MICROCOPY RESOLUTION TEST CHART

NATIONAL BUREAU OF STANDARDS-1963-A

AD-A160 773

REPORT DOCUMENTATION PAGE		READ INSTRUCTIONS BEFORE COMPLETING FORM
1. REPORT NUMBER AFIT/CI/NR 85-108D	2 GOVT ACCESSION NO	3 RECIPIENT'S CATALOG NUMBER
4. TITLE (and Subtitle) Axial Compressor Reversed Flow Performance		5 TYPE OF REPORT & PERIOD COVERED THESIS/DISSERTATION
		6 PERFORMING ORG. REPORT NUMBER
7. AUTHOR(s) Robert Normand Gamache		8 CONTRACT OR GRANT NUMBER(s)
9. PERFORMING ORGANIZATION NAME AND ADDRESS AFIT STUDENT AT: Massachusetts Institute of Technology		10. PROGRAM ELEMENT PROJECT, TASK AREA & WORK UNIT NUMBERS
11. CONTROLLING OFFICE NAME AND ADDRESS AFIT/NR WPAFB OH 45433 - 6583		12. REPORT DATE May 1985
		13. NUMBER OF PAGES 428
14. MONITORING AGENCY NAME & ADDRESS(if different from Controlling Office)		15. SECURITY CLASS. (of this report) UNCLASS
		15a. DECLASSIFICATION/DOWNGRADING SCHEDULE

16. DISTRIBUTION STATEMENT (of this Report)

APPROVED FOR PUBLIC RELEASE; DISTRIBUTION UNLIMITED

DTIC
ELECTE
OCT 3 1 1985
B

17. DISTRIBUTION STATEMENT (of the abstract entered in Block 20, if different from Report)

18. SUPPLEMENTARY NOTES

APPROVED FOR PUBLIC RELEASE: IAW AFR 190-1

LYNN E. WOLAVER
Dean for Research and
Professional Development
AFIT, Wright-Patterson AFB

19. KEY WORDS (Continue on reverse side if necessary and identify by block number)

20. ABSTRACT (Continue on reverse side if necessary and identify by block number)

ATTACHED

AFIT RESEARCH ASSESSMENT

The purpose of this questionnaire is to ascertain the value and/or contribution of research accomplished by students or faculty of the Air Force Institute of Technology (AU). It would be greatly appreciated if you would complete the following questionnaire and return it to:

AFIT/NR
Wright-Patterson AFB OH 45433

RESEARCH TITLE: <u>Axial Compressor Reversed Flow Performance</u>

AUTHOR: <u>Robert Normand Gamache</u>

RESEARCH ASSESSMENT QUESTIONS:

1. Did this research contribute to a current Air Force project?

( ) a. YES   ( ) b. NO

2. Do you believe this research topic is significant enough that it would have been researched (or contracted) by your organization or another agency if AFIT had not?

( ) a. YES   ( ) b. NO

3. The benefits of AFIT research can often be expressed by the equivalent value that your agency achieved/received by virtue of AFIT performing the research. Can you estimate what this research would have cost if it had been accomplished under contract or if it had been done in-house in terms of manpower and/or dollars?

( ) a. MAN-YEARS _____   ( ) b. $_____

4. Often it is not possible to attach equivalent dollar values to research, although the results of the research may, in fact, be important. Whether or not you were able to establish an equivalent value for this research (3. above), what is your estimate of its significance?

( ) a. HIGHLY   ( ) b. SIGNIFICANT   ( ) c. SLIGHTLY   ( ) d. OF NO
         SIGNIFICANT   SIGNIFICANT   SIGNIFICANCE

5. AFIT welcomes any further comments you may have on the above questions, or any additional details concerning the current application, future potential, or other value of this research. Please use the bottom part of this questionnaire for your statement(s).

NAME   GRADE   POSITION

ORGANIZATION   LOCATION

STATEMENT(s):

AXIAL COMPRESSOR
REVERSED FLOW PERFORMANCE

by

Robert Normand Gamache

B.S., University of Notre Dame (1977)
M.S., Air Force Institute of Technology (1978)

SUBMITTED IN PARTIAL FULFILLMENT
OF THE REQUIREMENTS FOR THE
DEGREE OF
DOCTOR OF PHILOSOPHY

at the
MASSACHUSETTS INSTITUTE OF TECHNOLOGY

May 1985

© Massachusetts Institute of Technology

Signature of Author _____
Department of Aeronautics
and Astronautics
1985

Certified by _____
Edward M. Greitzer
Thesis Supervisor
Professor of Aeronautics and Astronautics

Certified by _____
Eugene E. Covert
Professor of Aeronautics and Astronautics

Certified by _____
Jack L. Kerrebrock
Maclaurin Professor and Department Head
of Aeronautics and Astronautics

Accepted by _____
Prof. Harold Y. Wachman
Chairman, Department Graduate Committee

AXIAL COMPRESSOR
REVERSED FLOW PERFORMANCE

by

ROBERT NORMAND GAMACHE

Submitted to the Department of
Aeronautics and Astronautics
on May 7, 1985 in partial fulfillment of the
requirements for the Degree of
Doctor of Philosophy

ABSTRACT

The results of an analytical study of compression system forced response and an experimental investigation of the reversed flow performance of a three-stage axial-flow compressor are presented.

A one-dimensional lumped parameter description of the dynamics of a simple compression system was found to be capable of simulating the circumstances under which the imposition of a periodic external excitation can "force" a normally surging compression system into a small amplitude oscillation about the nonrecoverable stall point. This forced oscillation can then decay into a system stagnation upon termination of the external excitation. It was also found, however, that predictions of compression system forced response behavior were heavily dependent upon the model used for defining compressor post-stall performance, both steady state and transient, especially in the reverse flow and mass flow shutoff operating regimes.

The complete set of pressure rise and torque characteristics of a three-stage axial-flow compressor are presented. Two stable stalled flow modes have been observed in the multi-stage axial compressor builds tested: 1) rotating stall, and 2) full annulus stalled flow. The transition to each of the two stalled modes is accompanied by a discontinuous drop in overall time-averaged pressure rise and torque performance. Although a large hysteresis is associated with the unstall-rotating stall transition (which occurs at a relatively large positive flow coefficient), the transition from rotating stall to the annulus stall mode (which occurs at a negative flow coefficient near shutoff) has no hysteresis.

Detailed flowfield measurements at several reverse mass flow rates were obtained through the use of a synchronous event and rotor phase lock data acquisition triggering technique. Instantaneous traces of all three absolute velocity components as well as the total and static pressures at several representative axial, circumferential, and radial measuring positions have been included. An analysis of the experimental results indicates that a multi-lobed spinning pressure disturbance pattern exists at moderate and low reverse flow coefficients. The influence of the pressure disturbance pattern is most pronounced at the reverse flow coefficient which yields the overall pressure rise level corresponding to the level observed during operation in the rotating stall flow mode.

i

The detailed flowfield measurements also show that there is a significant radial redistribution of flow through the compressor. The existence of large radial velocity components and radial total and static pressure gradients have been documented. At low reversed flow coefficients, the formation of strong recirculatory flow patterns was observed. These three dimensional aspects of the flowfield tend to explain why previous two-dimensional cascade based theories have failed to correctly predict reversed flow performance in rotating turbomachinery. Finally, the strong similarities between the reverse flowfield structure measured and reported in the present work, with the rotating stall cell flowfield structure measured by others, provides support for the use of the basic parallel compressor concept for analyzing rotating stall.

Thesis Supervisor: Dr. Edward M. Greitzer
            Title: Professor of Aeronautics and Astronautics
                   and Director of the Plasma Dynamics and
                   Gas Turbine Laboratory

Accession
NTIS CRA&I
DTIC TAB
Unannounced
Justification

By
Distribution/
Availability Codes
Dist   Avail and/or
        Special
A-1

QUALITY
INSPECTED
5

ii

iii

TABLE OF CONTENTS

a = speed of sound (Chapters 1 and 2)

= fraction of compressor annulus admitting through-flow (Chapter 3)

a_0, a_1, a_2 = coefficients of second order curve fit of linearized anemometer signal

A = flow-through area

= constant in King's Law, defined in Equation 4-7 (Chapter 4)

A_B/A_C = blockage ratio (fraction of compressor annulus not admitting throughflow)

A_{RSC}/A_C = fraction of compressor annullus occupied by rotating stall cell

A_n = Fourier series coefficients

$b_0, ..., b_9$ = coefficients of slanted hot wire directional sensitivity curve fit

B = dimensionless number; defined in Equation 1-1

= constant in King's Law; defined in Equation 4-7 (Chapter 4)

c = speed of sound (Chapter 7)

c_p = specific heat capacity at constant pressure

c_0, c_1, c_2 = constants in correlation of case wall pressure drop across stationary bladerows

C = compressor pressure rise

= absolute velocity (Chapters 4 and 7)

C_x = absolute axial velocity component

---

* Symbols with more than one meaning are listed with general definition first. The alternate definition (along with the chapter where the secondary meaning is employed) is listed second.

C_θ, C_γ = absolute circumferential, tangential velocity component

C_r = absolute radial velocity component

C_0' = amplitude of upstream axial velocity fluctuations at axial station #9

$C1_{s.s.}$ = axisymmetric flow mode steady-state compressor pressure rise

$C2_{s.s.}$ = rotating stall flow mode steady-state compressor pressure rise

d_0, d_1, d_2 = constants in correlation of case wall static pressure drop across stationary bladerows

E = hot wire anemometer bridge output (volts)

E_ℓ = linearized hot wire anemometer bridge output (volts)

f = frequency (Hz)

F = throttle pressure drop

F' = partial derivative of throttle pressure drop with respect to throttle mass flow

g_r = gradient of body force in radial direction

G = body force

h = enthalpy

H_S, H_R = stationary, rotor bladerow case wall static pressure drop

K_{LE}, K_{TE} = leading edge, trailing edge blade angles

$K1$ = linearized component performance characteristic slope

$K2$ = linearized component performance characteristic y-intercept

L = effective length of equivalent duct

ℓ = blade chord length

$\vec{\ell}$ = unit vector along direction of slanted sensor element

x

$\dot{m}$ = mass flow

M = Mach Number

n = exponent constant in King's Law; defined in Equation 4-7
= Fourier series number (Chapter 7)

N = number of stages

$N_{R/S}$ = number of rotor revolutions elapsed before fully developed rotating stall condition is developed

N_σ = number of lobes in spinning pressure disturbance pattern

P = pressure

PR = compressor pressure ratio

P = plenum pressure rise, $(P_{plenum} - P_{ambient})$

P_{op} = orifice plate pressure drop

r = radius, radial direction

Re = Reynold's Number

r_m, R_m = compressor rotor mean radius

R_1, R_2 = electrical resistances in King's Law; defined in Equation 4-7

S = signal voltage (Chapter 4)
= pitchwise spacing (Chapter 3)
= entropy (Chapter 7)

t = time

t_{RSC} = rotating stall cell time duration (oscilloscope trace)

T = temperature

T_1 = hot wire sensor operating temperature in King's Law; defined in Equation 4-7

T_s = point in compression system dynamic simulation when external forcing function is introduced

T_{RSC} = rotating stall cell cycle period (oscilloscope trace)

$T_{R/S}$ = period of time elapsed before fully developed rotating stall condition is developed

ΔT = temperature difference (Chapter 7)
= elapsed time (Chapter 2)

T_∞ = large (infinite) time duration

U = mean rotor velocity

U_{RSC} = rotating stall cell propagation speed

U_σ = spinning pressure disturbance propagation speed

V = velocity

V_p = plenum volume

W = relative velocity

W_e = effective cooling velocity (scalar)

W_x, W_y, W_z = sensor based relative velocity components

X = axial direction

X_f = forcing function amplitude

α = absolute flow angle
= discharge coefficient (Chapter 4 and Appendix A)

α_o = initial sensor orientation angle

$\Delta\alpha$ = sensor turning angle increment (Chapter 4)

β = relative flow angle

β_s = blade stagger angle (Bammert and Zehner [35])

γ = specific heat ratio
= blade stagger angle (Chapter 3)

ϵ = streamtube radial offset from meanline radius

ζ = loss coefficient

θ = circumferential direction

θ_o = inclination angle of slanted hot wire sensor

θ_Y = yaw angle with respect to hot wire sensor

θ_P = pitch angle with respect to hot wire sensor

K = orifice plate calibraiton coefficient

μ = blockage ratio (fraction of compressor annulus not admitting throughflow)
= dynamic viscosity (Appendix A)

ν = kinematic viscosity

ρ = density

σ = angular propagation speed
= standard deviation (Chapter 4)

τ = torque
= time constant (Chapter 2)

ψ = pressure rise coefficient

ψ_τ = torque coefficient

ψ_θ = temperature coefficient

ω = frequency (radian)

ω_F = external forcing function periodic frequency

ω_H = Helmholtz resonator frequency; defined on p.13

ϕ = flow coefficient

ϕ_F = forcing function phase angle

ϕ' = velocity perturbation potential

Ω = rotor angular speed

Subscripts

C = compressor

duct = facility ducting (36" Dia.)

EA = ensemble average

F = external forcing function

0 = stagnation condition

op = orifice plate

r = radial

RSC = rotating stall cell

s.s. = steady state

S-S = static-to-static

t = total condition

T = throttle

T-S = total-to-static

T-T = total-to-total

UNS = unstalled

X = axial

Y = tangential
= yaw angle (Chapter 4)

η = random noise

θ = circumferential
= temperature (Chapter 5)

σ = multilobe disturbance pattern

τ = torque

ω = frequency

$*$ = design point

$\bullet$ = empirical term (Bammert and Zehner [35])

Superscripts

$\sim$ = non-dimensional variable

$\rightarrow$ = vector quantity

$\prime$ = fluctuating quantity

$\overline{}A_\theta$ = circumferential area average

TABLE LIST

Chapter 1

INTRODUCTION

During the development of gas turbine engines for aircraft propulsion applications in the 1940's and early 1950's, the phenomena of surge and rotating stall were observed to be the two modes of compression system response to an excursion past the stall limit of the compressor [1,2][1]. In 1955, Emmons, Pearson and Grant [3] distinguished between these distinct types of stall behavior by describing surge as a global compression system instability similar in manner to a "self-excited Helmholtz resonator," and by describing rotating stall as a localized compressor phenomenon in which one or more stall cells propagate around the compressor annulus at a constant rotational speed.

In aircraft engine applications, the desire to sustain a minimal level of efficient engine operation is the reason why most relevant surveys of post stall compression system behavior attempt to clearly identify those types of compressor stall that are "recoverable" and those which are not. Nonrecoverable stalls, sometimes called "hung stalls" or "engine stagnations," require complete engine shutdown and restart to recover from the stagnation condition. Because of this, surge has generally become the desired initial mode of compression system response to an excursion past the stall limit of the compressor. Surge stalls are considered to be "recoverable" because the compressor operates on its unstalled performance characteristic during a portion of the surge cycle. As a result, unstalled operation at the

---

[1]Numbers in brackets refer to the bibliography listing in the Reference Section of this thesis.

1

design point can often be reestablished sometimes automatically by the system, or by opening compressor bleed ports, or by taking other similar corrective measures to terminate the surge cycle in this operating regime.

On the other hand, fully developed rotating stall can be nonrecoverable in any practical gas turbine engine design. The occurance of steady state rotating stall is sometimes called an "engine stagnation" because the overall compression system (i.e. the gas turbine engine) responds to the localized rotating stall event in the compressor by establishing a new, stalled ("stagnated"), equilibrium operating condition at a lower rotational speed and with substantially reduced mass flow and pressure rise across the compressor. Since this new equilibrium point is almost always beyond the influence of any active engine control parameters (e.g. fuel and throttle controls), an engine stagnation is not recoverable. Prolonged operation at this new equilibrium condition can have severe consequences for both the integrity of the engine and the aircraft because the reduced mass flow and compressor pressure rise will result in sharply increased compressor and turbine metal temperatures as well as drastically reduced propulsive efficiency and thrust.

It was soon realized in the early 1950's by Huppert and Benser [1] and Pearson [4] in the United States, and Smith and Fletcher [2] in Great Britain, that an increase in the wheel speed of the compressor rotor and/or an increase in the combustor volume tended to promote the (more favorable) surge mode of compression system response rather than a rotating stall induced stagnation. Greitzer [5] in 1976 quantified these previously identified qualitative trends when he defined a dimensionless "B parameter" for compression systems as follows:

$$B = \frac{U}{2a} \sqrt{\frac{V_P}{A_c L_c}} \qquad (1-1)$$

2

where U is the mean wheel speed, 2_a is twice the characteristic speed of sound of the medium in the compressor, V_p is the volume of the combustor or exit plenum, A_c is the flowthrough area of the compressor, and L_c is the equivalent length of the compressor ducting.

According to the analytical and experimental evidence presented by Greitzer in [5,6], there is a critical value of the B parameter for each compression system. For compression systems with a value of B above their critical value, B_{crit}, the system will surge upon an excursion past the stall limit of the compressor. At B values below this critical value, the system will encounter equilibrium rotating stall at the operating point defined by the intersection of the throttle and the rotating stall characteristics.

Although Greitzer's "B parameter" first appeared in 1976, there was some qualitative empirical evidence during the 1950's and 1960's to suggest that nonrecoverable stagnation stall could be avoided by providing enough volume in the compressor and/or increasing the wheel speed and/or decreasing the flowthrough area and/or length of the compressor. Although it was not fully appreciated within the aircraft gas turbine industry, incorporation of these trends in the design process tended to insure that engines would surge following an excursion past the compressor's stall 'imit. Indeed, the compressor stall limit on a compressor map of pressure ratio vs. corrected weight flow became known as the "surge line".

By the mid-1970's, it became apparent that the development and deployment of high thrust-to-weight ratio afterburning turbofan engines had caused the stagnation stall phenomenon to appear with increased incidence. For instance, the operational stagnation rate of Pratt & Whitney's production lot IV F100 augmented turbofans had reached 12 stagnations

3

per 1000 engine flight hours (EFH) in early 1976 [7]. Although this incidence rate had leveled out to 2 stagnations/1000 EFH by 1978, a better statistical measure of the true magnitude or the technical gravity of the stagnation problem is the ratio of the number of nonrecoverable stagnations versus the number of stalls encountered.[2] Ground and flight tests revealed that the standard configuration F100 engines were experiencing a 44.9% stagnation stall rate, i.e. 178 stagnations occured in 396 stalls [7].

Ducted afterburning turbofans, as opposed to augmented turbojets, provide an inherent opportunity for direct communication between the afterburner and the front of the compressor via the fan bypass duct. According to Davis and Mazzawy [8], an initial large positive pressure pulse (pressurization) followed by many smaller negative pressure pulses (depressurizations) travelling up the fan duct (in a subsonic medium) were responsible for forcing the F100 compressor into a rotating stall condition and the engine into a subsequent stagnation. In most of the F100 engine stagnations, these external[3] pressure excitations induced a nonrecoverable stall while the engine was operating at full power in a speed regime where the engine should normally surge. Many of these "forced stagnations" typically occured after the engine had partially completed the first or second surge cycle immediately following the initial excursion across the compressor's stall limit. This outcome cannot be predicted by the critical B parameter criterion alone.

The incidence of stagnations per stall encounters was significantly reduced in the F100 engine by implementing several modifications designed to reduce the communication of events

---

[2]The number of engine stagnations per 1000 engine flight hours can be artificially reduced by restricting the operational flight envelope in order to encounter fewer total compressor stalls. Fewer total compressor stall encounters directly reduces the number of opportunities for engine stagnations to occur. Hence, a decrease in this statistical measure may merely reflect a loss in useful flight envelope rather than a technical or fundamental solution of the stagnation stall problem.

[3]"External" in this context means external to the compressor.

in the afterburner with the conditions at the compressor face. The forward extension of the splitter towards the compressor inlet has been a particularly effective design change in this regard. This was termed a proximate splitter. It and other "design fixes" have drastically reduced the severity of the F100 engine stagnation stall problem (with a slight loss in engine performance), these design solutions were based upon qualitative considerations of the need to isolate the compressor from an afterburner induced external forcing function rather than a complete quantitative understanding of post stall axial compressor fluid mechanics.

It is desirable to avoid this type of forced stagnation stall before production and deployment of an engine begins, and an important goal, therefore is to develop design criteria for rotating stall resistant compressors. There appear to be two conceptual strategies which one may pursue to accomplish this goal. First, one may be able to eliminate the existance of the stalled equilibrium operating point by designing the compressor in such a manner that the steady state rotating stall characteristic does not intersect the throttle characteristic. The second strategy is to design the compressor in a manner which causes the transient stalled performance of the compressor to dynamically drive the compression system away from the stalled equilibrium operating point (under all anticipated external forcing function conditions) before an engine stagnation can develop.

The pursuit of either strategy requires the development of a compressor performance prediction model that captures the relevant fluid mechanics and physics associated with the two- and three-dimensional flowfields which exist in stalled compressors. Adoption of the first strategy will require a compressor model that predicts the final steady state rotating stall performance of a compressor as a function of the free design parameters. The second strategy will require a post stall compressor model that is capable of predicting the transient as well as steady state stalled performance of a compressor. This latter transient compressor performance prediction model must be incorporated in an overall dynamic compression system

5

model to predict whether or not a particular compression system configuration will stagnate under a given set of external forcing function conditions (including the nul or free response case)

To the best of the author's knowledge, the first systematic study (at least in the open literature) directed towards the forced response of compression systems was undertaken by the author in 1982. This is reported in Chapter 2. The impetus for this analytical investigation stemmed from a view that the second stall resistant strategy, i.e. dynamically avoiding the stalled equilibrium operating point, may be more practical to implement than attempting to eliminate the stalled equilibrium point altogether. One of the results that emerged from this preliminary forced response study is that there are only two "locations" in a surge limit cycle where the imposition of a reasonable strength external pressure excitation can interrupt the surge cycle and then drive the compression system to the nonrecoverable stall point 1) near the stall onset of the compressor (at the "surge line") and 2) near the bottom of the reversed flow characteristic at zero mass flow. This result is consistent with the trends observed with respect to F100 engine stagnation stalls.

In addition, a sensitivity analysis revealed that the predicted response of the compression system can be *drastically* altered by slightly changing the location and shape of the compressor's stall characteristic in the neighborhood of the shutoff flow coefficient. Unfortunately, not much was known about the performance of multistage axial flow compressors immediately prior to the stall recovery portion of a surge cycle. In the past, the study of this type of axial compressor performance was neglected due to lack of a pressing need and because the flowfields are sufficiently complex that the then existing data acquisition technology and instrumentation techniques were inadequate for the task at hand. It was these factors that provided the initial motivation to investigate the reversed and zero mass flow performance of axial compressors.

6

In recent years, the development of "axisymmetric characteristic" based models of rotating stall flowfields by Moore [9] and Moore and Greitzer [10, 11] have also increased the interest in exploring the reversed flow performance of axial compressors. These models like the "parallel compressor" model proposed by Gray (and reported by Day [12]), assume that the stalled backflow portion of a compressor operating in rotating stall has a flowfield structure which is identical to the case where the entire compressor annulus is subjected to reverse flow. Hence, the performance defined by a compressor's reverse flow characteristic is taken to be the performance of the stalled backflow portion of the compressor when it is operating with rotating stall. The time-averaged, reversed flow, axial pressure and temperature profiles presented in this thesis tend to support this concept.

In the thesis, a complete set of overall compressor performance characteristics are presented. These characteristics reveal that a steady state rotating stall flow mode can be maintained while the compressor is operating at a negative average axial flow coefficient. In addition to the flow mode change which occurs at the stall limit of the compressor, the time-averaged data indicates that another flow mode change occurs in the neighborhood of the zero mass flow point. This flow mode change from a single, full span, rotating stall cell occupying about 90% of the annulus to a highly complex, but organized, annulus stalled flow pattern is accompanied by a sharp reduction in pressure rise and an off-loading of torque absorption by the compressor. Unlike the stall-unstall flow mode change which occurs at higher positive flow coefficients, no significant amount of hysteresis is associated with this flow mode change. From a stall recovery standpoint, the existence of a discontinuous rise in performance from the reverse flow characteristic to the rotating stall characteristic tends to promote an initial acceleration of the fluid in the compressor ducting towards stall recovery during a surge limit cycle.

Detailed high response flowfield measurements of the reversed flow pattern were made

7

using a double phase lock triggering technique to synchronize the two sources of unsteadiness which exist in the flowfield under investigation. Three dimensional measurements of the velocity field were made using a slanted hot wire sensor, rotated to three different orientations to obtain the three components of the instantaneous, periodically unsteady, velocity vector. The results obtained during this investigation are, to the author's knowledge the first measurements of this kind. An analysis of these results indicates that the reverse flowfield in modern, multistage, axial compressors is dominated by radial flows which produce a highly organized, non-uniform flow pattern. Based upon these findings, a descriptive kinematic model of the reverse flowfield is proposed.

The format of this thesis is as follows. In Chapter 2, the results of a compression system forced response study are presented. The results from this analytical study provided the primary motivation for the experimental investigation of axial compressor reversed flows. Although there is little published literature which specifically addresses reversed flow and performance near shutoff in multistage axial flow compressors, a number of related articles on the performance of other varieties of turbomachines operated under abnormal and reversed flow conditions have been published, and the most relevant of these are included in the literature review that appears in Chapter 3. The experimental facility, data acquisition system, instrumentation, and experimental techniques employed during the course of the investigation are fully described in Chapter 4. The time-averaged results are presented in Chapter 5. High response measurements of the detailed flowfield structure appear in Chapter 6. Chapter 7 contains an analysis of the flowfield data and presents a model of the reverse flowfield. The final summary of the conclusions drawn from this thesis effort as well as recommendations for further research appear in Chapter 8.

Chapter 2

COMPRESSION SYSTEM DYNAMICS

As a way of introducing or motivating the research effort, this chapter describes an initial study on the forced response of compression systems. It will be shown that the forced response behavior of simple compression systems is heavily dependent upon the reverse flow and shutoff performance of the compressor. In particular, a "forced stagnation event" can be simulated under certain conditions. However, only slight modifications of the compressor's low reverse flow performance characteristic can preclude this predicted outcome under an otherwise identical set of circumstances.

The primary objective of this preliminary forced response investigation was to evaluate the suitability of present analytical methods to deal with the problem of forced nonrecoverable stall. In other words, what we wished to determine was the set of circumstances under which the imposition of an external forcing function could force a normally surging compression system into a nonrecoverable stall, i.e. analytically reproduce the F100 engine stagnation scenario described qualitatively by Davis and Mazzawy in [8]. Another important objective was to explore the "robustness" of the results, i.e. to explore the sensitivity of the predicted compression system response to small changes in the scheme used to define the compression system dynamics and the transient post-stall performance of the compressor.

The implication associated with the tradeoff of these two competing objectives has paramount importance. There is not much to be gained by expending considerable effort to refine compression system dynamic models or devising more elaborate transient compressor performance prediction schemes if the (known unfavorable) event one wishes to avoid can be

9

predicted for almost any reasonable definition of a compression system and/or compressor performance model. On the other hand, one must be concerned with the methodology used to generate the model if the results are not "robust". As will be seen below, a basic conclusion from the study was that overall compression system forced response results are heavily dependent upon the assumptions made with regard to the reverse and zero flow operating regime performance of the compressor.

The subsequent sections of this chapter can be conceptually divided into a description of the methodology used to generate compression system dynamic simulations and a discussion of the simulation results. The overall compression system dynamic model and compressor performance prediction scheme appears in the next two sections. The latter two sections are concerned with presenting the free and forced response simulation results as well as providing an analysis of the observed trends.

2.1 COMPRESSION SYSTEM DYNAMIC MODEL

A lumped parameter dynamic model of the simple compressor-plenum-throttle compression system depicted in Figure 1 was used during this investigation. The equations of motion which govern the dynamic response of this simplified compression system were derived by applying the appropriate fluid conservation principle for each component in the system. In addition, these equations can be greatly simplified by considering the case of an incompressible fluid. This approach for modeling simple compression system dynamics is not new and has been well documented in the technical literature by Greitzer [5].

Greitzer used the following dimensional form of the equations of motion:

$$C - \Delta P = \frac{L_c}{A_c} \frac{d \dot{m}_c}{dt} \qquad (2-1)$$

10

$$\Delta P - F = \frac{L_T}{A_T} \frac{d\dot{m}_T}{dt} \qquad (2\text{-}2)$$

$$\dot{m}_c - \dot{m}_T = \frac{\rho V_P}{\gamma P} \frac{dP_P}{dt} \qquad (2\text{-}3)$$

Equations (2-1) and (2-2) are momentum balances that describe the flow in the compressor and throttle ducts respectively. The left hand side (LHS) of these equations represent the driving pressure differential which causes an acceleration of the fluid mass in the associated ducting. In both equations, ΔP represents the pressure difference between the plenum pressure and the pressure at ambient conditions. C and F represent the one-dimensional characteristic performance of the compressor and throttle components of the simplified compression system. If the flow in the associated ducting is uniformly axisymmetric, C and F are the respective pressure rise or drop (depending upon one's frame of reference) attributed to the operation of either component. If the flow is not axisymmetric, as is the case in rotating stall, then any changes in momentum across the associated component duct must be "lumped" into these terms. When the pressure rise or drop across either component's ducting, ΔP, is equal to the pressure rise or drop caused by the operation of that component, C or F; then the LHS[4] of Equations (2-1) and (2-2) are identically zero. As a result, there are no overall one-dimensional fluid accelerations or decelerations in either set of ducting and the system is said to be operating at a steady-state operating condition.

---

[4] LHS and RHS will be used throughout the remainder of this thesis to denote left and right hand sides of an equation respectively.

Equation (2-3) is derived from the mass conservation principle applied to the plenum volume. The form of this equation implies the use of several reasonable assumptions. First, the static pressure in the plenum is uniform throughout the volume at all times. Second, the process in the plenum volume is isentropic [5]. Third, for this incompressible fluid flow case, the ratio of density to pressure in the plenum is not appreciably different from that at ambient conditions.

If the system is operating at a steady state point, the mass flow rate into the volume through the compressor, $\dot{m}_c$, equals the mass flow rate out of the volume through the throttle, $\dot{m}_t$. In this case, the LHS of Equation (2-3) vanishes and the pressure in the plenum volume remains constant with time.

Since throttle ducting lengths are usually small, the amount of mass or fluid inertance in the throttle ducting is also small. Hence, if one assumes the throttle responds quasi-steadily to the changes in mass flow through the nozzle, then the performance of the throttle, F, is always nearly equal to the difference in the plenum and ambient pressures, ΔP. As a result, Equation (2-2) can now be eliminated from the set of dynamic equations, and the throttle performance characteristic can be expressed in terms of throttle mass flow by the following parabolic representation:

$$F = \frac{\dot{m}_T^2}{2\rho A_T^2} \qquad (2-4)$$

where A_t is the throttle flowthrough area at the discharge plane.

It is useful to non-dimensionalize these equations. One way to do this is to non-dimensionalize mass flows using the reference quantity $\rho U A_c$, pressure variables using

12

the blade dynamic head $1/2 \rho U^2$, and time with the Helmholtz Resonator Frequency for the compressor cavity, $\omega_H = a\sqrt{A_c/V_p L_c}$. Hence, the non-dimensional form of the basic compression system dynamic model becomes:

$$\frac{d\tilde{m}_c}{d\tilde{t}} = B(\tilde{C} - \Delta\tilde{P}) \qquad (2-5)$$

$$\frac{d\tilde{m}_T}{d\tilde{t}} = \frac{1}{B\tilde{F}'}(\tilde{m}_c - \tilde{m}_T) \qquad (2-6)$$

where the symbol ($\sim$) denotes dimensionless variables. The non-dimensional plenum pressure differential, $\Delta\tilde{P}$, and the derivative of throttle characteristic with respect to throttle mass flow are given by:

$$\Delta\tilde{P} = \tilde{F} = \left(\frac{A_c}{A_T}\right)^2 \tilde{m}_T^2 \qquad (2-7)$$

$$\tilde{F}' = 2\left(\frac{A_c}{A_T}\right)^2 \tilde{m}_T \qquad (2-8)$$

During the forced response investigation, a sinusoidal time dependent term was added to the RHS of Equation (2-5) in order to model the presence of an external pressure excitation. The addition of such a forcing function term to Equation (2-5) produces the following:

$$\frac{d\tilde{m}_c}{d\tilde{t}} = B\left[\tilde{C} - \Delta\tilde{P} + \delta\tilde{X}_F \sin\tilde{\omega}_F(\tilde{t} - \tilde{T}_s)\right] \qquad (2-9)$$

13

where;

$$\delta = \begin{array}{ll} 0 & \tilde{t} < \tilde{T}_s \\ 1 & \tilde{t} \geq \tilde{T}_s \end{array} \qquad (2\text{-}10)$$

and $\tilde{X}_f$ is the peak non-dimensional amplitude of the forcing function, $\tilde{\omega}_f$ is the non-dimensionalized forcing frequency, and $\tilde{T}_s$ is a non-dimensional time parameter which designates the point in the dynamic simulation when the external pressure excitation is introduced to the system.

Equations (2-6) and (2-9) are a set of first order, coupled, nonlinear ordinary differential equations which sufficiently describe the forced response dynamic behavior of the simple compression system illustrated in Figure 1. For a quasi-steady definition of compressor performance, $\tilde{C}$ is a function of compressor mass flow rate only. Typically, this functional relationship is highly nonlinear. This feature of the problem is the reason why dynamic simulations of even the simple compression system defined herein exhibit non-linear behavior. In addition, the problem becomes more complex when a non-quasi-steady formulation of compressor performance is employed.

To determine the forced response of the compression system, Equations (2-6) and (2-9) were solved numerically as an initial value problem. A time marching computer program using Hamming's Predictor-Corrector method for evaluating simultaneous sets of ordinary differential equations was written to accomplish this. A fourth order Runge Kutta scheme is used to "start" the more efficient predictor-corrector. A full discussion of the program's overall architecture and a logic flow are presented in [70].

14

2.2 COMPRESSOR PERFORMANCE PREDICTION METHODOLOGY

The most ellusive, yet most crucial, element of any compression system dynamic simulation scheme is the model which defines the quasi one-dimensional performance of the compressor, $\tilde{C}$. This model must capture the relevant two- and three-dimensional flowfield physics which exist in stalled and unstalled compressors. Whether the flowfield is computed in fine detail or broadly simulated, the one-dimensional performance prediction output of the model should be valid for every operating regime encountered by the compressor during any possible transient event.

2.2.1. Previous Lumped Parameter Prediction Schemes

In the past, compression system dynamic studies were conducted using the typical set of quasi-steady, non-linear compressor characteristics shown in Figure 2 (see Greitzer [5] and Wenzel and Bruton [13]). The characteristic curve depicted in Figure 2 has four component sections. First, there is the familiar negatively sloped unstalled compressor characteristic. Second, there is a relatively flat rotating stall curve. This curve represents the locus of steady state rotating stall equilibrium operating points when the throttle is positioned at these flow coefficient settings. Third, there are two positively sloped transition curves which join the rotating stall curve to the unstalled characteristic. The existence of two transition curves is indicative of a significant amount of stall-unstall hysteresis. Finally, there is another strongly negative sloped reversed flow characteristic which smoothly joins the rotating stall characteristic at zero mass flow.

This typical definition of a complete map of steady-state axial compressor characteristics was incorporated in these overall compression system dynamic models by setting these steady-state characteristics equal to the instantaneous value of the transient compressor

performance characteristic, i.e. $\tilde{c} = \tilde{c}_{s.s.}$, as a function of instantaneous mass flow rate, $\tilde{\dot{m}}_c$. In some simulations [5], a first order lag model is used to relate the transient and steady-state compressor performance as follows:

$$\tau \frac{d\tilde{c}}{d\tilde{t}} = (\tilde{c}_{ss} - \tilde{c}) \qquad (2-11)$$

In the hysteresis stall-unstall flow regime where the steady-state performance characteristic is double valued with respect to compressor mass flow rate, the appropriate characteristic was chosen based upon the prior history of the transient trajectory. If the compressor was in the process of stalling, the curve marked "stall" in Figure 2 would be used. Otherwise, the curve marked "recovery" would be employed.

Three modes of compression system free response non-equilibrium behavior have been predicted by dynamic simulations which incorporate this type of compressor performance model. Figures 3a, b and c qualitatively illustrate each of the three observed free response behavior trends. In this context, the term "free response" refers to the subsequent compression system dynamic behavior resulting from an initial destabilizing perturbation (rather than from the continuous imposition of an external forcing function). Figure 3a illustrates a typical surge limit cycle. This type of non-equilibrium free response behavior occurs when the value of the system B parameter is larger than the critical system value, $B > B_c$.

On the other hand, Figure 3b portrays the behavior associated with a system whose B value is slightly below the critical system value, $B < B_c$. One should carefully note that

this simulation predicts that the system initially establishes the first portion of a surge limit cycle. The implicit flowfield assumption inherent to this simulation is that "axisymmetric stalled" flow is established during the quasi-steady reverse flow or "plenum blowdown" phase of this eventual stagnation simulation. After the plenum blowdown phase is complete, the flowfield develops rotating stall cells (non-axisymmetric flow) *without* developing a sufficient pressure differential to drive the system to recovery. Instead, the system spirals into nonrecoverable stall. The new stable operating point is defined by the intersection of the throttle characteristic and the steady state rotating stall characteristic. This particular free response mode has not been generally observed in post stall tests of multistage axial flow compressors.

If the system B value is lowered significantly below the critical B value, i.e. $B \ll B_c$, then the behavior shown in Figure 3c is predicted. In this case, the flowfield implication is that stalled axisymmetric flow never exists. The compressor develops non-axisymmetric rotating stall directly after the initial departure from the unstalled operating regime. In turn, the compression system is predicted to stagnate.

The foregoing discussion presents a brief summary of the general behavior predicted by compression system dynamic response models which incorporate the compressor model illustrated in Figure 2. It should be recognized that if the pressure difference between the stall point on the unstalled characteristic and the pressure level of the rotating stall characteristic is not as great (as is the case with most radial flow machines and many single stage axial flow fans), then the stagnation behavior depicted in Figure 3b generally does not materialize during analytic simulations. Instead, the system critical B value determines whether a system will exhibit the surge behavior shown in Figure 3a or the stagnation behavior shown in Figure 3c.

17

2.2.2. Axisymmetric Stalled Performance Characteristic

The concept of axisymmetric stalled compressor performance was given much of its impetus by Moore [9] when he defined a "compressor pressure-rise coefficient in the absence of rotating stall." Moore suggested that this non-rotating stall pressure rise coefficient, ψ_c, is single valued with respect to mass flow and incorporates the reverse flow and unstalled performance characteristics illustrated in Figure 2. Koff [14] and Koff and Greitzer [15] proposed that this non-rotating stall pressure rise coefficient is actually an "axisymmetric stalled performance characteristic." References [14] and [15] describe a proposal for constructing the unstable portion of the curve, i.e. the low forward flow regime between reversed and unstalled flow, based on experimental surge data and using the momentum balance represented by Equation (2-1).

This axisymmetric characteristic is actually similar to the compressor surge characteristic set forth six years earlier by Horvath in his Doctoral Thesis at the Swiss Federal Institute of Technology in 1976 [16]. Gyarmathy [17] describes the shape of Horvath's compressor characteristic as "a third degree parabola, symmetric around [a central] saddle point."

Figure 4 presents a qualitative sketch of a proposed multistage axial compressor axisymmetric characteristic. This curve is composed of the unstalled characteristic, a reverse flow characteristic, and an unsteady low forward flow characteristic. The first two portions of the curve can be experimentally measured, while the unstable portion of the curve can not be measured because of its inherent nature.

The implication associated with the existence of an axisymmetric characteristic is that the standard practice of using the Figure 2 type characteristic in the manner just described in Section 2.2.1 may *not* be a valid method to employ in compression system dynamic response simulations. Specifically, if surge is essentially an axisymmetric flowfield

18

phenomenon, one would not expect to be able to use a steady-state non-axisymmetric rotating stall curve to model compressor performance during the highly transient portions of a surge cycle.

2.2.3 Basic Compressor Performance Prediction Scheme

The baseline set of quasi-steady compressor characteristics are depicted in Figure 5. These characteristics were chosen to be representative of the high performance, multi-stage axial compressors found in modern ducted turbofan engines. Because of the uncertainty associated with these characteristics, several variants of these baseline shapes were examined in this study (Section 2.4.4).

Given these quasi-steady characteristics, however, it still remains to develop an implementation scheme for defining the transient compressor characteristic at each instant in time and for all possible mass flow regimes. This scheme must be valid especially during the highly transient portions of the surge cycle when the flow through the compressor transitions from an initial axisymmetric flow mode to a certain amount of non-axisymmetric flow caused by the growth of rotating stall cells. In the case where the system "falls" into an equilibrium stagnation condition, the model must provide a method for "evolving" from the unstable stalled portion of the axisymmetric curve to the measured steady state rotating stall characteristic.

2.2.3.1. Definition

A non-steady compressor model is proposed which would account for the formation and growth of non-axisymmetric stall cells during the surge transients of an axial compressor by defining a time-dependent transient compressor characteristic. This concept is implemented by "transitioning" from the unstable axisymmetric characteristic to the stable or equilibrium

19

rotating stall characteristic. During the unstalled and reversed flow operating regimes of post stall surge cycles, the transient compressor performance would contine to be defined by the appropriate quasi-steady performance characteristics. The motivation for treating the reversed and unstalled flow regimes in this manner stems from the fact that these flow regimes are traversed relatively slowly or quasi-steadily. An equilibrium rotating stall condition (corresponding to a system stagnation) will be predicted by this model only when enough time has elapsed during either apparent surge transient to permit a complete "collapse" of the transient performance characteristic onto the steady state rotating stall characteristic.

A very important aspect of this conceptual approach is the selection of the procedure for "transitioning" from the unstable axisymmetric stalled curve to the steady-state rotating stall curve. The physical mechanism that is modeled by the transition schedule is the formation and growth of rotating stall cells. For the purpose of this preliminary study, a linear time rate-of-transition was assumed. This schedule can be defined mathematically as follows:

$$\tilde{C}\left(\tilde{m}_c, \tilde{t}\right) = \tilde{C}_1\left(\tilde{m}_c\right) + \frac{\Delta\tilde{T}}{\tilde{T}_{R/s}}\left[\tilde{C}_2\left(\tilde{m}_c\right) - \tilde{C}_1\left(\tilde{m}_c\right)\right] \qquad (2\text{-}12)$$

where

$$\Delta\tilde{T} = \begin{array}{ll} 0 & \tilde{t} < \tilde{t}_i \\ \tilde{t} - \tilde{t}_i & \tilde{t}_i \le \tilde{t} \le \tilde{T}_{R/s} \\ \tilde{T}_{R/s} & \tilde{t} > \tilde{T}_{R/s} \end{array} \qquad (2\text{-}13)$$

and $\tilde{t}_i$ is the point in the simulation when the stall limit of the compressor is reached, $\tilde{T}_{R/s}$

20

is the nondimensional time required to form a *fully* developed rotating stall cell, $\widetilde{C}_1(\widetilde{\dot{m}}_c)$ is the nondimensional axisymmetric pressure rise performance at a given mass flow rate, while $\widetilde{C}_2(\widetilde{\dot{m}}_c)$ is the nondimensional rotating stall pressure rise performance at the same given mass flow rate.

Greitzer has presented data (e.g. [18]) on the formation time of a fully developed rotating stall condition; very *roughly* 5-10 rotor revolutions. This general rule-of-thumb was used to specify the total duration of the transient performance curve during the transition from the axisymmetric to the rotating stall states. The non-dimensional rotating stall formation time, $\widetilde{T}_{R/S}$, is thus:

$$\widetilde{T}_{R_{/S}} \approx N_{R_{/S}} \left(60 / RPM \right) \omega_H \tag{2-14}$$

where $N_{R/S}$ is the number of rotor revolutions required to form a fully developed rotating stall cell, and ω_H is the Helmholtz resonator frequency defined in Section 2.1.

2.2.3.2. Transient Characteristic Implementation

It is important to emphasize that the dynamics of the system govern which operating conditions the compressor encounters, and hence, the mode of stall that will occur. The compressor model which makes no apriori decisions about which type of response mode will occur for a given set of system conditions. Perhaps the best way to explain the implementation of the compressor model is to review how it defines a transient characteristic for the standard surge or stagnation system response modes illustrated in Figures 3a and 3c respectively. In either case, we will assume that our hypothetical compression system is

21

initially operating at the unstalled design point of our example compressor as shown in Figure 6a. The system is then driven off the design point by an inlet flow perturbation which causes the plenum pressure to rise (and thus the compressor mass flow rate to decrease). In a ducted turbofan configuration, an afterburner hardlight or fan stall could cause this type of flow perturbation. Eventually, the stall limit of the compressor is encountered. This quasi-steady traverse up the unstalled characteristic is illustrated in Figure 6b. Since this portion of the transient was essentially quasi-steady, the compressor model defines the transient performance characteristic equal as the measured steady state unstalled characteristic.

Once the compressor departs from the stall point, it enters a highly transient, stalled, operating regime. The flow through the compressor in this regime is initially axisymmetric but is tending to transition to a non-axisymmetric condition as rotating stall cells begin to form and grow. To simulate the one-dimensional performance effect of this highly two- and probably three-dimensional unsteady sequence of events, Equations 2-12 and 2-13 are used to define an instantaneous transient compressor performance characteristic. The characteristic defined by these equations is a locus of points on a set of curves which evolve during the transition from the unstalled axisymmetric characteristic to the rotating stall characteristic at the linear rate prescribed by Eq. 2-14. This process is graphically portrayed in Figures 6c and 6d. The locus of left facing arrows in Figure 6c define the instantaneous transient performance of the compressor during this portion of a hypothetical surge cycle. Figure 6d depicts a higher resolution version of this transient characteristic without the clutter of superimposing the intermediate curves given by Equation 2-12.

The instantaneous transient performance curve illustrated in Figure 6d implies that the compressor has transitioned from unstalled flow to reverse flow before a fully developed rotating stall condition could be established. This observation is evidenced by the fact that the

22

instantaneous transient performance curve did not completely transition to the steady state
rotating stall characteristic; i.e.

$$\tilde{t} - \tilde{t}_i < \tilde{T}_{R_{/_s}} \qquad (2\text{-}15)$$

where $\tilde{t}_i$ is the non-dimensional time at which the stall limit of the compressor is first
encountered, and $\tilde{t} - \tilde{t}_i$ is the total elapsed time of the transient excursion to reverse flow.

If, however, the B parameter value of our hypothetical case were lowered; the fluid
deceleration in the compressor ducting would not have been as great, and it would have taken
more time to traverse the compressor map from the unstalled to the reverse flow
characteristic. For the case where the B parameter value of the system is below the critical
value, B_c, the inequality represented by Equation 2-15 would have reached an equality
condition. At this point, the compressor would operate on the steady state rotating stall
characteristic. As stated before at the beginning of this section, it should be pointed out that
the compressor model does not have apriori knowledge of the critical B parameter value. The
"decision" to terminate the transition schedule is governed by the relevant system dynamics
through the time scale criteria set forth in Equation 2-13.

For the case where $B > B_c$, the compressor encounters a third operating condition:
reversed flow over the complete circumference of the annulus. This condition is established
presumably when the lower mass flow limit of the steady state rotating stall curve is crossed.
In this operating regime, the plenum pressure is dissipated by a "blowdown" through both the
throttle and compressor. Since an axial compressor offers a significant amount of resistance
to reverse flow, there is a large drop in pressure rise for a relatively small change in
compressor mass flow rate and the overall system blows-down through the compressor in a

23

quasi-steady manner. Hence, the model sets the transient performance characteristic equal to the reversed flow characteristic.

After the blow-down transient, the overall system returns the compressor to operation at positive mass flow rates. The flow is initially axisymmetric at zero flow or shutoff, but tends to transition to a non-axisymmetric condition as rotating stall cells begin to form and grow during this recovery process. The same transition strategy is employed to define the transient performance characteristic of the compressor in this flow regime with Equations 2-12 and 2-13 used in the same way. The only modification is that the quantity, $\tilde{t}_i$, now refers to the point in the simulation when the low flow steady state rotating stall limit of the compressor is reached. It is assumed that this point is also the flow coefficient where the axisymmetric characteristic become unstable. Figures 6e and 6f portray such a recovery transition of a surge limit cycle.

Once the mass flow rate increases beyond the recovery point shown in Figures 6e-f (usually defined as the high mass flow limit of the steady state rotating stall characteristic), the rotating stall cell(s) begin to shrink or decay and the flowfield returns to an axisymmetric unstalled condition. The compressor model accounts for these actual physical processes by reversing the rate-of-transition of the characteristics.

2.3 FREE RESPONSE SIMULATION RESULTS

A compression system free response study was conducted to characterize the response of the baseline system. In particular, the critical value of the non-dimensional B parameter was determined. In addition, the qualitative transient compression system behavior predicted with the aid of the new unsteady compressor performance model seemed to generally agree with experimental observations of post stall compression system behavior.

24

2.3.1. B Parameter Critical Value

The critical value of the B parameter which divides the surge and stagnation response for the baseline set of quasi-steady compressor characteristics was found to be 0.1865. System simulations were performed for an initial coarse matrix of B parameter values which was then refined to bound the critical B parameter value. The system response trajectory illustrated in Figure 7b depicts a case of a compression system surge instability at a B parameter value of 0.187. The trajectory shown in Figure 7a illustrates the case where a system stagnation occurs at a B parameter value of 0.186.

The plotted points in these figures were generated at fixed time intervals (this practice was employed to generate the remaining system response trajectories shown throughout the remainder of this chapter). As a result, the relative spacing of the points in these figures can be interpreted as an indication of the fluid accelerations or decelerations which are simulated to occur in the compressor duct. For instance, the close spacing of the points immediately prior to final stagnation event shown in Figure 8 is an indication that the fluid accelerations and decelerations in the neighborhood of the rotating stall equilibrium operating point are negligible.

2.3.2. Baseline Free Response Simulations

Once the B parameter critical value had been determined the free response of the compression system was also studied at the two B parameter values that would be investigated during the forced response investigation. Figures 8a and 8b show free response surge limit cycle trajectories associated with these two B parameter values of 0.23 and 0.80 respectively. Of these two cases, the first case (B=0.23) is somewhat more realistic from a practical design standpoint. This B value is approximately 25% greater than the critical B value.

25

The second case (B = 0.80) represents a system whose B value is over 400% greater than the critical B value. The transient accelerations and decelerations are much greater in this case than the former case. Although, the overall surge cycle period is longer for this case. The increase in overall cycle period is mainly due to the larger amount of time spent traversing the dissipative legs of the cycle, i.e. the quasi-steady reversed flow and unstalled operating regimes. These features of the surge cycle trajectories are clearly evident in the relative spacing between the plotted points. The nondimensional period of the two baseline free response surge limit cycles are

$$\tilde{T}_{B = 0.23} \quad = \quad 1.77 \quad (B > B_{crit})$$

$$\tilde{T}_{B = 0.80} \quad = \quad 3.97 \quad (B \gg B_{crit})$$

If we assume that a "characteristic" speed of sound for a modern compressor is approximately 1500 ft/sec, an effective compressor length of 3 ft., a flowthrough area of 1.5 ft^2, and a combustor volume of 5 ft^3; then the Helmholtz resonator radian frequency for a modern gas turbine compression system is about ω_H = 475 rad/sec. Since time is nondimensionalized by the Helmholtz resonator radian frequency, i.e. $\tilde{t} = t \omega_H / 2\pi$, the period of the two baseline surge limit cycles are

$$T_{B=0.23} \quad = \quad 23.4 \quad msec \quad (B > B_{crit})$$

$$T_{B=0.80} \quad = \quad 52.5 \quad msec \quad (B \gg B_{crit})$$

26

2.3.3. Transient Compressor Characteristics

The time history locus of the instantaneous compressor performance values returned by the transient compressor model during two free response dynamic simulations are presented in Figures 9a and 9b. The Figure 9b compressor performance trace corresponds to the $B = 0.80$ system response case depicted in Figure 8b. Figure 9b illustrates the surge case implementation of the collapse schedule described in Section 2.2.3.2. and schematically represented in Figures 6a-f. The relative length and direction of the arrows which appear in Figure 9a (and 9b) are indications of how fast a mass flow regime was traversed and of the time history development of the instantaneous performance characteristic.

The transient compressor performance trace depicted in Figure 9a corresponds to the $B = 0.186$ system response case shown in Figure 7a. Figure 12 clearly illustrates an example of a complete transition from the axisymmetric characteristic to the steady state rotating stall characteristic at a B parameter value below B_{crit}. The number and close spacing of points in the trajectory is a clear indication that the time duration expressed by the LHS of the Equation 2-15 inequality became sufficient to cause an equality between the LHS and RHS to develop.

2.4 FORCED RESPONSE SIMULATION RESULTS

Until now, the primary purpose for conducting compression system dynamic simulations was to determine whether or not a given compression system would exhibit surge or stagnation behavior once the system had been subjected to an initial destabilizing perturbation. The major emphasis of this forced response study is to make a preliminary attempt at determining how the response behavior of a simple compression system is modified when an external forcing function is imposed.

In particular, the primary objective of the baseline forced response investigation was to identify the relevant parameter combinations which are capable of forcing either baseline compression system into a nonrecoverable stagnation from a pre-established surge limit cycle condition. Since the problem is nonlinear and several relevant parameters are involved, a multiple parameter variation study was conducted. The methodology used to conduct this study is explained in Section 2.4.1. A local analysis for the system about the equilibrium rotating stall point is presented in Section 2.4.2. This criterion was developed to limit the scope of the parametric variation study to realistic parameter combinations of the forcing function nondimensional peak amplitude, $\widetilde{X}_f$, and nondimensionalized frequency, $\widetilde{\omega}_f$. The overall results and trends observed from the baseline forced response investigation are presented in the subsections of Section 2.4.3.

Finally, another objective of this effort is to evaluate the suitability and major weaknesses associated with this lumped parameter approach for simulating post stall compression system dynamic response. This objective motivated a sensitivity analysis to test the robustness of the baseline case results. The findings associated with this subsequent sensitivity analysis appear in the subsections of Section 2.4.4.

2.4.1 Parametric Methodology

A brief inspection of Equations 2-9 and 2-10 reveals that there are at least four relevant parameters associated with the problem of external sinusoidal excitation of a simple compression system. These four parameters are: the system B parameter (B), the forcing function peak amplitude ($\widetilde{X}_f$), the forcing function frequency ($\widetilde{\omega}_f$), and the forcing function initial timing parameter ($\widetilde{T}_s$). At this point, it should be emphasized that a sinusoidal

28

excitation was chosen to simulate the effects of a periodic pressure pulse which can be generated from low frequency afterburner combustion instability phenomena (e.g. rumble).

The scope of the parameter variation study was limited to consideration of two values of the B parameter. A B value of 0.23 was selected to represent the case where the system B value was slightly greater than B_{crit}. The other selection, $B = 0.80$, represents a case where the system B value is significantly greater than B_{crit}. Prior to this forced response investigation, it was believed that this system (which has a B value that is 430% greater than B_{crit}) would be immune to any type of forced stagnation behavior.

A wide range of forcing function amplitude, frequency, and timing parameter combinations were explored for each of the two distinct B parameter baseline cases. It was quickly discovered, however, that only a very narrow range of the forcing function timing parameter yielded the proper timing condition for causing a (reasonable strength) forcing function to "interrupt" the pre-established surge limit cycle. As a result, both three-parameter variation matrices were reduced by one order to a two-parameter variation problem.

2.4.2. Local Analysis about Stagnation Point

In order for an externally imposed forcing function to induce nonrecoverable stall in a surging compression system, the forcing function must accomplish two tasks. First, this external excitation must be introduced with the proper timing and enough strength to break or interrupt the initial surge cycle and subsequently drive the system towards the equilibrium (nonrecoverable) stall point of the compression system. This equilibrium point has been defined previously as the point of intersection between the throttle and steady-state rotating stall characteristics.

The second task is equally important. The strength of the external excitation must not be too large else the system will be driven away from the neighborhood of the nonrecoverable stall point and return to a variant of the original surge limit cycle. In order to reduce the range of possible forcing function peak amplitude and frequency combinations which might be considered in the two-parameter variation matricies, a local stagnation point analysis was carried out to identify which amplitude-frequency combinations produce an excitation that is "too strong" to accomplish the second task.

The local stagnation point analysis is based upon a linearized description of the system dynamics in the neighborhood of the nonrecoverable stall point. By linearizing the compressor's rotating stall characteristic and the throttle characteristic at the point defined by their intersection, the governing coupled set of system dynamic equations can be combined into the following linear second order differential equation for compressor mass flow[5]

$$\frac{d^2\tilde{m}_c}{d\tilde{t}^2} + \frac{1}{BK_{1_T}} \frac{d\tilde{m}_c}{d\tilde{t}} + \tilde{m}_c = \frac{K_{2_C} - K_{2_T}}{K_{1_T}} +$$

(2-16)

$$B\tilde{X}_F \tilde{\omega}_F \sin\left(\tilde{\omega}_F \tilde{t} + \tilde{\phi}_F\right) - \frac{\tilde{X}_F}{K_{1_T}} \cos\left(\tilde{\omega}_F \tilde{t} + \tilde{\phi}_F\right)$$

where $K1_t$ is the slope of the throttle characteristic at the equilibrium stagnation point; $K2_t$ and $K2_c$ are the linearized throttle and compressor characteristics' y-intercept points; and ϕ_f is an arbitrary phase angle of the external forcing function.

---

[5] This equation has been derived for the baseline set of compressor characteristics for which the slope of the rotating stall characteristic is zero. A more general formulation of the homogeneous portion of this equation can be found in [5].

This equation has an analytic solution which consists of a homogenous part and a particular part. The homogeneous portion of the solution is fully defined once the initial conditions are supplied (i.e. the mass flow rate and the rate-of-change of the mass flow rate at time equal to zero). The derivation of Equation 2-16 as well as its solution are documented in [70]. The solution of Equation 2-16 yields compressor mass flow rate as a function of time for any combination of forcing function peak amplitude, $\tilde{X}_f$, and frequency, $\tilde{\omega}_f$, at a given system B parameter value.

The maximum allowable peak mass flow excursion about the nonrecoverable stall equilibrium condition, $\tilde{m}_{c\ max}$, is the point at which the system has effectively left the linearized neighborhood about the equilibrium point and enters a strongly nonlinear flow regime where forces are developed that drive the system further away from the equilibrium point. This maximum mass flow excursion point is either end of the steady state rotating stall curve. The linearized neighborhood about the equilibrium point along with the maximum mass flow excursion limit is schematically portrayed in Figure 10.

The solution of Equation 2-16 can be used to iteratively find the values of the forcing function peak amplitude, $\tilde{X}_f$, which cause the maximum mass flow excursion, $\tilde{m}_{c\ max}$, for a given system B parameter value and forcing function frequency. A local "domain of attraction" curve can be generated in this manner by holding the B parameter value fixed and varying the forcing function frequency. Figure 11 contains a set of these local domains of attraction curves for the baseline compression system B parameter values of 0.23 and 0.80.

For a given B value then, a forcing function with an amplitude frequency combination which lies above the appropriate curve will cause the overall compression system to be forced away from the neighborhood of the nonrecoverable stall point and return to the original surge mode. This local stagnation point criterion was used to greatly reduce the scope of the

31

parameter variation study by eliminating the forcing function amplitude-frequency combinations above the curves from serious consideration as potential candidates for inducing nonrecoverable stall.

2.4.3. Baseline Forced Response Simulations

The forced response behavior of the baseline compression system to an externally applied sinusoidal pressure excitation was characterized by conducting the extensive parameter variation study outlined earlier in Section 2.4.1. During each simulation, the compression system was allowed to freely respond to an initial destabilizing perturbation for the duration of one surge limit cycle. The external forcing function was introduced to the system via the $\tilde{T}_s$ parameter on the subsequent surge limit cycle. The first phase of the study was directed towards investigating forcing function timing considerations. The "timing" consideration results are represented in Section 2.4.3.1. The second phase of the study was directed at forcing function strength considerations and a check of the local domains of attraction criterion reported earlier in Section 2.4.2. The "strength" consideration results are summarized in subsection 2.4.3.2. Finally, the influence of removing the external excitation are addressed in Subsection 2.4.3.3.

2.4.3.1. Timing Considerations

The time at which the external forcing function is first introduced to the simulation is defined as the $\tilde{T}_s$ parameter. This parameter effectively determines the point in the second surge limit cycle trajectory where the forcing function is initiated. The results of this forced response investigation indicate that for a given B parameter value, there is a very narrow range of the $\tilde{T}_s$ parameter that is necessray, but not sufficient, to cause the applied forcing

32

function to drive either baseline system into a forced oscillation about the nonrecoverable stall equilibrium operating point. Figures 12a and 12b depict examples of the equilibrium point forced oscillation which results when a forcing function with the right timing and proper strength is introduced.

At a B parameter of 0.23, the "timing window" corresponds to the location in the surge limit cycle where the stall limit of the compressor is re-encountered following a quasi-steady traverse of the unstalled characteristic. For the 0.80 B parameter case, the timing window was at the mass flow shutoff point location of the cycle. These two locations are where the compressor characteristic transitions from a steep negative slope to zero slope. In addition, the transient trajectory indicates that the system is still responding quasi-steadily in these flow regimes.

Mathematically, these locations are the regions in the surge limit cycle where the following conditions exist simultaneously:

$$\frac{d\tilde{\dot{m}}_c}{d\tilde{t}} \approx 0 \tag{2-17a}$$

$$\frac{d\tilde{c}}{d\tilde{\dot{m}}_c} \approx 0 \tag{2-17b}$$

Taken together, these two conditions imply that the system is in a regime where small amounts of external excitation will have the greatest impact on increasing or decreasing the compressor duct mass flow. Individually, the first condition indicates that the pressure forces which accelerate or decelerate the fluid in the compressor duct are nearly balanced, i.e. the LHS of Equation 2-1 is zero. As a result, a small external pressure excitation need not

overcome the pressure force terms in order to influence the acceleration or deceleration of fluid in the compressor ducting. The second condition is also important. The net effect of this condition is to insure that large pressure forces do not develop with slight changes in compressor mass flow rate. In terms of our external pressure excitation, this condition insures that a small excitation term can have a reasonable effect on the system over a significant mass flow range before strong compressor performance forces are developed.

Figures 13a through 13b illustrate transient system response trajectories where the timing was improper. In the first two figures, the external forcing function was imposed "too soon". The quasi-steady condition represented by Equation 2-17a existed in these cases. However, the second condition was not met. Figures 14a and 14b depict the result of late timing. In these cases, the second condition was met but the system had enough time to develop sufficient inertial forces to overcome the effects of the forcing function.

One may obtain a reasonable feel for the relative size of the "timing windows" by inspecting Figures 15 and 16. These figures are plots which indicate which combinations of the $\tilde{T}_s$ timing parameter and forcing function amplitude, $\tilde{X}_f$, generate a forced oscillation about the nonrecoverable stall point while holding the forcing function frequency parameter fixed. The largest $\tilde{T}_s$ timing parameter windows occured at a forcing function frequency of $\tilde{\omega}_f = 0.5$. These windows were 0.1 and 0.16 Helmholtz resonator time units long for the B parameter values of 0.23 and 0.80 respectively. In Section 2.3.2, it was estimated that the Helmholtz frequency for a modern gas turbine engine to be $\omega_H = 475$ rad/sec. Using this estimate, the timing windows are 1.3 msec and 2.1 msec long respectively. These timing considerations help to explain the difficulty in reproducibly establishing the test conditions under which a forced nonrecoverable event occurs.

34

2.4.3.2. Amplitude-Frequency Considerations

In addition to timing considerations, the amplitude-frequency combination of the forcing function will have a significant impact on the problem. Again, it was determined that a very narrow "window" of forcing function amplitude-frequency combinations will drive a normally surging compression system into a forced oscillation about the nonrecoverable stall equilibrium point. In some cases, the amplitude-frequency combination does not produce a great enough effect to "break" the surge limit cycle. Figures 17a and 17b illustrate this case. In other cases, the amplitude-frequency combination lies above the appropriate local "domain of attraction" curve (defined in Section 2.4.2). These combinations produce a strong enough effect to drive the system away from the neighborhood of the nonrecoverable stall point (even after the initial surge cycle had been interupted). Representative simulations of these cases appear in Figures 18a and 18b.

Although Figures 15 and 16 illustrate the narrow forcing function peak amplitude "windows" which exist at a given forcing function frequency, an estimate of the size of the forcing function frequency window can be obtained by crossplotting all the forced nonrecoverable stall points on a single amplitude vs. frequency scale. Figure 19 is a crossplot of amplitude-frequency combinations which generated these forced nonrecoverable stall outcomes. The appropriate local stability curves for both B parameter value baseline cases have been superimposed on the crossplot to emphasize the relevance of the local domains of attraction analysis.

The Figure 19 crossplot shows a number of interesting features. First, it appears obvious that the local domain of attraction criterion developed earlier in Section 2.4.2 is a valid technique for predicting the forcing function amplitude-frequency combinations that will drive the baseline system away from the equilibrium rotating stall condition. Second, the forcing function frequency at which the compression system can be driven into nonrecoverable

35

stall appears to be concentrated in a very narrow band and is relatively independent of the B factor parameter for this set of steady state compressor characteristics. This forcing function frequency band is approximately centered at one-half of the Helmholtz Resonator Frequency, $\tilde{\omega}_f = 0.5$. Thirdly, the compression system with a B parameter value slightly greater than B_{crit} will require relatively large external pressure excitation amplitudes in order for the system to be forcibly driven into an oscillation about the nonrecoverable stall point. On the other hand, the compression system with a B parameter value greatly above B_{crit} (considered to be a "safe" design), did not require a significant large peak pressure amplitude to drive the system into the forced oscillation about the nonrecoverable stall point.

This last observation deserves further comment. From a free response standpoint, greater values of the B parameter are associated with reducing the likelihood of encountering a stagnation. However, from a forced response standpoint, it appears that the possibility of being driven into a stagnation is greatly increased for a range of B parameter values significantly above B_{crit}. Furthermore, there appears to be a mode of entering the stagnation condition. A low B-high $\tilde{X}_f$ combination caused the baseline system to enter the stagnation from the stall limit point of the surge limit cycle. A high B-low $\tilde{X}_f$ combination drove the system into a stagnation during the initial recovery portion of the surge cycle at the shutoff flow coefficient. If one assumes that the high B-low $\tilde{X}_f$ combination occurs more frequently in practice, an extension of the baseline results of this study would suggest that the most likely mode for entering a forced stagnation should be during the recovery portion of a surge cycle. This trend has been observed in practice.

36

The size of the amplitude-frequency "windows" are also small. The forcing function frequency window is approximately one tenth of a Helmholtz radian frequency unit, i.e. 0.1 ω_H or only about 7.5 Hz. In absolute terms, this window extends from 37.5 Hz to 45 Hz. It is interesting to consider that these frequencies are slightly lower than the frequency range associated with the longitudinal combustion instability mode of the F100 engine afterburner. The forcing function peak amplitude window ranges from a nondimensional value of 0.5 to 0.8 for the 0.23 B parameter value system. The reference blade dynamic pressure, $1/2 \rho U^2$, is assumed to be equal to a value of 25 psi (based upon HPC inlet condition). Hence, the dimensional range of the peak amplitude window extends from 12.5 to 20 psi. Likewise, the dimensional range for the B = 0.80 case is 5 to 7.5 psi.

2.4.3.3. Excitation Cessation Considerations

Although a stagnation condition is nearly established, an analysis of the behavior depicted in Figures 12a and 12b indicates that continued imposition of the periodic external excitation causes a nearly linear forced oscillation about the nonrecoverable stall point. The time-averaged effects of this condition are essentially identical to an actual stagnation in that the pressure rise and mass flow across the compressor are considerably reduced. The net effect may be to cause the external pressure excitation to cease.

At this point, it is important to consider whether or not the system "falls" into a subsequent stagnation or returns to the surge mode of instability. Both of these events are possible. Simulations of both phenomena are presented in Figures 20 and 21. Figures 20a and 20b illustrate the case where a stagnation occurs, while Figure 21 shows the reestablishment of a surge limit cycle instability. The difference between these two sets of figures is the point at which the external excitation was terminated. In mathematical terms, a

37

different set of initial conditions was provided for the resulting free response problem once the forced response problem was terminated.

2.4.4. Sensitivity Analysis Results

Since the primary objective of this forced response investigation was to evaluate the suitability of this lumped parameter method to deal with the problem of forced nonrecoverable stall, it is necessary to explore the "robustness" of the results presented in the previous subsections. If the results are not robust, especially with respect to small changes in the underlying assumptions one is forced to make because of inadequate knowledge or understanding; then the methodology is flawed. The results of this sensitivity analysis indicate that there are several crucial gaps in our knowledge of post-stall compressor performance.

2.4.4.1. Modified Zero Mass Flow Performance

The flow regime in the region around the shutoff flow coefficient was identified as one of the two critical points in a surge limit cycle where the imposition of an external forcing function can have a significant impact on the remaining compression system response. Unfortunately, almost nothing is known about the behavior of modern multistage axial compressors in this flow regime. The baseline set of quasi-steady performance characteristics depicted in Figure 5 were a best estimate of the "typical" performance of a multistage axial compressor. This estimate was completely arbitrary for the mass flow regime in the neighborhood of the shutoff flow coefficient.

As a measure of the sensitivity to changes in the compressor performance characteristic at the mass flow shutoff point, the axisymmetric curve was slightly altered as shown in Figure 22. These small changes significantly effected the forced response behavior of the overall compression system. Although the data associated with $B = 0.23$ baseline case was

38

unaffected by these changes, it was no longer possible to force the system into an oscillation about the nonrecoverable stall point from the "bottom" of the surge cycle at any value of the B parameter.

The effect of these small changes in the backflow and low positive flow rate portion of the curve is to sharply reduce the flow regime over which the compressor performance condition represented by Equation 2-17b is maintained. As a result, the rate at which the model increases the force terms which tend to drive the system towards recovery is increased. In order to drive the system off the recovery leg of the surge cycle the increased growth of the initial acceleration term must be balanced by an increase in the external forcing function peak amplitude. As a result, the required increase in the forcing function amplitude violates the local stability criterion around the neighborhood of the stagnation equilibrium operating point. In the final analysis, the system is forced back to the original surge limit cycle. A forced oscillation about the stagnation point is not achieved.

The shape of the axisymmetric curve was further modified at the zero mass flow point to insure that the condition represented by Equation 2-18b is never satisfied. Figure 23a displays this more drastic modification of the zero mass flow characteristic as well as the effect this change has on a transient system response trajectory.

2.4.4.2. Shifted Rotating Stall Performance

In addition to modifying the shape of the zero mass flow portion of the axisymmetric characteristic, the rotating stall performance characteristic was shifted relative to the axisymmetric curve to a higher pressure rise performance level. The principle effects of making this change were to further erode both conditions represented by Equation 2-17 and to move the stagnation equilibrium point further up the throttle characteristic (to a higher mass flow rate).

39

Moving the stagnation point in this manner increases the critical value of the B parameter. It also imposes a more severe limit upon the maximum allowable mass flow excursion about the stagnation point. For example, raising the rotating stall performance characteristic from a nondimensional pressure rise value of 1.1 to 1.5 shifts the critical B parameter value from 0.1865 to 0.244. The maximum allowable peak mass flow rate decreases from 0.20 to 0.15. This latter development accounts for a significant downward shift of the amplitude-frequency local domain of attraction curve (defined in Section 2.4.2) at a given B parameter value.

It is still no longer possible to force the system into an oscillation about the nonrecoverable stall point from the "bottom" leg of the surge cycle for any value of the B parameter. Figure 23b illustrates a typical case where the system is driven into a forced oscillation about the stagnation point from the "top" of the surge cycle. In this case, the B parameter value was 25% greater than B_{crit}. Finally, Figure 24 contains a crossplot of the forcing function amplitude-frequency combinations which caused the system to encounter forced oscillations about the stagnation point.

2.4.4.3. Single Pulse Excitation

A brief exploratory investigation was made of the forced response associated with nonperiodic forcing functions. In particular, a simple on-off pulse function with a constant amplitude was employed in several forced response simulations. This function was introduced during the initial portion of the recovery leg of a surge limit cycle for a system defined by the modified set of "more severe" quasi-steady performance characteristics considered in the previous section. Figure 25 illustrates a typical stagnation event which can occur under these circumstances.

This feat could not be accomplished for this set of compressor characteristics by imposing a sinusoidal forcing function. The reason for the success of the simple pulse function stems from the fact that the pulse function amplitude value is not constrained by a local domain of attraction criterion. Once the compression system is driven to neighborhood of the nonrecoverable stall point, shutting off the pulse function insures that the system will not be driven back to the original surge limit cycle. Hence, a much higher amplitude can be used to break the surge limit cycle at the desired location.

The importance of this result is that aperiodic forcing functions can sometimes cause a forced stagnation event to occur under conditions where a periodic excitation fails to produce this outcome. Hence, any serious attempt to investigate the forced stagnation stall phenomena of a particular turbine engine will have to be based upon an accurate description of the external excitation time history as well as the compressor's performance characteristics.

2.5 SUMMARY

Several important results have emerged during the course of this preliminary forced response investigation. First, a simple one-dimensional lumped parameter description of the compresssion system dynamics is capable of simulating the set of circumstances under which the imposition of a periodic external excitation can "force" a normally surging compression system into a small amplitude oscillation about the nonrecoverable stall point. This forced oscillation can decay into a system stagnation upon termination of the external excitation.

Second, there are small "windows" in parameter space which define a limited number of suitable forcing functions with the proper combination of timing and strength. In particular, there are only two locations in a surge limit cycle where the imposition of a reasonable strength external pressure excitation can interrupt the surge cycle and then drive the

compression system to the nonrecoverable stall point: 1) near the stall onset of the compressor, and 2) near the bottom of the reversed flow characteristic at zero mass flow.

Perhaps the greatest single conclusion reached during the course of this investigation is the realization that the predicted forced or free response behavior of even a simple compression system is heavily dependent upon the model for defining the compressor's post-stall transient performance. This is manifested in analytical simulations of compression system response by the sensitivity of the predicted response behavior to small changes in the basic assumptions of the compressor model. In particular, the predicted forced response of a compression system can be *drastically* altered by slightly changing the location and shape of the compressor's performance characteristic in the neighborhood of the shutoff flow coefficient.

Unfortunately, not much is known about the performance of multistage axial flow compressors immediately prior to the initial stall recovery portion of a surge cycle. As a result, the remainder of this thesis effort was directed towards an experimental investigation of axial compressor reversed flow performance. In particular, the desire to develop compression system dynamic simulation models for dealing with the problem of forced stagnation stall provides strong motivation for determining if a flow mode change occurs near the shutoff flow coefficient of multistage axial compressors.

42

Chapter 3

REVIEW OF PREVIOUS WORK

Although there is very little published literature which specifically addresses the fluid mechanics associated with the reverse flow and mass flow shutoff operating regimes of multistage axial flow compressors, there is a large body of related articles on the performance of a wider variety of turbomachines operated under abnormal conditions. With a few exceptions virtually none of this literature is authored by individuals in the aircraft gas turbine academic or industrial community. Until now, most of the interest in turbomachinery reverse flows has been centered in three areas: 1) hydraulics and the design of pumping machinery for hydro-electric power plants, 2) the process plant industry, and 3) the nuclear power industry.

By far, the largest body of articles with respect to reverse flow in turbomachines have been by hydraulics engineers concerned with water-hammer and the transient performance of centrifugal water pump installations under starting, stopping or emergency loss of power conditions. Most of the literature on "four-quadrant" turbomachine performance[6] was generated by the need to effectively deal with the safety issues raised by the possibility of operation under abnormal conditions, i.e. the need to consider turbine runaway speeds, hydraulic balance and radial thrust, dynamic system instabilities and the effects of cavitation.

---

[6] Four quadrant turbomachine performance refers to the performance (head or torque) associated with a turbomachine operating under a reversed or normal flow direction and a reversed or normal rotation direction.

43

A good example of this class of hydraulic "four-quadrant" performance articles is the paper published by Ritter and Rohling [20] on restarting large custom pumps against reverse flow.

Reverse flow can also occur in process plant applications where an axial compressor is used to pump flow into large plenum volumes. Naegel [21] gives an excellent review of the technical issues related to the operation of large, axial flow refrigeration turbocompressors for Liquid Natural Gas (LNG) plants. Although reverse flow is not a common mode of operation in the natural gas liquification process, safety analyses must consider the effects and consequences associated with possible operating faults which could cause a reverse flow condition to develop in these extremely large turbocompressors.[7] Blast furnace compressor installations provide another example of an industrial application where reversed flow in turbomachinery can occur. Suter [22] and Strub and Suter [23, 24] have published several articles on the nature of industrial compressor surging which occurs in these installations.

During the past two decades, the development of the nuclear power industry has helped spark renewed interest in the phenomenon of reversed flow in turbomachinery. Most of this new interest is based in Germany in response to a German federal program to develop nuclear closed-cycle gas turbine power generation technology. This cycle involves the use of a high temperature nuclear reactor and helium gas turbines (HHT). As a result, the German HHT related research in turbomachinery reverse flows has been primarily directed towards the four quadrant performance of gas (air) turbine stages.

Given this background review of the motivations for investigating turbomachinery reversed flows, the following sections of this chapter will present a detailed review of the

---

[7] The power requirements of these compressors can be immense. For example, it was reported that the U.S. and Japan have plans to build LNG plants which will have compression cycles that will consume 1,500,000 kw of insulated refrigeration compressor shaft power [21].

results and accomplishments of the more relevant technical efforts. Experimental results and measurements will be dealt with first. This will be followed by a review of the various analytical attempts to treat the phenomenon of reversed flow in turbomachinery.

3.1 EXPERIMENTAL LITERATURE

Although there are no detailed flowfield measurements of reversed flows in any type of turbomachine to date, there have been a number of attempts to measure the overall performance characteristics of various turbomachines operated under reverse flow conditions. The experimental literature on this subject can be generally classified into three categories: 1) Four-quadrant Performance Measurements, 2) Compressor Performance Estimates from Reduced Surge Data and 3) Annulus Stalled Flow Performance Measurements. The latter category of results refers to the measured flow mode change which sometimes occurs when a compressor in rotating stall is throttled to very low positive flow coefficients.

3.1.1. Four-Quadrant Performance Measurements

Four quadrant turbomachine performance was first measured on a centrifugal water pump by Thoma [25] in 1931. Since then, the four-quadrant performance of mixed-flow and axial water pumps have also been measured. In the last two decades, the four quadrant performance of an axial-flow fan, as well as single and multiple air turbine stages have been reported in the literature.

3.1.1.1. Hydraulic Pumps

One of the first known attempts to systematically measure the performance of pumps operated under abnormal conditions was the effort conducted in Germany by Thoma [25] in

45

1931 and reported later in the United States by Kittredge and Thoma [26]. A set of experiments were performed on a small centrifugal water pump. Head and torque performance data were reported as a function of mass flow rate for several shaft speeds. Performance data were obtained at both positive and negative mass flow rates as well as positive and negative rotational speeds. The motivation for these experiments was to determine the effects of water hammer in the discharge pipe of a centrifugal pump which suddenly loses power or is otherwise stopped.

In 1937, Knapp [27] published a similar paper on the abnormal operation of a larger, more efficient centrifugal water pump. At the suggestion of von Karman, Knapp presented his data by plotting contours of constant head and torque on a single flow capacity versus wheel speed diagram. Four quadrants of possible turbomachine operation were defined by this Karman-Knapp circle diagram: 1) Positive flow-positive rotation in Quadrant I; 2) Positive flow-negative rotation in Quadrant II; 3) Negative flow-negative rotation in Quadrant III; and 4) Negative flow-positive rotation in Quadrant IV.

Knapp postulated a method by which these quasi-steady four quadrant characteristics could be used to predict the transient variation of wheel speed and mass flow through a pump which suddenly looses power. Knapp's transient path always began in Quadrant I at the normal operating point of the pump. Once the power input to the pump was lost, the transient path proceeds through Quadrant IV, i.e. energy dissipative negative flow-positive rotation operating regime. Eventually, the transient path terminates in Quadrant III at the zero torque (turbine runaway speed) condition. In 1941, Knapp [28] published a second paper summarizing an attempt to apply this technique to predict the transient behavior of the pumping-plant for the Grand Coulee Dam Project. According to Knapp, the major weakness of the analysis was a lack of knowledge about the flowfield and pump operating characteristics during the Quadrant IV reversed flow-normal rotation portion of the transient.

46

A complete set of performance characteristics was obtained for the first time on an axial flow pump by Swanson [29,30] in 1951. Swanson's axial flow machine was a single stage water pump. In 1957, Stepanoff [31] presented a summary of the complete set of four quadrant characteristics for various water pump configurations. Although these early investigations addressed the problem of measuring turbomachine performance during reversed flow and mass flow shutoff, most of the configurations studied were centrifugal pumps and th working medium under consideration was water.

Since the late 1950's, there have been a considerable amount of papers published on the four quadrant performance of water pumps. These articles typically appear in most of the well and lesser known hydraulics and civil engineering journals. A review of the current state of knowledge with regard to the four quadrant steady-flow characteristics of water pumps is given by Martin [32] in 1983.

3.1.1.2. Axial-Flow Fan

Turner and Sparkes' [33] 1964 paper on the "Complete Characteristics for a Single-Stage Axial Flow Fan" described an effort to measure the complete four quadrant characteristics of a turbomachine which more closely resembled the fans of aircraft gas turbine engines. To the best of the author's knowledge, the effort reported in this paper is one of only two experimental investigations of axial-flow fan/compressor reverse flow regime performance that have been conducted on the part of the aircraft gas turbine engine development community.[8,9]

3.1.1.3. Single and Multiple Air Turbine Stages

During the mid-1970's, Bammert and Zehner [35,36] conducted an extensive set of reverse flow tests on a parametric series of two-dimensional (rectilinear) air turbine cascade

geometries. Their test program also included reversed flow tests of an annular cascade as well as a multistage turbine with the rotor locked at a zero rotation condition. The empirical relationships for pressure drop as a function of reverse mass flow rate that were obtained from these cascade tests formed the basis for proceeding with the prediction and measurement of the four quadrant performance of a single [37] and a seven stage [38] air turbine in the late 1970's.

Although there is not much similarity between reverse flow in axial turbines and reverse flow in axial compressors, the air turbine work conducted by Bammert and Zehner does raise some important issues which should be put into a general historical perspective on past thinking about reversed flows in high performance turbomachines. The first issue concerning these tests relates to the presentation of results. The definition of the four quadrant zones of operation by Bammert and Zehner is not consistent with the standard Karman-Knapp definition of turbomachine four quadrant operation. The major difference between the two conventions is that a Karman-Knapp representation defines the abscissa of the performance map as rotational speed and the ordinate as flow rate, while Bammert and Zehner adopt the opposite convention. These two conventions are depicted in Figures 26a and 26b. This difference in conventions must be realized in any attempt to compare the Bammert and Zehner four quadrant results with the standardized body of four quadrant performance results discussed in Section 3.1.1.1.

_____

[8] Turner and Sparkes performed this investigation under the auspices of Britain's Ministry of Aviation, Turbo Machinery Department, National Gas Turbine Establishment, Pyestock, Farnborough, Hants.
[9] The results of the "second" experimental investigation are not published in the open literature. This effort was conducted by Pratt & Whitney's Government Product Division in 1980. During this experimental investigation, a reverse flow performance characteristic was measured on a three-stage high speed compressor. This characteristic was first presented publicly by Davis[34] at a recent MIT Gas Turbine Laboratory seminar on December 4, 1984.

The second issue regarding these tests is that a pervasive predisposition towards casting this problem in the context of two-dimensional flow processes seems to exist. Like Turner and Sparkes [33] in 1964, there is heavy emphasis on obtaining steady-state or time averaged performance data and an on extensive use of two-dimensional velocity triangle diagrams to explain their reversed flow results. Their initial large investment of time and resources in a broad scope experimental parameter investigation of different blading geometries in a two-dimensional cascade (wind tunnel) as well as reverse flow tests on a multistage turbine with a locked (fixed) rotor demonstrate a significant preoccupation with a view that the reverse flowfield is dominated by essentially two-dimensional processes.

One major area of similarity among the flowfields associated with axial turbines and compressors are the relative velocity diagrams which result when one performs a simple two-dimensional analysis of the reversed flowfields for either case. The reverse flowfield velocity vector relationships for Karman-Knapp Quadrant IV or Bammert-Zehner Quadrant II operation show that the flow strikes each successive bladerow at the trailing edges of the blading with approximately perpendicular incidence angles. This similarity is illustrated in Figures 27a and 27b.

3.1.2. Indirect Measurements of Reversed Flow Performance

In many applications, the sheer size and power requirements associated with testing full scale high performance compressors prohibits the direct measurement of steady-state reversed flow performance characteristics. An indirect method for deducing a compressor's reversed flow performance is the procedure by which transient surge cycle data is inertially corrected to yield an instantaneous trace of the transient compressor characteristic. During the reverse flow or plenum blowdown portion of a compression system surge limit cycle, the transient process is nearly quasi-steady. As a result, the deduced transient compressor characteristic

49

is usually considered to be a good estimate of the steady state reversed flow performance characteristic of the compressor.

This data reduction scheme is an inverse application of the compression system dynamic model discussed earlier in Section 2.1. Rather than predict system performance at a future interval in time with the aid of a transient compressor model; this inverse calculation begins with a known set of system response data, i.e. $\dot{m}_c(t)$ and $P(t)$, and attempts to deduce the transient compressor performance characteristic, $C(t)$, through application of Equation 2-1. In order to employ Equation 2-1, the first derivative of the compressor mass flow must be numerically evaluated from the data. To perform this reduction, Equation 2-1 is usually rearranged as follows:

$$C(t) = P(t) + \frac{L_c}{A_c} \frac{d[\dot{m}_c(t)]}{dt} \qquad (3-1)$$

There are two major pitfalls associated with implementing this approach. The first major technical obstacle is the development of a suitable experimental technique for the accurate measurement of compressor mass flow rate as a function of time, i.e. $\dot{m}_c(t)$. The second pitfall is related to the first. The measurement of compressor mass flow rate must be resolved temporally to very small time increments to permit accurate numerical evaluation of instantaneous flow accelerations, i.e. $d[\dot{m}_c(t)]/dt$. Recall from the discussion of Section 2.3.2 that the entire surge cycle for a modern multistage axial compressor is of the order of tens of milliseconds. During the highly transient portions of the surge cycle, it is not uncommon to traverse the entire design mass flow range of the compressor in one or two

50

milliseconds. For the purposes of resolving reverse flow performance characteristics, the time resolution of mass flow data will be of the order of microseconds for a modern compressor like that found in the F100 engine.

Smith and Fletcher [2] in 1954 were among the first investigators to realize that the reversed flow portion of a gas turbine surge cycle was traversed in a gradual (quasi-steady) manner. Hence, it was theoretically possible to deduce the reversed flow performance of a compressor from transient surge cycle data. In 1963, Suter [22] determined the reversed flow characteristics of a 10-stage axial flow compressor by surging a Swiss prototype 3,000 kW gas turbine engine.

Suter's inertially corrected results showed that a strongly negative sloped reversed flow characteristic exists. This characteristic drops well below the design point pressure rise capability of the compressor as the zero mass flow condition is approached. At zero mass flow, there is a discrete pressure rise and the reverse flow characteristic extends continuously into low forward flow with a slightly less negative slope.

Koff [14], and Koff and Greitzer [15] in 1984, report the reverse flow characteristic of a 3-stage axial flow compressor by reducing the surge cycle data measured by Greitzer [6] in 1976. Again, the reverse flow characteristic is reported to be strongly negative sloped. However, the reverse flow characteristic is shown to transition to nearly zero slope at slightly negative flow coefficients immediately prior to the mass flow shutoff condition.

3.1.3. Annulus Stalled Flows

There is a significant amount of technical literature which report the results of experimental investigations of compressor rotating stall phenomena. Day's Ph.D. thesis at Cambridge University [12], Greitzer's 1980 Freeman Scholar Lecture on "The Stability of Pumping Systems" [19], and Stenning's review of "Rotating Stall and Surge" [39] contain

51

some of the better literature reviews of this subject. In several rotating stall oriented experimental studies, annulus stalled flow conditions were observed upon throttling a compressor in rotating stall to very low positive flow coefficients. Although these compressors are still operating at a net time-averaged positive mass flow rate, this flow mode change appears to be a transition to an extenstion of the general annulus stalled performance characteristic that defines the compressor's reverse flow performance.

In 1954, Iura and Rannie [40] conducted several sets of tests aimed at documenting the performance of single- and three-stage axial flow compressors in rotating stall. At mass flow shutoff, their normal three-stage compressor configuration exhibited stable rotating stall operation with a single full span stall cell covering 87% of the annulus. When the solidity of the original three-stage compressor build was decreased by one-half, "irregular axisymmetric pulsations" with no discernable flow patterns were encountered at flow coefficients less than 0.07. Moreover, both one-stage builds (full and half design solidity) exhibited the same type of axisymmetric irregular flow patterns at low positive flow coefficients. In addition, Iura and Rannie noted that a small amount of hysterisis existed at these low flow coefficients between the full span rotating stall and the axisymmetric stall flow mode transitions. Unfortunately, these observations were qualitatively reported without a quantitative presentation of the compressor performance in these low flow regimes.

Shaw and Lewkowicz [41] reported the results of "The Construction and Testing of a Large Axial Flow Compressor" at the University of Liverpool, England, in 1963. The major conclusion reached by these authors was that two "hysteresis loops" exist in the pressure rise vs. flow coefficient characteristic of their single-stage axial flow compressor. The first hysteresis occurs at the discontinuity between unstalled flow and full span rotating stall in the neighborhood of the stall flow coefficient of the compressor. At a very low flow

52

coefficient, i.e. $\bar{C}_x/U = 0.10$, there is another hysteresis loop at a discontinuity between full span rotating stall and "an axisymmetric stall" flow mode. At this second hysteresis point, the performance associated with the axisymmetric stall mode is less than that associated with the full span rotating stall immediately prior to the transition. In addition, the slope of the axisymmetric stall portion of the performance characteristic is negatively sloped and continuously extends to the mass flow shutoff point.

Day [12] reported the results of tests performed to determine the rotating stall performance of several axial flow compressor builds in his 1976 Ph.D. Dissertation at Cambridge University, England. At very low flow coefficients, Day observed a change in flow mode from a rotating stall to an axisymmetric stall in several of the compressor builds tested. Day's data indicates that the transition to axisymmetric stall generally involves a decrease in pressure coefficient performance. In addition, the flow coefficient at which transition occurs appears to decrease with increasing design flow coefficient and/or an increase in the number of compressor stages. This later trend is in general agreement with the trend first observed by Iura and Rannie [40] in 1954. Although Day's data does not conclusively indicate a trend with respect to the slope of the axisymmetric characteristics in this flow regime, it does appear that there is no hysteresis or flow coefficient overlap between the rotating stall and axisymmetric stall characteristics.

Das and Jiang [42] performed a similar investigation of the rotating stall performance of a three-stage axial flow compressor in 1983. Like Iura and Rannie [40] almost 30 years previously, they qualitatively report[10] a transition to "irregular non-periodic stall" at very

---

[10] Although this qualitative report of a transition to "irregular non-periodic stall" did not appear in the published version of their paper, this discussion did appear in the original manuscript submitted to the AIAA for review.

low flow coefficients without reporting the corresponding pressure rise vs. flow coefficient performance in this operating regime.

3.2 ANALYTICAL LITERATURE

The theoretical literature on the subject of reversed flows in axial compressors is virtually nonexistent. The primary reason for this state of affairs is the fact that there have been no detailed experimental measurements of reverse flow velocity and pressure fields with turbomachines. Without a working experimental description of the flowfield, it is very difficult to develop a credible analytical formulation of the kinematics and dynamics of reverse flow processes.

To date, most of the reverse flow analytical work has been directed towards predicting steady-state (time-averaged) head rise and torque characteristics. Invariably, the authors of these prediction schemes are forced to make two-dimensional, steady flow assumptions regarding the detailed nature of the complex unsteady flow processes which occur in turbomachine reverse flow operating regimes. As a result, these analytical performance prediction models usually generate results which compare reasonably well with cascade data where a reasonably steady two-dimensional flow pattern may well be established. However, these same models fail to predict the performance of multistage rotating turbomachinery.

The analytical literature on reversed flows in turbomachinery will be presented in the following three subsections. First, a generalized ideal reverse flow performance prediction method will be outlined. Next, some general cascade loss models dealing with highly separated flows will be discussed. Finally, the adaption of these cascade loss models to overall turbomachine prediction schemes will be explored in detail.

54

3.2.1. Ideal Performance Prediction

Swanson, [29,30] in 1951 was one of the first investigators to formulate a theoretical model for predicting the reversed flow characteristics of an axial flow pump. Swanson's analysis consisted of simply writing the energy equation and the conservation of angular momentum equation for a control volume around the entire pump. By assuming zero losses, the mechanical energy input was set equal to the hydraulic energy output.

This type of ideal analysis essentially treats the turbomachine as a "black box". Provision is made for mechanical power input to this unit via the shaft. The flowfield at the inlet is assumed to be axisymmetric with uniform and purely axial velocity. The flowfield at the discharge of the machine is also assumed to be axisymmetric with uniform velocity at an outlet flow angle fixed by the blading exit angle.

Swanson qualifies the usefulness of this model by noting that the actual flow departs from the assumptions of ideal flow in the reverse flow regime, since in reality, there is a substantial amount of power dissipation which occurs during reversed flow. Substantial pressure losses occur because the blading is set at extremely unfavorable angles to promote efficient pump operation. At that time, Swanson concluded that no mechanism had been developed to predict or define the amount of power dissipation which occurs during backflow. In 1964, Turner and Sparkes [33] made the same sort of ideal performance calculations for their single-stage axial fan, and also acknowledged that there is no information available to predict flow losses during reversed flow.

3.2.2. Cascade Loss Models

The present day analytical loss prediction models for turbomachine cascades subjected to reverse flows are derived from the original work of Betz and Peterson [43] in 1931. These investigators described a hodograph method for treating the potential flow in jets positioned

between adjacent "dead flow" regions. This approach was a direct application of the free streamline theory advanced by Helmholtz and Kirchoff [44] for the flow of a steady, incompressible, inviscid fluid that is free of all conservative and nonconservative body forces, i.e. a potential flow defined by the Laplace equation for velocity potential.

In 1954, Cornell [45] applied this method to the case of a stalled cascade of airfoils. Cornell replaced the cascade of cambered airfoils with a two-dimensional cascade of flat plates of length ℓ, pitchwise spacing S, and stagger γ. This geometry is depicted in Figure 28a. In this analysis, the inlet flow relative velocity W_1 is assumed to have an approach angle β_1 which is sufficient to cause the flow to separate at the leading edge of the flat plates. A free streamline between the resulting separated wake region on the suction surface of the plates and the potential flow in the jet regions is assumed to emanate from the leading edge separation point and extend infinitely far downstream (measuring plane 2 in Figure 28a). Likewise, a free streamline emanates from the trailing edge of the plates and extends infinitely far downstream to measuring plane 2. Between measuring planes 2 and 3[11], the jets and wakes are mixed while conserving continuity and momentum. This standard stream-thrust averaging technique accounts for the loss production associated with the separation of an otherwise inviscid fluid and accounts for the difference in outlet flow angles β_2 and β_3.

By the early 1970's, fault analyses of direct cycle nuclear plants revealed the possibility that backflow through the gas turbines could occur in the event of a catastrophic pipe rupture in the closed cycle circuit. In 1974, Bammert and Zehner [35] applied Betz and Peteron's method to reverse flows in turbomachine blading cascades. Figure 28b illustrates the relevant geometry and flow relationships associated with Bammert and Zehner's

---

[11] Physically, measuring plane 3 is a pseudo-downstream position from the already infinitely far downstream measuring plane 2.

formulation of the problem. Bammert and Zehner appear to have independently extended Cornell's formulation by defining an empirically based loss correction term which could be added to the mixing loss estimate given by the standard stream-thrust averaging technique. If the loss coefficient ζ is defined to be

$$\zeta = 1 - \left(\frac{W_{3,a}}{W_{3,s}}\right)^2 \qquad (3-2)$$

where $W_{3,a}$ is the actual velocity realized at measuring plane 3 (see Figure 28b) and $W_{3,s}$ is the isentropic ideal velocity possible at this station; then Bammert and Zehner's suggested form of the relationship for the losses through the cascade is

$$\zeta = \zeta_m + \zeta^* \qquad (3-3)$$

where ζ_m is the loss due to the stream-thrust averaged mixing process described previously, and ζ^* is the empirical loss correction term.

These two loss terms are defined by Bammert and Zehner as follows

$$\zeta_m = \frac{\left(1 - \frac{a}{s}\right)^2}{1 + \cot^2 \alpha_2 + 2\left(\frac{a}{s}\right)\left(\frac{a}{s} - 1\right)} \qquad (3-4)$$

57

$$\zeta^* = 0.417 + 0.815\left(\frac{\beta_s}{180}\right)\frac{s}{l} \qquad (3-5)$$

where (in the terminology of Figure 28b) o is the (tangential) width of the jets, α_2 is the measuring plane 2 outlet flow angle (relative to the tangential direction), and β_s is the relative tangential stagger of the flat plates (in degrees). The numerical coefficients in Equation 3-5 were obtained through an extensive set of parametric cascade tests (discussed in Section 3.1.1.3).

The results of the parametric experimental investigation further showed that the loss model represented by the solution of the two hodograph equations plus the empirical correction given by Equations 3-3 through 3-5 is valid for only slender, slightly cambered airfoil profiles. For typical turbine airfoils, the profiles are usually thicker and more cambered. A Coanda effect at the leading edge of the airfoils was believed to exert an influence on the problem. Bammert and Zehner developed a procedure for predicting losses for these realistic turbine profiles by completely abandoning the free streamline analytical theory. Instead, they developed a very detailed empirical procedure based upon the results of their cascade tests. This new procedure will not be outlined any further because it is not relevant to the study of axial compressor reversed flow phenomena.

A decade later, in 1983, Koff [14] proposed a reverse flow loss model for axial compressor cascades which was essentially identical to the analytical model considered by Bammert and Zehner. Figure 28c depicts Koff's representation of the relevant geometric relationships. Although Koff's model was developed independently of the work by Bammert and Zehner, the striking similarity arises from the fact that both models are based upon the original separated flow theories of Betz and Peterson [43] in 1931.

58

3.2.3. Multistage Performance Predictions

The preceeding discussion of cascade loss models was not presented because of the author's belief that these approaches show great promise. Rather, it will be shown in later chapters that an analytical approach based upon "stacking" of the static pressure drops through steady state two-dimensional cascades is inappropriate for the task of predicting multistage turbomachine reverse flow performance. In particular, it will be shown that these approaches are fundamentally flawed because radial flow effects tend to dominate the reverse flowfield of a modern multistage machine.

Unfortunately, all the multistage turbomachine reverse flow prediction schemes in existence today are extensions of the cascade theories presented in Section 3.2.2. The following sections will outline these cascade "stacking" approaches and report the limited attempts to compare the predictions of these models with actual experimental results.

3.2.3.1. Axial Turbines

Bammert and Zehner [35] developed a bladerow-by-bladerow iterative scheme to evaluate multistage turbine performance. Bladerow calculations were based upon their empirically derived polynomial relationship for predicting the pressure ratio vs. mass flow rate characteristic of a turbine cascade. This scheme was used to successfully predict the pressure drop performance of a four stage turbine *whose rotor was held fixed at zero rotational speed.*

Five years later, Zehner [46] published an article in 1979 which reported an attempt to compare the results from this cascade based prediction scheme with experimental data recently obtained from rotating tests of a one-stage and a seven-stage version of the same turbine test article. In all the rotating tests, the reverse flow correspondence between the predicted and experimental results were poor. Zehner explains the discrepancies by

59

highlighting several features of the rotating turbine rig's design that could be responsible for creating flow conditions which were beyond the range of validity of the cascade data base. A more probable explanation is that the structure of the flow in *rotating* turbomachinery is primarily three-dimensional. In Chapter 6, experimental data will be presented which illustrates the significance of radial flow effects in a rotating multistage axial compressor rig.

3.2.3.2. Axial Compressors

Meanwhile, Koff [14] extended the jets and wakes cascade theory to predict the pressure drop performance of a multibladerow axial compressor by marching through the machine using the steady-state Bernoulli equation to define the static pressure drop across each bladerow. At each interbladerow gap, the wakes and jets are assumed to mix out before encountering each successive bladerow. This process can be repeated through an N number of bladerows because a uniform velocity profile is *always* established (via the stream-thrust mixing procedure) prior to entering the inlet plane of each bladerow.

This model was used to predict the reversed flow pressure vs. flow coefficient characteristic measured by Turner and Sparkes [33] on their one-stage axial fan; the reverse flow characteristic reduced from the Greitzer [6] transient surge data (discussed in Section 3.1.2.); as well as the Compressor Build #1 reverse flow characteristic measured by the author and reported in Chapter 5 of this thesis. There was exceptionally good agreement between the prediction of the analytical model with the single stage results reported by Turner and Sparkes. However, in both of the multistage comparisons, the agreement between the predicted and the experimental results were poor. The net pressure losses predicted by the model tended to be more than 100% greater than the actual measured losses. In retrospect, the major weakness of the model appears to be a failure to adequately account for

the three-dimensional aspects of reversed flow flowfields (especially the presence of strong radial flows) within multistage axial flow compressors.

3.3 LITERATURE REVIEW SUMMARY

As one reviews the technical literature on the performance of various pump and compressor configurations, the general trends illustrated in Figure 29 begin to emerge. The Karman-Knapp Quadrant I and IV performance characteristics shown in Figure 29a appear to be typically representative of low lift pumps and centrifugal compressors and blowers. This characteristic is essentially continuous with smooth performance transitions from unstalled flow to rotating stall to reversed flow. There is a substantial amount of literature which indicates that abrupt flow changes do not usually occur in these machines.

In Figure 29b, a generalized performance characteristic of a single-stage axial flow fan or compressor is depicted. Although four discontinuous characteristics corresponding to unstalled flow, part span multi-cell rotating stall, full span rotating stall, and annulus stalled flow can be distinctly identified; the discontinuities between these flow modes do not appear to be great.

The most drastic flow mode changes occur in the multi-stage axial flow compressors usually found in aircraft gas turbine engine applications (Figure 29c). Three regimes of flow mode performance are identifiable: unstalled operation, full span rotating stall, and axisymmetric stall. A hysteresis loop appears to exist only at the flow mode transitions from unstalled flow to rotating stall.

Little is known about the transition from rotating stall to annulus stalled flow at low positive or negative flow coefficients. In fact, a complete set of measured steady state characteristics for a multistage axial flow compressor (like that depicted in Figure 29c) does

61

not appear to exist in the open literature. More importantly, detailed measurements of reversed flow or annulus stalled flowfields have never been performed and reported.

Currently, there are no reliable analytical methods for treating annulus stalled flowfields. Existing analyses are usually based upon overly simplistic steady two dimensional flow assumptions of the flowfield structure. Multistage analyses are merely extensions of isolated cascade loss models. To date, the effects of radial flows upon annulus stalled flowfield processes have not been seriously considered. In this thesis, it will be shown that the reversed flow flowfields of modern axial compressors are dominated by three dimensional throughflow and recirculatory flow patterns.

Chapter 4

EXPERIMENTAL APPARATUS AND TECHNIQUES

The original design and construction of the MIT 3-Stage Low Speed Compressor Test Facility was accomplished by Eastland [47]. At the time that this experimental investigation began, the existing facility was configured to generate time-averaged data of compressor rotating phenomena at positive axial flow rates. In order to conduct an experimental investigation of compressor reversed flow performance, a substantial facility redesign effort had to be initiated. Most of the major facility components (i.e. drive train, throttle, and data acquisition system) as well as the overall physical layout of the exhaust system ducting were modified from the original design. The first portion of this chapter will be dedicated to documenting these design changes and providing a general description of the test facility. A detailed description of the *unmodified* facility components will be omitted in lieu of a reference to the original work of Eastland [47].

The remaining two sections of the chapter deal with instrumentation, the data acquisition system, and experimental techniques. Although a prior capability existed to acquire steady-state performance data, there was no existing capability to acquire high response flowfield information. Section 4.2 describes the data acquisition system that was developed to acquire, record and reduce unsteady reversed flow velocity and pressure field data. One of the accomplishments associated with this phase of the investigation was the development of a synchronous or double phase-lock triggering system. Finally, the experimental techniques

63

used to acquire unsteady three-dimensional flowfield information will be reviewed in the remaining section of this chapter.

4.1 COMPRESSOR TEST FACILITY

A simplified schematic of the 3-stage compressor test facility which existed at the MIT Gas Turbine Laboratory prior to 1982 is displayed in Figure 30. Conceptually, the major components of this facility are a simple compressor-plenum-throttle compression system (described earlier in Section 2.1) plus two large downstream volumes (separated by an orifice throttle) and an exhaust fan. The two large downstream volumes correspond to the exhaust ducting which channels the test compressor's discharge flow out of the test cell. The exhaust fan is a high volumetric flow industrial blower. This fan was placed at the exit of the system to provide a capability for varying the slope of the test compressor's throttle characteristic by reducing the back pressure behind the conical throttle.

The main goal of the initial engineering redesign and facility modification portion of this thesis effort was to provide a means for establishing reverse and zero mass flow conditions in the test compressor. The reversed flow requirement was implemented by reversing the test compressor on its support stand and using the exhaust fan. The zero flow requirement was met by redesigning the conical throttle to seal the exhaust duct when in a fully closed position. The following subsections describe the resulting facility design that emerged from the reconstruction phase of the project.

4.1.1. Facility Design Considerations

A general layout of the modified test facility is presented in Figures 31 (overhead planform view) and 32 (side view). Photographs of the test facility appear in Figures 33 and 34. In the reverse flow configuration, air is drawn in from the test cell surroundings

64

through a flared inlet which is attached to the exit flange of the test compressor. The flared inlet forms the outside wall of the inlet annulus. The inner wall is defined by a cylindrical centerbody which supports the drive train. A FOD (Foreign Object Damage) screen is placed over the intake to prevent ingestion of solid objects which could damage the compressor.

After passing through the compressor (which is working against the direction of the flow), the fluid enters a relatively small plenum volume at sub-atmospheric pressures. The flow then passes through an adjustable conical nozzle which is used to control the mass flow rate through the facility. Once past the conical nozzle, the flow enters a series of flow straightening devices: a porous screen, followed by a honeycomb section, followed by a second porous screen. Next, the flow passes through a flow measurement orifice, an elbow section in the ducting, and then the centrifugal exhaust blower.

In order for reversed flow conditions to be established in the test compressor, the stalled[12] pressure rise performance of the exhaust fan must be equal to the sum total of all the losses associated with the flow through the facility ducting plus the pressure drop created by the test compressor. A system pressure loss analysis was conducted to determine the feasible range of operation for the facility. This analysis was formulated to provide a map of the possible flow coefficients and pressure rise coefficients which could be established in the test compressor as a function of test compressor rotational speed and a given static pressure rise capability of the exhaust fan. The results of this analysis are presented in Figure 35. In addition, the complete derivation and discussion of the equations and assumptions of the system feasibility analysis are presented in [71].

---

[12] The expected mass flow rates through the facility were predicted to range from 0-3 lbm/sec. Since the design mass flow rate of the exhaust fan is approximately 18 lbm/sec, the exhaust fan will be operating in a stalled flow regime throughout the reverse flow test series.

For an assumed exhaust fan static pressure rise capability of 16 in. H_2O, an inspection

of the general trends depicted in Figure 35 reveals that a maximum reverse flow coefficient

of $\bar{C}_x/U = -0.33$ is achievable at a test compressor rotational speed of 1000 RPM. At

lower flow coefficients, the same nondimensional conditions can be maintained at higher test

compressor rotational speeds for a given maximum pressure rise capability of the exhaust fan.

Subsequent tests showed that the maximum pressure rise capability of the exhaust fan was

considerably higher than originally estimated (about 24 in. H_2O). As a result, no difficulties

were encountered with respect to establishing a broad range of reverse flow operating

conditions in the test compressor.

4.1.2. Compressor Drive Train

The drive unit for the facility is a (50 year old) electric dynamometer[13] manufactured

by the Sprague Electric Works Division of General Electric Company (Serial #634869).

This 250 volt, 885 ampere dynamometer has a maximum rated shaft rotational speed of 1500

RPM and power output (at this speed) of 375 Hp. The belt drive system designed by

Eastland [47] uses 8 Browning 5vx Gripnotch belts on sheaves with a diameter ratio of 2.13.

This belt drive system sets the maximum compressor speed at 3200 RPM. At this speed,

the belts are rated to transmit a maximum of 228 Hp.

A diagram of the compressor drive train with the new modifications appears in Figure

36. The first section of the compressor drive train is a 26" length of 1-15/16" diameter

---

[13] A startup and shutdown checklist for the operation of this dynamometer is given in [71].
In order to maintain normal compressor shaft rotation, the direction of rotation of the
dynamometer was reversed by rewiring the dynamometer's motor field circuit.

steel shaft on which the smaller drive belt sheath is mounted. This shaft is supported by two SKF type SAF 22511 pillow blocks which house split taper roller bearings. A life expectancy safety analysis of this design is given by Eastland [47]. During operation, the oil lubricant escapes past the seals of the bearing housing as a fine mist at a low rate. Since the facility is intended to be in operation for long periods of time without a shutdown to check the oil level, surface Type K thermocouples were affixed to the bearing housing as a precaution. Real time continuous readout of the bearing temperatures is given by solid state Omega Model 115KF digital thermometers which are mounted on the operator's main control panel. The two thrust bearings in the test compressor and the two roller bearings on the exhaust fan drive train were similarly instrumented and monitored.

The remaining portion of the drive train is supported by the inlet cylinder through the torquemeter support mount. Since the test compressor is now being driven from the aft end of the rotor shaft, a new rigid coupling for the drive train and a new compressor mounting flange to support the cylindrical inlet centerbody piece were designed. The net effect of these modifications was to increase the length of the drive train on the compressor side of the torquemeter. Conversely, the location of the torquemeter and the supporting cylindrical inlet was canterlevered 5" further away from the internal aft mounting flange of the compressor. This redesign places a significant amount of moment on the supporting center body struts of the compressor (eight 1/2" diameter bolts). As a result, two adjustable turnbuckle supports with mounting studs were placed at the torquemeter end of the cylindrical inlet piece to relieve the moment about the main compressor center body support struts.[14]

---

[14] If the turnbuckles are not properly adjusted, these struts deflect and the entire compressor rotor becomes locked.

67

The new drive train rigid coupling is composed of a shaft adapter piece and a complementary stub shaft mating piece. The shaft adapter piece is attached to the aft end of the compressor shaft as shown in Figure 37. The entire shear load of transmitting the required power to the compressor is borne entirely by two 5/16" diameter UNBRAKO hardened dowel pins (heat treated alloy steel). These pins have a double shear strength of 23,000 lb_f and are placed at a 0.59" radius from the centerline of the shaft so the maximum expected torque which can be transmitted by these two pins is approximately 13,000 in-lb_f. At a rotational speed of 3200 RPM, this translates to a maximum power transmission capability of 110 Hp.

The drive train is assembled by bolting the shaft adapter to the aft end of the compressor shaft with two modified 1/4-28 socket head cap screws. The stub shaft mating piece is bolted to the shaft adapter piece as indicated in Figure 37. Next, the nominal 18" length 1-1/2" diameter shaft piece is connected to the stub shaft with a Browning CSP rigid coupling. This coupling employs a tapered sleeve fit and slotted keyway mechanical arrangement. At this point, the entire compressor assembly can be physically rotated from its normal vertical orientation during assembly to a horizontal position. After installing the flared inelet and cylindrical inlet support piece to the compressor's aft end O.D. and I.D. mounting flanges respectively, the entire assembly can be mounted on the test stand using the facility's overhead crane. Once on the test stand, the cylindrical inlet support turnbuckles should be immediately adjusted to insure that the compressor rotor spins freely (see footnote 13).

Before the torquemeter is installed on its mounting platform inside the cylindrical inlet piece (see Figure 34), the 1-15/16" diameter drive belt shaft must be aligned with 18" length 1-1/2" diameter shaft using tooling specially designed for this purpose. Axial and

68

angular alignment is accomplished by adjusting the main compressor mount turnbuckles as described by Eastland in [47]. Finally, assembly of the drive train consists of installing the torquemeter and the two Browning GC15E gear type flexible couplings. Great care should be taken to insure that the flexible couplings are installed according to the specifications set forth in [48].

4.1.3. Test Compressor

The three-stage test compressor was originally designed in the late 1960's during Pratt & Whitney's JT9D high pressure compressor development program. This compressor was used to test proposed blading for the thirteenth, fourteenth and fifteenth stages of the JT9D compressor [49]. From September 1, 1973 to August 1, 1974, this compressor was tested at United Technologies Research Center (UTRC) with cantilevered stators using low aspect ratio-redesigned endwork (LAR-REW) blading in all three stages [50]. In 1980, this compressor was removed from storage, inspected, assembled, dynamically balanced, and shipped to the MIT Gas Turbine Laboratory for the rotating stall measurement test series conducted by Eastland [47].

4.1.3.1. Builds Tested

A detailed assembly drawing of the test compressor is shown in Figure 38. The general specifications for this compressor are given by Christianson in [51], Eastland in [47] and are reproduced in Table 1. The compressor assembly has a constant flowpath annulus with a casing inside diameter of 24.000" and a hub diameter of 21.115" (0.88 hub-to-tip ratio). The three stages are non-repeating. The aspect ratio of the LAR-REW blading averages 0.8 for the rotors and 1.17 for the stators. A picture of the blading is shown in Figure 39.

69

During the present test series, two compressor builds were tested. Both builds used the same blading and had the same meanline based design flow coefficient (about $\bar{C}_x/U = 0.6$). However, the first build was tested at blading stagger settings which corresponded to a reaction of 0.64 and the second build was tested at a reaction of 0.74. Table II contains a list of the predicted performance for the two builds and Table III contains a listing of all the pertinent blading information of the two builds. (Figure 40 defines the blade angle relationships given in Table III).

An inspection of Table III reveals that the rotor angle stagger settings were increased by 5° to generate the second build configuration and the stator stagger angle settings were decreased by 10°. Figure 41 shows the location of these two builds on a map of stator and rotor stagger angle settings for a given value of flow coefficient and overall reaction at a 2400 RPM operating condition.[15] Henceforth, the 0.64 reaction build will be referred to as the medium reaction build. The 0.74 reaction build will be designated as the high reaction build. All the high response flowfield measurements were obtained from the high reaction build.

4.1.3.2. Restagger Procedure

To restagger the compressor's blading, a complete disassembly of the compressor is required. Next, individual blades must be removed, cleaned and then reinstalled with the special tooling that was designed for this process during this thesis effort. Finally, the compressor must be reassembled by restacking each individual bladerow on top of the previous bladerow.

---

[15] This parametric map was generated by J.T. Lewis [52] at Pratt & Whitney GPD.
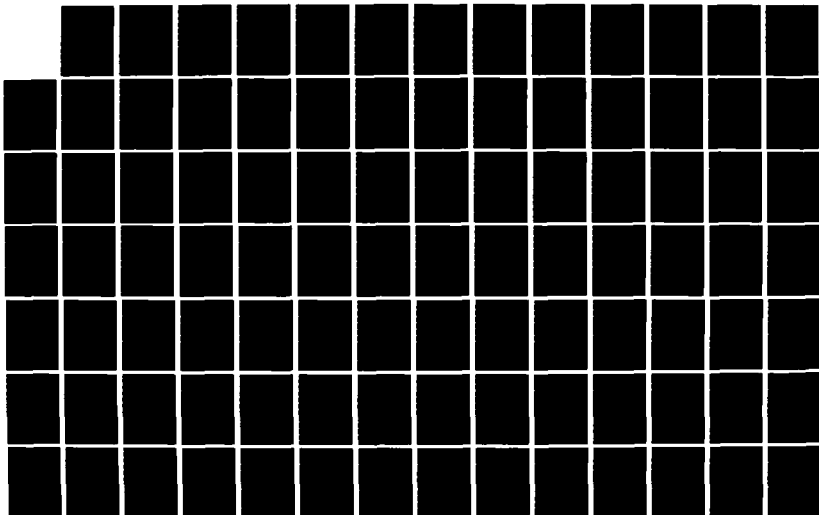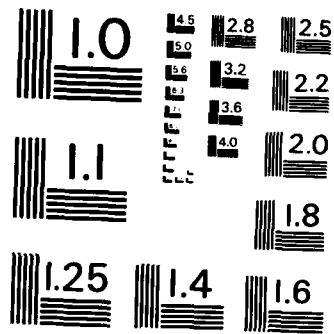
A special compressor disassembly stand was designed and frabricated. The stand is essentially an I-beam reinforced 3/4" thick steel flat plate with a 6" deep steel flange. The inner and outer diameter of this flange matches the main front end mounting flange of the compressor. Disassembly begins by disconnecting the drive train, removing the torquemeter and both inlet pieces, and vertically stacking the compressor on the disassembly stand with the front end down and the aft end up. The four-phase, 13-step complete compressor builddown procedure that was developed is summarized in Table IV.

Once the compressor has been disassembled, each individual blade was removed, cleaned and inspected for damage. The existing blades are cast aluminum and should be replaced[16] if any cracks are detected (especially along the roots of the rotor blades). In order to set the blade stagger angles, a set of low cost stagger tooling was designed and fabricated to reproduce the blade assembly technique employed by UTRC [53]. This tooling allows a skilled machinist to set the stagger angle of each blade to within (conservatively) ± 0.25 degrees of the required value.

Compressor reassembly is accomplished by restacking the individual bladerows and stages. Extreme care must be exercised to insure that each of the casing rings and rotor disks are completely free of dirt and metal chips during reassembly. Otherwise, the cummulative effect of stacking even subtly misaligned components will cause potentially severe axial misalignments and a reduction of the already tight hub (0.034 in.) and tip (0.037 in.) clearances.

---

[16] Bradbury [54] is the reference which contains the design specifications for the existing blading.

71

4.1.3.3. Instrumentation Slots

A major goal of the detailed flowfield characterization measurements was to resolve the flowfield to spatial scales less than the order of a single blade passage. To achieve the circumferential direction spatial resolution requirement, the interbladerow case spacing rings had to be modified. Figure 42 depicts the case spacing ring modification that was required to provide a capability for circumferentially traversing the flowpath annulus. Figure 43 shows the instrumentation support mount which slides through the 30° arcs that were machined into the case spacer rings.

The two designs illustrated in Figures 42 and 43 provide a capability for traversing probes, up to a maximum diameter of 3/8", through a circumferential arc of 10°. The inside diameter of the sliding support mount extends over a 20° arc and provides a continuous annulus wall over several blade passages on either side of the instrumentation port. The sliding support mount was designed to be equal to the task of supporting a computer controlled probe traversing mechanism[17] for performing radial and yaw angle sweeps at a given axial and circumferential position. Twelve of these high response instrumentation ports were added. The location of stations 2 through 11 are shown in Figure 36; while the remaining two instrumentation slots were placed on the inlet and exit case spacing flanges of the compressor.

4.1.4 Exhaust System

There were two immediate impacts upon the design of the exhaust system ducting associated with physically reversing the orientation of the compressor and lengthening the drive train. First, a new downstream annulus assembly had to be designed to connect the front end of the compressor with the exhaust plenum and the throttle assembly (while

---

[17] The computer controlled traversing mechanism is described further in Section 4.2.2.1.

72

maintaining the integrity of the flowpath annulus). A toroidal inlet with a 2:1 ellipse section was attached to the inner diameter of this new downstream connection assembly to avoid a step increase in the flowpath during low positive or forward flow rate operation[18]. This new assembly is illustrated along with the modified throttle assembly in Figure 44.

The second major impact on the exhaust system design was the need to shift the ground level exhaust ducting 6-1/4" further aft. This need was satisfied by relocating the turnbuckle support mounts on the main support frame and by inserting a 6" honeycomb duct section (with a 1/4" neoprene gasket) in the upper level duct work. This "deswirling" section was placed in the approach leading to the orifice mass flow measurement station as shown in Figures 31 and 32 to preclude the possibility of streamwise vorticity induced mass flow measurement errors.

The next two subsections deal with the conical throttle redesign effort and the exhaust fan which establishes the reverse flow conditions in the test compressor.

4.1.4.1. Throttle Assembly

A good discussion of the fabrication of the basic mechanical components of the conical throttle assembly is given by Eastland [47] and will not be repeated here. However, some features of the mechanical design made the existing throttle assembly inadequate for achieving zero mass flow conditions.[19] In addition, a complimentary control system for positioning the throttle had to be designed and implemented.

---

[18] A step increase in the return flowpath could cause flow separation and a radial distortion of the inlet velocity profile to the compressor at low positive mass flow rates.
[19] In fairness to Eastland [47], it should be pointed out that the establishment of zero mass flow conditions was not an original facility design requirement.

The mechanical modifications that were implemented are illustrated in the throttle assembly depicted in Figure 44. Two leak paths had to be sealed. The first leak path was at the point where the movable throttle piece meets the inside wall of the dump plenum. Part of the problem at this location was the fact that the conical throttle piece was fabricated by rolling and welding a section of 1/4" aluminum plate. As a result, the conical section was out-of-round and could not seal over the entire circumference of the entrance duct[20] leading to the dump plenum. To alleviate this problem, an aluminum flat plate contact surface was bolted to the inner wall of the dump plenum. In addition, a concentric aluminum ring with a matching flat surface was welded to the conical surface as shown in Figure 44. Gasket material was epoxied to both surfaces to insure that a good seal is achieved.

The second physical leak path was through the center of the conical throttle piece past the two power screws and D.C. gear motors. To block this leak path, the entire throttle drive system was enclosed by welding a cylindrical extension to the downstream side of the movable conical piece. A rear access plate was bolted to this extension to complete the seal and provide a means for accessing the throttle drive and control system.

The basic components of the throttle control system are a main power circuit, a safety control circuit, and a throttle position indication circuit. The main power circuit controls the speed and direction of rotation of the two D.C. gear motors which drive the power screws that linearly displace the conical throttle assembly. This main D.C. power circuit is wired in parallel through the contacts of a normally open and a normally closed power relay.

The coils of these power relays are part of two separate microswitch activated safety circuits. These microswitch activated safety circuits are energized by a dedicated 12 VDC 1.2A unregulated power supply. These safety circuits provide the means for disengaging the

---

[20] The entrance duct was also out-of-round.

existing direction of rotation of the D.C. gear motors and illuminating a control panel lamp when the throttle has reached a fully open or closed position. A normally open and a normally closed power relay were required to disengage one direction of rotation, while maintaining the ability to command the opposite direction of rotation.

The position indication circuit consists of a 6" range Trans-Tek Series 240 linear voltage-displacement transducer (LVDT), a regulated 15 VDC power supply, and a Nonlinear Systems Model PM-349 digital panel meter. The Trans-Tek LVDT produces a linear D.C. voltage output as a function of throttle position. This signal is offset and scaled by a series of operational amplifiers and adjustable potentiometers to display a 0-100% throttle position reading on the digital panel meter.

4.1.4.2. Exhaust Fan

The facility exhaust fan was a Champion Design Eleven [55] size 300 SISW double camber airfoil centrifugal fan. A Litton Industries' Pacemaker[R] continuous three-phase 75 Hp electric motor was used to drive the fan via a belt drive. As a unit, the exhaust fan had a design point static pressure rise of 23 in. H_2O at a volumetric flow of 14,600 cubic feet per minute and a shaft rotational speed of 2660 RPM.

The general shape of the stalled performance characteristic of this fan is roughly given by the characteristic displayed in Figure 29a. In order to conduct the series of low flow and zero flow tests reported in this thesis, it was essential that the stalled performance characteristic of the exhaust fan actually be as shown in Figure 29a. If the stalled performance characteristic of the exhaust fan had decreased sharply with a decrease in mass flow rate, two problems would have surfaced. First, the exhaust fan would not have been able to produce enough pressure rise to overcome the pressure loss generated by the test

75

compressor and the facility loss producing sources. In terms of the facility performance map shown in Figure 33 (see Section 4.1.1.), the constant fan performance curve represented by a straightline on Figure 33 would have dropped sharply with decreasing flow coefficient.

The other problem that could have arisen is related to compression system dynamics. If the stalled performance characteristic of the exhaust fan had been positively sloped (i.e. a drop in performance with a decrease in mass flow), there is a possibility that the simple compression system formed by the fan, the second large downstream volume depicted in Figure 30, and the orifice throttle could have become dynamically unstable. In the parlance of Chapter 2, this portion of the test facility could have undergone surge limit cycle oscillations.

In addition to the favorable stalled performance characteristic, the exhaust fan is equipped with variable inlet guide vanes. A Bodine Type NCI-12 1/50 Hp A.C. motor was installed to control the position of these inlet guide vanes. A power circuit with microswitch interrupts and an IGV position indication circuit (similar to the throttle circuits described in the previous section) were designed and installed to control the exhaust fan IGV position from the test facility's main control panel.

4.1.5. Orifice Plate

Although it is possible to use a calibrated inlet to measure flow rate while the test compressor is operating in the annulus stalled reverse flow (and the unstalled flow) operating regime, Greitzer [6] and Day [12] have shown that serious flow measurement errors will occur during operation in rotating stall. These flow measurement errors occur because the presence of a rotating stall cell creates a non-uniform inlet flowfield. In order to measure a complete set of Kármán-Knapp Quadrant I and IV characteristics, including operation in rotating stall, it became necessary to use a downstream orifice plate as a flow measurement device.

76

An excellent discussion on the use of orifice plates as flow measurement devices is given by Ower and Pankhurst [56]. In principle, mass flow is determined by measuring the pressure drop across a constriction in the flow. As a result, the size of the pressure drop associated with a given mass flow rate becomes the basic design tradeoff when sizing an orifice plate constriction for an application. If the constriction is not great enough (large hole); the pressure drop is small and can fall below the accuracy of the pressure measurement instrumentation. In addition, the orifice plate based[21] Reynold's Number can fall below a value of 10^4. Below this value, the relationship between pressure drop and mass flow becomes Reynold's Number dependent. On the other hand, if the constriction is too great (small hole); the pressure drop is high and can seriously limit the facility's range of operation (see the system pressure loss analysis in [71]).

The constriction of the orifice plate designed by Eastland [47] was sized to operate at a test compressor flow coefficient of 0.8. During the planned reverse flow test series, it was estimated that the maximum flowrate through the facility would be a flow coefficient $\bar{C}_x/U$ = -0.25. As a result, an orifice plate sizing design study and a subsequent calibration of the selected design was conducted at the outset of this thesis effort.

4.1.5.1. Design Summary

The basic relationship between mass flow and pressure drop across an orifice plate can be derived by combining the incompressible continuity and Bernoulli equations to yield the

---

[21] The orifice plate based Reynold's Number is defined as the velocity of the jet through the constriction multiplied by the diameter of the constriction and divided by the kinematic viscosity of the fluid at the constriction.

77

following expression

$$\dot{m} = A_{op} \sqrt{\frac{2\rho\Delta P_{op}}{1-(A_{op}/A_{duct})^2}} \qquad (4-1)$$

where A_{op} is the area of the orifice hole and A_{duct} is the crossectional area of the upstream ducting (7.068 ft^2).

In reality, there are some frictional and turbulent energy losses as well as flow separation associated with flow through a constriction. The flow separation causes a "vena contrasta" or a minimal flowthrough area to become established. To account for these losses, Ower and Pankhurst [56] recommends multiplying through the RHS of Equation 4-1 by the following empirically based discharge coefficient

$$\alpha = 0.5959 + 0.0312 \left(\frac{A_{op}}{A_{duct}}\right)^{1.05} - 0.184 \left(\frac{A_{op}}{A_{duct}}\right)^4$$

$$+ 0.0029 \left(\frac{A_{op}}{A_{duct}}\right)^{1.25} \left[\frac{10^6 \sqrt{A_{op}/A_{duct}}}{Re_{op}}\right]^{0.75} \qquad (4-2)$$

If there are no leaks in the ducting between the test compressor and the orifice plate measurement station, Equation 4-1 can be rewritten in the following convenient form

$$\frac{\bar{C}_x}{U} = K \frac{\sqrt{\rho_{op} \Delta P_{op}}}{\rho_c U} \qquad (4-3)$$

where K is defined as the orifice plate calibration coefficient.

K is defined by the following empirical relation

$$K = \alpha \frac{A_{op}}{A_c} \sqrt{\frac{2}{1 - (A_{op}/A_{duct})^2}} \qquad (4-4)$$

where the discharge coefficient α is given by Equation 4-2 and A_c is the flowthrough area of

the compressor annulus (0.7087 ft^2).

A parametric design study was conducted by varying the average flow coefficient, the

compressor rotational speed, and the orifice plate hole diameter as the independent variables.

The resulting analysis produced an orifice plate design with a 6.0 in. diameter hole.

In the Reynold's Number invariant regime, the predicted orifice plate calibration

coefficient for this design was $K = 0.234$. Furthermore, the pressure drop associated with a

$\bar{C}_x/U = -0.25$ and a rotational speed of 1200 RPM was predicted to be $\Delta P_{op} = 7.29$ in.

H_2O. The suitability of this orifice pressure drop was evaluated during the system pressure

loss analysis [71] and the design was judged to be reasonable in terms of this system design

constraint. At a rotational speed of 2400 RPM, a pressure drop of $\Delta P_{op} = 1.17$ in H_2O

would be realized at a flow coefficient as low as $\bar{C}_x/U = -0.05$. Since the accuracy of

79

the scanivalve pressure transducer is of the order of 0.025 in. H_2O, this pressure drop was judged to be sufficient for adequate accuracy.

4.1.5.2. Calibration Results

An orifice plate and compressor inlet mass flow calibration was accomplished by using the exhaust fan to establish a flow through the facility. During the calibration test series, the test compressor was allowed to freely windmill. The conical throttle assembly was used to adjust the flow rate through the facility. In this way, an inlet Reynold's Number range of 2.98×10^4 to 2.64×10^5 and an orifice plate Reynold's Number range of 3.58×10^4 to 3.58×10^5 were established.

The mass flow through the facility and the blockage associated with the inlet boundary layers was determined by performing radial traverses of the test compressor's inlet annulus with a standard United Sensor cobra type total pressure probe. Wall static pressure taps on the inner and outer diameter of the inlet annulus were used to measure the inlet static pressure. In addition, wall static pressure taps on either side of the orifice plate were used to measure the orifice plate pressure drop.

A brief description of the orifice and inlet calibration data acquisition and reduction as well as several measured inlet dynamic pressure profiles are presented in Appendix A. The results of the inlet calibration are plotted in Figure 45 and given by the following expression for inlet blockage ratio

$$\frac{A_B}{A_c} = 1.3004 \left(Re_{Inlet}\right)^{-0.2397} \tag{4-5}$$

where Re_{inlet} is the inlet based Reynold's Number. The above expression represents the best least squares curve fit of the measured blockage data. The standard deviation of this blockage ratio vs. inlet Reynold's Number curve fit is $\sigma = 0.0033$. Table V contains the results of a flow coefficient probable error analysis at several facility flow rates and test compressor rotational speeds.

The results of the orifice plate calibration are plotted in Figure 46 and represented by the following expression for the orifice plate calibration coefficient

$$K = 0.2339 - 8.4743(Re_{op})^{-0.5086} \qquad (4-6)$$

where Re_{op} is the orifice plate based Reynold's Number. Again, this expression represents the best least squares curve fit of the calibration coefficient vs. orifice plate Reynold's Number data with a standard deviation of $\sigma = 0.0043$. In an analogous fashion, Table VI contains the results of an orifice plate based flow coefficient probable error analysis. The results of the error analysis reported in Tables V and VI were considered acceptable levels of mass flow measurement error.

4.2 DATA ACQUISITION SYSTEM

The automated data acquisition system that evolved during this axial compressor reverse flow experimental effort can be conceptually treated in three categories. First, there are the computer based data acquisition components of the facility. Each component acquires the relevant data according to programmed software instructions and transmits this information to

81

the dedicated on-line digital computer through a series of interfaces. The function and operation of this generic data acquisition equipment will be briefly summarized in Section 4.2.1. The second category deals with the actual instrumentation and signal conditioning equipment required to measure time-averaged physical processes and convert these measurements into an electrical signal for input into the facility's generic data acquisition equipment. This category is treated in Section 4.2.2. Finally, the last category deals with the instrumentation and signal conditioning associated with the measurement of unsteady physical processes.

4.2.1. Overall Acquisition Architecture

A schematic diagram which summarizes the basic relationships between the various computer based data acquisition hardware components is shown in Figure 47. The sheer volume of the data acquisition software that is required to operate these hardware components prohibits inclusion of source listings in an appendix. Instead, source listings of all the data acquisition, reduction and plot software can be found in an attachment to [71].

4.2.1.1. Dedicated Computer

A Digital Equipment Corporation (DEC) LSI-11/23 minicomputer was used to acquire and process all the data reported herein. Although this minicomputer runs on a RSX-11M Plus multiuser operating system, this computer was dedicated to the 3-Stage Compressor Test Facility during tests by task building all data acquisition programs on a privileged account with a priority level just below the system operating level. Access to the minicomputer is provided by a DEC VT-100 terminal. Data and software storage is accomplished through the use of either a floppy disk drive or a Winchester hard disk drive (3 disks). Plotted and printed output can be obtained from a Versatec V-80 printer. Finally, one of the RS-232

terminal lines was reconfigured on a slave mode to integrate an Analog Devices Model μMAC-4000 temperature multiplexer into the system. Fink [57] gives a similar, and in some circumstances, a more detailed description of this basic system.

4.2.1.2. Parallel Interface Bus

The LSI-11/23 is equipped with a GPIB parallel interface bus. This bus gives the minicomputer the capability of directly transmitting or receiving information to/from any IEEE-488 compatible instrument. Three such real time data analysis instruments were interfaced with the LSI-11/23 in this manner: a Hewlett-Packard 3501B frequency counter, a Tektronix 468 digital storage oscilloscope, and Hewlett-Packard 3582A digital storage spectrum analyzer. The software required to acquire data from each of these instruments through the GPIB interface is listed in the attachment to [71].

4.2.1.3. Analog-to-Digital Converter

A software programmable Datel A/D Converter is directly mounted in the LSI-11/23 printed circuit board rack assembly. User access to the Datel A/D Converter is provided by a specially constructed multiplexing interface box. This interface gives the user the capability to multiplex up to 16 analog signals and introduce an external trigger through standard BNC connectors. The analog voltage scale, digitizing frequency, internal or external triggering mode, and the desired channel(s) to be converted are controlled by software programming.

The maximum resolution is set by the selected voltage scale and the 12 bit length constraint of the A/D converter. To determine voltage resolution, one must remember that

one bit is used to define the sign of the analog voltage. This leaves 11 bits to resolve the entire voltage range, i.e. 2^{11} or 2048 divisions. For the minimum voltage scale option of ±1.25 volts, this A/D converter is capable of resolving voltage to within 0.61 millivolts.

The maximum conversion frequency was determined through tests to be 43 KHz. Analog-to-digital conversion breakdown occurs at higher sampling rates. In addition, the LSI-11/23 line timer clock must be manually switched off before attempting to acquire high response voltage time traces with the Datel A/D converter. Otherwise, the LSI-11/23 time updating system interupts the data transmission enable signal between the A/D converter and the minicomputer and time trace data can be lost.

4.2.1.4. Automated Probe Traverser

Through interactive or pre-programmed software, a user can instruct the LSI-11/23 to position an instrumentation probe at a precise radial position (±0.004 in.) and angular orientation (±0.180 deg) in the test compressor. Without this capability, the detailed flowfield measurements reported in Chapter 6 would have been nearly impossible to acquire. The minicomputer controls the position of an instrumentation probe through a DRV-11 driver board and the Datel A/D converter.

J1 and J2 strip-wire cables connect the DRV-11 board with an intermediate interface connection box. A single 13 conductance cable connects this interface with a specially modified L.C. Smith traverse mechanism controller. Finally, a standard configuration L.C. Smith model BBS-8 SM-360 SM 1/4" probe actuator with stepping motor drive is used to translate and rotate the instrumentation probe. Probe position is detected through the use of 10 turn, $1K\Omega$, 0.1% linearity potentiometers. The signal generated by this potentiometer circuit is transmitted by the controller through the intermediate interface to A/D converter channel #1 (translation position) and #2 (orientation) as 0-10 volt scale analog signals.

84

4.2.1.5. Scanivalve

A DRV-11 board is used by the LSI-11/23 minicomputer to control the operation for a 48 pressure port scanivalve. The J1 and J2 40 conductance strip lines from this second DRV-11 board are routed to a scanivalve interface designed by Eastland [47]. This interface is directly connected to a standard Scanivalve SSS-48C pneumatic scanner. Fink [57] gives a complete description of the detailed operation of this circuit.

A single Spectra strain gauge type ±2.5 psid pressure transducer is mounted in the scanivalve assembly along with an amplifier signal condition unit with zero and span adjustment controls. A calibration of this pressure transducer was performed on this transducer using a MKS Baratron as a reference standard. The calibration results indicate that there is a linear curve fit standard deviation of $\sigma = 0.025$ in. H_2O. These results are presented in Appendix B.

4.2.1.6. Real Time Clock

A Data Translation DT2769 programmable real time clock was installed in the LSI-11/23 to synchronize the Datel A/D conversion with an external real time pulse from a specially developed synchronous trigger circuit. This programmable clock operates as follows.

A MACRO language computer subroutine (DUMBLE) enables or "cocks" the DT2769 clock. This software controlled enable command instructs the clock to test for an output signal from one of the clock's two internal Schmidt Triggers (ST #2). This Schmidt Trigger generates an output when the analog (TTL) voltage signal at the trigger's input is of a prescribed slope and above a prescribed threshold level. When the next Schmidt Trigger #2 output signal is detected, the clock generates ("fires") an overflow pulse train at a software prescribed

frequency. Once the Datel A/D converter has completed the desired number of software prescribed conversions; the MACRO program "resets" the clock by terminating the pulse train.

In this way, the data acquisition is synchronized to a real time periodic or random external triggering pulse. The synchronous trigger circuit that was developed to provide this external triggering pulse will be discussed in the next section (4.2.1.7.). User access to the DT2769 real time clock is provided by a specially designed rack mounted modular interface. This interface has two sets of Schmidt Trigger threshold and slope controls as well as BNC connectors for the Schmidt Trigger inputs/outputs and a BNC connector for the clock overflow pulse train output.

4.2.1.7. Synchronous Trigger

The triggering circuit depicted in Figure 48 was developed to synchronize or phase lock the data acquisition with rotor position, a periodic flowfield phenomenon, or a synchronization of both phenomena. A rotor phase locked triggering pulse is generated using a fiber optic transmission cable to detect the passage of a uniquely identifiable rotor blade. While the compressor was disassembled, the tips of all but one of the blades from each of the three rotor bladerows were painted flat black. In addition, a compatible port for the fiber optic cable was machined into the case rings above each rotor. The output from an adjustable light emitting diode (LED) is transmitted by an outgoing fiber optic cable to the rotor blade tip clearance region. This illumination is reflected by the one polished blade back through the return fiber optic cable to a photo-detector.

The photo-detector generates an analog voltage signal proportional to the intensity of the light received. This analog signal is input to a Schmidt Trigger which fires a 5 VDC output signal as long as the analog signal is above a preset voltage level. For the given thickness of the rotor blade and an 1170 RPM shaft rotational speed, this Schmidt Trigger output signal

86

has a duration on the order of 50 microseconds. The duration of this signal is reduced to 1 msec by inserting a one-shot in the circuit. This rotor synchronized pulse train can also be sent to the output BNC connector via a three position rotary switch.

To phase lock to a flowfield event (like a rotating stall cell - Day [12]), the analog signal from a flow measurement sensor like a hotwire anemometer or pressure transducer amplifier is input to the synchronous trigger module via a standard BNC connector. This signal is then introduced to a Schmidt Trigger with an adjustable input threshold level. An adjustable one-shot component is used to reduce the duration of this signal to a range between 5-50 msec. Again, the output of this circuit can be directly sent to the output BNC connector by selecting the proper setting on the rotary switch.

A synchronous rotor and flowfield event signal is generated by inputing both output signals to a summing component. This component generates an output pulse when both input signals overlap. Proper selection of the rotary switch setting will direct this synchronized signal to the output connector. This synchronous circuit was a critical component of the system for resolving the unsteady flow processes which exist in axial compressor reverse flowfields.

4.2.1.8. Baratron

A MKS Baratron 170 Series electronic pressure measurement system was interfaced with the DEC LSI-11/23 minicomputer. The minicomputer accesses the Baratron interface module through a DRV-11J board. The binary coded decimal output from the back of the Baratron 170M-27D digital readout unit is transmitted to this interface via a 25 twisted pair shielded cable (25 feet long).

87

4.2.2. Time-Averaged Measurement Instrumentation

4.2.2.1. Pressure

Conceptually, a time-average pressure data acquisition system is composed of a measurement probe, some pressure line tubing, and a pressure measurement device. Figure 49 illustrates the time-average pressure data acquisition system that was employed. During the steady-state reverse flow performance characterization tests (results reported in Chapter 5), 7-element Kiel Head total pressure rakes (illustrated in Figure 50) and wall static pressure taps were used to acquire total and static pressure at the locations indicated in Figure 51. Flexible, color-coded, Tygon Tubing was used to transmit the pressure signal from these probes either directly to a 48 port scanivalve or to an input manifold. From the output manifold, averaged pressure signals could be transmitted to a high accuracy 100 torr Baratron pressure measurement head or a Dwyer Manometer gage. Scanivalve pressure transducer zero drift measurement errors were corrected by dedicating several ports as atmospheric reference ports. The output from the scanivalve pressure transducer was directly connected by coaxial patch cord to channel #15 of the Datel A/D converter.

During the inlet calibration tests described earlier in Section 4.1.5.2., a United Sensor type CA-120-24-F-22-CD cobra head two dimensional probe was used for the radial traverses of the inlet velocity profile. This probe has three measuring ports: one port in the center, and one port on either side of the center position. The advantage of using this type of probe to perform an inlet calibration is that the center port can be used to measure the desired total pressure profile while the two side ports can be continuously monitored to insure that there is no swirl in the flow during the calibration.

A United Sensor type KBC-24 Kiel head probe with a 1/8" diameter sensing head shroud was used to check the time-averaged total pressures at the various axial, circumferential and radial locations of the unsteady reverse flowfield. Kiel head probes are required in this

application because the inherent unsteadiness of the flow causes the instantaneous velocity vector to switch directions. The wider angle of acceptance afforded by the Kiel head design makes this type of probe more suitable for this measurement although caution must be exercised to insure that the instantaneous flow direction changes are not greater than the +40 to 50 degree range of directional insensitivity of this probe.

Finally, a United Sensor type PCC-8-KL pitot static probe was used to measure the velocity of the hot wire calibration jet. These probes return a static and total pressure signal at the desired point in the calibration jet.

4.2.2.2. Temperature

Temperatures were measured with Omega CASS-18E-6 quick-disconnect, exposed junction, type K thermocouple probes. These probes were positioned at the axial and circumferential positions indicated in Figure 51. In addition, two thermocouple probes were positioned 3 feet upstream of the orifice measurement station.[22] These thermocouples were directly wired to an Analog Devices μMAC-4000 temperature multiplexer. The μMAC-4000 has a programmable gain amplifier, a 13-bit dual slope analog-to-digital converter, and a microcomputer which uses an 8-bit processor with 6K of Read-Only Memory (ROM) and 1K of Random Access Memory (RAM). Although the resolution of the μMAC-4000 is approximately $\pm 1/2°F$, the probable accuracy of the measurement is of the order of $2°F$. Since the temperature differences at the low speed conditions under investigation are sometimes small, the quantitative usefulness of the acquired temperature data is somewhat limited on these occasions.

---

[22] These later two temperature measurements were used to evaluate the fluid density at the orifice plate station.

4.2.2.3. Torque and Shaft Rotational Speed

The data acquisition system for acquiring time-average torque and shaft rotational speed is diagrammed in Figure 52. A Lebow model 1105-5K slip ring torque sensor is used to measure torque. Excitation for the torque sensor strain gauge bridge as well as amplification of the bridge output is provided by a precalibrated Lebow model 7530-100 signal conditioning unit. The torque sensor has a maximum capacity of 5,000 in-lb$_f$, a maximum speed rating of 15,000 RPM, and a torque protection overload up to 7,500 in-lb$_f$.

The analog output from the signal conditioning unit is linearly proportional to torque at the rate of 1 volt per 1,000 in-lb$_f$ of torque. This analog signal is input directly to the Datel A/D converter (channel #14). During the operation of the compressor, the output from the torquemeter signal conditioning unit was monitored on the digital storage oscilloscope. At steady state speed conditions, the torque analog signal was observed to fluctuate about a steady state value. To obtain a steady state average torque value, 3000 A/D conversions were performed at an internal pacer clock defined sampling frequency of 512 Hz. It is believed that the gear type flexible couplings at either end of the torque sensor cause these fluctuations by introducing forced torsional vibration in the shaft.

The measured torque value is corrected for the tare torque of the compressor (a function of shaft rotational speed) by using the calibration given by Christianson [50]. This calibration was obtained by removing the compressor blading and measuring the torque input as a function of shaft rotational speed. Shaft rotational speed is measured by a magnetic pickup over a 60 tooth gear. This signal is read directly by an IEEE-488 instrument bus compatible frequency counter.

90

4.2.3. High Response Instrumentation

4.2.3.1. Miniature Pressure Transducers

High response measurements of the unsteady pressure field were made with four miniature pressure transducers mounted in specially constructed probes. A set of rack mounted modular signal conditioning units were designed and constructed to provide the necessary input excitation as well as output amplification for these pressure transducers. The analog output from these signal conditioning units was typically patched through a low pass filter to the Datel A/D converter for the acquisition of the quantitative results reported in Chapter 6. Real time observation and spectrum analysis of the signal was accomplished by connecting the analog output(s) to the digital storage oscilloscope and the digital storage fast fourier transform (FFT) spectrum analyzer described earlier in Section 4.2.1.2. Synchronous triggering of the Datel A/D converter and the digital storage oscilloscope was accomplished by the methods described in Sections 4.2.1.6. and 4.2.1.7. An overall schematic of this data acquisition process is given in Figure 53.

The four pressure transducers were manufactured by Gaeltec Ltd. These transducers have four active strain gages arranged in a wheatstone bridge configuration on a thin silicon wafer. The natural frequency of these transducers is of the order of 50 KHz and the full scale range is ±0.1 psid. The reference pressure for these differential mode transducers was set to atmospheric conditions. The sensitivity of the four transducers ranged from a low of 78.7 μV/in. H_2O to a high of 168.5 μV/in. H_2O. at a D.C. excitation of 5 volts. This sensitivity could be improved somewhat by increasing the excitation voltage. This was not done because the resulting I^2R heating of the transducer caused temperature gradients that seriously affected the zero drift characteristics of the transducers.

91

Even with the low 5 volt D.C. excitation level, zero drift difficulties were experienced with these transducers. Day [12] reports similar zero shift problems. In order to obtain accurate pressure field measurements, these transducers were statically calibrated in a specially constructed calibration chamber located next to the test compressor before and after each set of tests. In addition, the test compressor was given time to warm up before each set of measurements. These precautions became the dominant time-consuming steps associated wtih acquiring the pressure field data. Appendix B contains a pre-test and post-test calibration of one of these pressure transducers.

Since pressure differences on the order of several inches of water were expected at the 1170 RPM operating condition of the compressor,[23] the unamplified output of these transducers was well below the maximum 610 μV resolution of the analog-to-digital converter (see discussion in Section 4.2.1.3.). As a result, an amplifier circuit tailored to the requirements of these presssure transducers was designed. Five amplifiers were constructed (1 spare). The basic amplifier circuit was designed around an Analog Devices model 2B31K signal conditioning unit. A gain-frequency response tradeoff study indicated that the gain of these amplifiers should be set at 500. This gain value produces a resultant transducer output sensitivity range of 39.3 mv/in. H_2O to 84.2 mv/in. H_2O. The measured -3dB cutoff frequency for these amplifiers is about 6 KHz at a gain of 500. Appendix B contains plots of the measured frequency response of the amplifiers. Finally, the amplifier output was filtered by a Thermo Systems Incorporated model 1057 5 KHz low pass filter.

---

[23] This low rotational speed was selected as the best compromise between the desire to cause large pressure differences versus the desire to reduce the temperature gradients and blade passing frequency. The temperature gradients caused by operation at high speed would seriously compromise the usefulness of the hot wire sensors as well as create zero drift problems with the pressure transducers. Higher blade passing frequencies would decrease the resolution of the related unsteady flow processes because both the signal amplifiers and the A/D converter have limited maximum frequency performance.

Two of the pressure transducers were fitted in specially modified Kiel Head total pressure probes. The remaining two pressure transducers were installed at the end of a 2 in. length of 8 gage hypodermic tubing (0.160 in. outer diameter). Both types of probes are illustrated in Figure 54. The original design of these probes was made by Eastland [47]. He calculated a 6.1 KHz frequency response associated with the ducting ahead of the pressure transducer in the Kiel Head probe assembly. Since the static probe is flush mounted, the frequency response associated with this probe is essentially that of the transducer itself. The Kiel Head probe was fitted with a 2 ft. long, 1/4" diameter reinforcement support (holder) in order to traverse the entire assembly using the computer controlled traversing equipment described previously in Section 4.2.1.4.

4.2.3.2. Slanted Hot Wire Sensors

The unsteady velocity field was measured with a slanted hot wire sensor. This sensor was the active leg of a constant temperature anemometer wheatstone bridge circuit. In this type of standard arrangement, the voltage output from the anemometer is a nonlinear function of fluid velocity as defined by King's Law [58,59]:

$$\frac{E^2 R_1}{(R_1 + R_2)} = \left[A + B (\rho V)^{\frac{1}{n}} (T_1 - T) \right]$$

(4-7)

where   A,B = empirical coefficients which vary as a function of fluid properties and type of sensor, i.e. thermal conductivity, viscosity and Prandtl Number.

n = empirical exponent (close to 2);

R_1, T_1 = sensor operating resistance and temperature;

p, V, T = fluid density, velocity and temperature;

R_2 = bridge resistor in series with the sensor;

E = bridge output voltage.

It was more convenient to work with a linearized version of the anemometer analog output signal. Hence, this signal was linearized and filtered before being sent either to the A/D converter, digital storage oscilloscope, or spectrum analyzer as shown in Figure 55.

The slanted hot wire sensors used during this investigation were inclined 45° to the axis of the probe as indicated in Figure 56. These sensors are standard Thermo Systems Incorporated model 1213T1.5 hot wire sensors. The wires of these sensors are platinum coated tungsten and were operated at an overheat ratio of 1.8[24]. The sensing lengths are typically 0.050 in. while the diameters are 0.00015 in. The distance between the probe supports is about 0.060 in. The typical frequency response of these sensors in air at 300 feet per second using a Thermo Systems Inc. model 1050 anemometer is about 600 KHz [58].

These sensors were placed in a 1/4" diameter shielded probe support to permit utilization of the computer controlled traversing mechanism described earlier. In addition, a conventional single wire sensor in a second anemometer circuit was used to provide the flowfield signal for the synchronous trigger described in Section 4.2.1.7. This second sensor was placed just upstream of the test compressor blading as shown in Figure 51. At this

---

[24] Tungsten was chosen as a wire material because of its relative durability. A relatively high overheat ratio was chosen to minimize the effects of freestream temperature variations.

94

location, a "clean" event locked triggering signal could be obtained that was free of any blade passing related unsteadiness. During the course of the testing, this hot wire sensor was replaced with one of the high response total pressure probes. Since it turned out that a more reproducible analog signal could be generated by the pressure transducers for triggering purposes.

4.3 EXPERIMENTAL TECHNIQUES

Before proceeding with a detailed discussion of the experimental techniques that were developed to study unsteady reverse flow phenomena, a few comments about some of the more conventional techniques used to acquire the time-average performance data (reported in Chapter 5) will be briefly summarized. Compressor flow coefficient was determined by measuring the pressure drop across the orifice plate and using a Newton-Raphson numerical root solving scheme to solve the implicit set of equations given by 4-3 and 4-6. Where appropriate, the inlet mass flow calibration given by Equation 4-5 was used to check the values derived from the orifice plate.

An independent measurement check strategy was applied to the acquisition of compressor pressure rise data. Critical pressure difference measurements made by the scanivalve pressure transducer were rechecked using the manifold arrangement described earlier (Section 4.2.1.1.) to transmit the pressure difference signals to the more accurate Baratron or a Dwyer gage manometer. This type of redundancy in the experimental technique increases run time but helps to prevent acquisition of bad data from a faulty instrument. The next three subsections wi... describe the techniques used to acquire rotating stall cell size and speed, and the unsteady three dimensional reverse flow pressure and velocity fields.

4.3.1. Rotating Stall Cell Properties

Although the measurement of rotating stall phenomena was not the primary focus of this investigation, rotating stall conditions were encountered during some of the flow regimes under investigation. Stall cell size and speed data could be easily measured using an uncalibrated hot wire sensor and the digital storage oscilloscope. An uncalibrated hot wire sensor was installed in the test compressor at a midspan radial position just downstream of the inlet guide vanes as shown in Figure 51. When the compressor was operated with a rotating stall cell present, a voltage-time trace similar to the trace shown in Figure 57 would be present on the screen of the digital storage oscilloscope. In this figure, the relatively smooth voltage peaks correspond to the unstalled flow. The low voltage (erratic) portion of the trace corresponds to the flow within the rotating stall cell.

Stall cell duration t_{rsc} is defined as the portion of the trace occupied by the stall cell. Stall cell period T_{RSC} is the time associated with one complete cycle of the voltage-time trace waveform. These two conceptual definitions are depicted on the Figure 57 signal waveform. Assuming only one stall cell is present[25], the rotating stall size and speed can be reduced as follows

$$A_{RSC} = \left(\frac{t_{RSC}}{T_{RSC}}\right) A_c \tag{4-8}$$

---

[25] This assumption can be intuitively checked by computing the resulting stall cell speed as a percentage of the known blade speed. If this percentage is higher than the previously observed trends by day [12] and others, then two or more rotating stall cells are probably present. A single hot wire sensor can not be used to definitively establish the number of rotating stall cells present.

$$U_{RSC} = \frac{2\pi r_m}{T_{RSC}} \qquad \text{(4-9)}$$

In practice, this technique tends to predict stall cell speed with better precision than stall cell size. The reason for this outcome can be explained with respect to the inherent nature of the signal waveform shown in Figure 54. Usually, there is no ambiguity associated with estimating a typically well defined cycle period, i.e. T_{RSC}. Since this variable is the only unknown quantity in the stall cell speed calculation, stall cell speed estimates are reproducibly consistent and the scatter bands are narrow. However, the stall cell size calculation requires an additional estimate of the stall cell duration t_{RSC}. This quantity is usually ill-defined on an oscilloscope trace.

4.3.2. Unsteady Flowfield Measurements

The flowfield of an axial compressor operating under reverse flow conditions is both unsteady and three dimensional. In this section, the experimental techniques that were developed to cope with reverse flow unsteadiness are discussed. Section 4.3.3. will deal with techniques associated with using a single slanted hot wire sensor to acquire three dimensional flow data. To cope with the unsteadiness aspects of the problem, suitable techniques had to be developed for locating the time-averaged mean flow direction and to acquire phase locked ensemble averaged time traces of the instantaneous flowfield variables.

4.3.2.1. Mean Flow Direction

At a given spatial coordinate position in the flowfield, the mean flow direction of a periodically unsteady flow can be conceptually viewed as the time-average direction about

97

which the instantaneous velocity vector fluctuates. In a general periodic unsteady flow, both the magnitude and the direction of the velocity vector will vary. To illustrate the concept of mean flow direction, consider the case where the magnitude of the velocity vector is constant, i.e. $|\vec{C}(t)|$ = constant, but the velocity vector direction fluctuates periodically about a mean direction. For the general compressor coordinate system depicted in Figure 58, this periodic, 3-D, directional unsteadiness case can be expressed mathematically as follows;

$$\alpha_Y(t) = \overline{\alpha}_Y + |\alpha_Y'| \sin(\omega t + \phi_Y) \qquad (4-10)$$

$$\alpha_P(t) = \overline{\alpha}_P + |\alpha_P'| \sin(\omega t + \phi_P) \qquad (4-11)$$

and the following periodicity relations apply

$$\alpha_Y(t) = \alpha_Y\left(t + \frac{2\pi}{\omega}\right) \qquad (4-12)$$

$$\alpha_P(t) = \alpha_P\left(t + \frac{2\pi}{\omega}\right) \qquad (4-13)$$

where $\alpha_y(t)$ and $\alpha_p(t)$ are the instantaneous yaw and pitch angles depicted in Figure 58; $\overline{\alpha}_y$ and $\overline{\alpha}_p$ are the time-average mean yaw and pitch angles (invariant with time)

$\left|\alpha_y'\right|\sin\left(\omega t+\phi_y\right)$ and $\left|\alpha_p'\right|\sin\left(\omega t+\phi_p\right)$ are the periodic fluctuating

components of the instantaneous yaw and pitch angles; ω is the periodic frequency; and ϕ_y

and ϕ_p are arbitrary phase angles.

For reverse flows in the test compressor, the time-average pitch angle and periodic

fluctuating pitch angle were found to be small at the axial gap measurement stations. In

front of the rotor bladerows, the presence of extremely large tangential velocity components

were responsible for the creation of small pitch angles even though significant radial velocity

components were present. In terms of experimental technique, these conditions simplify the

mean flow direction determination problem to two dimensions, i.e. to locating the mean yaw

angle $\overline{\alpha}_y$.

The mean yaw angle $\overline{\alpha}_y$ was determined by rotating the high response Kiel Head probe

upon its axis. The analog signal from the probe was displayed on the digital storage

oscilloscope as well as inputed to the Datel A/D converter. In an interactive fashion, the

probe would be rotated to a commanded orientation by the LSI-11/23 minicomputer and a

time-average sample acquired through the Datel A/D converter. By performing enough of

these interactive measurements, the maximum total pressure reading could be obtained.

This interactive process can be conceptually illustrated by considering the

two-dimensional, constant magnitude, periodic directional unsteadiness case illustrated in

Figures 59a and 59b. The relevant geometry of the measurement problem is illustrated in

Figure 59a. A constant magnitude velocity vector $\overrightarrow{\overline{C}}$ passes through the spatial coordinate at

some unknown time average yaw angle $\overline{\alpha}_y$ with respect to the general compressor reference

frame X-Y. About this mean position, the velocity vector fluctuates by an amount

$$\alpha_y'(t) = |\alpha_y'| \sin(\omega t + \phi_y) \qquad (4\text{-}14)$$

The range of possible time-average pressure readings that will be realized using this Kiel Head probe rotation technique is illustrated in Figure 59b as a function of probe orientation angle α_{yprobe}. The contours plotted in Figure 59b correspond to varying amounts of directional unsteadiness. If the flow is completely steady, i.e. $|\alpha_y'| = 0$, then the uppermost flat contour will be generated. The time average pressure reading $\overline{P}$ at the flat portion of the contour will be the actual total pressure of the flow. The angular range of the flat portion will correspond to the directional insensitivity of the Kiel head probe (about $\pm 50^\circ$). The midpoint of this flat section corresponds to the mean flow direction yaw angle $\overline{\alpha}_y$. On an oscilloscope trace, there will be no fluctuations of voltage vs. time.

As the flow becomes unsteady, the flat section decreases in angular range until only one angular point remains. This is the condition where the fluctuations associated with the flow unsteadiness are just within the maximum directional insensitivity of the Kiel Head probe, i.e. the following condition is reached

$$|\alpha_y'| = 50^\circ$$

Again, an oscilloscope trace will show no evidence of the directional unsteadiness when the probe is aligned with the mean flow direction. However, as the probe is rotated away from this orientation; larger amounts of fluctuations in the voltage-time trace will be observed on an oscilloscope trace.

Finally, an extremely unsteady flowfield will generate fluctuations greater than the range of directional insensitivity of the Kiel Head probe. In this case, the curves begin to fall off

100

from the actual total pressure level. Although a maximum pressure reading can be obtained which corresponds to the mean flow direction, this pressure reading is not the total pressure associated with constant magnitude velocity vector. This case can be distinguished easily by observing that the oscilloscope trace corresponding to this peak point shows a fluctuating voltage-time trace.

This preceeding discussion of a simplified two-dimensional, constant magnitude velocity vector case illustrates how the mean flow direction can be obtained. In reality, the magnitude of the velocity vector and the static pressure can vary with time also. In this event, the measured flow direction will be a magnitude weighted mean value and an oscilloscope voltage-time trace of even a directionally steady flow will show unsteady fluctuations. At this point, the discussion of how to completely resolve this unsteady three-dimensional flowfield is deferred to the following sections of this chapter. Unsteadiness will be treated in Section 4.3.2.2 while techniques aimed at resolving the three-dimensionality of the flowfield are considered in Section 4.3.3.

4.3.2.2. Synchronous Data Acquisition

Since the reverse flow flowfield is dominated by two sources of periodic unsteadiness, the output signal from any high response instrument will be of a form which is analogous to Equations 4-10 and 4-11 as follows

$$S(t) = \overline{S} + S'_{\omega_1}(t) + S'_{\omega_2}(t) + S_\eta(t) \tag{4-15}$$

and the following periodicity relations apply

$$S'_{\omega_1}(t) = S'_{\omega_1}\left(t + \frac{2\pi}{\omega_1}\right) \qquad (4\text{-}16)$$

$$S'_{\omega_2}(t) = S'_{\omega_2}\left(t + \frac{2\pi}{\omega_2}\right) \qquad (4\text{-}17)$$

and the stationary random component generated by noise or turbulence is negligibly small

$$\frac{S_\eta(t)}{S(t)} << 1 \qquad (4\text{-}18)$$

Synchronous data acquisition is the method by which the time-average mean signal $\overline{S}$ plus the two periodically fluctuating components of the signal are acquired (or by which the stationary random component of the signal $S_\eta(t)$ is discarded). The implementation of this technique requires synchronous triggering of the data acquisition system plus ensemble averaging of doubly phase-locked measurements.

Synchronous triggering was accomplished by placing a reference hot wire sensor or a high response total pressure probe in the upstream location depicted in Figure 51, and mounting the probe end of the fiber optic cable (see Section 4.2.1.7.) above the first stage rotor bladerow. In this configuration, the hot wire or total pressure probe produces a reliable reference pulse which is phased to a specific point in the periodic cycle caused by the reverse flow flowfield itself. This signal is reliable ("clean") because the flowfield event

sensor is in a location where unsteadiness associated with the rotating turbomachinery is not present.

The fiber optic circuit produces an extremely reliable pulse ($1\ \mu$sec) based upon rotor position. By adjusting the duration of the pulse from the reference event sensor (5-50 μsec), phase resolution can be sacrificed to speed the data acquisition process by providing a greater opportunity for the two pulse signals to overlap. The duration of the reference event sensor pulse was set to $25\ \mu$sec. This corresponds to a phase lock synchronization to within 40 KHz or about twice the data acquisition sampling rate.

This synchronized triggering pulse was used to commence the acquisition of 1000 data samples at a 20 KHz sampling rate. This sampling rate and number of conversions provided a fine enough resolution to resolve the flowfield to a scale which is an order of magnitude finer than the width of the rotor blade passages for an overall time period duration associated with one rotor revolution at the 1170 RPM operating condition. The signal time trace obtained in this manner corresponds to the instantaneous signal $S(t)$ given by Equation 4-15.

In order to discard the stationary random component generated by noise or turbulence, several sets of these time traces had to be acquired and ensemble averaged. The number of sets which must be acquired and averaged is directly a function of the signal to noise ratio. A large signal to noise ratio is synonymous with the condition expressed by Equation 4-18. As the LHS of Equation 4-18 becomes smaller, the acquisition of fewer data sets are required to discard the noise or turbulence component of the signal $S_{\eta}(t)$ through ensemble averaging. During this set of tests, 128 sets of synchronous data were required to produce a noise free ensemble average time trace which could be reduced by the three-dimensional methods described in Section 4.3.3.2. Table VIII depicts a symbolic representation[26] of the ensemble averaging process employed.

103

Since the ensemble averaging process is accomplished on a real time basis, it was deemed prudent to take some precautionary measures to insure that the ensemble averaged representation of the signal accurately reflects the true nature of the instantaneous signal, i.e.

$$\overline{S}_{EA}(t) = S(t) - S_{\eta}(t)$$

(4-19)

or from Equation 4-17

$$\overline{S}_{EA}(t) = \overline{S} + S'_{\omega_1}(t) + S'_{\omega_2}(t)$$

(4-20)

where $\overline{S}_{EA}(t)$ is the ensemble averaged signal time trace.

The most obvious precaution one can take is to save a record of an instantaneous signal trace. The provision for recording an instantaneous trace was automatically programmed into the data acquisition software. Comparisons between the instantaneous traces and the ensemble averaged representations will be shown in Chapter 6. The comparisons generally show good agreement (see Figure 94) with little loss in signal detail. This result provides convincing evidence that the unsteadiness associated with the flowfield is doubly periodic and that the synchronous triggering system is functioning properly.

---

[26] This symbolic representation is identically analogous to the ensemble averaging scheme reported by Day in [12].

Another precautionary measure that was taken deals with the issue of reproducibility of results. Several test points were re-acquired. The ensemble average results were then compared to demonstrate reproducibility. Again, the comparisons show good agreement.

4.3.3. Three-Dimensional Flowfield Measurements

The technique of rotating a single, inclined hot wire sensor to acquire three synchronized measurements of the flowfield velocity vector was employed to acquire three-dimensional flowfield data. This basic approach is not a fundamentally new experimental technique. The measurement of three dimensional flowfields using a single inclined hot wire technique has been reported in the literature by many previous investigators [60,61,62, 63]. Although the basic approach is similar, the actual equations used to define the inclined hot wire geometry and form of the basic directional sensitivity relation as well as the velocity component reduction technique have been modified to tailor the overall approach to the problem of acquiring reverse flow flowfield data. The three following subsections document the three-dimensional flowfield measurement technique that was used to generate the instantaneous results reported in Chapter 6.

4.3.3.1. Slanted Sensor Calibration

Figure 60 illustrates the right-handed probe fixed coordinate system that was adopted during this thesis effort. The Z-axis of this system runs through the center of the probe, i.e. along the axis of the probe. The sensing section of the probe lies in the X-Z plane with the shorter of the two support prongs positioned over a positive X-axis location. The Y-Z plane is perpendicular to the sensing length of the probe as shown. The sensor is inclined with respect to the X-axis at an angle θ_0.

The instantaneous velocity vector $\vec{W}$ can be defined relative to this probe fixed coordinate system by adopting the pitch angle θ_p and yaw angle θ_y convention shown.[27] Finally, the angle that the velocity vector $\vec{W}$ makes with respect to the unit vector along the axis of the sensor $\vec{\ell}$ is defined as the sensor fixed yaw angle of the flow β. The geometric relationships between the angles β, θ_o, θ_p, θ_y, are found by taking the dot product of the unit velocity vector $\vec{W}/|\vec{W}|$ with the sensor unit vector $\vec{\ell}$ as follows

$$\vec{\ell} = \cos\theta_o\, \vec{i} \; + \; \sin\theta_o\, \vec{k} \tag{4-21}$$

$$\frac{\vec{W}}{|\vec{W}|} = -\cos\theta_p \cos\theta_y\, \vec{i} \; - \; \cos\theta_p \sin\theta_y\, \vec{j} \; + \; \sin\theta_p\, \vec{k} \tag{4-22}$$

$$\vec{\ell} \cdot \frac{\vec{W}}{|\vec{W}|} = -\cos\beta = -\cos\theta_o \cos\theta_p \cos\theta_y \; + \; \sin\theta_o \sin\theta_p \tag{4-23}$$

$$\cos\beta = \cos\theta_o \cos\theta_p \cos\theta_y \; - \; \sin\theta_o \sin\theta_p \tag{4-24}$$

A velocity magnitude calibration of a slanted hot wire sensor was performed by placing the sensor in a known uniform velocity field at a sensor based relative yaw angle β of $90°$.

---

[27] This particular convention was recommended by Johnson [64].

106

This orientation can be accomplished by mounting the hot wire probe in front of a calibration jet at a pitch angle $\theta_p = 0^o$ and a yaw angle $\theta_y = 90^o$. By varying the velocity of the calibration jet, recording the linearized output from the anemometer, and performing a second order least squares curve fit of the acquired calibration data, a slanted sensor velocity magnitude calibration was obtained. This calibration can be expressed as follows

$$|\vec{W}| = a_o + a_1 E_\ell + a_2 E_\ell^2 \qquad (4\text{-}25)$$

where a_0, a_1, a_2 are the second order least squares curve fit coefficients; E_ℓ is the linearized signal from the anemometer; and $|\vec{W}|$ is the magnitude of the velocity vector. Appendix B contains a typical velocity magnitude calibration for a sensor which is inclined 45° to the X-axis. If the anemometer signal is properly linearized with zero output at zero flow velocity; the a_0 and a_2 calibration coefficients will be nearly equal to zero. The a_1 coefficient corresponds to the slope of the linear relationship between velocity magnitude and voltage.

A directional sensitivity calibration is performed by placing the sensor in front of the calibration jet and recording the linearized signal from the anemometer while the known yaw angle θ_y, pitch angle θ_p and jet velocity $|\vec{W}|$ are systematically varied. A calibration matrix of 3 jet velocities, 6 pitch angles, and 31 yaw angles is sufficient to produce a good directional sensitivity calibration. The directional sensitivity calibration data is recorded in the following normalized form

107

$$\frac{W_e}{|\vec{W}|} = \frac{a_0 + a_1 E_{\slashed{I}} + a_2 E_{\slashed{I}}^{2}}{|\vec{W}|} \qquad (4\text{-}26)$$

where W_e is the effective cooling velocity (a scalar quantity); $|\vec{W}|$ is the known magnitude

of the calibration jet velocity; a_0, a_1, and a_2 are the previously determined velocity

magnitude calibration coefficients; and $E_{\slashed{I}}$ is the linearized signal from the anemometer.

The next step in the directional sensitivity calibration sequence is to perform a multiple

parameter least squares curve fit of the normalized effective cooling velocity calibration data.

The recommended[26] form of the least squares curve fit is given by the following expression

$$\frac{W_e}{|\vec{W}|} = b_0 + b_1\beta + b_2\,\theta_P + b_3\,|\vec{W}| + b_4\,\beta^2 +$$

$$(4\text{-}27)$$

$$b_5\,\theta_P^2 + b_6\,\beta\theta_P + b_7\,\beta\,|\vec{W}| + b_8\,\theta_P\,|\vec{W}| + b_9\,\beta^3$$

where b_0 through b_9 are the directional sensitivity calibration coefficients that are

determined from the least squares curve fit. A largest pivotal divisor Gaussian matrix

reduction scheme is used to numerically solve the set of ten linear simultaneous equations

---

[26] Recommended by Dr. Hyoun-Woo Shin, a senior researcher on the staff of the MIT Gas
Turbine Laboratory.

generated by forming the least squares partial derivatives of Equation 4-27. A typical directional sensitivity calibration for the same 45° sensor is also contained in Appendix B.

4.3.3.2. Data Acquisition Procedure

The basic three step data acquisition procedure for acquiring sufficient information to resolve a three-dimensional flowfield consists of 1) initially aligning the sensor with the time-average mean flow direction; 2) acquiring a synchronous triggered ensemble average representation (time trace) of the linearized anemometer signal, and 3) rotating the sensor to acquire two more ensemble averaged traces at alternate sensor orientations. The basic geometry associated with this acquisition technique is depicted in Figure 61. Wire positions A, B, and C correspond to the three data acquisition orientations of the slanted sensor. The time-average mean velocity vector $\overrightarrow{W}$ is at an angle $\overline{\alpha}_y$ with respect to the axial direction of the compressor coordinate frame.

The sensor is initially aligned with the mean velocity vector $\overrightarrow{W}$ on the basis of a previous mapping of the mean flow direction using the Kiel Head total pressure probe technique described earlier in Section 4.3.2.1. Figure 61 illustrates a typical case where the initial sensor orientation, i.e. position A, is slightly misaligned from the mean flow direction by a sensor based coordinate frame yaw angle θ_{yA}. After the synchronous data acquisition technique explained in Section 4.3.2.2. is employed to obtain an ensemble average signal trace (of the linearized anemometer bridge output), the sensor is rotated on its axis to position B by a turning angle increment $\Delta\alpha$. At wire positions B and C, the sensor based mean yaw angles, θ_{yB} and θ_{yC}, are

$$\theta_{YB} = \theta_{YA} + \Delta\alpha \qquad (4-28)$$

109

$$\theta_{YC} = \theta_{YA} - \Delta\alpha \qquad\qquad (4\text{-}29)$$

Although the same turning angle increment was used to establish positions B and C as indicated by Equations 4-28 and 4-29, equal turning angle increments are not an inherent requirement associated with this technique. The magnitude of the turning angle increment is governed by the yaw angle range of the slanted sensor's directional sensitivity calibration and the amount of directional unsteadiness associated with the instantaneous flowfield.

In order for the results to be valid, the instantaneous velocity vector should never be beyond the yaw angle calibration range of the inclined sensor. For the 45° slanted sensor used during this work, the effective yaw angle calibration range is about $\pm 75^{o}$ (see Slanted Sensor Directional Sensitivity Calibration in Appendix B). To measure a possible $\pm 50^{o}$ amount of directional unsteadiness about the mean direction, the turning angle increment was set equal to 25°.

4.3.3.3. Velocity Component Reduction

The data acquisition procedure described in the previous section provides three ensemble average time traces of effective cooling velocity, i.e. $W_{eA}(t)$, $W_{eB}(t)$, and $W_{eC}(t)$. These time traces correspond to three independent measurements of the same instantaneous velocity vector because of the synchronous triggering technique that was used to obtain the data. At each instant in time, i.e. t_j where $j = 1,1000$, each of these three effective velocities can be used to eliminate an unknown variable in Equation 4-27 (the numerator in the LHS of the

110

equation). Three more equations are generated on the basis of the Equation 4-24 geometric relationship which must exist at each of the three sensor orientations. As a result, a set of 6 simultaneous nonlinear algebraic equations are generated to solve for the 6 unknowns β_A, β_B, β_C, θ_{YA}, θ_P, $|\vec{W}|$ as follows

Sensor Position A

$$\frac{W_{e_A}(t_j)}{|\vec{W}|} = b_0 + b_1 \beta_A + b_2 \theta_P + b_3 |\vec{W}| + b_4 \beta_A^2 + \qquad (4\text{-}30)$$

$$b_5 \theta_P^2 + b_6 \beta_A \theta_P + b_7 \beta_A |\vec{W}| + b_8 \theta_P |\vec{W}| + b_9 \beta_A^3$$

$$\cos \beta_A = \cos \theta_0 \cos \theta_P \cos \theta_{YA} - \sin \theta_0 \sin \theta_P \qquad (4\text{-}31)$$

Sensor Position B

$$\frac{W_{e_B}(t_j)}{|\vec{W}|} = b_0 + b_1 \beta_B + b_2 \theta_P + b_3 |\vec{W}| + b_4 \beta_B^2 + \qquad (4\text{-}32)$$

$$b_5 \theta_P^2 + b_6 \beta_B \theta_P + b_7 \beta_B |\vec{W}| + b_8 \theta_P |\vec{W}| + b_9 \beta_B^3$$

$$\cos \beta_B = \cos \theta_0 \cos \theta_P \cos \left(\theta_{YA} + \Delta\alpha \right) - \sin \theta_0 \sin \theta_P \qquad (4\text{-}33)$$

111

Sensor Position C

$$\frac{W_{e_C}(t_i)}{|\vec{W}|} = b_0 + b_1\beta_C + b_2\theta_P + b_3|\vec{W}| + b_4\beta_C^2 + \tag{4-34}$$

$$b_5\theta_P^2 + b_6\beta_C\theta_P + b_7\beta_C|\vec{W}| + b_8\theta_P|\vec{W}| + b_9\beta_C^3$$

$$\cos\beta_C = \cos\theta_0 \cos\theta_P \cos\left(\theta_{YA} - \Delta\alpha\right) - \sin\theta_0 \sin\theta_P \tag{4-35}$$

To solve the above set of equations, a hybrid variant of a classical Newton-Raphson iteration scheme is employed. This method was developed by M.J.D. Powell [65] and is similar to the Levenberg/Marquardt iteration [66,67] which uses a least squares technique for estimating the values for each of the variables at a future step in the iteration. This method, however, does not require explicit expressions for the partial derivatives of the residual equations.[29] Instead, successive values of the computed residuals are used to build up a numerical approximation for the matrix of partial derivatives of these residuals (Jacobian Matrix).

This method requires an initial guess of the velocity vector to begin the solution procedure. Since the time required to yield a converged solution is about 10 seconds on the

---

[29] The residual equations are formed by subtracting the LHS of Equations 4-32 through 4-37 from both sides of each respective equation. A solution is obtained by driving these residuals to a small value.

LSI-11/23 minicomputer, it would be inconvenient to have the user interactively input this initial guess when even a small portion of the 1000 element trace was being reduced. As a result, a simple, but extremely effective algorithm for automatically generating this initial guess was developed. This algorithm is based upon an analysis of the directional sensitivity calibrations of the sensor and requires only the measured values of the three effective velocities to generate a reasonable initial guess. This algorithm was programmed into the data reduction software as follows

$$\theta_p = 0 \tag{4-36a}$$

$$|\vec{W}| = 1.3 \, W_{emax} \tag{4-36b}$$

$$\theta_{y_A} = 80 \left[\frac{W_{e_a}(t_j)}{|\vec{W}|} - \frac{W_{e_c}(t_j)}{|\vec{W}|} \right] \tag{4-36c}$$

where W_{emax} is the largest effective velocity of the three measured effective velocity of the three measured effective velocities and θ_{y_A} is defined in degrees.

Once a converged solution is obtained, the velocity vector is known in terms of two angles and a magnitude with respect to the sensor based coordinate frame at position A. This velocity vector is resolved into relative velocity components in the sensor coordinate frame as follows

$$(W_x)_A = -|\vec{W}|\cos \theta_p \cos \theta_{y_A} \tag{4-37a}$$

113

$$(W_y)_A = -|\vec{W}| \cos \theta_p \sin \theta_{yA} \qquad\qquad (4\text{-}37b)$$

$$(W_z)_A = |\vec{W}| \sin \theta_p \qquad\qquad (4\text{-}37c)$$

where W_x, W_y, and W_z are the relative velocity components in the sensor based reference frame depicted in Figure 60.

A coordinate transformation of these components back to a compressor based coordinate frame (depicted in Figure 57) is accomplished as follows

$$C_X = -|\vec{W}| \cos \theta_p \cos (\alpha_o - \theta_{yA}) \qquad\qquad (4\text{-}38a)$$

$$C_\theta = -|\vec{W}| \cos \theta_p \sin (\alpha_o - \theta_{yA}) \qquad\qquad (4\text{-}38b)$$

$$C_r = |\vec{W}| \sin \theta_p \qquad\qquad (4\text{-}38c)$$

It should be pointed out that Equations 4-38a through 4-38c are only valid for an initial sensor orientation angle $-90^0 < \alpha_o < 90^0$. If greater or lesser initial orientation angles are dictated by the flowfield, a suitable algorithm has been coded into the data reduction software to correct the Equation 4-38 expressions.

114

4.3.4. Summary

Before concluding this chapter, the following summary of the experimental procedure used to acquire unsteady three-dimensional reverse flowfield data is offered.

1) A velocity magnitude and directional sensitivity calibrations of the 45° slanted hot wire sensor is performed prior to the actual test date.

2) A reference sensor is mounted just upstream (less than one blade pitch spacing) of the first bladerow (Stator #3). The fiber optic cable is mounted above the Rotor #1 bladerow. The output from both probes is connected to the synchronous trigger circuit. The output from the synchronous trigger is fed to the real time clock and the digital storage oscilloscope.

3) A pretest static calibration of the Kiel Head probe is performed. The probe is mounted in the automatic traversing mechanism which is then positioned at the appropriate axial and circumferential measuring station. The radial position and orientation of the probe is initialized with respect to the compressor coordinate frame.

4) The mean flow direction is interactively determined via computer commanded rotation of the Kiel Head probe, generation of a time-average mean total pressure using the Datel A/D converter, and operator monitoring of the instantaneous oscilloscope trace.

5) The mean flow direction is recorded. The synchronous acquisition of a total pressure trace at the mean flow angle is accomplished as follows

a) the synchronous trigger circuit provides a reference pulse to the real time clock

b) the real time clock provides a prescribed 20 KHz overflow pulse train to the Detel A/D converter;

c) 1000 discrete measurements are acquired and stored in a memory location in the LSI-11/23

d) steps a) through c) are repeated 128 times;

e) the ensemble average time trace and instantaneous trace #64 are stored on hard disk in a direct access data file.

6) After the acquisition of the total pressure field and a post-test static calibration of the Kiel Head probe, acquisition of the three-dimensional velocity field is ready to proceed (usually on another day). On the morning of the velocity field measurements, a pre-test velocity magnitude calibration check of the sensor is accomplished. Steps 2) and 3) are repeated for the hot wire probe.

7) The sensor is initially positioned at an orientation aligned with the mean flow direction determined in step 4). Steps 5a) through 5e) are reaccomplished for the acquisition of the hot wire sensor ensemble average trace and one instantaneous trace.

8) The sensor is rotated 25^0 to a second orientation via preprogrammed computer control. Again, steps 5a) through 5e) are reaccomplished for the acquisition of the hot wire traces at this second position.

9) The sensor is rotated back through -50^0 of rotation to a third orientation. Again, a new set of synchronous traces are acquired in an analogous fashion.

10) After the acquisition of the velocity field is accomplished, a post-test velocity magnitude calibration of the hot wire sensor is performed.

After this acquisition process is completed, the data reduction phase begins. Since enormous amounts of time are required to reduce the raw data on the LSI-11/23 minicomputer, the data reduction software was written to be self contained. This permitted automated data reduction to proceed overnight.[30] This automated data reduction philosophy was implemented by incorporating the following features in the software code

   a) automatic initial guess algorithm (see Section 4.3.3.3.)

   b) provision to select from 1 to 5 of the 1000 point time trace strings for reduction;

   c) provision to select any number of continuous 20 point portions of the overall trace for reduction;

   d) automatic restart of the reduction process for points which fail to converge on a first reduction attempt (initial guess is the last set of computed results);

   e) generation of an error file listing the unconverged data points and their last computed solutions for data points that do not converge after two reduction attempts;

   f) provision for an interactive reduction option to reduce individual data points appearing in the error file.

Finally, it should be noted that the primary limitations of this technique are 1) the nature of the flowfield unsteadiness, and 2) the range of flowfield directional unsteadiness. If

---

[30] In fact, the standard operating procedure became one of around-the-clock 24 hour data acquisition and reduction. Early in the morning, the pre-test calibration of the sensor would be accomplished. Data acquisition would proceed throughout the day. Post-test calibrations, creation of floppy disk data file backups, and initiation of an overnight data reduction program would be accomplished during early evening. The data reduction program would run continuously throughout the night until the cycle was repeated on the following morning.

117

the flowfield unsteadiness is not periodic, the data acquisition system cannot be triggered to acquire ensemble average traces (sharp spikes in the instantaneous traces are impossible to reduce with any sort of consistency). More importantly though, an aperiodically unsteady flow would imply that three independent effective velocity traces corresponding to the identical flowfield could not be obtained. Aside from the nature of the unsteadiness, the flow direction changes must be within the working range of the high response instrumentation. The present procedure and instrumentation can tolerate flow angle changes by as much as 100° ($\pm 50^{\circ}$ about the mean flow direction).

Chapter 5

TIME-AVERAGE PERFORMANCE RESULTS

During this investigation of axial compressor reversed flow phenomena, overall time-averaged performance and detailed flowfield measurements were made. This chapter will present the time-average performance results. Chapter 6 will present the results associated with the high response measurements of the compressor's detailed flowfield structure. The interpretation of these results, including a kinematic and dynamic analysis of the flowfield, is given in Chapter 7.

The time-average measurements of the compressor pressure rise performance characteristics are presented and discussed in Section 5.1. With the exception of Pratt & Whitney's unpublished HSR data [34], these characteristics are the only complete set of Karman-Knapp Quadrant I and IV compressor performance characteristics in existence (to the best of the author's knowledge) for a multistage axial compressor which is representative of aircraft gas turbine engine applications. In an analogous fashion, Section 5.2 presents the measured set of torque characteristics for the two compressor builds.

Section 5.3 is devoted to a presentation of time-averaged measurements of the axial pressure and temperature profiles through the compressor. Since little is known about the zero mass flow and reversed flow performance of axial compressors, the major portion of the axial profile results and discussion will be concerned with the profiles in these flow regimes. Quantitative measurements of steady-state rotating stall cell properties are given in Section 5.4. Finally, a qualitative summary of the stalled flow operating regimes is presented in

Section 5.5. This summary includes a discussion of the two stalled flow modes observed during the present test series: 1) rotating stall, and 2) annulus stalled flow.

5.1 PRESSURE RISE CHARACTERISTICS

The overall total-to-static, total-to-total, and static-to-static pressure rise coefficients for an axial comrpessor are defined in the following subsections. These three measures of compressor pressure rise performance are presented as a function of flow coefficient for the two builds tested. In addition, the static-to-static pressure rise characteristics for each individual compressor stage are presented in the final subsection.

5.1.1. Total-to-Static Performance

The total-to-static definition of pressure rise coefficient is usually the preferred approach for representing overall compressor performance. The popularity of this definition stems, in part, from the fact that this quantity is precisely the one-dimensional measure of compressor performance required by many compression system dynamic models. For instance, the compressor characteristic C which appears in the Chapter 2 compression system model is actually a compressor total-to-static characteristic. Also in rotating stall studies, Day [12] showed that the total-to-static characteristic should be used in preference to other overall characteristics because this measure of performance is not influenced by the relative size of the stall cell.

In terms of the compressor measuring planes given in Figure 51, the overall total-to-static pressure rise coefficient ψ_{T-S} of the test compressor is given by the following equations

$$\psi_{T-s} = \frac{(P_{13} - \bar{P}_2)}{\frac{1}{2}\rho U^2} \qquad \text{(Reverse Flow)} \qquad (5-1)$$

$$\psi_{T-S} = \frac{(\bar{P}_9 - \bar{P}_0)}{\frac{1}{2}\rho U^2} \qquad \text{(Forward Flow)} \qquad (5\text{-}2)$$

where $\bar{P}$ is the time-average static pressure, and the numerical subscript corresponds to the measuring plane. Reverse flow corresponds to a net axial airflow from left-to-right in the compressor shown in Figure 51. Forward flow conditions correspond to the opposite net flow direction.

The total-to-static characteristics of the medium and high reaction builds are shown in Figures 62 and 63 respectively.[31] In both cases, the complete total-to-static characteristic is composed of three discrete segments corresponding to unstalled flow, rotating stall, and an annulus stalled reverse flow mode. Each segment of the characteristic is separated from an adjacent segment by a discontinuous transition. The first, or high flow rate, transition occurs at a stall inception flow coefficient of $\bar{C}_x/U = 0.49$. This transition from unstalled flow to a full span, single cell rotating stall flow mode is accompanied by an abrupt change in the total-to-static pressure rise performance of the compressor. Upon opening the throttle, this transition is not repeated in the reverse direction, i.e. the transition from rotating stall to unstalled flow. Instead, there is a significant amount of hysteresis, or flow coefficient overlap, in the unstalled and rotating stall segments of the characteristic. This phenomenon has been well documented by previous investigators (see Day [12]).

In these compressor builds, the full span rotating stall flow mode is stable over a broad range of flow coefficients including a net reverse (negative) axial flow coefficient. To the

---

[31] The unstalled characteristic and the high flow coefficient portion of the rotating stall characteristic were measured and reported by Eastland [47] prior to this experimental effort.

best of the author's knowledge, this possibility was suspected by some but never measured before the present effort. The stable, fully continuous rotating stall portion of the characteristic extends to a reverse flow coefficient of $\bar{C}_x/U = -0.04$. At this flow coefficient, the characteristic becomes discontinuous due to an abrupt change in flow mode to an annulus stalled flow mode. Unlike the transition between unstalled flow and rotating stall, there is no hysteresis associated with this negative flow coefficient transition. This trend was observed by Day [12] at a low positive flow coefficient transition between rotating stall and what he described as an "axisymmetric stall." Although the annulus stalled flow mode is not completely axisymmetric (as will be shown by the high response flowfield results presented in Chapter 6),[32] Day's observation that there was no hysteresis loop in the performance curves is consistent with the trends observed in the present effort.

The reverse flow, backflow, or annulus stalled characteristic at negative flow coefficients is strongly negatively sloped. Although this characteristic is slightly parabolic (or quadrant with flow coefficient), the slope of the characteristic is about 17:1. This result indicates that the compressor presents a substantial amount of resistance to reverse flow. Furthermore, the difference in reaction between the two builds tested produced no change in the reverse flow characteristic or the transition point, (i.e. $\bar{C}_x/U = -0.04$) between annulus stalled flow and the rotating stall flow mode.

In both cases, the annulus stalled flow mode becomes unstable on the strongly negative sloped portion of the total-to-static performance characteristic. The unpublished Pratt &

---

[32] The degree of nonasymmetry associated with annulus stalled flows is of the order of several blade passages. The context of Day's use of the term "axisymmetric" was with respect to the nonasymmetry caused by the presence of rotating stall cells. These nonasymmetries are of the order of the entire circumference of the compressor.

Whitney HSR data [34] demonstrates the same trend. For these compressors then, it appears that a compressor flowfield instability, rather than a one-dimensional compression system instability, accounts for the flow mode transition between annulus stalled flow and rotating stall.

Finally, the three different symbols plotted in Figures 62 and 63 correspond to shaft rotational speeds of 1170, 1800 and 2400 RPM. Each of these three speedlines collapse to the same nondimensional annulus stalled flow characteristic as shown in the figures. In the case of rotating stall, however, a slight speed dependence becomes apparent at nearly zero flow coefficient. The reason for this slight speed dependence lies in the fact that there is a significant amount of power input to the compressor without a net airflow through the machine. As a result, the fluid within the compressor and the compressor blading heats up and this is the cause of the speed dependence indicated by Figures 62 and 63 in the zero mass flow portion of the rotating stall curve.

5.1.2. Total-to-Total Performance

The total-to-total pressure rise coefficient is defined in terms of the compressor measuring planes shown in Figure 51 as

$$\psi_{\text{T-T}} = \frac{(\bar{P}_{t_{10}} - \bar{P}_{t_2})}{\frac{1}{2}\rho U^2} \tag{5-3}$$

where $\bar{P}_t$ is the time-average (Kiel probe measured) total pressure, and the numerical subscript corresponds to the measuring plane. In reverse flow, the left facing total pressure rakes shown in Figure 51 are used to obtain the time-average total pressure readings. In forward flow, the right facing rakes are used.

123

The utility of this performance measure is somewhat limited. In unstalled flow and annulus stalled reverse flow, the total pressure reading given by a Kiu. Head total pressure probe will reflect the true total pressure of the flow only if the amount of swirl and/or the directional unsteadiness of the flow does not exceed the $\pm 50^{\circ}$ directional insensitivity limit of the probe. In rotating stall, the flow direction can change by as much as 120° [12]. As a result, the total pressure probe is usually never aligned with the flow in the presence of a rotating stall flowfield. Hence, the time-average total-to-total characteristic of a rotating stall flow regime is usually purely academic and has little useful value.

Perhaps the greatest value associated with total-to-total pressure rise data is the relationship between this measure of performance and other alternative methods for characterizing compressor performance. For instance, a compressor's total pressure ratio is a standard performance index. The total-to-total pressure coefficient is related to total pressure ratio as follows

$$ PR = \frac{\bar{P}_{t_{10}}}{\bar{P}_{t_2}} = \frac{\frac{1}{2}\rho U^2 \, \psi_{\text{T-T}}}{\bar{P}_{t_2}} \tag{5-4} $$

where the flow regime under consideration is assumed to be either unstalled or annulus stalled reverse flow.

In unstalled forward flow, the total-to-total chartacteristic can be related to the total-to-static characteristic by assuming that

$$ \bar{P}_{t_2} = P_o \tag{5-5a} $$

124

$$\overline{P}_{t_{10}} = \overline{P}_{t_9} \tag{5-5b}$$

$$= \overline{P}_9 + \tfrac{1}{2}\rho\overline{C}_9^{\,2}$$

$$= \overline{P}_9 + \tfrac{1}{2}\rho\overline{C}_x^{\,2}\sec^2\alpha_{y_9}$$

and hence,

$$\frac{\left(\overline{P}_9 - P_0\right)}{\tfrac{1}{2}\rho U^2} = \frac{\left(\overline{P}_{t_{10}} - \overline{P}_{t_2}\right)}{\tfrac{1}{2}\rho U^2} - \left(\frac{\overline{C}_x}{U}\right)^2 \sec^2\alpha_{y_9} \tag{5-5c}$$

or

$$\psi_{T-S} = \psi_{T-T} - \left(\frac{\overline{C}_x}{U}\right)^2 \sec^2\alpha_{y_9} \tag{5-6}$$

where α_{y_9} is the absolute swirl angle of the flow in the circumferential direction at measuring station 9 (see Figure 58).

During annulus stalled reverse flow, these pressure rise measures of performance are related by a similar logic as follows

$$\overline{P}_{t_{10}} = P_{13} \tag{5-7a}$$

$$\overline{P_{t_2}} = \overline{P_2} + \frac{1}{2}\rho\,\overline{C_2}^2 \tag{5-7b}$$

$$= \overline{P_2} + \frac{1}{2}\rho\,\overline{C_x}^2 \sec^2\alpha_{y_2}$$

and thus

$$\frac{\left(P_{13} - \overline{P_2}\right)}{\frac{1}{2}\rho U^2} = \frac{\left(\overline{P_{t_{10}}} - \overline{P_{t_2}}\right)}{\frac{1}{2}\rho U^2} + \left(\frac{\overline{C_x}}{U}\right)^2 \sec^2\alpha_{y_2} \tag{5-8}$$

which is

$$\psi_{T-S} = \psi_{T-T} + \left(\frac{\overline{C_x}}{U}\right) \sec^2\alpha_{y_2}$$

where α_{y_2} is the absolute swirl angle of the flow in the circumferential direction at

measuring station 2.

The total-to-total characteristics of both builds appear in Figures 64 and 65. In the

unstalled and annulus stalled flow regimes, a comparison between these total-to-total

characteristics with the total-to-static characteristics presented in Section 5.1.1. confirms the

relationships predicted by Equations 5-6 and 5-8 respectively, i.e. a $(\overline{C_x}/U)^2$ difference

exists between the two characteristics. This difference is more easily seen in the unstalled

flow regime because the flow coefficients are greater in magnitude ($\overline{C_x}/U$ = 0.6 rather than

$\overline{C_x}/U$ = -0.1). Comparisons between the two sets of characteristics in the rotating stall

operating regime should be avoided because of the inherent difficulty associated with generating

126

valid time-average total pressure measurements just upstream and downstream of the compressor blading.

The discrepancy in the total-to-total characteristics reported by Eastland [47] with those measured by the author (shown in Figure 64) is attributed to the placement of the upstream total pressure instrumentation at different axial stations. In the presence of a rotating stall flowfield, the difference in total pressures retrieved by the total pressure rakes accounts for the slight discontinuity in the rotating stall portion of the total-to-total characteristic.

5.1.3. Static-to-Static Performance

Static-to-static characteristics are another alternative measure of overall compressor pressure rise performance:

$$\left(\psi_{s-s}\right)_{9-2} = \frac{\left(\overline{P}_9 - \overline{P}_2\right)}{\frac{1}{2}\rho U^2} \tag{5-9}$$

where plane 9 is just aft of the third stage stator bladerow and plane 2 is just in front of the inlet guide vane blading. When comparing compressors with a different number of stages, it is useful to define a static-to-static characteristic in terms of planes 9 and 3:

$$\left(\psi_{s-s}\right)_{9-3} = \frac{\overline{P}_9 - \overline{P}_3}{\frac{1}{2}\rho U^2} \tag{5-10}$$

where measuring plane 3 is in the interbladerow gap between the first stage rotor and the IGV's.

127

The static-to-static characteristics for the two builds tested during this experimental effort are given in Figures 66 and 67. An inspection of these figures reveals that there is little difference between whether Equation 5-9 (before IGV's) or Equation 5-10 (after IGV's) is used to define static-to-static performance in the unstalled flow regime. The IGV's in the test compressor are slightly cambered and staggered. Hence, they produce little flow turning and pressure drop in the unstalled flow regime. This trend appears to be the case in rotating stall at high flow coefficients where the majority of the annulus circumference is unstalled. However, as more of the circumference is enveloped in rotating stall, the two measures of static-to-static compressor performance tend to diverge. Finally, annulus stalled reverse flow is encountered. Once again, these two characteristics diverge sharply as larger reversed flow operating conditions are imposed upon the compressor. These trends tend to support a parallel compressor concept of rotating stall and will be addressed further in Chapter 7.

Day [12] has shown that the static-to-static characteristic measured before the IGV's is related to the total-to-static characteristic in the unstalled flow regime as follows

$$P_0 = \bar{P}_2 + \tfrac{1}{2}\rho \bar{C}_x^{\,2} \qquad (5\text{-}11)$$

and thus

$$\frac{\left(\bar{P}_9 - P_0\right)}{\tfrac{1}{2}\rho U^2} = \frac{\left(\bar{P}_9 - \bar{P}_2\right)}{\tfrac{1}{2}\rho U^2} - \left(\frac{\bar{C}_x}{U}\right)^2 \qquad (5\text{-}12)$$

which is

$$\psi_{T\text{-}s} = \left(\psi_{s\text{-}s}\right)_{9\text{-}2} - \left(\frac{\bar{C}_x}{U}\right)^2$$

In annulus stalled reverse flow, a similar rationale applies:

$$P_{13} = \overline{P}_9 + \tfrac{1}{2}\rho\overline{C}_x^{\,2} \tag{5-13a}$$

and hence,

$$\frac{\left(P_{13} - \overline{P}_2\right)}{\tfrac{1}{2}\rho U^2} = \frac{\left(\overline{P}_9 - \overline{P}_2\right)}{\tfrac{1}{2}\rho U^2} + \left(\frac{\overline{C}_x}{U}\right)^2 \tag{5-13b}$$

or

$$\psi_{T-S} = \left(\psi_{s-s}\right)_{9-2} + \left(\frac{\overline{C}_x}{U}\right)^2 \tag{5-14}$$

The trends predicted by Equations 5-12 and 5-14 are observed in the data reported herein when one compares the total-to-static characteristics plotted in Figures 62 and 63 with the static-to-static characteristics plotted in Figures 66 and 67.

A major portion of Day's Ph.D. thesis [12] is devoted to documenting the relationship between these two types of pressure rise characteristics while the compressor is operating in rotating stall. For this reason, Day's original analysis will not be reproduced here. However, it is important to point out that the experimental results obtained during this effort are consistent with Day's interpretation of the relative relationship between total-to-static and static-to-static performance during rotating stall. In particular, the static-to-static characteristic measured after the IGV's $(\psi_{s-s})_{9-3}$ crosses the total-to-static characteristic ψ_{T-S} as lower valued flow coefficients $\overline{C}_x/U$ are encountered.

This "crossover" phenomenon seems to occur because the relative size of the stall cell increases with decreasing flow coefficient. Since time-average static pressure is also an annulus circumference weighted average of the static pressure associated with the rotating stall cell and unstalled flowfields, increasing the size of the stall cell tends to cause the time-average static pressure in the interbladerow gap between the IGV's and first stage rotor to reflect the static pressure condition which exists in front of a rotor during rotating stall. In Chapter 6, the high response flowfield results of the annulus stalled flow condition will show that there is a significant radial pressure gradient at this measuring plane. If the flowfield within a rotating stall cell at this measuring plane is similar to an annulus stalled flow, this "crossover" phenomen appears to be the direct time-average result of a parallel compressor interpretation of rotating stall.

5.1.4 Stage Performance

The sum of the individual stage static pressure rise coefficients yield the overall static-to-static pressure rise coefficient measured after the IGV's $(\psi_{s-s})_{9-3}$. The three individual stage pressure rise coefficients are defined by the following expressions:

$$\left(\psi_{s-s}\right)_{5-3} = \frac{\left(\overline{P}_5 - \overline{P}_3\right)}{\frac{1}{2}\rho U^2} \qquad \text{(Stage 1)} \qquad (5\text{-}15)$$

$$\left(\psi_{s-s}\right)_{7-5} = \frac{\left(\overline{P}_7 - \overline{P}_5\right)}{\frac{1}{2}\rho U^2} \qquad \text{(Stage 2)} \qquad (5\text{-}16)$$

$$\left(\psi_{s\text{-}s}\right)_{9\text{-}7} = \frac{\left(P_9 - P_7\right)}{\frac{1}{2}\rho U^2} \qquad \text{(Stage 3)} \qquad (5\text{-}17)$$

The individual stage characteristics for the medium and high reaction builds tested are given in Figures 68 and 69. In both cases, the unstalled portions of the characteristics indicate that stages 2 and 3 perform similarly while stage 1 yields about a 30% increase in pressure rise performance. These trends are explained by the fact that the stages are nonrepeating. At high flow coefficients, the rotating stall performance of each stage is decreased, but the basic stage relationship trends observed in unstalled flow are preserved, i.e. stages 2 and 3 perform similarly and stage 1 has significantly improved performance.

The performance of all three stages decreases significantly as the flow coefficient is reduced by throttling the test compressor deeper into rotating stall. Although the performance of all three stages decreases with decreasing flow coefficient, the rate of decrease in performance is different among the three stages. Initially, the *rate of decrease* in performance of stages 1 and 3 are identical in the high flow coefficient regime. However, the performance reduction rate associated with stage 2 is less drastic then either of the other two stages. Eventually, the performance of stages 1 and 2 level out to a stage pressure rise coefficient of 0.29 at the transition flow coefficient of $\bar{C}_x/U = -0.04$. On the other hand, the stage 3 pressure rise performance continues to fall off until a stage pressure rise coefficient equal to zero is reached.

After the transition to annulus stalled flow, stages 1 and 2 continue to perform identically while stage 3 continues to exhibit drastically different pressure rise performance. In fact, there is a net pressure rise across stage 3 in the direction of the average axial flow

(indicated by the negative pressure rise coefficient in Figures 68 and 69). Conversely, stages 1 and 2 offer a net resistance to reverse flow as indicated by the positive stage pressure coefficients.

The fact that the performance of stage 2 "switches over" from the pressure rise level associated with stage 3 at high flow coefficients to the performance level associated with stage 1 at low and negative flow coefficients tends to support a parallel compressor concept of rotating stall. Under this concept, the time-average performance is the weighted average of the annulus stalled reverse flow performance characteristic (stall cell) and the unstalled characteristic. As the stall cell grows in size relative to the unstalled portion of the flow, the performance behavior associated with stages 1 and 2 should be similar because each of these stages is followed by a moving bladerow. This point was first made by Day in [12]. In Chapter 6, we shall see that the radial pressure gradients before and after a moving bladerow under reverse flow conditions are very much different. A further discussion of these results will appear in Chapter 7.

5.2 TORQUE CHARACTERISTIC

A nondimensional torque coefficient ψ_T can be defined as follows

$$\psi_T = \frac{T}{\frac{1}{2}\rho U^2 A_c R_M} \tag{5-18}$$

where T is the torque absorption by the compressor (corrected for tare torque), A_c is the annulus flowthrough area of the compressor, and R_m is the mean radius of the compressor blading.

132

The torque versus flow coefficient characteristic of the two compressor builds tested are given in Figures 70 and 71. At stall inception, the torque absorbed by the compressor falls off discontinuously by roughly 10%. As the compressor is throttled into deep rotating stall, the torque coefficient gradually drops off to a level which is about 66% of the peak unstalled value. With the exception of the stall inception discontinuity, these trends have been previously observed by Day [12].

As the zero mass flow regime is encountered, the torque loading level begins to increase. This slight increase in torque level continues as the compressor is throttled through negative net axial flow coefficients. Once the reverse flow annulus stalled transition point is reached, the torque level significantly drops off in a discontinuous fashion. This discontinuity in the torque characteristic is of the order of 60% for both reaction builds. As larger reversed flows are imposed across the compressor, the torque absorbed by the compressor increases sharply. At a reverse flow coefficient $\overline{C}_x/U = -0.20$, the torque absorbed by the compressor is approximately twice the peak torque absorption level of the compressor in the unstalled flow regime. Finally, the torque characteristics for the two reaction builds are identically the same in the reverse flow regime (as were the pressure rise characteristics).

At this point, it is beneficial to make several comments with respect to the nature of the reverse flow torque characteristics. First, the method for nondimensionalizing the torque measurements appears to be an effective reference value for the reverse flow regime. Figures 70 and 71 contain the torque characteristics generated at three different shaft rotational speeds. In both reaction builds, the reverse flow speedline characteristics are virtually indistinguishable.

Another point which deserves further discussion is the agreement between the measured torque absorption and the measured total temperature rise through the machine. A nondimensional temperature coefficient ψ_θ can be defined as follows

$$\psi_\theta = \frac{\left(\overline{T}_2 - T_{13}\right)}{\frac{1}{2} \frac{U^2}{c_p}} \qquad \text{(Reverse Flow)} \qquad (5\text{-}19)$$

$$\psi_\theta = \frac{\left(\overline{T}_9 - T_0\right)}{\frac{1}{2} \frac{U^2}{c_p}} \qquad \text{(Forward Flow)} \qquad (5\text{-}20)$$

where T is the time-average total temperature, the numerical subscript indicates the measuring plane indicated on Figure 51, and c_p is the constant pressure specific heat of the fluid. The reference quantity $^1/_2 U^2 / c_p$ is the blade dynamic temperature. At shaft rotational speeds of 1170, 1800, and 2400 RPM, the value of this reference temperature quantity is 1.10°F, 2.61°F, 4.64°F respectively.

To relate the torque coefficient to the temperature coefficient, an energy balance is written for a control volume around the compressor:

$$T \Omega = \dot{m} \, c_p \left(\overline{T}_2 - T_{13}\right) \qquad (5\text{-}21)$$

where Ω is the shaft rotational speed, and $\dot{m}$ is the time average mass flow rate through the compressor. The left hand side of Equation 5-21 is the mechanical work input to the

134

compressor. The right hand side of this equation is the net stagnation enthalpy convected

away from the compressor. Dividing both sides of Equation 5-21 by $\frac{1}{2}\rho U^2 A_c R_M \Omega$

and defining a mean blade speed and average mass flow rate;

$$U = R_m \Omega$$

$$\dot{m} = \rho A_c \bar{C}_x$$

Equation 5-21 can be rewritten in the following form:

$$\frac{T}{\frac{1}{2}\rho U^2 A_c R_M} = \left(\frac{\bar{C}_x}{U}\right) \frac{(\bar{T}_2 - T_{13})}{\frac{1}{2}\frac{U^2}{C_P}} \qquad (5-22)$$

which is the desired result

$$\psi_T = \left(\frac{\bar{C}_x}{U}\right) \psi_\theta \qquad (5-23)$$

This relationship was used to express the measured torque characteristic in terms of the temperature coefficient. Figure 72 shows a plot of the measured temperature rise across the medium reaction build compressor at a 2400 RPM condition. Superimposed upon this plot is the measured torque characteristic data. Good agreement exists between the two curves. The measured torque characteristic falls with the probable $4^\circ F$ error bands associated with the type K thermocouple instrumentation. The only exceptions are the two points corresponding to data acquisition runs that were performed immediately after the compressor was transitioned

from a rotating stall state at zero mass flow. These points are *not* indicative of the energy balance given by Equation 5-21 because the compressor was just previously run at a "hot" operating condition. As a result, residual heat transfer from the still hot compressor blading is causing the flow to experience a greater temperature rise than would have otherwise occured from the mechanical work input to the compressor alone.

For a given temperature measurement accuracy, lower reference temperatures and temperature differences across the compressor made this type of comparison extremely difficult at the lower rotational speeds. However, the lower speedline temperature-torque coefficient comparisons show the same type of general torque level agreement (but with considerably more scatter in the temperature data). These comparisons are useful with respect to providing greater confidence in the torque level measurements.

Before leaving this discussion of the time-average torque measurement results, it is instructive to consider some of the torque level predictions which result from a steady-state, two-dimensional, axisymmetric flowfield interpretation of reverse flow in axial compressors. Although one of the major findings of the present effort is that the reverse flowfield in axial compressors is unsteady, and three-dimensional; the reverse flow theories presented by previous investigators [14, 46] tend to advance this flowfield description as a basis for computing overall turbomachine time-average performance. To proceed with this type of analysis, consider the two-dimensional uniform flowfield depicted in Figure 73.

At the inlet to the moving rotor bladerow, the flow exits the stationary bladerow at an absolute uniform velocity C_b with an absolute yaw angle $-\alpha_{yb}$. At the outlet to the moving rotor bladerow, the flow exits with a relative velocity W_c with a relative yaw angle β_{yc}. Conservation of angular momentum across the three moving rotor bladerows in the three-stage test compressor yields the following expression

136

$$\mathcal{T} \; = \; \dot{m} \, R_M \sum_{i=1}^{3} \left(C_{Y_c} - C_{Y_b} \right)_i \qquad (5\text{-}24)$$

where the index $i = 1, 2, 3$ represents each of the three stages in the compressor and the mass flow rate through the compressor is $\dot{m} = \rho A_c \bar{C}_x$.

Dividing each side of Equation 5-24 by the square of the mean blade speed and further rearrangement yields

$$\frac{\mathcal{T}}{\frac{1}{2} \rho U^2 A_c R_M} \; = \; 2 \left(\frac{\bar{C}_x}{U} \right) \sum_{i=1}^{3} \left(\frac{C_{Y_c}}{U} - \frac{C_{Y_b}}{U} \right)_i \qquad (5\text{-}25)$$

where from geometry

$$\left(\frac{C_{Y_b}}{U} \right)_i = \left[\left(\frac{\bar{C}_x}{U} \right) \tan \left(-\alpha_{Y_b} \right) \right]_i \qquad (5\text{-}26a)$$

$$\left(\frac{C_{Y_c}}{U} \right)_i = \left(\frac{W_{Y_c}}{U} \right)_i + 1 = \left[\left(\frac{\bar{C}_x}{U} \right) \tan \beta_{Y_c} + 1 \right]_i \qquad (5\text{-}26b)$$

and hence,

137

$$\psi_T = 6\left(\frac{\bar{C}_x}{U}\right) + 2\left(\frac{\bar{C}_x}{U}\right)^2 \sum_{i=1}^{3}\left(\tan\alpha_{Y_b} + \tan\beta_{Y_c}\right)_i \qquad (5\text{-}27)$$

which is a steady-state, meanline, axisymmetric representation for the reverse flow torque coefficient of a three stage axial compressor.

In general, previous attempts to model reverse flows in axial turbomachinery have resulted in a slight modification of the uniform flow assumption. Zehner [46] and Koff [17] both assume that the flow in each individual blade passage separates into a series of jets and wakes as shown in Figures 28b and 28c. Equation 5-27 can be modified to include this blade-to-blade degree of non-uniformity by including a blockage factor in the second order flow coefficient term:

$$\psi_T = 6\left(\frac{\bar{C}_x}{U}\right) + \frac{2\left(\frac{\bar{C}_x}{U}\right)^2}{\left(1 - \frac{A_B}{A_c}\right)} \sum_{i=1}^{3}\left(\tan\alpha_{Y_b} + \tan\beta_{Y_c}\right) \qquad (5\text{-}28)$$

where A_B/A_c is the blockage ratio. On a blade-to-blade basis, the blockage ratio is the fraction of the blade passage spacing which admits no flow. (In terms of Figure 29a or 29c, $A_B/A_c = \mu$.)

The above torque coefficient equation was evaluated for the first compressor build by defining α_{Y_b} and β_{Y_c} as the arithmetic average of the stagger angle setting and the leading edge mean camber angle of the stators and rotors respectively. The blockage ratio was varied

138

as a sensitivity variable for the purpose of this preliminary illustrative analysis. If a free streamline theory had been applied to the problem, two hodograph equations would have been solved simultaneously to yield the exit flow angles and blockage ratio. Table IX lists the computed flow angles and results generated during this preliminary analysis. A plot of the computed torque coefficient characteristics as a function of blockage ratio is given in Figure 74. This figure also includes the measured torque characteristic for comparative purposes.

An inspection of the trends indicated in Figure 74 reveals that steady-state two dimensional interpretations of the reverse flowfield tend to underpredict the actual torque characteristic. In order to achieve a good fit of the data, extremely large blockage ratios and substantial jet velocities are required to generate a sufficient amount of angular momentum change. In Chapter 6, the detailed flowfield results will show that this type of flowfield is generated by a significant radial redistribution of the mass flow.

5.3 TIME-AVERAGED PROFILE MEASUREMENTS

The axial static pressure and total temperature profile data presented herein strongly suggests that the annulus stalled reverse flowfield is similar to the instantaneous flowfield *within* a rotating stall cell. Detailed flowfield measurements which confirm this interpretation of the time-average profile results will be presented in Chapter 6. These sections will be concerned with presenting a representative set of time-average axial profiles which characterize the annulus stalled reverse flow regime and zero mass flow rotating stall operating condition.

5.3.1. Axial Pressure Profiles

Time-average axial pressure profiles were obtained through the use of case wall static pressure taps located at each interbladerow axial measuring station (see Figure 51). If there

139

is a substantial amount of swirl (i.e. tangential or circumferential direction velocity components) at these stations, the static pressure in the annulus gap could be somewhat lower in value than the measured case static pressures. The static pressures at the IGV inlet station (#2) and the third stage stator exit (#9) were acquired by averaging the measured tip and hub wall static pressure measurements.

Although an axial static pressure profile was acquired for each of the 250+ time-average data acquisition runs for the two compressor builds, a representative set of profiles will be presented here. For convenience, the axial profiles of both reaction builds at similar flow coefficients are superimposed upon each other on the same graph. The axial static pressure coefficients plotted in Figures 75 through 79 are referenced to the IGV inlet static pressure and nondimensionalized by the reference blade dynamic head

$$\left(\psi_{s-s}\right)_{x-2} = \frac{\overline{P}_x - \overline{P}_2}{\frac{1}{2}\rho U^2} \tag{5-29}$$

where x represents the axial station measuring plane under consideration (as given by Figure 51).

5.3.1.1. Annulus Stalled Flow

The axial static pressure profiles for both reaction builds in the annulus stalled reverse flow operating regime are given in Figures 75, 76 and 77. Figure 75 depicts the axial profiles associated with a relatively large reverse flow coefficient. Figure 76 depicts a moderate reverse flow coefficient case. Most of the detailed reverse flowfield measurements reported in Chapter 6 were acquired at this operating condition. Finally, Figure 77 depicts

140

the annulus stalled axial pressure profile immediately prior to the transition back to rotating stall.

At high reverse flow coefficients, large pressure drops occur across the IGV and the stage 1 and 2 stator bladerows. Recall that the net axial flow direction is from right to left in Figure 75. Small pressure drops are observed across the moving rotor bladerows and the stage 3 stator bladerow. A comparison between the medium and high reaction builds reveals that there are almost no differences in the axial static pressure profiles at this flow coefficient. The small differences in the pressure drops across the moving rotor bladerows can be barely detected with the stage 1 rotor static pressure difference being the greatest. In the medium reaction build, there is a slight pressure rise across the first stage rotor bladerow; while in the high reaction build, a measurable pressure drop occurs.

At the moderate and low flow coefficient reverse flow operating regimes (see Figures 76 and 77), the small differences between the rotor performance of the two reaction builds cease to exist. The majority of the imposed pressure drop across the machine still occurs across the IGV and the stage 1 and 2 stator bladerows. However, significant pressure rises occur across each of the three moving rotor bladerows. The pressure rises across the rotors reach maximum values at the transition reverse flow coefficient. This time-average phenomenon is fundamentally different from the axial pressure profiles which tend to be predicted by steady-state, two-dimensional, cascade "jets and wakes" formulations of the reverse flowfield [14, 35]. Chapters 6 and 7 will provide detailed flowfield measurements and analysis which explains this phenomenon.

5.3.1.2. Rotating Stall Flow

The axial static pressure profiles of the two builds during rotating stall operating conditions are plotted in Figures 78 and 79. Figure 78 depicts the case where the rotating

141

stall cell occupies 90% of the compressor annulus immediately prior to the annulus stalled reverse flow transition. The average axial flow coefficient is approximately -0.04 for this case. On the other hand, Figure 79 corresponds to a low positive flow coefficient condition, i.e. $\bar{C}_x/U = 0.08$. The similarity between the annulus stalled axial profiles (shown earlier in Figures 76 and 77) with these profiles is probably the best time-averaged performance indication that the basic assumption underlying a parallel compressor interpretation of rotating stall is valid; i.e. the flowfield within the stall cell is essentially identical to the annulus stalled reverse flowfield.

Perhaps the most appropriate method for explaining the similarity between the time-average profiles shown in Figures 76 and 77 with those shown in Figures 78 and 79 is by formally defining the time-averaged static pressure $\bar{P}$ at a particular axial station x in terms of the assumption which underlies the parallel compressor concept. If one assumes that the instantaneous static pressure in the stall cell and in the unstalled part of the annulus are relatively constant, then an area weighted average of these characteristic pressures gives a simple expression for the time average static pressure measurements

$$\bar{P}_x = \left(\frac{A_{RSC}}{A_c}\right) P_{x_{RSC}} + \left(1 - \frac{A_{RSC}}{A_c}\right) P_{x_{UNS}} \qquad (5\text{-}30)$$

where A_{RSC}/A_c is the fraction of the annulus occupied by the stall cell, and the subscripts RSC and UNS refer to the rotating stall cell and the unstalled flow regimes respectively.

In terms of Equation 5-30, the time-average axial profiles depicted in Figure 78 should be almost entirely due to the first term of this equation because the fraction of the annulus

occupied by the stall cell is almost 90%, i.e. $A_{RSC}/A_C = 0.9$. In effect, Equation 5-30 reduces to the following approximate condition

$$\bar{P}_X \approx P_{X\,RSC}$$

A comparison of the axial profiles depicted in Figures 76 and 78 reveal a striking similarity. In fact, the time-average profile of the rotating stall condition is almost identical to the time-average profile of the annulus stalled condition. Since the time-average rotating stall profile is essentially the instantaneous rotating stall profile as indicated above, this profile data strongly suggests that the flowfield within the rotating stall cell is identical to the annulus stalled reverse flowfield.

As the compressor is throttled out of deep rotating stall to larger positive axial flow coefficients, the size of the rotating stall cell decreases. In terms of Equation 5-30, the relative influence of the unstalled term increases at the expense of the rotating stall cell term. As a result, the "staircase" profile associated with the annulus stalled reverse flowfield within the stall cell begins to give way to a smoother profile typically associated with unstalled flow. This trend is clearly evident in Figure 79.

The first significant difference between the performance of the two reaction builds becomes evident in Figure 79. As the flow coefficient increases, the unstalled portion of the annulus has a greater effect upon the time-average static pressure performance of the machine. In this way, the reaction of the build begins to effect the overall time-average rotating stall performance of the compressor even though reaction has no apparent effect upon the annulus stalled reverse flowfield (assumed to characterize the flowfield within the rotating stall cell itself).

5.3.2. Axial Temperature Profiles

Time-average axial temperature profiles were acquired through the use of exposed thermocouple probes which were positioned at the midspan location of each interbladerow axial measuring station (see Figure 51). The axial total temperature profile data is nondimensionalized in the following coefficient form

$$\left(\psi_\theta\right)_{x-13} = \frac{\overline{\overline{T}}_x - T_{13}}{\frac{1}{2}\ \frac{U^2}{C_P}} \qquad \text{(Reverse Flow)} \qquad (5\text{-}31)$$

$$\left(\psi_\theta\right)_{x-0} = \frac{\overline{\overline{T}}_x - T_0}{\frac{1}{2}\ \frac{U^2}{C_P}} \qquad \text{(Forward Flow)} \qquad (5\text{-}32)$$

where x represents the axial station measuring plane under consideration (see Figure 51).

5.3.2.1. Annulus Stalled Flow

The axial total temperature profiles which correspond to the annulus stalled pressure profiles discussed in Section 5.3.1.1. are plotted in Figures 80, 81 and 82. These profiles indicate that the total temperature of the airflow increases as it passes through the compressor. In general, total temperature increases are observed across the stationary bladerows. Since no mechanical work is performed upon the flow in these passages, the flow must not be two-dimensional or steady or both. If the flow is not two-dimensional, radial shifts in the streamtube which passes through the bladerow inlet thermocouple could cause the

144

exit thermocouple to measure the total temperature of a different, higher energy streamtube. This time-average total temperature profile evidence strongly suggests that the previous attempts to apply steady, two-dimensional cascade assumptions to the reverse flow problem may be fundamentally flawed.

A comparison of the total temperature profiles associated with each of the reaction builds tested shows a significant difference. In the high reaction build, a "hot spot" occurs at the first stage interbladerow gap between the rotor and stator. As the reverse flow coefficient is reduced, this localized "hot spot" becomes more pronounced. At the transition flow coefficient, this temperature rise peak is clearly evident.

5.3.2.2. Rotating Stall Flow

The axial total temperature profiles corresponding to the rotating stall axial pressure profiles considered earlier are presented in Figures 83 and 84. Again, the time-average total temperature can be represented as an area weighted average of the instantaneous temperatures in the stall cell and in the unstalled portion of the annulus:

$$\overline{T}_x = \left(\frac{A_{RSC}}{A_c}\right) T_{x_{RSC}} + \left(1 - \frac{A_{RSC}}{A_c}\right) T_{x_{UNS}} \qquad (5\text{-}33)$$

A similar rationale can be applied to the total temperature profile as was applied to the static pressure profile. At the transition point flow coefficient, the rotating stall cell occupies 90% of the annulus. Therefore, the time-average total temperature profile is essentially the profile within the stall cell, i.e.

145

$$\overline{T}_x \approx T_{x \, RSC}$$

If the parallel compressor concept is valid, then the total temperature profile at this transition point rotating stall condition should appear much like the total temperature profile of the annulus stalled flow condition. The agreement between the total temperature profiles plotted in Figures 81 and 83 tends to support this conclusion. Although the profiles associated with each of the two reaction builds are easily distinguishable from each other, the similarity between the profiles of the same build is unmistakable.

Finally, as the flow coefficient is increased, the total temperature profile patterns shown in Figure 84 are observed. Net temperature rises across the rotor bladerows of stages 2 and 3 are still not observed because the stall cell occupies a considerable portion of the compressor annulus. This fact is confirmed by the continued existence of the localized "hot spot" in the high reaction build of the stage one rotor-stator measuring plane.

5.4 STALL CELL PROPERTY MEASUREMENTS

Although rotating stall measurements were not a primary focus of this experimental effort, stall cell size and speed information could be obtained with the existing data acquisition system and a single reference hot wire sensor. The experimental technique used to acquire stall cell property data is fully described in Section 4.3.1.

In general, stall cell speed and size vary as a function of axial flow coefficient. Figures 85 and 86 are plots of stall cell speed as a function of flow coefficient for the medium and high reaction compressor builds respectively. In these figures, stall cell speed is expressed as a percentage of the shaft rotational speed. These figures clearly show a decrease in stall cell speed with decreasing flow coefficient until a minimum stall cell speed is encountered at

146

an axial flow coefficient of 0.08. At lower positive flow coefficients and net reverse flow coefficients, the stall cell speed increases sharply. This trend is evident in both the medium and high reaction builds. In both cases, a minimum stall cell speed occurs at a flow coefficient $\bar{C}_x/U = 0.08$. The only difference between the two builds is that the minimum stall cell speed for the medium reaction build is slightly lower than that of the high reaction build. In both cases, the data points for all three speedlines collapse to a well defined curve. To the best of the author's knowledge, the establishment of a clear minimum stall cell speed at low forward flow and a subsequent increase in the stall cell speed immediately prior to annulus stalled transition has never been documented before.

The rotating stall cell size measurements for both reaction builds are depicted in Figures 87 and 88. There is somewhat more scatter in this data because of the additional judgements which are required to generate stall cell size information (see Section 4.3.1. for a detailed explanation). In the case of the medium reaction build, there is a noticeable shift in the data acquired by the author with that previously acquired by Eastland [47]. However, the slope of the size vs. flow coefficient curve is consistent. Section 4.3.1 also gives a detailed explanation for the shift in this data. In general, this discrepancy arises from the additional judgements which are required to reduce stall cell size information from a somewhat ambiguous oscilloscope trace such as the one given in Figure 57. In both builds, the stall cell size increases linearly with decreasing flow coefficients. At the transition flow coefficient to annulus stalled flow, the maximum stall cell size is approximately 90% of the compressor annulus.

5.5 FLOW MODE SUMMARY

Two recognizable stalled flow modes have been observed: 1) rotating stall, and 2)

147

annulus stalled flow. A large amount of hysterisis accompanies the transition from unstalled operation to the rotating stall mode. The pressure rise performance of the compressor falls off sharply at this transition. Torque level falls off gradually. A stable, full span rotating stall cell condition is maintained thereafter through the lower valued positive flow coefficients without any discontinuities in performance. This rotating stall condition is also stable at net reverse flow coefficients until a second transition point is reached at a flow coefficient of

$$\bar{C}_x/U = -0.04.$$

The second transition signals a change in stalled flow mode. A discontinuous drop in overall pressure rise performance is realized as a new, annulus stalled flow condition is established. The torque absorbed by the compressor falls off drastically. In addition, the acoustic signature is noticeably different. The real time output of a hot wire placed in front of the IGV bladerow reveals that the large scale asymmetry caused by the presence of the rotating stall cell has ceased. A spectrum analysis of the hot wire output confirms that all low harmonic periodicity in the signal is no longer present. In the following chapter, the results of a detailed flowfield characterization of this annulus stalled condition will be presented.

Chapter 6

HIGH RESPONSE FLOWFIELD RESULTS

The velocity and pressure field information obtained from high response measurements of a multistage axial compressor reverse flowfield are presented in this chapter. Aside from several introductory comments regarding the general nature of the complex flow processes which exist in axial compressor reversed flowfields, the discussion in this chapter will be limited to the purpose of providing a coherent presentation of the unsteady, three-dimensional flowfield data acquired during this research effort. In Chapter 7, the results of a kinematic and dynamic analysis of the relevant fluid mechanics associated with reversed flows are presented.

This experimental investigation is the first attempt to study the detailed structure of axial compressor reversed flowfields using high response instrumentation and automated digital computer data acquisition techniques. As a consequence, there was very little prior information on the type of fluid flow phenomena which might be encountered or how such phenomena could be measured and documented. The best "conventional wisdom" at the start of this investigation were the two dimensional cascade models proposed by Bammert and Zehner [35] and Koff [14] (see Sections 3.2.2. and 3.2.3.) and it was known that these models had fundamental weaknesses. Hence, it was necessary to adopt a broad based experimental program aimed at initially identifying and then documenting the types of unsteadiness and spatial movements of fluid which are present in axial compressor reversed flowfields.

149

A discussion of a few introductory concepts concerning the nature of the experiment is presented at the beginning of this chapter. The next section, Section 6.1, presents this general introduction. The principal measuring positions, the flow coefficient operating conditions investigated, and some phase-lock triggering considerations are identified in this discussion.

Section 6.2 is concerned with presenting the experimental data to document the upstream flowfield ahead of the compressor blading. Velocity and pressure field information at several radial and circumferential coordinates as well as several flow coefficient operating conditions are given. The next section, Section 6.3 deals with presenting the unsteady velocity and pressure field data which were obtained in the axial gap between the third stage rotor and stator bladerows. In a reverse flow operating condition, these two bladerows are the first two bladerows encountered by the fluid stream. In an analogous fashion, Section 6.4 presents the velocity and pressure field data at the next downstream condition where the fluid exits the third stage rotor and impinges upon the trailing edges of the second stage stator bladerow.

The presentation of representative downstream flowfield information is lumped together in Section 6.5. The two remaining downstream stages perform similiarly to stage 3 (whose detailed flowfield was presented earlier in Sections 6.3 and 6.4). The final section summarizes the flowfield characterization results presented in this chapter.

6.1 INTRODUCTORY CONSIDERATIONS

As mentioned earlier, the nature of this experimental effort was both an exploratory investigation of the structure of axial compressor reversed flowfields and a detailed documentation of that structure at several representative flow coefficients. During the course of the investigation, it was soon discovered that detailed flowfield measurements at low,

150

moderate, and high reverse flow coefficients would be necessary to give a representative characterization of axial compressor reverse flows.

The low flow coefficient operating condition selected for detailed flowfield measurements was a $\bar{C}_x/U = -0.05$. The flowfield that exists at this flow coefficient is indicative of the annulus stalled flowfield structure which exists in the compressor in the neighborhood of the transition to rotating stall. The total-to-static characteristic depicted in Figure 63 shows that the overall pressure rise performance across the compressor at this point is approximately $\psi_{T-S} = 0.45$.

Since many parallel compressor theories of rotating stall are based upon the idea that an annulus stalled reverse flowfield exists at the center of a rotating stall cell; it was decided to investigate a flow coefficient at which the pressure rise performance across the compressor is nearly the same as the pressure rise level associated with rotating stall operation. For this reason, a moderate reverse flow coefficient was chosen for detailed flowfield characterization at a $\bar{C}_x/U = -0.10$. At this point, the overall total-to-static pressure rise coefficient has a value nearly equal to unity. The kinematic analysis given in Chapter 7 will show that the flowfield at this rotating stall pressure level is fundamentally different than at other levels on the annulus stalled reverse flow characteristic.

As an upper limit on the maximum reverse flow condition which might be encountered during the surge or rotating stall operation of an aircraft gas turbine engine, a reverse flow coefficient commensurate with the peak unstalled pressure rise capability of the machine was selected. For this build of the MIT 3-Stage Research Compressor, the peak unstalled pressure rise coefficient of the compressor occurs at a value of $\psi_{T-S} = 2.2$. Hence, a high reverse

151

flow coefficient operating condition of $\bar{C}_x/U = -0.19$ was selected in accordance with the measured performance characteristic illustrated in Figure 63.

In addition to the selection of representative average flow coefficients, a decision on where and how to acquire high response velocity and pressure field data was necessary. The principal measuring position coordinate grid and phase-lock data acquisition techniques that evolved over the course of the investigation were tailored to deal with the unsteady and three-dimensional processes which naturally occur in axial compressor reverse flowfields. The following two subsections present a brief introduction to the spatial resolution and phase-lock triggering considerations which have an impact on the acquisition of instantaneous reverse flow information. It is hoped that these comments may aid anyone interested in conducting similar experiments.

6.1.1. Principle Measuring Positions

The reverse flowfield of an axial compressor can be generally categorized as being both unsteady and three-dimensional. The flow is unsteady primarily because of the rotating turbomachinery, but also because one or more acoustic spinning modes can be excited. The three-dimensionality of the flow is evidenced by strong radial and circumferential variations in the velocity and total pressure fields.

The amount of three-dimensionality in the flow mandates the minimum number (and maximum spacing) of the radial and circumferential measuring positions which are deemed adequate to describe flow variations at each of the axial stations. Behind moving bladerows, the requirement for rotor frame resolution of circumferential variations must be satisfied by proper selection of compressor rotor speed and data acquisition rate. Finally, the minimum

152

spatial resolution associated with the physical size of the sensing element effectively limits the minimum practical spacing of circumferential measuring stations.

These factors guided the selection of the principle measuring positions used during this investigation. These positions are illustrated in Figure 89. A total of 5 radial planes, 11 circumferential planes and 8 axial stations are defined in this figure. The 5 radial planes, numbered 1 through 5, are located at the 15, 30, 50, 70, and 85% blade span locations respectively. (The blade span of this constant annulus compressor is approximately 1.44 inches).

The circumferential positions are located at 0.125 inch intervals (at the 12.000 inch case inner wall radius). At an average stator bladerow pitch spacing of approximately 0.750 inches, these circumferential positions represent a 17% pitchwise blade passage resolution. The IGV bladerow has a greater solidity and as a result, these circumferential positions yield a 25% blade passage resolution for the IGV bladerow.

This measuring location grid pattern allowed adequate resolution of the radial and circumferential variations of velocity and total pressure. Typically, measurements were made at all five radial locations once the computer controlled probe traversing mechanism and instrumentation probe were positioned at a given axial and circumferential coordinate. It should be noted that radial traverses of the annulus are *required* to document the strongly three-dimensional character of axial compressor reverse flowfields. In addition, the instrumentation used to measure the velocity field must be capable of resolving radial velocity components due to the fact that simple radial equilibrium conditions (i.e. the condition represented by Eq. 7-32) certainly do not exist in the interbladerow axial gaps downstream of the rotor bladerows.

Although detailed velocity and total pressure radial traverses were not made at each of the 88 potential axial-circumferential coordinate combinations defined in Figure 89, a

153

significant number of these locations were used to acquire a 50 msec duration[33] time trace at a 20 Khz sample rate. Only selected examples will be presented to support the conclusions reached in Chapter 7. It should be noted, however, that the wider body of results accumulated during this experimental effort *has* been used to substantiate these conclusions.

6.1.2. Phase-Lock Triggering

In Chapter 4, a detailed discussion of the phase-lock triggering circuit that was developed for reverse flow measurements was presented. Three triggering circuits were identified: rotor locked, event locked, and synchronous triggering. This section addresses the question of which type of phase-lock triggering should be used to acquire instantaneous flowfield information under a given set of circumstances.

At the outset of this discussion, it is important to recall why phase-locked measurements are necessary. One important reason is the desire to obtain enhanced ensemble average representations of periodically unsteady analog data signals. Typically these signals have aperiodic or random noise components imbedded in the waveform of interest. Phase-locking allows the ensemble averaging process, illustrated in Table VII, to enhance the individual raw analog signals by allowing the mean and periodic fluctuating components to be retained, while averaging to zero any non-periodic random components (e.g. noise or turbulence).

Perhaps a more important reason for phase-locking the high response measurements is the inherent nature of the technique employed to acquire 3-D velocity field information. The use of a single slanted hot wire sensor requires that three independent measurements of the

---

[33] This time duration corresponds to the elapsed time during one complete rotor revolution.

same or an identical flowfield be made. Phase-locking insures that this requirement is met for acquiring measurements of periodically unsteady flowfields. Another reason for obtaining phase-locked measurements is the similar desire to align independent pressure and velocity measurements of a periodically unsteady flow with respect to a common stationary reference signal. A final reason is the requirement to identify the number and frequency of steady rotating disturbances. This requirement is satisfied by phase-locking independent measurements of the rotating phenomenon at different circumferential positions with respect to a common stationary reference signal.

Given these reasons for obtaining phase-locked measurements, the nature of the periodic unsteadiness in the flow is a very important consideration in evaluating the suitability of employing a particular type of phase lock trigger technique. One must be certain to identify all the relevant frequencies contained in the analog voltage signal. Next, a suitable method for initiating a triggering signal which is phase-locked to a given point in the period of all the fundamental frequencies must be developed.

During this experimental investigation of reversed flows, the first task, i.e. identifying the relevant frequencies in the analog signal, was accomplished by monitoring the quasi-instantaneous spectral trace of the signal on the screen of a Hewlett-Packard Model 3582A digital spectrum analyzer. This particular model produces nearly real time spectral traces of the instantaneous analog voltage signal by using digital methods to filter and store the input signal before employing a digital microprocessor to perform a Discrete Fast Fourier Transform on the stored data. This eliminated the need to store and post process instantaneous analog signals to identify the relevant frequencies contained in the analog waveform.

In most cases, a spectral trace of the analog signals received from high response hot wire or pressure transducer sensors placed in the reverse flow environment reveals that the

155

blade passing frequency is the dominant source of unsteadiness. In these cases then, phase-locking the measurements to the rotor via the fiber-optic technique outlined in Chapter 4 is sufficient to acquire instantaneous flowfield information.

At the moderate flow coefficient operating condition, a multi-lobed spinning pressure field disturbance was observed to occur at a fundamental frequency which is approximately 20% greater than the stage 3 rotor blade passing frequency. Since this frequency is not an interger multiple of the shaft rotational speed, the synchronous phase-lock trigger must be employed to avoid averaging away the effects of the spinning flow mode "event". Phase synchronization of these two fundamental frequencies can be accomplished by placing a reference high response sensor in the upstream flowfield outside of the compressor blading. At this location, the influence of the spinning pressure field disturbance is still present, however, the unsteadiness associated with the blade potential field is no longer present.

The need to successfully employ a synchronous triggering technique to acquire instantaneous information is highlighted by the following illustrative example. A typical instantaneous time trace of the wall static pressure at axial station #8, circumferential position #6, and the moderate reverse flow coefficient operating condition is given in Figure 90. A spectrum analysis of this signal is depicted in Figure 91. The spectral trace clearly shows periodic unsteadiness is present at three frequencies: 477 Hz, 955 Hz, and 1125 Hz. The first two frequencies are one-half of blade passing and the blade passing frequency respectively. The highest spectral peak occurs at the frequency associated with the multi-lobed rotating pressure pattern.

Figures 92 and 93 respectively illustrate ensemble averaged traces which are produced by phase-locking the measurements to the rotor or the spinning flow mode "event" only. In both cases, the averaging process has caused information to be lost. This fact can be easily verified by comparing the ensemble averaged waveforms plotted in Figures 92 and 93 with

156

the original instantaneous trace in Figure 90. On the other hand, if the synchronous phase-lock triggering technique is employed; then an ensemble averaged trace is produced which is representative of the original waveform. Figure 94 illustrates this point. In this figure, a plot of a synchronous triggered ensemble average trace is superimposed upon the original instantaneous trace. The agreement between the two traces is a firm indication that the ensemble averaged result is a good representation of the instantaneous signal.

During the remainder of this thesis, the majority of the results reported will be ensemble averaged representations of the required instantaneous signals. The phase-lock technique used to acquire these ensemble averaged traces will be always identified. Occasionally, spectrum traces and superimposed plots of ensemble averaged and instantaneous results will be presented to support the conclusions reached.

6.2 UPSTREAM FLOWFIELD

The upstream flowfield measuring plane, axial station #9, is located behind the trailing edges of the third stage stator bladerow. The axial spacing between this measuring plane and the stationary stator bladerow is about 0.300 inches or about 25% of the stator bladerow axial chord and 37% of the pitch (blade spacing). The velocity, static pressure and total pressure measurements of the flowfield which exists at this axial station during reverse flow operation are summarized in the following subsections.

6.2.1. Velocity Measurements

A slanted hot wire sensor was used to acquire the velocity field. Phase-locked ensemble averaged measurements of the flow were required at three different spatial orientations of the sensor. The axial, tangential, and radial components of the absolute velocity vector are reduced from the three phase locked ensemble averaged raw voltage-time traces by first

157

applying the appropriate second order velocity magnitude calibration to generate effective cooling velocity ensemble averaged time traces.

Along with the known orientations and directional sensitivity calibration coefficients of the slanted hot wire sensor, each of the individual corresponding points on the effective cooling velocity traces are further reduced. This directional sensitivity phase of the velocity reduction process is accomplished through the simultaneous solution of the governing set of six nonlinear algebraic equations by the methods described in Chapter 4.

6.2.1.1. Flow Coefficient Survey

A representative time trace of the upstream velocity field at the moderate reverse flow coefficient operating condition is given by the axial, tangential, and radial component traces depicted in Figure 95. The legend at the top of this figure indicates that a synchronous phase lock trigger was used to acquire a 128 trace ensemble average representation of the effective cooling velocity at each slanted wire orientation. The probe position data portion of the legend indicates that these velocity component traces were acquired at the upstream axial station #9, circumferential position #2, and at radial position #4 (70% blade span location). Finally, the mean flow coefficient portion of the legend indicates that the time average axial flow coefficient at this radial position is approximately equal to a value of -0.11 while there are essentially no mean radial or tangential velocity components.

This figure illustrates that small amplitude, high frequency fluctuations in all three components of the velocity field are present. The amplitude of these fluctuations is about 4.5% of the mean axial flow coefficient through the machine. The frequency of the fluctuations corresponds to the 1145 Hz spinning pressure disturbance which exists at this particular reverse flow coefficient. There are no observable circumferential variations in this basic representation of the upstream velocity field.

158

Before proceeding to the next flow coefficient, it is instructive to review the effective cooling velocity traces from which the absolute velocity component traces depicted in Figure 95 were reduced. The ensemble averaged representation as well as an actual instantaneous trace of the measured effective cooling velocities are plotted in Figure 96. The sensor orientations which appear in the legend at the top of this figure are defined by the geometry conventions given earlier in Figure 61. A sensor orientation of zero degrees corresponds to a probe alignment where the sensor lies in the X-R plane with the long support closest to the compressor blading. The excellent agreement between the ensemble average and instantaneous effective velocity traces is an indication that the reduced velocity components plotted in Figure 95 accurately correspond to the instantaneous velocity field upstream of the compressor blading.

Figure 97 presents the reduced local flow coefficient components of the upstream flowfield at the low ($\tilde{C}_x/U = -0.05$) mean axial flow operating condition. The high frequency fluctuations associated with a spinning pressure disturbance have shifted to nearly the stage 3 rotor blade passing frequency (about 980 Hz). A comparison of the ensemble averaged and instantaneous effective cooling velocity traces reveals that the unsteadiness in the flowfield is more random.

The reduced local flow coefficient components of the velocity field at the high flow coefficient operating condition ($\bar{C}_x/U = -0.19$) are given in Figure 98. This flowfield is essentially uniform with no tangential and radial components and no high frequency periodic fluctuations. The absence of any organized periodicity in the flowfield mandated the use of arbitrary rotor locked triggering to acquire these mean velocity component traces.

159

6.2.1.2. Radial Traverse Results

The time traces presented in the previous section are generally representative of each respective upstream flowfield condition at the 85%, 70%, 50% and to a lesser extent, the 30% blade span radial locations. At the 15% blade span location, the velocity field is dominated by a significant amount of random unsteadiness. This trend is present at all three flow coefficient operating conditions. To illustrate this phenomenon, the instantaneous and ensemble averaged effective cooling velocity measurements at the first radial position closest to the hub are shown in Figure 99 for the moderate flow coefficient condition. Large, aperiodic fluctuations in the instantaneous effective velocity trace are clearly evident. An ensemble average of this signal tends to produce the time average mean effective velocity levels.

The radial profiles of the circumferential area averaged mean flow coefficient components are listed in Table IX. These profiles tend to support the conclusion that a slight tangential swirl in the direction of rotor rotation is present at the lowest radial position. This effect is most pronounced in the low flow coefficient operating condition. The large, aperiodic fluctuations and the time average swirl at the hub position are the direct effects associated with the moving hub inner surface or even possibly flow through the aft hub seal. At this point, one should recall that this particular axial measuring station is several chord lengths downstream of the seal which separates the moving and stationary portions of the flowpath's inside surface. In this respect, these phenomena are effects associated with the specific design of the canterlevered stator compressor.

6.2.2. Static Pressure Measurements

High response measurements of the instantaneous static pressure field were made with the specially constructed probe shown earlier in Figure 54. A miniaturized differential strain

160

gage type pressure transducer was flush mounted at the end of a length of stainless hyperdermic tubing. The reference relief tube was left vented to the atmospheric conditions in the test cell. The entire assembly was then flush mounted at the inner case wall.

Pre- and post-test static calibrations of the pressure transducers revealed that significant amounts of zero point drift can occur during a normal one-hour test series. In order to avoid zero shift problems and provide a standard reference condition, direct time average measurements of the static pressure level with respect to the compressor inlet supply conditions were made using an extremely accurate Baratron electronic pressure sensor. These measurements were used to correct the average output level from the high response miniature pressure transducers. The resulting static pressures were normalized with respect to the mean blade dynamic pressure. Throughout the remainder of this thesis, the pressure transducer calibration data as well as the dimensional pressure normalizing information will appear with the pressure coefficient time traces.

The discussion of the upstream velocity field implies that a spinning pressure field disturbance is probably present at the moderate flow coefficient operating condition. Before proceeding with the presentation of wall static pressure coefficient time traces, it is useful to review the spectral signature of the analog signals from wall static pressure instrumentation at several mean axial reverse flow coefficients.

6.2.2.1. Spectral Signature

The wall static pressure spectral signatures shown in Figures 100a through f illustrate the change in frequency content of the upstream pressure field disturbances which exist at various points on the reverse flow characteristic. At high reverse flow coefficients, there are virtually no periodic static pressure disturbances. At moderate flow coefficients, a single periodic pressure disturbance centered at 1145 Hz exists over a very narrow range of

161

flow coefficients. This narrow range of flow coefficients, however, is precisely the range of flow coefficients where the overall total-to-static pressure rise across the compressor is essentially the same as that of the rotating stall characteristic (see Figure 63). At lower reverse flow coefficients, the 1145 Hz pressure disturbance frequency mode disappears and is replaced by a 980 Hz near blade passing frequency mode. This lower frequency mode persists until the transition point to rotating stall is reached.

6.2.2.2. Circumferential Survey

The instantaneous and ensemble averaged representation of the upstream wall static pressure at the moderate flow coefficient operating condition appears in Figure 101. This wall static pressure trace was acquired at circumferential position #2 using synchronous phase lock triggering. Although the agreement between the traces is good, the ensemble average trace represents a mean waveform pattern which is better suited to the purpose of making phase relationship comparisons. For this reason, the ensemble average static pressure traces acquired at circumferential positions #6 and #10 are shown in Figure 102 along with the ensemble average trace from circumferential position #2.

The phase shift present in Figure 102 is clear evidence that the periodic pressure disturbances in the upstream flowfield are rotating around the annulus of the compressor. The direction and speed at which the multi-lobed pressure disturbance pattern propagates will be discussed in Chapter 7.

6.2.3 Total Pressure Measurements

High response total pressure measurements of the upstream flowfield were accomplished with a specially constructed Kiel Head total pressure probe (also shown earlier in Figure 54). As was the case for the high response static pressure measurements, pre-test and

162

post-test calibrations were performed. Pressures were referenced to the subatmospheric compressor inlet conditions and normalized by the mean blade dynamic pressure.

Figure 103 contains a representative set of instantaneous and ensemble average traces of the fluctuating upstream total pressure field at radial positions #4. These traces are fairly representative of the total pressure measurements made at the moderate reverse flow coefficient condition. In Chapter 7, the relationships between the acquired velocity, static pressure and total pressure data presented here will be analyzed in greater detail.

6.3 THIRD STAGE ROTOR-STATOR INTERACTION FLOWFIELD

The intermediate rotor-stator interaction flowfield at axial measuring station #8 is dominated by periodic unsteadiness. This measurement station is located directly in the center of the 0.750 inch axial gap which exists between the stage 3 moving and stationary blade rows. Of the three operating conditions investigated, the moderate flow coefficient flowfield is the most complex. An alternating flow pattern in the rotor frame appears to exist. In addition, at least two modes of periodic unsteadiness exist in the pressure field. This case will be treated first. The flowfields at the high and low flow coefficients are simpler. These cases will be addressed in later subsections.

6.3.1. Moderate Reverse Flows ($\bar{C}_x/U = -0.10$)

The two sources of periodic unsteadiness which are present at this flow coefficient appear to be related to the fundamental blade passing frequency of the rotating bladerow and the occurance of a spinning multi-lobe pressure disturbance pattern. In the following subsections, the alternating pattern associated with the velocity field and the rather complex unsteadiness of the pressure field are reviewed in detail.

6.3.1.1. Velocity Field Alternating Flow Pattern

The alternating flow pattern of the velocity field can be clearly seen in the reduced time trace of the absolute velocity components at radial station #5 (85% blade span location). These velocity components are plotted in Figure 104. The axial flow coefficient profile shows regions of relatively high throughflow at slightly greater than 2 millisecond intervals. Regions of highly retarded flow also occur at the same periodic intervals. These time intervals correspond to a cyclic period which is *twice* the inverse of the blade passing frequency.

The tangential flow coefficient profile contains the same type of cyclic frequency content. Furthermore, a definite phase relationship exists between the perturbations in the axial and tangential flow coefficient profiles. This phase relationship indicates that regions of highly retarded axial throughflow are always preceeded by a change in the direction of the tangential velocity component. At these points, the tangential velocity component reverses directions from the direction of the moving blade row rotation (positive C_Θ/U) to a direction against the direction of rotation (negative C_Θ/U). In terms of the absolute flow direction convention illustrated in Figure 58, the flow has no tangential velocity component at the 2.15 msec point in the time trace. At 2.65 msec, a maximum positive yaw angle direction of 38^0 to the X-R plane of the compressor is achieved. In the next 100 microseconds, the flow changes directions by 106^0 to a maximum negative yaw angle direction of -68^0. This flow direction change is slightly greater than the calibration range of the hot wire sensor, and as a result, sharp "spikes" occur in the radial velocity component time trace. These "spikes" correspond to the points where convergence was not achieved during the velocity reduction process.

164

The drastic change in the absolute direction of the flow indicates the passage of a rotor blade. In front of the pressure surface side of the blade, the maximum axial velocity vector appears to be 50% greater than in front of the suction surface side of the blade. At the next blade passing position in the time trace, about the 3.75 msec location, positive tangential velocity components are not generated in front of the pressure surface of the blade. It appears from these high response time traces that the flow through this bladerow is diverted about every other rotor blade passage. Hence, the alternating pattern in the velocity field is of the order of every other rotor blade passage.

The reduced flow coefficient profiles in Figure 104 were derived from the ensemble average effective cooling velocity traces presented in Figure 105. An instantaneous effective cooling velocity trace is superimposed to illustrate the agreement between the two traces. The degree to which the ensemble average trace corresponds to the fluctuations in the instantaneous waveform is a direct indication of how well the reduced local flow coefficients will correspond to the instantaneous velocity field.

Rotor locked triggering was used to produce the agreement between the traces in Figure 105. Real time spectral analysis of the linearized analog voltage signals from the constant temperature anemometer bridge output indicated that this type of phase lock triggering would be sufficient to retrieve the peridically unsteady instantaneous effective cooling velocity waveforms. Synchronous triggering measurements were performed to confirm this observation. As expected, the synchronous measurements failed to improve the agreement between the two traces. Aperiodic fluctuations in the flow appear to be responsible for the slight discrepancies which do exist.

6.3.1.2. Spatial Survey of the Velocity Field

In the previous section, the existence of a basic alternating pattern in the velocity field

was documented. This section is concerned with presenting an understanding of how that velocity field varies along the span and across the pitch spacing of the blades. Figures 106 through 109 depict a radial traverse of the velocity field at the same circumferential position. These figures show that the alternating flow pattern which exists at the 85% blade span location extends downward through the 50% midspan location, i.e. every other rotor blade passage appears to be blocked at the higher radial locations.

At radial station #2 (30% blade span), the every other rotor blade passage alternating pattern fades into a blade-to-blade flow pattern. The agreement between the ensemble average and instantaneous traces of the effective cooling velocities at the 70%, 50% and 30% blade span positions is similar to the agreement at the 85% blade span location. Figure 110 depicts the effective velocity comparison at radial station #2.

However, the flowfield at the closest radial position to the hub is extremely turbulent and subject to large aperiodic fluctuations. There is considerable lack of agreement between the ensemble average and instantaneous traces of effective cooling velocity at this radial position. As a consequence, the local flow coefficients presented in Figure 109 should not be interpreted as a representation of the instantaneous flowfield. Significant aperiodic components in the instantaneous flowfield have been lost in the ensemble averaging process.

A constant radius circumferential survey of the axial and tangential components of the velocity field are presented in Figures 111 and 112 respectively. This "waterfall" presentation format clearly shows the propagating nature of the disturbances associated with the motion of the rotor blades. A comparison of the waveform phase relationships in these figures shows that the waveform measured at circumferential position #8 lags the circumferential position #4 waveform by 340 microseconds. Since these circumferential positions are approximately 0.491 inches apart at this radius, the speed of the propagating

166
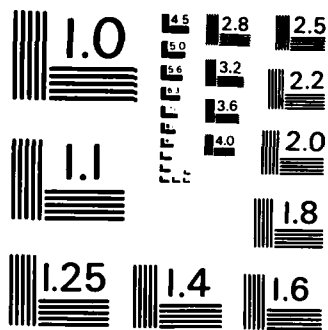
MICROCOPY RESOLUTION TEST CHART

NATIONAL BUREAU OF STANDARDS-1963-A

disturbance predicted by the waveform phase relationships is approximately 120 ft/sec, which is the blade passing speed at the 1170 RPM test condition.

6.3.1.3. Pressure Field Unsteadiness

A representative case wall static pressure trace has been previously presented in Figures 90 and 94. Although it might be assumed that the dominant frequency associated with the fluctuations in this trace is the blade passing frequency of the third stage rotor, i.e. 955 Hz, closer inspection reveals that the period of these fluctuations is approximately 890 microseconds. This period suggests that the 1145 Hz characteristic frequency associated with the spinning pressure disturbance (observed in the upstream flowfield) dominates the case wall static pressure field at this axial station.

This observation was confirmed by the spectral analysis of the static pressure trace waveform shown earlier in Figure 91. This figure also indicated that there is considerable strength in the coefficients associated with blade passing frequency and one-half of the blade passing frequency. The combined effect of these sources of unsteadiness is the waveform illustrated earlier in Figure 90.

Total pressure traverses of the rotor-stator interaction flowfield at axial measurement station #8 were performed also. Figures 113 and 114 contain time traces of the total pressure measurements made at the 85% and 30% blade span locations respectively. The corresponding spectrum traces of these total pressure traces are given in Figure 115. The total pressure traces and the spectrum plots clearly show that the total pressure fluctuations are predominantly due to the unsteadiness associated with the 1145 Hz spinning pressure disturbance. The effects associated with blade passing frequencies have no significant impact on the total pressure fluctuations at this axial station.

167

6.3.2. High Reverse Flows ($\bar{C}_x/U = -0.19$)

As the compressor is throttled deeper into reverse flow, the spinning pressure disturbance source of unsteadiness disappears along with the alternating flow pattern. At the high reverse flow coefficient condition, a single source of periodic unsteadiness exists. This source is the fundamental blade passing frequency of the stage 3 rotor blades.

The velocity field which exists at the 85% blade span location, unlike the moderate reverse flow condition, is non-alternating to within a blade-to-blade variation. The instantaneous components of the absolute velocity vector at this radial location are shown in Figure 116. The fluctuations in the axial velocity profile are practically sinusoidal with a peak perturbation amplitude that is nearly 20% of the mean axial flow coefficient. There is a large mean tangential swirl against the direction of rotor rotation, i.e. a swirl greater than the swirl associated with flow which exits at the stator exit blade angle. The fluctuations in the tangential velocity profile have peak perturbation amplitudes which are approximately equal to the magnitude of the mean swirl value. The tangential velocity waveform leads the axial component waveform by a 90° phase shift.

The instantaneous and ensemble averaged effective cooling velocities (from which this velocity field information has been derived) are presented in Figure 117. The very good agreement between these traces is further proof that the flowfield at this high reverse flow condition is well organized and periodically unsteady at the blade passing frequency. Radial traverses of the velocity field at this flow coefficient show no change in the representative profiles given in Figures 116 and 117 for the 85% blade span position.

A representative wall static and total pressure time trace at this axial station and operating condition are depicted in Figures 118 and 119. The corresponding spectral

168

signatures are plotted in Figure 120. These figures essentially indicate that a single source of unsteadiness is present - the unsteadiness associated with the moving rotor blades.

6.3.3. Low Reverse Flows ($\bar{C}_x/U$ = -0.05)

Upon throttling the compressor to lower reverse flow coefficients, the organized flowfield structure observed at high reverse flows transitions into the organized alternating flow pattern observed at moderate reverse flows. Further throttling of the compressor to very low reverse flow coefficients causes the organized alternating flow pattern and spinning pressure disturbance mode to be replaced with a more disorganized flowfield structure. This fact is evidenced by the representative effective cooling velocity traces shown in Figure 121.

Although the ensemble averaged representation of the sensor effective velocity qualitatively suggests that a time averaged blade-to-blade periodic unsteadiness is present in the flowfield, the instantaneous trace gives a good indication of the amount of randomness which is present in the flow. As a result, it was impossible to obtain detailed quantitative information about the flowfield structure at this low reverse flow coefficient condition. Figure 122 depicts the rotor locked time averaged absolute velocity components which were reduced from the ensemble average effective velocity trace given in Figure 121.

To complete the documentation of the flowfield at this axial station and flow coefficient, a representative set of wall static and total pressure time traces are presented in Figures 123 and 124. Spectral analysis plots of these waveforms are contained in Figure 125.

6.3.4 Station #8 Mean Flowfield Summary

Before proceeding to the next axial station, it is useful to review the area-averaged mean flowfield results at this measuring plane. Tables X and XI contain a listing of the

169

measured circumferential area averaged mean values of the absolute velocity vector components and the pressure field as a function of radial position. It should be noted that the information present in these tables represent circumferential average of a simple time invariant mean average of the velocity vector and pressure at the midpoint of the gap between the rotor and stator bladerows. This flowfield is heavily unsteady. Hence, these results should not be misconstrued as the instantaneous velocity profile leaving the stator bladerow and entering the rotor bladerow. Table X does show that a greater percentage of the throughflow through the compressor at this axial station appears to be through the hub region of the machine.

6.4 THIRD STAGE ROTOR EXIT FLOWFIELD

As shown in Figure 89, the axial gap immediately downstream of the third stage rotor bladerow is the location of axial measurement station #7. The high response instrumentation access slot that was installed at this station provided an opportunity to gather information about the detailed structure of the flowfield in front of the rotor bladerows. The velocity and pressure measurements of the alternating flow pattern at moderate flow coefficients will be presented first. The structure of this flowfield is fundamentally different from either the pattern at high reverse flows or the transition flow coefficient structure. The measurements of these two latter flowfields will be represented in subsequent subsections.

6.4.1. Alternating Flowfield Structure at Moderate Reverse Flow

In the previous Section 6.3.1. presentation of the upstream rotor-stator interaction station flowfield, an alternating flow pattern (where every other rotor blade passage appears to be bypassed) was observed at the moderate reverse flow condition. This pattern was most pronounced at the tip radial stations. The flowfield structure present at the downstream

170

station is manifested by a series of high velocity jets from the pressure surface of every other rotor blade. Again, this phenomenon is most prominent at the tip radial positions. In addition to rotor frame circumferential and radial variations in the velocity field, pressure measurements indicate that there are significant radial gradients in the total and static pressure fields.

6.4.1.1. Absolute Frame Velocity Measurements

The temporal signals produced by fixed flow measurement instrumentation behind a moving bladerow are sometimes considered to be a circumferential direction spatial record of the rotor frame instantaneous flowfield. This conclusion is subject to the important qualification that the presence of upstream or downstream components do not produce standing circumferential distortions in the flowfield. Several traverses at different circumferential positions with respect to the downstream stator bladerow were performed. Blade-to-blade circumferential variations in the velocity field were observed. Due to space limitations, a representative circumferential position was selected to present typical time record information of the rotor exit flowfield.

If the flow within the rotor passages is steady, then any rotor phase locked time trace of the analog signal generated by a stationary, high response flow measurement probe should be identical to any other similiarly acquired trace at the same fixed position. This set of circumstances existed at axial station #7 behind the third stage rotor bladerow. The representative instantaneous and ensemble averaged effective velocity traces shown in Figures 126 and 127 tend to support this observation. As a result, an investigation into the detailed flow structure of the rotor exit flowfield was possible.

The reduced absolute velocity component time traces presented in Figures 128 through 131 define the rotor exit flowfield at five radial positions. These figures clearly illustrate

171

several striking features of the flowfield. First, extremely large tangential or swirl components of velocity in the direction of rotor rotation are present. The swirl components are greater than the local blade speed at all five radial locations. At the 85% blade span position, these swirl velocity components can attain maximum speeds in excess of 150% of the local blade speed. A flowfield characterized by simple solid body rotation is not suggested by this experimental evidence.

The presence of predominantly negative radial flow components towards the hub of the machine is another striking feature of the flow. The existence of these radial velocity components suggests that simple radial equilibrium conditions are not present at this axial gap measurement plane. The fully three-dimensional nature of the flow is further evidenced by the radial variations in the mean and fluctuating components of the velocity vector.

6.4.1.2. Rotor Frame Flow Pattern

The temporal periodicity and phase relationships of the waveforms depicted in Figures 128-132 tend to support the conclusion that an alternating flow pattern exists in the rotor bladerow. Since the blade passing frequency is approximately 1.046 msec at the 1170 RPM test condition, the predominant two millisecond periodicity of the waveforms suggests the existence of a flow structure in which every other rotor blade passage appears to be enveloped in a recirculatory flow pattern. The remaining alternating passages issue high velocity "jets" which account for most of the axial throughflow across the bladerow.

For instance, the 85% blade span axial flow coefficient profiles depicted in Figure 128 clearly shows the formation of high velocity "jets" at 2 msec intervals. Since each 1 msec increment of this temporal trace can be interpreted as the rotor frame steady velocity profile exiting a single rotor blade passage, it appears that each of the "jets" issue from the

172

pressure surface of alternating rather than adjacent rotor blades. In addition, a large positive radial component is in phase with each of these throughflow jets.

At the time intervals corresponding to the intermediate blade passages, the negative or reverse flow defect in the axial flow coefficient trace is less pronounced. Moreover, the radial velocity component is negative. In addition, there is a smaller rise in the tangential velocity component trace. These measurements clearly show the presence of a downward directed jet in every other rotor blade passage. Higher velocity upward directed jets issue from the pressure surface of the alternating rotor blades. Inspection of the 15% blade span flow coefficient profiles (plotted in Figure 132) will reveal the existence of a net positive axial flow into these alternating "recirculatory" blade passages.

These distinct alternating flow patterns become more apparent by adopting a rotor frame of reference. Figure 133 contains a rotor frame spatial crossplot of the tangential and radial velocity component information given in a representative two millisecond segment of the temporal traces depicted in Figures 128-132. This two millisecond segment spatially corresponds to two adjacent rotor blade passages. These two blade passages are illustrated in Figure 133 from the perspective of a downstream observer at the second stage stator bladerow who is looking upstream. In this frame of reference, the direction of rotor rotation is from right-to-left. The relative lengths of the velocity vectors depicted in this figure are directly proportional to magnitude. Finally, the X's and O's at the tail of the arrows denote axial flow components into and out of the figure plane respectively.

In an analogous fashion, a circumferential direction crossplot of the relative axial and tangential velocity components is given in Figure 134 at each of the five radial measuring positions. These crossplots help to identify the two basic types of rotor blade passage flows: 1) a recirculation passage, and 2) a throughflow passage. The recirculation passage is characterized by reversed flow at the tip radial positions and by forward axial flows at the

173

hub radial locations. The throughflow passage issues a strong reverse flow jet from the rotor blade pressure surfaces. The strength of this jet steadily decreases as one proceeds radially downward from the tip to the hub radii of the blades.

6.4.1.3. Pressure Field Measurements

A representative high response measurement of the wall static pressure at this axial station appears in Figure 135. The spectral analysis plot of this wall static pressure trace is presented in Figure 137. These figures show that the previously observed spinning pressure disturbance aet the upstream axial stations is also present at this axial location. However, the fluctuations associated with blade passing flowfield periodicity are less prominent than at the previous axial station immediately upstream of the rotor.

High response total pressure measurements were made at all five radial positions along the blade span. Although the time averaged total pressure levels are particularly important and will be treated in a later section (Section 6.4.4.), the high response total pressure measurements provide an opportunity to independently observe the flowfield phenomena documented earlier using the slanted hot wire sensor 3-D velocity measurement technique. In this context, a single high response total pressure trace at radial station #5 (85% blade span) is presented in Figure 136. The corresponding spectral analysis plot follows in Figure 137.

Unlike the high response wall static pressure, the effect of the 1145 Hz spinning pressure disturbance has far less overall impact upon the resulting total pressure fluctuations. Both the one and two millisecond periodicity associated with the passage of the high velocity reverse flow jets is clearly evident in the total pressure trace waveform and the spectral content of the signal. Blade passage effects become more pronounced because the

174

dynamic pressure changes which occur as the probe passes through the high velocity jets are greater than the static pressure change associated with the spinning pressure disturbance.

6.4.2. Three-Dimensional Axisymmetric Flowfield Structure at High Reversed Flows

The organized flow pattern observed at moderate flow coefficients disappears at higher reverse flow coefficients. An axisymmetric flow structure continues to exist at the high reverse flow coefficient operating condition. This flowfield is defined by the absolute velocity time traces presented in Figures 138 and 139. Rotor frame velocity component crossplots appear in Figures 140 and 141.

The flowfield data presented in these figures characterizes a highly three-dimensional flow. In the circumferential direction, an unmistakable pattern of alternating high and low velocity flow is present. This pattern is periodic on the order of a rotor blade passage. In the radial direction, the overall magnitude of the velocity vectors is greatest at the larger blade span locations and falls off consistently along the span of the blades.

Probably the most obvious feature of the flowfield is the complete absence of simple radial equilibrium in the flow. This fact is evidenced by the strong negative radial velocity components towards the hub of the machine. Representative high response wall static and total pressure traces of this operating condition are given in Figures 142 and 143. Corresponding spectral traces appear in Figure 144. These traces confirm the absence of a spinning pressure disturbance phenomenon. The periodicity of the unsteady fluctuations in these traces is the inverse of blade passing frequency.

6.4.3. Transition Flowfield Structure at Low Reverse Flows

At low reverse flow coefficients, i.e. immediately prior to transition to rotating stall, the flowfield in front of the third stage rotor develops a distinct recirculatory pattern with each

175

rotor blade passage exhibiting identical phenomena. These trends are readily apparent in the axial velocity component profiles presented in Figures 145 through 147 and the rotor frame velocity component crossplots in Figures 148 and 149.

In general, there is a significant amount of positive (i.e. forward) axial flow into the rotor blade passages at the lower blade span radii. These positive axial flow components are accompanied by negative relative tangential velocity components. In the absolute frame, the swirl is in the direction of rotor rotation, but, the magnitude of the absolute tangential velocity component is less than the local blade speed.

Reverse axial flows exist at the blade tip radii. Large downward radial flow components are present at all radial stations. At midspan, the flow is entirely directed radially downward. This evidence suggests a recirculation pattern in which the flow may never enter the downstream stator blading. Instead, strong radial pressure gradients in the axial gap between the stator and rotor bladerows force the flow downward towards the roots of the rotor blading. Once the flow enters the rotor bladerow, the absolute tangential motion of the blading causes the fluid to be accelerated in the circumferential direction also. This causes the fluid to be transported up the pressure surface of the rotor blading to the tip radii.

6.4.4. Station #7 Mean Flowfield Summary

Table XII reports the circumferential area averaged rotor exit flowfield velocity components. The superscript, A_θ, is used to explicitly signify a circumferential area average quantity in this table. In Chapter 7 (Section 7.1.4), a precise definition of what is meant by a "circumferential area averaged" quantity will be given.

The radial variation in the circumferential area averaged mean flow coefficients is significant at all three flow coefficients. Most of the axial throughflow occurs at the tip radii

176

In all three cases. In addition, there is a significant amount of swirl in front of the rotors at all three flow coefficients.

The existence of large radial flows suggests the presence of significant radial pressure gradients. The time averaged radial distribution of static pressure was computed from the measured distributions of the absolute velocities and total pressures. Table XIII contains a listing of all three quantities. A strong radial static pressure gradient is clearly indicated by the reduced profile listed in this table.

6.5   FIRST AND SECOND STAGE FLOWFIELDS

The downstream stage flowfields can be conceptually divided into two categories: 1) the intra-stage rotor-stator interaction flowfields, and 2) the stage exit flowfields (at the axial stations in front of the rotors). These two flowfield categories will be characterized in the following subsections. The downstream intra-stage rotor-stator interaction flowfields (at axial positions #6 and #4) are somewhat different than the flowfield previously characterized at axial station #8. These differences will be highlighted next in Section 6.5.1. However, the stage exit flowfields in front of the rotor bladerows at axial stations #5 and #3 are essentially identical to the flowfield presented at axial station #7. These similiarities will be substantiated in Section 6.5.2.

6.5.1.   Stage Rotor-Stator Interaction Flowfields

As previously discussed in Chapter 4, the signals generated by high response flowfield measurement instrumentation generally have three components: 1) a time invariant mean value; 2) one or more periodic fluctuating component(s); and 3) an aperiodic or random unsteadiness component. In this conceptual framework, both the time invariant mean levels

177

and the relative significance of the random unsteadiness are greater in the signals generated at the downstream rotor-stator interaction stations.

Although the downstream rotor-stator interaction stations differ from the third stage station in these respects, the periodic content of the signals show identical trends. At the high and low reverse flow operating conditions, the periodic unsteadiness associated with blade passing frequency is clearly evident in the reduced temporal profiles of the absolute velocity components. At the moderate flow condition, the alternating flow pattern associated with the blockage of every other blade passage appears in the velocity component traces. Figure 150 illustrates this phenomena as it exists at the second stage rotor-stator interaction station.

A word of caution with regard to the utility of the information presented in Figure 150 is appropriate at this point. Although the velocity field information presented in Figures 104 and 106-108 are accurate representations of the instantaneous flowfield which exists at the third stage rotor-stator interaction station, Figure 150 is not an accurate portrayal of the instantaneous flowfield at the stage 2 rotor-stator interaction station. The information contained in this figure was reduced from a 128 trace rotor phase locked ensemble-average representation of the flowfield. As a result, the significant aperiodic components associated with the random unsteadiness present in the flow at this location have been lost. The instantaneous and ensemble averaged effective cooling velocities depicted in Figure 151 illustrate the general level of random unsteadiness in the flow.

The time invariant velocity and total pressure measurements at the downstream rotor-stator interaction stations contain useful information about the structure of the flowfield. The results of a detailed circumferential and radial survey of the mean velocity field at axial station #6 are presented in Table XIV for the moderate flow condition. Absolute frame crossplots of the axial and tangential velocity components are given in Figure 152 at each radial position. The circumferential and radial distribution patterns present in these

178

results suggests the formation of higher velocity throughflow streamtubes on the pressure surfaces of the upstream stator blades. Most of the axial throughflow occurs between the 15% and 50% blade span locations. Lack of significant radial velocity components implies the establishment of simple radial equilibrium conditions.

The circumferential area averages of these velocity components and of the velocity components measured at the other flow coefficient operating conditions are given in Table XV. This table clearly shows that most of the axial throughflow at this station is concentrated in the hub region at all the flow coefficient operating conditions. High levels of swirl *against* the direction of rotor rotation are clearly apparent. At the moderate flow coefficient, absolute yaw angles in excess of -80° exist at the tip radial positions. At the 30% blade span location, these yaw angles never dip below -50°.

The area averaged mean total pressures at the second stage rotor-stator interaction station are listed in Table XVI. This table also contains the area averaged measured magnitude of the absolute velocity vector as well as computed static pressures. The radial variation of total pressure at this station corresponds with the variation in velocity to produce a nearly constant static pressure profile.

Before proceeding with the characterization of the downstream stage exit flowfields a final word on the nature of the high frequency fluctuations in the pressure field is in order at this point. The spinning pressure disturbance observed at upstream positions is the dominant source of pressure field fluctuations at the downstream rotor-stator interaction stations also. Figures 153 and 154 depict a representative high response time trace of the wall static and total pressures at axial station #6. The corresponding plots of the frequency spectrum of these signal waveforms appears in Figure 155.

179

6.5.2. Stage and IGV Exit Flowfields

The energy introduced to the flow by the third stage rotor causes the flow to experience a rise in total temperature before it reaches the second stage at axial station #6. In addition, the energy increase due to the action of the second stage rotor causes a similar increase in total temperature. Likewise, the same type of conditions prevail at the first stage exit station. The net effect of the prior upstream temperature increases in the fluid is to cause flow conditions which are out of the calibration range of the uncompensated hot wire sensor.

At the second stage exit station, i.e. axial station #5, the amount of fluid temperature increase is not as severe. In general, a good qualitative investigation of the detailed flowfield structure is still possible at this axial station. However, quantitative velocity measurements will be slightly less than the actual fluid velocities. The worst case error at the 85% blade span location was estimated by comparing the measured mean total pressure level at this location, the measured mean wall static pressure, and the magnitude of the time averaged absolute velocity vector. The maximum velocity magnitude error is approximately -20% at the moderate flow condition.

The reduced absolute velocity components depicted in Figure 156 illustrate the type of detailed flowfield structure information which can be acquired at the downstream stage exit stations with uncompensated hot wire instrumentation. If these moderate flow condition axial station #5 results are compared with the results depicted in Figure 136 for axial station #7, the similarity in the flowfields becomes more evident. Furthermore, the agreement between the corresponding effective velocity traces shown in Figure 157 indicates that these absolute velocity component traces accurately portray the detailed structure of the instantaneous flowfield (subject to the slight error in the magnitude of the velocity vectors discussed earlier).

180

Table XVII is a listing of the mean wall static and total pressures at the remaining downstream axial stations for the moderate flow coefficient condition. Again, the high total pressures of the fluid exiting the rotor bladerows is significantly greater than the total pressure of the fluid leaving the first stage stator bladerow or the inlet guide vanes.

6.6 SUMMARY

Since the present work is the first attempt to study the detailed three-dimensional structure of axial compressor reversed flowfields, some introductory considerations which may aid others interested in conducting similar experiments were presented in Section 6.1. The need to establish a measuring position coordinate grid pattern with several radial planes was identified. Instrumentation capable of resolving all three velocity components are essential for the study of reversed flows. Phase-lock triggering of the data acquisition system is a key ingredient in the experimental procedure. Phase-locking is a data acquisition technique which permits independent measurements of a periodically unsteady flow to be properly aligned with respect to the common stationary reference. Data storage, file management, and signal post processing operations are considerably simplified when phase-locked data signals are acquired. A dual phase-lock technique was employed during this effort to deal with some of the special types of periodic unsteadiness which can be encountered during axial compressor reverse flow operation. In particular, a synchronous trigger capable of phase-locking both the position of the rotor shaft and the position of a spinning pressure disturbance was developed.

Section 6.2 presented the results of the upstream flowfield measurements. The methods used to acquire high response time resolved measurements of the upstream flowfield were reviewed. Representative velocity and pressure time traces were given at three reversed flow coefficients: low ($\bar{C}_x/U = -0.05$), moderate ($\bar{C}_x/U = -0.10$), and high ($\bar{C}_x/U =$

-0.19). Instantaneous and ensemble averaged representations of the raw effective cooling velocity measurements (from which the absolute velocity components are derived) are compared. It was observed that a spinning pressure disturbance appears at a narrow range, almost unique value, of flow coefficients about the moderate flow coefficient condition ($\overline{C}_x/U$ = -0.10). This narrow range of reverse flow coefficients are precisely the flow conditions under which the overall reversed flow pressure drop performance across the compressor is equal to the level of the compressor's rotating stall pressure rise characteristic. The characteristic frequency of the spinning pressure disturbance is approximately 1145 Hz. This pressure disturbance causes fluctuations in the velocity field with amplitudes which are about 4.5% of the mean axial flow level.

Section 6.3 dealt with the flowfield which exists in the axial gap between the third stage rotor and stator bladerows. At the moderate reverse flow condition, the time resolved traces of the absolute velocity components suggests the presence of a rotor frame alternating flow pattern in which every other rotor blade passage appears to be blocked. Radial traverse data indicates that this pattern becomes less pronounced at lower blade span locations. At the high and low reverse flow coefficient conditions, the flow is three dimensionally axisymmetric with blade passing periodic variations in the flow. Significant tangential or swirl velocity components against the direction of rotor rotation are present in the flow at all three flow coefficients. High response wall static pressure measurements indicate the presence of the spinning pressure disturbance at the low and moderate flow coefficients. No significant radial gradients in the pressure field exist at this axial location.

Section 6.4 is concerned with documenting the structure of the flowfield immediately in front of the third stage rotor bladerow. The flowfield at this axial station can be characterized as having extremely large tangential velocity components in the direction of

182

rotor rotation. Absolute swirl components on the order of 150% of the blade passing speed are not uncommon. In addition to large components of tangential velocity, significant amounts of radial inflow towards the hub of the machine were measured. Large radial gradients in the static pressure field were shown to exist at this axial station. Most of the time averaged axial throughflow occurs at the tip radial positions. The high flow coefficient condition is characterized by the presence of high velocity jets issuing from the pressure surface tip radii of every rotor blade passage. At moderate flow coefficients, the high velocity jets issue from the pressure surface of every other blade passage. The remaining rotor blade passages exhibit a recirculatory flow pattern. In these passages, there is a net forward flow into the blade passages at the hub positions and reverse flow at the tip locations. At low flow coefficients, the recirculatory and high velocity jet patterns appear to be combined in every rotor blade passage.

Finally, Section 6.5 presents representative flowfield measurement results from the first and second stage axial stations. These results tend to support the conclusion that these downstream flowfields exhibit the same fundamental structure as was observed at the third stage axial stations. The only notable exception is the flowfield at the downstream stage rotor-stator interaction stations. At these stations, a significantly greater portion of the axial throughflow occurs at the lower radial positions. At the moderate flow coefficient, this greater throughflow is manifested by a 65% increase in the axial velocity component at the 30% blade span location. In addition, higher tangential swirl velocities against the direction of rotor rotation were observed. Finally, a greater amount of random flow unsteadiness is present.

183

Chapter 7

DISCUSSION AND ANALYSIS OF EXPERIMENTAL RESULTS

To the best of the author's knowledge, the reversed flow data presented in the previous chapter is the first set of detailed experimental results which document this type of three-dimensional, unsteady flowfield. The principal objective of this chapter is to provide a conceptual framework for understanding the nature of behavior trends seen. To this end, the results of a preliminary kinematic and dynamic analysis of the high response reverse flowfield measurements will be presented in the following sections.

Section 7.1 deals with the kinematics of axial compressor reversed flows. An unsteady potential flow analysis of the compressor upstream flowfield is presented. The unsteady influence of the spinning disturbance pattern which was observed at the moderate and low reversed flow operating conditions is explained with respect to the relations given by this potential flow analysis. The overall flow structure and patterns of fluid motion within the compressor blading are given. These flow patterns provide a basis for addressing continuity, angular momentum and torque absorption considerations.

In Section 7.2, some of the relevant dynamics of axial compressor reversed flows are considered. Periodic pressure fluctuations in the upstream flowfield are related to the velocity field unsteadiness through an integral form of the momentum equation. The difference in radial pressure gradients before and after the moving rotor bladerows are addressed in detail.

The next section, Section 7.3, presents an overall physical model for explaining time averaged reversed flow performance behavior. Axial wall static pressure profile data given in Chapter 5 are explained in terms of this model. In addition, the performance of individual stages are addressed.

7.1 AXIAL COMPRESSOR REVERSED FLOW KINEMATICS

This section will define the structure of the reversed flow velocity field. The unsteadiness present in the upstream flowfield at certain flow coefficients is described by a relatively straightforward velocity potential solution of a two dimensional formulation of the wave equation. Within the compressor blading, the flowfield is more complex. An overall three-dimensional flow pattern is presented for the bladed region of the compressor at each of the three flow coefficients investigated. This overall structure will serve as a basis for describing annulus stalled axial compressor behavior trends.

7.1.1 Analysis of Upstream Periodic Unsteadiness

The experimental evidence presented in Chapter 6 confirms the existence of periodic unsteadiness in the flowfield upstream of the compressor blading. The spectral signatures of the upstream wall static pressure high response analog signals, shown in Figure 100, indicate that most of the periodic unsteady phenomena occurs at the lower reversed flow coefficients. The establishment of a multi-lobed travelling disturbance pattern is first encountered (and is most pronounced) at the $\bar{C}_x/U = -0.10$ moderate reverse flow condition. At a narrow range of flow coefficients centered about this reverse flow coefficient, the disturbance appears to propagate around the compressor annulus at a characteristic frequency from 1120 Hz to 1170 Hz. This frequency range is higher than the 955 Hz frequency associated with the

185

passage of the third stage rotor blades. As a result, the velocity field is subjected to the periodic unsteady distortions illustrated in Figure 95.

The following paragraphs will present an approximate two-dimensional analytic description of the upstream periodic unsteadiness observed at moderate and low reversed flow coefficients. The approach will be to formulate a velocity perturbation potential, ϕ', for the general periodic unsteady case of an N-lobed disturbance pattern which propagates around a compressor annulus at a fixed angular speed, σ. This will be used to establish an analytical basis for explaining the phase relationships of the absolute velocity components as well as the axial direction attenuation of the disturbance. In turn, these relationships will be used to help confirm the of propagation, the number of lobes, and the speed of the upstream propagating disturbance pattern. In Section 7.2.1, this velocity perturbation potential and an integral form of the momentum equation will be used to dynamically relate the phase differences between the velocity and pressure fields.

The coordinate system illustrated in Figure 158 depicts a segment of the compressor annulus which has been unwrapped at the mean radius, R_m. As shown in this figure, the common origin of the $X-\theta$ coordinate system is fixed at an arbitrary circumferential position at axial station #9. An initial condition axial velocity profile with a circumferential direction periodic disturbance wavelength equal to $2\pi/N_\sigma$ is shown at $x = 0$. This particular wavelength definition implies the existence of an N-lobed disturbance pattern around the compressor annulus.

The absolute velocity components in the upstream region will be represented by a mean velocity component and a superimposed perturbation as shown in Figure 158 and defined as follows

$$C_x\left(x, \theta, t\right) = \overline{C}_x + C_x'\left(x, \theta, t\right) \qquad (7-1)$$

186

$$C_\theta(x,\theta,t) = \bar{C}_\theta + C'_\theta(x,\theta,t) \qquad (7\text{-}2)$$

where $\bar{C}_x$ is the mean axial throughflow velocity component and $\bar{C}_\theta$ is a mean swirl velocity component. Under most circumstances, there is no mean swirl present in the upstream flowfield.

The further assumption of irrotational flow disturbances implies the existence of a velocity perturbation potential

$$\vec{C}' = \nabla \phi' \qquad (7\text{-}3)$$

such that the two perturbation velocities can be defined as follows

$$C'_x(x,\theta,t) = \frac{\partial \phi'}{\partial x}(x,\theta,t) \qquad (7\text{-}4)$$

$$C'_\theta(x,\theta,t) = \frac{1}{R_m} \frac{\partial \phi'}{\partial \theta}(x,\theta,t) \qquad (7\text{-}5)$$

If the fluid at upstream infinity is assumed to be homentropic and the motion started from rest, the subsequent flow of an inviscid fluid, free of non-conservative body forces, is irrotational. The equation governing unsteady irrotational subsonic flow of a homentropic gas is the wave equation

$$\nabla^2 \phi' = \frac{1}{c^2} \frac{\partial^2 \phi'}{\partial t^2} \qquad (7\text{-}6)$$

187

or in terms of the simplified two-dimensional coordinate system

$$\frac{\partial^2 \phi'}{\partial x^2} + \frac{1}{R_m^2}\frac{\partial^2 \phi'}{\partial \theta^2} = \frac{1}{c^2}\frac{\partial^2 \phi'}{\partial t^2} \tag{7-7}$$

where c is the speed of sound and R_m is the mean radius of the compressor.

Equation 7-7 can readily be solved using separation of variables to form three second order ordinary differential equations. The characteristic eigenvalues and corresponding eigenfunctions associated with the solution of these O.D.E.'s are evaluated by first applying the following periodic boundary conditions

$$\phi'\!\left(x,\theta,t\right) = \phi'\!\left(x,\theta-\sigma t\right) \tag{7-8}$$

$$\phi'\!\left(x,0,0\right) = \phi'\!\left(x,\tfrac{2\pi}{N_\sigma},0\right) \tag{7-9}$$

The periodicity condition represented in Equation 7-8 relates the angular and time coordinates for a travelling wave in the θ-direction where σ is the angular speed of the propagating disturbance. Positive σ values correspond to propagation in the θ-direction, while negative σ values denote propagation in the opposite direction. The condition specified by Equation 7-9 simply requires the perturbation potential to be periodic on the disturbance wavelength interval shown in Figure 158.

At upstream infinity, Sommerfeld's radiative condition [68] is applied. This condition excludes the possibility of "inward travelling" waves from infinity and insures the damped

188

solution. Given the initial condition axial velocity profile depicted in Figure 158, the following homogeneous initial condition exists at the X-axis origin:

$$\frac{\partial \phi'}{\partial x}(\infty, \theta, t) = \frac{1}{R_m} \frac{\partial \phi'}{\partial \theta}(\infty, \theta, t) = 0 \qquad (7\text{-}10)$$

Application of these conditions yields a solution to the wave equation (Eq 7-7) for the perturbation velocity potential of the form

$$\phi' = \sum_{n=1}^{\infty} A_n e^{-nN_\sigma \sqrt{\left[\frac{1}{R_m}\right]^2 - \left[\frac{\sigma}{c}\right]^2} X} \sin nN_\sigma(\theta - \sigma t) \qquad (n=1,2,3,\cdots) \qquad (7\text{-}11)$$

A propagation mach number, M_σ, can be defined as $M_\sigma = \sigma R_m / C$. Substitution of this definition into Equation 7-11 yields the desired general result

$$\phi' = \sum_{n=1}^{\infty} A_n e^{-\frac{nN_\sigma}{R_m}\sqrt{1-M_\sigma^2} X} \sin nN_\sigma(\theta - \sigma t) \qquad (n=1,2,3,\cdots) \qquad (7\text{-}12)$$

The remaining coefficients, A_n, can be determined by satisfying a specific velocity perturbation profile. The experimental evidence given in Figure 95 at axial station #9, i.e. X = 0, suggests the following first harmonic axial velocity perturbation profile

189

$$C'_x(0,\theta,t) = \frac{\partial \phi'}{\partial x}(0,\theta,t) = C'_0 \sin N_\sigma(\theta - \sigma t) \qquad (7\text{-}13)$$

where C'_0 is the amplitude of the velocity perturbation or about 0.45% of the mean blade speed, i.e. $C'_0/U = 0.0045$.

The first harmonic coefficient, A_1, can be determined by differentiating Equation 7-12 with respect to x and setting the result equal to the Equation 7-13 profile to yield the following

$$A_1 = \frac{-C'_0 R_m}{N_\sigma \sqrt{1 - M_\sigma^2}} = \frac{-0.0045 \, U \, R_m}{N_\sigma \sqrt{1 - M_\sigma^2}} \qquad (7\text{-}14)$$

Hence, the solution for the perturbation velocity potential which fits the experimental data is given by

$$\phi' = \frac{-C'_0 R_m}{N_\sigma \sqrt{1 - M_\sigma^2}} \, e^{-\frac{N_\sigma}{R_m}\sqrt{1 - M_\sigma^2} \, x} \sin N_\sigma(\theta - \sigma t) \qquad (7\text{-}15)$$

The axial and tangential direction perturbation velocities are found by evaluating the partial derivatives in Equations 7-4 and 7-5 to give the following results

$$C'_x(x,\theta,t) = C'_0 \, e^{-\frac{N_\sigma}{R_m}\sqrt{1 - M_\sigma^2} \, x} \sin N_\sigma(\theta - \sigma t) \qquad (7\text{-}16)$$

190

$$C_\theta'(x,\theta,t) = \frac{-C_0'}{\sqrt{1-M_\sigma^2}} \, e^{-\frac{N_\sigma}{R_m}\sqrt{1-M_\sigma^2}\,x} \cos N_\sigma(\theta - \sigma t) \qquad (7\text{-}17)$$

The above expressions for the perturbation velocities indicate that a definite 90° phase relationship exists between the axial and tangential direction velocity components. At a fixed (x,θ) coordinate location, the above expressions predict a 90° phase lead in the tangential direction velocity component temporal trace over the corresponding axial velocity component trace for a disturbance which propagates in the positive θ-direction. A disturbance propagating in the negative θ-direction will produce temporal profiles in which the tangential component lags the axial component by 90°. The experimental evidence obtained at axial station #9 leads to the conclusion that the upstream multi-lobed disturbance pattern propagates in the negative θ-direction, i.e. against the direction of rotor rotation. Figure 95 clearly illustrates the 90° phase lag pattern associated with a negative value of σ.

Although the direction and frequency of the propagating disturbance pattern have been determined, more information is required to estimate the number of lobes and rotational propagation speed of the spinning disturbance pattern. This task is accomplished by analyzing the phase relationships among the temporal traces of either the axial or tangential direction perturbation velocity components from three circumferential positions. Each temporal trace must be synchronized to a common stationary reference signal. Figure 159 depicts the first 5 msec of the tangential direction perturbation velocity component traces acquired at axial station #9, radial position #4 (70% blade span) and circumferential positions #2, #6 and #10.

Since the direction of propagation is opposite to the direction of rotor rotation, a disturbance observed at circumferential position #10 will propagate to circumferential

191

position #2 over a finite period of time Δt. As a result, the negatively sloped lines shown in Figure 159 identify the two most plausible time histories of the disturbance which arrives at circumferential position #2 about 2.225 msec after the synchronized reference trigger pulse is generated. The first possible spinning mode produces a 0.1 msec phase shift between circumferential positions #10 and #2. At radial station #4, the mean radius normalized arc length, $r\,\Theta_{10}/R_m$, is roughly equal to a value of 0.0854. This temporal phase shift and arc length can be combined to estimate a rotational propagation speed which is 6.98 times greater than the mean blade speed. The number of lobes, N_σ, associated with this rotational propagation speed can be estimated from the following relation

$$ N_\sigma = \frac{2\pi\left(\dfrac{r_4}{R_m}\right) R_m}{\dfrac{1}{f_\sigma}\left(\dfrac{U_\sigma}{U}\right) U} \qquad (7\text{-}18) $$

$$ \approx 8 \text{ lobes} $$

where r_4/R_m is the normalized radius at 70% blade span (1.026), $1/f_\sigma$ is the inverse of the rotational propagation frequency (1145 Hz), and U_σ/U is the normalized rotational propagation speed (6.98).

The second possible spinning mode has a much larger temporal phase shift, and consequently, a much lower propagation speed and increased number of lobes. For a phase shift of 1.846 msec, the normalized propagation speed is 38% of the mean blade speed. Equation 7-18 predicts the presence of a 158 lobed disturbance pattern associated with this

192

propagation speed. In order to determine which possible spinning mode is the correct disturbance pattern; the axial velocity perturbation axial direction decay characteristics predicted by Equations 7-16 and 7-17 will be compared with an actual measurement of the decay at axial station #10.

The exponential decay term in either Equation 7-16 or 7-17 contains three variables: the number of disturbance lobes N_σ, the rotational propagation Mach number M_σ, and the normalized upstream distance X/R_m. This latter parameter has a value of 0.2615 at axial station #10. The first possible spinning mode has an 8-lobed disturbance pattern and propagates at a Mach number of $M_\sigma = 0.705$. According to the perturbation velocity potential solution, these parameter values indicate that the peak amplitude of the periodic disturbances at axial station #10 should be about 22% of the value observed at station #9. For the relatively low rotational propagation speed ($M_{\sigma 2} = 0.038$) and large number of lobes ($N_{\sigma 2} = 158$) associated with the second possible spinning mode, virtually no periodic unsteadiness should be observed at axial station #10.

The measured decay at axial station #10 indicates that the peak amplitude of the periodic velocity component fluctuations have decayed to a level which is 26% of the original value at axial station #9. This evidence supports the conclusion that the high rotational propagation speed, 8-lobed pattern is the spinning disturbance mode which exists in the upstream flowfield at the moderate reverse flow coefficient operating condition. The relatively large rotational propagation Mach number associated with the 8-lobed pattern also accounts for the fact that amplitude of the tangential perturbation velocity component is larger than the axial perturbation velocity by a factor of $1/\sqrt{1 - M_\sigma^2}$ as predicted by Equations 7-16 and 7-17 and shown in Figure 95.

7.1.2 Overall Flow Structure

The existence of a strongly three-dimensional reverse flow structure with significant radial flow effects is perhaps one of the most important discoveries made during the present experimental effort.   Radial movement of fluid dominates the annulus stalled reverse flow structure throughout the relevant range of reverse flow coefficients likely to be encountered during post stall operation of an aircraft gas turbine compressor. Figure 160 illustrates the overall radial structure of axial compressor reversed flowfields at low, moderate and high flow coefficients. At this point, one should realize that these radial flow patterns were observed in a relatively high hub-tip ratio compressor design ($r_h/r_t = 0.88$).

Figure 160 depicts the circumferential area averaged axial velocity profiles entering and exiting the stage N + 1 rotor and stage N stator bladerows. At high reverse flows, there is radial movement of fluid but no evidence of a recirculatory pattern. The flow is essentially axisymmetric on a blade-to-blade periodic basis. The temporal velocity traces shown in Figures 116, 138 and 139 confirm this observation at selected radial stations aft and in front of the third stage rotor bladerow. In addition, the velocity component vector crossplots depicted in Figures 140 and 141 illustrate this axisymmetric behavior in a pictorial sketch. These figures as well as the area averaged mean velocity components listed in Tables X, XI, XII, and XV support the flow pattern depicted in part A of Figure 160.

Prior to this work, it had been assumed by previous investigators that the flow was two dimensional in the X-θ plane at these relatively large reversed flow coefficients. As a result, separated flow cascade models were applied to deal with the phenomenon of reversed flows in axial flow turbomachinery. Instead, the picture of reverse flow which emerges here is one of strong radial flows to the outer wall casing in the rotor bladerows and downward towards the hub in the interbladerow gap in front of the rotor bladerow. At moderate and

194

low reversed flows, a recirculatory flow pattern develops in front of the rotor bladerow as shown in parts B and C of Figure 160.

The moderate reversed flow recirculatory pattern alternates on an every other rotor blade passage scale. However, at low reversed flows the recirculatory pattern involves every rotor blade passage and can be considered to be non-alternating around the circumference of the compressor. Finally, the area averaged tangential movement of fluid in the interbladerow gaps is clearly *against* the direction of rotor rotation behind the rotor bladerows at axial stations #8, #6 and #4. In front of the rotors at axial stations #7, #5 and #3, the flow is in the direction of rotor rotation. The tangential vs. axial velocity component crossplots presented in Figures 134, 141, 149 and 152 support these conclusions.

7.1.3 Detailed Rotor Bladerow Flow Structure

The unsteady, three-dimensional velocity measurements indicate the presence of a different rotor bladerow flow structure at each of the reverse flow operating conditions investigated. At all three flow coefficients, the mean velocity profile into the trailing edges of the rotor bladerow is almost completely oriented in the negative Θ-direction, i.e. absolute swirl angles of $-80°$ are common. These angles are much greater than the leading edge blade angles of the preceeding stator bladerow. Most of the axial throughflow is concentrated at the 30% blade span radial location. These observations are well supported by the experimental evidence presented in Chapter 6 at axial stations #8 and #6.

Although the area averaged mean rotor inlet velocity profiles are roughly similiar at all three flow coefficients, the instantaneous inlet profile at the tip radial locations is drastically different during moderate reversed flows. In this case, every other rotor blade passage appears to be bypassed as was first described in Chapter 6. In addition to the abnormality in

195

the inlet profile observed at the moderate flow coefficient, the structure of the flow exiting the rotor blade passages is disimiliar at each flow coefficient.

The movement of fluid through the rotor bladerow is pictorially sketched in Figure 161 for the high reverse flow case. The flow enters the rotor bladerow at predominately the 30% blade span location and must negotiate an extremely large obtuse turning angle. For a relative trailing edge rotor angle of 38^0, an absolute mean flow angle of -80^0, plus the wheel speed of the rotor, this initial turning angle can exceed 120^0 as shown in Figure 161. The low axial drift velocity through the bladerow and the high tangential velocity imparted to the fluid cause relative frame body forces to centrifuge the fluid to high radial locations against the pressure surfaces of the rotor blades. The presence of a strong radial pressure gradient in front of the rotor bladerows causes the fluid to be ejected from the rotor bladerow at the tip radial locations with a significant negative radial velocity component as shown in Figure 161.

Although the dynamic mechanism is not yet completely understood, the lower axial drift velocity associated with moderate reversed flows cause the complex, alternating pattern depicted in Figure 162 to develop. Alternating recirculatory and throughflow passages are established. The throughflow passages in this pattern account for most of the mass flow through the compressor. Fluid enters these passages along the entire blade span from the hub-to-tip radial positions. Some fluid enters the throughflow passage at the hub position in front of the bladerow from the preceeding recirculatory blade passage as shown.

The recirculatory blade passages receive a certain amount of throughflow fluid at the lower radial positions at the trailing edges of the blades plus a sizeable amount of recirculatory fluid from the previous recirculatory blade pasage as shown in Figure 162. This alternating flow pattern is supported by the experimental evidence given in Figures 105-109 and 128-132. Perhaps the best indication of these recirculatory flow patterns is

196

given by the relative tangential velocity vs. absolute radial velocity crossplot appearing in Figure 133.

Finally, extremely low reversed flow axial drift rates cause the mixed throughflow and recirculatory flow pattern shown in Figure 163 to become established immediately prior to transition to rotating stall. Fluid predominately enters each bladerow at the hub regions of both the trailing and leading edges of the blade passages. Some fluid enters the blade passage at higher radial locations along the trailing edges of the blading. All fluid is ejected with strong negative radial velocity components at the tip radial positions of the blade leading edge pressure surfaces. Some of this ejected fluid continues to drift axially into the downstream stator bladerow where it impinges at high angles upon the trailing edges of the blading in an unsteady fashion. The remainder of the ejected fluid is forced to the hub region where the absolute tangential velocity actually drops below the local blade speed. In the relative coordinate frame shown in Figure 148, the fluid appears to move against the direction of rotor rotation to enter the next rotor blade passage as a recirculatory flow.

7.1.4 Continuity and Angular Momentum Considerations

In Chapter 6, circumferential area averaged mean flow velocity components were presented in Tables IX, X, XII, and XV for several axial stations. The normalized circumferential area averaged profiles of the axial velocity component were sketched in Figure 160. The first portion of this section is concerned with providing a definition of these circumferential area averaged quantities and presenting an overall axial direction continuity check of these results. The latter half of this section will be directed towards presenting a simple model for estimating torque absorption during reverse flow.

At this point, consider the case of an unsteady, three dimensional flow. For this case, there are radial, circumferential and temporal variations in the flow at any given axial

197

station. Temporal variations are averaged by taking a time average mean as follows

$$\frac{\overline{C}_x[r,\theta]}{U} = \frac{\int_0^{T_\infty} \frac{C_x[r,\theta,t]}{U} \, dt}{T_\infty} \qquad (7\text{-}19)$$

where T_∞ is an interval of time much greater than the periodic unsteadiness in the flow. In addition to the time average mean of the axial flow coefficient (shown above), time average representations of the other absolute velocity components can be expressed in the same manner. During the present work, this time average was performed by taking a simple arithmetic average of the acquired 50 msec time traces. Since the blade passing period is approximately 1 msec, this duration was considered to be an acceptable time interval for retrieving representative time averaged results.

The circumferential area average representation of the time averaged flow quantities is formally defined for the axial velocity component as

$$\frac{\overline{C}_x^{A_\theta}[r]}{U} = \frac{\int_0^{2\pi} \frac{\overline{C}_x[r,\theta]}{U} \, r \, d\theta}{2\pi r} \qquad (7\text{-}20)$$

where 2π is a complete angular sweep around the circumference of the compressor. During the present effort, it was possible to obtain circumferential area averaged information without sampling circumferential positions around the entire compressor annulus. Instead,

198

measurements at several circumferential positions across the pitch interval of the adjacent stationary bladerow were sufficient to average circumferential variations in the flow.

Continuity requires the average axial flow coefficient to remain constant at each axial station through the machine. This requirement is given in terms of the (circumferential area averaged) axial flow coefficient radial profile as

$$\frac{\bar{C}_x}{U} = \text{constant} = \frac{\int_{r_{hub}}^{r_{tip}} \frac{\overline{C_x^{A}}[r]}{U} 2\pi r \, dr}{\pi \left[r_{tip}^2 - r_{hub}^2 \right]} \qquad (7\text{-}21)$$

A continuity check of the results presented herein can be obtained by using a straight line approximation to interpolate between the circumferential area averaged axial flow coefficient values given in Tables IX, X, XII, and XV. Additional simplification is achieved by taking advantage of the high hub-to-tip ratio geometry of the compressor to neglect radial variations in the projected flow area. Simple trapezoidal integration confirms that overall axial flow continuity is satisfied by the circumferential area average radial profile data listed in these tables. At all three flow coefficients, the discrepancies between the evaluated values of the mean axial flow coefficient are less than ± 0.01. For example, the average axial flow coefficient $\bar{C}_x/U$ at axial stations #8, #7, and #6 were evaluated to be 0.18, 0.20, and 0.19 respectively for the high flow coefficient condition.

Although the flowfield associated with reverse flows is sufficiently complex to prohibit a first principles flowfield solution at the present time, the detailed flowfield measurements

reported herein do suggest an approximate conceptual framework for addressing the task of estimating torque absorption. In particular, the meanline torque relation given by Equation 5-28 can be modified to account for radial shifts in the primary axial throughflow streamtube across the rotor bladerows, the presence of recirculatory flow patterns at lower reverse flow coefficients, and the large deviation of the flow from the leading edge angles of the upstream stator blades. Inclusion of these effects into the simple meanline result given by Equation 5-28 leads to the following expression for an N-stage axial compressor

$$
\psi_T = \psi_{T,o} + 2\left(\frac{\overline{C}_x}{U}\right)\left[N + \frac{\left(\frac{\overline{C}_x}{U}\right)}{\left(1 - \frac{A_B}{A_C}\right)} \right.
$$

$$
\sum_{i=1}^{N}\left[\left(1 - \frac{\epsilon_b(r_{tip} - r_{hub})}{R_m}\right)\tan\left(K_{LE,b} + \Delta\alpha_{Y_{b,\delta}}\right)\right. \tag{7-22}
$$

$$
\left. \left. + \left(1 + \frac{\epsilon_c(r_{tip} - r_{hub})}{R_m}\right)\tan\left(K_{LE,c}\right)\right]_i \right]
$$

where $\psi_{T,o}$ = the base torque level associated with the presence of a recirculatory flow pattern

N = number of stages

ϵ_b, ϵ_c = the offset from the midspan radius of the uniform throughflow streamtube entering and leaving the rotor bladerow (expressed as a fraction of blade span).

$\Delta\alpha_{Y_{b,\delta}}$ = the increased deviation angle of the flow leaving the upstream stator bladerow

$K_{LE,b}, K_{LE,c}$ = the leading edge blade angles of the stator and rotor blades respectively (defined in Figure 40).

200

Unfortunately, many of the above variables can not be fully evaluated on the basis of the present set of results for a single compressor build. The base torque level $\psi_{T,o}$ is most certainly a function of the amount of recirculation present and the angular momentum change associated with the recirculatory flow. The high response results from the present test series tends to show that this term is zero at high reverse flows and is negligible compared to the throughflow term at lower reverse flows in the current build. An extrapolation of the time-average torque results presented in Figure 71 to the zero mass flow point tends to support this observation.

Another set of variables that vary as a function of compressor geometric design are the radial locations of the idealized uniform flow streamtubes which enter and leave the rotor bladerows. For the present build, Tables XII and XV indicate that the mass flow entering the rotor bladerows tends to be centered about the 30% bladespan location at all three mean flow coefficients. These tables also indicate that the flow exiting the rotor bladerow is primarily concentrated at about 70% of the blade span, and as a result, $\epsilon_b \approx \epsilon_c \approx 0.20$.

The information presented in Chapter 6 tends to support the observation that the flow exits the rotor blade passages at the leading edge angle of the blades. However, the unsteady effects associated with the moving bladerow downstream of the stator blades apparently causes the low velocity fluid exiting the stator bladerow to deviate from the leading edge blade angle. Although the mechanism for this phenomenon is not yet completely understood, the net effect is to cause large deviation angles and high tangential swirl against the direction of rotor rotation, i.e. $\Delta\alpha_{Y_{b,\delta}} \approx 30^\circ$. Finally, effective blockage ratios on the order of 60% of the projected flow through area tend to be supported by the detailed flowfield measurements.

At this point, it is important to emphasize that these rough estimates of effective blockage ratio and flow deviation angle are derived from flowfield measurements made in the

201

middle of the axial gap between the moving and stationary bladerows. It is possible that a higher velocity flow issues from the stator bladerows at the leading edge stator blade angle. This implies the existence of correspondingly larger effective blockage ratios at the stator bladerow exit plane. However, a lower velocity flow with larger swirl components and reduced effective blockage ratio is measured at the downstream mid-gap instrumentation location due to mixing of the high and low velocity streams (while angular momentum is conserved).

Substitution of the measured blockage and deviation angle values into Equation 7-22 yields predicted torque values which are in good agreement with the measured torque data presented in Figure 71. At a mean axial flow coefficient $\bar{C}_x/U = -0.20$, the computed torque coefficient is approximately 3.04. Ultimately, more detailed flowfield measurements on different compressor builds are required to extend the utility of Equation 7-22 past the current compressor build to a wide range of axial compressor designs.

7.2 AXIAL COMPRESSOR REVERSED FLOW DYNAMICS

In the previous section, the kinematics of axial compressor reversed flows were considered by studying the results of the velocity field measurements. This section addresses some of the dynamic considerations through an analysis of the unsteady and circumferential area averaged mean pressure measurements. In particular, an analysis of the unsteady periodic pressure fluctuations in the upstream flowfield as well as analysis of the radial pressure gradients which exist within the axial gaps between the compressor bladerows will be presented.

202

7.2.1 Upstream Periodic Pressure Fluctuations

Earlier, in Section 7.1.1, a perturbation velocity potential ϕ' was derived to establish an analytical basis for describing the periodic unsteadiness present in the upstream flowfield during the moderate reverse flow operating condition. In this section, the total pressure fluctuations associated with the spinning disturbance will be related to the velocity field fluctuations through an integral form of the Euler momentum equation.

The general equation of motion for an inviscid, compressible flow is

$$\frac{D\vec{c}}{Dt} = \frac{\partial \vec{c}}{\partial t} + (\vec{c} \cdot \nabla)\vec{c} = -\frac{1}{\rho}\nabla P - \nabla G \qquad (7-23)$$

In the absence of conservative body forces, the last term on the RHS of Equation 7-23 is zero, i.e. $\nabla G = 0$. Rearrangement and substitution of the following thermodynamic relation

$$\nabla h = T\nabla S + \frac{1}{\rho}\nabla P \qquad (7-24)$$

into Equation 7-23 yields the Crocco form of the momentum equation

$$\frac{\partial \vec{c}}{\partial t} - \vec{c} \times \vec{\omega} = T\nabla S - \nabla h_o \qquad (7-25)$$

where $\vec{\omega}$ is the vorticity vector (i.e. $\nabla \times \vec{c} = \vec{\omega}$), ∇S is the gradient of entropy, and ∇h_o is the gradient of stagnation enthalpy. This form of the momentum equation is particularly useful because it relates vorticity (a Kinematical property) to dynamical and thermodynamic properties.

203

Since the flow is assumed to be irrotational and homentropic, Equation 7-25 reduces to the following expression

$$\frac{\partial \vec{c}}{\partial t} = -\nabla h_o \qquad (7\text{-}26)$$

and if the following approximation is made

$$\nabla h_o \approx \frac{\nabla P_o}{\rho} \qquad (7\text{-}27)$$

(which is exact in the incompressible limit) then upon substitution of the velocity perturbation potential, Equation 7-26 can be integrated to yield

$$\frac{\partial \phi'}{\partial t} = -\frac{P_o'}{\rho} \qquad (7\text{-}28)$$

Finally, substitution of the velocity perturbation potential solution defined by Equation 7-15 yields the following analytical expression for the periodic total (stagnation) pressure fluctuations in the upstream flowfield

$$P_o'(x,\theta,t) = \frac{-\rho C_o \sigma R_m}{\sqrt{1-M_\sigma^2}} \ e^{-\frac{N_\sigma}{R_m}\sqrt{1-M_\sigma^2}\,x} \cos N_\sigma(\theta - \sigma t) \qquad (7\text{-}29)$$

The phase relationship predicted by the above expression requires the total pressure fluctuations to be identically 180° out of phase with the tangential velocity component fluctuations. For the previously established propagation direction against the rotor rotation, a temporal trace of the total pressure fluctuations should appear to lead the axial velocity component fluctuations. These trends are confirmed by the total pressure fluctuations shown in Figure 103 and the velocity component fluctuations presented in Figure 95.

The magnitude of the total pressure fluctuations is proportional to the amplitude of the tangential velocity component fluctuation, $C_o' / \sqrt{1 - M_\sigma^2}$, and the rotational propagation speed of the multi-lobed disturbance pattern, $U_\sigma = \sigma R_m$. In normalized form, the total pressure fluctuation amplitude is given as

$$\left| \frac{P_o'}{\frac{1}{2}\rho U^2} \right| = \left| \frac{\sigma R_m}{U} \right| \left(\frac{C_o'}{U} \right) \frac{2}{\sqrt{1 - M_\sigma^2}} \qquad (7\text{-}30)$$

$$\approx \quad 0.09$$

where C_o'/U is the normalized axial velocity component perturbation (0.0045), R_m/U is the rotational propagation speed of the disturbance (6.98), and M_σ is the rotational Mach number of the propagating disturbance (0.705). This result compares well with the total pressure fluctuations given in Figure 103.

7.2.2 Radial Pressure Gradients

The existence of strong radial pressure gradients at certain axial gap locations within the compressor is perhaps the most important dynamic feature of the flow within the bladed region. The circumferential area averaged pressure field information presented in Table XIII (axial station #7) clearly shows the existence of strong radial gradients of static and total pressure in front of the third stage rotor bladerow. Likewise, Table XVII shows the same large radial gradient of total pressure in front of the second and first stage rotor bladerows at axial stations #5 and #3. Tables XI, XVI and XVII indicate that large radial pressure gradients *do not exist behind* the moving bladerows. The remaining paragraphs of this section will address these differences in greater detail.

At this point, a few comments concerning the nature of the static pressure radial profile data reported in the tables referenced above are appropriate. The static pressures reported in these tables were not measured directly. Instead, these static pressure results were calculated from the measured total pressure and absolute velocity from the following expression

$$\frac{\overline{P}_s^{A_\theta}}{\frac{1}{2}\rho U^2} = \frac{\overline{P}_T^{A_\theta}}{\frac{1}{2}\rho U^2} - \left(\frac{\overline{C}^{A_\theta}}{U}\right)^2 \qquad (7\text{-}31)$$

Since the absoulte velocity measurement must be squared to obtain the static pressure value, small errors in the measurement of velocity tend to produce large errors in the estimated static pressure. For this reason, the measured case wall static pressures have been included in the mean pressure field tables to check the accuracy of the static pressure calculation. The agreement between the measured and calculated static pressure results is good at all locations and operating conditions except at axial station #7 for the low and moderate average flow coefficient cases. Although not shown, a comparison between measured and calculated static pressures at axial stations #5 and #3 reveal the same trends as was observed at axial station #7. These axial stations, as shown in Figure 89, are in front of the three rotor bladerows.

In these cases, the calculated static pressures at the 85% blade span radial position exceed the measured value at the case wall. Since the wall static and total pressure measurements could be acquired with a greater amount of confidence, this trend indicates that the absolute velocity measurement (i.e. the circumferential averaged value) is slightly lower than the actual velocity. An error analysis of the static pressure discrepancies reported in Table XIII indicates that the velocity measurement error is about 15% for the moderate flow

206

case and 24% for the low flow case. This velocity measurement error arises from two probable sources: 1) improper averaging of the circumferential variations in the time averaged velocity field, and 2) the presence of local temperature gradients.

The first source of error will yield artificially low estimates of velocity if not enough circumferential positions with respect to the downstream stationary blade passage have been included in the circumferential averaging process (Equation 7-20). This source of error can be eliminated by performing a larger amount of circumferential surveys of the flowfield. The other cause of error is the presence of large temperature gradients which can be caused by an uneven radial distribution of work input to the fluid stream as well as the static temperature increases which accompany the subsequent dissipation of the high energy fluid stream at the trailing edges of the downstream stator bladerow. This error source explains why the velocity measurement errors occur primarily at the axial locations immediately downstream of the rotor bladerows and why the errors become progressively greater at the downstream axial locations.

An estimate of the temperature increase required to produce these velocity measurement errors can be obtained by considering King's Law (Equation 4-7). For air at low velocities, the coefficient A in Equation 4-7 is small. Hence, the following first order expression can be written to relate the velocity error ΔC due to a change in fluid temperature ΔT above the calibration temperature T (see Goldstein [69]):

$$\frac{\Delta C}{C} \simeq \frac{n \Delta T}{T_{wire} - T} \qquad (7-32)$$

where n is the denominator of the exponent in King's Law (approximately equal to 2 for air), and T_{wire} is the temperature of the hot wire sensor. For a resistive overheat ratio of

207

1.7 and a tungsten temperature coefficient resistance of 0.0023/°F, the difference between the sensor operating temperature and the reference cold calibration temperature is $T_{wire} - T = 304°F$. According to Equation 7-32, temperature changes of about 23°F and 36°F are required to cause the respective 15% and 24% errors in the measured velocity.

Although these temperature levels are somewhat large, some recirculation is present and the streamtubes exiting the rotor tip locations have experienced a larger amount of work input than the flow exiting the rotors at lower radial locations. These effects tend to support the theory that large temperature gradients just downstream of the rotors can cause velocity measurement errors on the order of 20%.

A conservatively low estimate of the radial pressure gradient at axial station #7 is the difference between the measured case wall static pressure and the calculated static pressure at radial position #1. The overall differential equation of motion which governs the radial distribution of static pressure is

$$\frac{Dc_r}{Dt} - \frac{c_\theta^2}{r} = -\frac{1}{\rho}\frac{\partial P}{\partial r} + g_r + \nu\left[\nabla^2 c_r - \frac{c_r}{r^2} - \frac{2}{r^2}\frac{\partial c_\theta}{\partial \theta}\right] \quad (7\text{-}33)$$

If the effects of body forces and viscosity are negligible, then the last two terms on the RHS of Equation 7-33 can be dropped. Simple radial equilibrium exists when there are no radial flows, i.e. $Dc_r/Dt = 0$. Hence, the simple radial equilibrium expression for the radial pressure gradient is

$$\frac{\partial P}{\partial r} = \rho\frac{c_\theta^2}{r} \quad (7\text{-}34)$$

Dividing through both sides of the above equation by $1/2 \rho U^2$ and integrating from the first radial position to the case wall yields the following result

$$\frac{P_{s_{case \atop wall}} - P_{s_{r_1}}}{\frac{1}{2}\rho U^2} = \int_{r_1}^{r_{case \atop wall}} \frac{2\left(\frac{C_\theta}{U}\right)^2}{r} \, dr \qquad (7-35)$$

If the tangential direction velocity component profile listed in Table XII is corrected to account for the measurement error identified earlier and subsequently inserted into the above integral, then the radial pressure difference which should exist under radial equilibrium conditions can be predicted. Table XVIII contains a comparison between the pressure difference derived from actual measurement and application of Equation 7-31 with that predicted by simple radial equilibrium theory (Equation 7-35).

Three general trends are indicated by the results given in Table XVIII. First, the size of the pressure difference from the case wall to the 15% blade span location decreases as the compressor is throttled to lower reverse flow operating conditions. This trend is evident in the results generated from either Equation 7-31 or 7-35. A second trend is the relationship between the relative magnitudes of the pressure differences given by either method at a particular operating condition. In all cases, the quasi-measured pressure difference (subject to the shortcomings of the Equation 7-31 calculation discussed earlier) is greater than that predicted by simple radial equilibrium. However, the final trend indicated by the results is

that the quasi-measured pressure difference approaches the simple radial equilibrium result at lower overall flow coefficients.

The fact that the measured pressure difference is greater than the simple radial equilibrium result explains the existence of large radial velocity components directed towards the hub region of the compressor. In terms of the governing equation of motion (Equation 7-33), the material derivative term on the LHS of the equation is non-zero. The most probable cause for this absence of radial equilibrium is the conversion of dynamic head into useful static pressure rise at the trailing edges of the stator bladerow just downstream of the rotor bladerow. A static pressure gradient in the radial direction occurs because the fluid stream exiting the rotors at the tip radial positions have larger dynamic pressures. This radial distribution of dynamic head is well supported by the detailed flowfield measurements presented in Chapter 6.

7.3 OVERALL TIME AVERAGE PERFORMANCE MODEL

The newly acquired experimental results provide a better understanding of steady-state annulus stalled reverse flow phenomena. However, the complexity associated with the inherent unsteadiness and three-dimensionality of these flowfields still presents formidable obstacles to a complete definition of axial compressor reversed flows. Although a first principles performance prediction is not possible at the present time, the available experimental information can be used to formulate a physically plausible model which explains the time average static pressure performance trends presented earlier in Chapter 5.

Figure 164 schematically depicts the overall time-average performance model which is supported by the cumulative set of experimental evidence presented in the preceeding chapters. This representation of the axial profiles of the case and hub wall static pressure profiles highlights a number of previously unknown features of axial compressor reversed flows.

210

First, the definition of an axial compressor stage during annulus stalled reverse flow should be redefined to group the stator (or IGV) of the previous stage N with the rotor of the N + 1 stage. This bookkeeping arrangement tends to remove the mystery surrounding the apparent dissimilar performance of the third stage as compared to the two first stages (illustrated in Figures 68 and 69).

The existence of large radial pressure gradients in front, but not behind, the rotor bladerows accounts for the wide disparity in the axial profiles of the case and hub wall static pressure. This conceputal model clearly indicates that the pressure drop across the stage occurs in the rotor bladerows at the hub wall, and in the stator bladerows at the case wall. At most reverse flow coefficients, there is a rise in static pressure across the rotors at the case wall.

The magnitude of the static radial pressure gradient in front of a particular rotor bladerow is usually greater than the static pressure drop across the entire stage. Although not shown in Figure 164, the radial gradient in *total pressure* in front of the rotor bladerows is slightly greater than the static pressure drop across the entire compressor.

According to this overall model of reverse flow performance, the pressure drop across a particular stage ψ_{stage_i} is a function of the pressure drop across the stator bladerow H_S and the pressure rise across the rotor bladerow H_R

$$\psi_{stage_i} = H_{s_{i-1}} - H_{R_i} \tag{7-36}$$

For a general N stage compressor, the overall static-to-static pressure drop is given as

$$\psi_{s-s} = \sum_{i=1}^{N} \left[H_{s_{i-1}} - H_{R_i} \right] \tag{7-37}$$

where the static pressure drop or rise across the rotor and stator bladerows is a function of the compressor design variables and flow coefficient, i.e.

$$H_S = H_S \ (\overline{C}_x/U, \ \text{geometry})$$

$$H_R = H_R \ (\overline{C}_x/U, \ \text{geometry})$$

One possible scheme for correlating the stator and rotor bladerow static pressure head changes is given by the following relations

$$H_s = c_0 + c_1 \left(\frac{\overline{C}_x}{U}\right)^{c_2} \tag{7-38a}$$

$$H_R = d_0 + d_1 \left(\frac{\overline{C}_x}{U}\right)^{d_2} \tag{7-38b}$$

where the coefficients c_0, c_1, c_2, d_0, d_1, and d_2 are functions of compressor design parameters. Any future experimental efforts aimed at evaluating these coefficients should not neglect the possibility that the individual stator and rotor head rise coefficients may be coupled with respect to each other.

If Equations 7-38a and b are substituted into Equation 7-37 and the resulting expression is combined with the Equation 5-14 relationship, then the following general expression for the total-to-static pressure drop across an N-stage axial compressor is obtained:

$$\psi_{T-s} = \left(\frac{\overline{C}_x}{U}\right)^2 + \sum_{i=1}^{N} \left[\left[c_0 + c_1\left(\frac{\overline{C}_x}{U}\right)^{c_2}\right]_{i-1} - \left[d_0 + d_1\left(\frac{\overline{C}_x}{U}\right)^{d_2}\right]_i \right] \tag{7-39}$$

Unfortunately, the experimental results from these two compressor builds are not sufficient for the purpose of evaluating the coefficients in the above equation for a wide variety of multistage axial compressor designs. An extensive parametric test matrix will be required to obtain a good predictive capability with the methodology represented by Equation 7-39.

213

Chapter 8

CONCLUSIONS AND RECOMMENDATIONS

The instantaneous flowfield which exists in a multistage axial compressor during reverse flow and mass flow shutoff operating conditions is both unsteady and three-dimensional. Until the present work, experimental investigation of these flow regimes was generally avoided because of an absence of a pressing practical need and the inability of existing experimental techniques to deal with the special problems posed by the complex and even hostile environments associated wtih these flows.

The serious stagnation stall problems which accompanied the development of afterburning turbofan engines in the 1970's gave new impetus to the study of post stall axial compressor performance. The compression system forced response analytical investigation undertaken at the outset of this research effort appears to be the first systematic attempt to evaluate the suitability of existing simple lumped parameter compression system models to deal with the problem of forced nonrecoverable stall.

It was found that predicitons of the forced response of a compression system can be drastically altered by slightly changing the shape of the assumed steady-state compressor reverse flow characteristic in the neighborhood of the shutoff flow coefficient. In addition, subsequent develoments in the theories for predicting steady-state rotating stall performance have also increased the interest in investigating axial compressor reversed flow performance.

At the same time, the development and widespread application of low cost digital microprocessor technology made the acquisition of reverse flowfield data technically practical

with the development of appropriate experimental techniques. During this effort, the development of a synchronous phase lock triggering circuit as well as the application of slanted hot wire three-dimensional velocity measurement techniques made the study of axial compressor reversed flowfields possible.

A wide variety of significant conclusions have been reached during this research investigation. In order to present these ideas in the most easily understood and concise manner possible, the conclusions reported in this chapter will be divided into one of the following five general areas: 1) Compression System Dynamics; 2) Experimental Techniques; 3) Time Average Performance Measurements; 4) Reverse Flowfield Measurements; and 5) Rotating Stall Implications. Finally, recommendations for further work in the area of axial compressor post-stall behavior and performance are offered.

Compression System Dynamics

Although a detailed discussion of the major findings of the compression system forced response study can be found in Section 2.5, the significant original contributions made during this phase of the research effort are outlined as follows:

1) A simple one-dimensional lumped parameter description of a compression system appears to be capable of simulating a forced nonrecoverable stagnation stall event similiar to the phenomena observed in actual turbofan engine stagnation tests.

2) Only a small number of forcing functions have the proper timing and strength to cause this forced stagnation event. According to the results of a parametric analysis, there are small "windows" in parameter space which define the forcing functions capable of

215

interrupting a pre-established surge limit cycle and driving the system to the nonrecoverable stall point.

3) There are two locations in a surge limit cycle where the imposition of reasonable strength external excitation can cause a forced stagnation event:

        a) near the stall onset of the compressor, and

        b) at the bottom of the reversed flow characteristic near zero mass flow.

4) The predicted forced response of even a simple compression system is extremely dependent upon the assumptions implicit in the transient post-stall compressor performance model. In particular, the predicted response behavior is critically sensitive to the assumed shape of the compressor steady-state reverse flow characteristic near zero mass flow.

Experimental Techniques

Perhaps the most significant contribution made during this thesis effort is the detailed documentation of a highly unsteady, and three-dimensional stalled compressor flowfield. These results were obtained only after the development of some specialized experimental techniques designed to overcome some of the difficulties posed by the peculiar characteristics of axial compressor reversed flowfields. From an experimental measurement standpoint, the more notable conclusions are as follows:

1) The presence of a spinning pressure disturbance at several reverse flow coefficients caused two sources of periodic unsteadiness to be present in the reverse flowfield. The developemnt of a synchronous trigger circuit for aligning the phase of the propagating

216

disturbance and the position of the rotor shaft was essential for obtaining ensemble averaged high response pressure data within the compressor blading.

2) The best location for placement of a pressure sensitive high response sensor to generate a phase lock triggering signal with respect to the spinning pressure disturbance is immediately upstream of the compressor blading. At this location, the unsteadiness associated with the potential fields of the moving blades is not present. In addition, the analog output from this sensor as well as the resultant digital trigger signal should be monitored on an oscilliscope to prevent the zero drift characteristics of the sensor to cause phase shift synchronization errors. Constant adjustment of the threshold trigger level was required to obtain well synchronized results.

3) The use of phase locked triggering to initiate data acquisition sampling was an essential prerequisite for obtaining three-dimensional velocity measurements using a single slanted hot wire in a periodically unsteady flow. It was found that a 45° slanted sensor offered the best tradeoff between yaw and pitch angle sensitivity range for reversed flow measurements.

4) The strongly three-dimensional character of reverse flowfields requires measurements at several radial positions to document radial movement of fluid in throughflow and recirculatory flow patterns. In addition, circumferential variations in the flow require radial traverses at a large number of circumferential positions with respect to the stationary stator bladerows.

5) The reduction of the acquired effective cooling velocity measurements into absolute velocity components involves the numerical soution of a set of six non-linear algebraic equations. In order to reduce substantial amounts of three-dimensional velocity data, the data reduction software should be structured to permit an automatic, unattended data reduction option as well as a user oriented manual reduction option. The automatic reduction option should incorporate the following features; an automatic initial guess algorithm (based upon the sensor directional sensitivity calibration), provision to reduce selected discrete segments of a given data trace, and generation of an error file to list unconverged data points encountered during the reduction run.

Time Average Performance Measurements

With the exception of Pratt & Whitney's unpublished High Speed Rig (HSR) data [34], the compressor pressure rise and torque characteristics presented herein are the only *complete* set of characteristics in existence for a multistage axial compressor representative of aircraft gas turbine engine applications. Several conclusions with respect to these time averaged stalled performance results have been drawn as follows:

1) Although a large amount of hysteresis accompanies the transition from unstalled flow to rotating stall, virtually no hysteresis was observed at the transition between rotating stall and annulus stalled reversed flow. This latter transition is characterized by a precipitous drop in the overall pressure rise across the compressor as well as a drop in the torque absorbed by the compressor. In terms of the results of the compression system forced response study, this discontinuous drop in the pressure performance characteristic narrows the range of forcing function combinations with the proper timing and strength to cause a forced nonrecoverable stall event to occur.

2) The overall reversed flow performance of the high and moderate reaction builds tested were essentially identical. This observation leads to the conclusion that the reversed flowfields in both builds were roughly identical regardless of the blade stagger angle setting changes. Differences in the axial temperature profiles between the two builds suggests the slight movement of streamtubes with different total temperature levels.

3) A stable rotating stall condition was clearly evident at overall net negative flow rates. Rotating stall cell property measurements indicate that the stall cell grows to nearly 90% of the compressor annulus before transition to the annulus stalled reverse flow condition is encountered. The precipitous drop in pressure rise and torque absorption performance at the reverse flow transition point is due to the stalling of the remaining 10% of the compressor annulus.

Reverse Flowfield Measurements

Analysis of the unsteady, three-dimensional reverse flow velocity and pressure field measurements has led to a number of conclusions about the detailed nature of axial compressor reversed flows. In particular, the most fundamental conclusions are:

1) The unsteady fluctuations in the pressure fields upstream, within, and downstream of the compressor are primarily due to the presence of a spinning acoustic disturbance mode. These spinning pressure disturbance patterns usually occur at the moderate and low reverse flow coefficient conditions where recirculatory flow patterns are generated in front of the rotor bladerows. The phase relationships between the upstream absolute velocity components as well as the results of an unsteady potential flow analysis of the upstream inlet

219

region leads to the conclusion that the multi-lobed pressure disturbance patterns which exist at the moderate flow condition spins *against* the direction of rotor rotation.

2) The temporal phase relationships of several circumferentially offset, but reference signal phase locked, high response flowfield measurements plus the measured frequency and upstream decay characteristics of the spinning pressure disturbance leads to the conclusion that an 8-lobed pattern propagating at a relative Mach number of 0.7 exists at the moderate flow condition. The high relative Mach number at which the disturbance sweeps the compressor annulus explains the noticeable difference in acoustic signature as various reverse flow coefficients are encountered.

3) Although the magnitude of the total pressure fluctuations associated with the spinning disturbance pattern is approximately 10-15% of the pressure drop performance across the compressor, this magnitude is small in comparison with the total pressure levels which are generated within the compressor blading, especially in front of the rotor bladerows where total pressures three times greater than the overall total pressure drop across the compressor have been observed. At the present time, the reason for the establishment of a spinning disturbance mode is not known.

4) It has been established that the reversed flowfield developes alternating flow patterns at this flow coefficient synonymous with the rotating stall pressure rise level. In particular, the 8-lobed spinning pressure disturbance pattern and the alternating recirculatory and throughflow passages in the rotor bladerow at the moderate reverse flow condition are direct evidential support of this conclusion. The reverse flow characteristic *should not* be classified unequivocably as an axisymmetric characteristic in the two dimensional, non-rotating

disturbance sense of the term. Rather, the details of the reverse flowfield structure support the conclusion that the reverse flow characteristic should be more appropriately referred to as an *annulus stalled characteristic.*

5) The analysis of the overall structure of the reverse flowfield indicates that strong radial flows and pressure gradients dominate the reverse flowfield at all relevant flow coefficients. In effect, each rotor bladerow acts as an inefficient centrifugal compressor stage in which most of the axial throughflow is pumped from the hub to the tip radial positions. These conclusions explain why two dimensional cascade based models which seek to predict multistage axial flow turbomachinery reversed flow performance have failed in the past.

6) The radial static pressure gradients in front of the rotor bladerows are greater than those predicted by simple radial equilibrium of the swirling fluid in front of the rotor bladerows. The large static pressures which exist at the tip radial positions are probably caused by the conversion of a portion of the large dynamic heads associated with fluid exiting the rotor bladerow into useful static pressure rise at the trailing edges of the downstream stator bladerow. The resulting non-radial equilibrium condition causes fluid to be forced towards the hub of the machine in the axial gap in front of the rotor bladerows. These facts account for the development of strong recirculatory flows even in a high hub-tip ratio design and suggest a non-zero shutoff head rise in the annulus stalled characteristic (if transition to rotating stall is not encountered first).

7) The tangential movement of fluid within the axial gaps between the compressor bladerows suggests that the rotors do not act merely as passive "paddle wheels" where fluid is brought into a general solid body rotation across the compressor annulus. The large tangential

221

velocities in front of the rotor bladerows is in the direction of rotor rotation with absolute velocities in the range of 1.5 U. In back of the rotors, consistently large tangential velocities *against* the direction of rotor rotation have been measured. The large velocities in front of the rotors can be explained in terms of the radial redistribution of axial throughflow in the rotors and the consequent formation of high velocity "jets" issuing from the pressure surfaces of the rotor blading. However, the large magnitude of the reverse rotation tangential swirl observed behind the rotor bladerow is not yet fully understood. Apparently, the movement of the rotor bladerow causes the high and low energy fluid leaving the stator bladerow to mix rapidly (in an unsteady fashion) while conserving angular momentum.

Rotating Stall Implications

The present investigation of axial compressor reversed flow performance has uncovered a number of flow similarities between the detailed flowfield structure of rotating stall and annulus stalled reversed flows. In particular, there is strong support for a parallel compressor view of rotating stall in which the flow at the center of the stall cell is identical to the flow found in annulus stalled reverse flow. If true, the detailed reverse flowfield structure reported herein is also a description of the flowfield which exists at the center of a rotating stall cell.

The time averaged axial wall static pressure and midspan temperature profiles presented in Figures 76 and 81 for reverse flow and Figures 78 and 83 for rotating stall firmly support this hypothesis. In addition, the instantaneous wall static pressure profile obtained by Day [12] at the circumferential center of a stall cell (in a similar low speed three stage compressor) corresponds well to the profiles shown in Figure 76. These figures show the same characteristically "kinked" staircase axial static pressure profile associated with high wall static pressures in front of the rotors and low pressures behind the rotors.

222

The general shape of these profiles as predicted by the overall reverse flow performance model presented in Chapter 7 is attributed to the radial redistribution of throughflow in the rotors, the subsequent ejection of this throughflow in concentrated jets at the tip radial position, and the resulting static pressure recovery of a portion of the dynamic head of these jets at the trailing edges of the stator bladerows.

Detailed flowfield measurements by Das and Jiang [42] and Day [14] show the same high tangential velocities in front of the rotors at the center of rotating stall cells. Although not equipped with the proper experimental techniques to measure radial velocity components, both sets of investigators concede that strong radial flows (of the type presented in this thesis) are present in rotating stall cells. Hence, the detailed flow structure of rotating stall cells reported by others is similar to the reverse flowfield structure reported herein.

In the final analysis, the parallel compressor concept of rotating stall is not conclusively proven beyond a reasonable doubt by the existing experimental evidence. However, the present work does significantly extend the evidential support in favor of this particular rotating stall theory. At this point, recommendations for further axial compressor post stall work are offered.

Recommendations

The complexity of the unsteadiness and three-dimensionality associated with multistage axial compressor annulus stalled and rotating stall flowfields presents formidable long term obstacles to the development of post-stall analytical flowfield models capable of generating assured stall resistant compressor designs. It is the author's opinion that the greatest opportunities for furthering the goal of designing stall resistant compressors lie in continued post-stall experimental tests aimed at understanding the detailed flow structure and performance behavior of multistage axial compressors.

The double phase lock synchronous techniques developed during the present investigation should be employed to investigate the detailed blade resolved flowfield structure during rotating stall. If the current MIT 3-Stage Axial Compressor build is used to perform these experiments, a direct comparison between the annulus stalled flowfield reported in this thesis and the flowfield within the rotating stall cell will be possible for the first time. These tests should be conducted with the objectives of either verifying the parallel compressor concept or documenting the fundamental differences between the two flowfields.

It is recommended that future post-stall tests be conducted with temperature compensated instrumentation and experimental techniques. During the current investigation, large temperature gradients in the downstream compressor stages prevented acquisition of error free quantitative velocity field information. The impingement of high velocity fluid streams can cause localized static temperature increases which seriously effect the velocity magnitude calibrations of the hot wire sensors. The present experimental technique need only be slightly modified to increase the number of phase locked measurements from three to six. Setting the anemometer to a different overheat ratio, or constant current operation (if enough bandwidth exists), will permit acquisition of the instantaneous temperature field to compensate the velocity measurements.

With respect to annulus stalled reverse flow performance, the two builds tested showed little difference in the overall performance characteristics. Evidently, the overall flowfield structure is invariant to changes in the reaction of the compressor blading at the present design flow coefficient. It is recommended that more compressor builds be tested in a parametric matrix to determine the sensitivity of reversed flow steady-state performance with respect to design variable changes. Attention should be focused upon the low flow shape of the time averaged performance characteristic as well as the location of the transition point prior to rotating stall inception.

This investigation of multistage axial compressor reversed flows is a first attempt to study a previously unknown post-stall flowfield. Although a firm basis for the investigation of unsteady, three-dimensional stalled flows has been established, future experimental and analytical research efforts are required to accomplish the final objective of *insuring* that stagnation stall is permanently eliminated as a potential problem in aircraft gas turbine engines.

REFERENCES

1 Huppert, M.C., and Benser, W.A., "Some Stall and Surge Phenomena in Axial Flow Compressors," *Journal of the Aeronautical Sciences*, Vol. 20, No. 112, Dec 1953, pp. 835-845.

2 Smith, A.G., and Fletcher, P.J., "Observations on the Surging of Various Low-Speed Fans and Compressors," *NGTE Memorandum No. M.219*, July 1954.

3 Emmons, H.W., Pearson, C.E., and Grant H.P., "Compressor Surge and Stall Propagation," *Transactions of the ASME*, Vol. 77, No. 4, Apr. 1955, pp. 455-469.

4 Pearson, C.E., "Surge Behavior in a Three-Stage Compressor," *Journal of the Aeronautical Sciences*, Vol. 22, No. 11, Nov. 1955, pp. 799-802.

5 Greitzer, E.M., "Surge and Rotating Stall in Axial Flow Compressors - Part I: Theoretical Compression System Model," *ASME Journal of Engineering for Power*, Vol. 98, No. 2, Apr. 1976, pp. 190-198.

6 Greitzer, E.M., "Surge and Rotating Stall in Axial Flow Compressors - Part II: Experimental Results and Comparison With Theory," *ASME Journal of Engineering for Power*, Vol. 98 No. 2, Apr. 1976, pp. 199-217.

7 Wetmore, W.C., "F100 Stagnation Stall Fixes To Be Tested," *Aviation Week & Space Technology*, No. 27, 1978, pp. 44-47.

8 "Good-bye Stagnation: America's Finest Fighter Engine Outgrows a Childhood Ailment," *Aircraft Engineering*, Vol. 511, No. 11, Issue 609, Nov. 1979, pp. 15-17.

9 Moore, F.K., "A Theory of Rotating Stall of Multistage Axial Compressors," *NASA Contractor Report 3685*, July 1983.

10 Moore, F.K., and Greitzer, E.M., "A Theory of Post-Stall Transients in Axial Compression Systems: Part I - Development of Equations," *ASME Paper No. 85-GT-171*, for Meet March 1985.

11 Greitzer, E.M., and Moore, F.K., "A Theory of Post-Stall Transients in Axial Compression Systems: Part II - Application," *ASME Paper No. 85-GT-172*, for Meet March 1985.

12 Day, I.J., "Axial Compressor Stall," *Ph.D. Dissertation*, Christ's College (Cambridge University), 1976.

226

13 Wenzel, L.M., and Bruton, W.M., "Analytical Investigation of Nonrecoverable Stall," NASA Technical Memorandum 82792, February 1982.

14 Koff, S.G., "Stalled Flow Characteristics for Axial Compressors," M.S. thesis, Massachusetts Institute of Technology, 1983.

15 Koff, S.G., and Greitzer, E.M., "Stalled Flow Performance for Axial Compressors - I: Axisymmetric Characteristic," ASME Paper No. 84-GT-93, for Meet June 1984.

16 Horvath, A.J.T., "Der Pumpvorgang von Verdichtern und Kreiselpumpenals nichtlineare Schwingung," Ph.D. thesis, Swiss Federal Institute of Technology at Lausanne, 1976.

17 Gyarmathy, G., "Nonlinear Analysis of Surge Cycles," ASME Journal of Fluids Engineering, March 1977, pp. 258-9.

18 Greitzer, E.M., "Review - Axial Compressor Stall Phenomena," ASME Journal of Fluids Engineering, Vol. 102, June 1980, pp. 1134-151.

19 Greitzer, E.M., "The Stability of Pumping Systems - The 1980 Freeman Scholar Lecture," ASME Journal of Fluids Engineering, Vol. 103, June 1981, pp. 193-242.

20 Ritter, H.K., and Rohling, T.A., "Starting Large Custom Pumps Against Reverse Flow," Allis-Chalmers Engineering Review, Vol. 37, No. 2, Feb. 1972, pp. 26-31.

21 Naegeli, J.P., "Refrigeration Turbocompressors for Base-Load LNG Plants," Sulzer Technical Review, No. 4, 1973, pp. 213-224.

22 Suter, I.P., "Surge Tests on a Gas Turbine Compressor," Oil Engine and Gas Turbine, October 1963, pp. 49-51.

23 Strub, R.A., and Suter, I.P., "Compressor Surge in Gas Turbines and Blast Furnace Compressor Installations," ASME Journal of Engineering for Power, April 1965, pp. 193-6.

24 Strub, R.A., and Suter, I.P., "Compressor Surge in Gas Turbines and Blast Furnace Compressor Installations," Sulzer Technical Review, No. 2, Feb. 1966, pp. 80-3.

25 Thoma, D., "Vorgange beim Ausfallen des Antriebes von Kreiselpumpen," Mitteilungen des Hydraulischen Institute der Technischen Hochschule Munchen, Vol. 4, 1931, pp. 102-4.

26 Kittredge, C.P., and Thoma D., "Centrifugal Pumps Operated Under Abnormal Conditions," Power, June 2, 1931, pp. 881-884.

27 Knapp, R.T., "Complete Characteristics of Centrifugal Pumps and Their Use in the Prediction of Transient Behavior," Transactions of the ASME, Vol. 59, No. 8, Nov. 1937, pp. 683-689.

28 Knapp, R.T., "Centrifugal-Pump Performance as Affected by Design Features," Transactions of the ASME, Vol. 63, No. 3, Apr. 1941, pp. 251-260.

29 Swanson, W.M., "Complete Circle Characteristic Diagrams for Turbomachinery," Mechanical Engineer's thesis, California Institute of Technology, 1951.

30 Swanson, W.M., "Complete Characteristic Circle Diagrams for Turbomachinery," Transactions of the ASME, Vol. 75, July 1953, pp. 819-826.

31 Stepanoff, A.J., "Special Operating Conditions of Centrifugal Pumps," Chap. 13, Centrifugal and Axial Flow Pumps (New York: John Wiley and Sons, Inc.), 1957, pp. 269-292.

32 Martin, C.S., "Representation of Pump Characteristics for Transient Analysis," Performance Characteristics of Hydraulic Turbines and Pumps, ASME FED - Volume 6, 1983, pp. 1-113.

33 Turner, R.C., and Sparkes, D.W., "Complete Characteristics for a Single-Stage Axial-Flow Fan," Paper #29, Thermodynamics and Fluid Mechanics Convention, Cambridge, 9-10th Apr 1964 (Institution of Mechanical Engineers).

34 Davis, R.E., "Compressor Stall Recovery Design Technology," MIT Gas Turbine Laboratory Seminar, December 4, 1984.

35 Bammert, K., and Zehner, P., "Back Flow Characteristics of Turbine Cascades," Atomkernenergie, Vol. 24, No. 4, 1974, pp. 225-232.

36 Bammert, K., and Zehner, P., "Back Flow in Turbines of Nuclear Closed-Cycle Gas Turbine Plants in Case of Circuit Pipe Rupture," ASME Journal of Engineering for Power, April 1975, pp. 189-194.

37 Bammert, K., and Zehner, P., "Measurements of the Performance of an Air Turbine Stage at Positive and Negative Mass Flow and Rotational Speed (Four-Quadrant Characteristics)," ASME Journal of Engineering for Power, Vol. 100, Jan. 1978, pp. 22-29.

38 Bammert, K., and Zehner, P., "Measurements of the Four-Quadrant Characteristics on a Multi-Stage Turbine, ASME Paper No. 79-GT-107, for Meet March 12-15, 1979, 6 pgs.

39 Stenning, A.H., "Rotating Stall and Surge," ASME Journal of Fluids Engineering, Vol. 102, Mar 1980, pp. 14-20.

40 Iura, T., and Rannie, W.D., "Experimental Investigations of Propagating Stall in Axial-Flow Compressors," ASME Transactions, Apr 1954, pp. 463-471.

41 Shaw, R., and Lewkowicz, A., "The Construction and Testing of a Large Axial Flow Compressor," 1963 Aeronautical Research Council Current Paper, C.P. No. 620, May 1962.

42 Das, D.K., "Flow Measurements within Rotating Stall Cells in Single and Multistage Axial-Flow Compressors," AIAA International Symposium on Air Breathing Engines, 6th, Paris, France, June 6-10, 1983, Symposium Paper No. A83-35801 16-07, pp. 623-631.

43 Betz, A., and Petersohn, E., "Anwendung der Theorie der frein Strahlen," Ingenieur-Archiv 2 Nr. 2 (1931), pp. 190-211.

44 Lamb, H., Hydrodynamics, 6th edition, Dover Publications, New York, 1945.

45 Cornell, W.G., "The Stall Performance of Cascades," Proceedings 2nd National Conference Applied Mechanics (Michigan) ASME, New York, 1954.

46 Zehner, P., "Calculation of Four Quadrant Characteristics of Turbines," ASME Paper No. 80-GT-2, for Meet March 10-13, 1980, 13 pgs.

47 Eastland, A.H.J., "Investigation of Compressor Performance in Rotating Stall: I-Facility Design and Construction and Initial Steady State Measurements," MIT Gas Turbine and Plasma Dynamics Laboratory Report No. 164, June 1982.

48 "Browning Gear Couplings," Browning Catalog GC-1, December 1980, p. 6.

49 Goepner, B., "Three-Stage JT9D Research Compressor Investigation," United Aircraft Research Laboratory Report No. H233698-2, December 29, 1969.

50 Christianson, M.B., "An Experimental Investigations of a Three-Stage Axial-Flow Compressor with Cantilevered Stators Using Low Aspect Ratio-Redesigned Endwork Blading in All Stages," United Aircraft Research Laboratory Report No. R232752-1, February 11, 1975.

51 Christianson, M.B., "Assembly of a P&WA Three-Stage Axial Flow Compressor for use at MIT," United Technologies Research Center Report No. R80-232806, September 19, 1980.

52 Lewis, J.T., "MIT Compressor Re-Stagger," P&WA GPD correspondence, dated 26 June 1984.

53 Christianson, M.B., "Compressor Blade Assembly Technique at UTRC for the Three-Stage Compressor Test Rigs," Report No. UTRC 76-159, December 20, 1976.

54 Bradbury, R., "Compressor Blade Design and Inspection Technique at UTRC for the Three-Stage Compressor Test Rigs,": Report No. UTRC77-8, February 3, 1977.

55 "Design II Centrifugal Airfoil Fans," Champion Blower & Forge, Inc., Catalog CAF 100-9-75, 1967, p. 22.

56 Ower, E., and Pankhurst, R.C., "The Orifice Plate, Shaped Nozzle, and Venturi Tube", Chapter 7, The Measurement of Airflow, (London: Pergammon Press), 1966, pp.152-180.

57 Fink, D.A., "An Experimental Investigation of Centrifugal Compressor Surge and Stall Phenomena in Turbochargers," M.S. thesis, Massachusetts Institute of Technology, May 1984.

58 King, L.V., "On the Convection of Heat from Small Cylinders in a Stream of Fluid: Determination of the Convective Constants of Small Platinum Wires with Applications to Hot-Wire Anemonetry," _Proceedings of the Royal Philosophical Society (London)_, Series A, Vol. 214, p. 273 (1914).

59 "Model 1050/1050A Constant Temperature Anemometer," Thermo Systems, Inc., _Manual P/N 1990215_, 1984.

60 Whitfield, C.E., Kelly, J.C., and Barry, B., "A Three-Dimensional Analysis of Rotor Wakes," _Aeronautical Quarterly_, Vol XXIII, Part 4, Nov. 1972, pp. 285-300.

61 Hirsch, Ch., and Kool, P., "Measurement of the Three Dimensional Flow Field Behind an Axial Compressor Stage," _ASME Journal of Engineering for Power_, April 1977, pp. 168-180.

62 Kool, P., De Ruyek, J., and Hirsch, Ch., "The Three-Dimensional Flow and Blade Wake in an Axial Plane Downstream of an Axial Compressor Rotor," _ASME Paper No. 78-GT-66_, for Meet April 9-13, 1978.

63 Schmidt, D.P., and Okishi, T.H., "Multistage Axial-Flow Turbomachine Wake Production, Transport, and Interaction," _AIAA Journal_, Vol. 15, No. 8, August 1977, pp. 1138-1145.

64 Johnson, M., private communciation, December 1984.

65 Powell, M.J.D., "A Hybrid Method for Nonlinear Equations," Chapter 6, 1970, pp. 87-114.

66 Levenberg, K., "A Method for the Solution of Certain Nonlinear Problems in Least Squares," _Quarterly Journal of Applied Mathematics_, Vol. 2, 1944, pp. 164-168.

67 Marquardt, D.W., "An Algorithm for Least Squares Estimation of Nonlinear Parameters," _Journal of the Society of Industrial Applied Mathematics_, Vol. 11, 1963, pp.431-441.

68 Sommerfeld, A., "The Condition of Radiation," Section 28, _Partial Differential Equations in Physics_ (New York: Academic Press, Inc.), 1949, p. 189.

69 Goldstein, R.J., ed., "Thermal Anemometers", Chapter 4, _Fluid Mechanics Measurements_ (New York: Hemisphere Publishing Corporation), 1983, p. 123.

70 Gamache, R.N., "Forced Non-Recoverable Stall in Compression Systems," _Unpublished Doctoral Committee Memorandum_, Sep. 1982.

71 Gamache, R.N., "Design and Operation of the MIT-3 Stage Compressor Test Facility", _Unpublished GTL Notes_, May 1985.

TABLE I

COMPRESSOR SPECIFICATIONS

OVERALL ASSEMBLY

UTRC Drawing No.	1233-566
Number of stages	3 (non-repeating)
Tip Diameter, in.	24.000
Hub Diameter, in.	21.115
Hub-Tip Ratio	0.88
Static Tip Clearance, in.	
Rotor #1	0.038
Rotor #2	0.037
Rotor #3	0.035
Static Hub Clearance, in.	
Stator #1	0.032
Stator #2	0.037
Stator #3	0.034

BLADING DESIGN

Bladerow	No. of Blades	Chord, in.	Aspect Ratio	Midspan Camber, deg.
Inlet Guide Vanes	124	0.826	1.746	11
Rotor Blades				
Stage 1	54	1.779	0.811	17
Stage 2	55	1.764	0.817	18
Stage 3	49	1.996	0.722	20
Stator Blades				
Stage 1	85	1.235	1.168	27
Stage 2	88	1.232	1.170	25
Stage 3	90	1.235	1.168	53

TABLE II

COMPRESSOR PERFORMANCE SUMMARY

NOMINAL DESIGN POINT (Build #1)

Speed, RPM	5926.0
Mean Blade Speed, U, ft/sec.	583.3
Mass Flow Rate, lb_m/sec	19.2
Flow Coefficient, C_x/U	0.619
Pressure Ratio	1.489
Reference Pressure, $1/2 \rho U^2$, psi	2.754
Pressure Coefficient, $\Delta P / 1/2 \rho U^2$	2.610
Efficiency, η, %(measured)	86.2

COMPRESSOR BUILDS TESTED (Lewis [52])

Reference Speed, RPM	2400.0
Flow Coefficient, C_x/U	
Build #1	0.596
Build #2	0.594
Pressure Rise Coefficient, $\Delta P / 1/2 \rho U^2$	
Build #1	2.343
Build #2	2.343
Efficiency, η, % (estimated)	
Build #1	85.2
Build #2	80.8
Reaction, R	
Build #1	0.642
Build #2	0.738

TABLE III

MIDSPAN BLADE ANGLE* SETTING SUMMARY

Bladerow	Stagger Angle, Deg.		Leading Edge Blade Angle, Deg.		Trailing Edge Blade Angle, Deg.	
	Build#1	Build#2	Build#1	Build#2	Build#1	Build#2
Inlet Guide Vanes	8.1	8.1	0.0	0.0	10.0	10.0
Rotor Blades						
Stage 1	37.8	42.8	45.0	50.0	36.0	41.0
Stage 2	38.5	43.5	49.5	54.5	31.5	36.5
Stage 3	39.6	44.6	53.0	58.0	33.0	38.0
Stator Blades						
Stage 1	21.0	11.0	28.0	18.0	9.0	-1.0
Stage 2	23.0	12.0	37.5	27.5	12.5	2.5
Stage 3	15.5	5.5	46.0	36.5	-7.0	-17.0

* Blade angle definitions and conventions are given in Figure 40.

TABLE IV

COMPRESSOR DISSASSEMBLY PROCEDURE

Phase I – AFT FLANGE DISASSEMBLY (Partial)

    Step 1) Remove Aft Flange Retention Plate
    Step 2) Remove Aft Bearing Thrust Load Plate
    Step 3) Remove Aft Bearing Load Spring Assembly
    Step 4) Loosen and Remove Axial Tie Rod Aft Retention Nuts (4)

Phase II – AFT FLANGE ASSEMBLY REMOVAL

    Step 5) Insert Eyebolts (4) in Aft Mount
    Step 6) Pull Assembly (Overhead Crane)

Phase III – AFT BEARING REMOVAL

    Step 7) Remove Aft Case Ring Spacer
    Step 8) Pull Aft Bearing Assembly
    Step 9) Slide Aft End Disk Off Shaft

Phase IV – REMOVAL OF COMPRESSOR BLADEROWS

    Step 10) Remove Stage Three

        a) Interbladerow Case Ring
        b) Stator Case Ring
        c) Interbladerow Case Ring
        d) Rotor Case Ring
        e) Stator Hub Disk
        f) Rotor Disk

    Step 11) Remove Stage Two (a-f)
    Step 12) Remove Stage One (a-f)
    Step 13) Remove Inlet Guide Vane Bladerow

234

TABLE V

INLET CALIBRATION ERROR ANALYSIS*

Re_{inlet}	A_B/A_C (Eq. 4-5)	C_x (ft/sec)	Operating Speed RPM	Operating Speed U (ft/sec)	$\frac{C_x}{U}$	Error
50,000	0.097 ± 0.003	6.11 ± 0.02	1170	115.2	0.053 ± 0.0002	0.4%
			1800	177.2	0.034 ± 0.0001	
			2400	236.3	0.026 ± 0.0001	
250,000	0.066 ± 0.003	31.60 ± 0.11	1170	115.2	0.274 ± 0.0001	0.4%
			1800	177.2	0.178 ± 0.0006	
			2400	236.3	0.134 ± 0.0005	

* Based upon one standard deviation of the blockage ratio vs. inlet Reynold's Number curve fit.

235

TABLE VI

ORIFICE PLATE CALIBRATION ERROR ANALYSIS*

$Re_{o.p.}$	K (Eq. 4-6)	$\overline{C}_x$ (ft/sec)	Operating Speed RPM	U (ft/sec)	$\dfrac{\overline{C}_x}{U}$	Error
50,000	0.199 ± 0.0004	4.69 ± 0.10	1170	115.2	0.041 ± 0.0009	2%
			1800	177.2	0.026 ± 0.0006	
			2400	236.3	0.020 ± 0.0004	
350,000	0.221 ± 0.004	32.69 ± 0.63	1170	115.2	0.284 ± 0.0055	2%
			1800	177.2	0.184 ± 0.0036	
			2400	236.3	0.138 ± 0.0027	

* Based upon one standard deviation of the orifice plate calibration coefficient vs. Reynold's Number curve fit

236

TABLE VII

ENSEMBLE AVERAGING PROCESS

	t_1	t_2	t_3	...	t_{1000}
Trace #1	$S_1(t_1)$	$S_1(t_2)$	$S_1(t_3)$	...	$S_1(t_{1000})$
Trace #2	$S_2(t_1)$	$S_2(t_2)$	$S_2(t_3)$	...	$S_2(t_{1000})$
...	...	...	...	...	...
Trace #128	$S_{128}(t_1)$	$S_{128}(t_2)$	$S_{128}(t_3)$	...	$S_{128}(t_{1000})$
ENSEMBLE AVERAGE TRACE $S_{EA}(t_j)$	$\dfrac{\sum_{k=1}^{128} S_k(t_1)}{128}$	$\dfrac{\sum_{k=1}^{128} S_k(t_2)}{128}$	$\dfrac{\sum_{k=1}^{128} S_k(t_3)}{128}$	...	$\dfrac{\sum_{k=1}^{128} S_k(t_{1000})}{128}$

TABLE VIII

MEANLINE TORQUE ANALYSIS
(Moderate Reaction Build)

	α_{y_b} (Deg)	β_{y_c} (Deg)
Stage 1	-30.5	46.3
Stage 2	-30.3	44.0
Stage 3	-28.5	41.4

$$T / 1/2 \rho U^2 A_c R_m$$

$\dfrac{C_x}{U}$	A_B/A_C			
	0	0.2	0.4	0.6
-0.05	0.323	0.329	0.338	0.358
-0.10	0.692	0.715	0.754	0.830
-0.15	1.107	1.159	1.246	1.419
-0.20	1.569	1.661	1.815	2.122

TABLE IX

AREA AVERAGED UPSTREAM MEAN VELOCITY FIELD

Reverse Flow Operating Condition

Radial Position	Low $\overline{C_x}^{A_0}/U$	Low $\overline{C_\theta}^{A_0}/U$	Low $\overline{C_r}^{A_0}/U$	Moderate $\overline{C_x}^{A_0}/U$	Moderate $\overline{C_\theta}^{A_0}/U$	Moderate $\overline{C_r}^{A_0}/U$	High $\overline{C_x}^{A_0}/U$	High $\overline{C_\theta}^{A_0}/U$	High $\overline{C_r}^{A_0}/U$
5	-0.06	0	0.02	-0.11	0	0	-0.21	0.01	0
4	-0.07	0	0	-0.11	0	0	-0.22	0.01	-0.01
3	-0.08	0	0	-0.12	0	0	-0.23	0.01	-0.02
2	-0.09	0.02	0.02	-0.12	0	0	-0.24	0.01	-0.02
1	-0.05	0.12	0.05	-0.10	0.07	0.04	-0.23	0.02	-0.01

TABLE X

AREA AVERAGED THIRD STAGE STATOR EXIT MEAN VELOCITY FIELD

Reverse Flow Operating Condition

Radial Position	Low			Moderate			High		
	$\dfrac{\overline{C}_x^A}{U}$	$\dfrac{\overline{C}_\theta^A}{U}$	$\dfrac{\overline{C}_r^A}{U}$	$\dfrac{\overline{C}_x^A}{U}$	$\dfrac{\overline{C}_\theta^A}{U}$	$\dfrac{\overline{C}_r^A}{U}$	$\dfrac{\overline{C}_x^A}{U}$	$\dfrac{\overline{C}_\theta^A}{U}$	$\dfrac{\overline{C}_r^A}{U}$
5	0	0.19	0.04	-0.10	-0.04	0.03	-0.20	-0.09	0.02
4	-0.07	0.06	0.06	-0.11	-0.05	0.02	-0.20	-0.09	0.01
3	-0.08	-0.05	0.04	-0.12	-0.06	0.01	-0.20	-0.100	0.01
2	-0.10	-0.03	0.04	-0.15	-0.05	0.01	-0.22	-0.110	-0.01
1	-0.11	0.14	0.08	-0.18	0.09	0.05	-0.27	-0.100	0

TABLE XI

AREA AVERAGED THIRD STAGE STATOR EXIT
MEAN PRESSURE FIELD

Reverse Flow Operating Condition

Radial Position	Low			Moderate			High		
	$\dfrac{\overline{P}_T A_\theta}{1/2\rho U^2}$	$\dfrac{\overline{C} A_\theta}{U}$	$\dfrac{\overline{P}_S A_\theta}{1/2\rho U^2}$	$\dfrac{\overline{P}_T A_\theta}{1/2\rho U^2}$	$\dfrac{\overline{C} A_\theta}{U}$	$\dfrac{\overline{P}_S A_\theta}{1/2\rho U^2}$	$\dfrac{\overline{P}_T A_\theta}{1/2\rho U^2}$	$\dfrac{\overline{C} A_\theta}{U}$	$\dfrac{\overline{P}_S A_\theta}{1/2\rho U^2}$
Case Wall	---	---	0.45	---	---	1.05	---	---	2.81
5	0.53	0.19	0.49	1.07	0.11	1.06	2.83	0.22	2.78
4	0.44	0.11	0.43	1.07	0.12	1.06	2.83	0.22	2.78
3	0.44	0.10	0.43	1.07	0.13	1.05	2.84	0.22	2.79
2	0.44	0.11	0.43	1.07	0.16	1.04	2.83	0.25	2.77
1	0.46	0.20	0.42	1.07	0.21	1.03	2.84	0.29	2.76

241

TABLE XII

AREA AVERAGED THIRD STAGE ROTOR EXIT
MEAN VELOCITY FIELD

Reverse Flow Operating Condition

Radial Position	Low			Moderate			High		
	$\dfrac{\overline{C_x}^{A_\theta}}{U}$	$\dfrac{\overline{C_\theta}^{A_\theta}}{U}$	$\dfrac{\overline{C_r}^{A_\theta}}{U}$	$\dfrac{\overline{C_x}^{A_\theta}}{U}$	$\dfrac{\overline{C_\theta}^{A_\theta}}{U}$	$\dfrac{\overline{C_r}^{A_\theta}}{U}$	$\dfrac{\overline{C_x}^{A_\theta}}{U}$	$\dfrac{\overline{C_\theta}^{A_\theta}}{U}$	$\dfrac{\overline{C_r}^{A_\theta}}{U}$
5	-0.14	1.07	-0.10	-0.22	1.22	-0.14	-0.34	1.44	-0.07
4	-0.09	1.06	-0.13	-0.16	1.19	-0.16	-0.31	1.42	-0.11
3	-0.03	1.00	-0.16	-0.11	1.15	-0.19	-0.19	1.33	-0.16
2	-0.03	0.85	-0.12	-0.10	1.06	-0.16	-0.19	1.33	-0.20
1	0.01	0.73	-0.09	-0.09	0.95	-0.13	-0.18	1.23	-0.14

TABLE XIII

AREA AVERAGED THIRD STAGE ROTOR EXIT MEAN PRESSURE FIELD

Reverse Flow Operating Condition

Radial Position	Low			Moderate			High		
	$\dfrac{\overline{P}_T A_\theta}{1/_2 \rho U^2}$	$\dfrac{\overline{C} A_\theta}{U}$	$\dfrac{\overline{P}_S A_\theta}{1/_2 \rho U^2}$	$\dfrac{\overline{P}_T A_\theta}{1/_2 \rho U^2}$	$\dfrac{\overline{C} A_\theta}{U}$	$\dfrac{\overline{P}_S A_\theta}{1/_2 \rho U^2}$	$\dfrac{\overline{P}_T A_\theta}{1/_2 \rho U^2}$	$\dfrac{\overline{C} A_\theta}{U}$	$\dfrac{\overline{P}_S A_\theta}{1/_2 \rho U^2}$
Case Wall	---	---	0.54	---	---	1.14	---	---	2.77
5	2.13	1.08	0.96	3.31	1.25	1.57	4.91	1.48	2.72
4	1.91	1.07	0.76	2.84	1.21	1.37	4.73	1.46	2.61
3	1.56	1.01	0.53	2.44	1.17	1.07	3.78	1.35	1.95
2	1.15	0.86	0.41	2.04	1.08	0.88	3.37	1.36	1.53
1	0.87	0.74	0.33	1.72	0.96	0.79	3.16	1.25	1.60

TABLE XIV

TIME AVERAGED SECOND STAGE STATOR EXIT VELOCITY FIELD
(MODERATE REVERSE FLOW)

Radial Position	Circumferential Position										
	1	2	3	4	5	6	7	8	9	10	11

C_x/U

Radial	1	2	3	4	5	6	7	8	9	10	11
5	-0.04	-0.08	-0.07	-0.09	-0.11	-0.08	-0.02	-0.04	-0.02	-0.08	-0.04
4	-0.09	-0.11	-0.28	-0.13	-0.17	-0.11	-0.07	-0.07	-0.03	-0.09	-0.05
3	-0.17	-0.20	-0.26	-0.25	-0.27	-0.15	-0.24	-0.14	-0.14	-0.18	-0.17
2	-0.54	-0.24	-0.27	-0.30	-0.30	-0.18	-0.30	-0.20	-0.20	-0.27	-0.23
1	-0.13	-0.15	-0.11	-0.15	-0.10	-0.11	-0.05	-0.10	-0.04	-0.13	-0.06

C_θ/U

Radial	1	2	3	4	5	6	7	8	9	10	11
5	-0.45	-0.41	-0.72	-0.40	-0.63	-0.38	-0.44	-0.41	-0.48	-0.40	-0.42
4	-0.55	-0.48	-1.098	-0.49	-0.73	-0.44	-0.55	-0.48	-0.54	-0.46	-0.47
3	-0.50	-0.48	-0.57	-0.46	-0.54	-0.36	-0.70	-0.43	-0.48	-0.43	-0.42
2	-0.77	-0.44	-0.50	-0.39	-0.47	-0.29	-0.66	-0.40	-0.47	-0.40	-0.40
1	-0.55	-0.38	-0.42	-0.36	-0.49	-0.34	-0.55	-0.38	-0.41	-0.37	-0.41

C_r/U

Radial	1	2	3	4	5	6	7	8	9	10	11
5	-0.03	0	-0.03	0.02	0	0.01	-0.02	0	-0.03	-0.01	-0.03
4	-0.09	-0.03	-0.35	0	-0.03	0	-0.10	-0.01	-0.04	-0.02	-0.05
3	-0.02	-0.04	-0.10	-0.01	0.11	0.02	-0.20	0	-0.02	-0.01	-0.01
2	-0.39	-0.03	-0.04	-0.01	0.02	0.04	-0.21	-0.01	-0.05	-0.03	-0.01
1	0.12	0.01	-0.03	0	-0.02	0	0	0	-0.02	-0.02	-0.03

TABLE XV

AREA AVERAGED SECOND STAGE STATOR EXIT VELOCITY FIELD

Reverse Flow Operating Condition

Radial Position	Low			Moderate			High		
	$\frac{\bar{C}_x A_\theta}{U}$	$\frac{\bar{C}_\theta A_\theta}{U}$	$\frac{\bar{C}_r A_\theta}{U}$	$\frac{\bar{C}_x A_\theta}{U}$	$\frac{\bar{C}_\theta A_\theta}{U}$	$\frac{\bar{C}_r A_\theta}{U}$	$\frac{\bar{C}_x A_\theta}{U}$	$\frac{\bar{C}_\theta A_\theta}{U}$	$\frac{\bar{C}_r A_\theta}{U}$
5	-0.04	-0.21	0.04	-0.06	-0.45	-0.01	-0.10	-0.55	-0.04
4	-0.05	-0.27	0	-0.09	-0.52	-0.03	-0.14	-0.55	-0.03
3	-0.08	-0.30	-0.02	-0.19	-0.48	-0.02	-0.29	-0.51	-0.07
2	-0.10	-0.29	-0.03	-0.25	-0.44	-0.03	-0.37	-0.48	-0.03
1	-0.04	-0.24	-0.01	-0.09	-0.41	-0.01	-0.20	-0.45	-0.03

245

TABLE XVI

AREA AVERAGE SECOND STAGE STATOR EXIT PRESSURE FIELD

Reverse Flow Operating Condition

Radial Position	Low			Moderate			High		
	$\dfrac{\bar{P}_T A_\theta}{1/2\rho U^2}$	$\dfrac{\bar{C} A_\theta}{U}$	$\dfrac{\bar{P}_S A_\theta}{1/2\rho U^2}$	$\dfrac{\bar{P}_T A_\theta}{1/2\rho U^2}$	$\dfrac{\bar{C} A_\theta}{U}$	$\dfrac{\bar{P}_S A_\theta}{1/2\rho U^2}$	$\dfrac{\bar{P}_T A_\theta}{1/2\rho U^2}$	$\dfrac{\bar{C} A_\theta}{U}$	$\dfrac{\bar{P}_S A_\theta}{1/2\rho U^2}$
Case Wall	---	---	0.31	---	---	0.70	---	---	1.80
5	0.41	0.22	0.36	0.80	0.45	0.59	1.94	0.56	1.63
4	0.39	0.27	0.31	0.87	0.53	0.59	2.03	0.57	1.71
3	0.42	0.31	0.32	0.93	0.52	0.66	2.06	0.59	1.71
2	0.41	0.29	0.33	0.90	0.51	0.64	2.12	0.61	1.75
1	0.38	0.24	0.32	0.85	0.42	0.67	1.97	0.49	1.73

TABLE XVII

AREA AVERAGE DOWNSTREAM PRESSURE MEASUREMENTS
(MODERATE REVERSED FLOWS)

$$\frac{\overline{P_T}^{A_\theta}}{1/2\,\rho\,U^2}$$

	AXIAL STATION			
Radial Position	5	4	3	2
5	2.96	0.60	2.64	-0.02
4	2.87	0.78	2.65	0.03
3	2.61	0.84	2.37	0.05
2	2.17	0.66	2.03	0.07
1	1.69	0.56	1.50	0.06

TABLE XVIII

RADIAL PRESSURE GRADIENT COMPARISON
(Third Stage Rotor Exit at Axial Station #7)

$$\frac{\Delta\overline{P_T}^{A_\theta}}{1/2\,\rho\,U^2}$$

Reverse Flow Operating Condition (C_x/U)	Measured (Eq. 7-31)	Radial Equilibrium (Eq. 7-35)
High	1.17	0.38
Moderate	0.35	0.29
Low	0.21	0.20
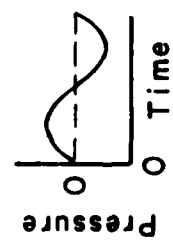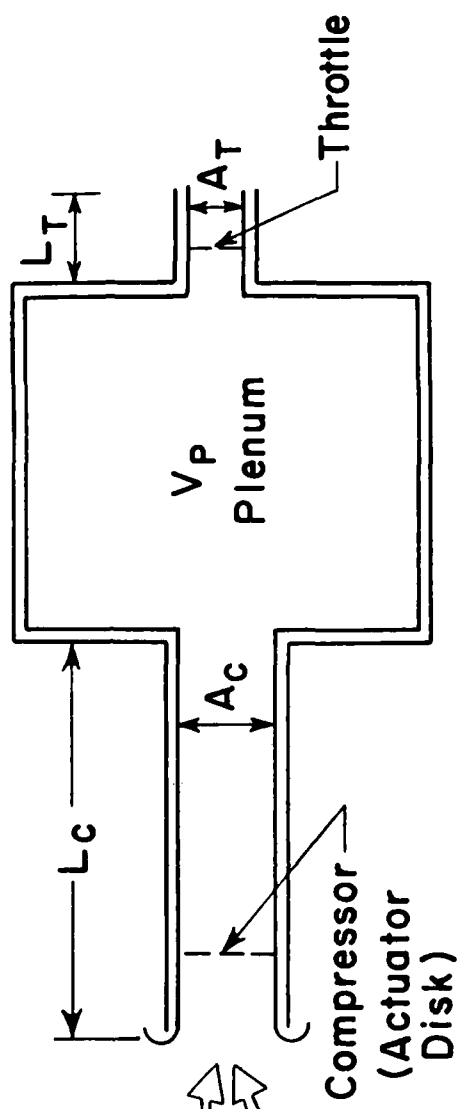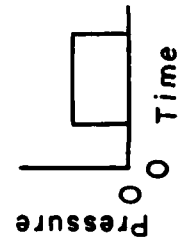
Figure 1   Compression System Dynamic Model

248
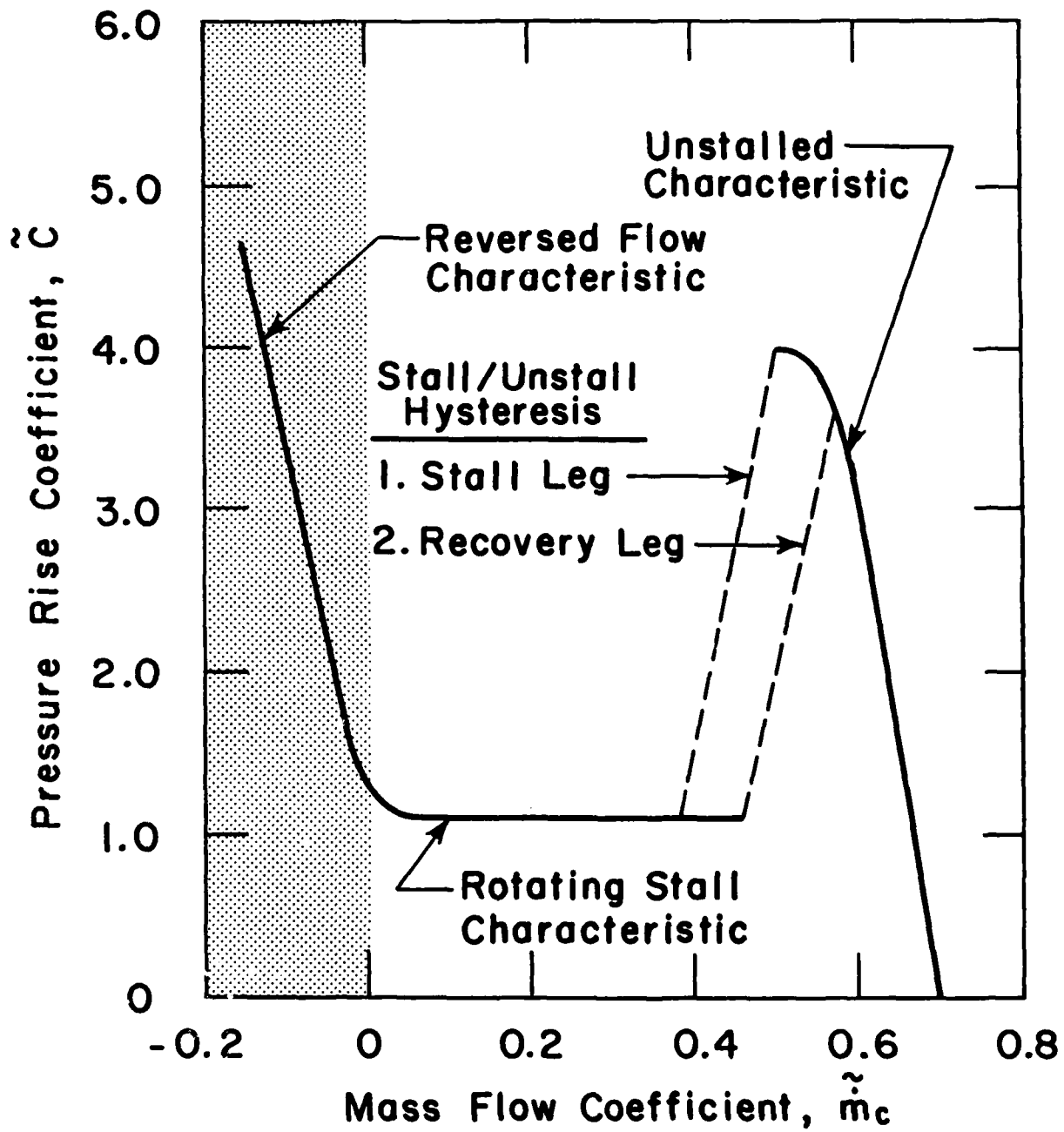
Figure 2   Representative Multistage Axial Compressor Performance
(Steady State)

—— Compressor Performance Characteristic, $\tilde{C}$

--- Transient System Response Trajectory, $\Delta \tilde{P}(\tilde{t})$

B > B$_{crit}$

B < B$_{crit}$

B << B$_{crit}$

Mass Flow Coefficient

Mass Flow Coefficient

Mass Flow Coefficient

a) Surge Limit Cycle

b) Stagnation (Indirect)

c) Stagnation (Direct)

Pressure Rise Coefficient
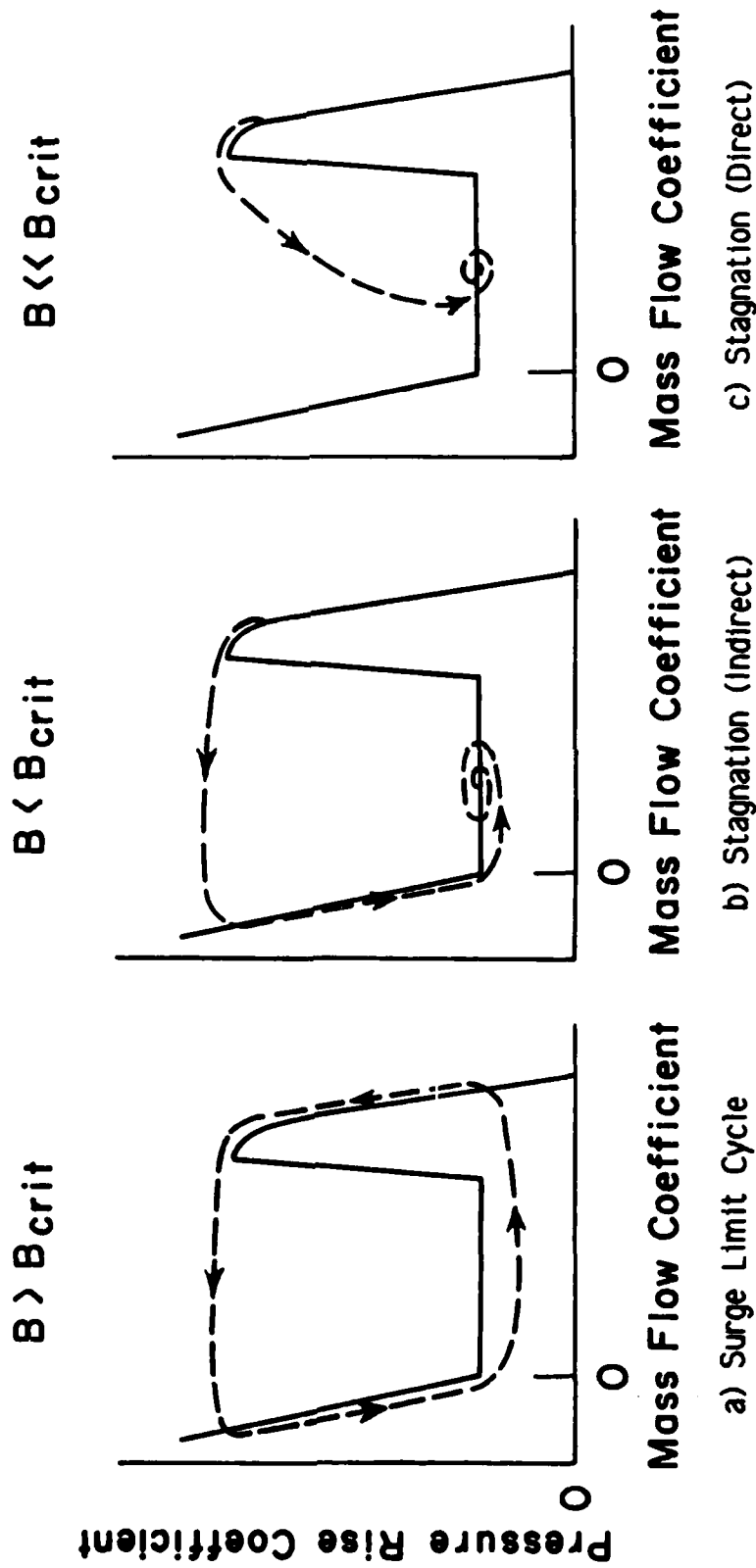
Figure 3   Post Stall Compression System Behavior Modes
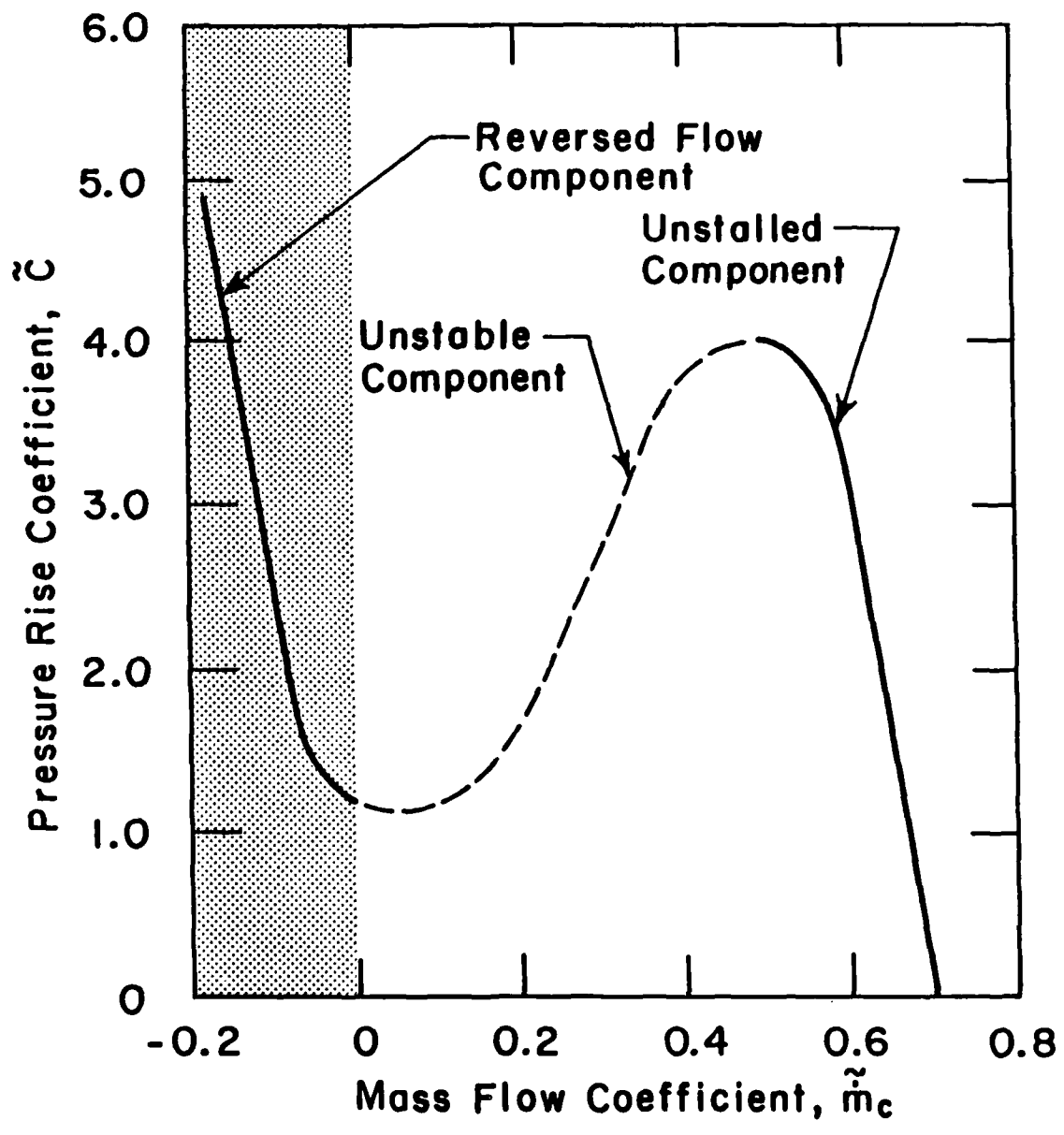
Figure 4   Representative Axisymmetric Characteristic
(Ref: Koff [14])

251
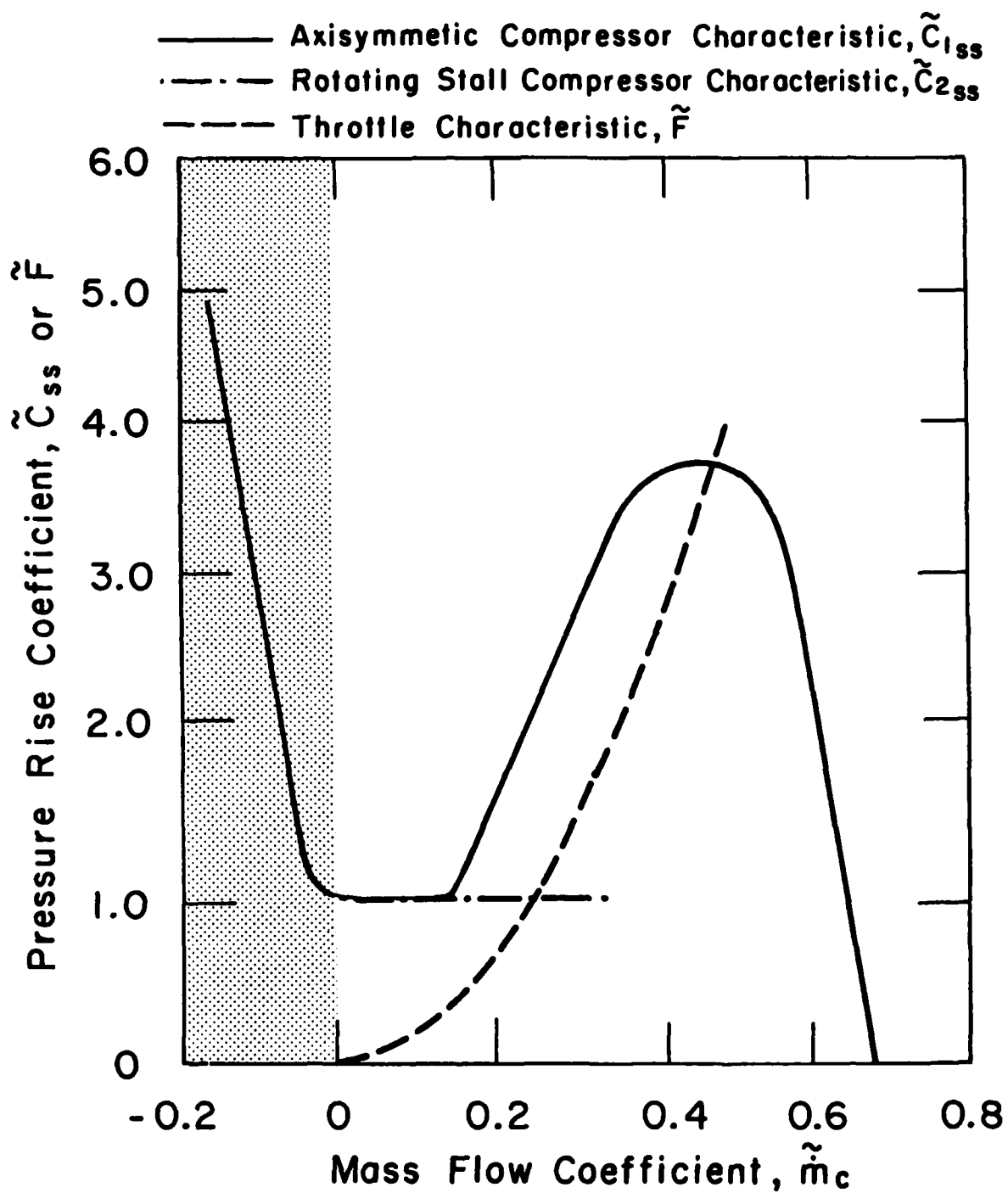
Figure 5   Baseline Performance Characteristics (Steady State)
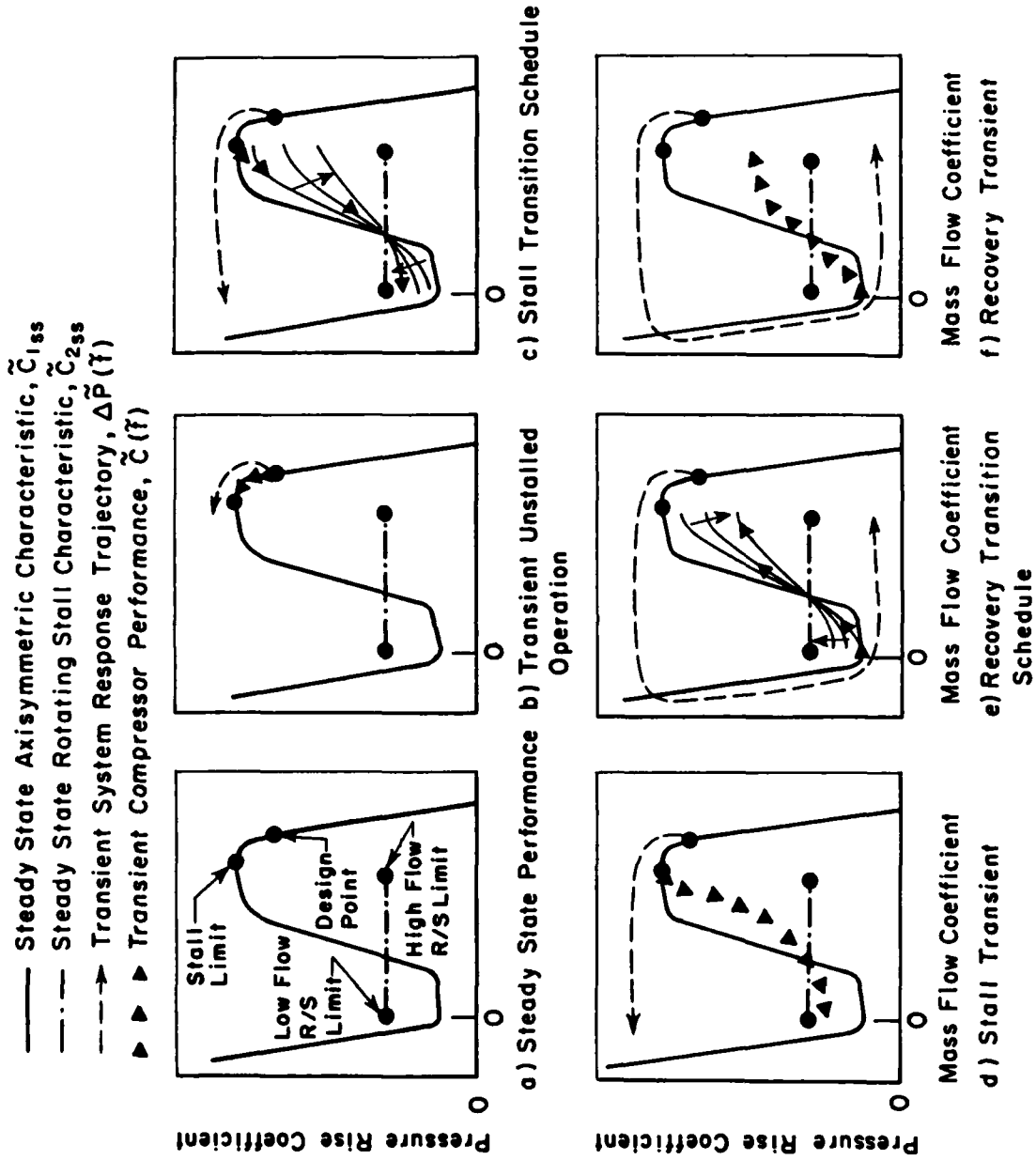
Figure 6   Transient Compressor Performance Prediction

253
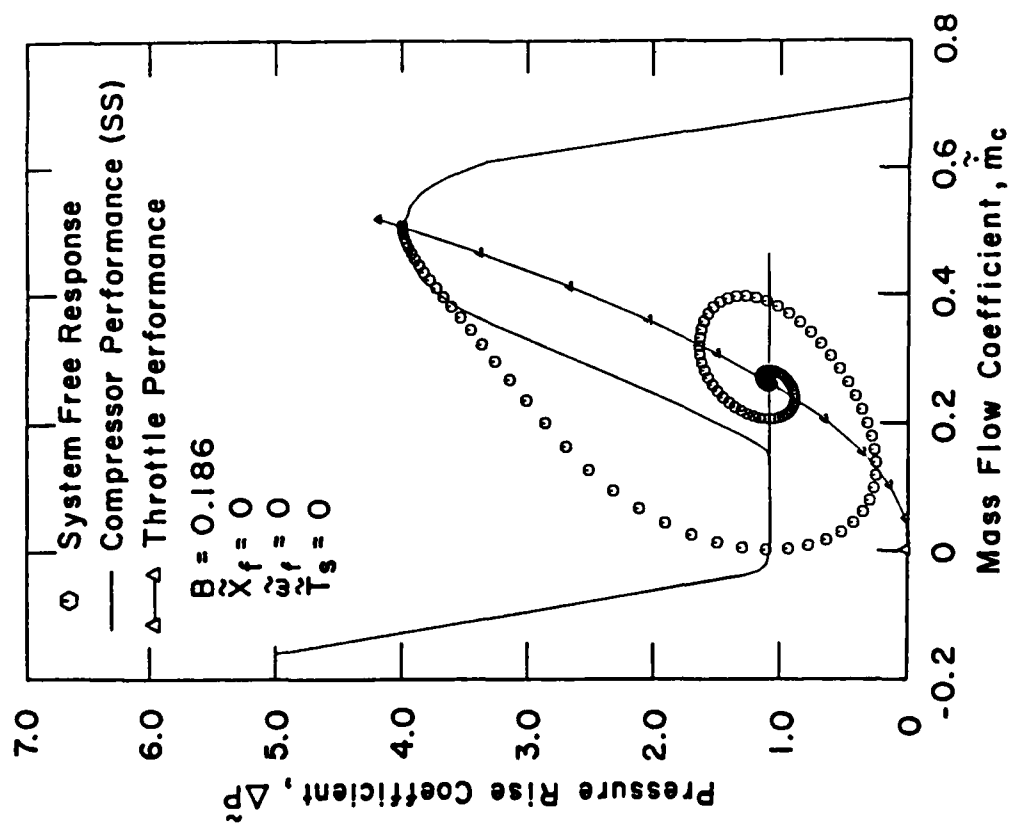
a) Stagnation $(B < B_{crit})$
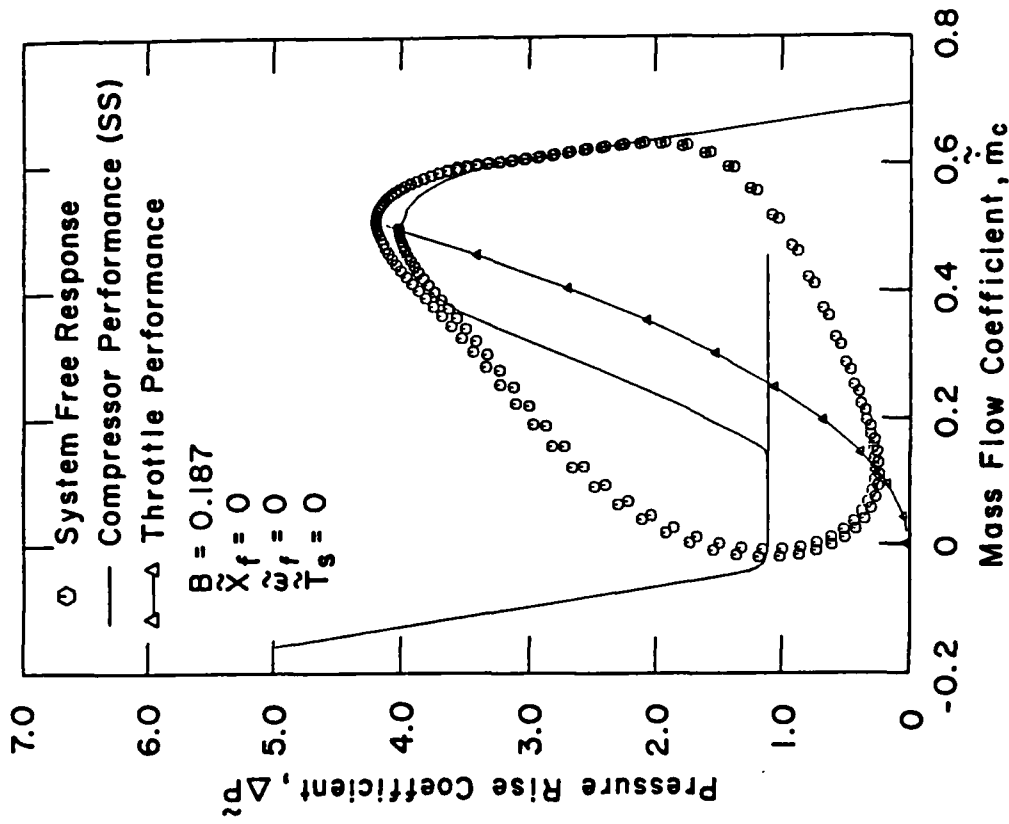
b) Surge Limit Cycle $(B > B_{crit})$

Figure 7   Compression System Free Response

254
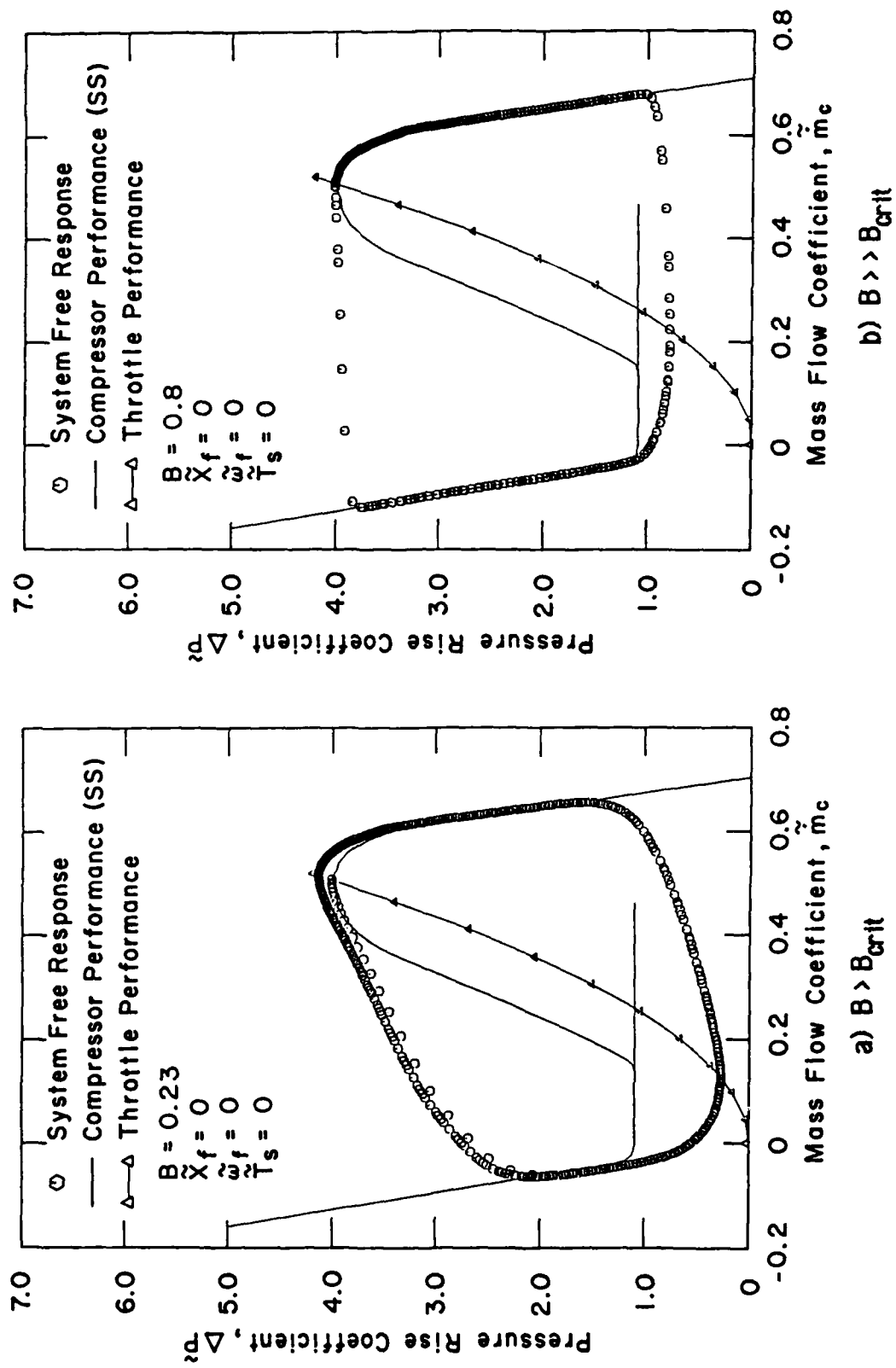
Figure 8   Baseline System Surge Limit Cycles
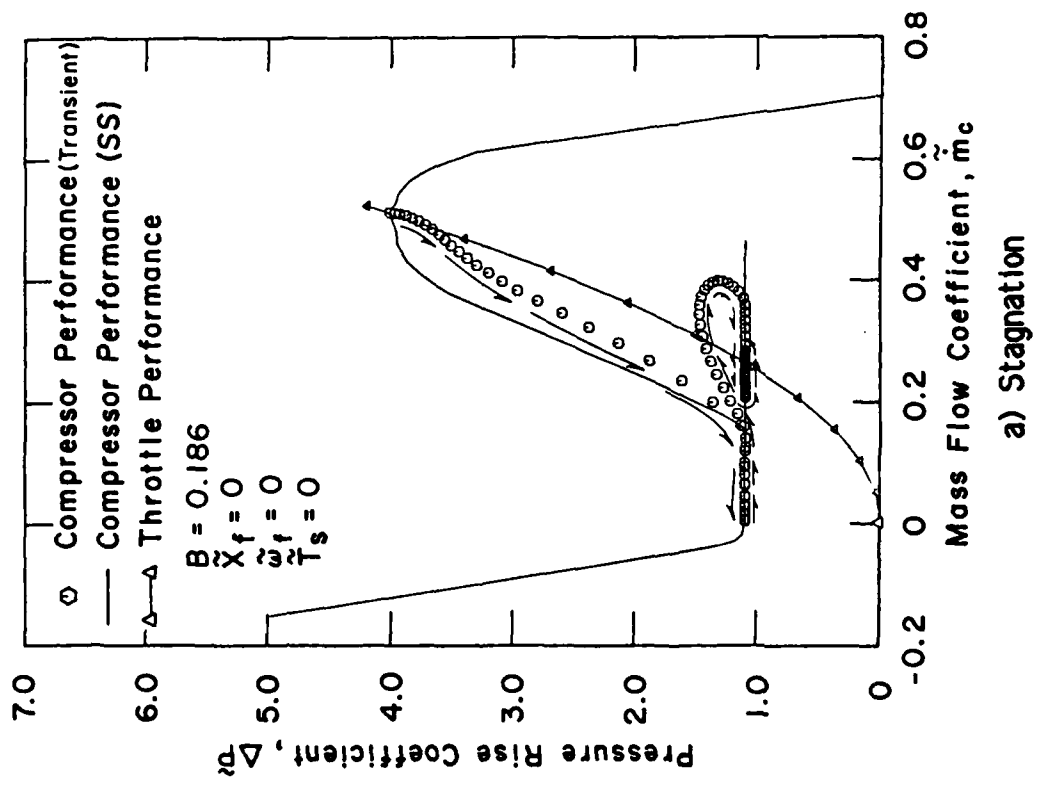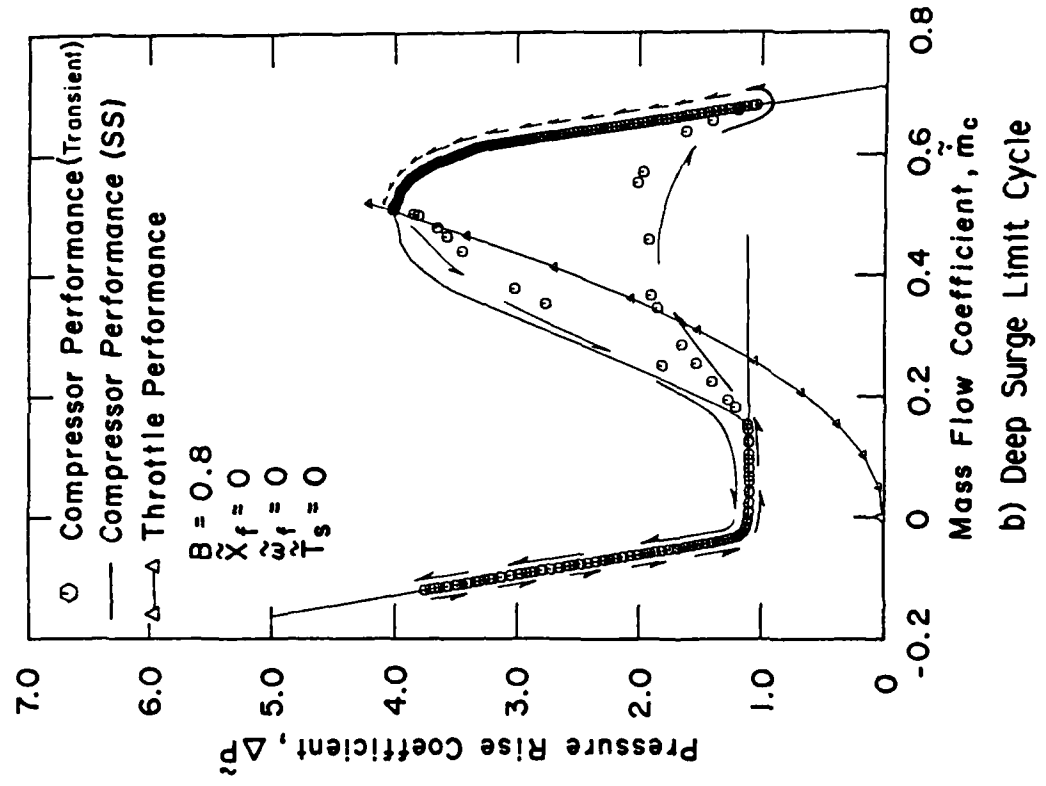
Figure 9   Transient Compressor Performance
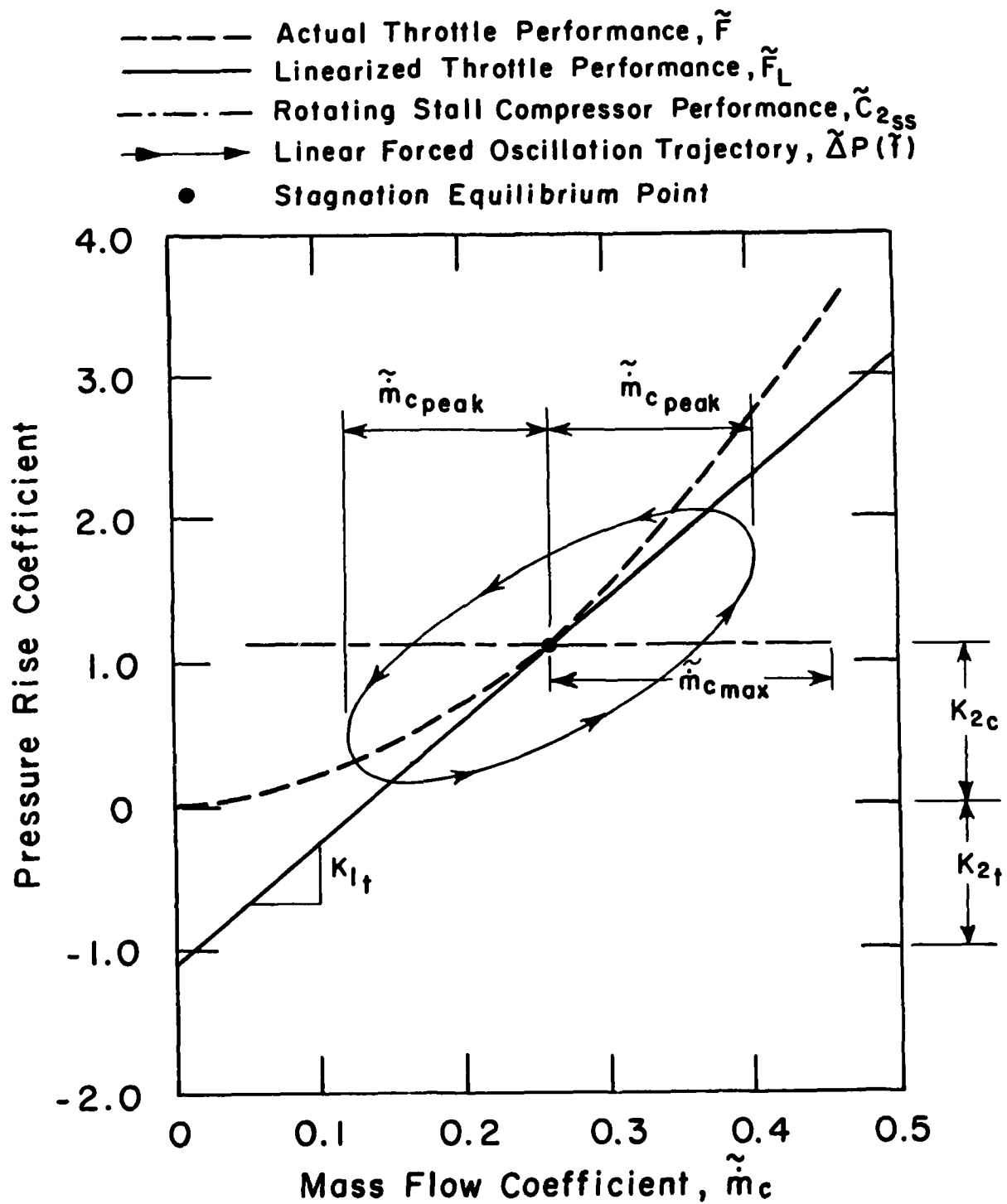
Figure 10   Linearized Stagnation Point System Dynamics
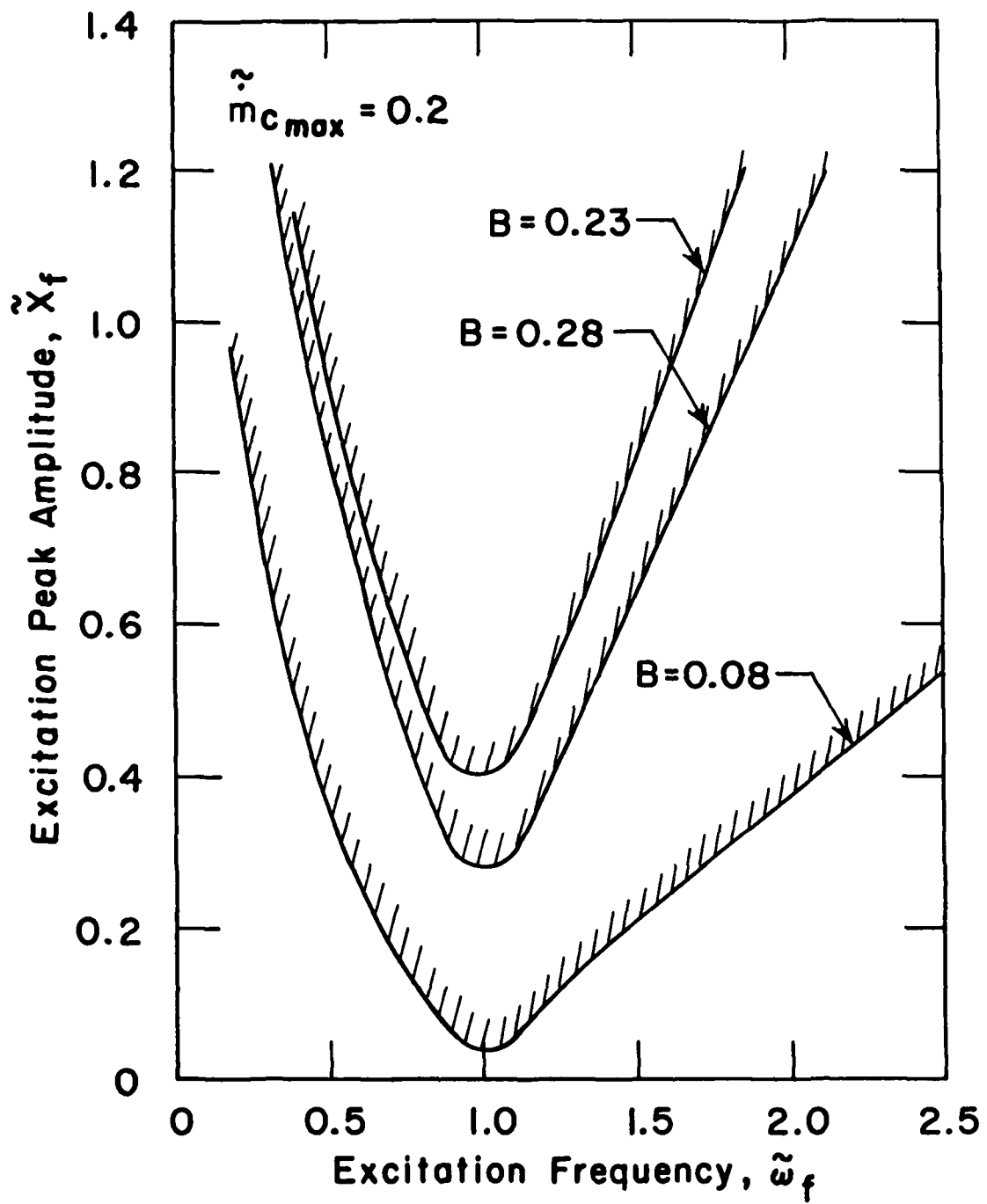
Figure 11   Domains of Attraction from Local Linear Analysis
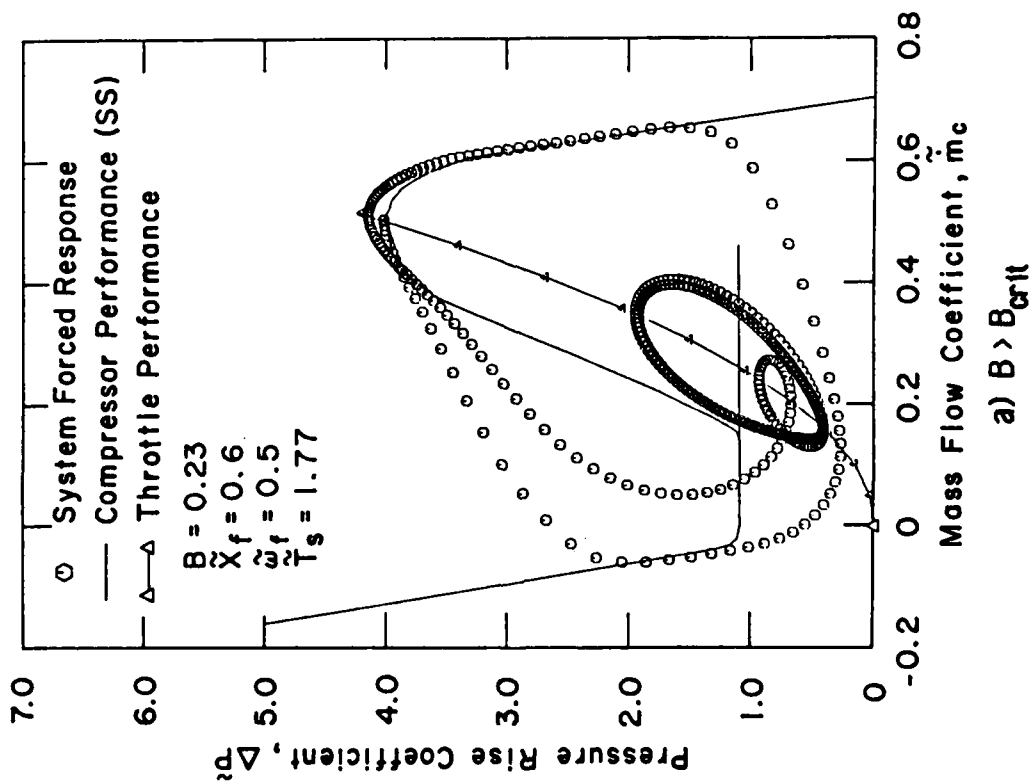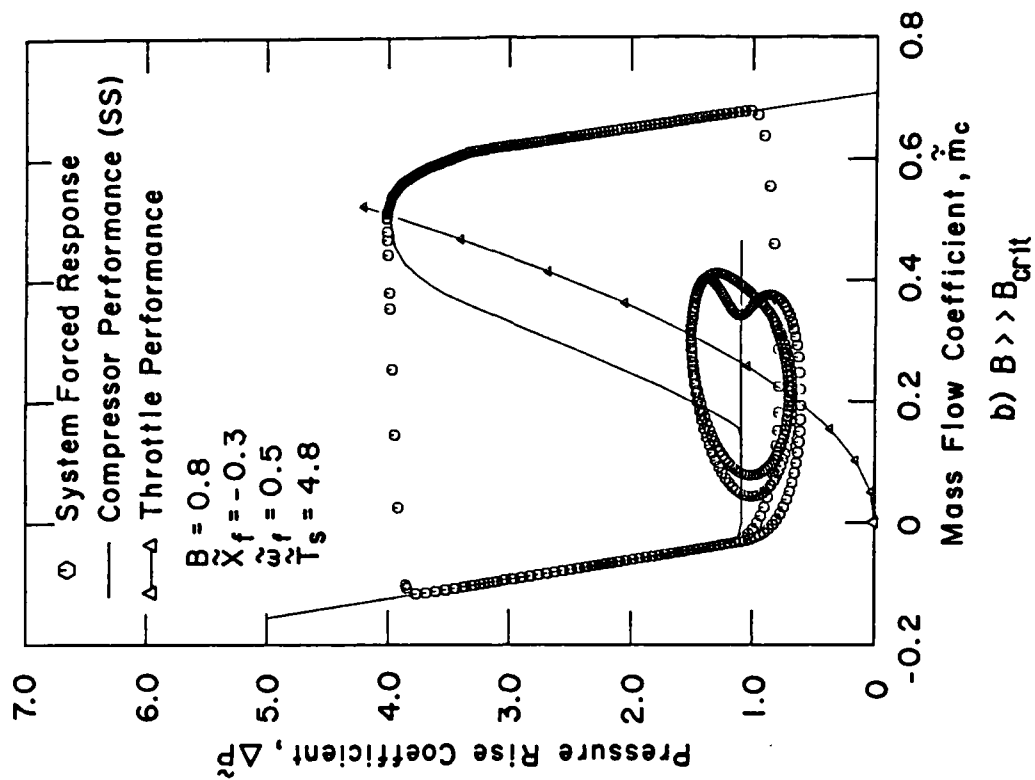
Figure 12   Stagnation Point Forced Oscillation

259
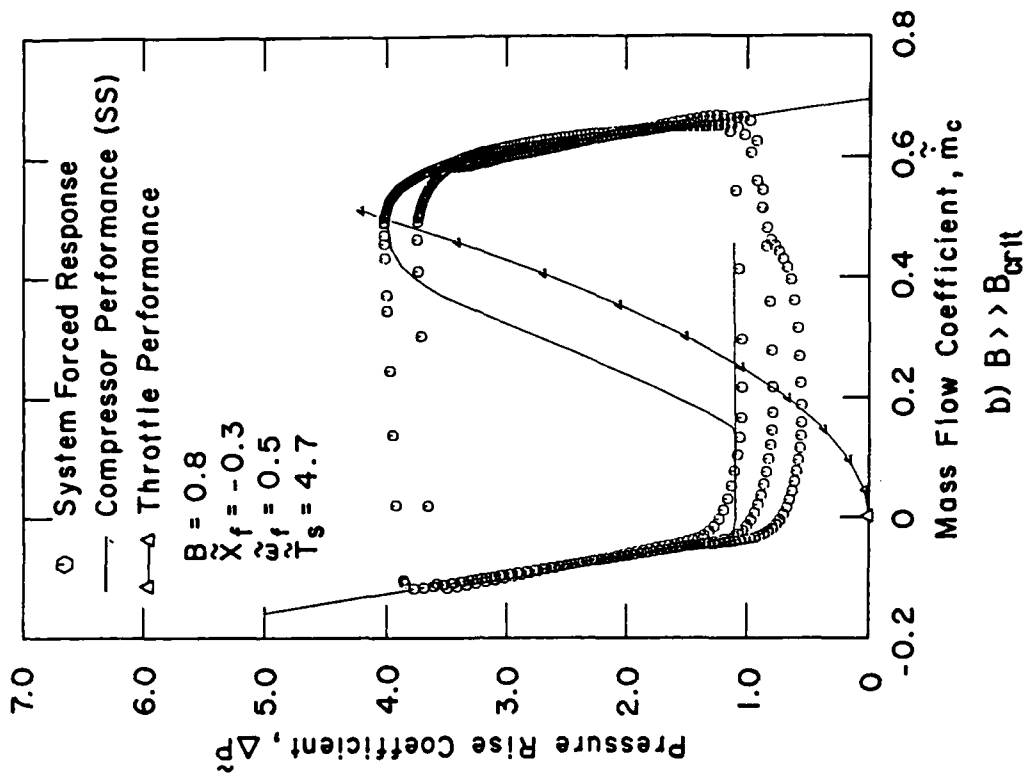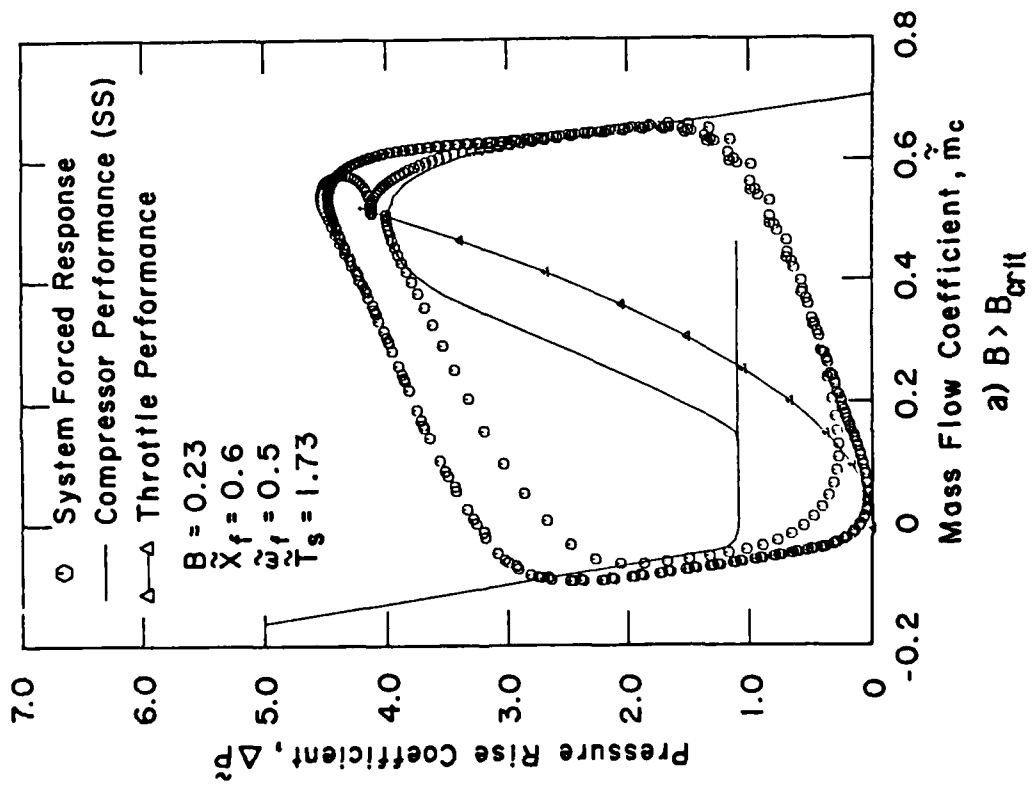
Figure 13   Effect of Early Imposition of External Pressure Excitation
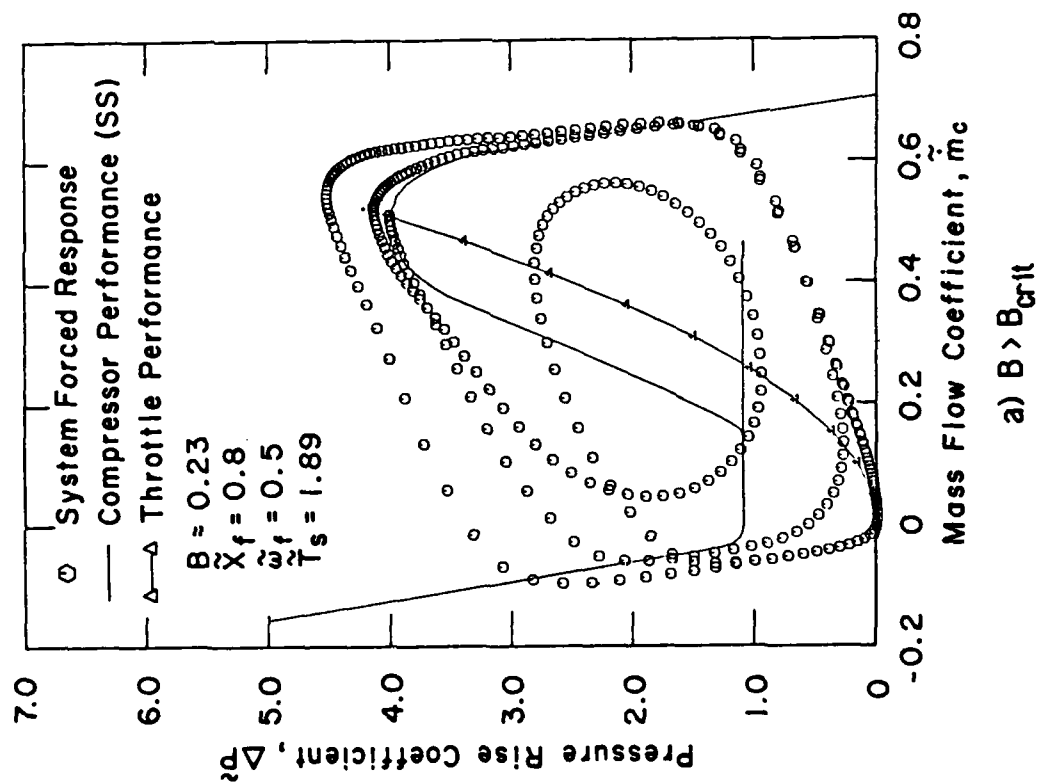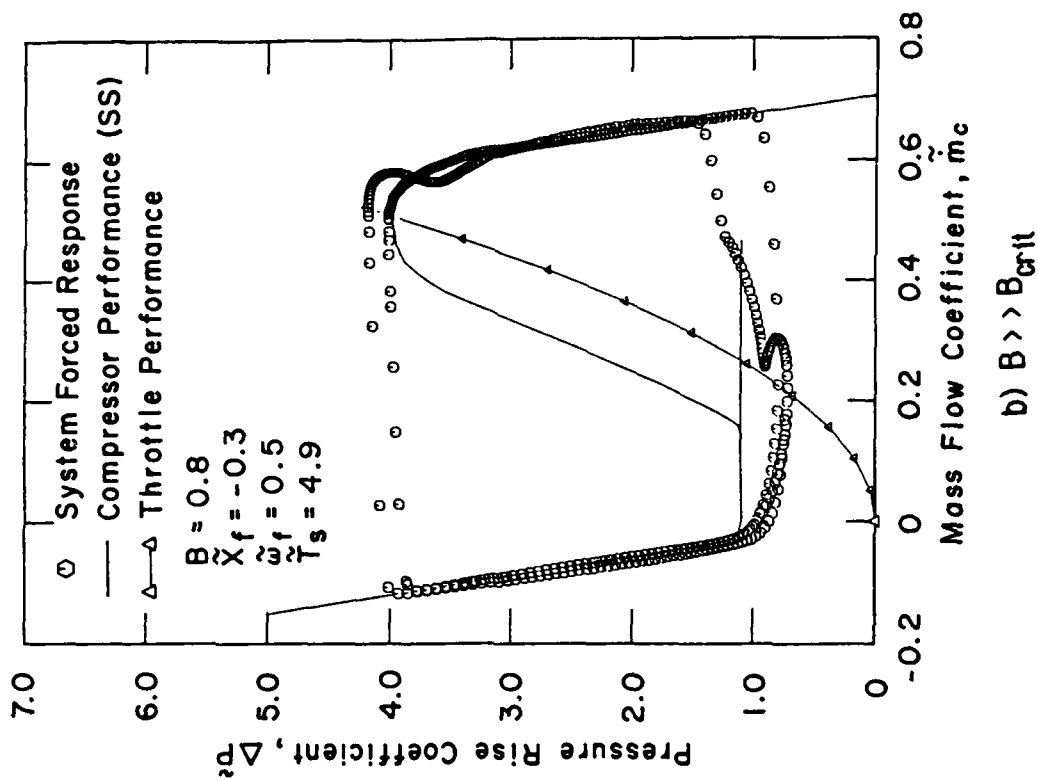
Figure 14   Effect of Late Imposition of External Pressure Excitation
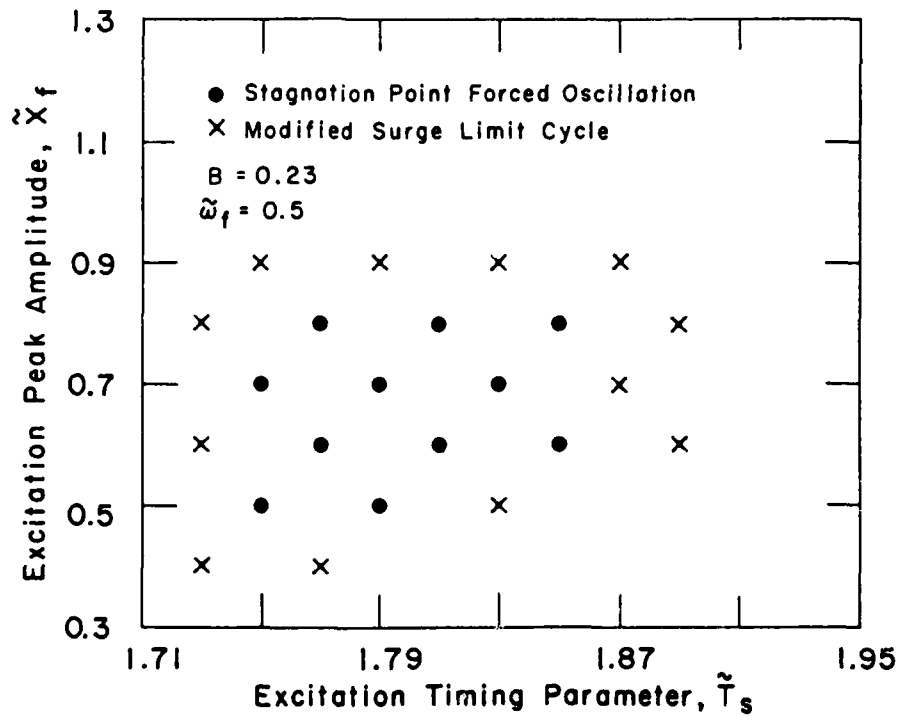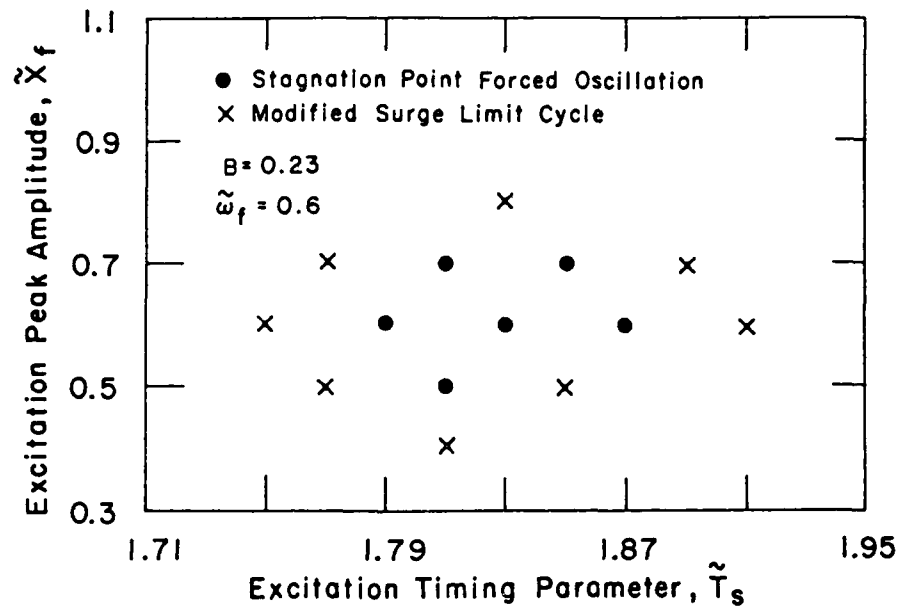
Figure 15   External Excitation Timing Window $(B > B_{crit})$
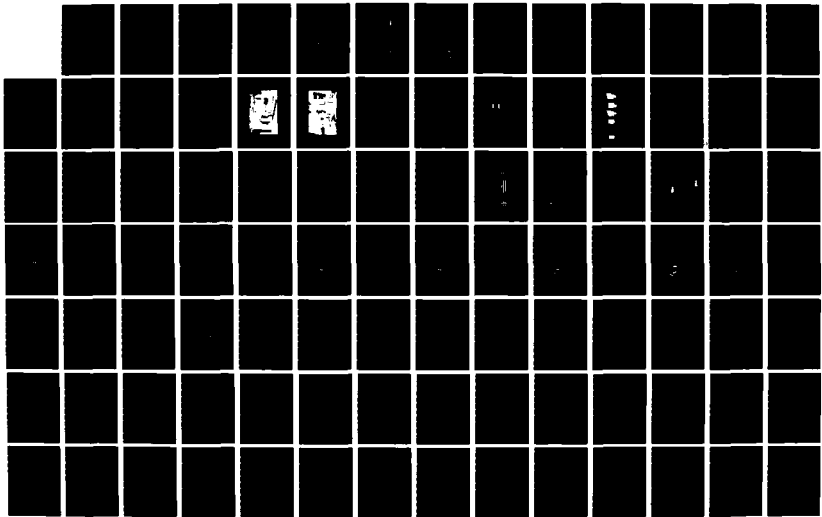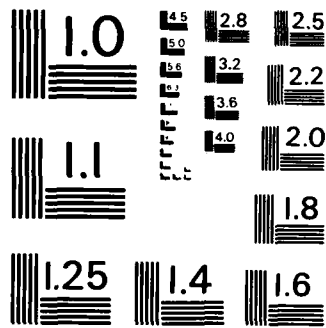
MICROCOPY RESOLUTION TEST CHART

NATIONAL BUREAU OF STANDARDS-1963-A
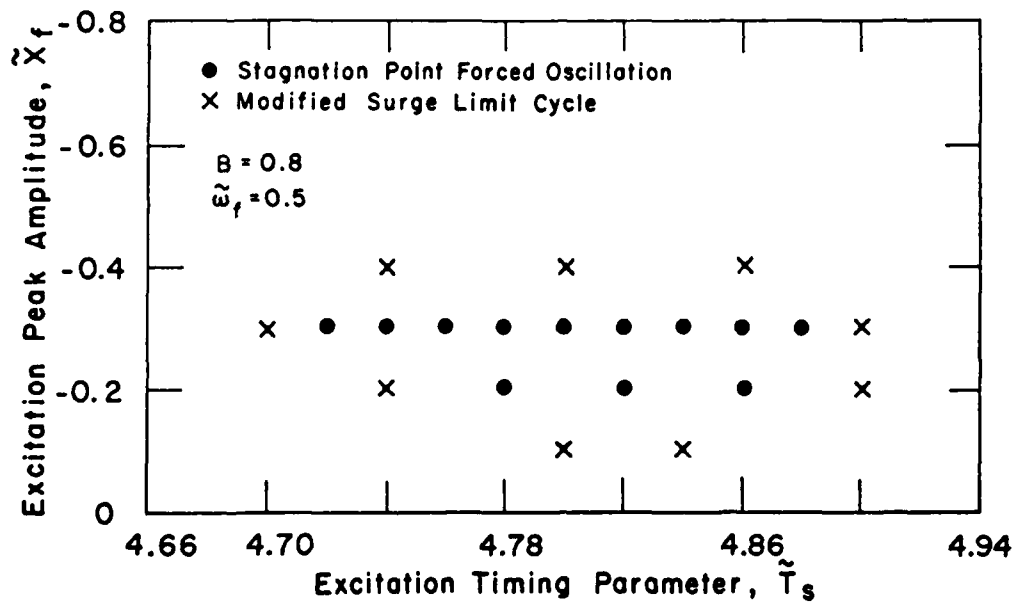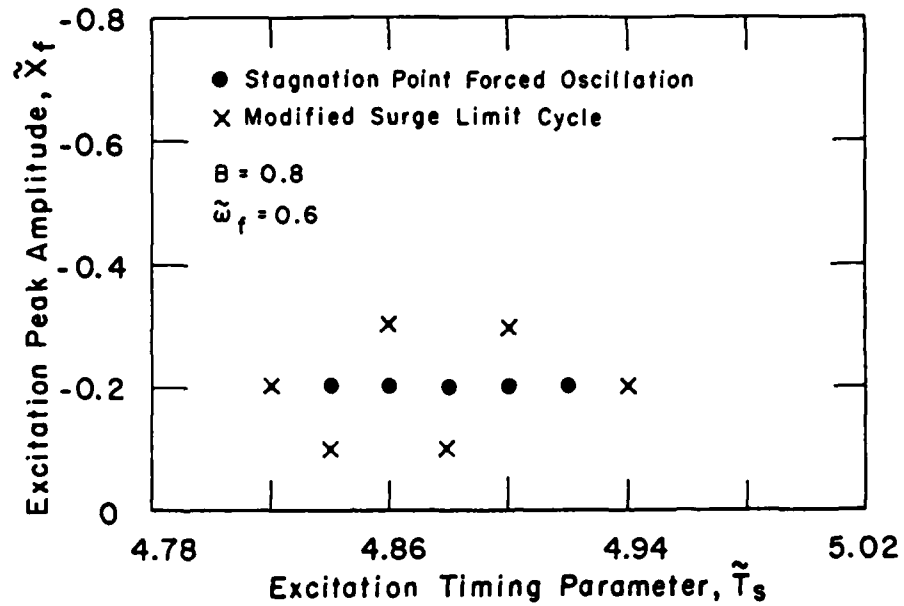
Figure 16   External Excitation Timing Window (B >> B_crit)
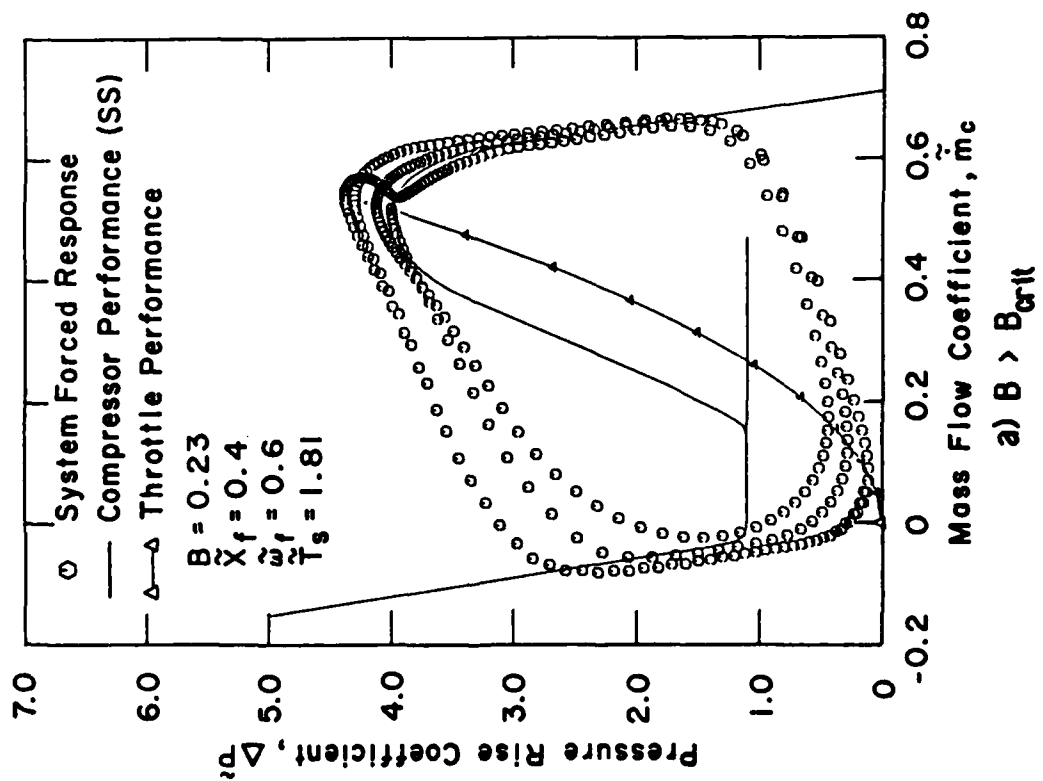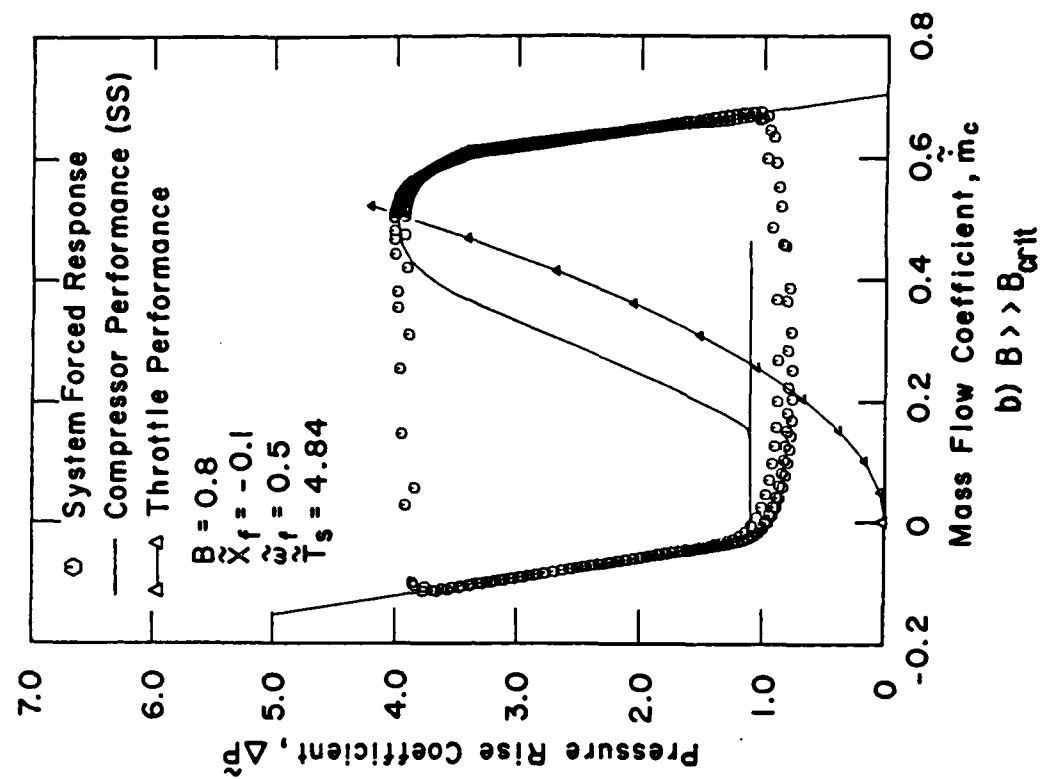
Figure 17   Effect of Imposing a Weak External Pressure Excitation
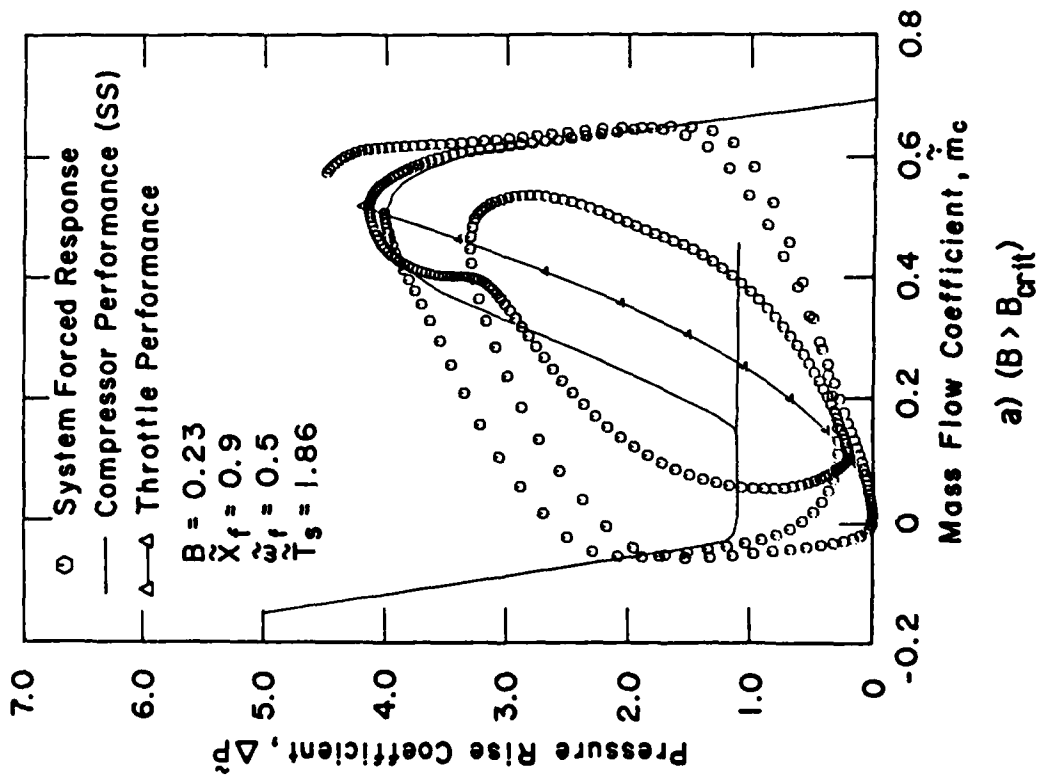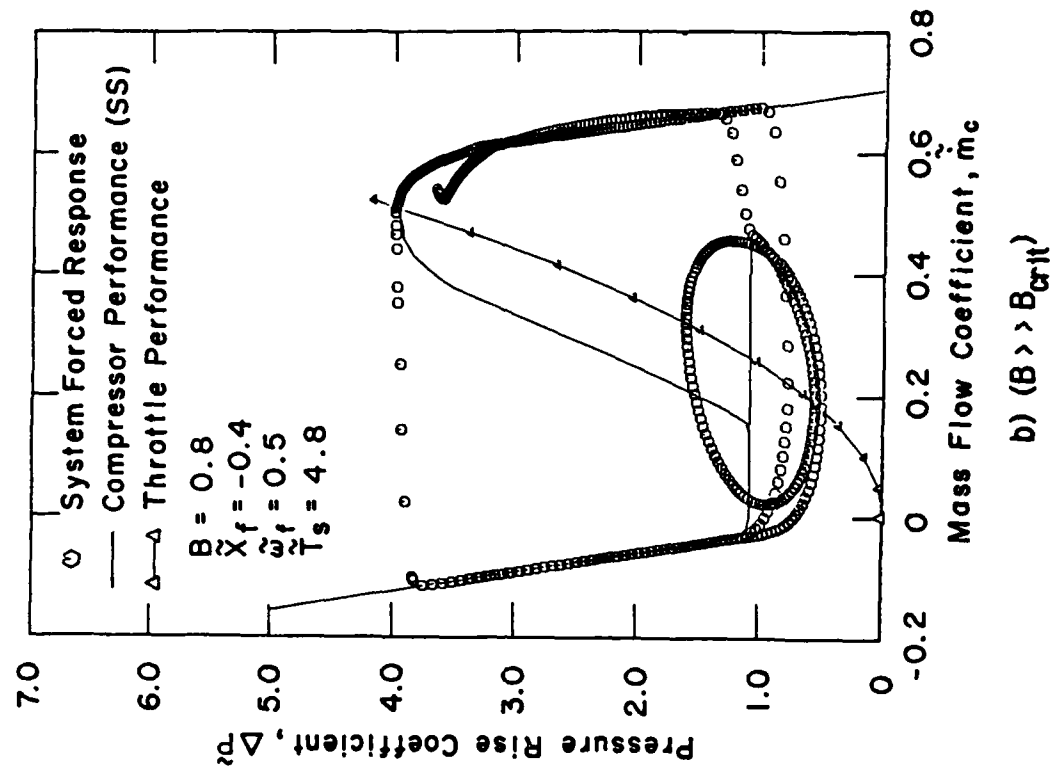
Figure 18   Effect of Imposing a Strong External Pressure Excitation
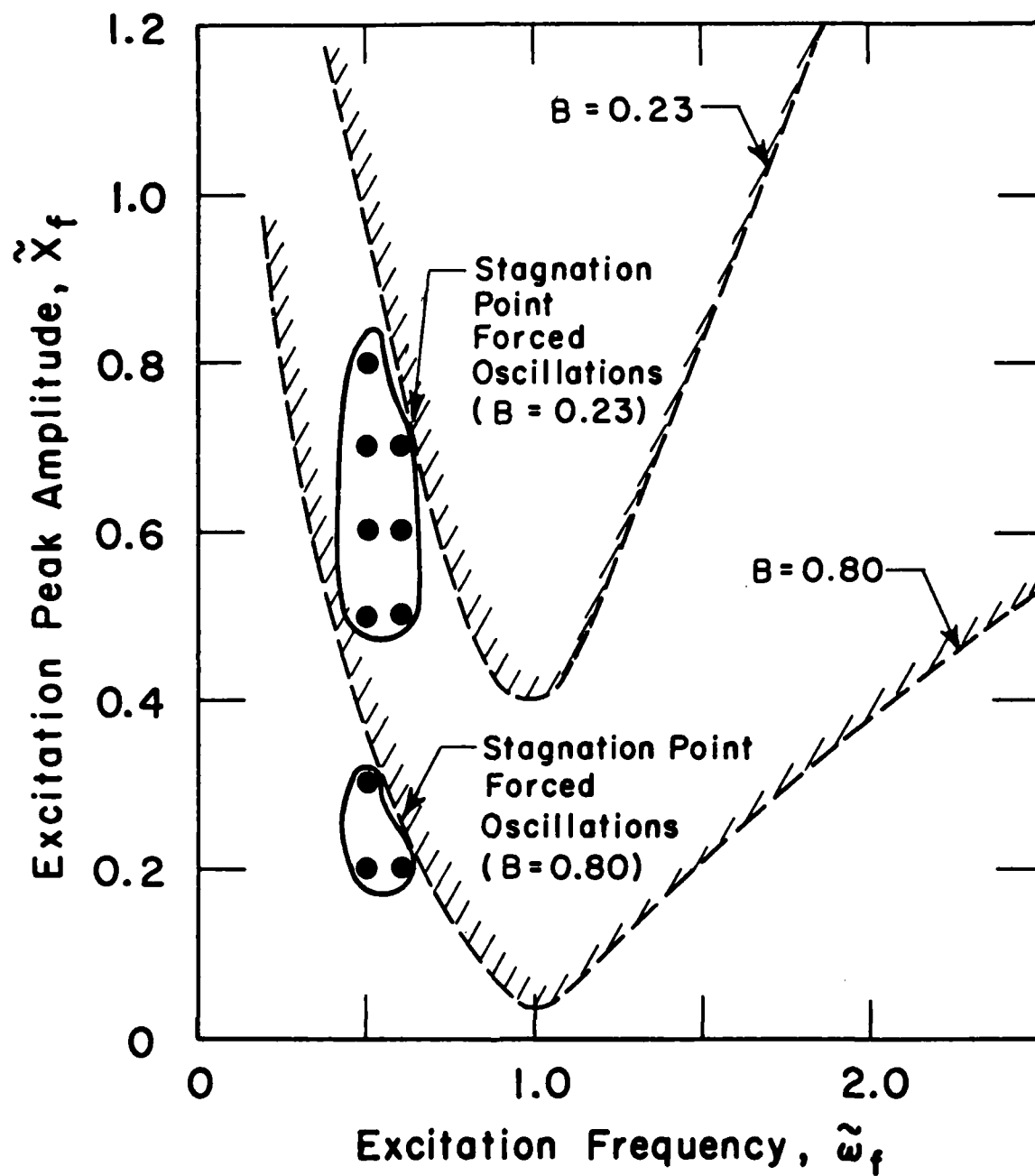
Figure 19   External Excitation Amplitude – Frequency Window
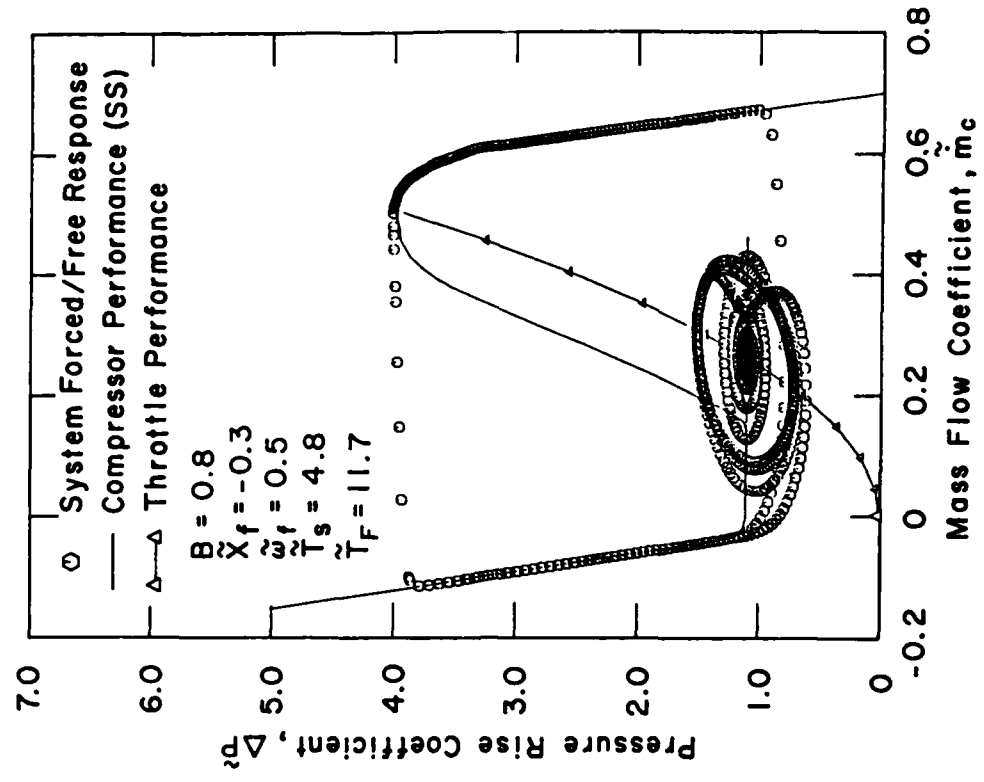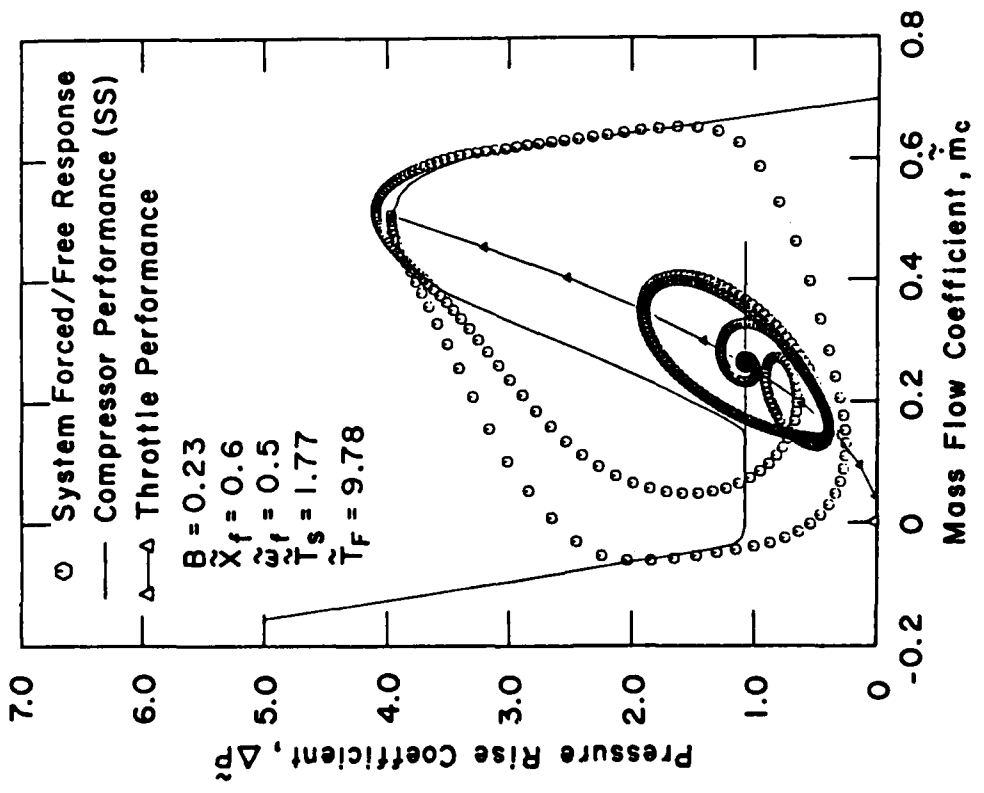
Figure 20   Stagnation Spiral Upon External Excitation Termination

Figure 22   Modified Compressor Performance
Characteristic (Zero Mass Flow Regime)

Figure 21   Surge Limit Cycle Reestablishment
Upon External Excitation Termination

268
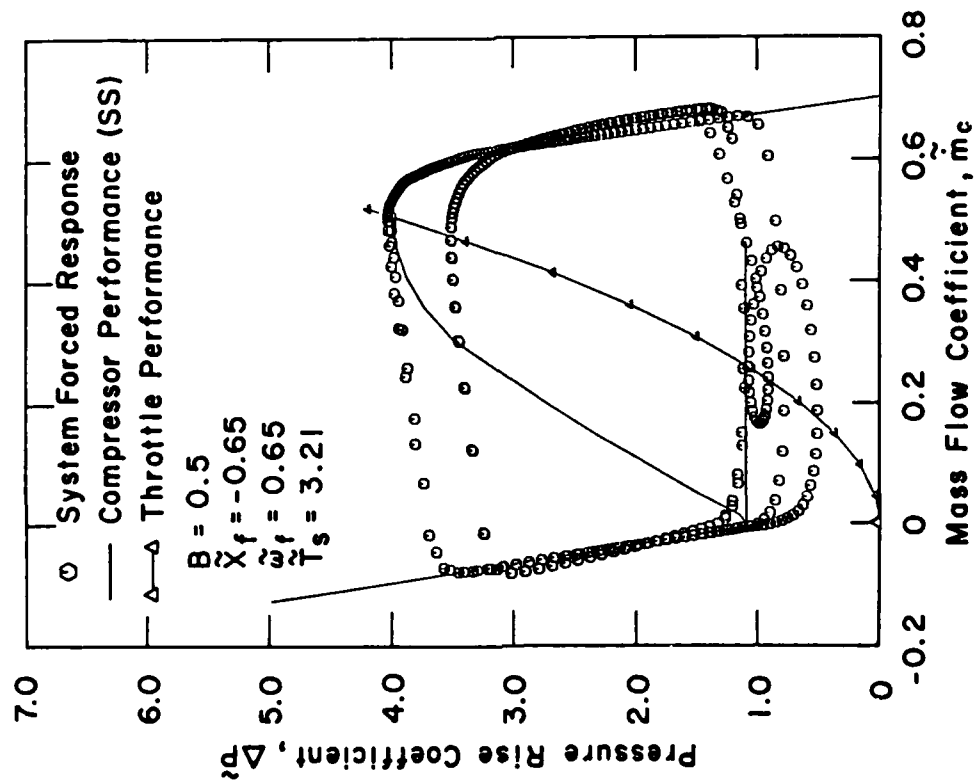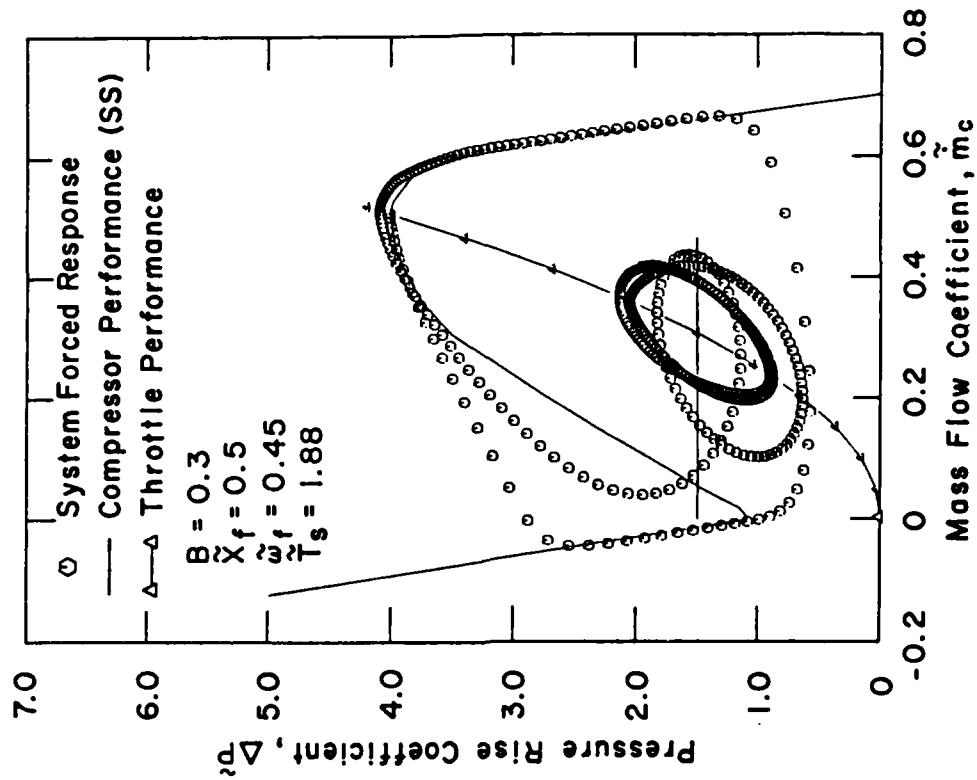
a) Modified Zero Mass Flow Regime Characteristic

b) Shifted Rotating Stall Characteristic

Figure 23   Off Baseline Transient Forced Response
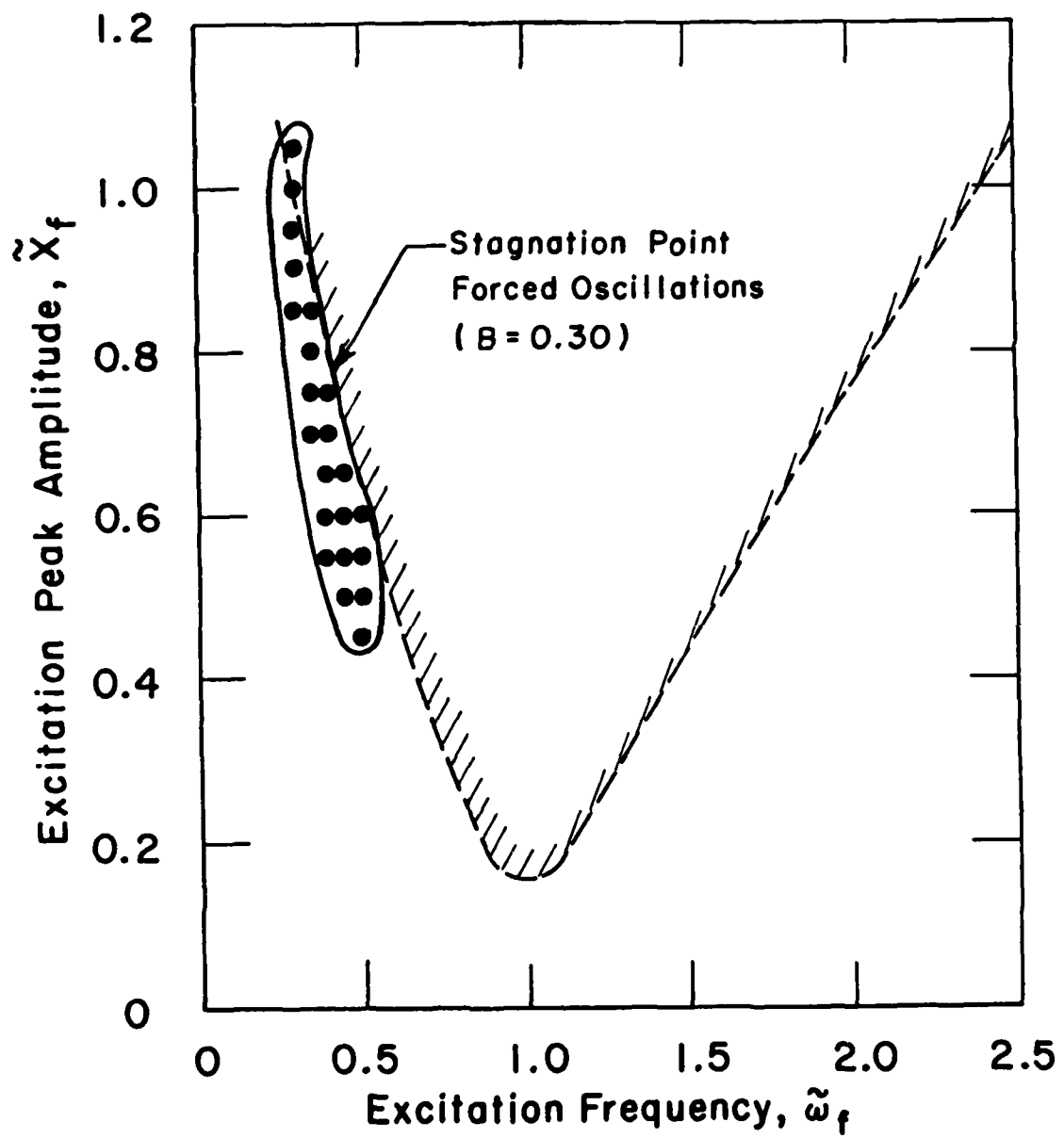
Figure 24   External Excitation Amplitude – Frequency Window
(Off-Baseline)
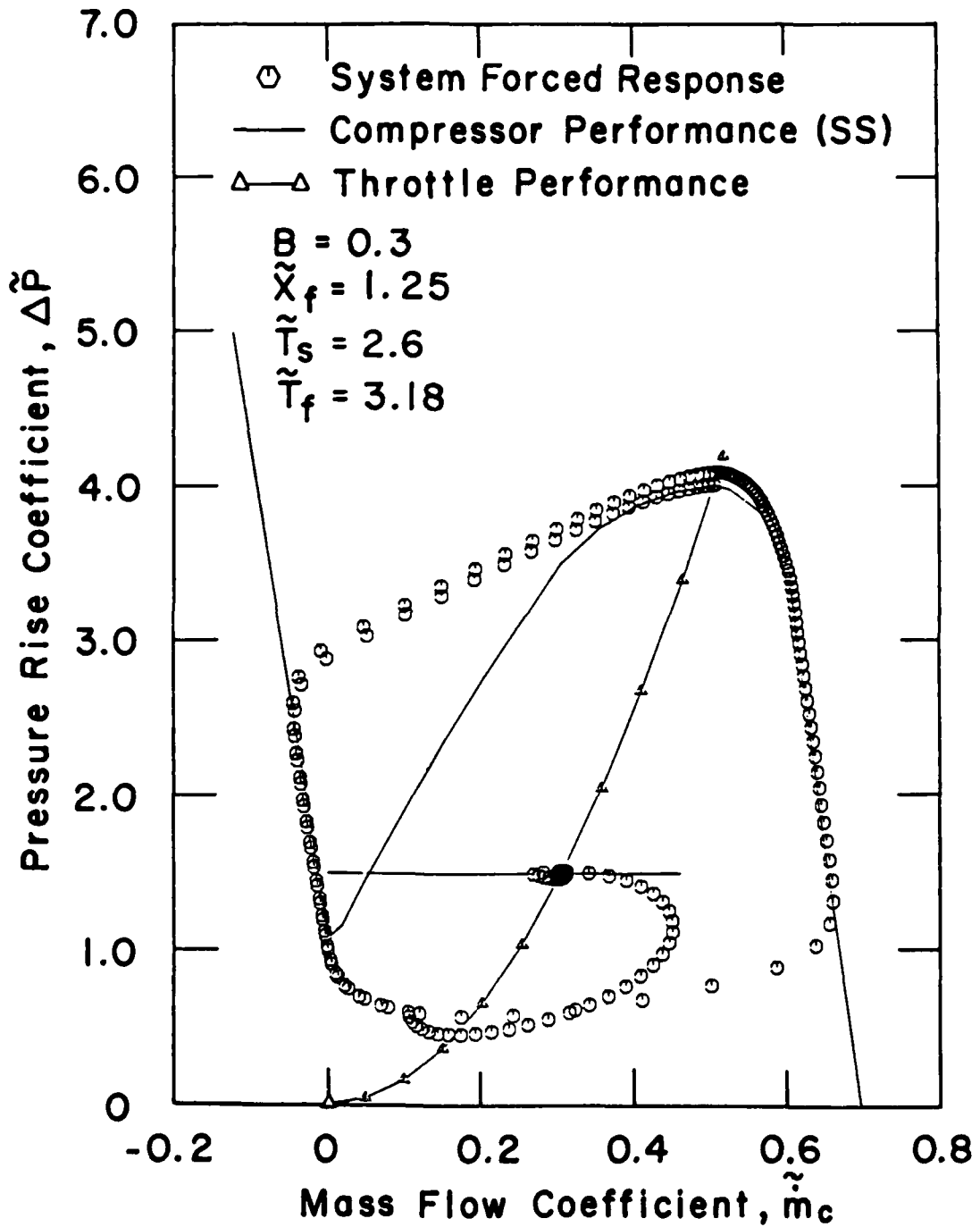
Figure 25   Off Baseline Transient Forced Response (Discrete Pulse)
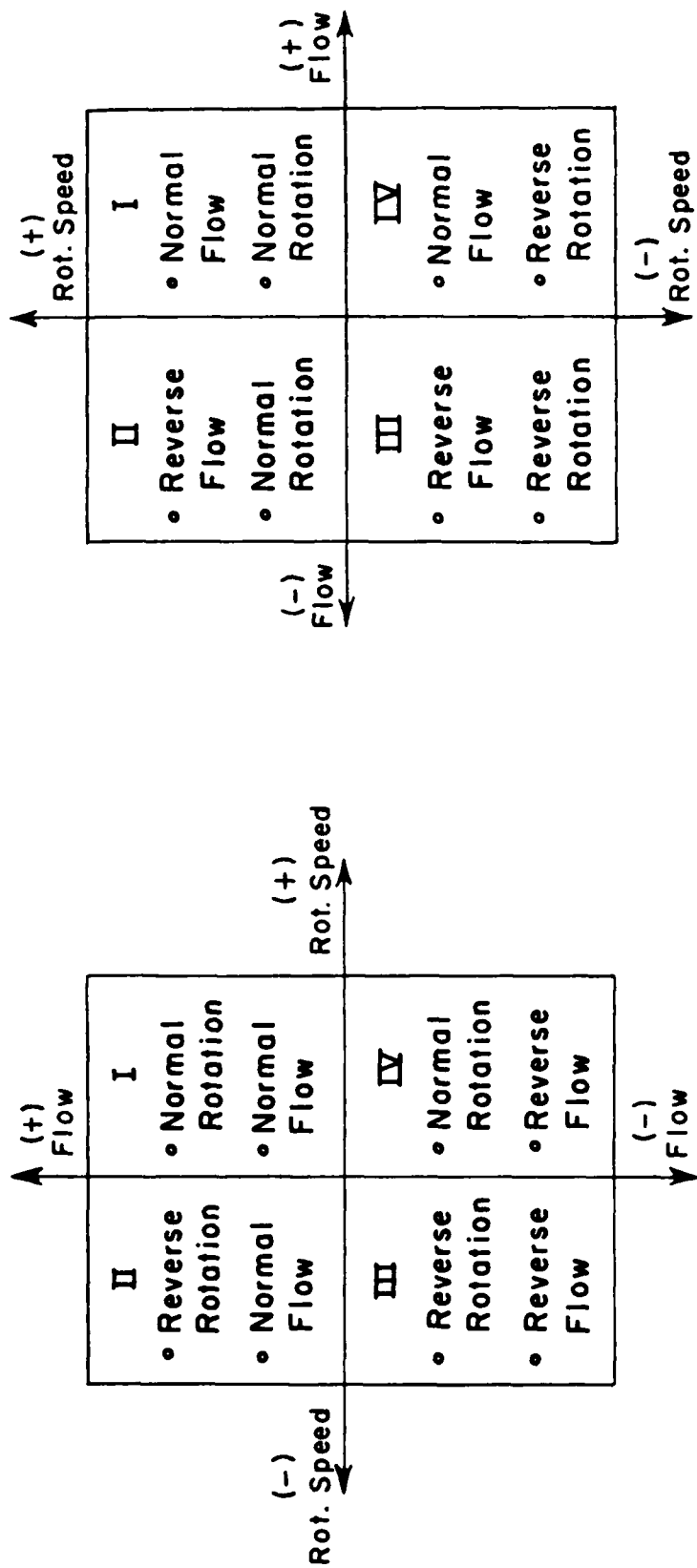
a) Karman-Knapp (1937)

b) Bammert-Zehner (1978)

Figure 26   Four Quadrant Performance Conventions
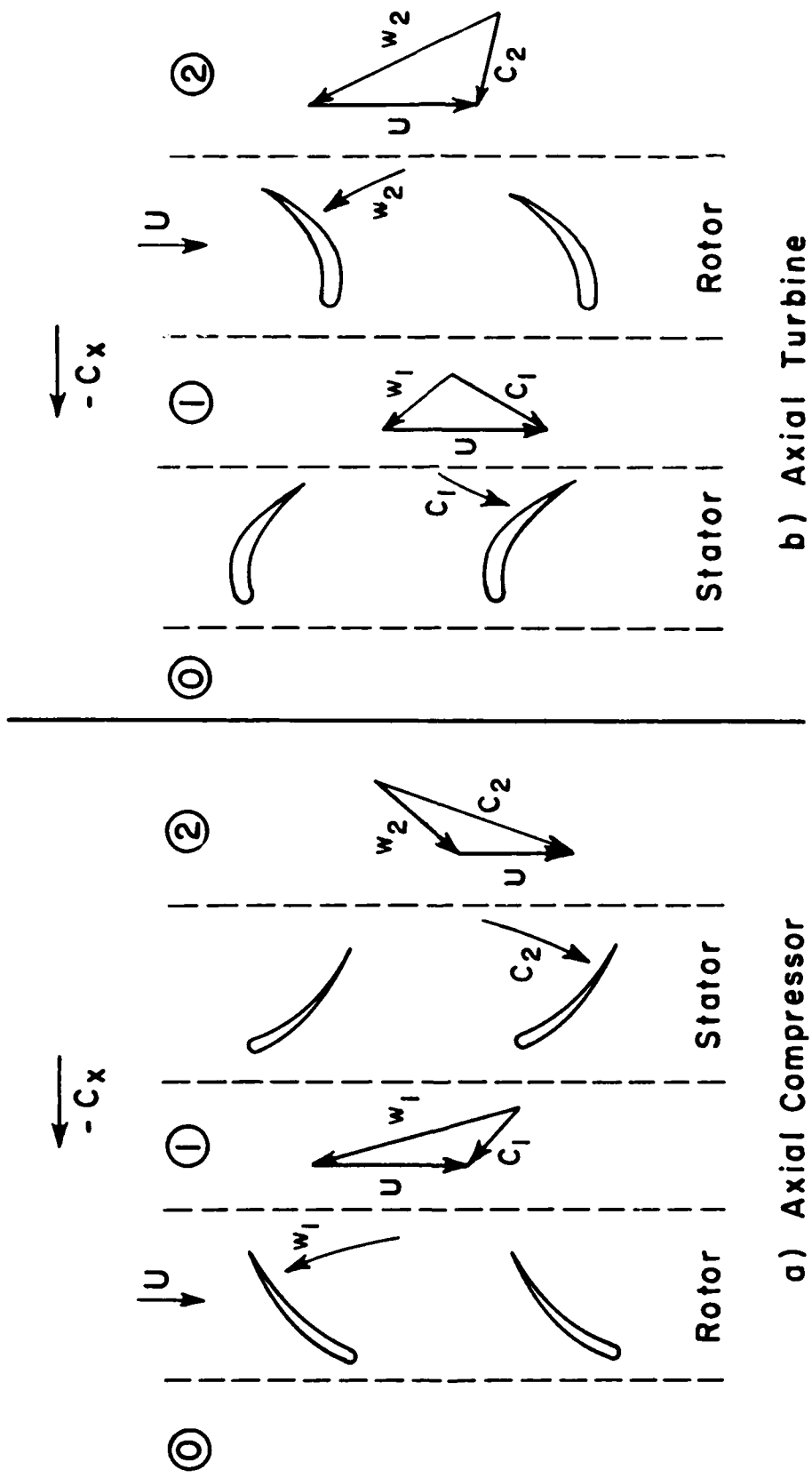
Figure 27   Conceptual Reverse Flow Velocity Diagrams

273

a) Cornell's 1954 Stalled Cascade [43]

b) Bammert And Zehner's 1974 Reverse Flow Turbine Cascade [35]

c) Koff's 1983 Reverse Flow Compressor Cascade [14]
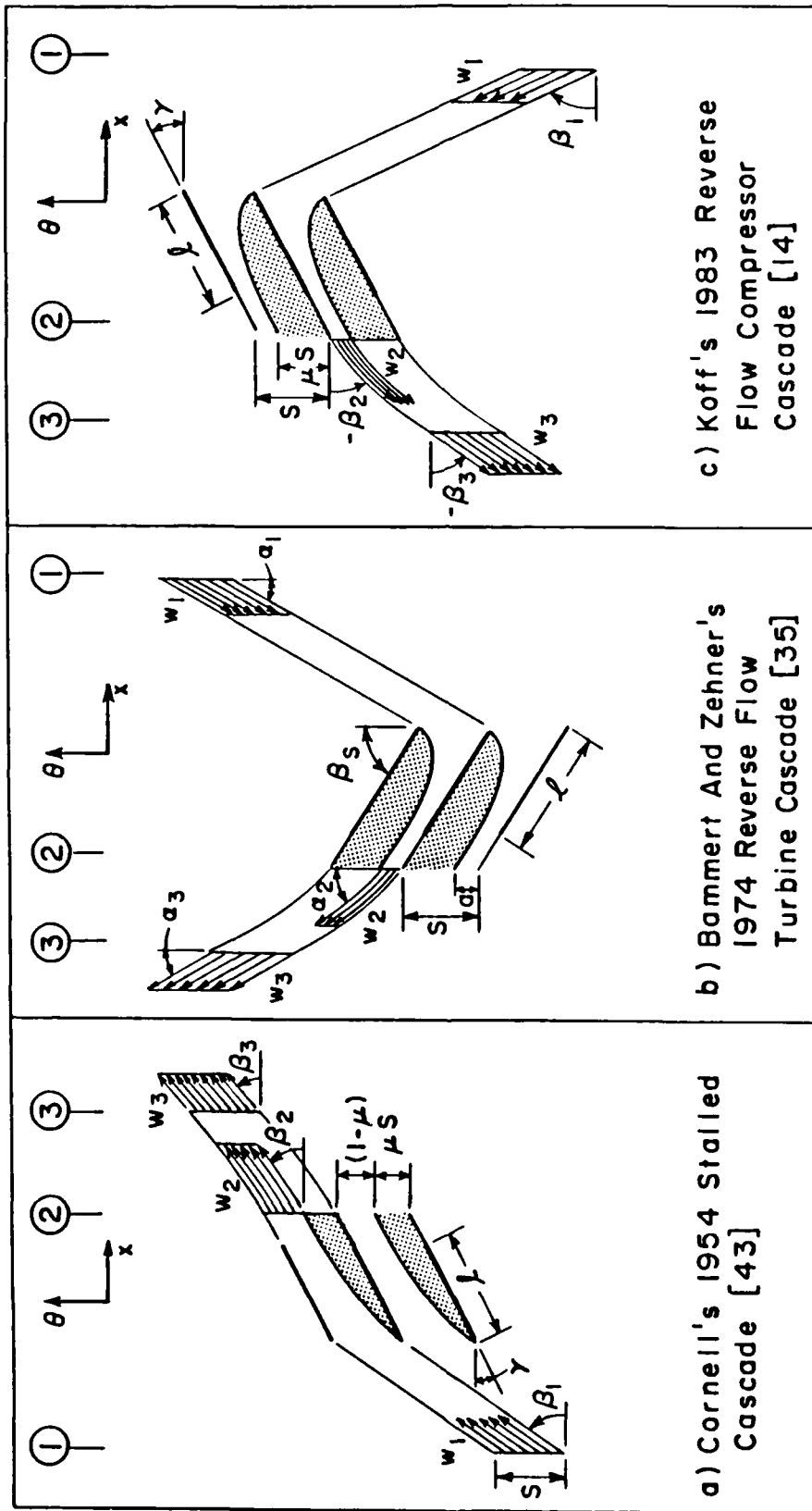
Figure 28   Cascade Loss Models
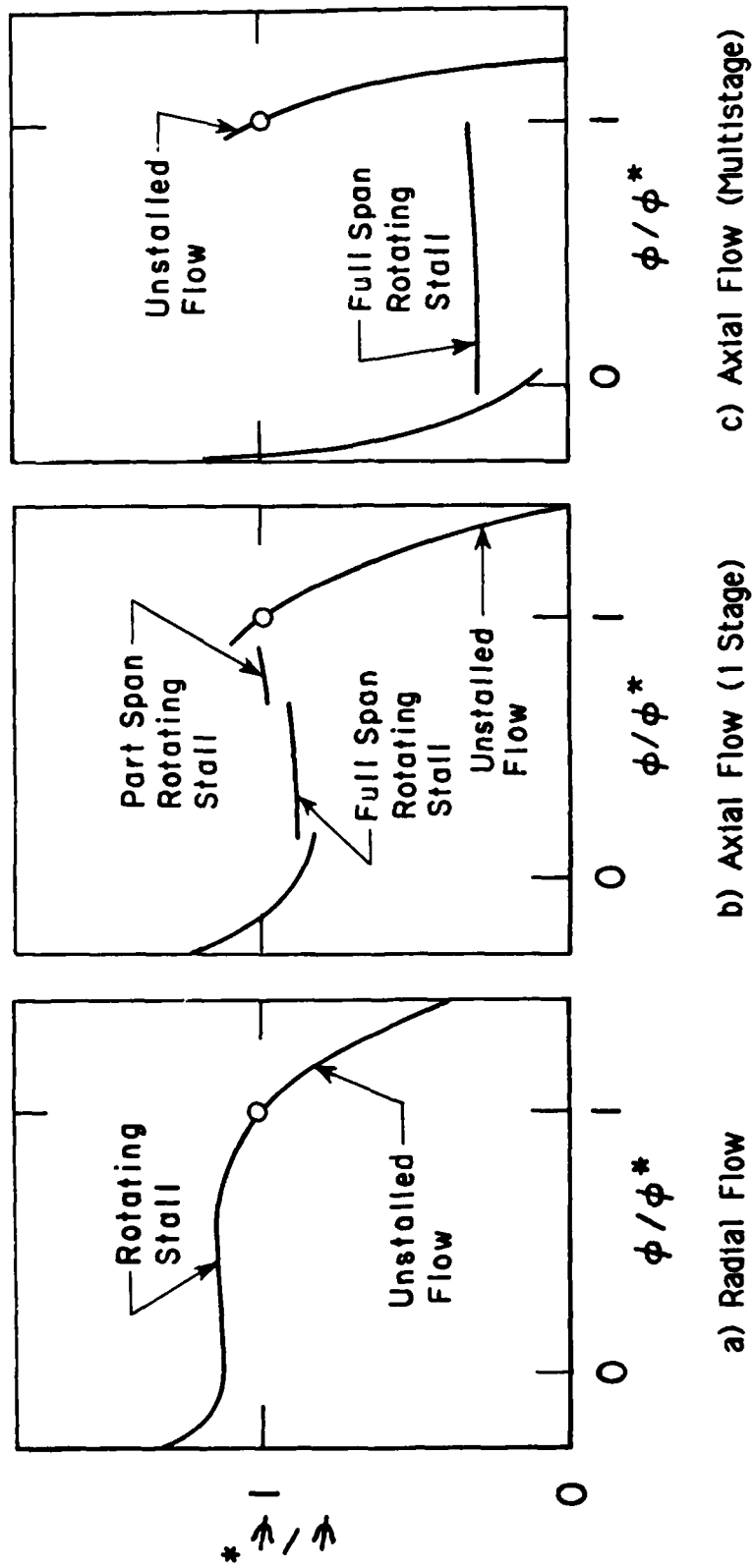
Figure 29   General Compressor Performance Trend

275
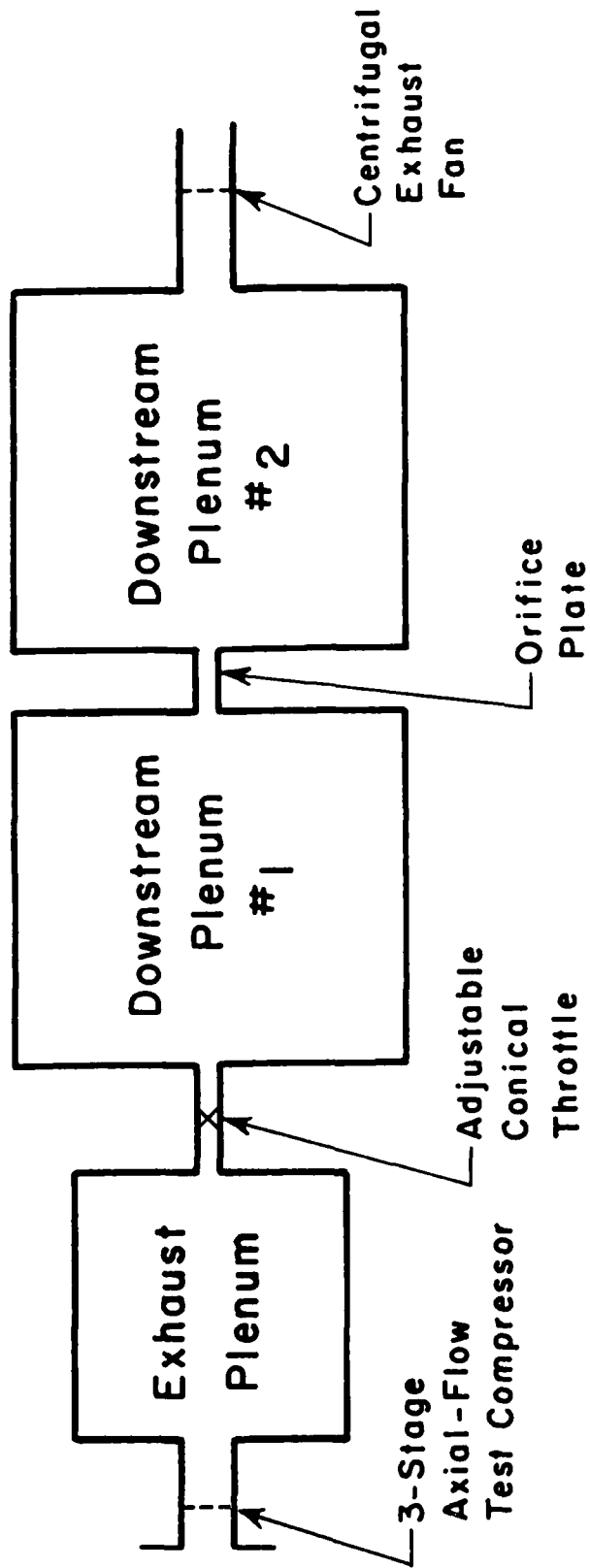
Figure 30   Test Facility Compression System Schematic
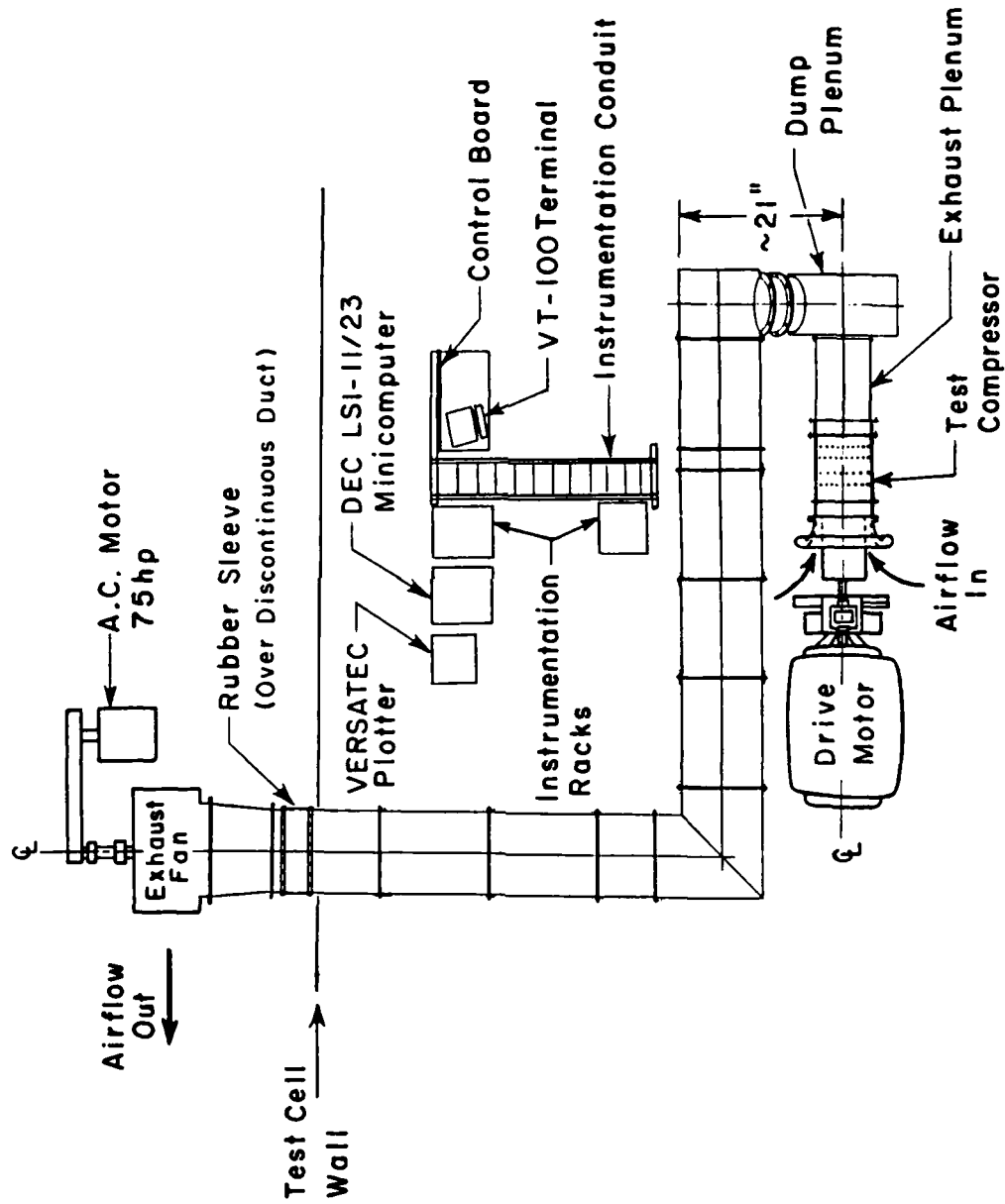
Figure 31   Overhead Planform Schematic of Test Facility

277
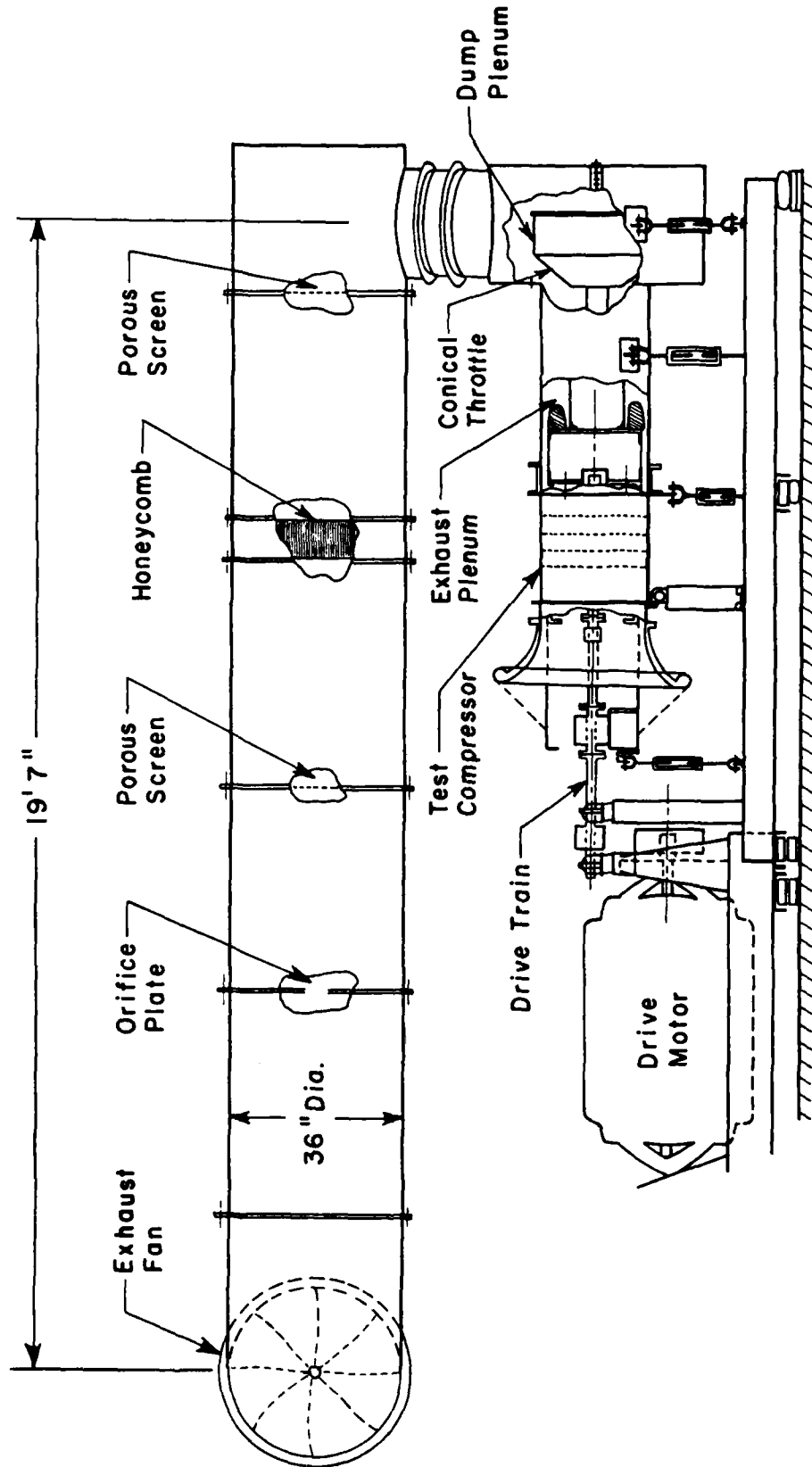
Figure 32   Side View Schematic of Test Facility
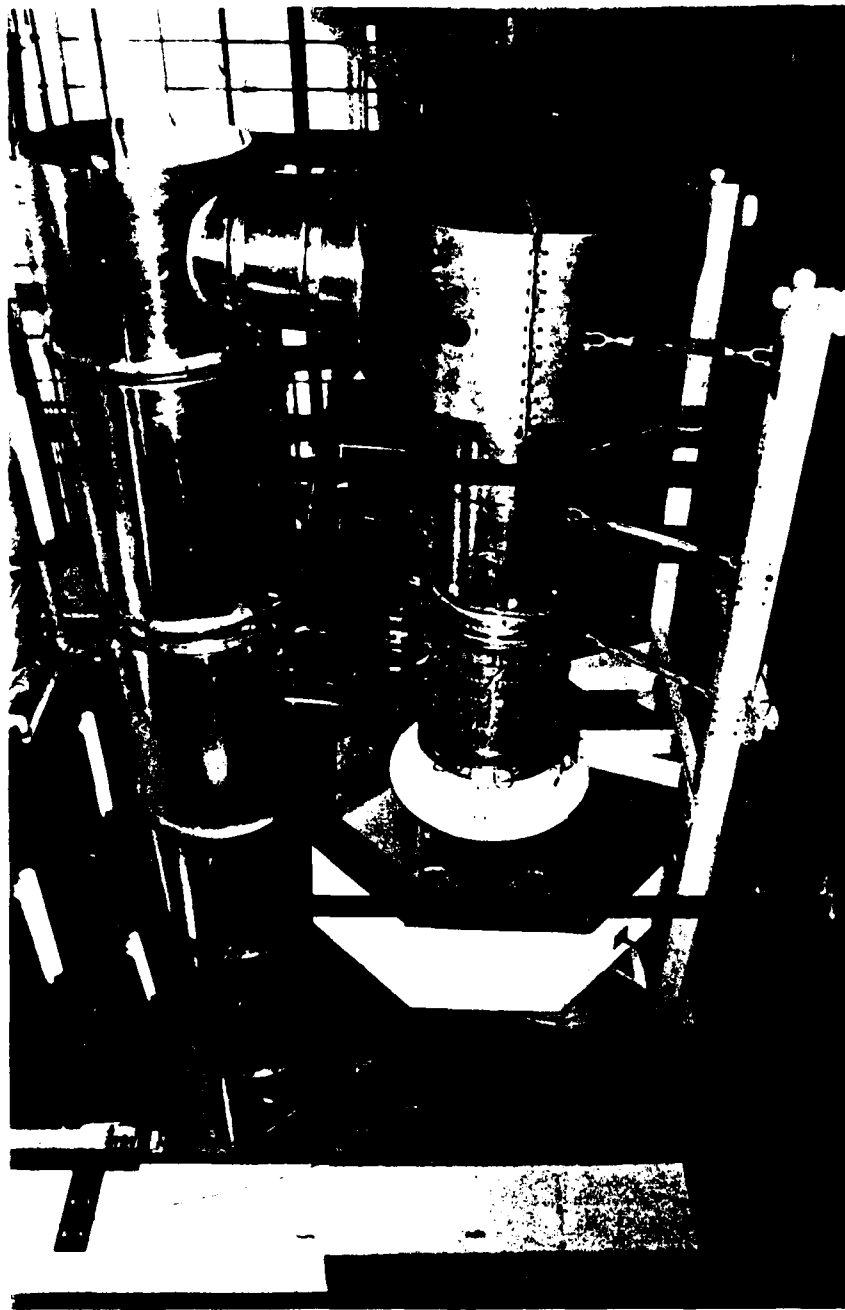
Figure 33   Photograph of MIT 3-Stage Axial Compressor Test Facility
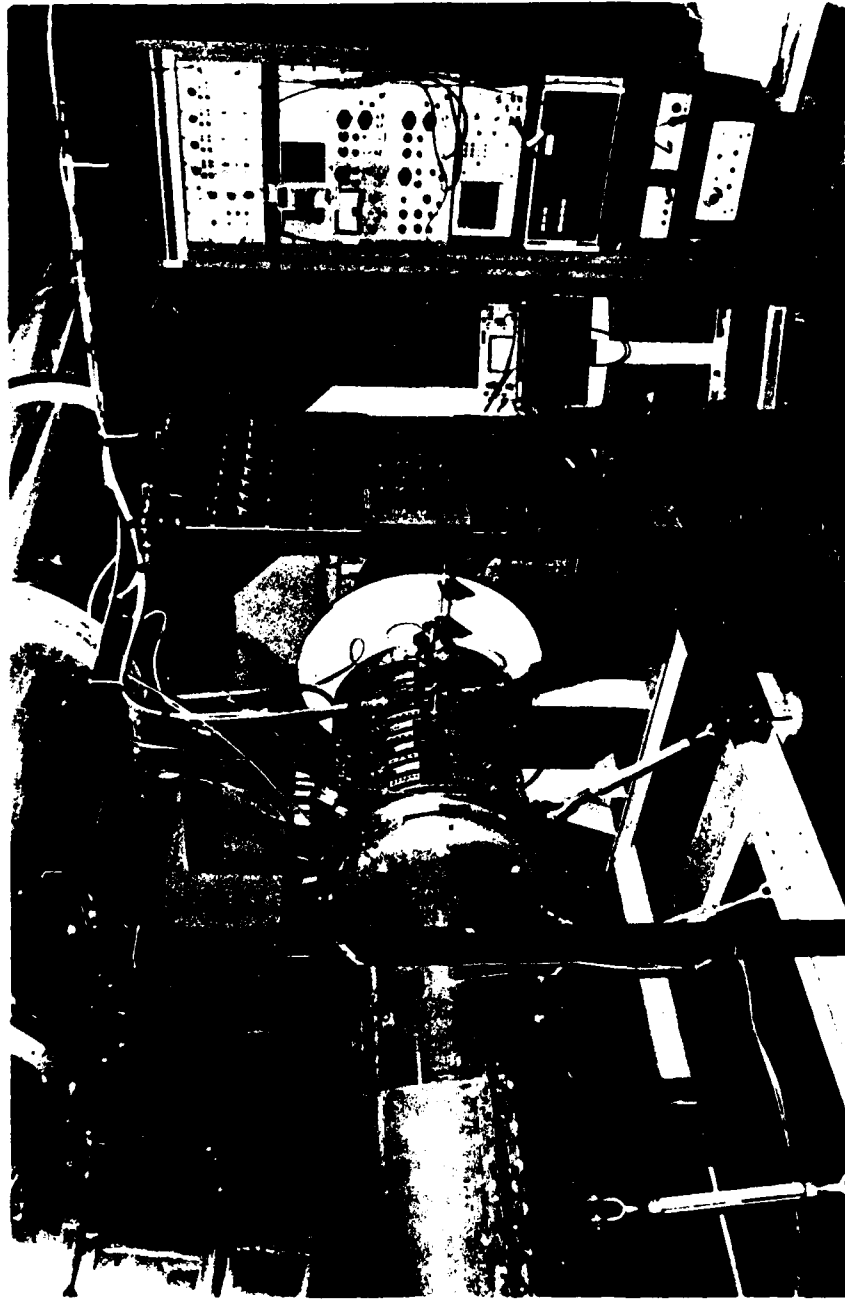
Figure 34   Photograph of Facility Data Acquisition Hardware
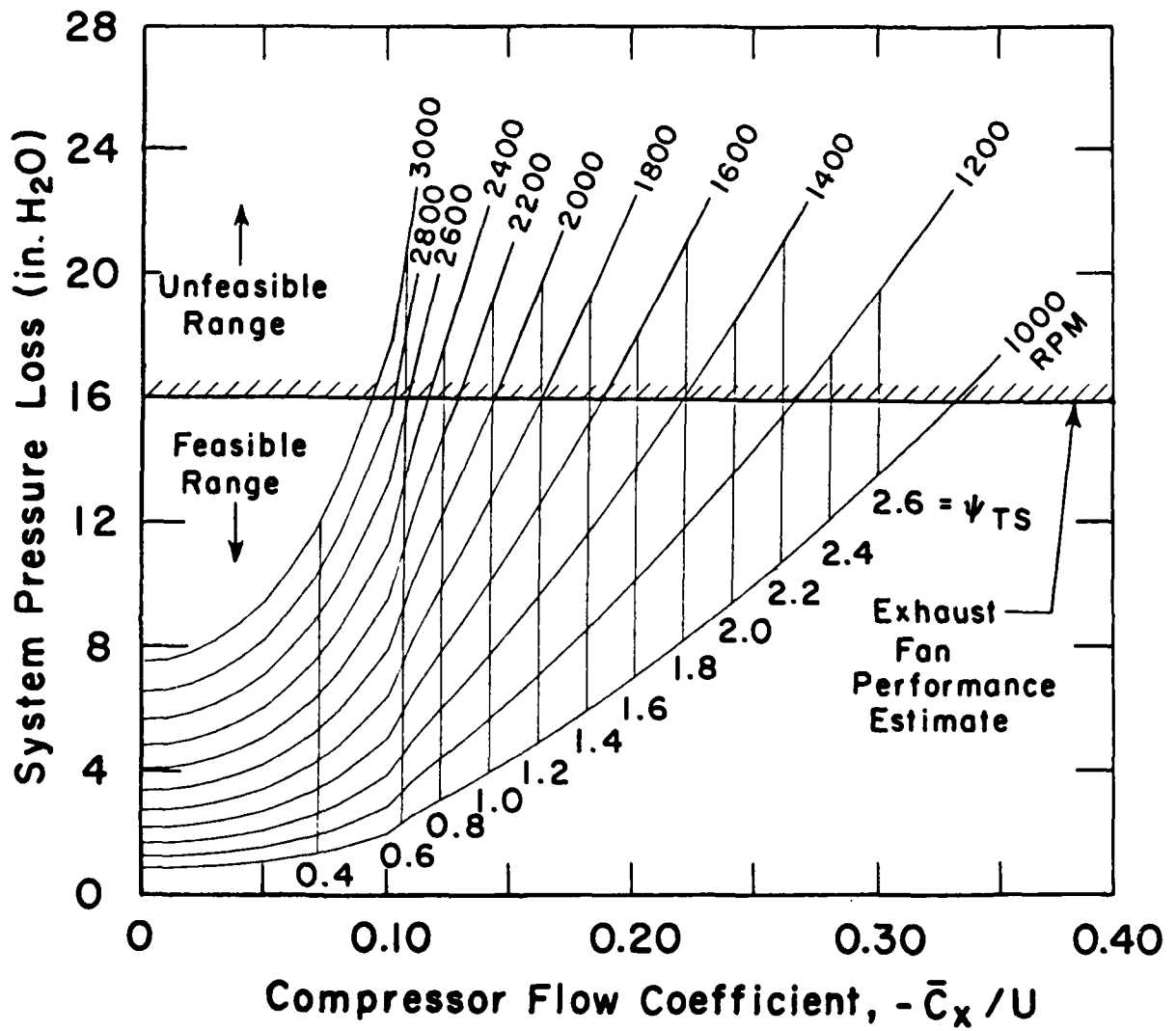
Figure 35   System Pressure Loss Summary
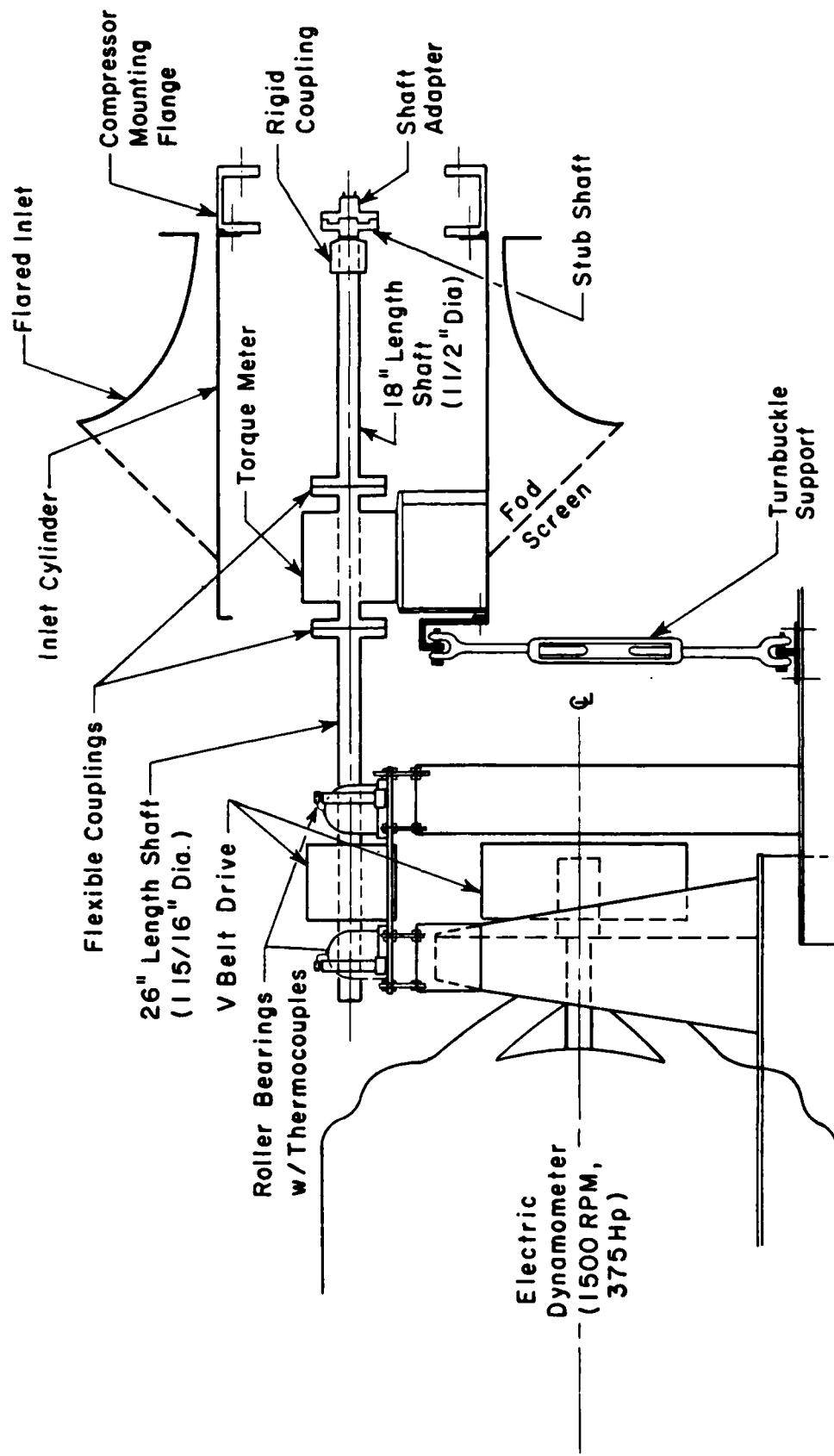
Figure 36   Compressor Drive Train

282
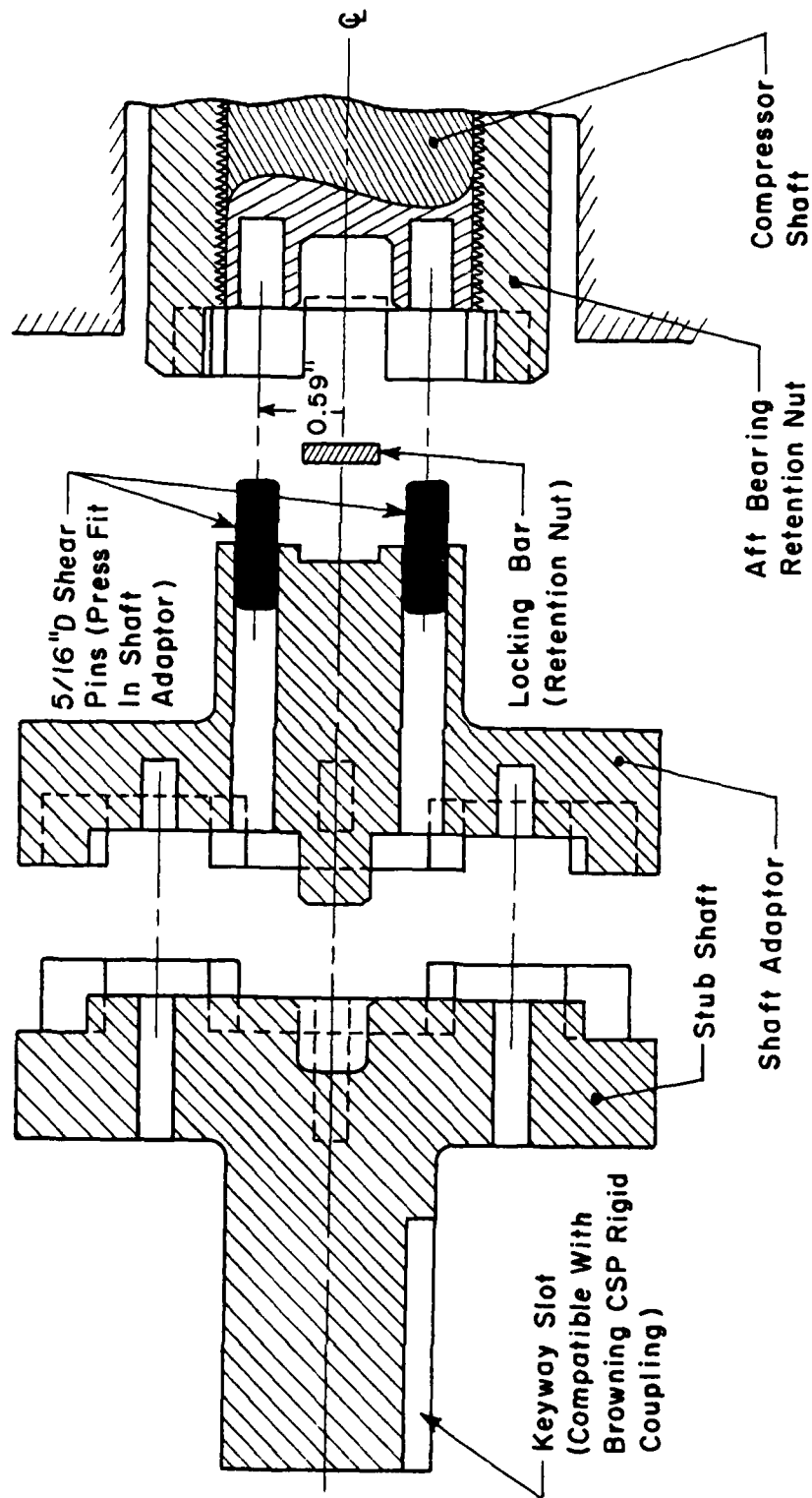
Figure 37   Drive Shaft-Compressor Aft End Rotor Connections

Compressor
Shaft

Aft Bearing
Retention Nut

5/16"D Shear
Pins (Press Fit
In Shaft
Adaptor)

Locking Bar
(Retention Nut)

Stub Shaft

Shaft Adaptor

Keyway Slot
(Compatible With
Browning CSP Rigid
Coupling)

0.59"

283
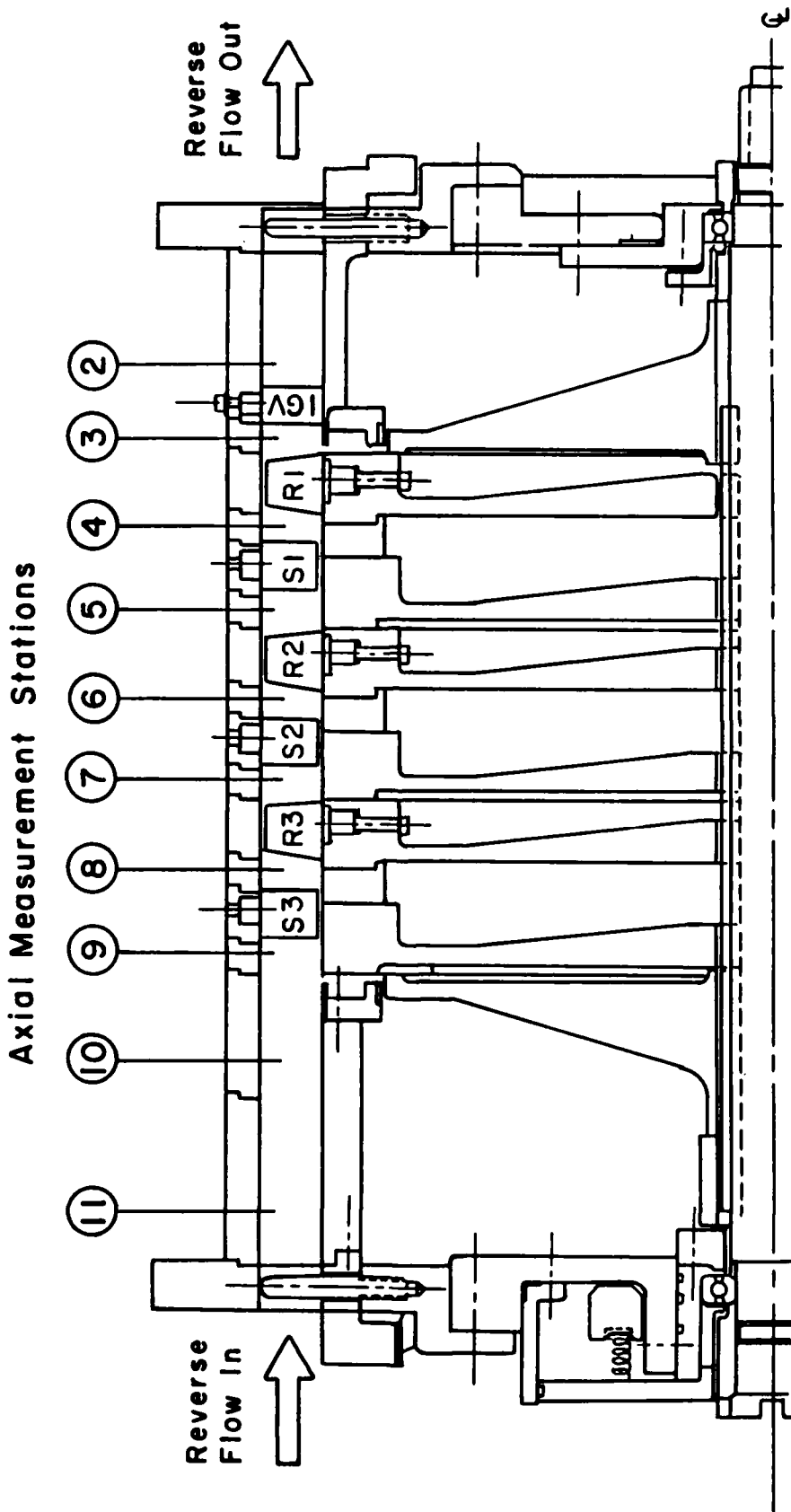
Figure 38 MIT 3-Stage Axial Compressor

284
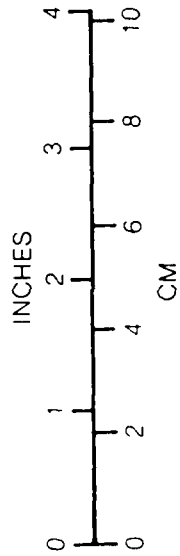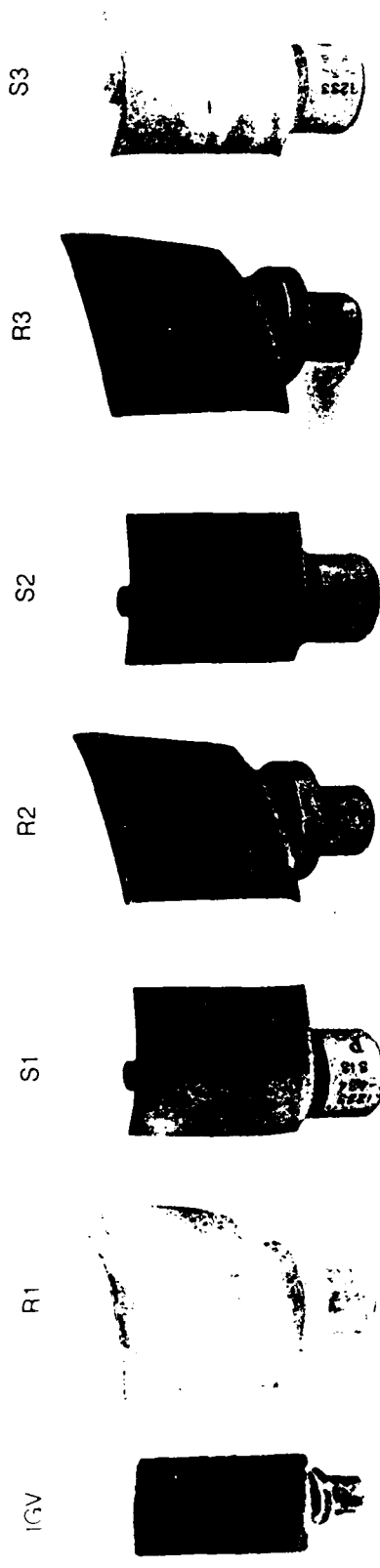
Figure 39   Compressor Blading

K_{LE} - Loading Edge Blade Angle

K_{TE} - Trailing Edge Blade Angle

γ - Stagger Angle

IGV

Rotor

Stator

Direction Of Rotation

Leading Edge Tangent

Mean Camber

Chord K_{LE} Line

Trailing Edge Tangent

Axial Direction
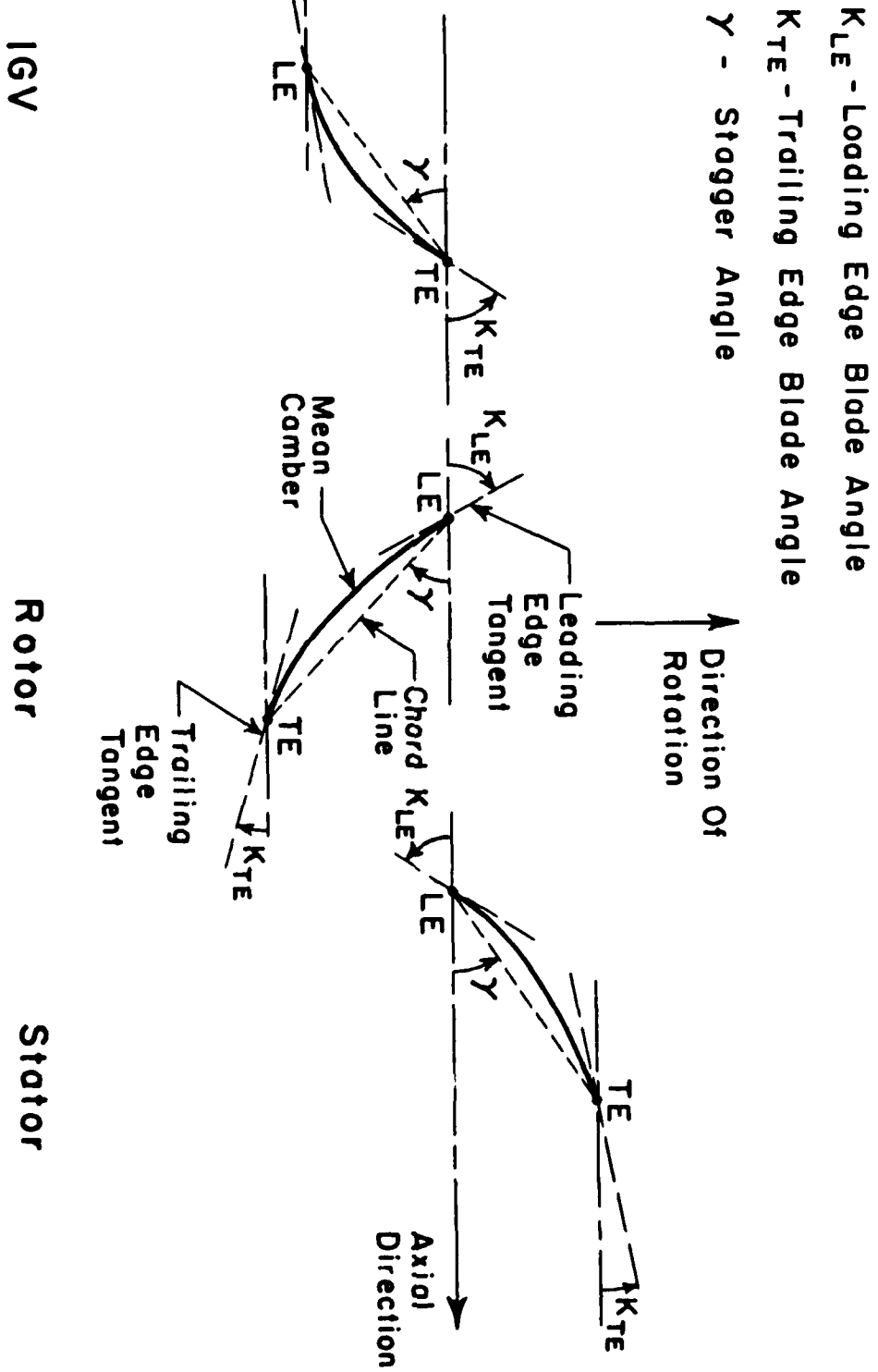
Figure 40   Blade Angle Definitions
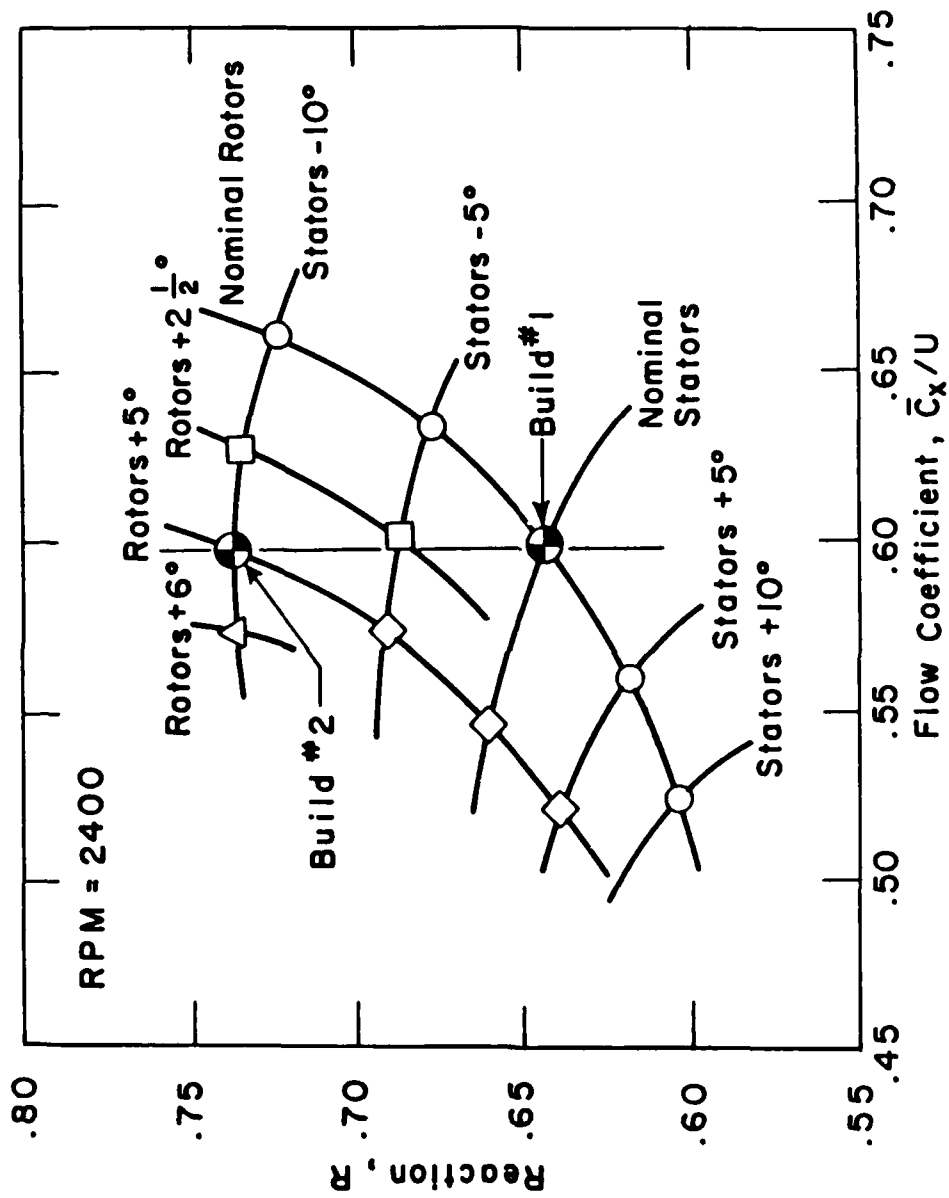
Figure 41 Reaction vs. Design Flow Coefficient Parametric Results
(Lewis [52])
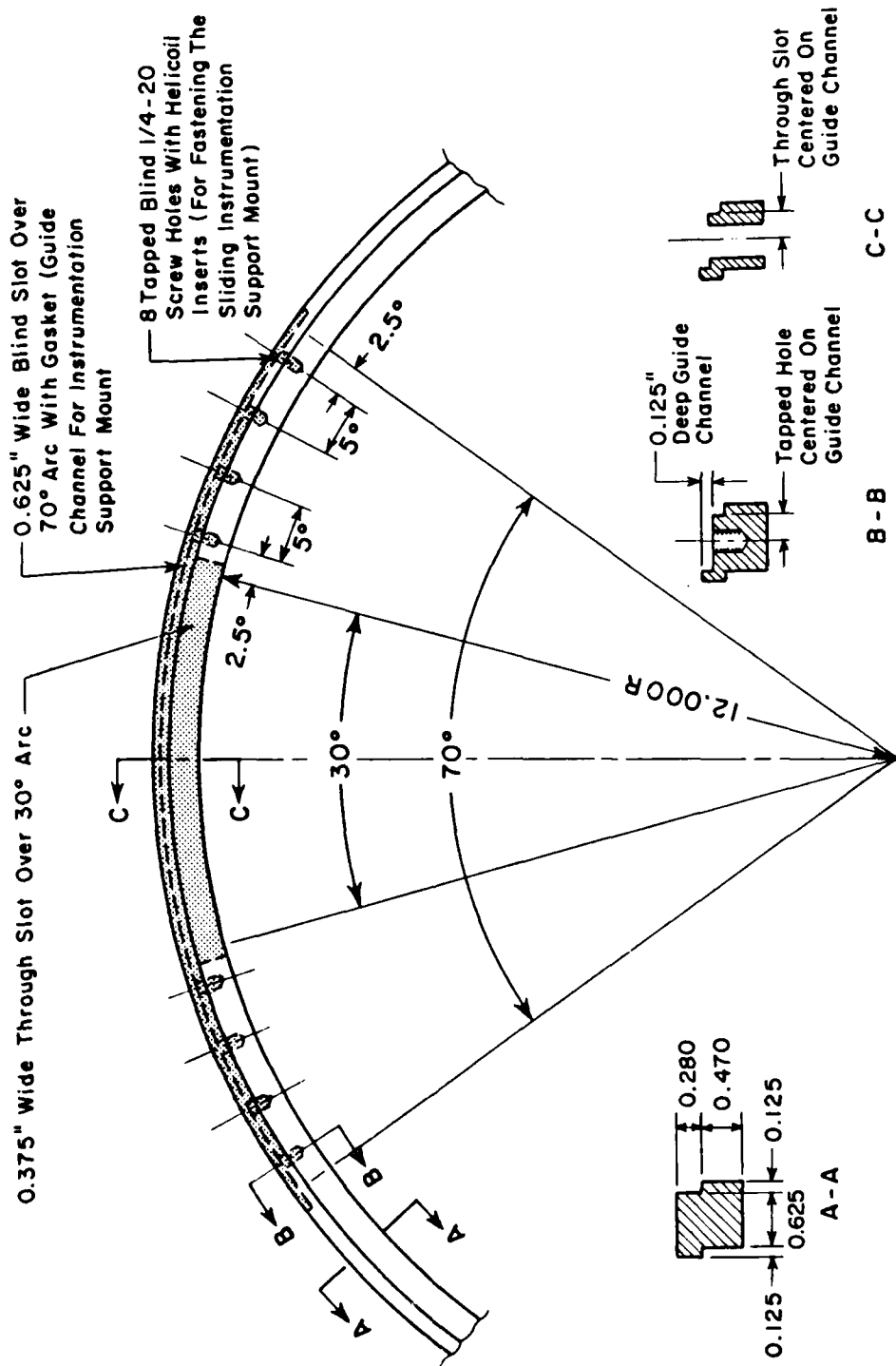
Figure 42   Case Spacer Ring Instrumentation Slot

288

Instrumentation Port (Accomodates Probe Diameters Up To 0.312")

2 Receptacles For Alignment Pins

2 Tapped Blind 1/4-20 Screw Holes (For Fastening Probe Traversing Mechanism)

2.5°

5°

12.000 R

60°

20°

0.625

Sliding Contact Surface

0.625   0.625

0.375

B - B

Centered Through Slot Over 5° Arc (For Continuous Range Of Position Locations)

0.375"

A A
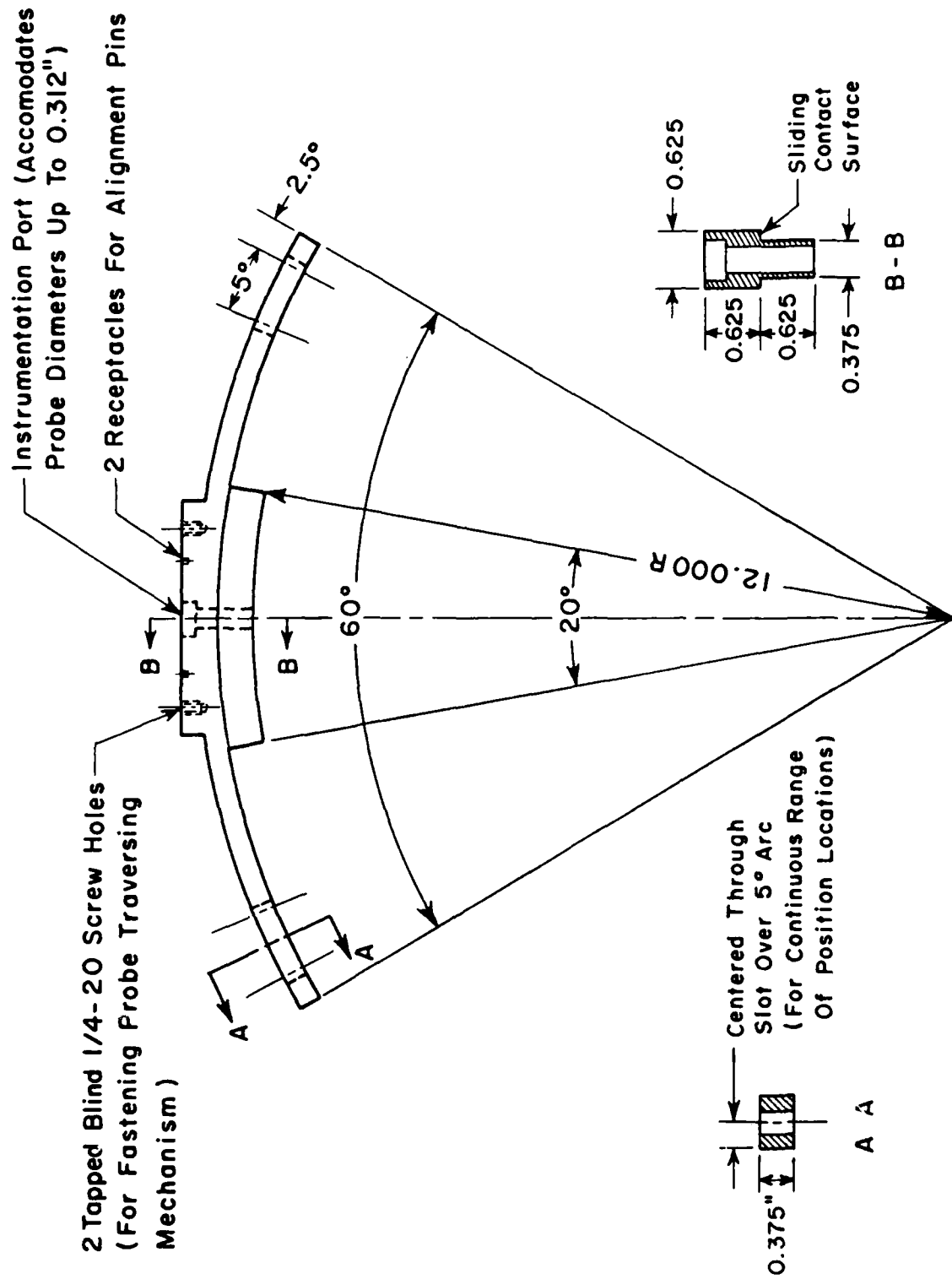
Figure 43   Instrumentation Support Mount

THROTTLE ASSEMBLY

COMPRESSOR
CONNECTION ASSEMBLY

Drive System Enclosure

D.C. Drive Motor

Microswitch (Fully Open Limit)

Throttle Ring Seal w/Gasket

Dump Plenum

Flat Plate Ring Seal w/Gasket
(Reinforcement Split Ring On
Outside Of Dump Plenum Wall)

Power Screw

Microswitch (Fully Closed Limit)

Throttle Centerbody

Conical Throttle

Centerbody Support Struts

Torridal Inlet (2:1 Ellipse)

Compressor Shaft Protective Cover

Exhaust Plenum

Case Flange
(Instrumentation Axial Station #1)

Figure 44   Exhaust Plenum and Conical Throttle Assembly
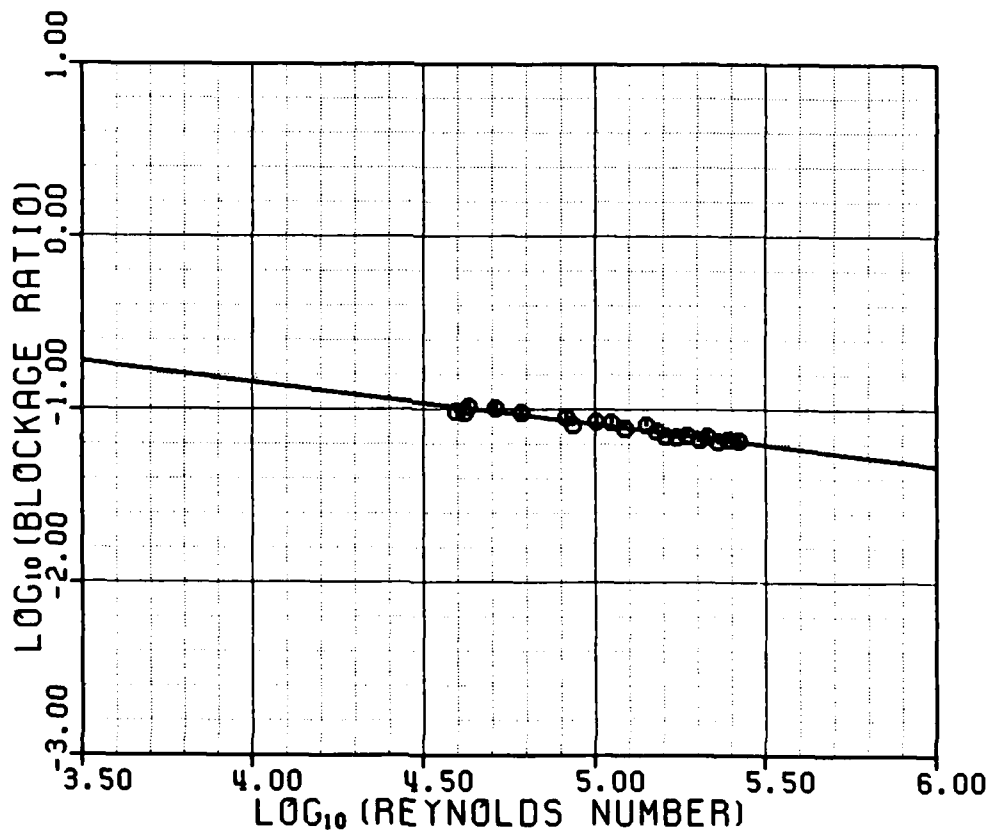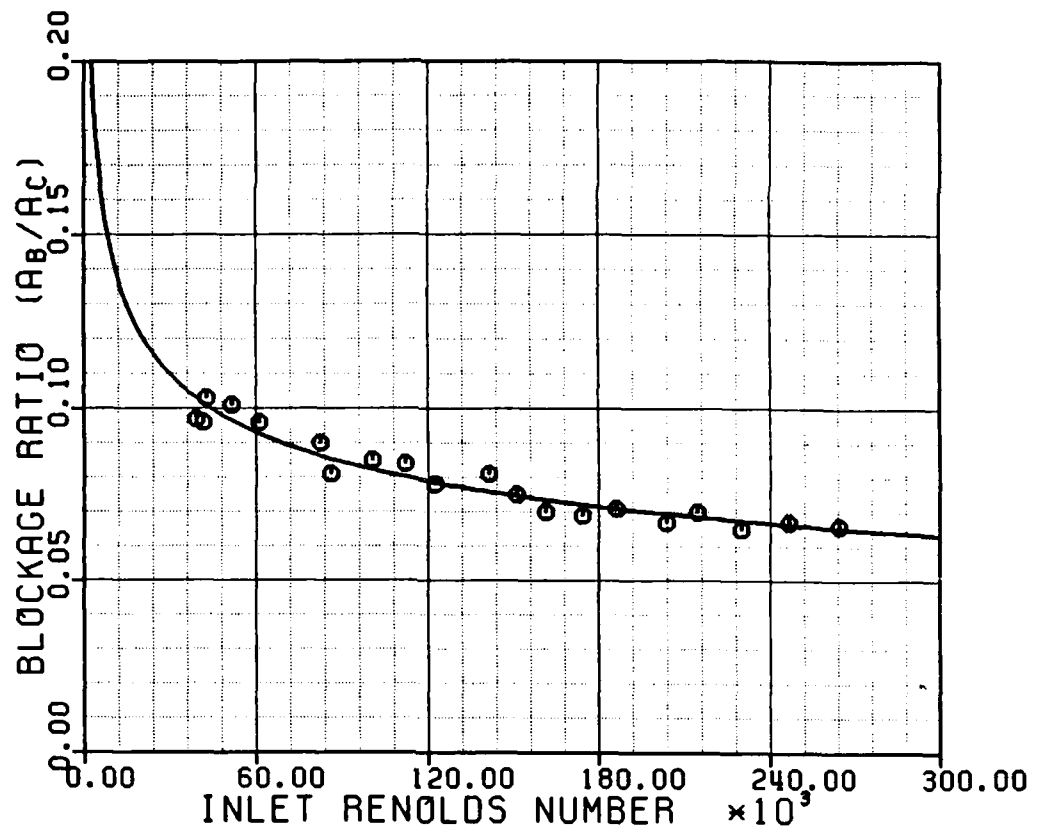
Figure 45   Inlet Mass Flow Calibration
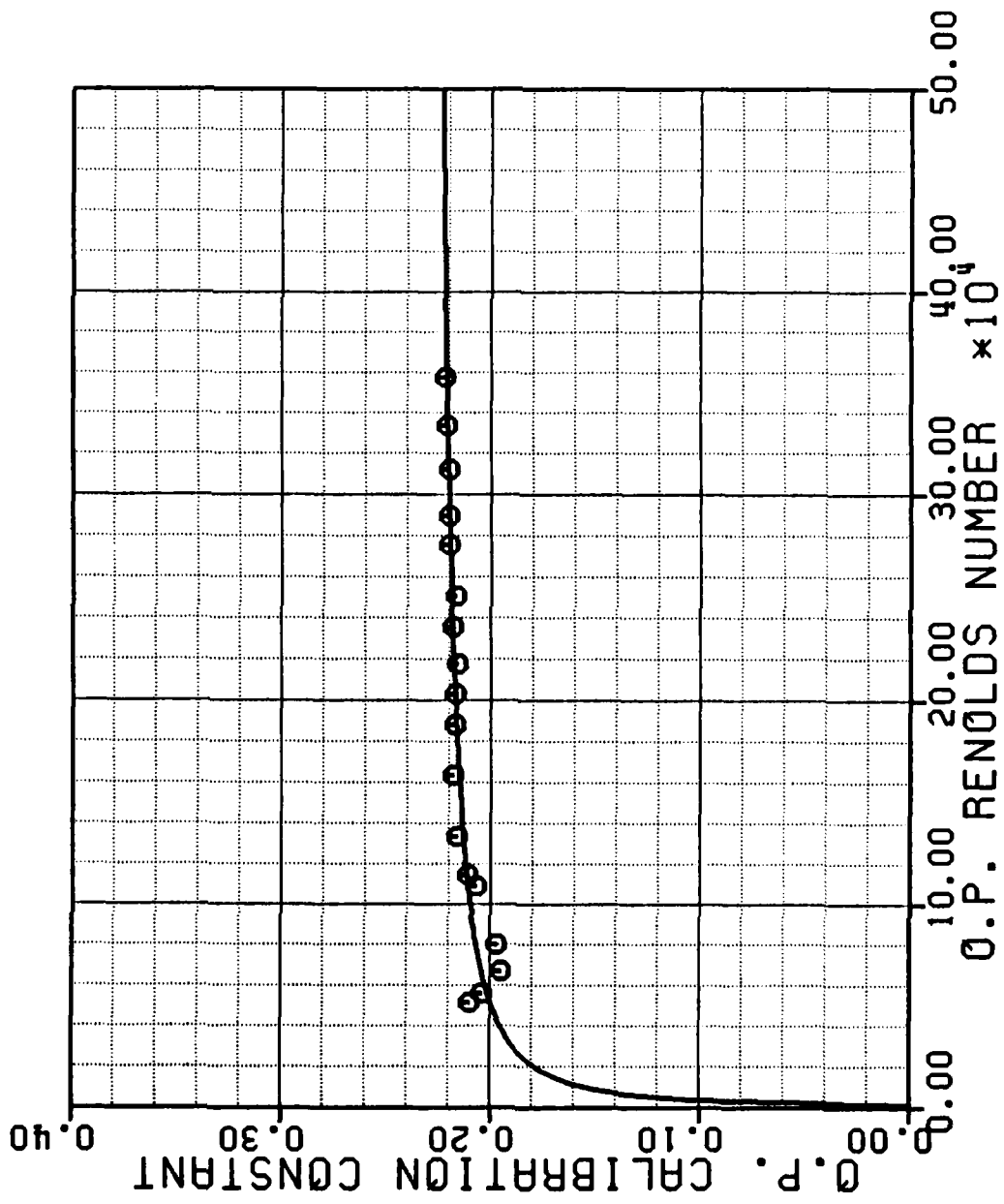
Figure 46 Orifice Plate Mass Flow Calibration
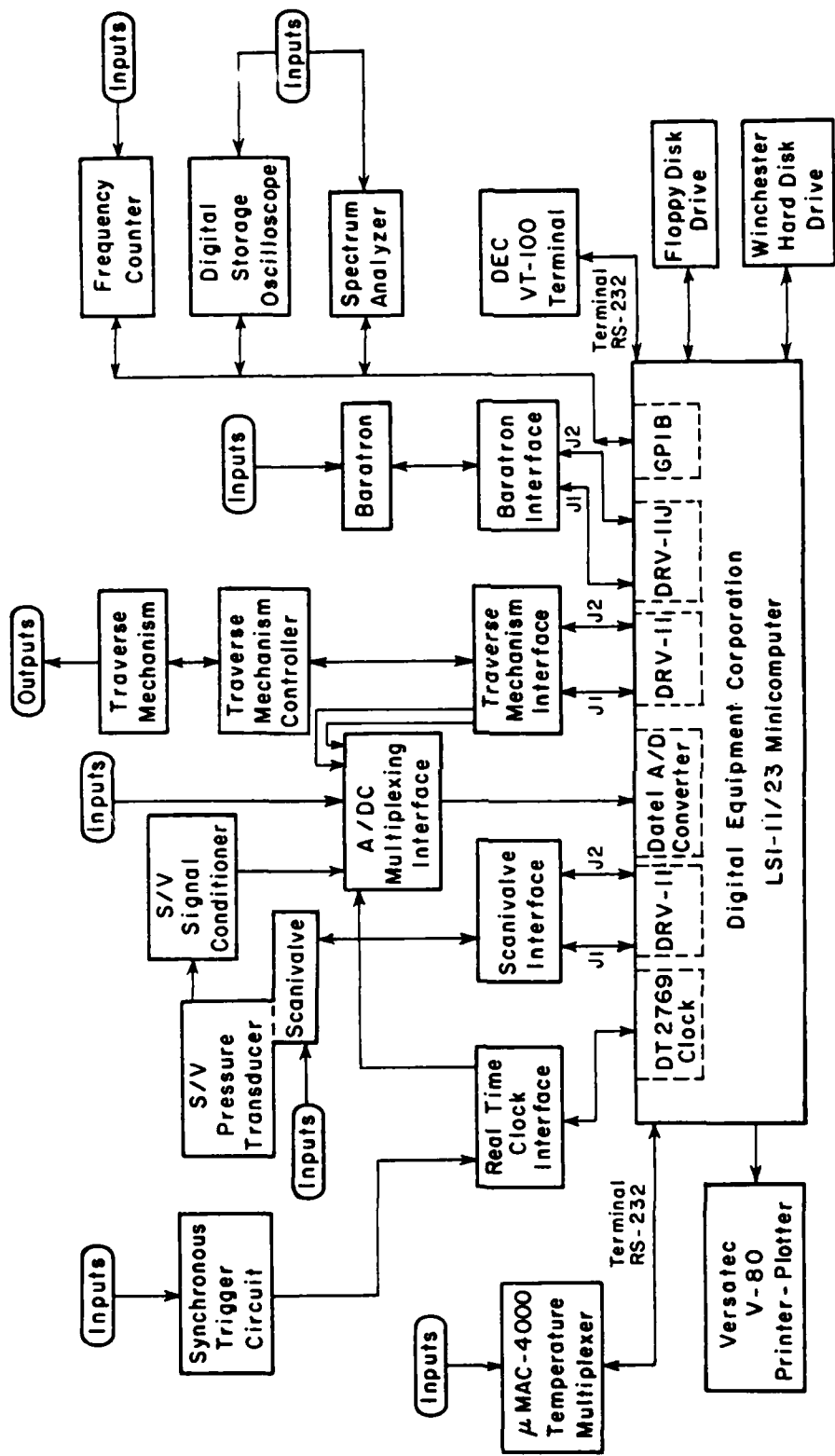
Figure 47 Test Facility Data Acquisition System

293
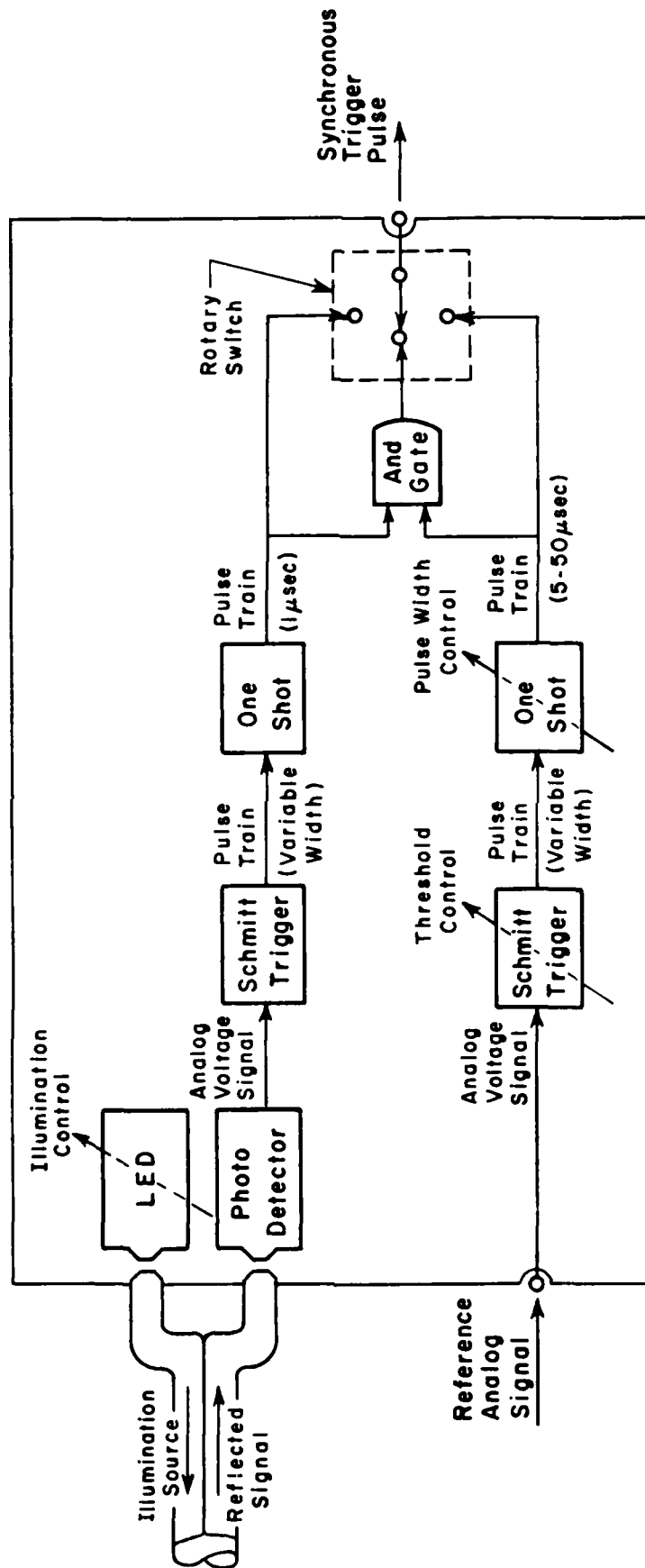
Figure 48 Synchronous Trigger Circuit Schematic

294
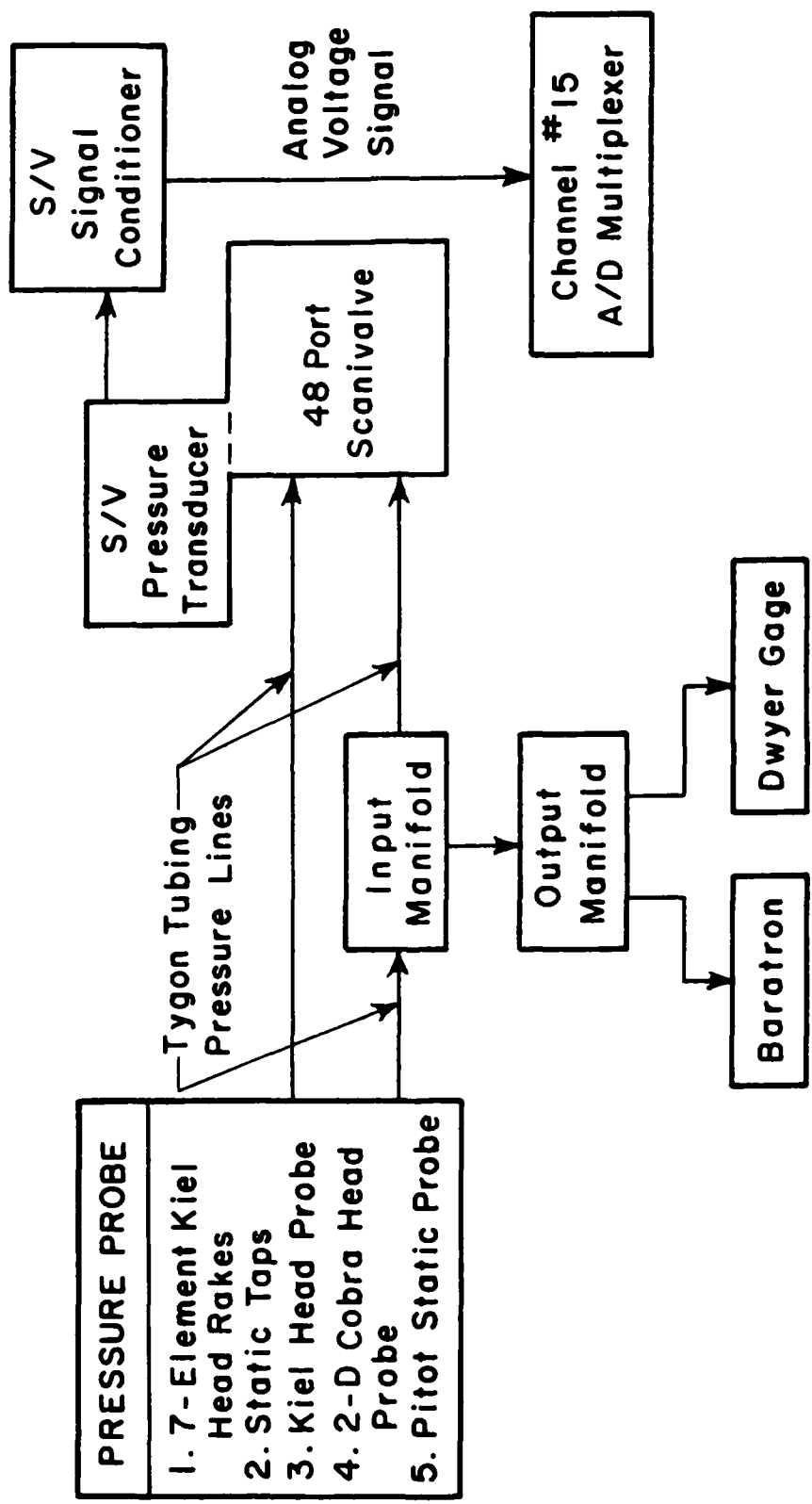
Figure 49   Time Average Pressure Data Acquisition Schematic
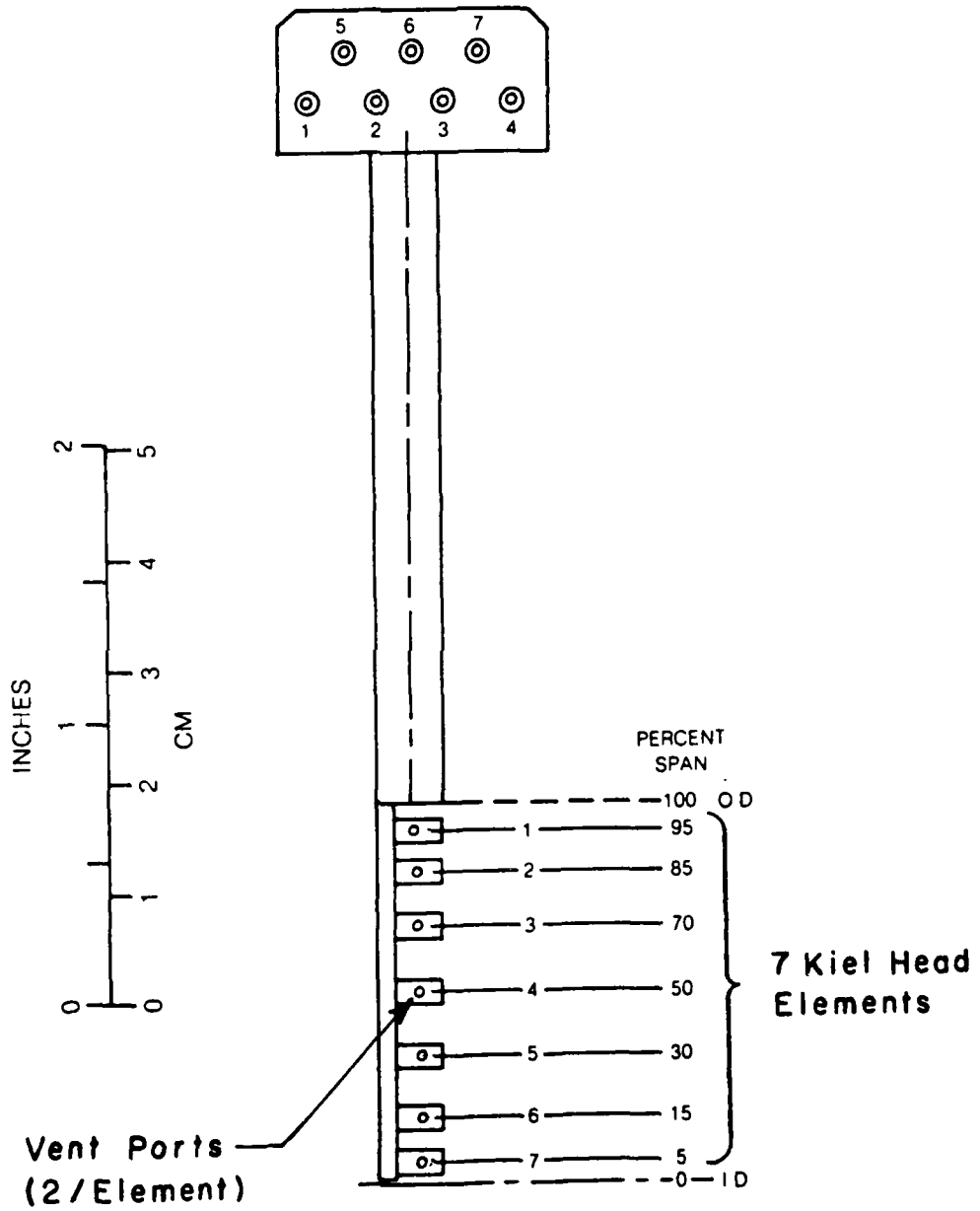
Figure 50   Total Pressure Rake
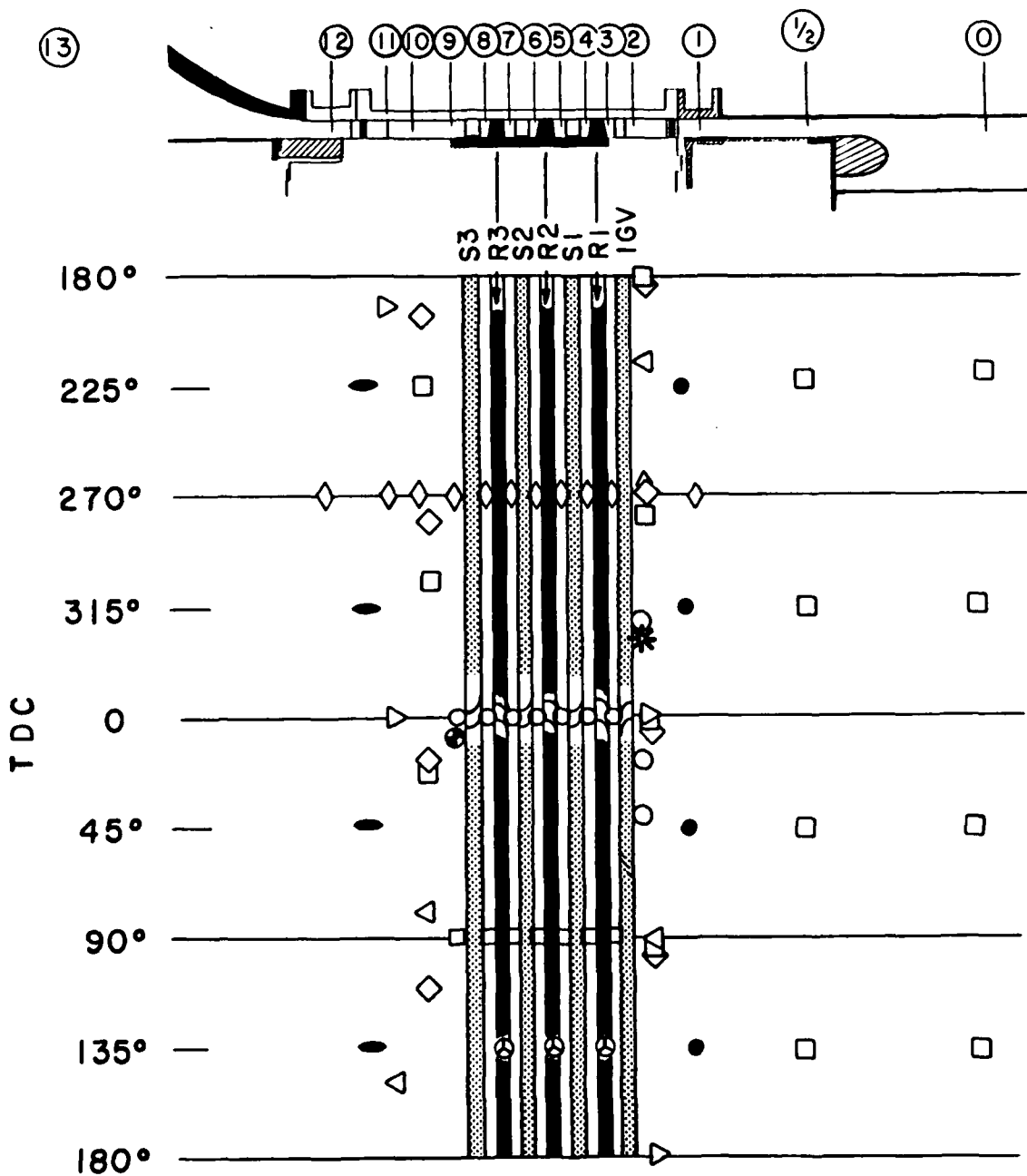
Figure 51   Compressor Instrumentation Locations

297
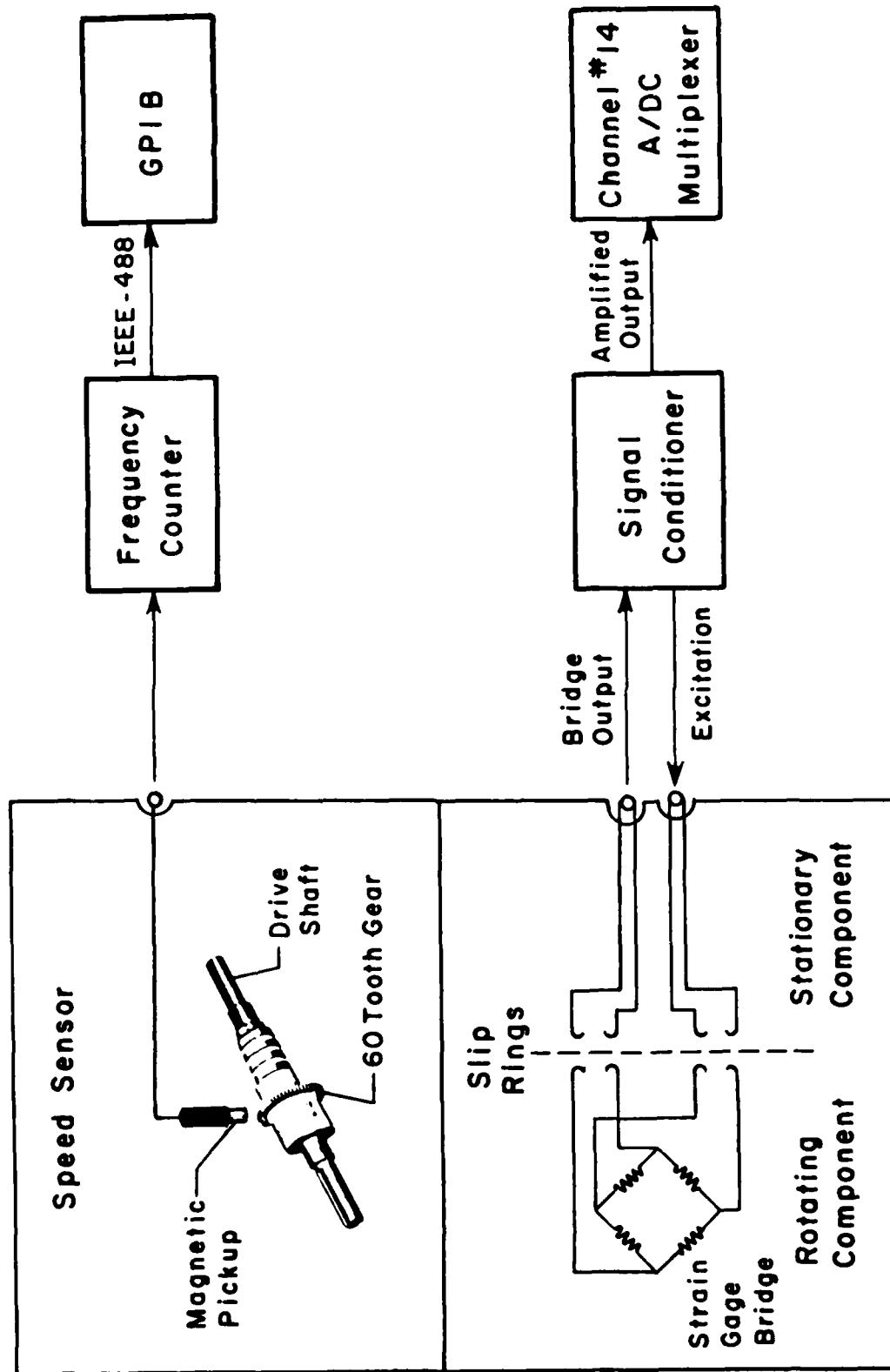
Figure 52   Torque and Shaft Rotational Speed Data Acqusition Schematic
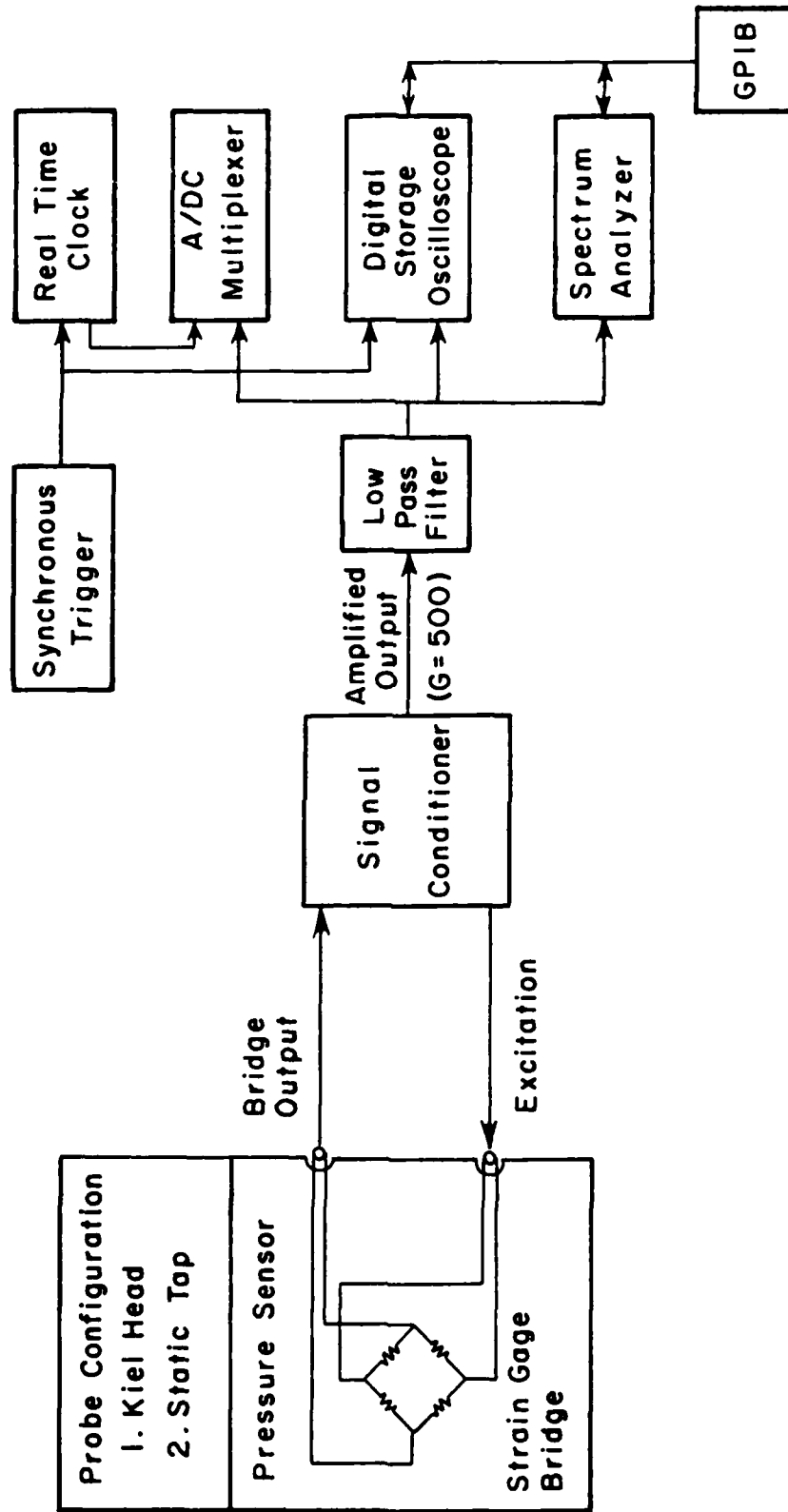
Figure 53   High Response Pressure Data Acquisition Schematic

299
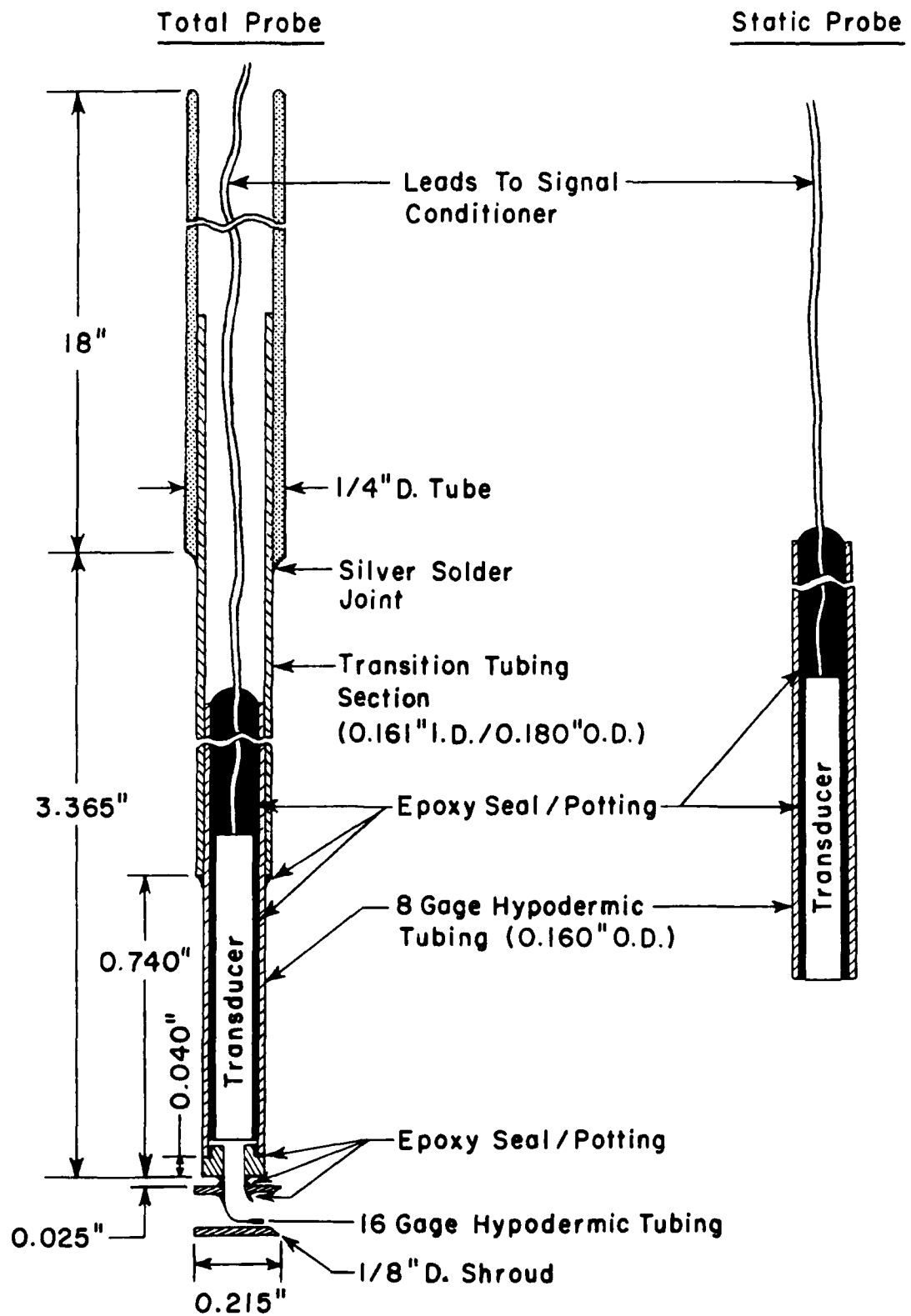
Figure 54   High Response Pressure Probes

300
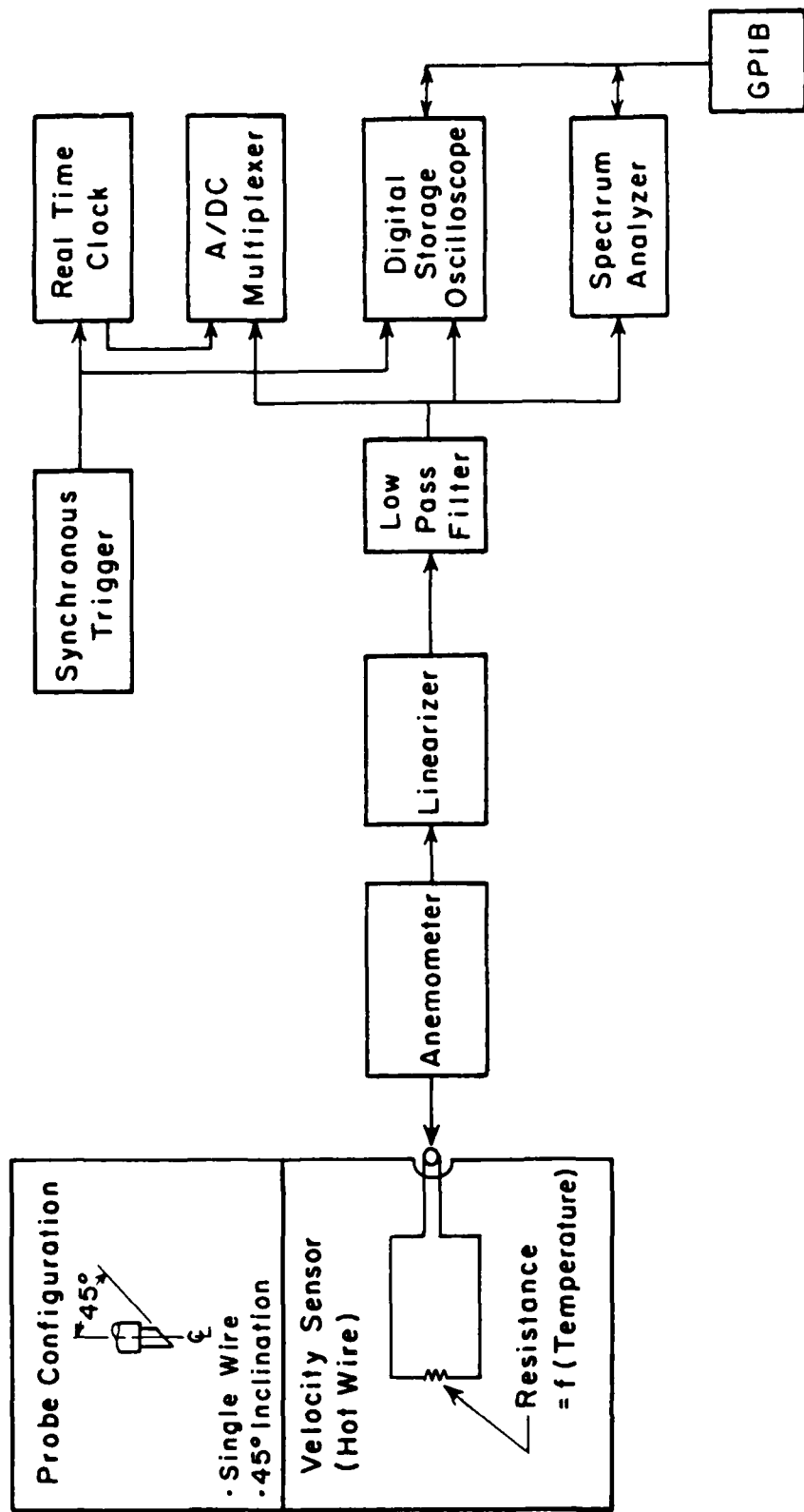
Figure 55   Hot Wire Data Acquisition Schematic

301

Platinum Coated Tungsten Sensing Area
0.050" Length
0.00015" Diameter

Gold Plated
Sensor Supports

0.375"

45°

0.050" Sensing
Length

0.060" Distance
Between Supports
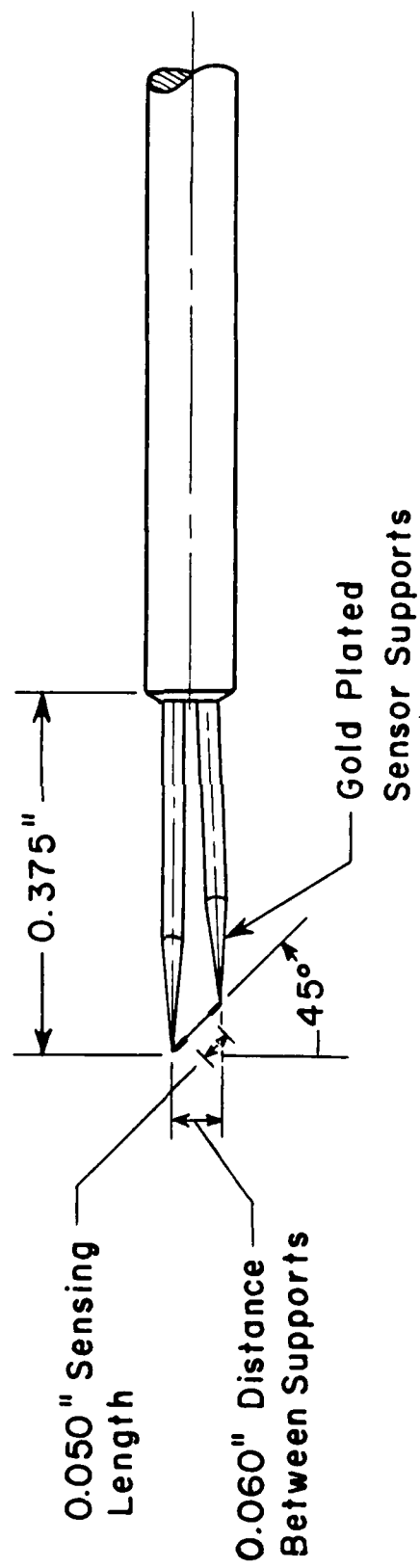
Figure 56   Slanted Hot Wire Probe
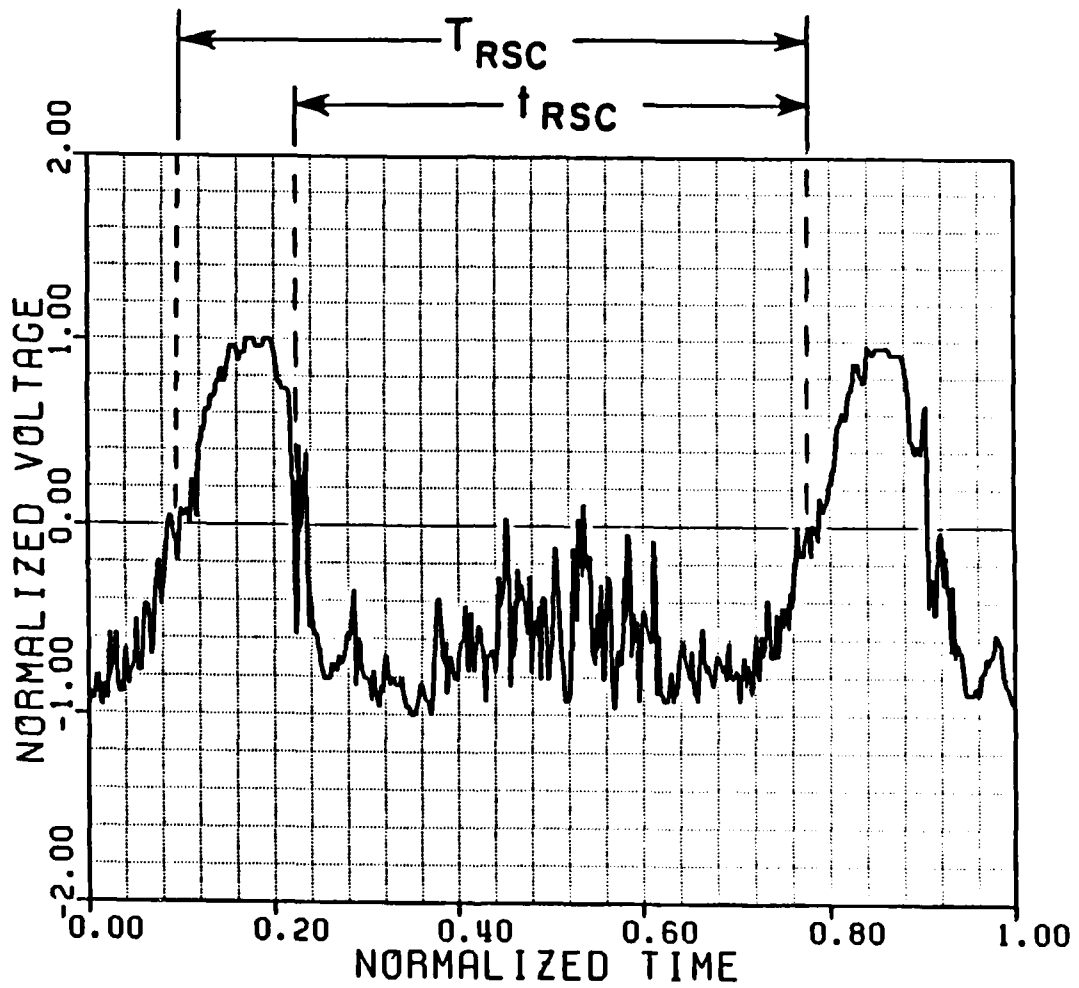
Figure 57   Rotating Stall Cell Oscilloscope Trace

303

α_P – Absolute Pitch Angle

α_Y – Absolute Yaw Angle

$\vec{C}$ – Absolute Velocity Vector At Point O
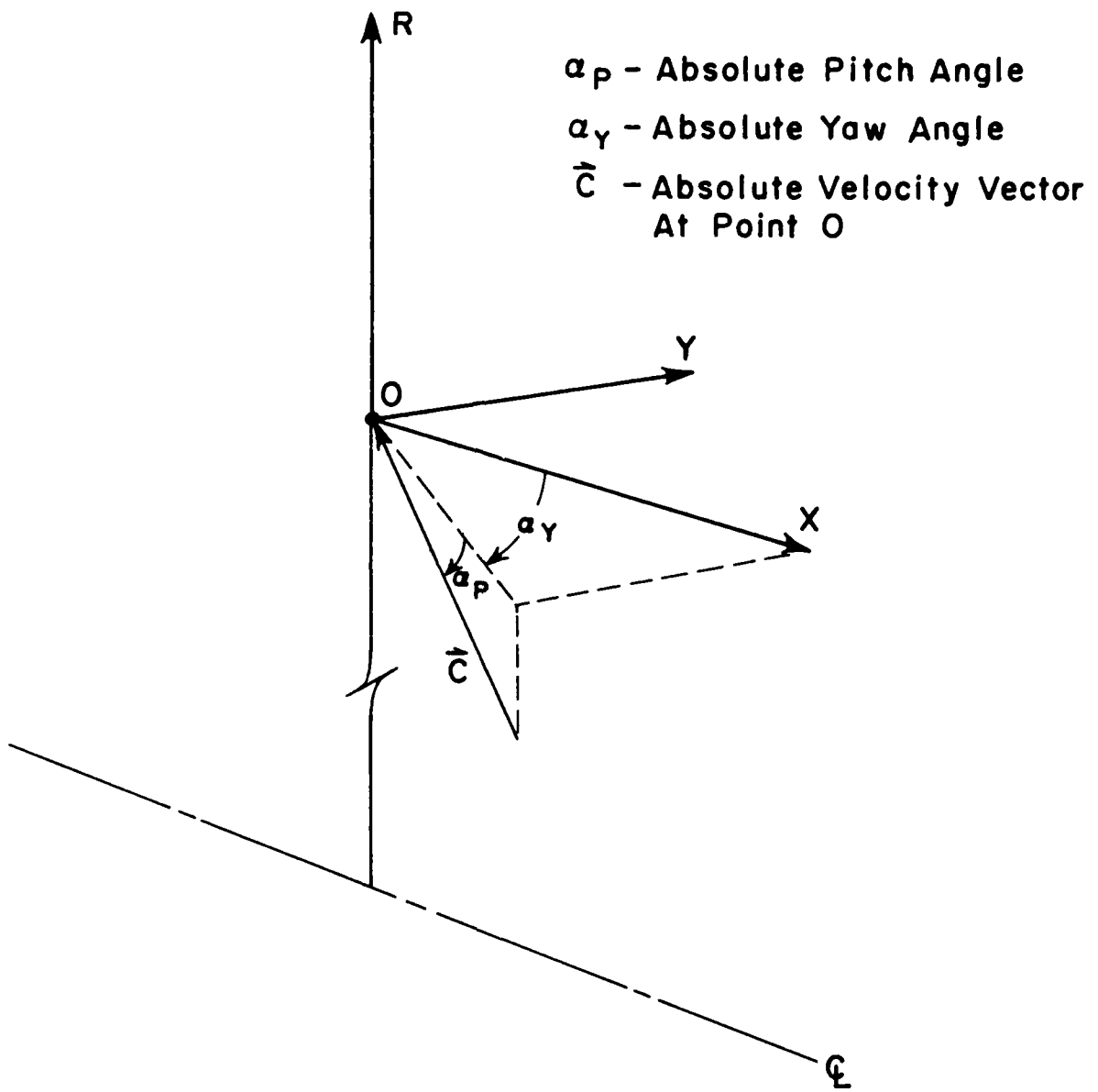
Figure 58   General Compressor Coordinate Frame

304

$$a_y(t) = \bar{a}_y + |a_y'| \sin(\omega t + \phi)$$

$$|\tilde{C}(t)| = \text{Constant}$$

$|a_y'| \gg 50°$

$|a_y'| > 50°$

$|a_y'| = 50°$

$|a_y'| < 50°$

$|a_y'| = 0$

$$\frac{\Delta p}{\frac{1}{2}\rho C_a^2}$$

$-100°$ 0 $100°$

$\bar{a}_y - a_{y_{Probe}}$
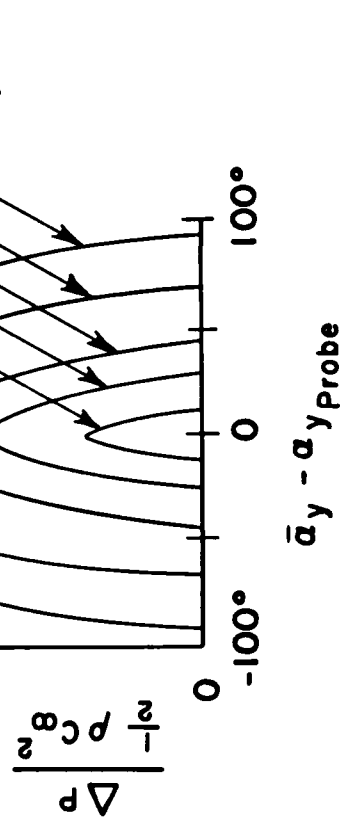
b) Time Average Results
(Kiel Head Probe)

$a_{y_{probe}}$

$\bar{a}_y$

R

$\bar{C}$

$2\,|a_y'|$

y

x

$\mathbb{C}$

a) Geometric Relationships

Figure 59   Periodic Directional Unsteadiness about a Time Average Mean

305

θ_o –Sensor Inclination
θ_p –Probe Pitch Angle
θ_y –Probe Yaw Angle
$\overline{w}$ –Relative Velocity Vector
At Sensor Center
β –Relative Yaw Angle
(WRT Sensor)

Long
Support

Short
Support
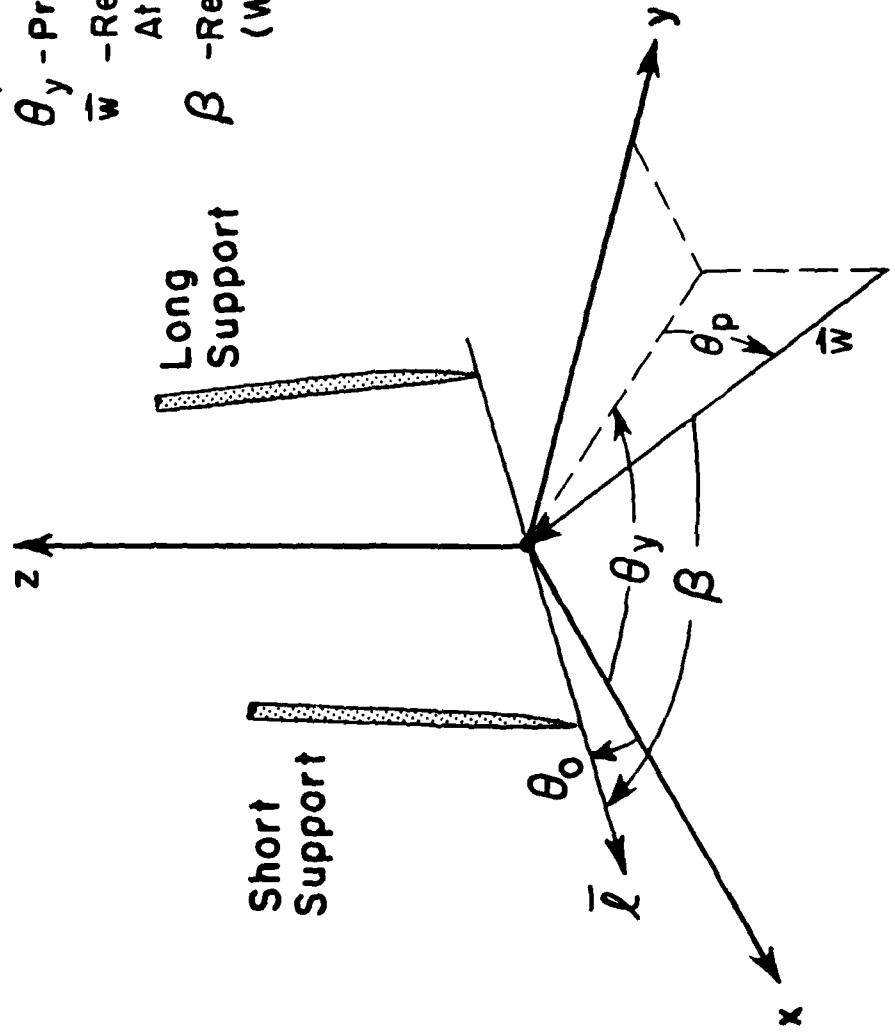
Figure 60   Hot Wire Probe Fixed Coordinate Frame
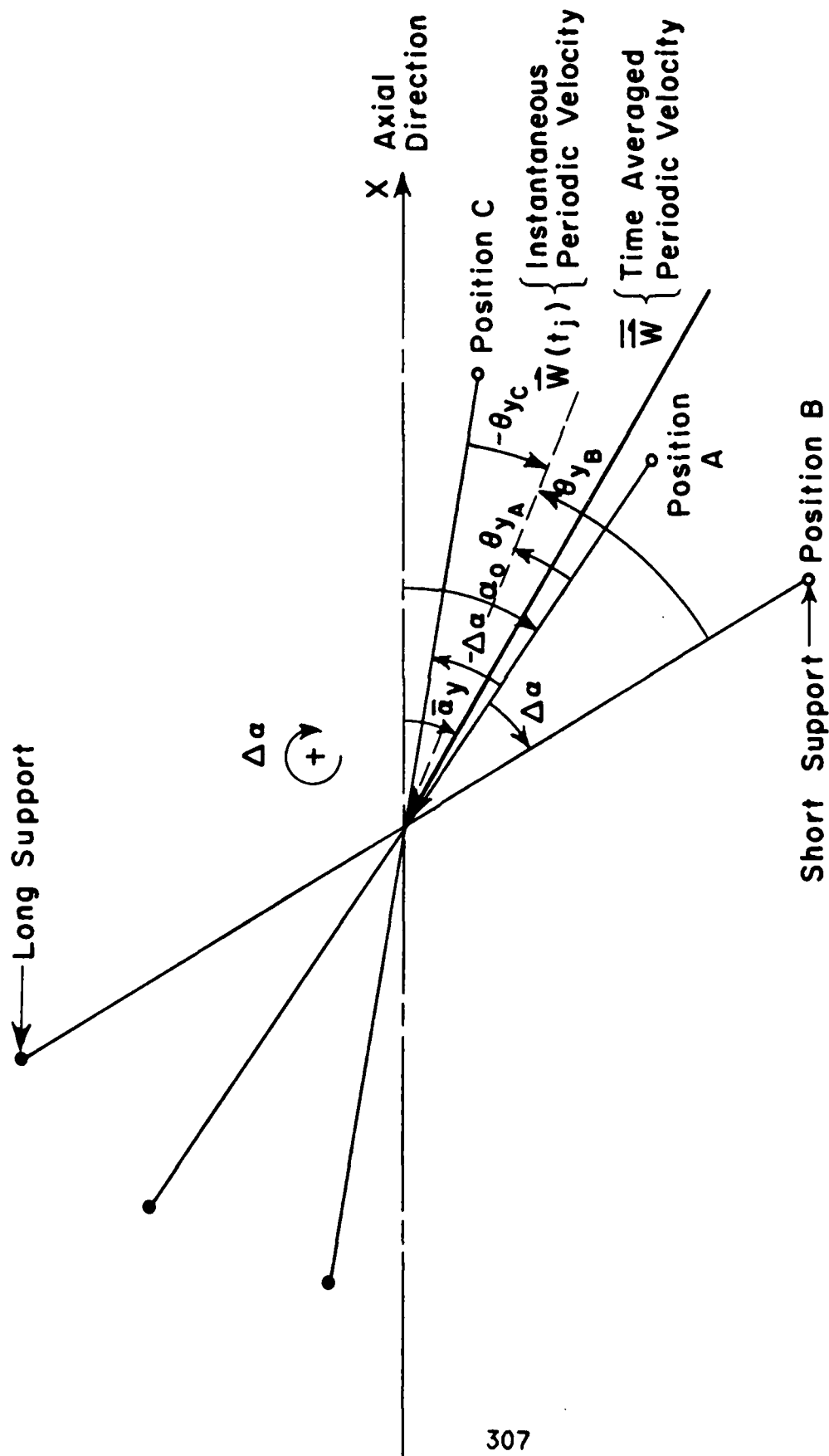
Figure 61   Slanted Sensor Data Acquisition Geometry

307

Figure 62   Medium Reaction Build Total-to-Static Characteristic

Figure 63   High Reaction Build Total-to-Static Characteristic

Legend:
- ⊙ 1170 RPM SPEEDLINE
- ⊡ 1800 RPM SPEEDLINE
- ✕ 2400 RPM SPEEDLINE
- ◇ EASTLAND (47)
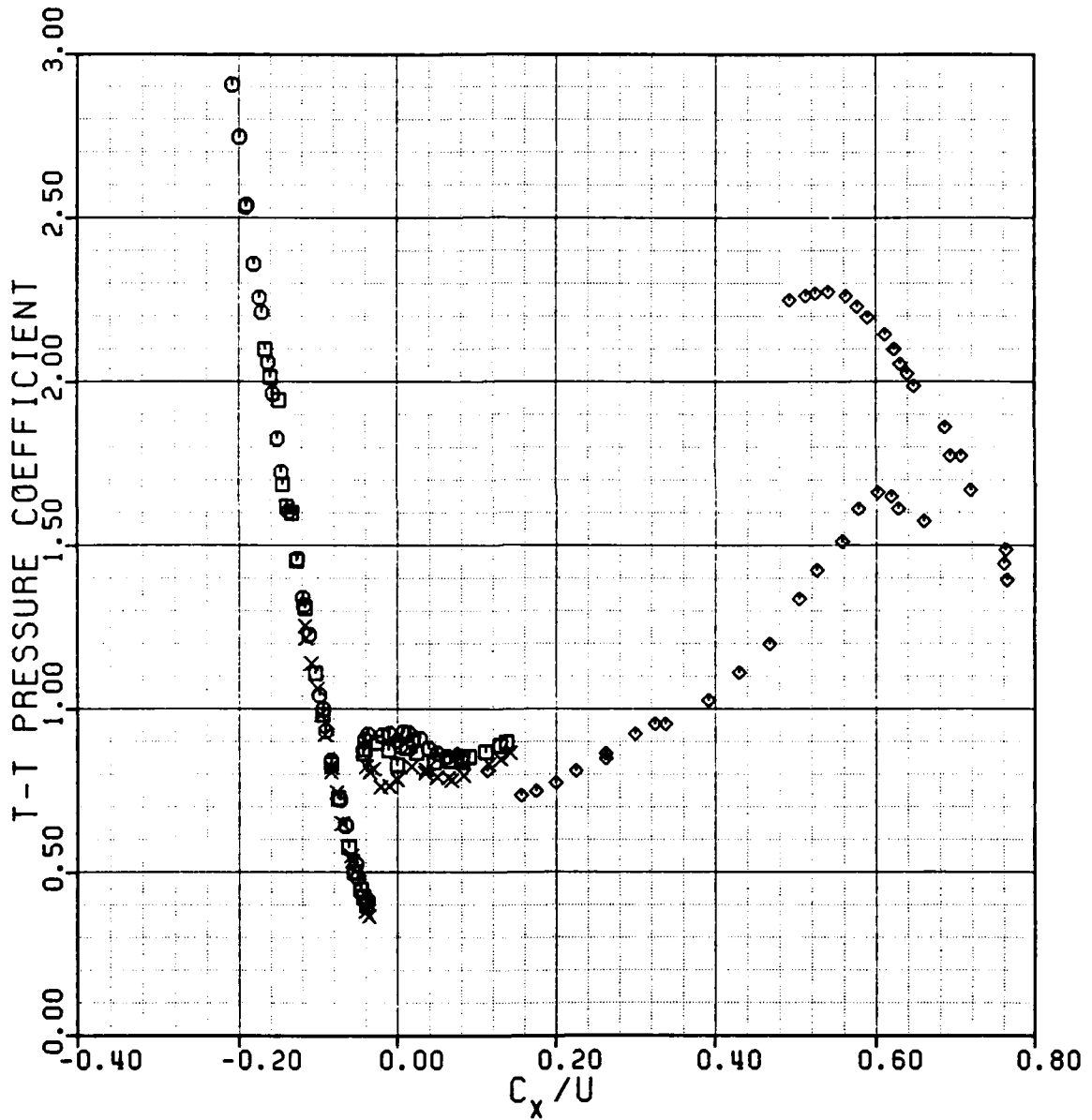
Figure 64   Medium Reaction Build Total-to-Total Characteristic

310
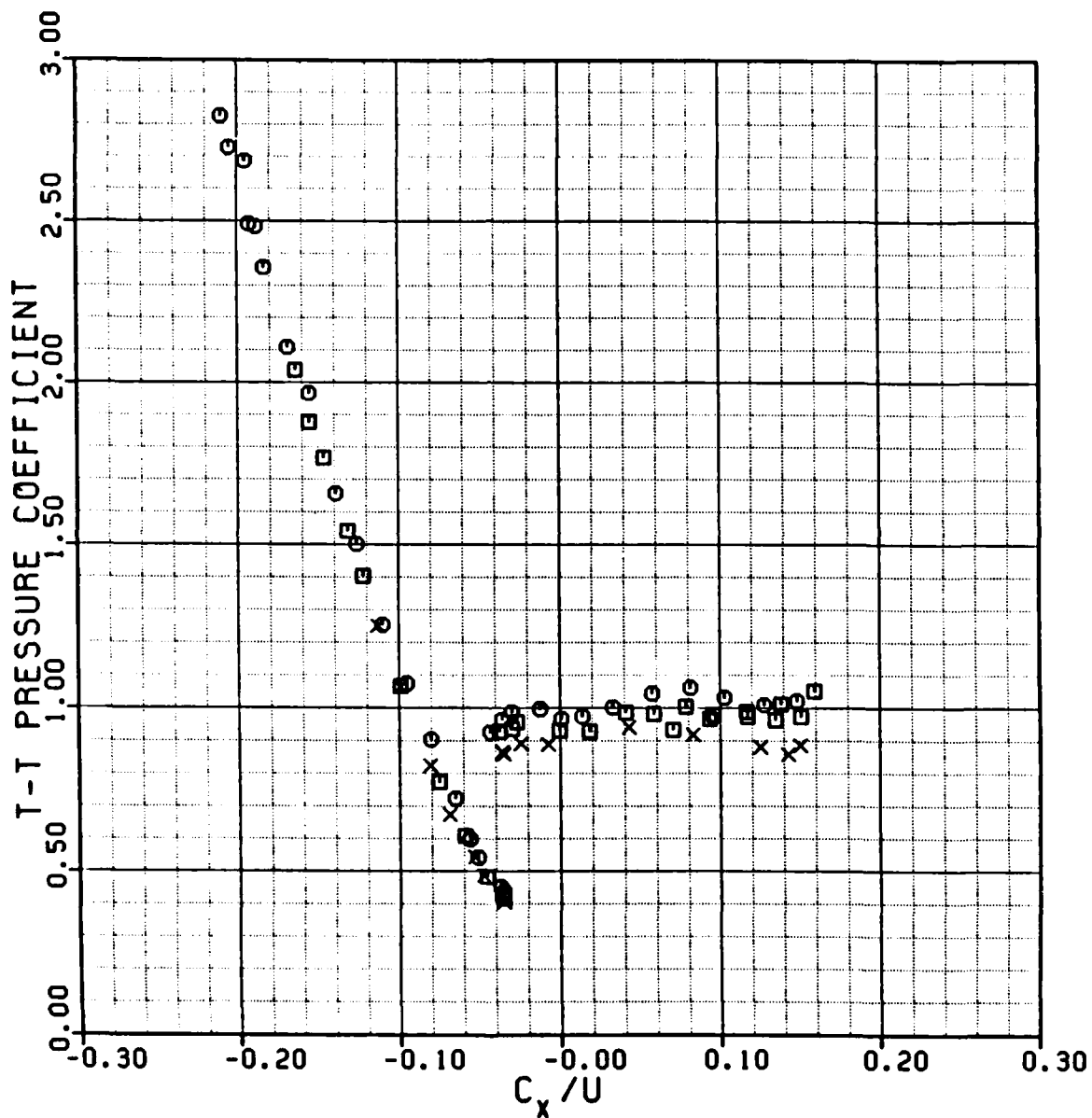
Figure 55   High Reaction Build Total-to-Total Characteristic
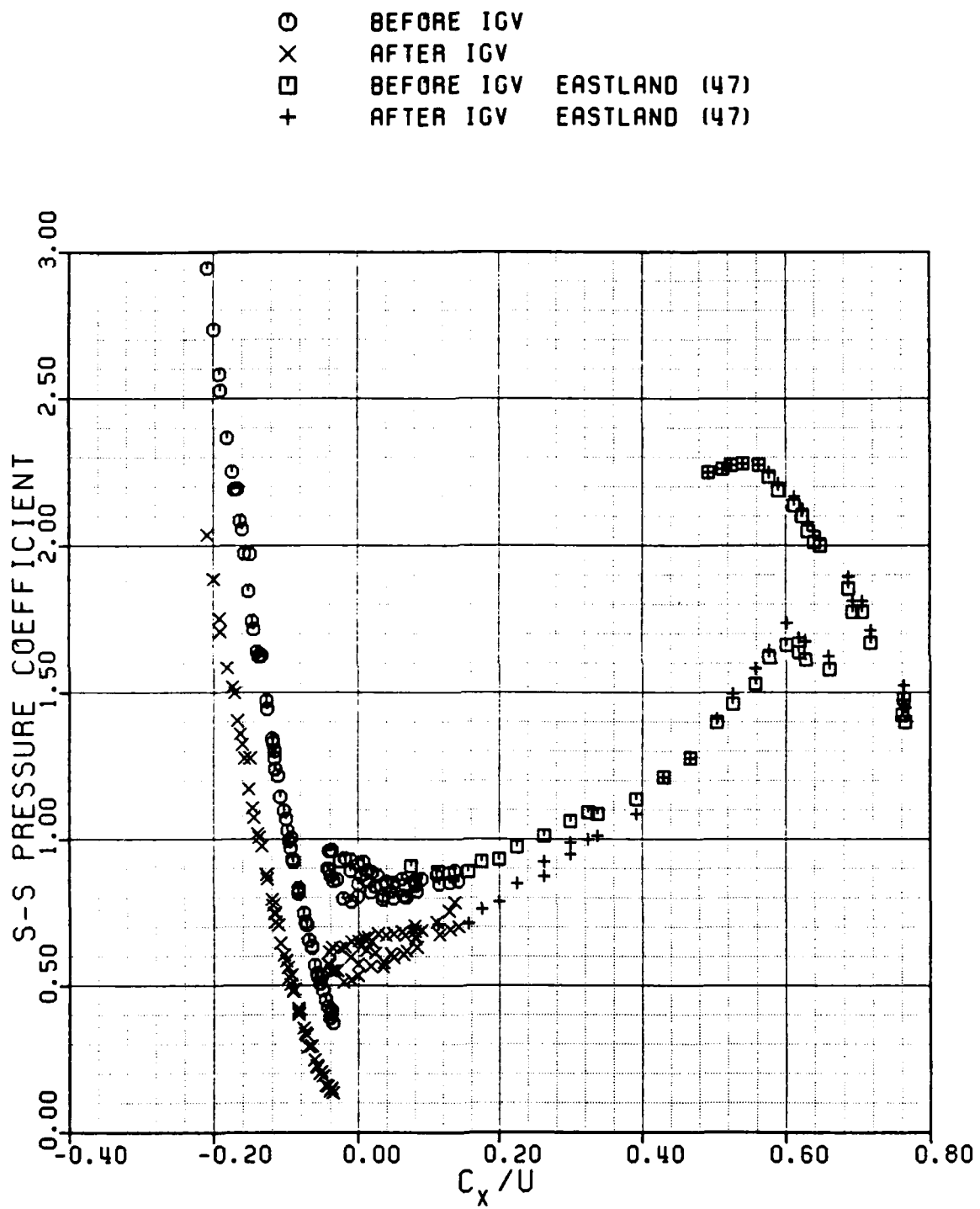
Figure 66   Medium Reaction Build Static-to-Static Characteristics

312
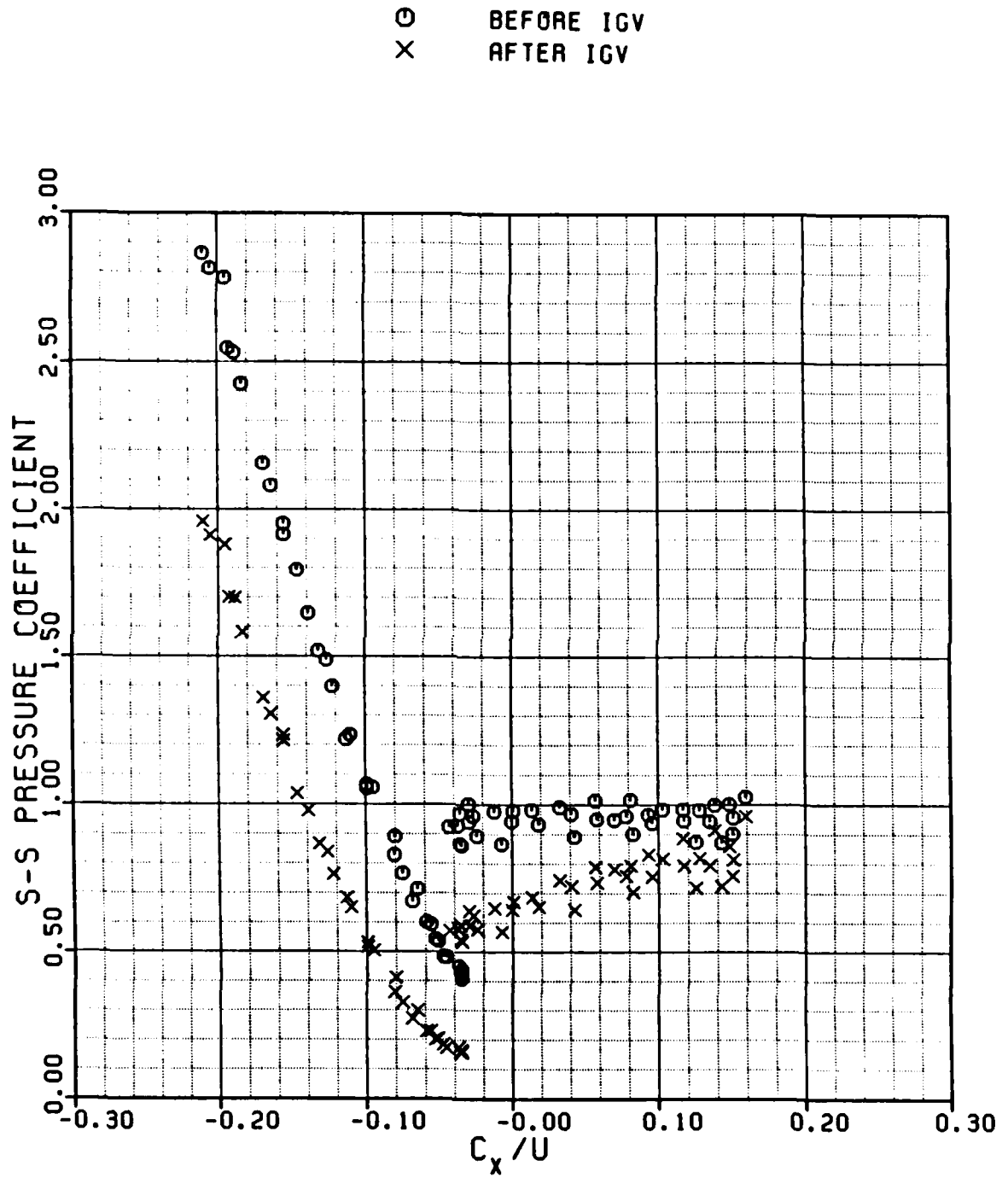
Figure 67   High Reaction Build Static-to-Static Characteristics
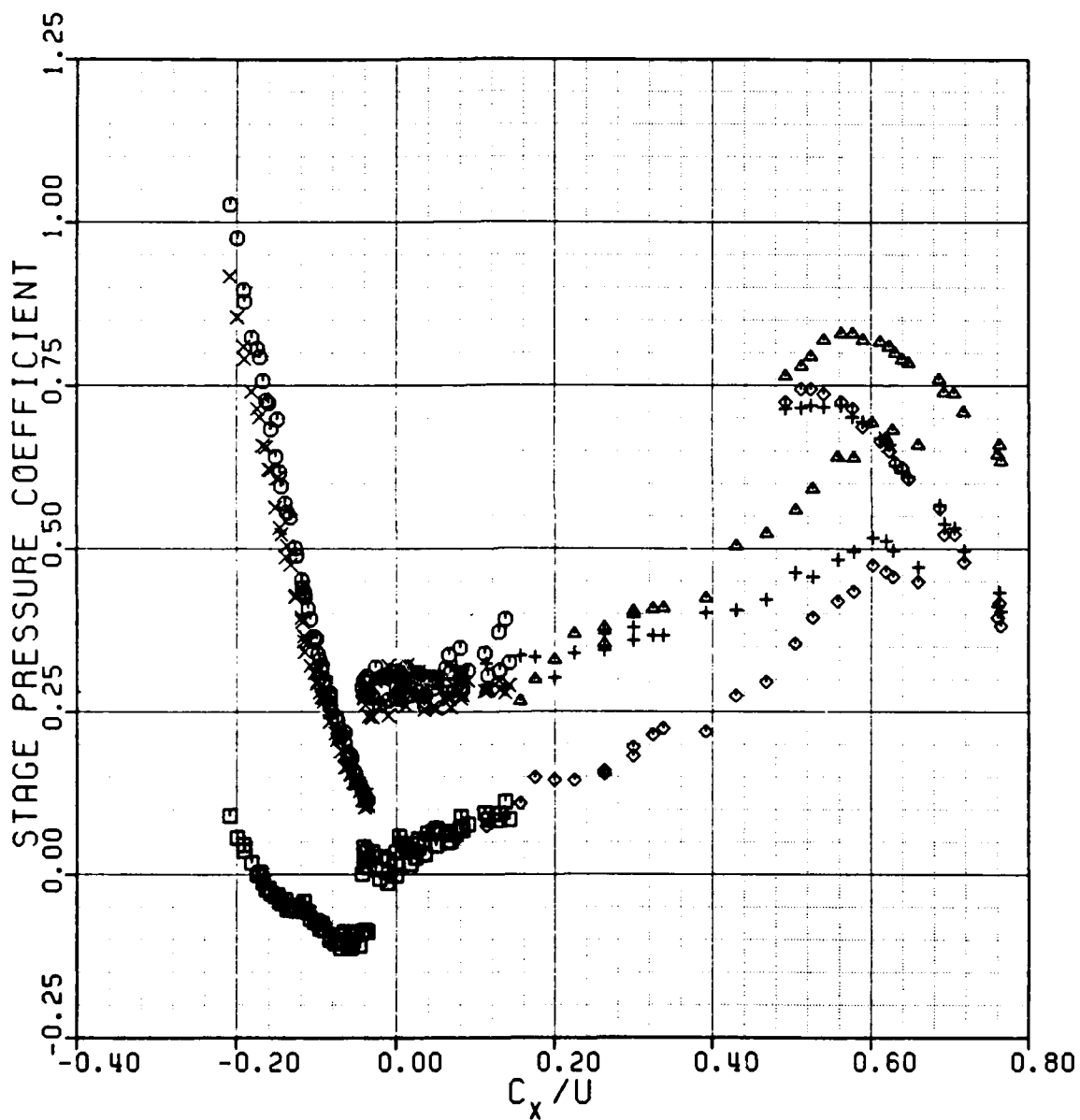
Figure 68   Medium Reaction Build Individual Stage Characteristics

314
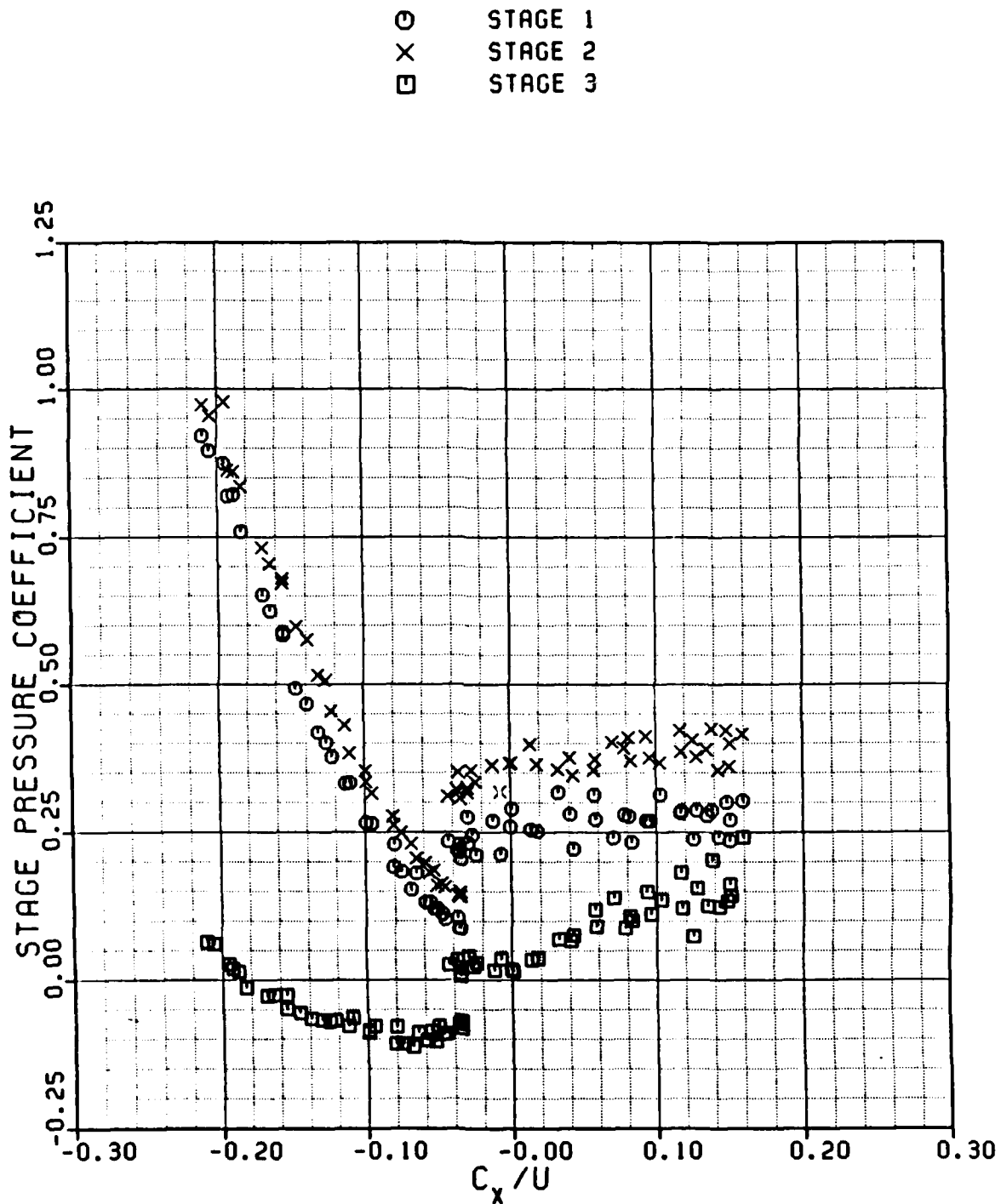
Figure 69   High Reaction Build Individual Stage Characteristics

Figure 70   Medium Reaction Build Torque Characteristic

Figure 71   High Reaction Build Torque Characteristic
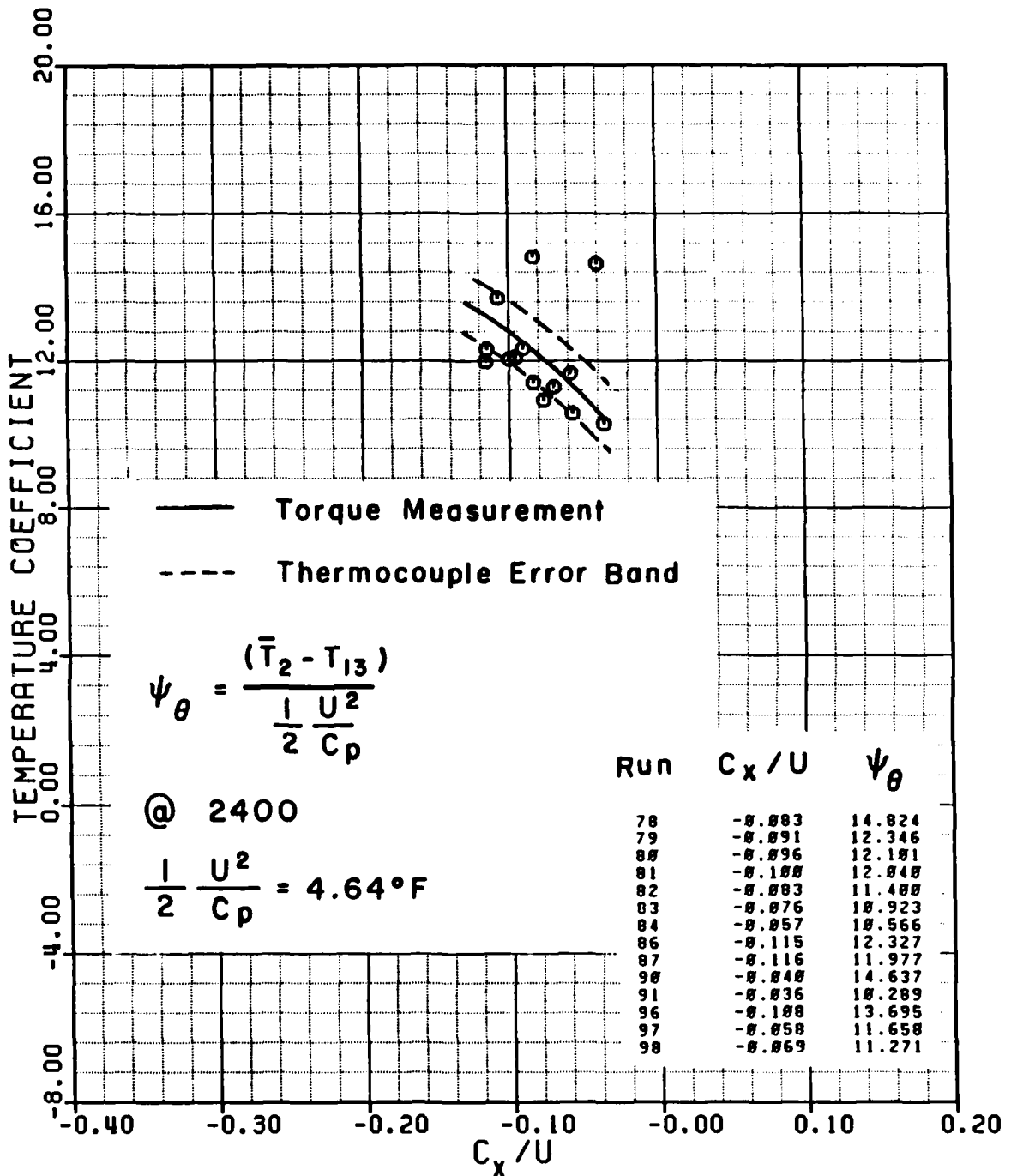
Figure 72   Total Temperature Characteristic Comparison

Figure 73 Two Dimensional Geometry for Reverse Flow Torque Analysis
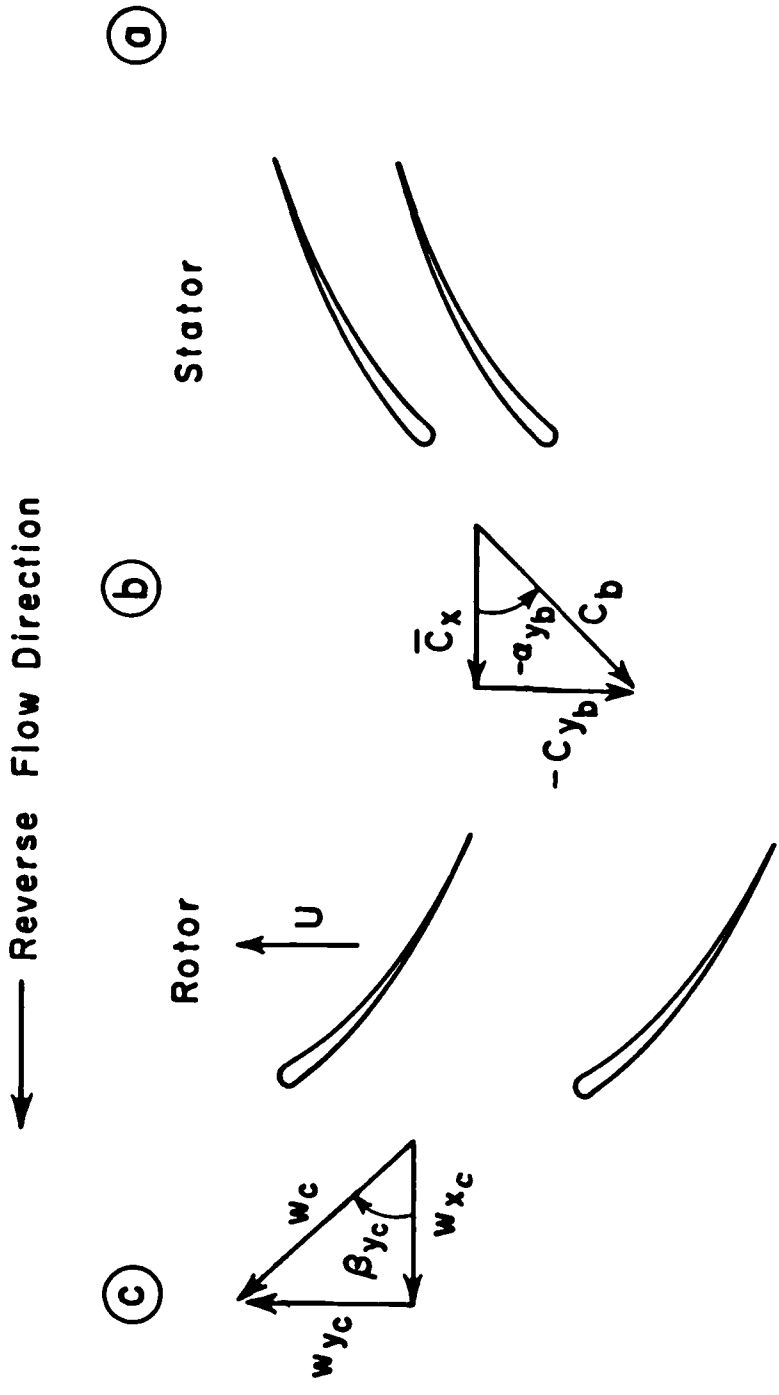
w - Rotor Frame
c - Absolute Frame
$w_{x_c} = \bar{C}_x$
$w_{y_c} + U = C_{y_c}$
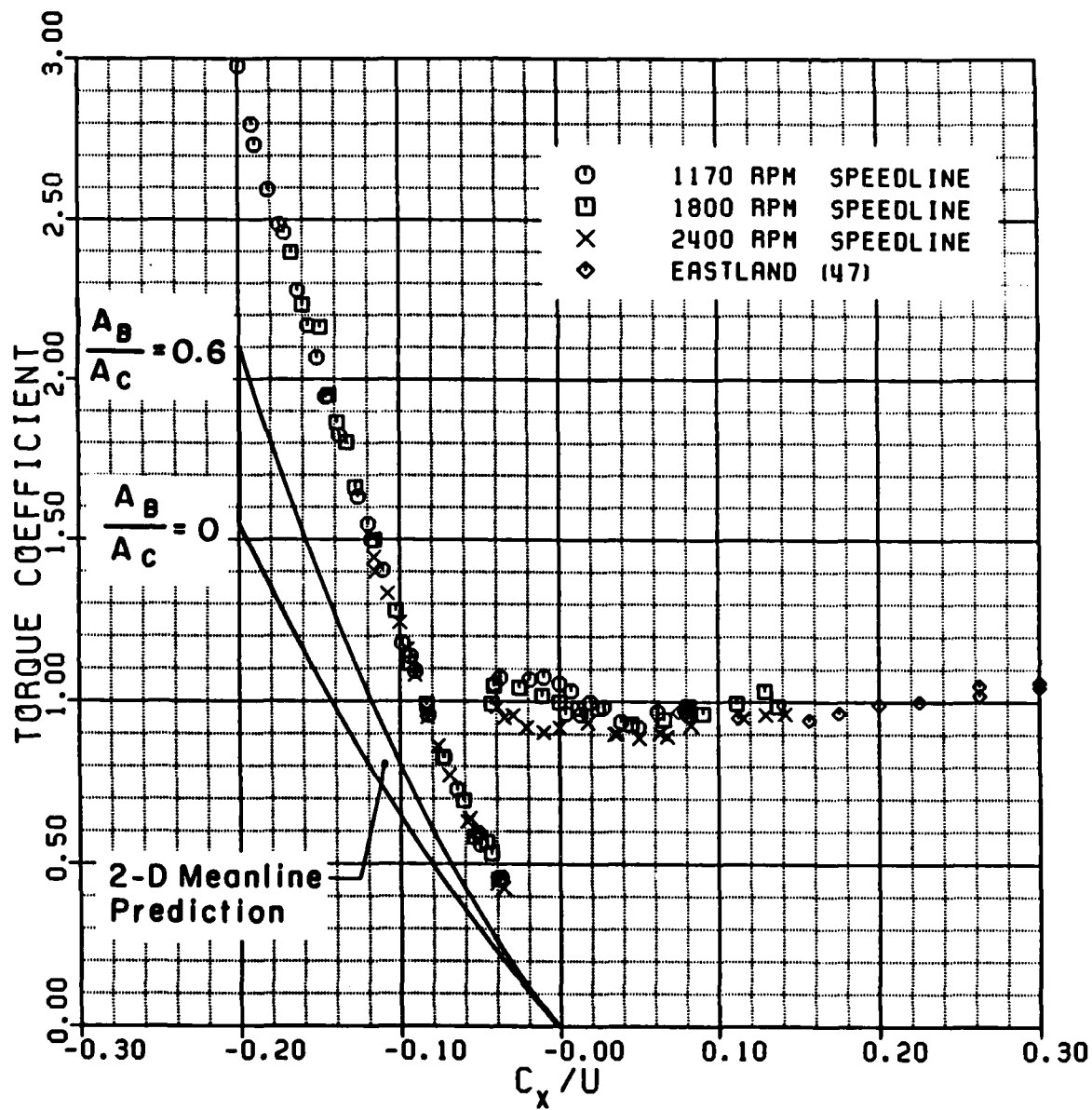
Figure 74   Reverse Flow Torque Absorption Analysis Results
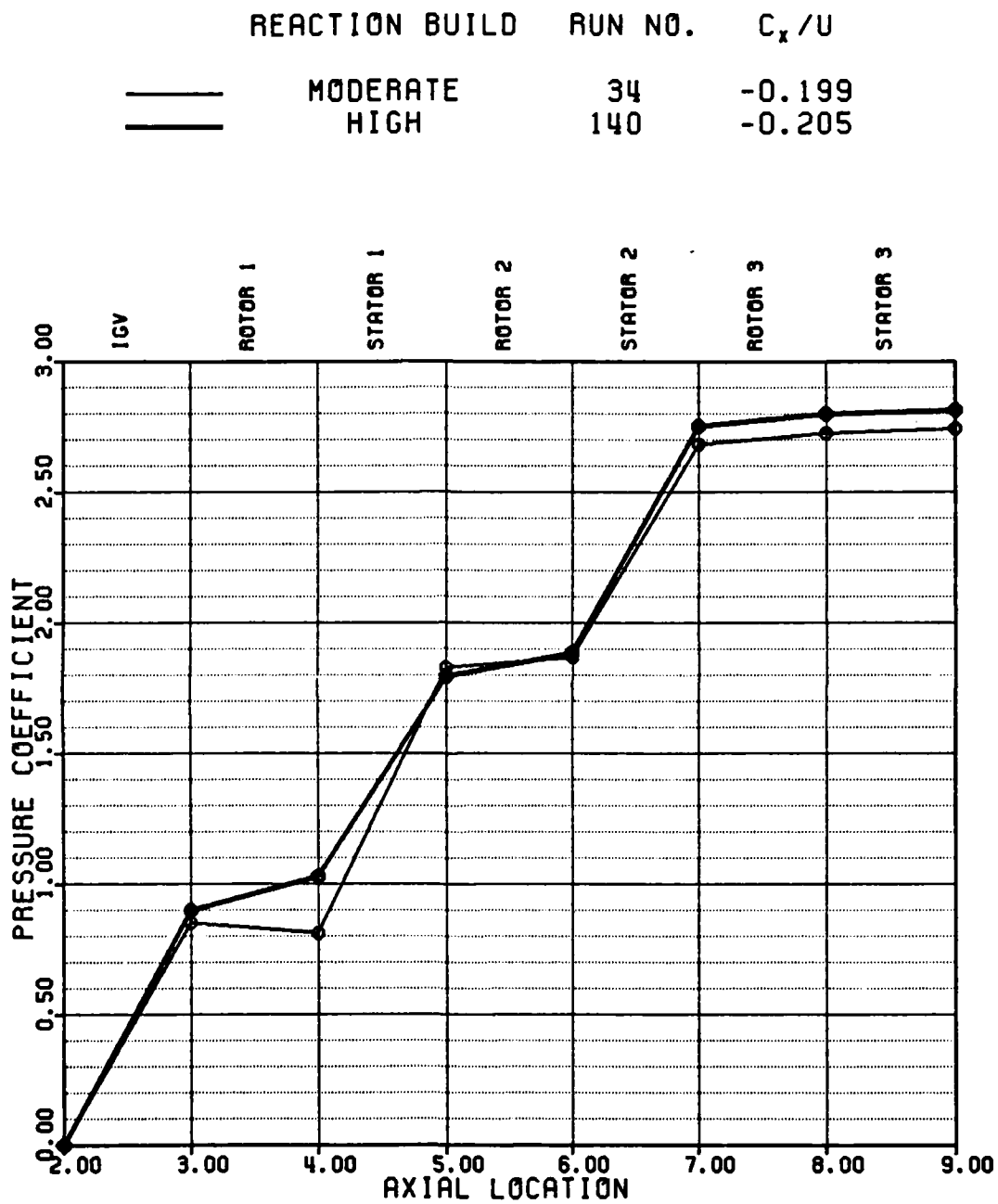
Figure 75   Annulus Stalled Axial Pressure Profile

at High Reverse Flow

Figure 76   Annulus Stalled Axial Pressure Profile
at Moderate Reverse Flow

Figure 77   Annulus Stalled Axial Pressure Profile at Transition Point

REACTION BUILD	RUN NO.	C_x/U
—— MODERATE	42	-0.041
—— HIGH	137	-0.043
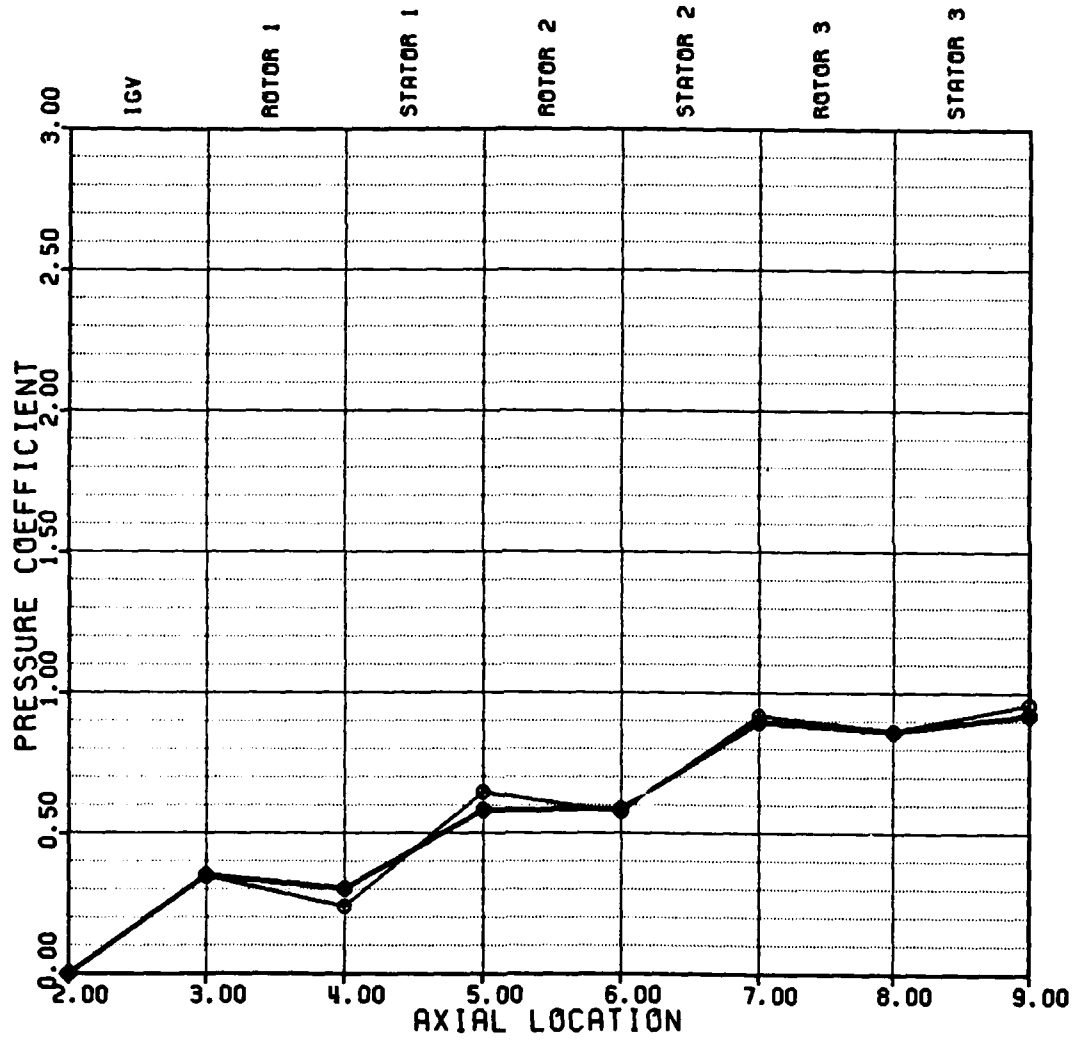
Figure 78   Rotating Stall Axial Pressure Profile at Transition Point

324

REACTION BUILD   RUN NO. C_x/U

——————   MODERATE   32   0.081
——————   HIGH   119   0.081
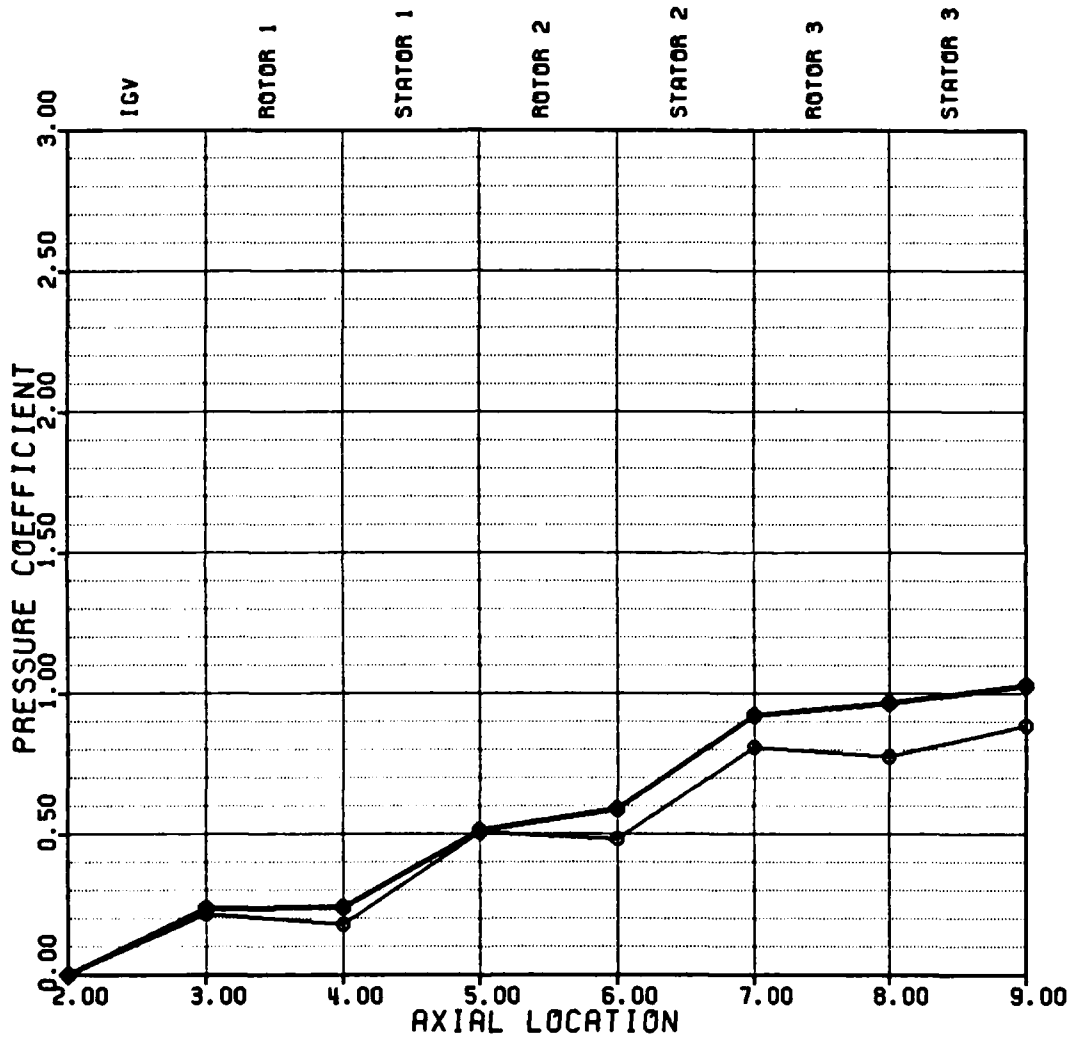
Figure 79   Rotating Stall Axial Pressure Profile at Low Forward Flow
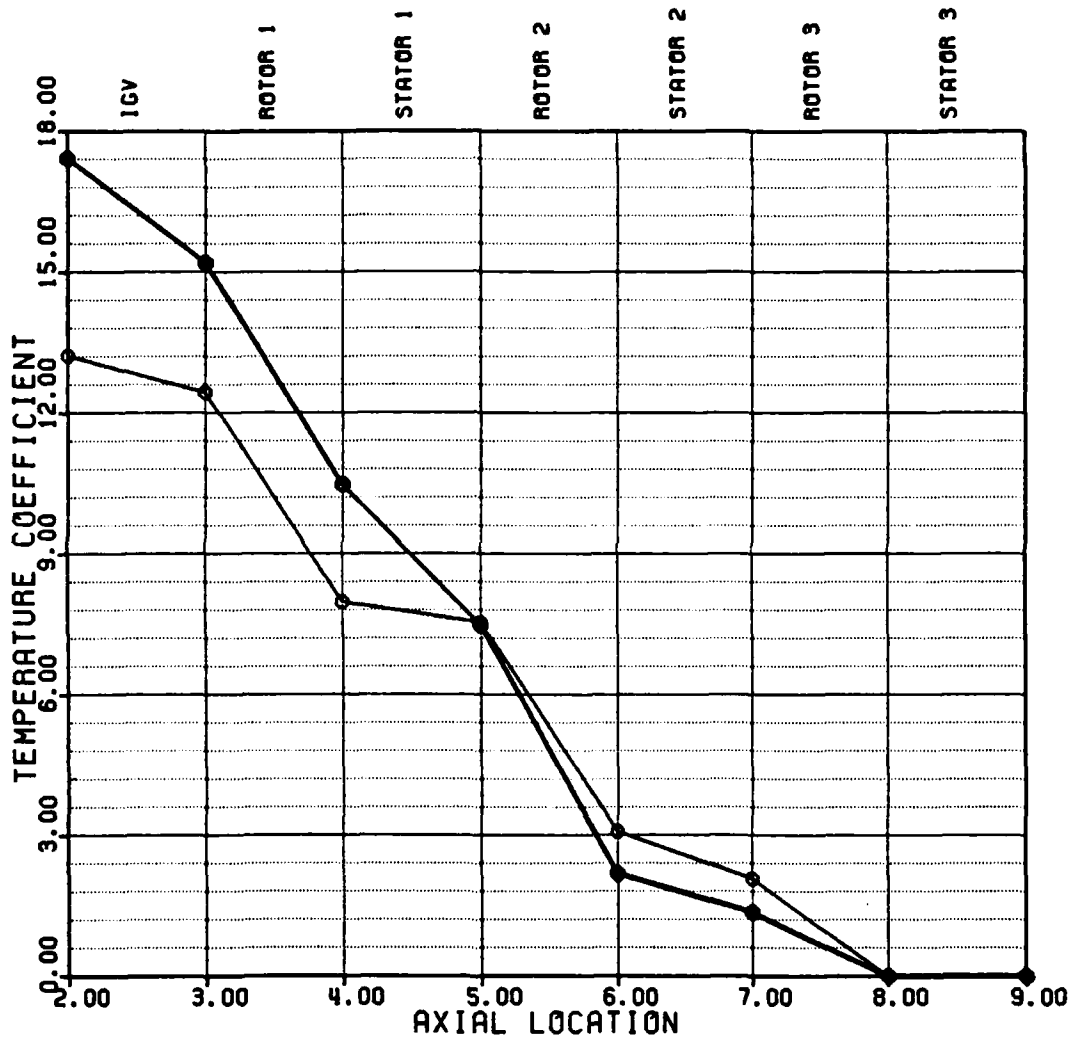
Figure 80   Annulus Stalled Axial Temperature Profile
at High Reverse Flow

REACTION BUILD   RUN NO. C_x/U

——	MODERATE	18	-0.098
——	HIGH	190	-0.095
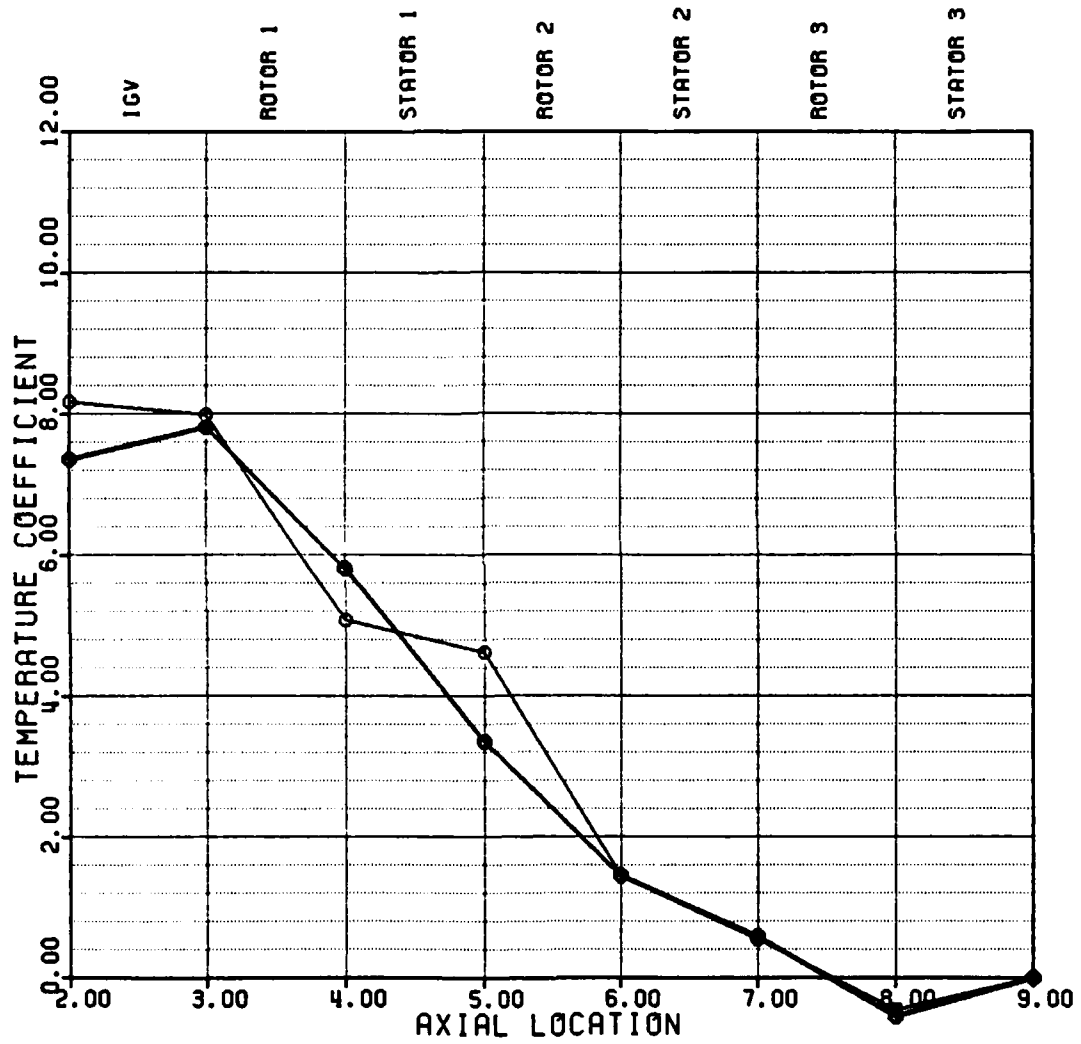
Figure 81   Annulus Stalled Axial Temperature Profile
at Moderate Reverse Flow

REACTION BUILD   RUN NO. C_x/U

	MODERATE	40	-0.038
	HIGH	133	-0.035
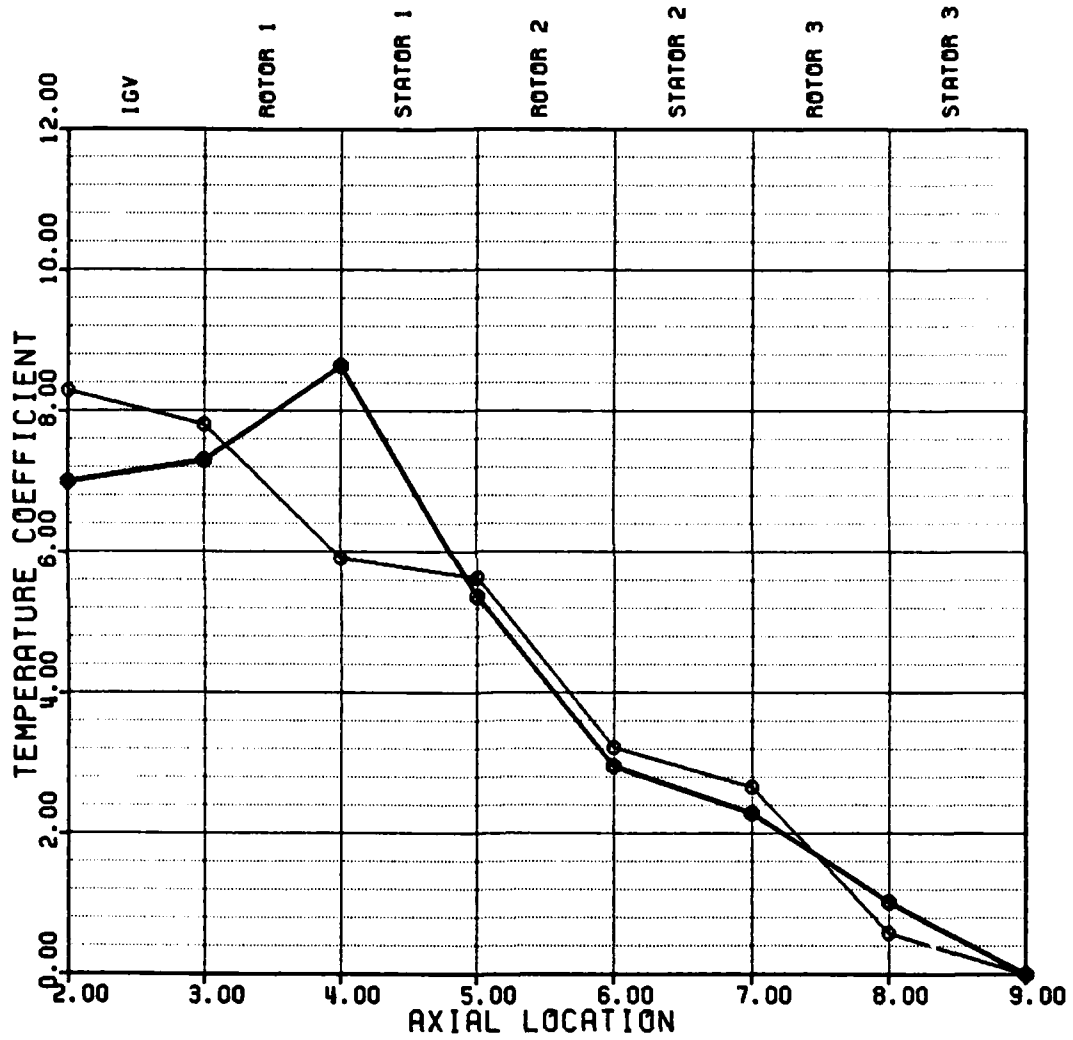
Figure 82   Annulus Stalled Axial Temperature Profile
at Transition Point

Figure 83   Rotating Stall Axial Temperature Profile
at Transition Point

Figure 84   Rotating Stall Axial Temperature Profile
at Low Forward Flow

Figure 85   Medium Reaction Build Stall Cell Speed
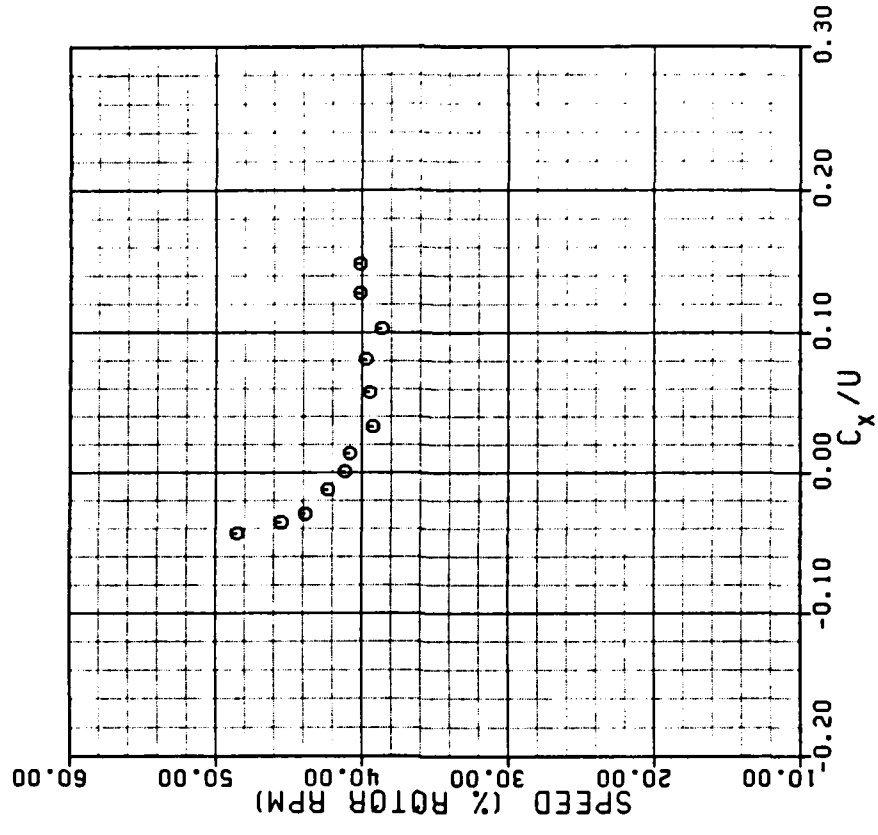
Figure 86   High Reaction Build Stall Cell Speed

331
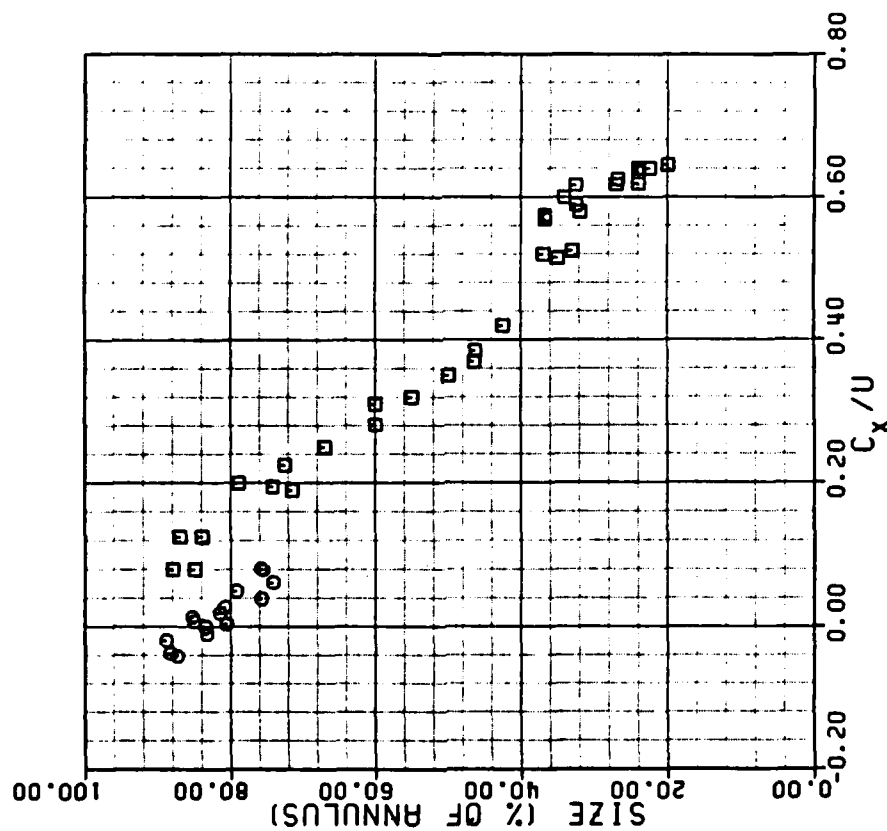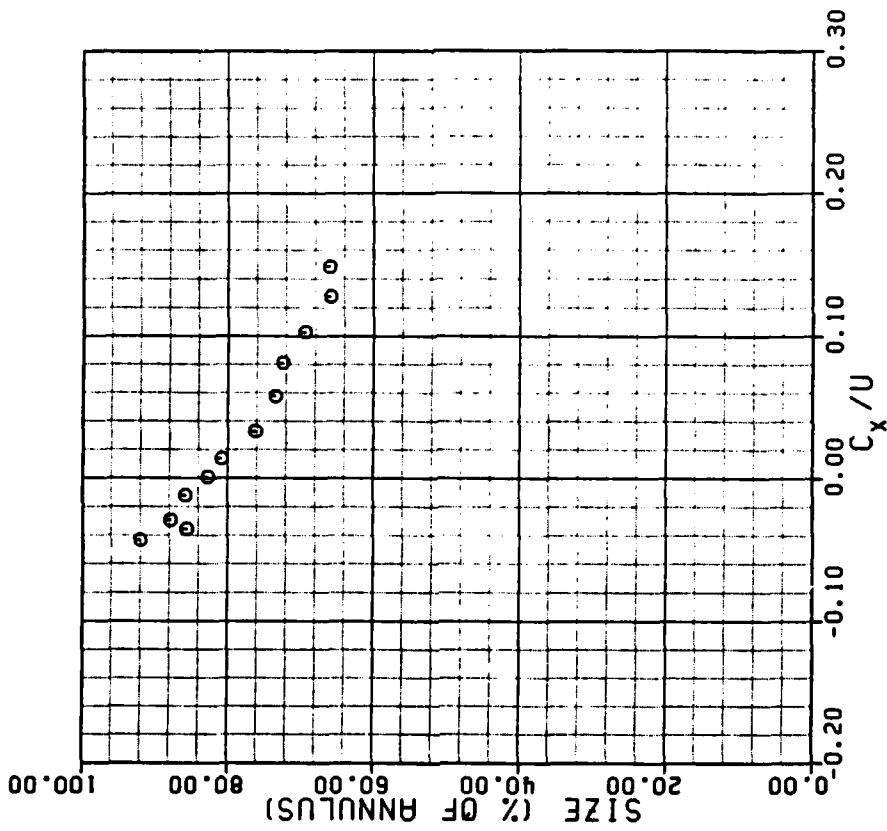
Figure 87   Medium Reaction Build Stall Cell Size

Figure 88   High Reaction Build Stall Cell Size

332
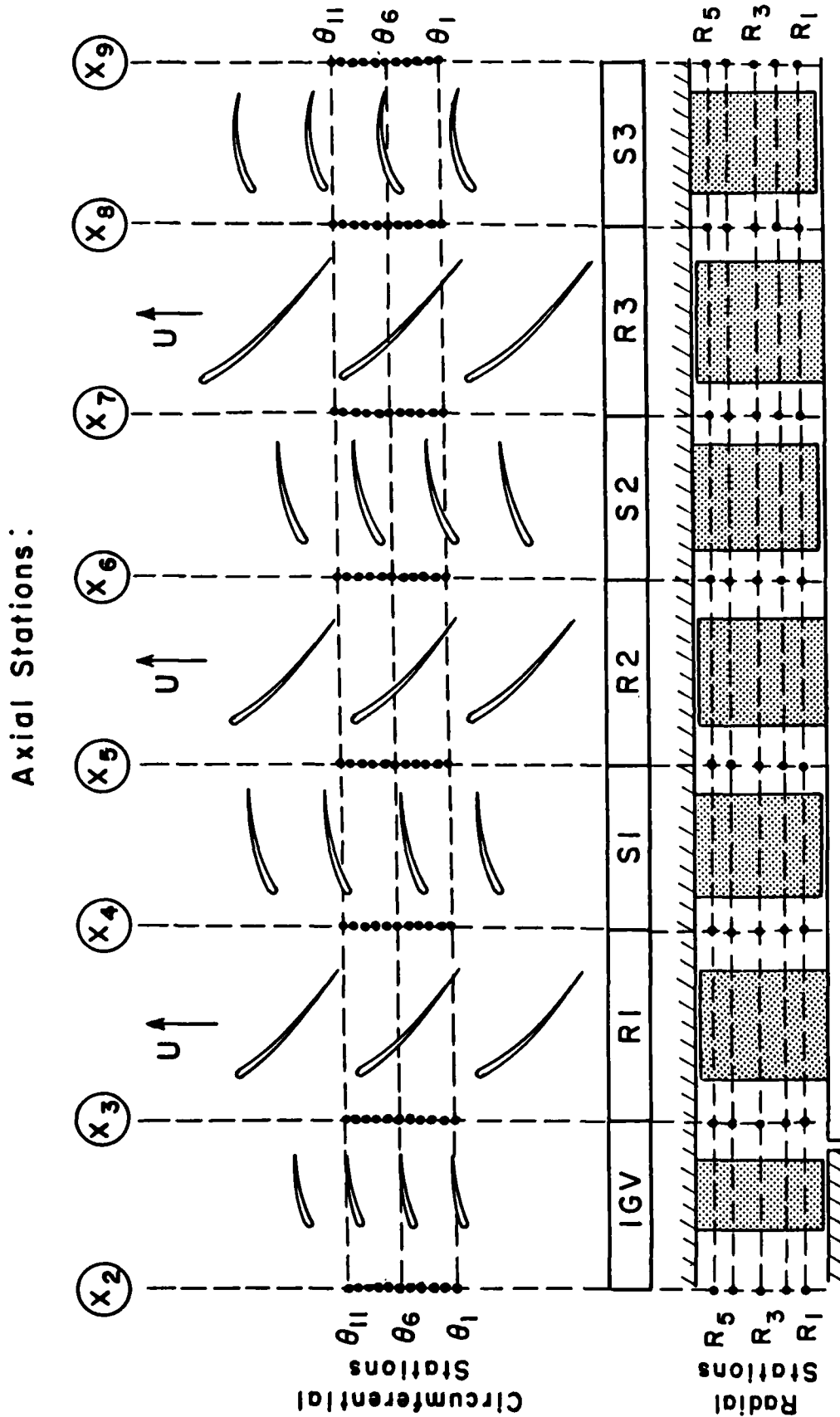
Figure 89   Principal Measuring Positions

333

(INSTANTANEOUS TRACE)

DATE: 3 /29/85

SYNCHRONOUS TRIGGER
TRANSDUCER SERIAL NO.   C260
AMPLIFIER NO.   3
AXIAL STATION 8
CIRCUMFERENTIAL POSITION 6

CALIBRATION DATA:

	ZERO DRIFT (MV)	SENSITIVITY (MV/IN H_2O)	STD DEV (IN H_2O)
PRE-RUN	29.8	45.1	0.053
POST-RUN	-19.0	47.2	0.042
RUN AVG	-7.8	46.7	

PRESSURE DATA (IN H_2O):

AVERAGE . . . . . . -0.955
MAXIMUM 0.299
MINIMUM . . . . . . -2.029
CORRECTED AVG . . .   3.096
BLADE REFERENCE . .   2.949
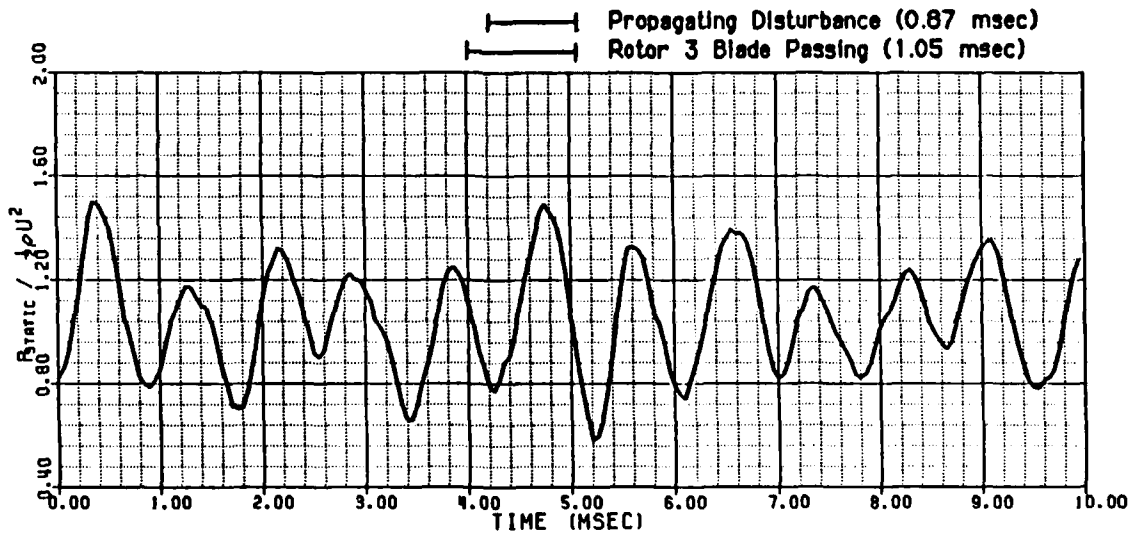
Figure 90   High Response Wall Static Pressure Temporal Trace
(Axial Station #8)

SPECTRAL ANALYSIS

(WALL STATIC PRESSURE TRACE)

DATE: 3 /29/85

$C_x/U = -0.10$

TRANSDUCER SERIAL NO.   C260
AMPLIFIER NO.   3
AXIAL STATION 8
CIRCUMFERENTIAL POSITION 6
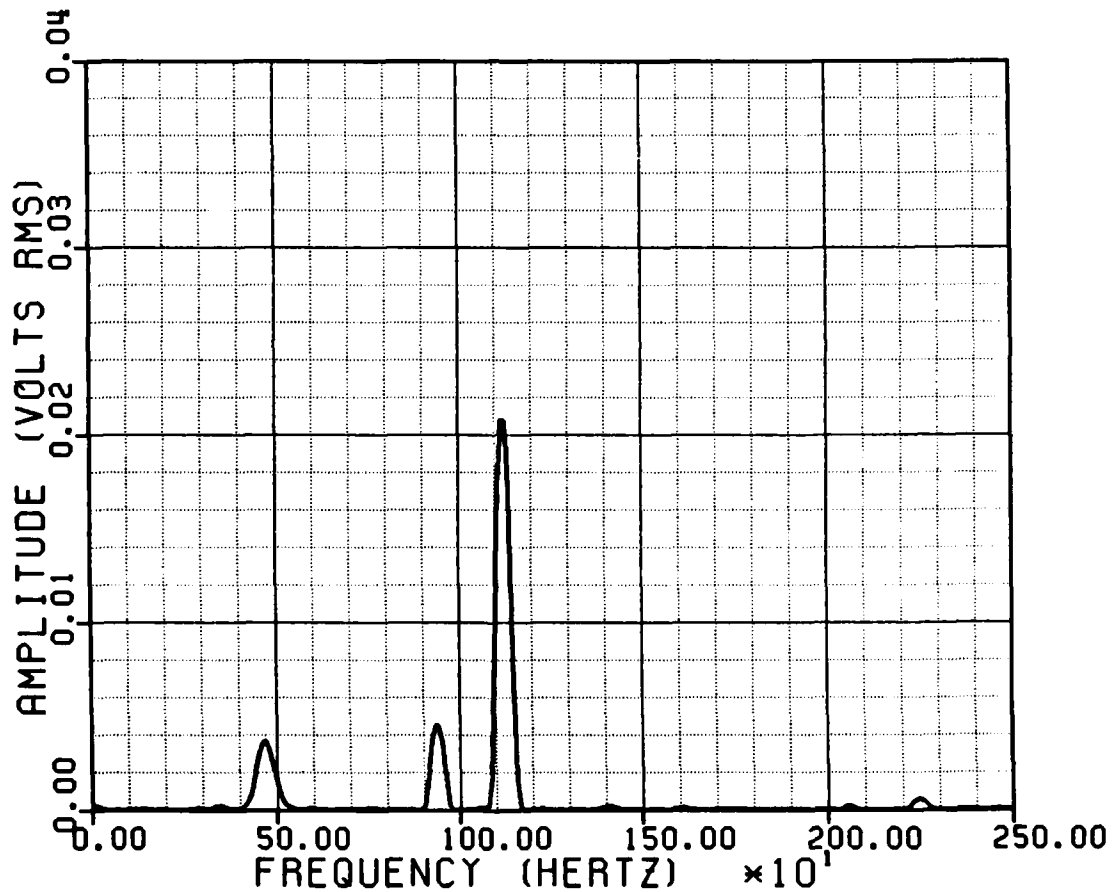
Figure 91   Wall Static Pressure Spectral Signature

(Axial Station #8)

(032 TRACE ENSEMBLE AVERAGE)

DATE: 3 /29/85

ROTOR LOCKED TRIGGER
TRANSDUCER SERIAL NO.   C260
AMPLIFIER NO.   3
AXIAL STATION 8
CIRCUMFERENTIAL POSITION 6

CALIBRATION DATA:

	ZERO DRIFT (MV)	SENSITIVITY (MV/IN H_2O)	STD DEV (IN H_2O)
PRE-RUN	29.8	45.1	0.053
POST-RUN	-19.0	47.2	0.042
RUN AVG	-9.3	46.8	

PRESSURE DATA (IN H_2O):

AVERAGE . . . . . . -0.949
MAXIMUM . . . . . . -0.253
MINIMUM . . . . . . -1.392
CORRECTED AVG . . . 3.096
BLADE REFERENCE . . 2.949

├─────┤ Propagating Disturbance (0.87 msec)
├─────────┤ Rotor 3 Blade Passing (1.05 msec)
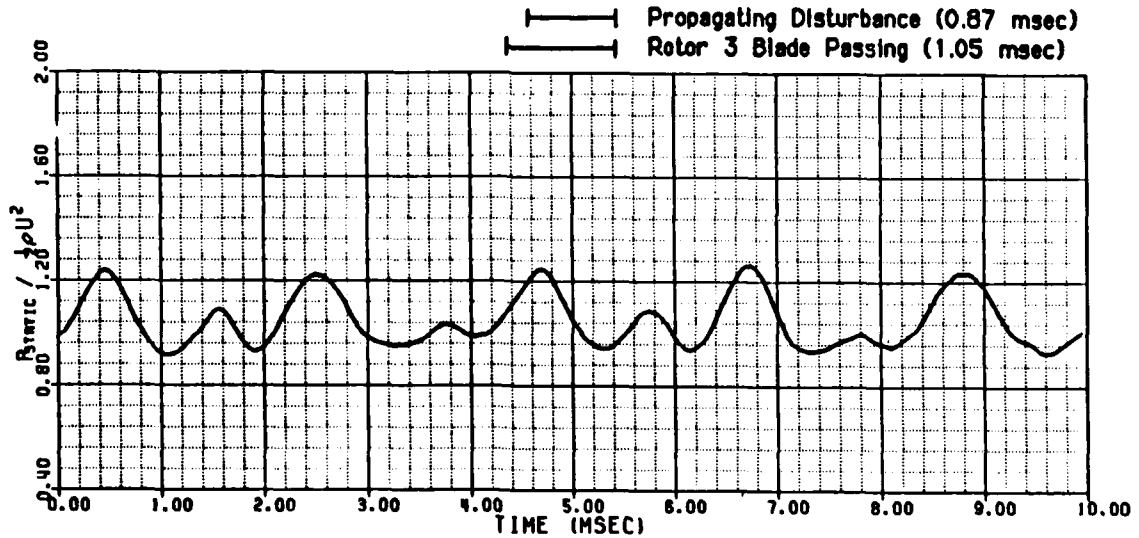
Figure 92   Rotor Locked Ensemble Averaged Wall Static Pressure
(Axial Station #8)

336

(032 TRACE   ENSEMBLE AVERAGE)

DATE: 3 /29/85

EVENT LOCKED TRIGGER
TRANSDUCER SERIAL NO.   C260
AMPLIFIER NO.   3
AXIAL STATION 8
CIRCUMFERENTIAL POSITION 6

CALIBRATION DATA:

	ZERO DRIFT (MV)	SENSITIVITY (MV/IN H_2O)	STD DEV (IN H_2O)
PRE-RUN	29.8	45.1	0.053
POST-RUN	-19.0	47.2	0.042
RUN AVG	-8.7	46.7	

PRESSURE DATA (IN H_2O):

AVERAGE . . . . . . -0.932
MAXIMUM . . . . . . -0.194
MINIMUM . . . . . . -1.736
CORRECTED AVG . . .   3.096
BLADE REFERENCE . .   2.949

├─────┤ Propagating Disturbance (0.87 msec)
├─────┤ Rotor 3 Blade Passing (1.05 msec)
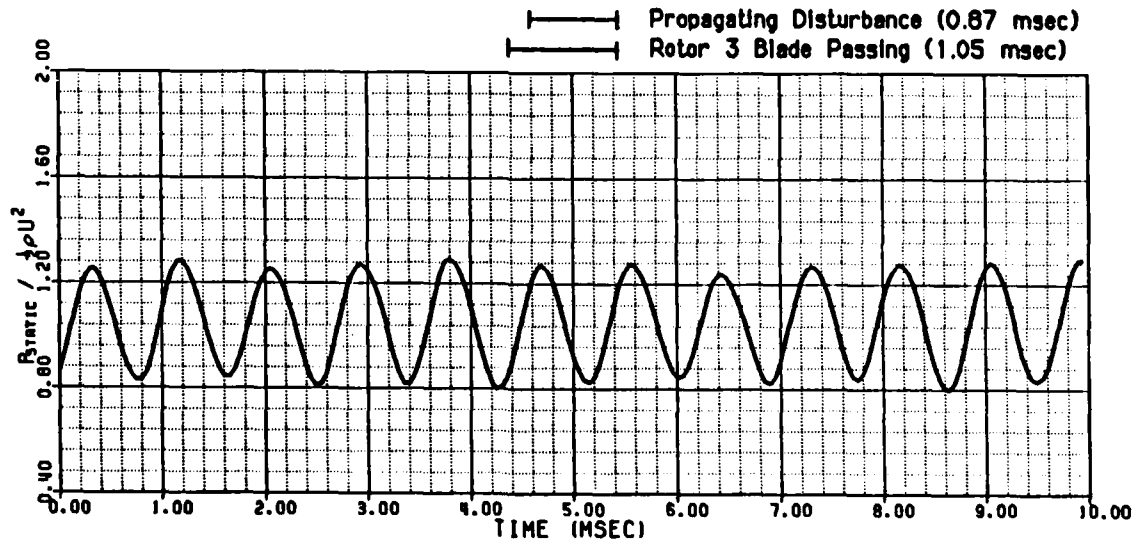
Figure 93   Event Locked Ensemble Averaged Wall Static Pressure
(Axial Station #8)

337

Figure 94 Synchronous Locked Ensemble Averaged Wall
Static Pressure   (Axial Station #8)

338

DATE: 3/28/85	PROBE POSITION DATA:	MEAN FLOW COEFFICIENTS:
SENSOR SERIAL NUMBER: 1	AXIAL STATION 9	C_X/U = -0.117
SYNCHRONOUS TRIGGER	CIRCUMFERENTIAL POSITION . 2	C_θ/U = -0.006
SAMPLE RATE [KHZ]: 20.0	RADIAL POSITION 4	C_R/U = -0.005

Propagating Disturbance (0.87 msec)
Rotor 3 Blade Passing (1.05 msec)
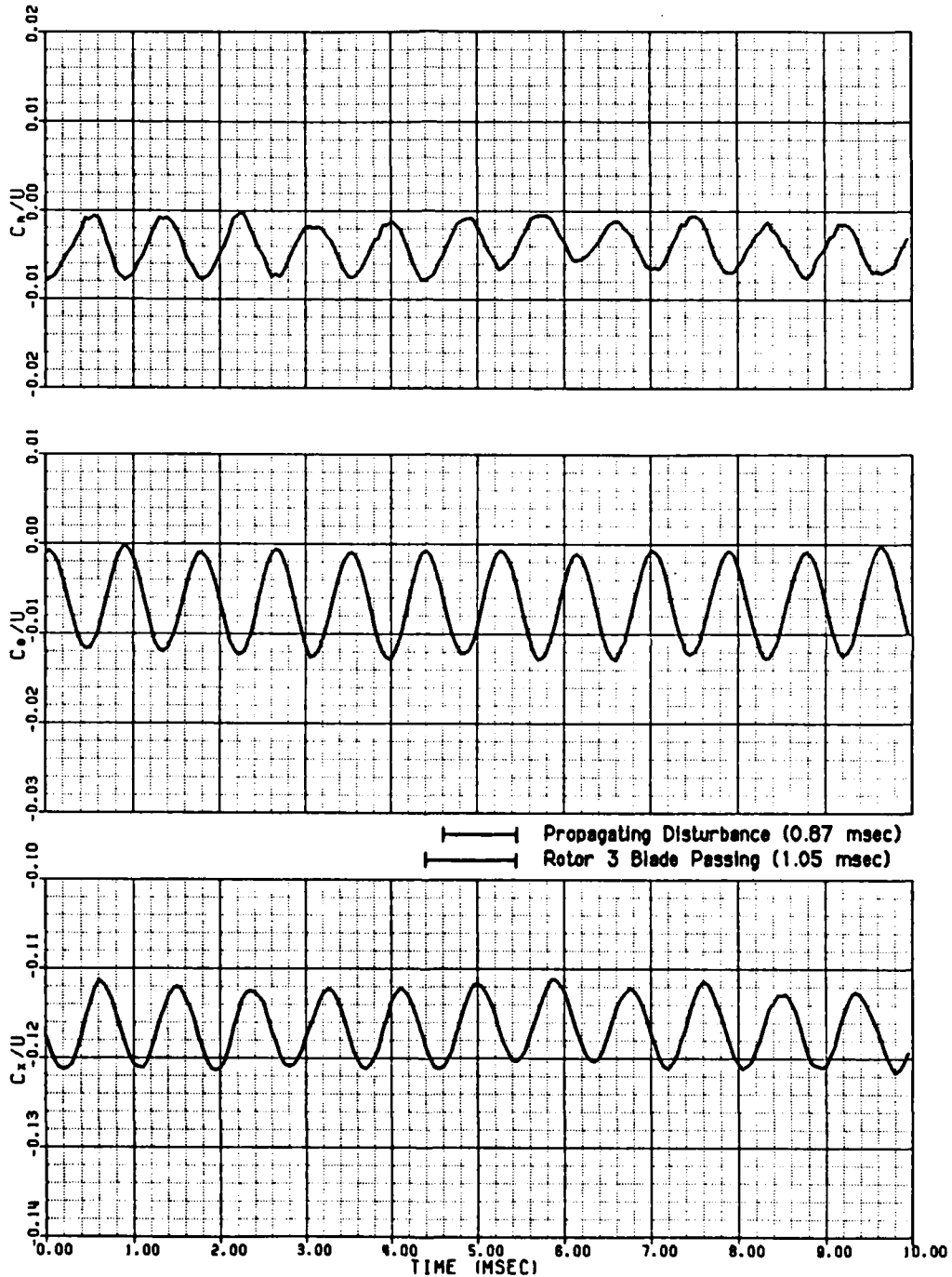
Figure 95   Upstream Velocity Field at Moderate Reversed Flows

339

Figure 96   Upstream Effective Cooling Velocity Measurements
at Moderate Reversed Flows

340

LOCAL FLOW COEFFICIENTS
(128 TRACE ENSEMBLE AVERAGE)
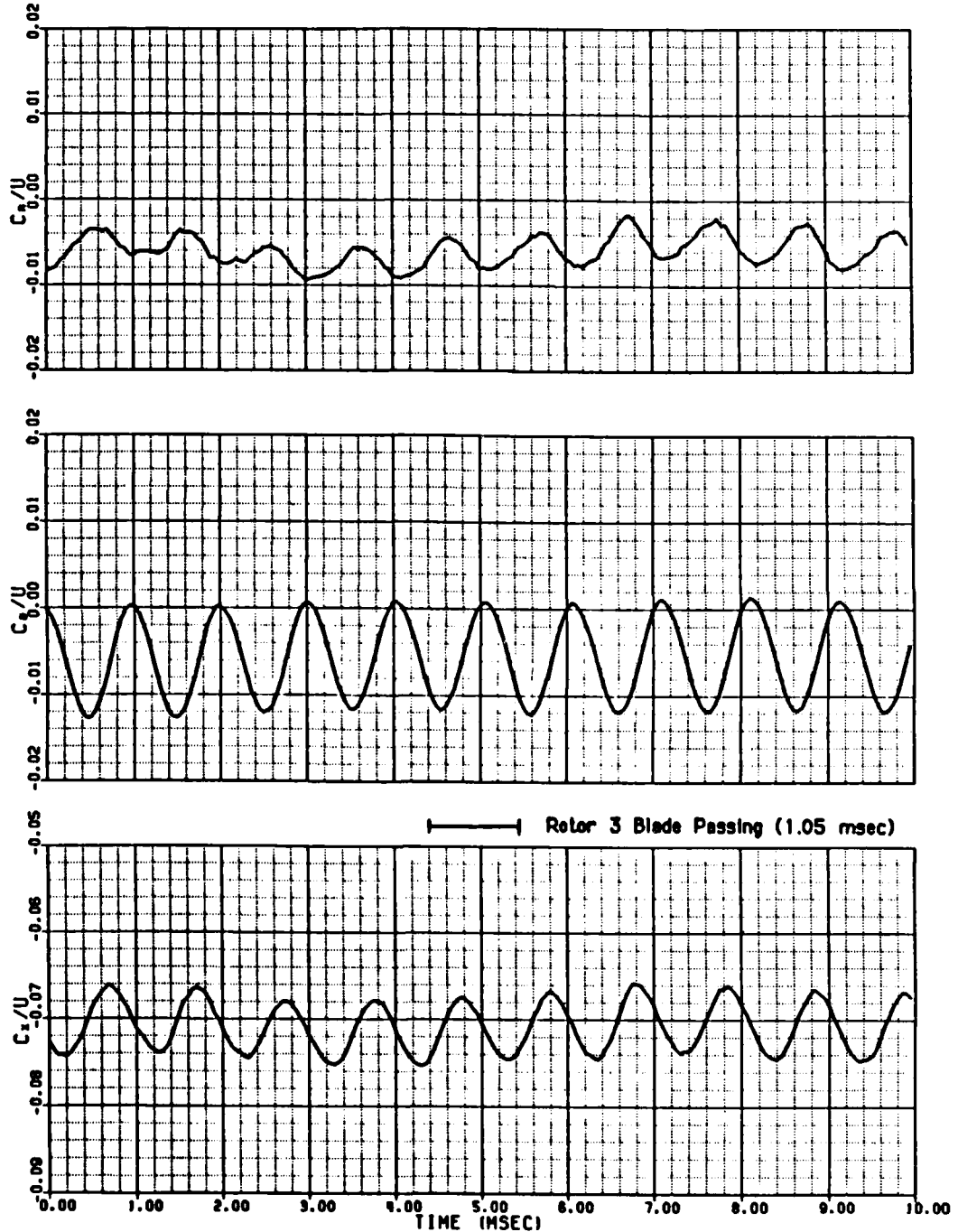
Figure 97   Upstream Velocity Field at Low Reversed Flows

341

LOCAL FLOW COEFFICIENTS
(128 TRACE ENSAMBLE AVERAGE)

DATE:	9/27/85	PROBE POSITION DATA:		MEAN FLOW COEFFICIENTS:	
SENSOR SERIAL NUMBER:	1	AXIAL STATION 9		C_X/U =	-0.199
SYNCHRONOUS TRIGGER		CIRCUMFERENTIAL POSITION .2		C_θ/U =	-0.012
SAMPLE RATE [KHZ]:	20.0	RADIAL POSITION 4		C_R/U =	-0.016

Rotor 3 Blade Passing (1.05 msec)

TIME (MSEC)

Figure 98   Upstream Velocity Field at High Reversed Flows

342

DATE: 9/28/85   PROBE POSITION DATA: SENSOR ORIENTATIONS [DEG]:
SENSOR SERIAL NUMBER: 1   AXIAL STATION 9   ANGLE "A" . .   35.0
     SYNCHRONOUS TRIGGER   CIRCUMFERENTIAL POSITION . 2   ANGLE "B" . .   55.0
SAMPLE RATE [KHZ]: 20.0   RADIAL POSITION 1   ANGLE "C" . .   15.0

Propagating Disturbance (0.87 msec)
Rotor 3 Blade Passing (1.05 msec)

Figure 99   Random Unsteadiness in the Moderate Reversed Flow
Upstream Flowfield at 15% Blade Span Location
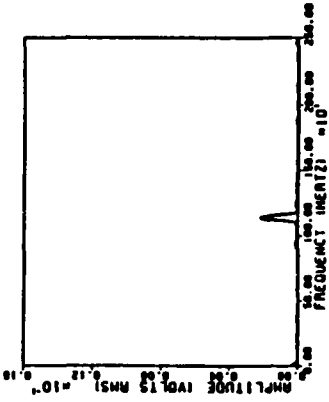
a) $C_x/U = -0.19$

b) $C_x/U = -0.16$

c) $C_x/U = -0.13$

d) $C_x/U = -0.12$
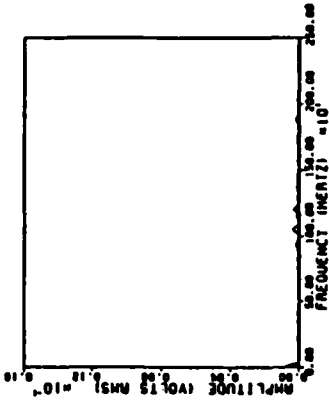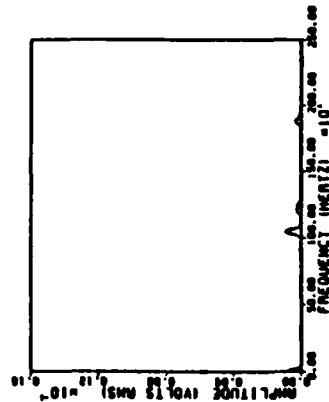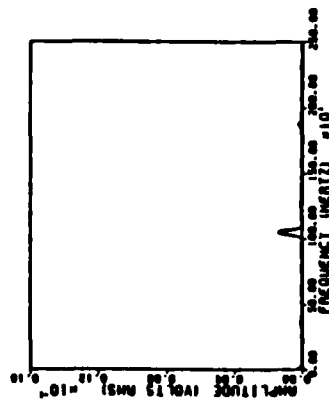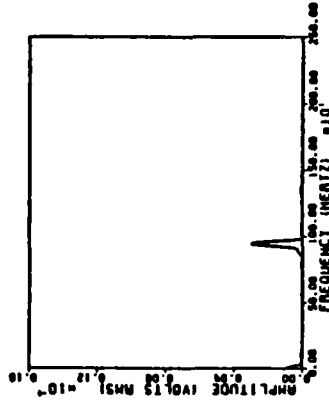
e) $C_x/U = -0.10$

f) $C_x/U = -0.07$

g) $C_x/U = -0.06$

h) $C_x/U = -0.04$
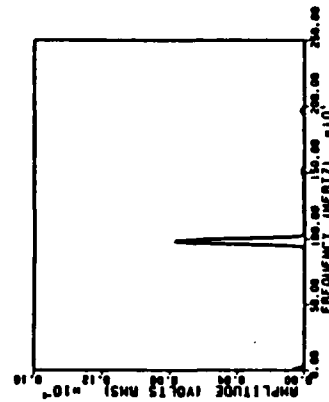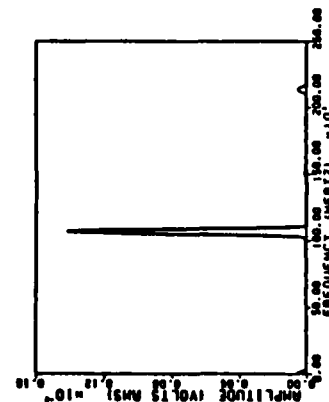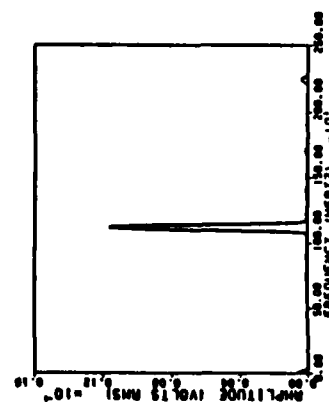
Figure 100   Upstream Wall Static Pressure Spectral Signatures at Several Flow Coefficients

─── INSTANTANEOUS TRACE
─── 128 TRACE ENSEMBLE AVERAGE

DATE: 3 /29/85

SYNCHRONOUS   TRIGGER
TRANSDUCER SERIAL NO.   C260
AMPLIFIER NO.   3
AXIAL STATION 9
CIRCUMFERENTIAL POSITION 2

CALIBRATION DATA:

	ZERO DRIFT (MV)	SENSITIVITY (MV/IN H_2O)	STD DEV (IN H_2O)
PRE-RUN	29.8	45.1	0.053
POST-RUN	-19.0	47.2	0.042
RUN AVG	14.3	45.7	

PRESSURE DATA (IN H_2O):

AVERAGE . . . . . . -0.971
MAXIMUM . . . . . . -0.552
MINIMUM . . . . . . -1.377
CORRECTED AVG . . .   3.126
BLADE REFERENCE . .   2.949

├────┤ Propagating Disturbance (0.87 msec)
├────────┤ Rotor 3 Blade Passing (1.05 msec)
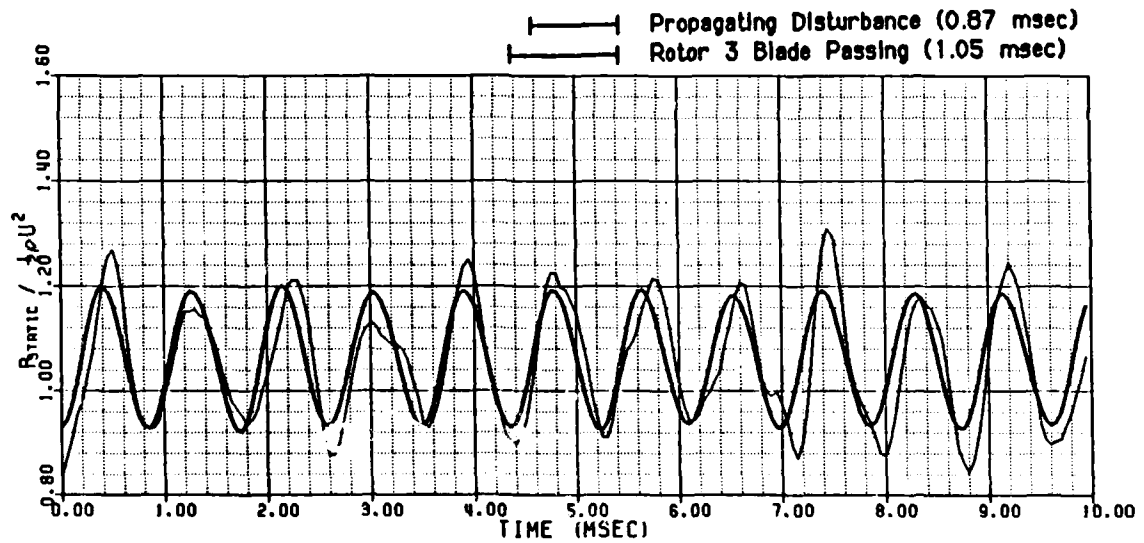
Figure 101   Upstream Wall Static Pressure at Moderate
Reversed Flows

345

(128 TRACE ENSEMBLE AVERAGE)

DATE: 3 /29/85

SYNCHRONOUS TRIGGER
TRANSDUCER SERIAL NO. C260
AMPLIFIER NO. 3

AXIAL STATION 9
CIRCUMFERENTIAL POSITION 10

AXIAL STATION 9
CIRCUMFERENTIAL POSITION 2
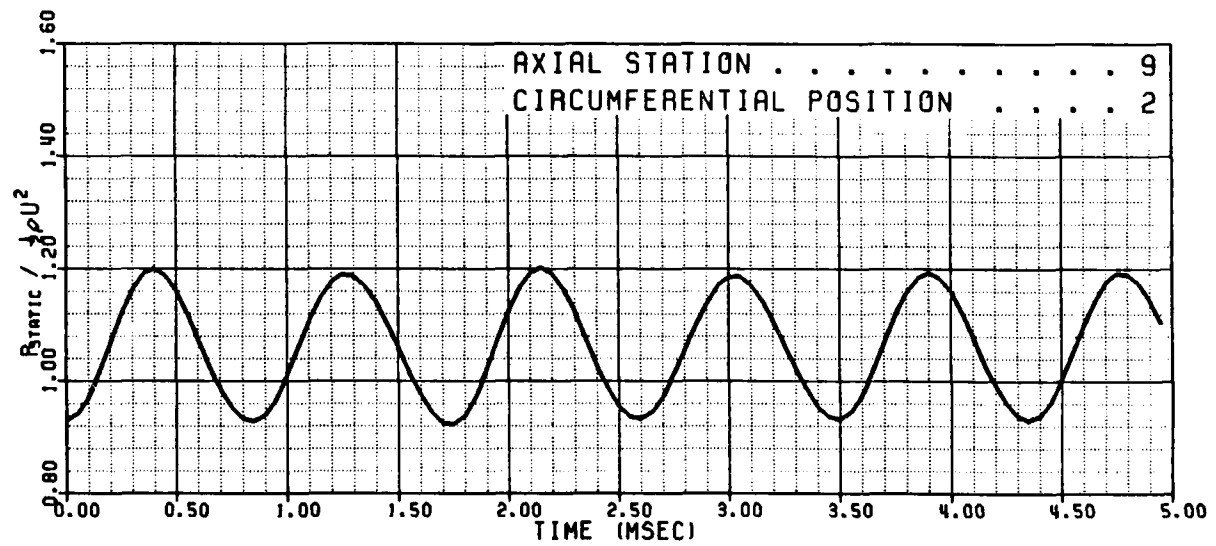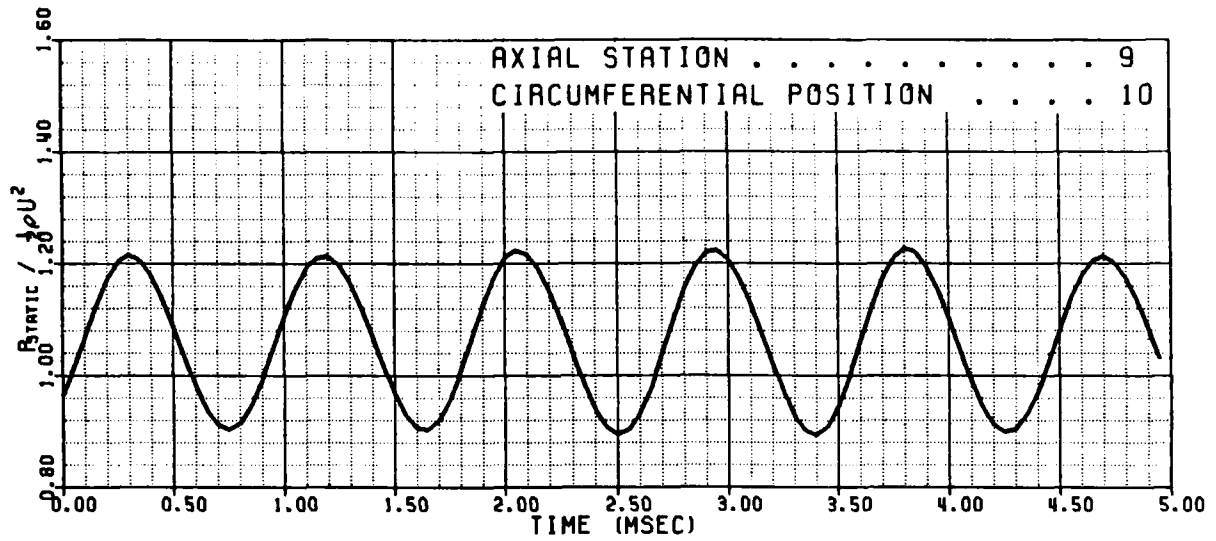
Figure 102   Upstream Wall Static Pressure Circumferential Survey
at Moderate Reversed Flows

346

```
────── INSTANTANEOUS TRACE
────── 128 TRACE  ENSEMBLE AVERAGE

        DATE:        3 /28/85

            SYNCHRONOUS  TRIGGER
        TRANSDUCER SERIAL NO.    C259
          AMPLIFIER NO.               3
      AXIAL STATION . . . . . . . . . . 9
      CIRCUMFERENTIAL POSITION  . . . . 2
      RADIAL POSITION . . . . . . . . . 4
      PROBE YAW ANGLE (DEG TDC) . . . . 0
```

CALIBRATION DATA:

	ZERO DRIFT (MV)	SENSITIVITY (MV/IN H_2O)	STD DEV (IN H_2O)
PRE-RUN	-2.7	78.2	0.013
POST-RUN	-41.3	82.5	0.077
RUN AVG	-18.3	79.9	

PRESSURE DATA (IN H_2O):

```
            AVERAGE . . . . . .  -0.145
            MAXIMUM . . . . . .   0.190
            MINIMUM . . . . . .  -0.474
            CORRECTED AVG . . .   3.185
            BLADE REFERENCE . .   2.949
```
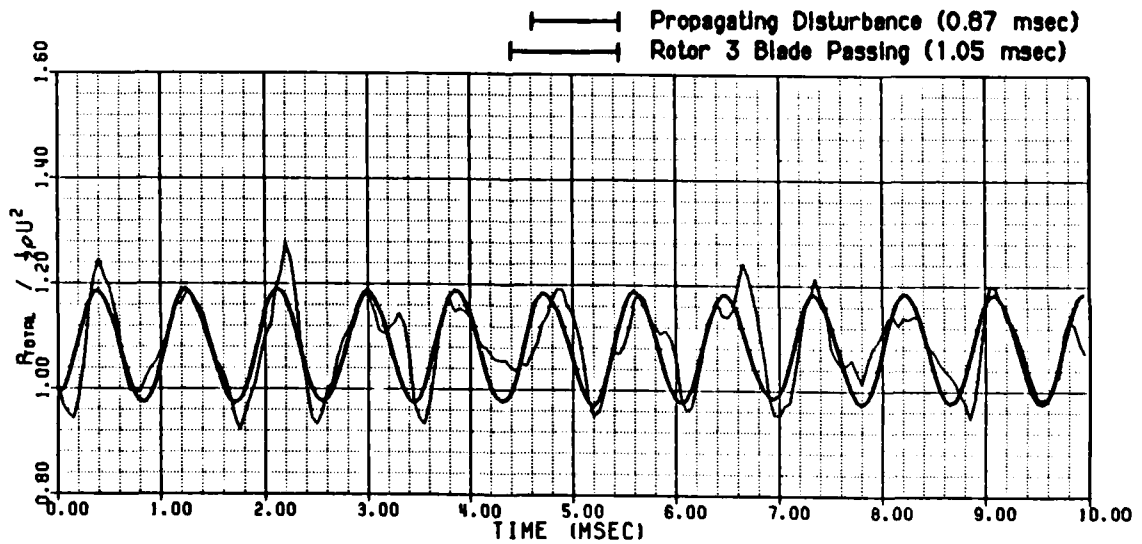

Figure 103 Upstream Total Pressure at Moderate Reversed Flow

Figure 104 Axial Station #8 Velocity Field at Moderate
Reversed Flows and the 85% Blade Span Location

348

Figure 105   Axial Station #8 Effective Cooling Velocity Measurements
at Moderate Reversed Flows and the 85% Blade Span Location

DATE: 2 /22/85
SENSOR SERIAL NUMBER: 1
ROTOR LOCKED TRIGGER
SAMPLE RATE [KHZ]: 20.0

PROBE POSITION DATA:
AXIAL STATION 8
CIRCUMFERENTIAL POSITION . 4
RADIAL POSITION 4

MEAN FLOW COEFFICIENTS:
C_X/U =   -0.118
C_θ/U =   -0.029
C_R/U =   0.036

Propagating Disturbance (0.87 msec)
Rotor 3 Blade Passing (1.05 msec)

TIME (MSEC)
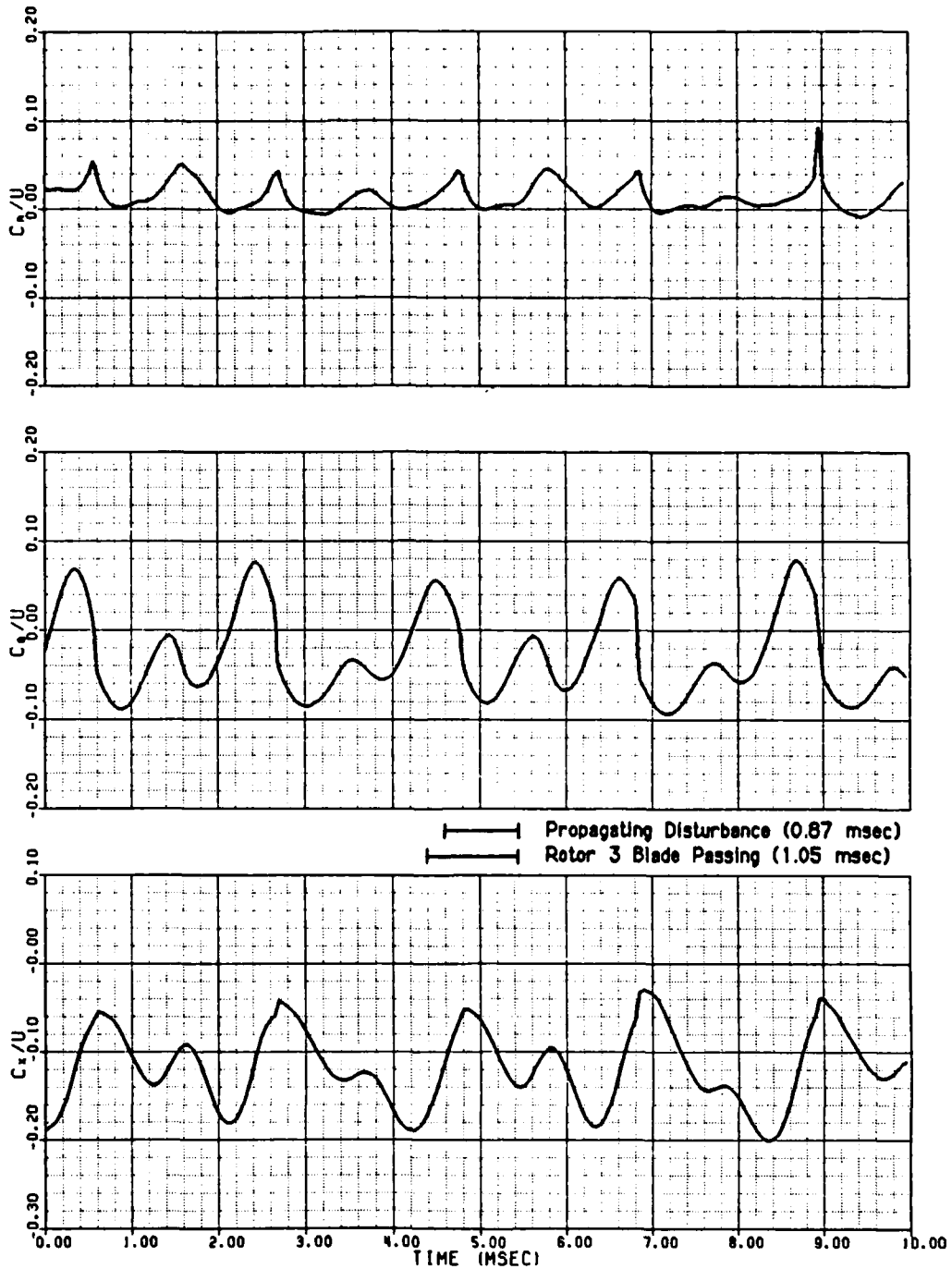
Figure 106   Axial Station #8 Velocity Field at Moderate
Reversed Flows and the 70% Blade Span Location

350

DATE: 2/22/85   PROBE POSITION DATA: MEAN FLOW COEFFICIENTS:
SENSOR SERIAL NUMBER: 1   AXIAL STATION . . . . 8 C_X/U =   -0.123
ROTOR LOCKED TRIGGER   CIRCUMFERENTIAL POSITION . 4 C_θ/U =   -0.045
SAMPLE RATE [KHZ]: 20.0   RADIAL POSITION . . . . . . 3 C_R/U =   0.048

Propagating Disturbance (0.87 msec)
Rotor 3 Blade Passing (1.05 msec)

Figure 107   Axial Station #8 Velocity Field at Moderate
Reversed Flows and the 50% Blade Span Location

351

Figure 108 Axial Station #8 Velocity Field at Moderate
Reversed Flows and the 30% Blade Span Location

(128 TRACE ENSAMBLE AVERAGE)

Propagating Disturbance (0.87 msec)
Rotor 3 Blade Passing (1.05 msec)

Figure 109   Axial Station #8 Velocity Field at Moderate
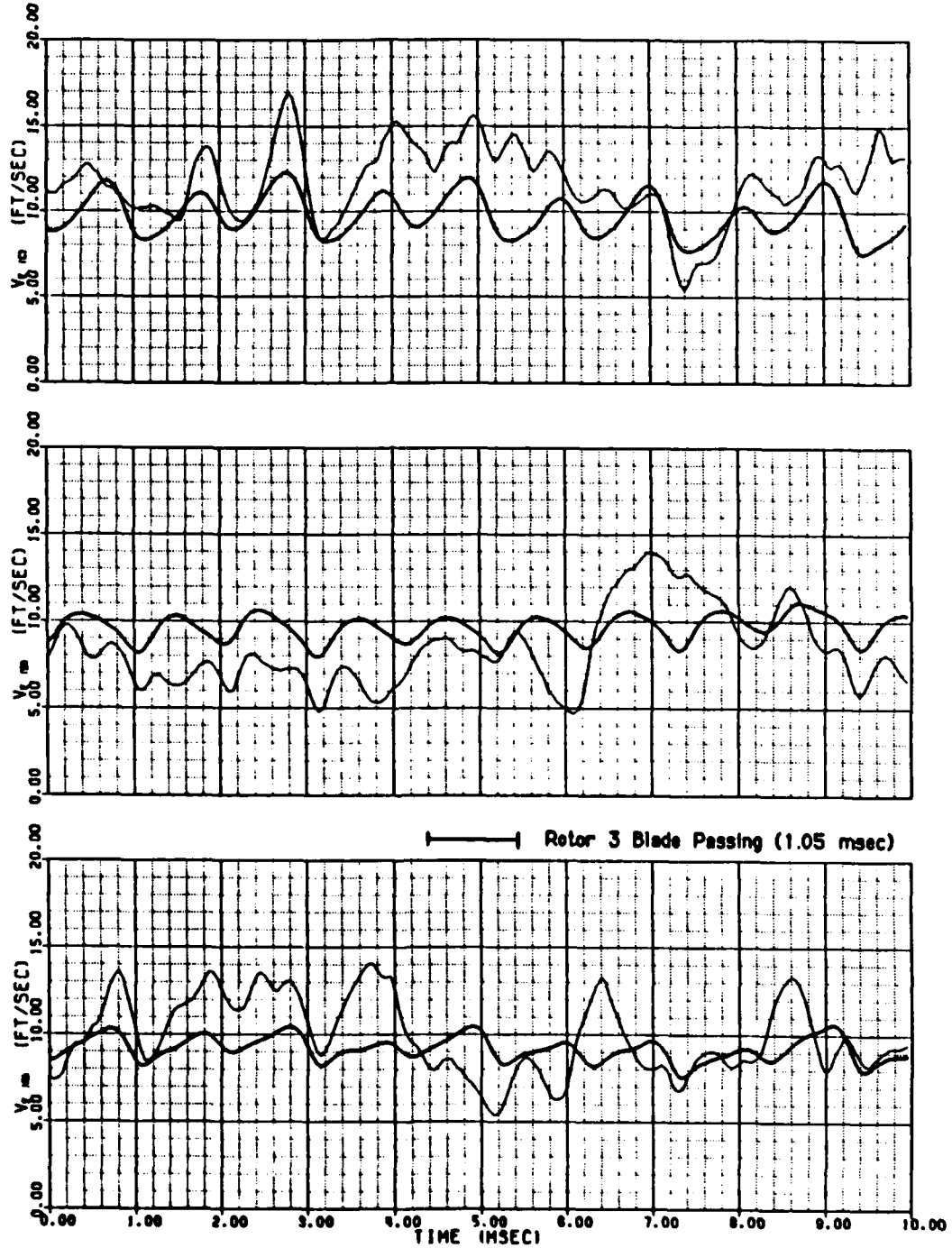Reversed Flows and the 15% Blade Span Location

353
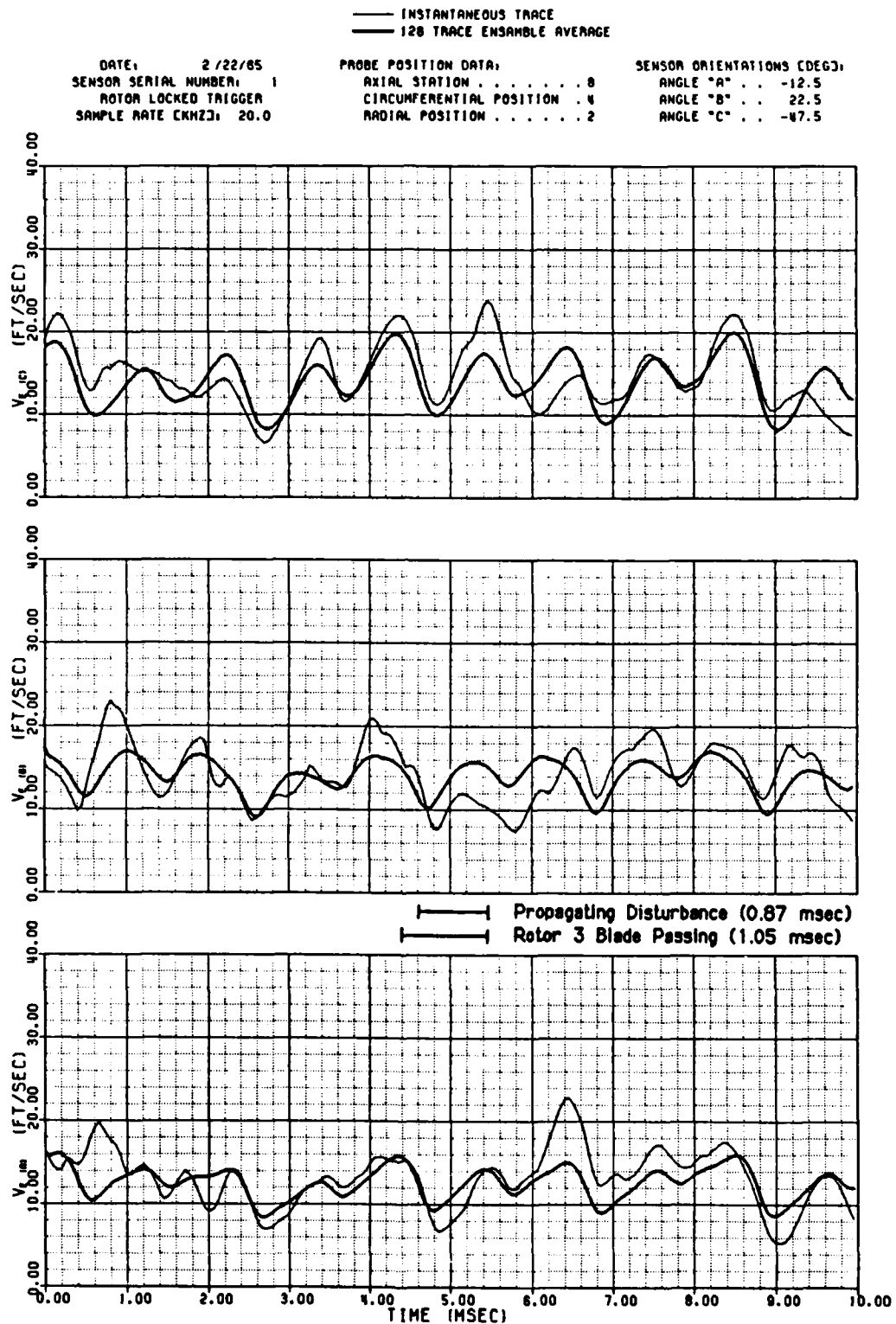
Figure 110 Axial Station #8 Effective Cooling Velocity Measurements
at Moderate Reversed Flows and the 30% Blade Span Location
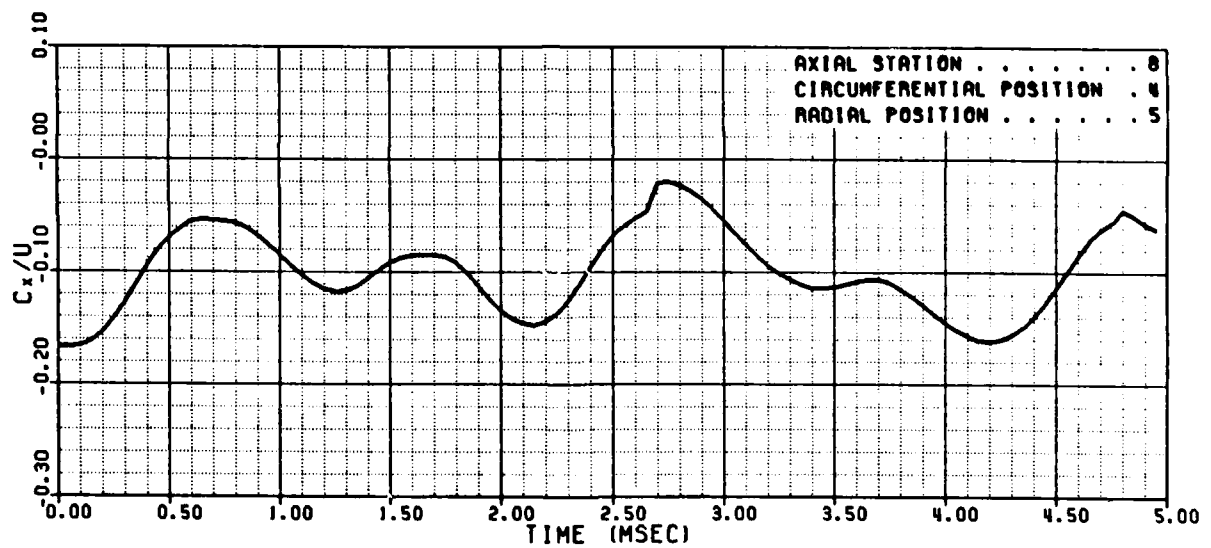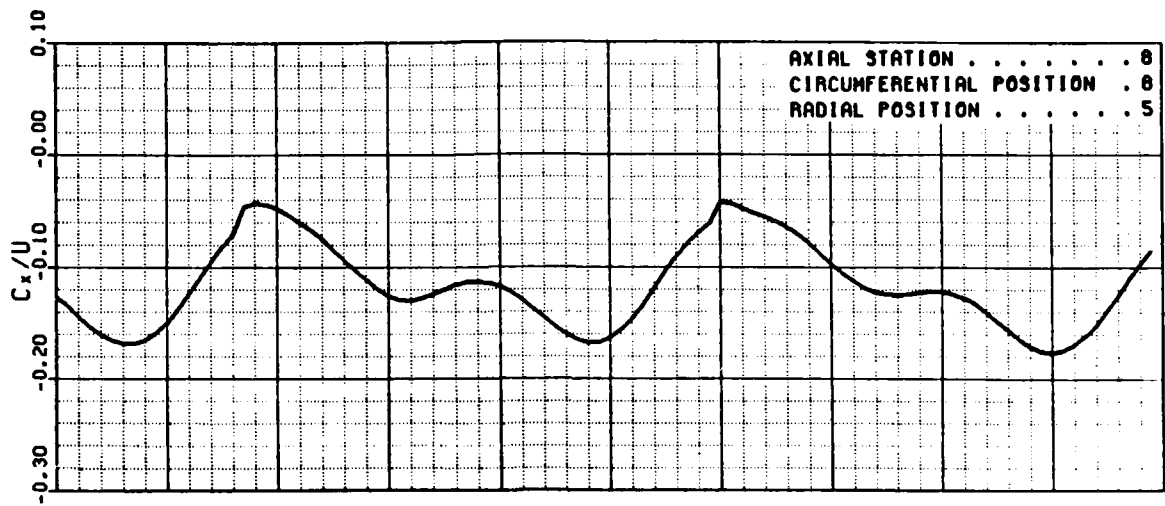
Figure 111 Axial Station #8 Axial Velocity Component
Circumferential Survey at Moderate Reversed Flows
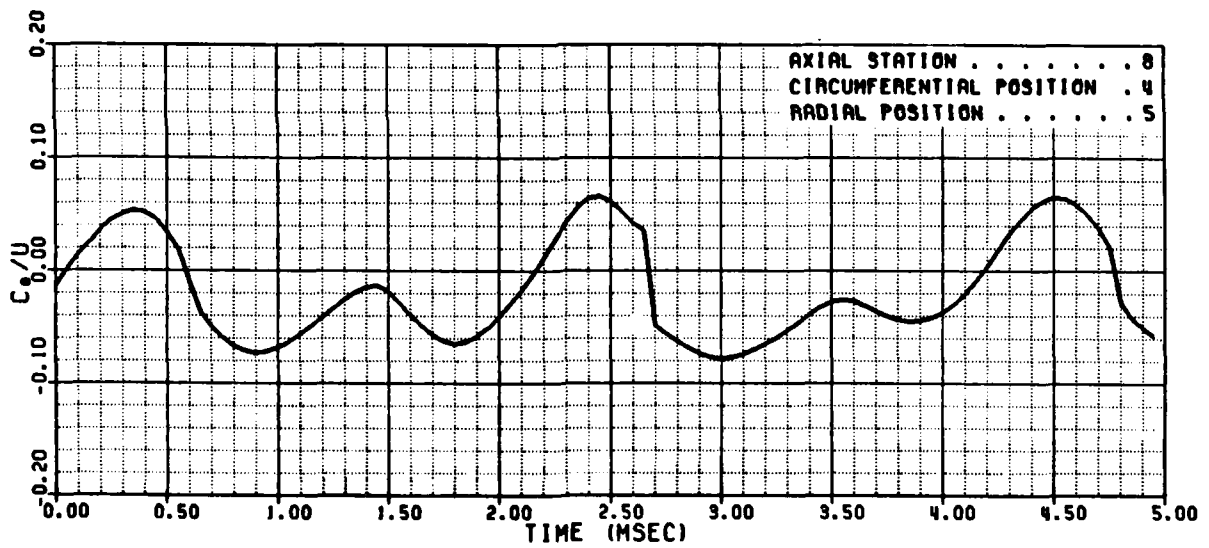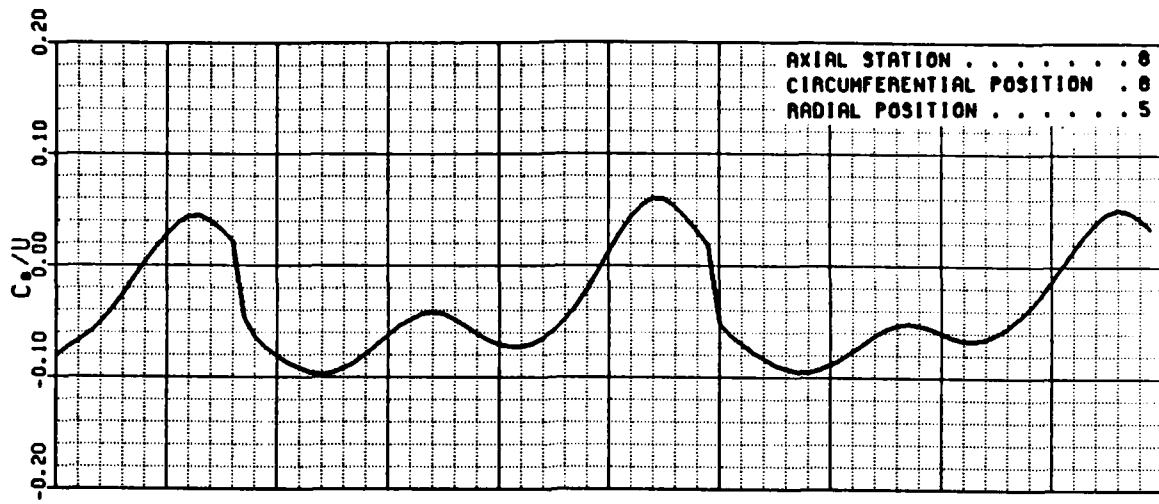
Figure 112   Axial Station #8 Tangential Velocity Component
Circumferential Survey at Moderate Reversed Flows

356

─── INSTANTANEOUS TRACE
─── 032 TRACE ENSEMBLE AVERAGE

DATE: 3 /29/85

SYNCHRONOUS TRIGGER
TRANSDUCER SERIAL NO.   C259
AMPLIFIER NO.   3
AXIAL STATION 8
CIRCUMFERENTIAL POSITION 6
RADIAL POSITION 5
PROBE YAW ANGLE (DEG TDC) . . . . -10

CALIBRATION DATA:

	ZERO DRIFT (MV)	SENSITIVITY (MV/IN H_2O)	STD DEV (IN H_2O)
PRE-RUN	26.9	82.6	0.047
POST-RUN	398.2	79.2	0.043
RUN AVG	324.4	79.9	

PRESSURE DATA (IN H_2O):

AVERAGE 0.243
MAXIMUM 1.145
MINIMUM . . . . . . -0.585
CORRECTED AVG . . .   3.155
BLADE REFERENCE . .   2.949
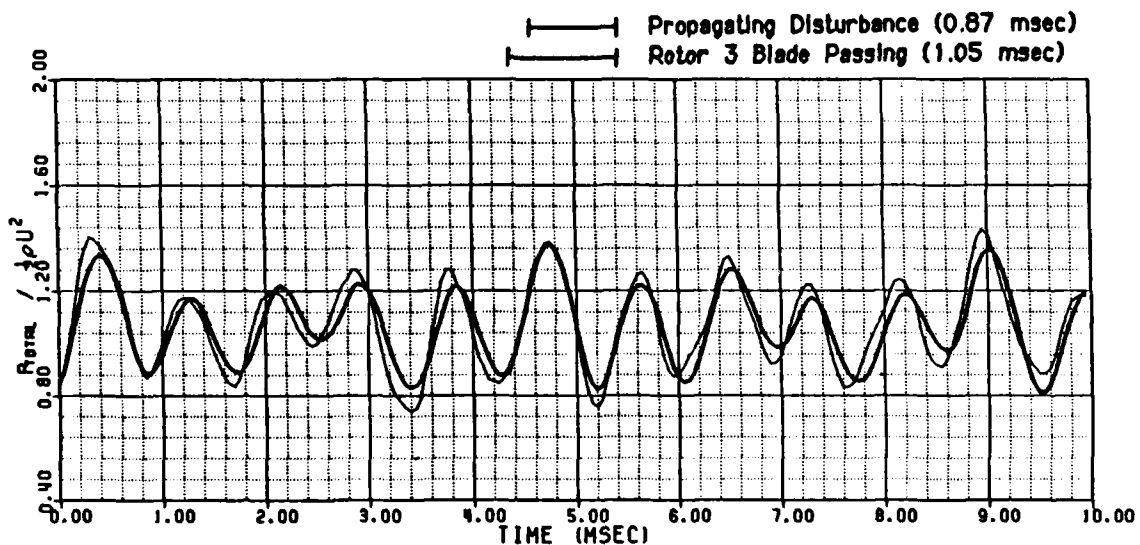
Figure 113 Axial Station #8 Total Pressure Measurement at Moderate Reversed Flows and the 85% Blade Span Location

───── INSTANTANEOUS TRACE
───── 032 TRACE ENSEMBLE AVERAGE

DATE: 3 /29/85

SYNCHRONOUS TRIGGER
TRANSDUCER SERIAL NO.   C259
AMPLIFIER NO.   3
AXIAL STATION 8
CIRCUMFERENTIAL POSITION 6
RADIAL POSITION 2
PROBE YAW ANGLE (DEG TDC) . . . . -10

CALIBRATION DATA:

	ZERO DRIFT (MV)	SENSITIVITY (MV/IN H$_2$O)	STD DEV (IN H$_2$O)
PRE-RUN	26.9	82.6	0.047
POST-RUN	398.2	79.2	0.043
RUN AVG	336.6	79.8	

PRESSURE DATA (IN H$_2$O):

AVERAGE 1.084
MAXIMUM 1.960
MINIMUM 0.168
CORRECTED AVG . . .   3.160
BLADE REFERENCE . .   2.949

├──────┤ Propagating Disturbance (0.87 msec)
├──────┤ Rotor 3 Blade Passing (1.05 msec)
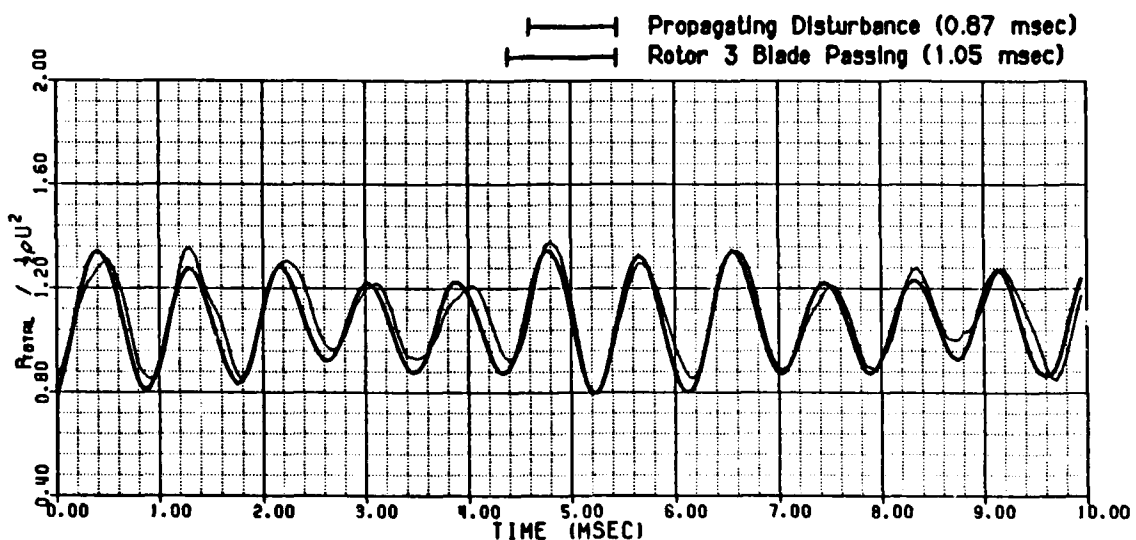
Figure 114 Axial Station #8 Total Pressure Measurement at
Moderate Reversed Flows and the 30% Blade Span Location

358

END

FILMED

DTIC
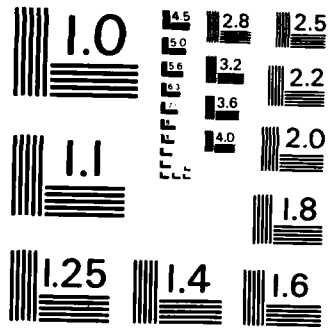
MICROCOPY RESOLUTION TEST CHART

NATIONAL BUREAU OF STANDARDS-1963-A

SPECTRAL ANALYSIS
(TOTAL PRESSURE TRACE)

DATE: 3 /29/85
$C_x/U = -0.10$

TRANSDUCER SERIAL NO.   C259
AMPLIFIER NO.   3

AXIAL STATION 8
CIRCUMFERENTIAL POSITION . . . 6
RADIAL POSITION 5
YAW ANGLE SETTING (DEG TDC) . . -10

SPECTRAL ANALYSIS
(TOTAL PRESSURE TRACE)

DATE: 3 /29/85
$C_x/U = -0.10$

TRANSDUCER SERIAL NO.   C259
AMPLIFIER NO.   3

AXIAL STATION 8
CIRCUMFERENTIAL POSITION . . . 6
RADIAL POSITION 2
YAW ANGLE SETTING (DEG TDC) . . -10
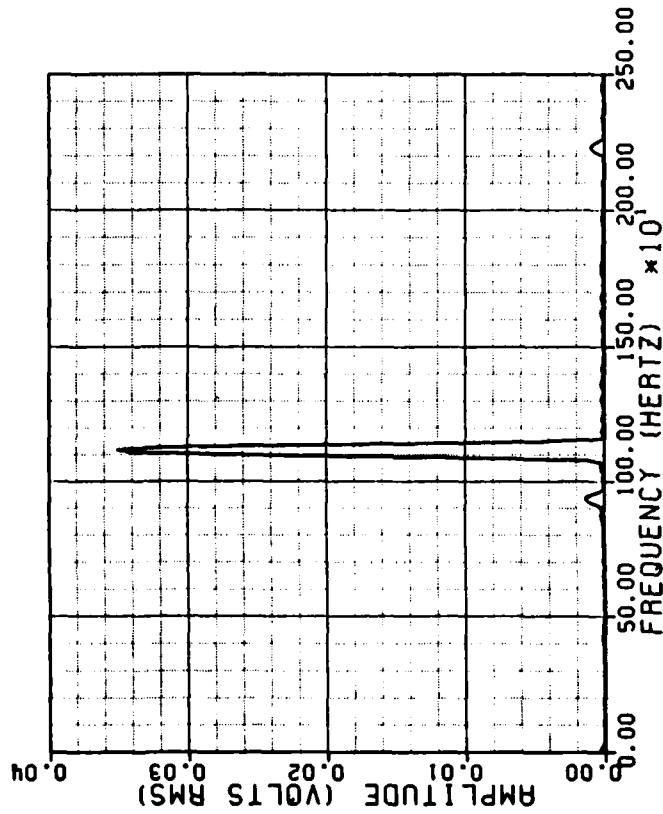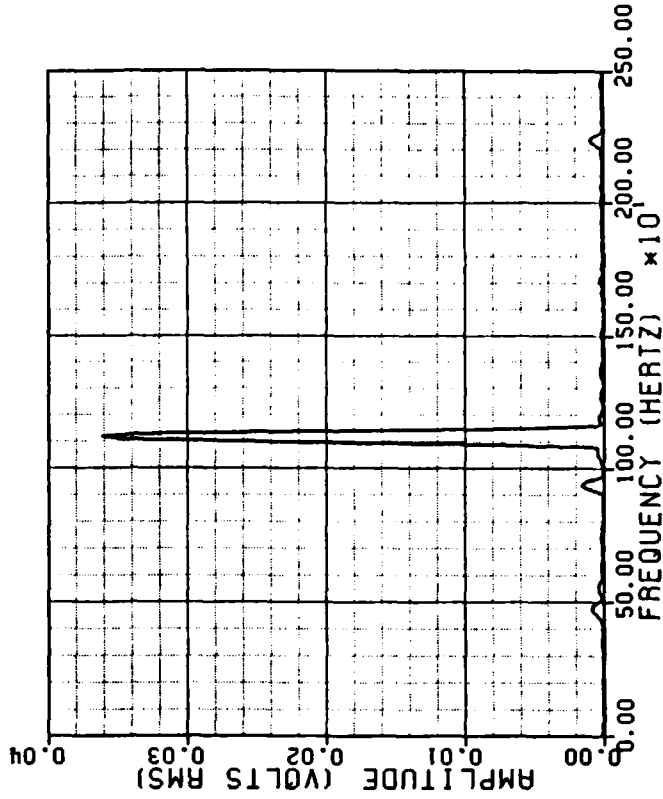
Figure 115   Axial Station #8 Total Pressure Spectral Signatures
at Moderate Reversed Flows

359

(128 TRACE ENSAMBLE AVERAGE)

DATE: 9/26/85	PROBE POSITION DATA:	MEAN FLOW COEFFICIENTS:
SENSOR SERIAL NUMBER: 1	AXIAL STATION 8	C_X/U = -0.173
ROTOR LOCKED TRIGGER	CIRCUMFERENTIAL POSITION . 6	C_θ/U = -0.088
SAMPLE RATE [KHZ]: 20.0	RADIAL POSITION 5	C_R/U = 0.028
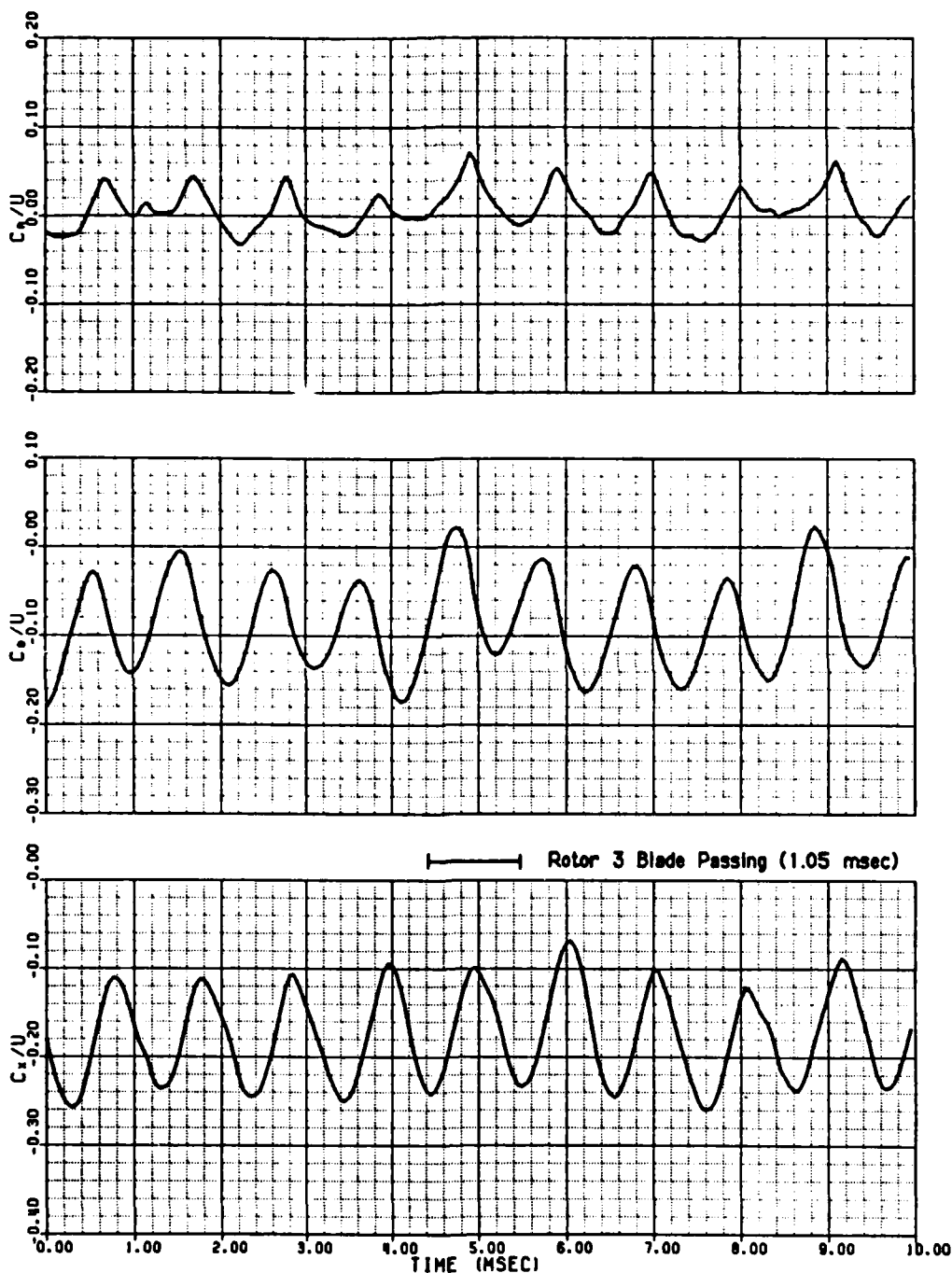
Figure 116 Axial Station #8 Velocity Field at High
Reversed Flows at the 85% Blade Span Location
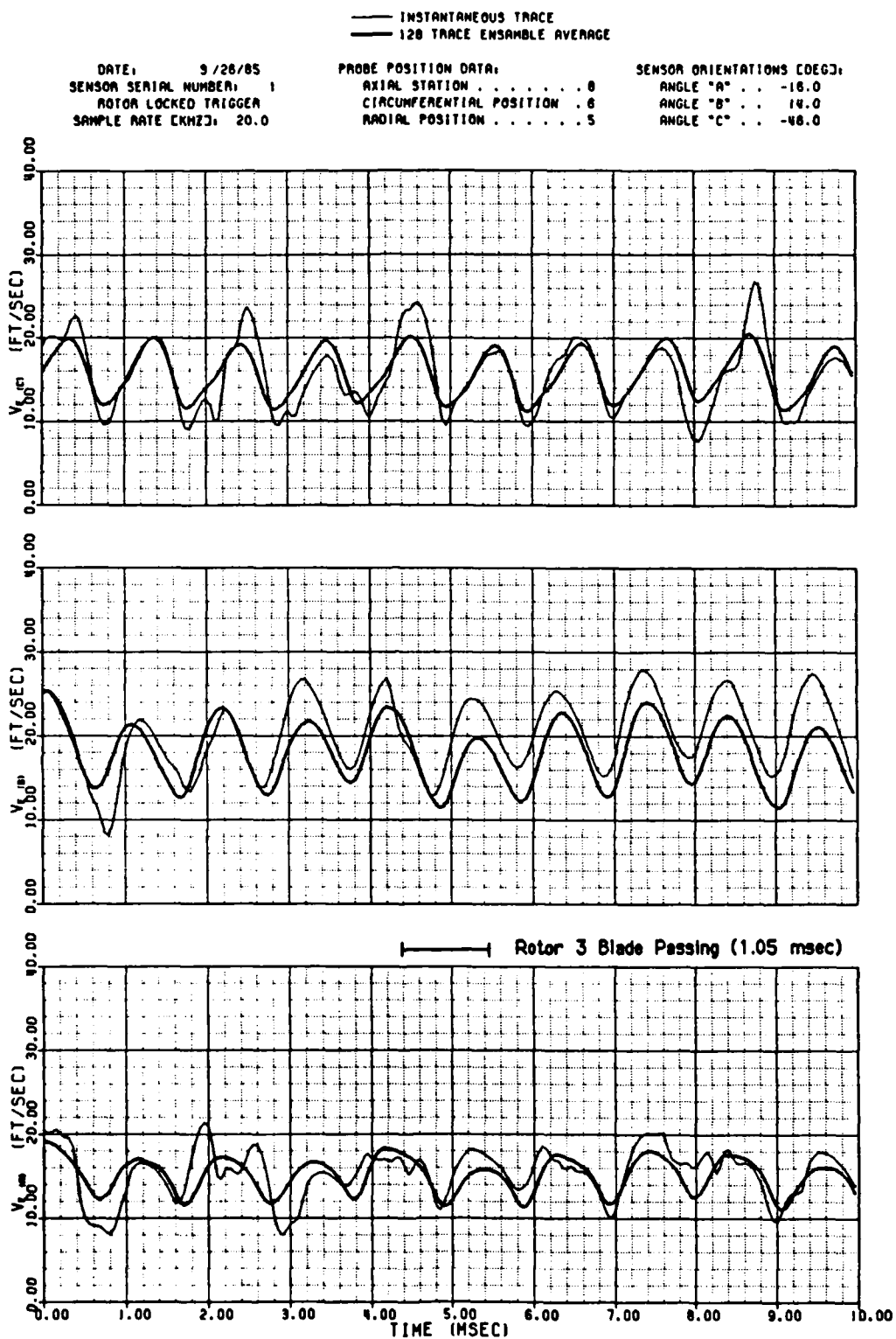
Figure 117 Axial Station #8 Effective Cooling Velocity Measurements at High Reversed Flow and the 85% Blade Span Location

361

———— INSTANTANEOUS TRACE
———— 128 TRACE ENSEMBLE AVERAGE

DATE: 3 /29/85

ROTOR LOCKED TRIGGER
TRANSDUCER SERIAL NO.   C260
AMPLIFIER NO.   3
AXIAL STATION 8
CIRCUMFERENTIAL POSITION 6

CALIBRATION DATA:

	ZERO DRIFT (MV)	SENSITIVITY (MV/IN H_2O)	STD DEV (IN H_2O)
PRE-RUN	29.8	45.1	0.053
POST-RUN	-19.0	47.2	0.042
RUN AVG	-1.6	46.4	

PRESSURE DATA (IN H_2O):

AVERAGE . . . . . .   -1.424
MAXIMUM . . . . . .   -0.728
MINIMUM . . . . . .   -2.128
CORRECTED AVG . . .   8.287
BLADE REFERENCE . .   2.949
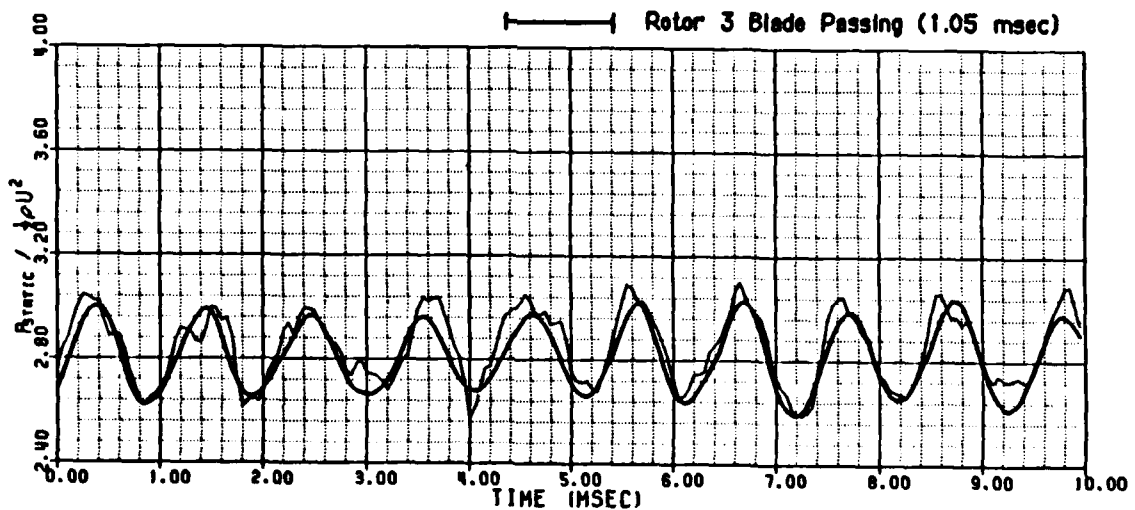
Figure 118   Axial Station #8 Wall Static Pressure Measurement
at High Reversed Flow

362

─── INSTANTANEOUS TRACE
─── 128 TRACE ENSEMBLE AVERAGE

DATE: 3 /29/85

ROTOR LOCKED TRIGGER
TRANSDUCER SERIAL NO.   C259
AMPLIFIER NO.   3
AXIAL STATION 8
CIRCUMFERENTIAL POSITION 6
RADIAL POSITION 5
PROBE YAW ANGLE (DEG TDC) . . . . -16

CALIBRATION DATA:

	ZERO DRIFT (MV)	SENSITIVITY (MV/IN H_2O)	STD DEV (IN H_2O)
PRE-RUN	26.9	82.6	0.047
POST-RUN	398.2	79.2	0.043
RUN AVG	376.5	79.4	

PRESSURE DATA (IN H_2O):

AVERAGE . . . . . . -0.300
MAXIMUM 0.194
MINIMUM . . . . . . -0.841
CORRECTED AVG . . . 8.346
BLADE REFERENCE . . 2.949
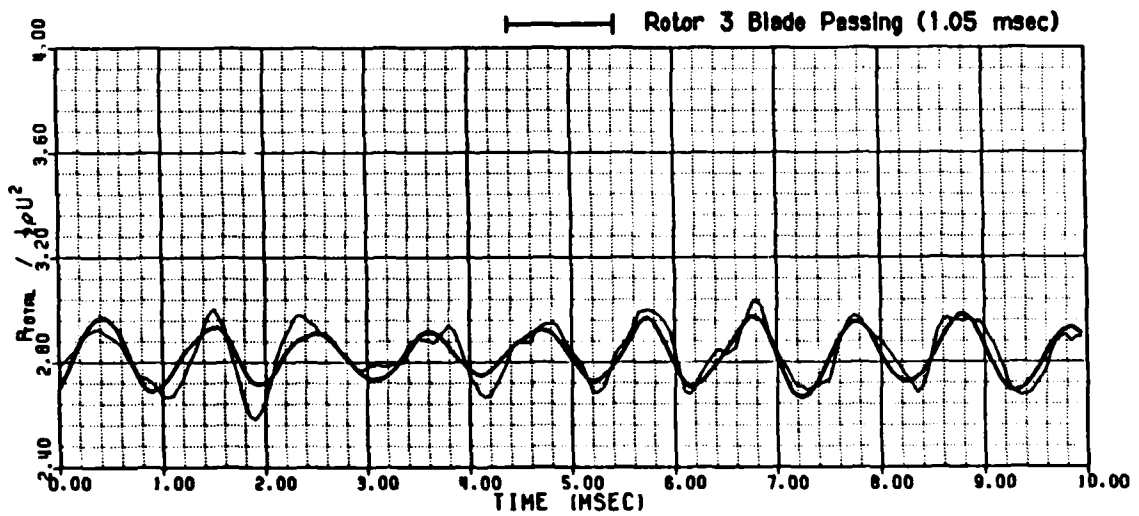
Figure 119 Axial Station #8 Total Pressure Measurement at High
Reversed Flow and the 85% Blade Span Location

Figure 120 Axial Station #8 Wall Static and Total Pressure Spectral Signatures at High Reversed Flows

SENSOR EFFECTIVE VELOCITY

—— INSTANTANEOUS TRACE
—— 120 TRACE ENSAMBLE AVERAGE

DATE: 9/26/85	PROBE POSITION DATA:	SENSOR ORIENTATIONS [DEG]:
SENSOR SERIAL NUMBER: 1	AXIAL STATION 8	ANGLE "A" . . -45.0
ROTOR LOCKED TRIGGER	CIRCUMFERENTIAL POSITION . 10	ANGLE "B" . . -15.0
SAMPLE RATE [KHZ]: 20.0	RADIAL POSITION 3	ANGLE "C" . . -75.0

Figure 121   Axial Station #8 Effective Cooling Velocity Measurements
at Low Reversed Flows and the 50% Blade Span Location

365

LOCAL FLOW COEFFICIENTS
(128 TRACE ENSAMBLE AVERAGE)
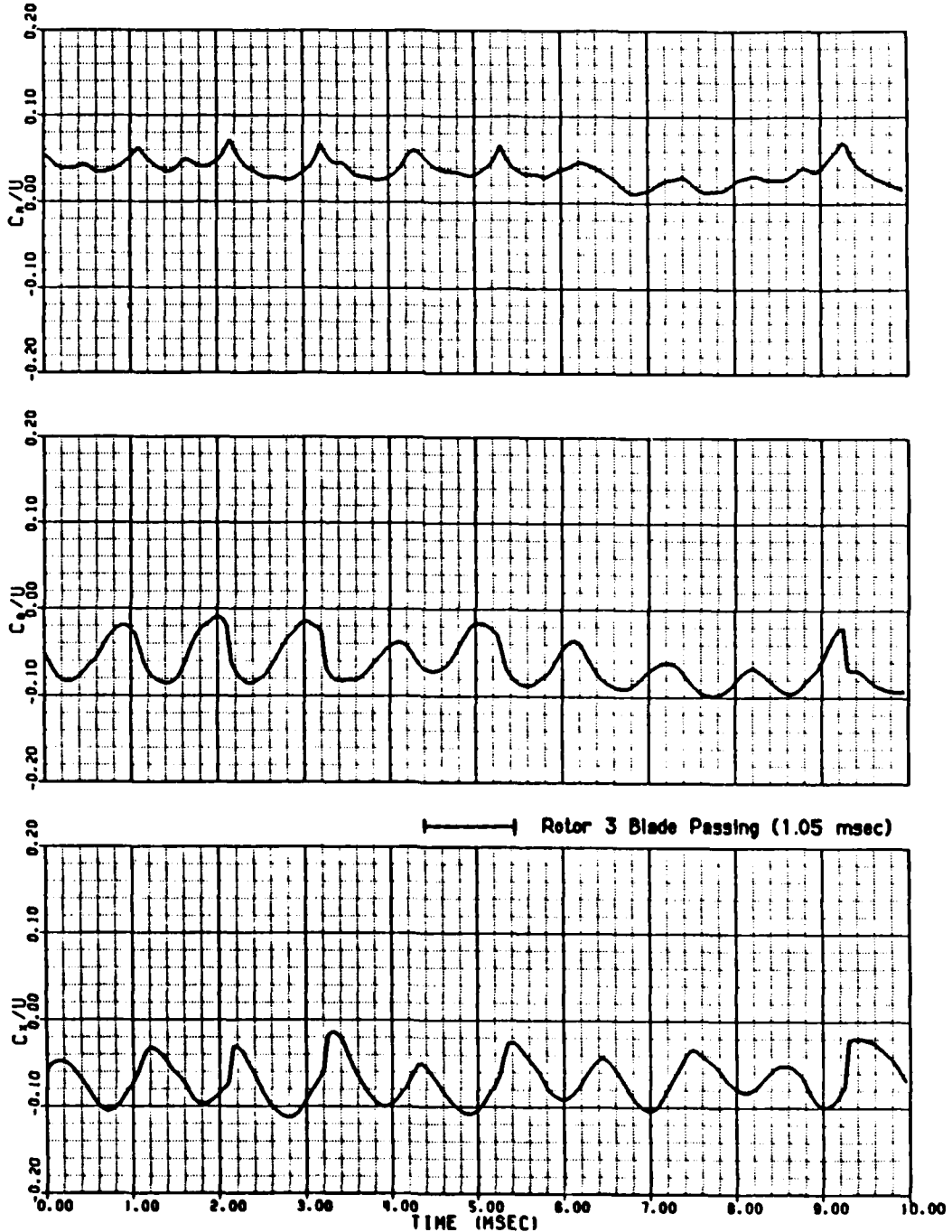
Figure 122   Axial Station #8 Velocity Field at Low Reversed Flow
and the 50% Blade Span Location

366

INSTANTANEOUS TRACE

032 TRACE ENSEMBLE AVERAGE

DATE: 3 /29/85

SYNCHRONOUS TRIGGER
TRANSDUCER SERIAL NO.   C260
AMPLIFIER NO.   3
AXIAL STATION 8
CIRCUMFERENTIAL POSITION 6

CALIBRATION DATA:

	ZERO DRIFT (MV)	SENSITIVITY (MV/IN H$_2$O)	STD DEV (IN H$_2$O)
PRE-RUN	29.8	45.1	0.053
POST-RUN	-19.0	47.2	0.042
RUN AVG	-0.3	46.4	

PRESSURE DATA (IN H$_2$O):

AVERAGE . . . . . . -0.946
MAXIMUM . . . . . . -0.454
MINIMUM . . . . . ·. -1.458
CORRECTED AVG . . . 1.340
BLADE REFERENCE . . 2.949

Figure 123   Axial Station #8 Wall Static Pressure Measurement
at Low Reversed Flow

DATE: 3 /29/85

SYNCHRONOUS TRIGGER
TRANSDUCER SERIAL NO.   C259
AMPLIFIER NO.   3
AXIAL STATION 8
CIRCUMFERENTIAL POSITION 6
RADIAL POSITION 5
PROBE YAW ANGLE (DEG TDC) 85

CALIBRATION DATA:

	ZERO DRIFT (MV)	SENSITIVITY (MV/IN H₂O)	STD DEV (IN H₂O)
PRE-RUN	26.9	82.6	0.047
POST-RUN	398.2	79.2	0.043
RUN AVG	352.2	79.6	

PRESSURE DATA (IN H_2O):

AVERAGE 0.430
MAXIMUM 1.167
MINIMUM . . . . . . -0.204
CORRECTED AVG . . .   1.590
BLADE REFERENCE . .   2.949
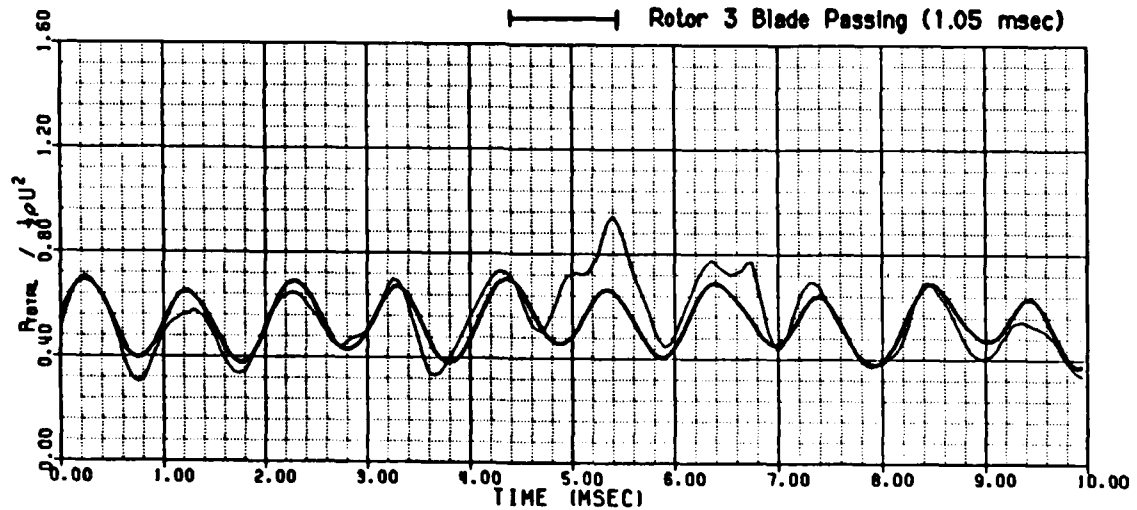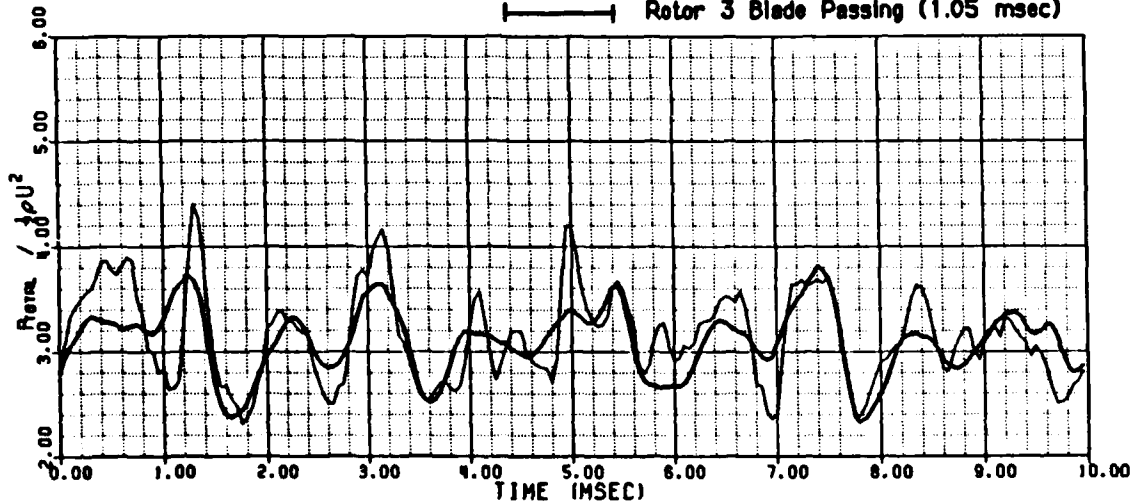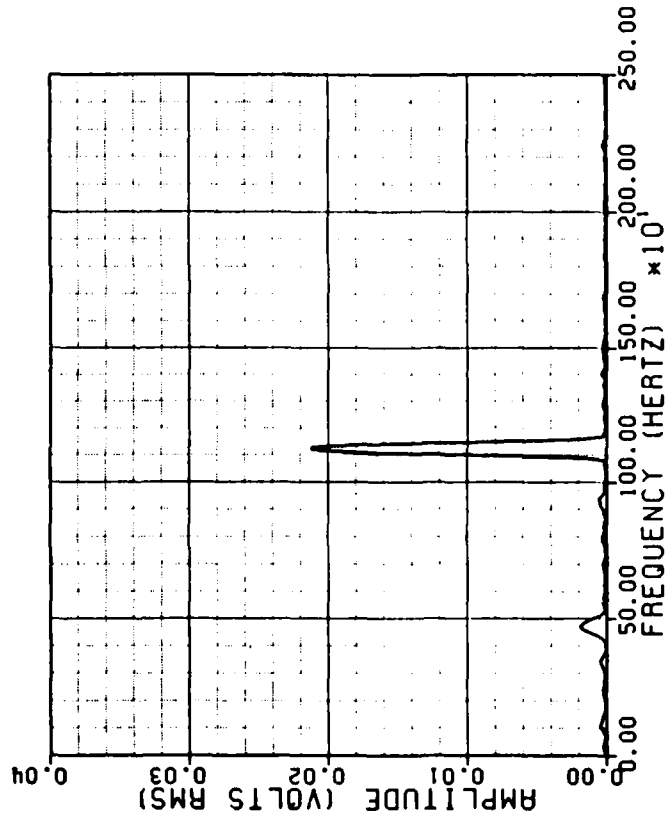

Figure 124   Axial Station #8 Total Pressure Measurement at Low
Reversed Flow and the 85% Blade Span Location

SPECTRAL ANALYSIS
(TOTAL PRESSURE TRACE)

DATE: 3 /29/85
$C_x/U = -0.05$

TRANSDUCER SERIAL NO. C259
AMPLIFIER NO. 3
AXIAL STATION 8
CIRCUMFERENTIAL POSITION . . 6
RADIAL POSITION 5
YAW ANGLE SETTING (DEG TOC) . 85
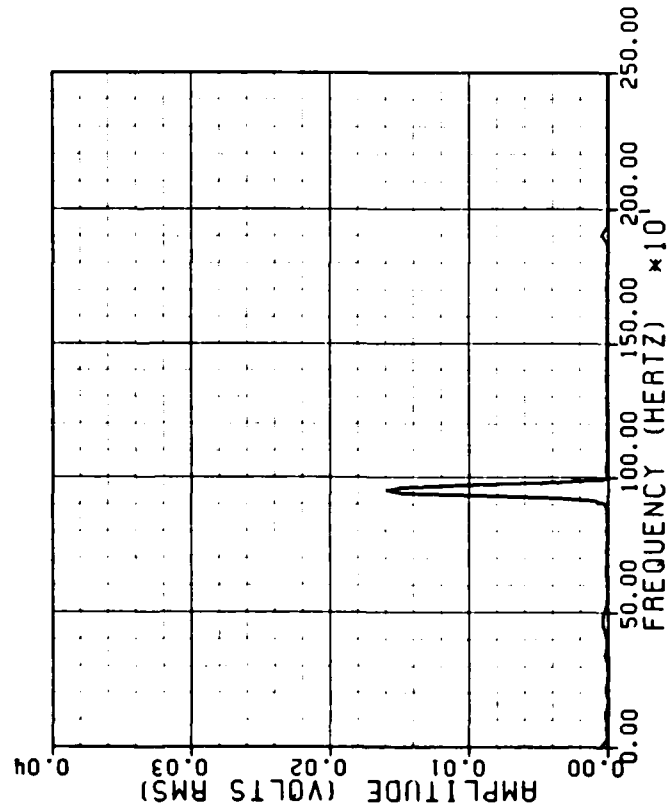
SPECTRAL ANALYSIS
(WALL STATIC PRESSURE TRACE)

DATE: 3 /29/85
$C_x/U = -0.05$

TRANSDUCER SERIAL NO. C260
AMPLIFIER NO. 3
AXIAL STATION 8
CIRCUMFERENTIAL POSITION . . 6
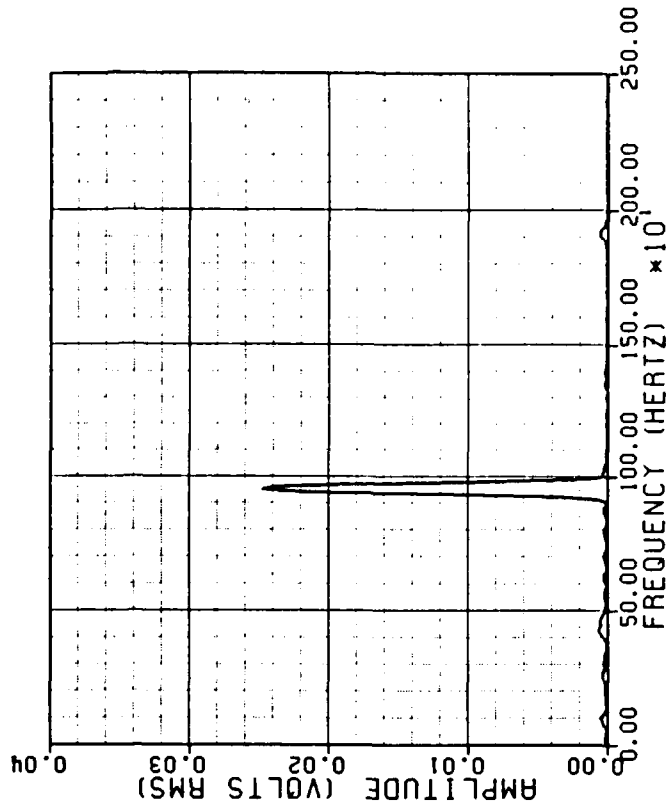
Figure 125 Axial Station #8 Wall Static and Total Pressure Spectral Signatures at Low Reversed flow

369

Figure 126 Axial Station #7 Effective Cooling Velocity Measurements at Moderate Reversed Flows and the 85% Blade Span Location

Propagating Disturbance (0.87 m·sec)
Rotor 3 Blade Passing (1.05 msec)

Figure 127   Axial Station #7 Effective Cooling Velocity Measurements
at Moderate Reversed Flows and the 15% Blade Span Location

371

(128 TRACE ENSAMBLE AVERAGE)

DATE: 2/25/85	PROBE POSITION DATA:	MEAN FLOW COEFFICIENTS:
SENSOR SERIAL NUMBER: 1	AXIAL STATION 7	C_X/U = -0.098
ROTOR LOCKED TRIGGER	CIRCUMFERENTIAL POSITION . 10	C_θ/U = 1.372
SAMPLE RATE [KHZ]: 20.0	RADIAL POSITION 5	C_R/U = -0.032

Propagating Disturbance (0.87 msec)
Rotor 3 Blade Passing (1.05 msec)

Figure 128   Axial Station #7 Velocity Field at Moderate
Reversed Flows and the 85% Blade Span Location

372

DATE: 2/25/85   PROBE POSITION DATA: MEAN FLOW COEFFICIENTS:
SENSOR SERIAL NUMBER: 1   AXIAL STATION . . . . 7 C_X/U =   -0.029
ROTOR LOCKED TRIGGER   CIRCUMFERENTIAL POSITION . 10 C_θ/U =   1.362
SAMPLE RATE [KHZ]: 20.0   RADIAL POSITION . . . . . . 4 C_R/U =   -0.055

Propagating Disturbance (0.87 msec)
Rotor 3 Blade Passing (1.05 msec)

Figure 129   Axial Station #7 Velocity Field at Moderate
Reversed Flows and the 70% Blade Span Location

373

(128 TRACE ENSAMBLE AVERAGE)

DATE: 2/25/85   PROBE POSITION DATA: MEAN FLOW COEFFICIENTS:
SENSOR SERIAL NUMBER: I   AXIAL STATION . . . . . . .7 C_X/U =   0.028
        ROTOR LOCKED TRIGGER   CIRCUMFERENTIAL POSITION . 10 C_θ/U =   1.298
SAMPLE RATE [KHZ]: 20.0   RADIAL POSITION . . . . . .3 C_R/U =   -0.085

Figure 130   Axial Station #7 Velocity Field at Moderate
Reversed Flows and the 50% Blade Span Location

374

DATE: 2/25/85
SENSOR SERIAL NUMBER: 1
ROTOR LOCKED TRIGGER
SAMPLE RATE [KHZ]: 20.0

PROBE POSITION DATA:
AXIAL STATION 7
CIRCUMFERENTIAL POSITION . .10
RADIAL POSITION 2

MEAN FLOW COEFFICIENTS:
C_X/U =   0.095
C_θ/U =   1.174
C_R/U =   -0.061

|———| Propagating Disturbance (0.87 msec)
|———| Rotor 3 Blade Passing (1.05 msec)

TIME (MSEC)
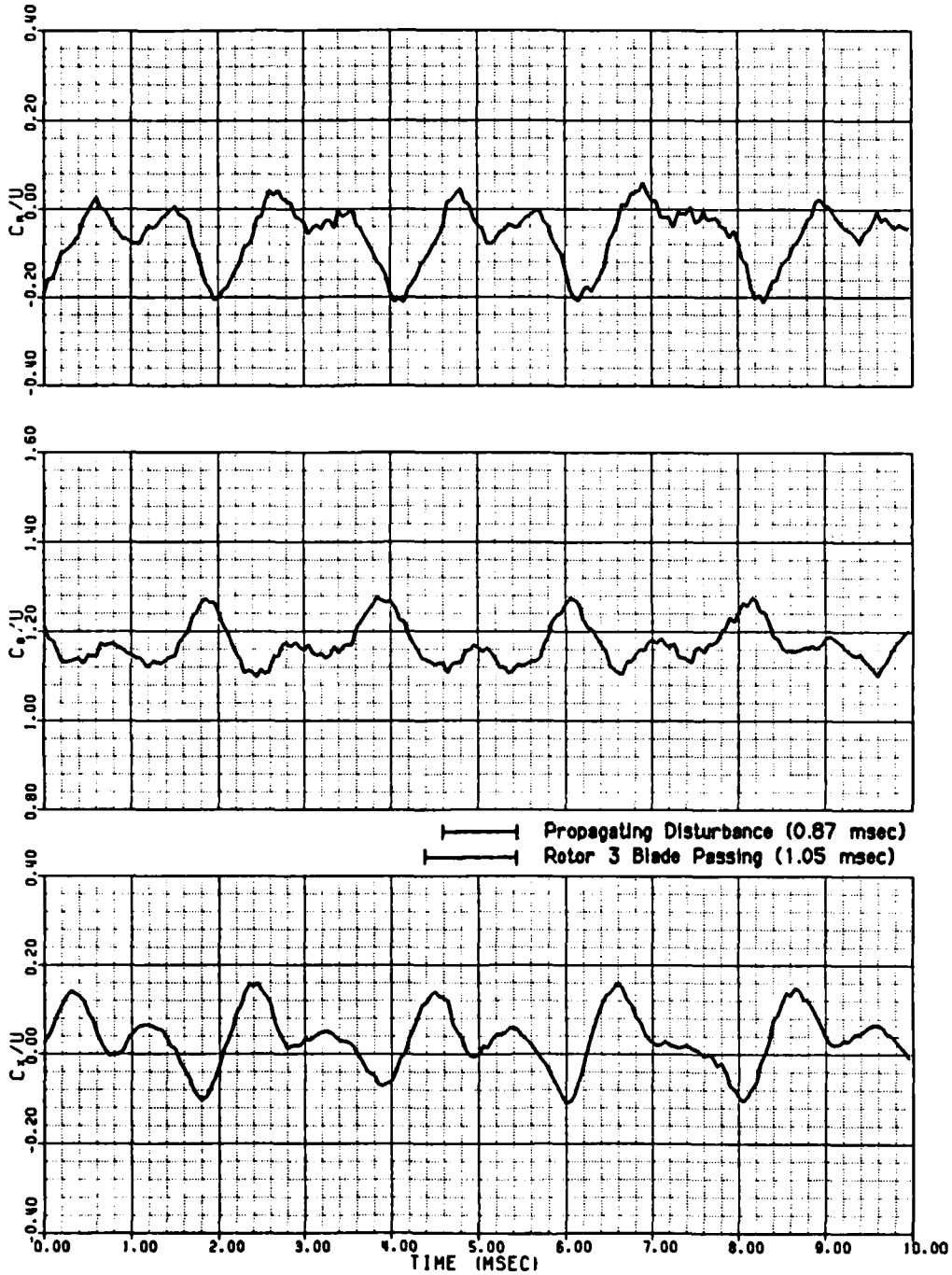
Figure 131   Axial Station #7 Velocity Field at Moderate
Reversed Flows and the 30% Blade Span Location

DATE: 2 /25/85   PROBE POSITION DATA: MEAN FLOW COEFFICIENTS:
SENSOR SERIAL NUMBER: 1   AXIAL STATION . . . . . . .7 C_X/U =   0.019
ROTOR LOCKED TRIGGER   CIRCUMFERENTIAL POSITION .10 C_θ/U =   1.066
SAMPLE RATE [KHZ]:   20.0   RADIAL POSITION . . . . . .1 C_R/U =   -0.043

Propagating Disturbance (0.87 msec)
Rotor 3 Blade Passing (1.05 msec)

TIME (MSEC)
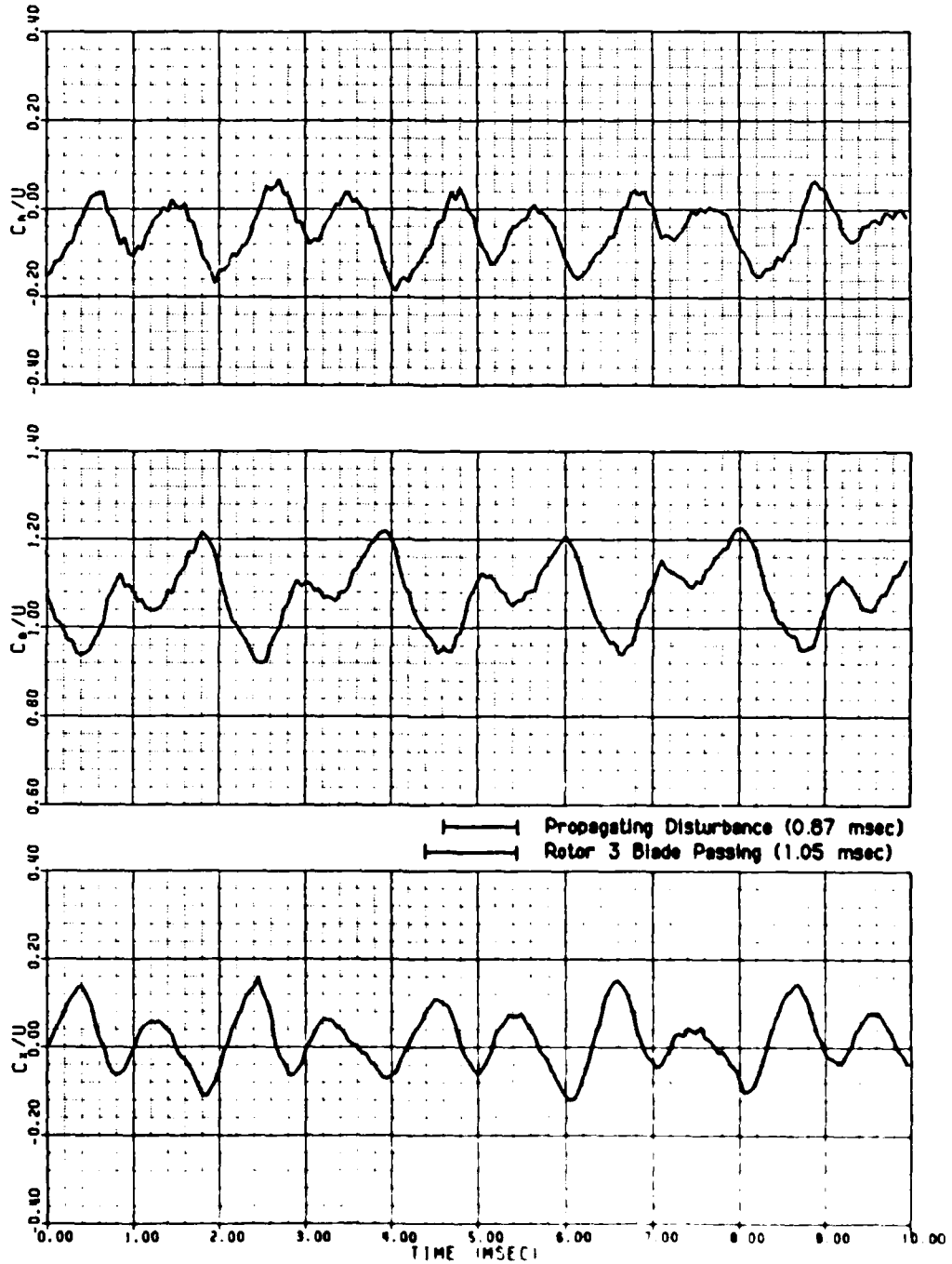
Figure 132   Axial Station #7 Velocity Field at Moderate
Reversed Flows and the 15% Blade Span Location

376

Moderate Reverse Flow

Axial Station #7

Upstream View (Rotor Relative Frame)
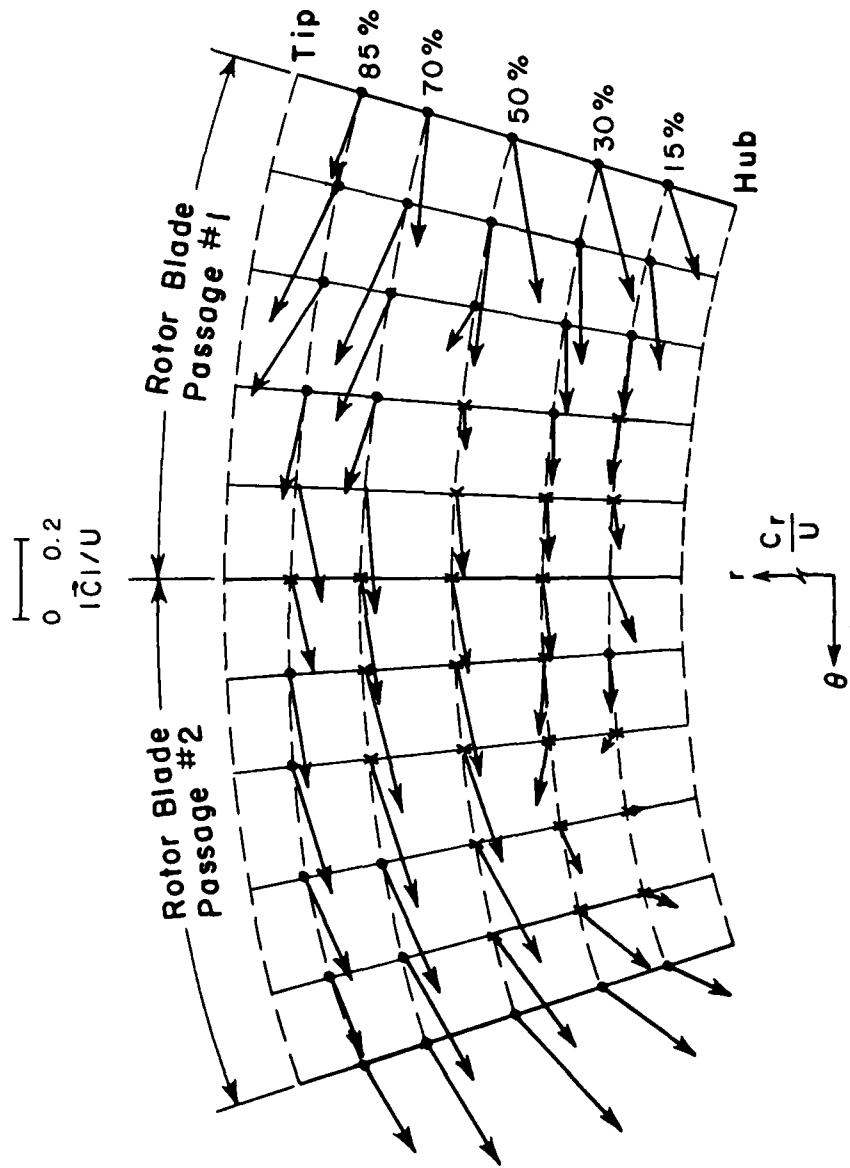
Figure 133   Relative Tangential Velocity vs. Absolute Radial Velocity Crossplot
of the Moderate Reverse Flow Rotor Exit Flowfield
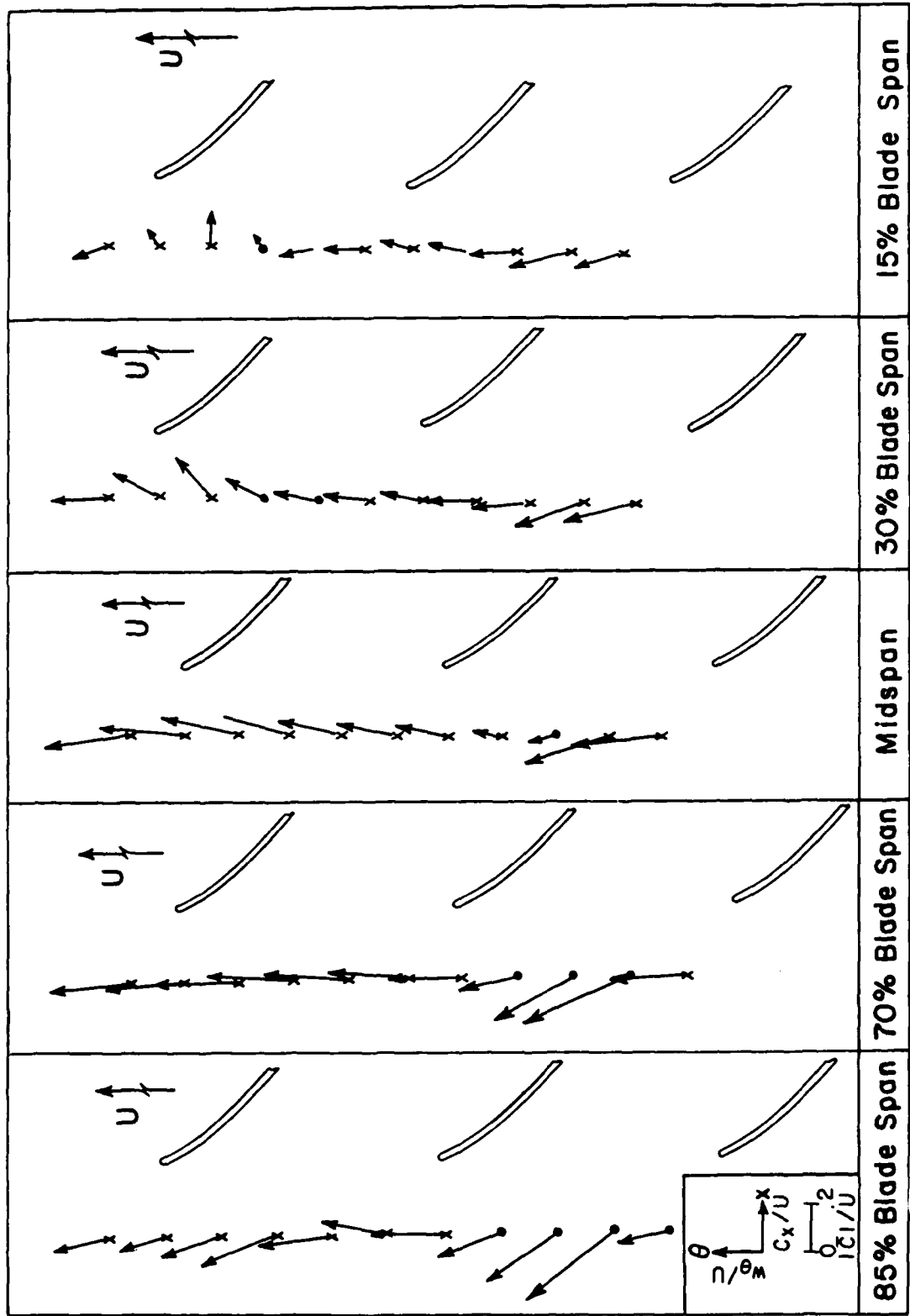
Figure 134   Absolute Axial Velocity vs. Relative Tangential Velocity Crossplot of the Moderate Reverse Flow Rotor Exit Flowfield

378

INSTANTANEOUS TRACE

032 TRACE ENSEMBLE AVERAGE

DATE: 3 /29/85

SYNCHRONOUS TRIGGER
TRANSDUCER SERIAL NO.   C260
AMPLIFIER NO.   3
AXIAL STATION 7
CIRCUMFERENTIAL POSITION 6

CALIBRATION DATA:

	ZERO DRIFT (MV)	SENSITIVITY (MV/IN H_2O)	STD DEV (IN H_2O)
PRE-RUN	29.8	45.1	0.053
POST-RUN	-19.0	47.2	0.042
RUN AVG	-11.2	46.9	

PRESSURE DATA (IN H_2O):

AVERAGE . . . . . . -0.225
MAXIMUM 0.974
MINIMUM . . . . . . -1.489
CORRECTED AVG . . .   3.362
BLADE REFERENCE . .   2.949
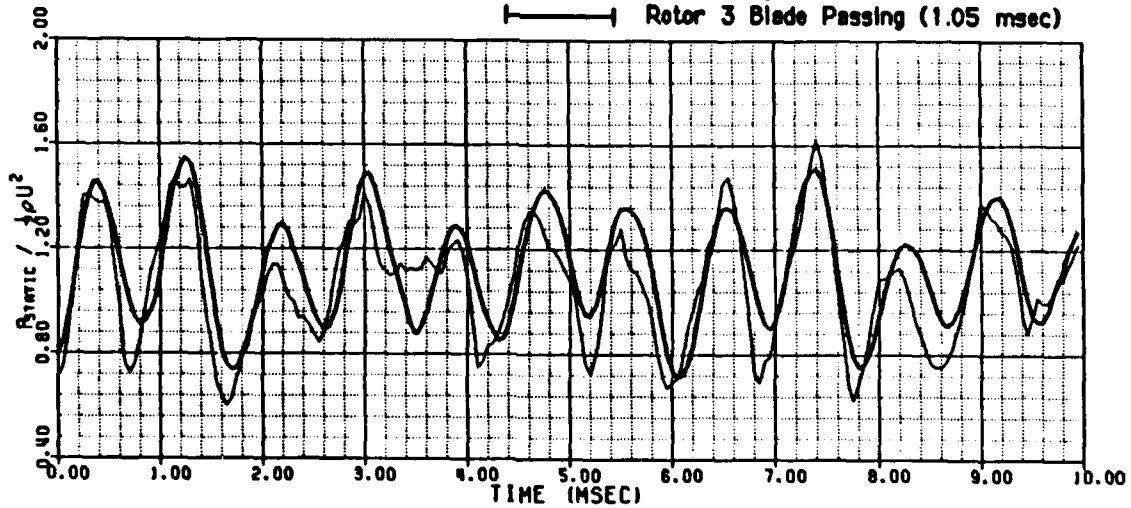
Figure 135   Axial Station #7 Wall Static Pressure Measurement
at Moderate Reverse Flow

——— INSTANTANEOUS TRACE
——— 032 TRACE   ENSEMBLE AVERAGE

DATE: 3 /29/85

SYNCHRONOUS   TRIGGER
TRANSDUCER SERIAL NO.   C259
AMPLIFIER NO.   3
AXIAL STATION 7
CIRCUMFERENTIAL POSITION 6
RADIAL POSITION 5
PROBE YAW ANGLE (DEG TOC) 85

CALIBRATION DATA:

	ZERO DRIFT (MV)	SENSITIVITY (MV/IN H_2O)	STD DEV (IN H_2O)
PRE-RUN	26.9	82.6	0.047
POST-RUN	398.2	79.2	0.043
RUN AVG	224.7	80.8	

PRESSURE DATA (IN H_2O):

AVERAGE 6.935
MAXIMUM 8.966
MINIMUM 4.564
CORRECTED AVG . . .   9.220
BLADE REFERENCE . .   2.949

├———┤ Propagating Disturbance (0.87 msec)
├———————┤ Rotor 3 Blade Passing (1.05 msec)

Figure 136   Axial Station #7 Total Pressure Measurement at
Moderate Reverse Flow and 85% Blade Span Location

380

SPECTRAL ANALYSIS
(TOTAL PRESSURE TRACE)

DATE: 3 /29/85
$C_x/U = -0.10$

TRANSDUCER SERIAL NO.   C259
AMPLIFIER NO.   3

AXIAL STATION   7
CIRCUMFERENTIAL POSITION . .   6
RADIAL POSITION   5
YAW ANGLE SETTING (DEG TDC) . .   85

SPECTRAL ANALYSIS
(WALL STATIC PRESSURE TRACE)

DATE: 3 /29/85
$C_x/U = -0.10$

TRANSDUCER SERIAL NO.   C260
AMPLIFIER NO.   3

AXIAL STATION   7
CIRCUMFERENTIAL POSITION . . .   6
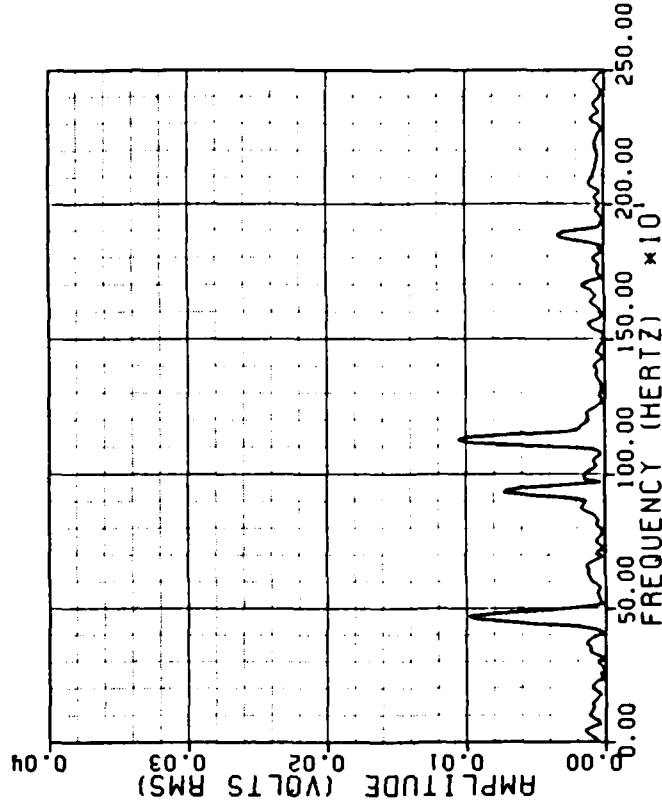
Figure 137   Axial Station #7 Wall Static and Total Pressure Spectral Signatures
at Moderate Reversed Flows
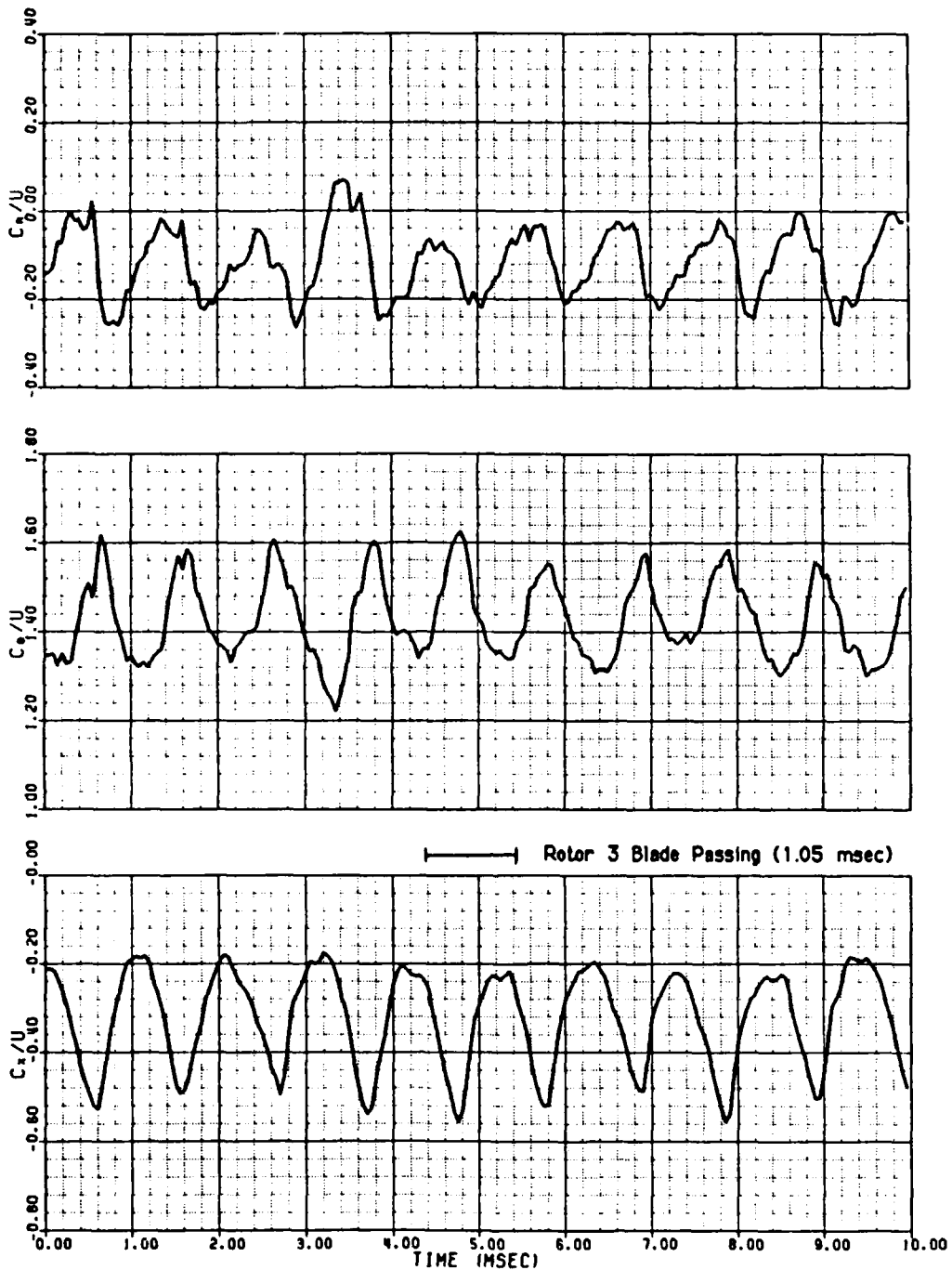
Figure 138   Axial Station #7 Velocity Field at High
Reversed Flows and the 70% Blade Span Location

382

DATE: 3/27/85   PROBE POSITION DATA: MEAN FLOW COEFFICIENTS:
SENSOR SERIAL NUMBER: 1   AXIAL STATION . . . . 7 C_X/U =   -0.195
ROTOR LOCKED TRIGGER   CIRCUMFERENTIAL POSITION . 10 C_θ/U =   1.331
SAMPLE RATE (KHZ): 20.0   RADIAL POSITION . . . . . . 2 C_R/U =   -0.199

Rotor 3 Blade Passing (1.05 msec)

TIME (MSEC)

Figure 139   Axial Station #7 Velocity Field at High
Reversed Flows and the 30% Blade Span Location

383

High Reverse Flow
Axial Station #7
Upstream View (Rotor Relative Frame)
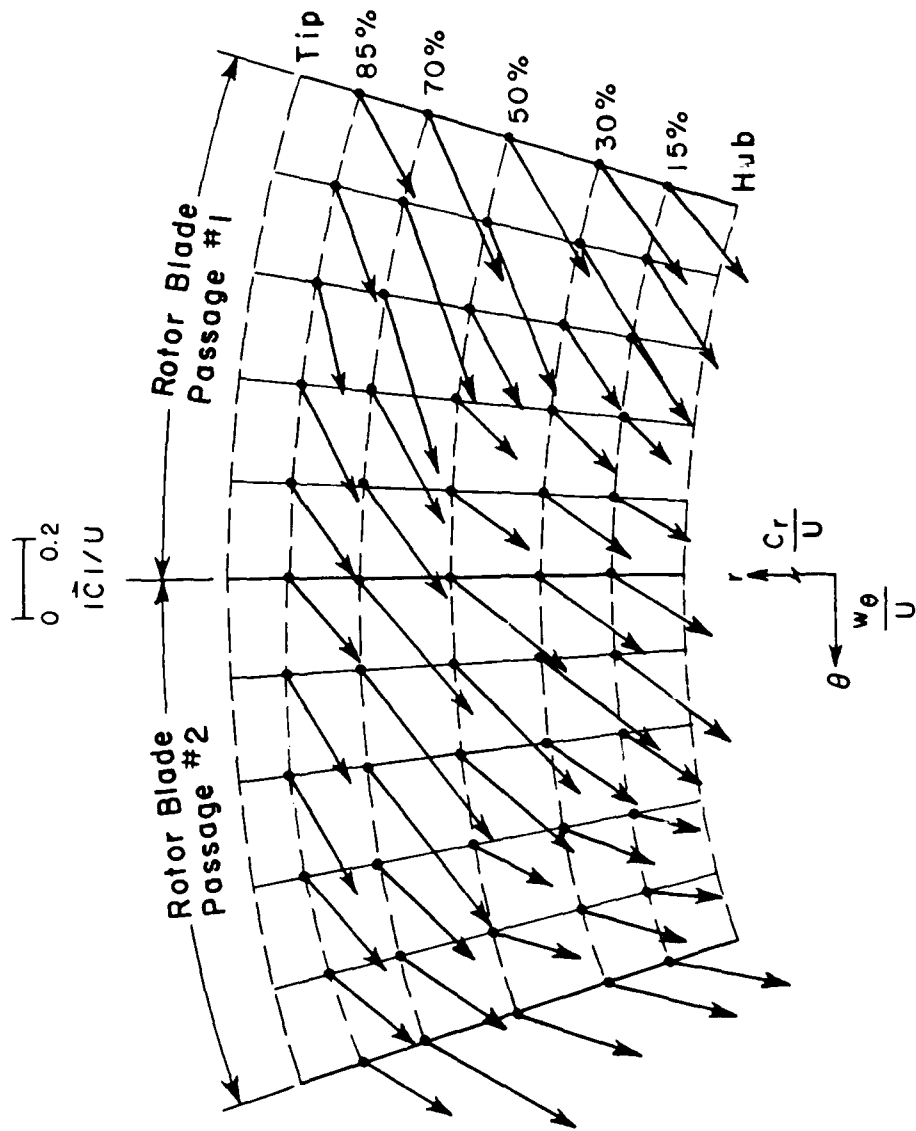
Figure 140   Relative Tangential Velocity vs. Absolute Radial Velocity Crossplot
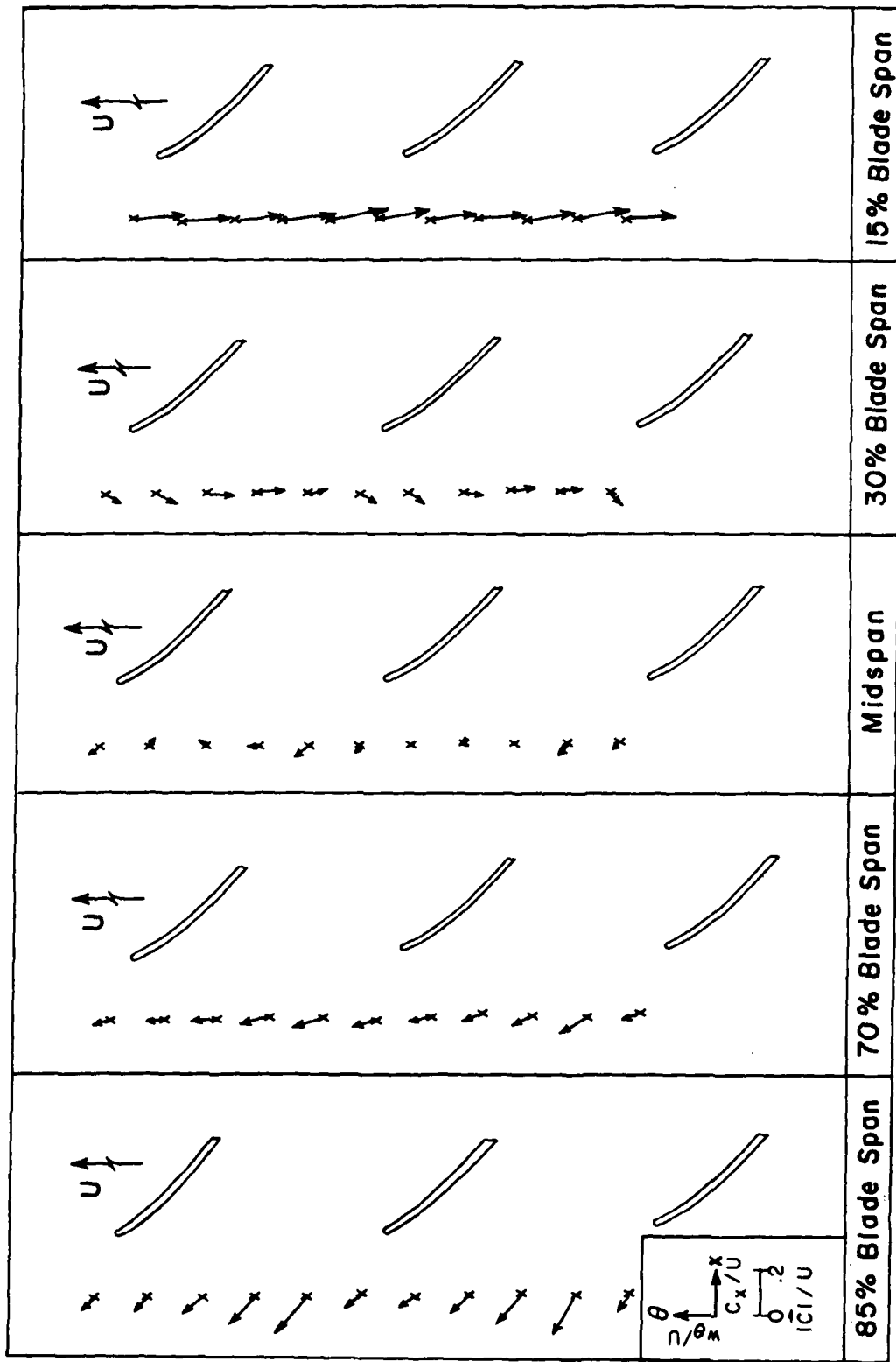of the High Reverse Flow Rotor Exit Flowfield

Figure 141   Absolute Axial Velocity vs. Relative Tangential Velocity Crossplot
of the High Reverse Flow Rotor Exit Flowfield

Figure 142 Axial Station #7 Total Pressure Measurement at High
Reverse Flow and 50% Blade Span Location

—— INSTANTANEOUS TRACE
—— 128 TRACE ENSEMBLE AVERAGE

DATE: 3 /29/85

ROTOR LOCKED TRIGGER
TRANSDUCER SERIAL NO.   C259
AMPLIFIER NO.   3
AXIAL STATION 7
CIRCUMFERENTIAL POSITION 6
RADIAL POSITION 5
PROBE YAW ANGLE (DEG TDC) 80

CALIBRATION DATA:

	ZERO DRIFT (MV)	SENSITIVITY (MV/IN H$_2$O)	STD DEV (IN H$_2$O)
PRE-RUN	26.9	82.6	0.047
POST-RUN	398.2	79.2	0.043
RUN AVG	290.6	80.2	

PRESSURE DATA (IN H$_2$O):

AVERAGE 7.916
MAXIMUM 10.669
MINIMUM 5.353
CORRECTED AVG . . . 14.480
BLADE REFERENCE . . 2.949

Figure 143   Axial Station #7 Total Pressure Measurement at High
Reverse Flow and 85% Blade Span Location

387
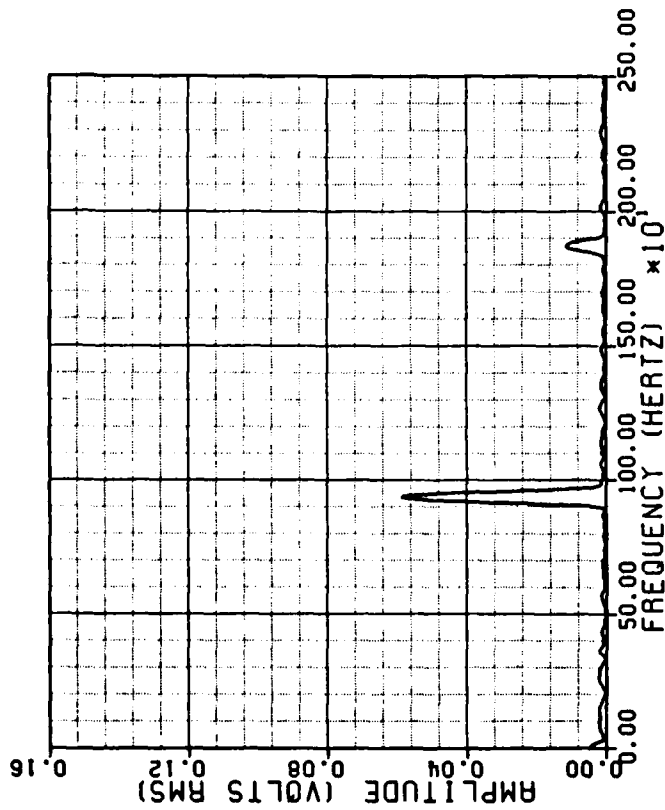
Figure 144 Axial Station #7 Total Pressure Spectral Signatures at High Reversed Flows

Figure 145   Axial Station #7 Velocity Field at Low
Reversed Flows and the 85% Blade Span Location

389

DATE: 2-27-85
SENSOR SERIAL NUMBER: 1
ROTOR LOCKED TRIGGER
SAMPLE RATE (KHZ): 20.0

PROBE POSITION DATA:
AXIAL STATION 7
CIRCUMFERENTIAL POSITION . . 10
RADIAL POSITION 9

MEAN FLOW COEFFICIENTS:
C_X/U = -0.009
C_θ/U = 1.019
C_R/U = -0.146

Rotor 3 Blade Passing (1.05 msec)

TIME (MSEC)
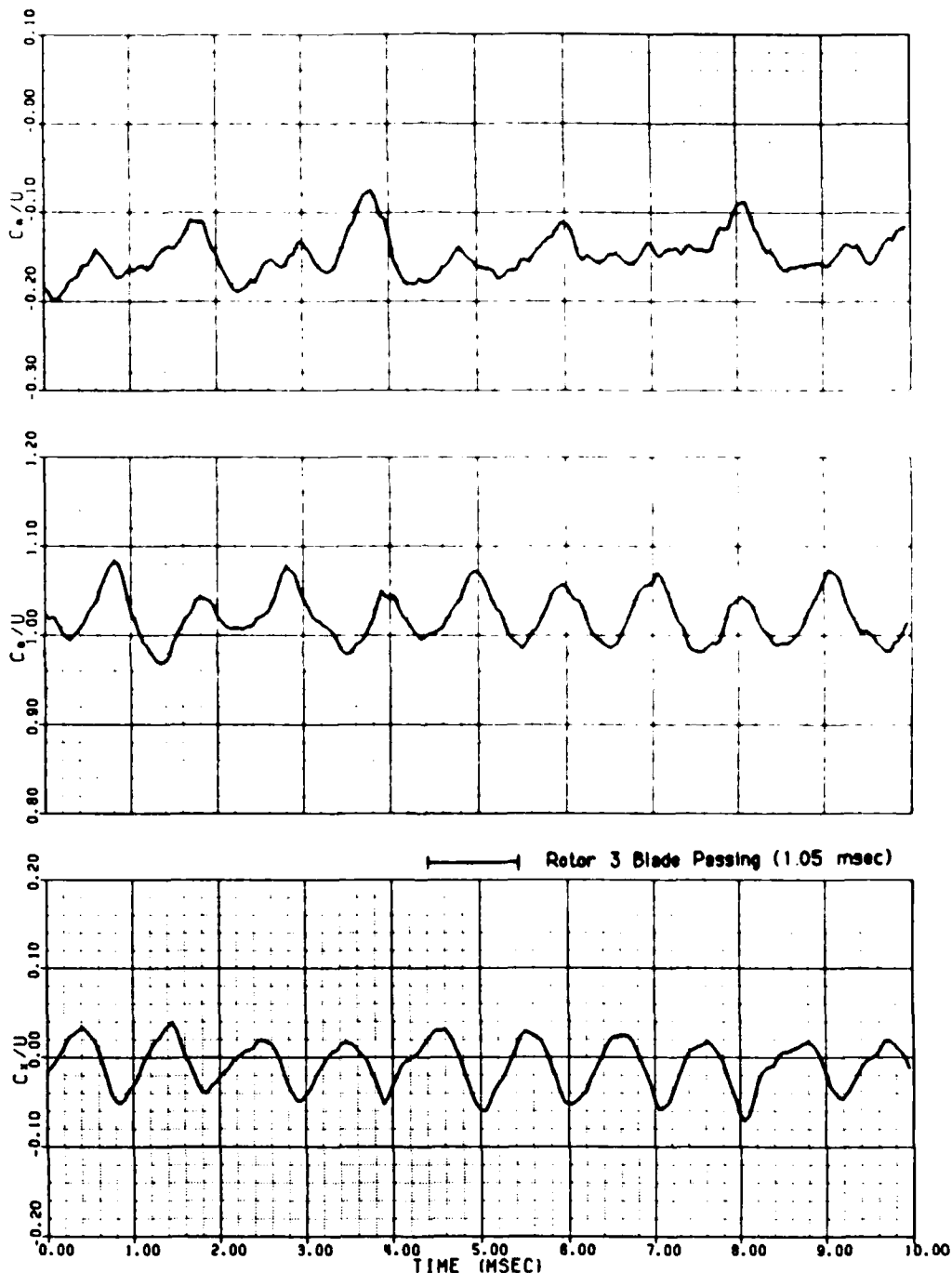
Figure 146   Axial Station #7 Velocity Field at Low
Reversed Flows and the 50% Blade Span Location

390

DATE: 2/27/85   PROBE POSITION DATA: MEAN FLOW COEFFICIENTS:
SENSOR SERIAL NUMBER: 1   AXIAL STATION . . . . . . .7 C_X/U = 0.028
ROTOR LOCKED TRIGGER   CIRCUMFERENTIAL POSITION .10 C_θ/U = 0.710
SAMPLE RATE [KHZ]: 20.0   RADIAL POSITION . . . . . .1 C_R/U = -0.081
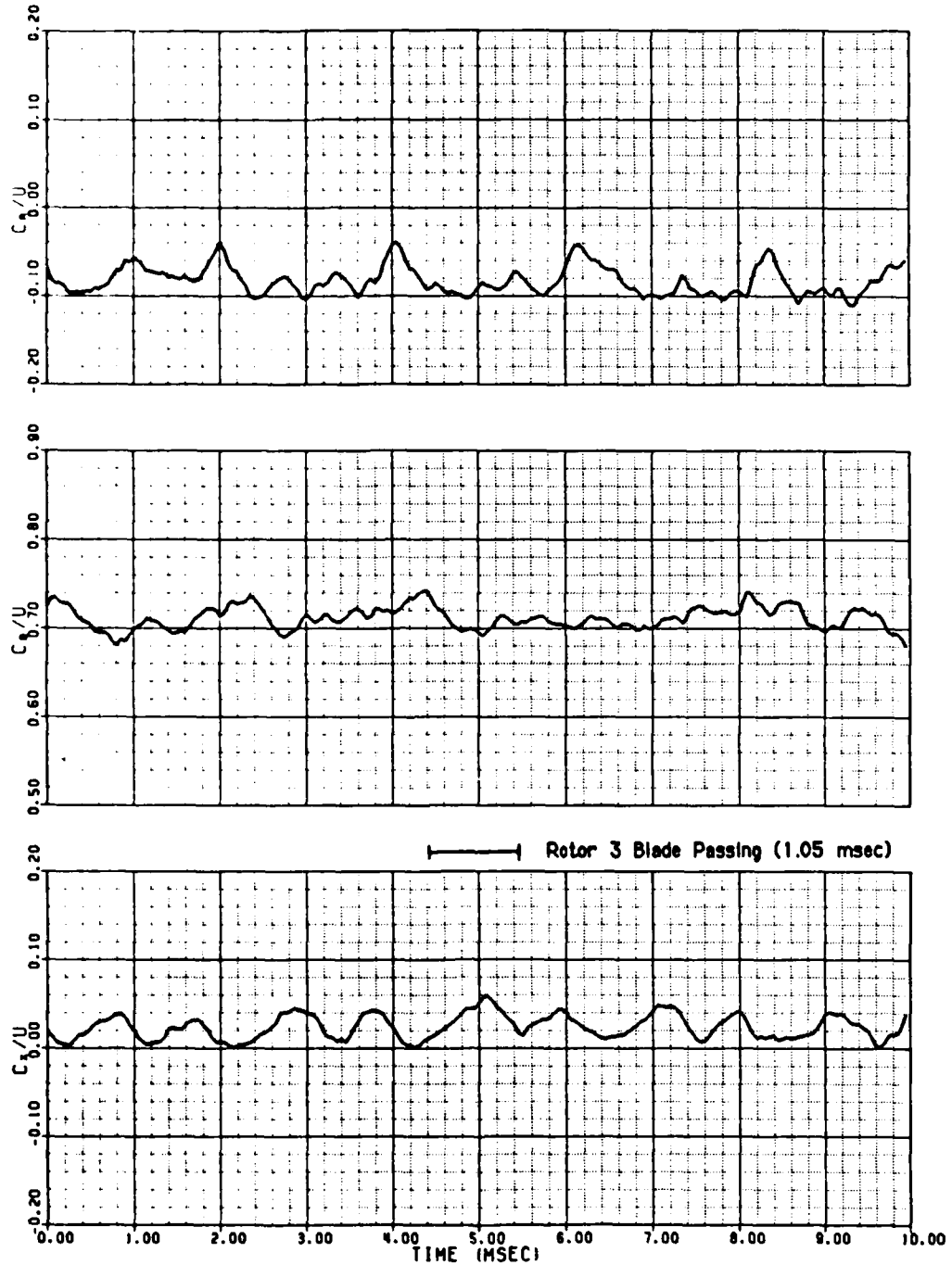
Figure 147   Axial Station #7 Velocity Field at Low
Reversed Flows and the 15% Blade Span Location

391

Low Reverse Flow
Axial Station #7
Upstream View (Rotor Relative Frame)
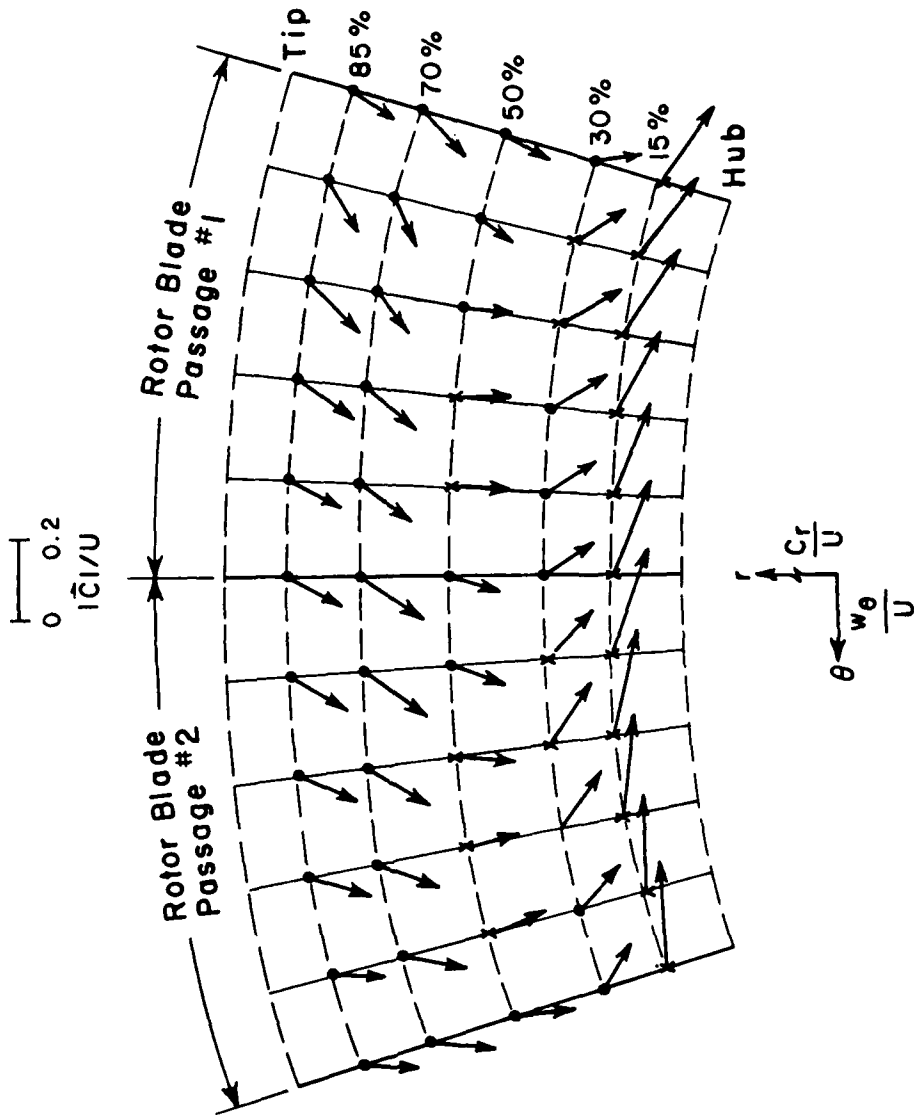
Figure 148 Relative Tangential Velocity vs. Absolute Radial Velocity Crossplot
of the Low Reverse Flow Rotor Exit Flowfield

Figure 149 Absolute Axial Velocity vs. relative Tangential Velocity Crossplot
of the Low Reverse Flow Rotor Exit Flowfield

(128 TRACE ENSAMBLE AVERAGE)

DATE: 2/21/85   PROBE POSITION DATA: MEAN FLOW COEFFICIENTS:
SENSOR SERIAL NUMBER: 1   AXIAL STATION . . . . . . .6 C_X/U =   -0.106
ROTOR LOCKED TRIGGER   CIRCUMFERENTIAL POSITION . 6 C_θ/U =   -0.436
SAMPLE RATE [KHZ]: 20.0   RADIAL POSITION . . . . . .4 C_R/U =   0.004

Propagating Disturbance (0.87 msec)
Rotor 2 Blade Passing (0.93 msec)

TIME (MSEC)
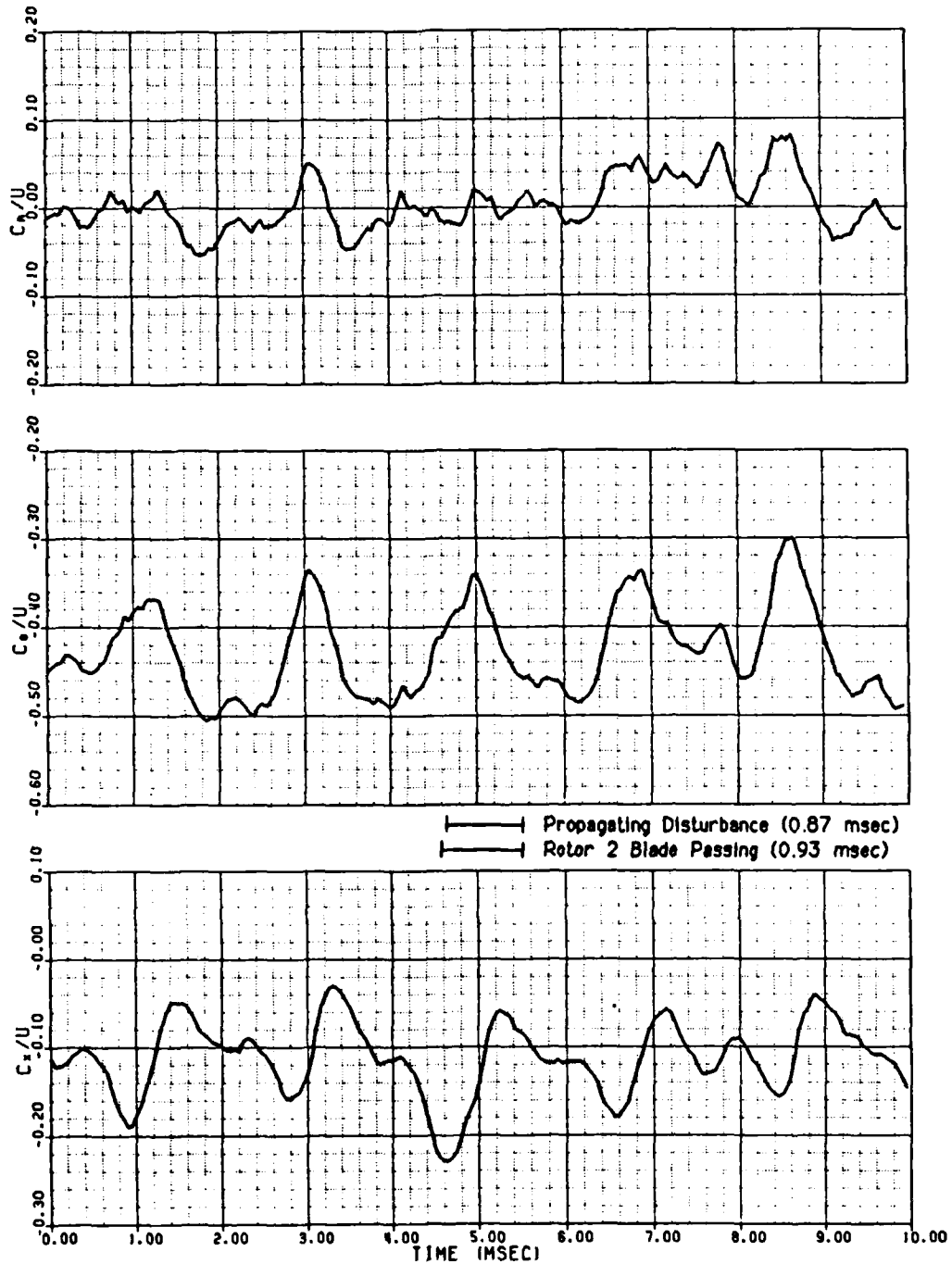
Figure 150   Axial Station #6 Velocity Field at Moderate
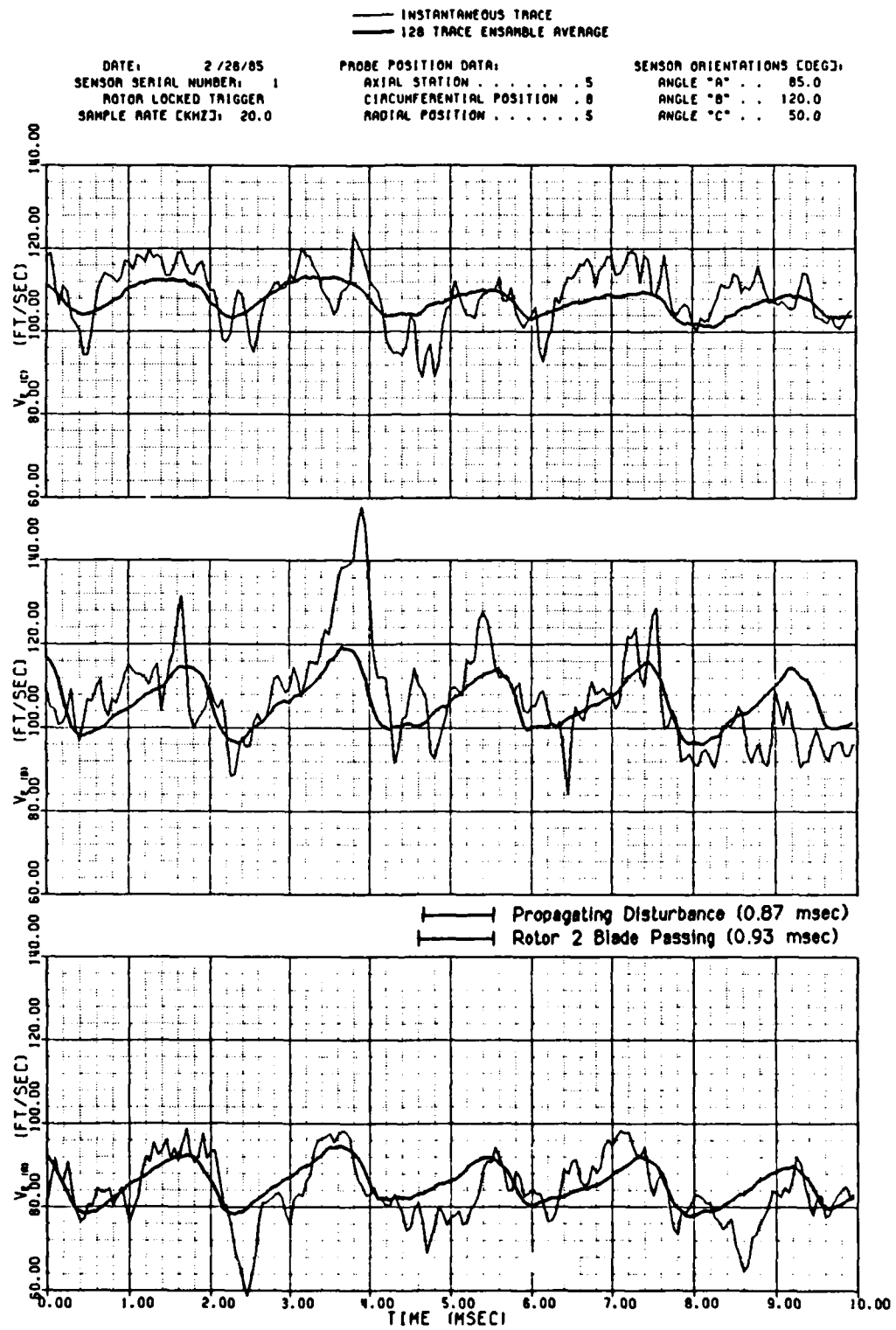Reverse Flow and the 70% Blade Span Location

394
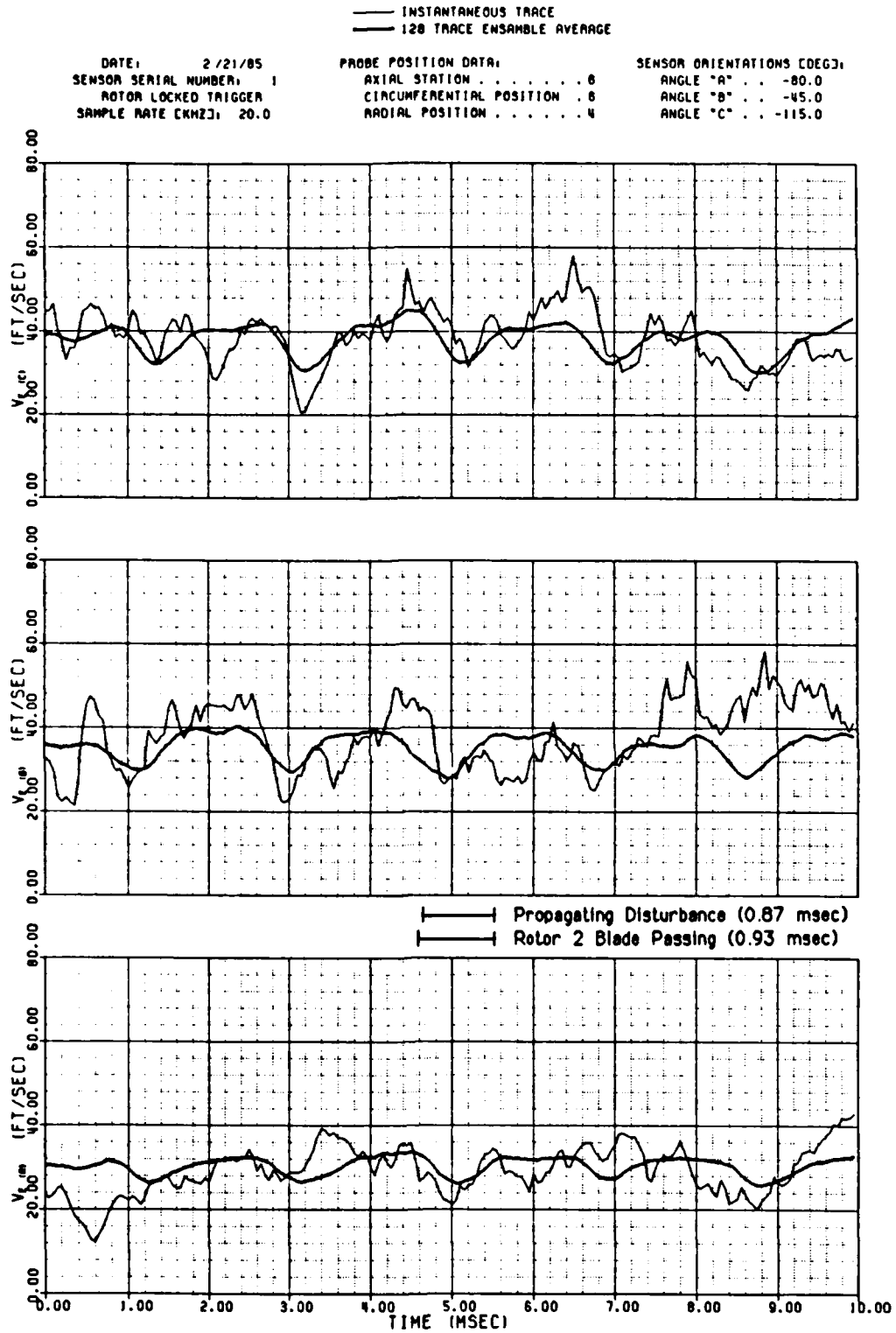
Figure 151   Axial Station #6 Effective Cooling Velocity Measurements
at Moderate Reversed Flow and the 70% Blade Span Location
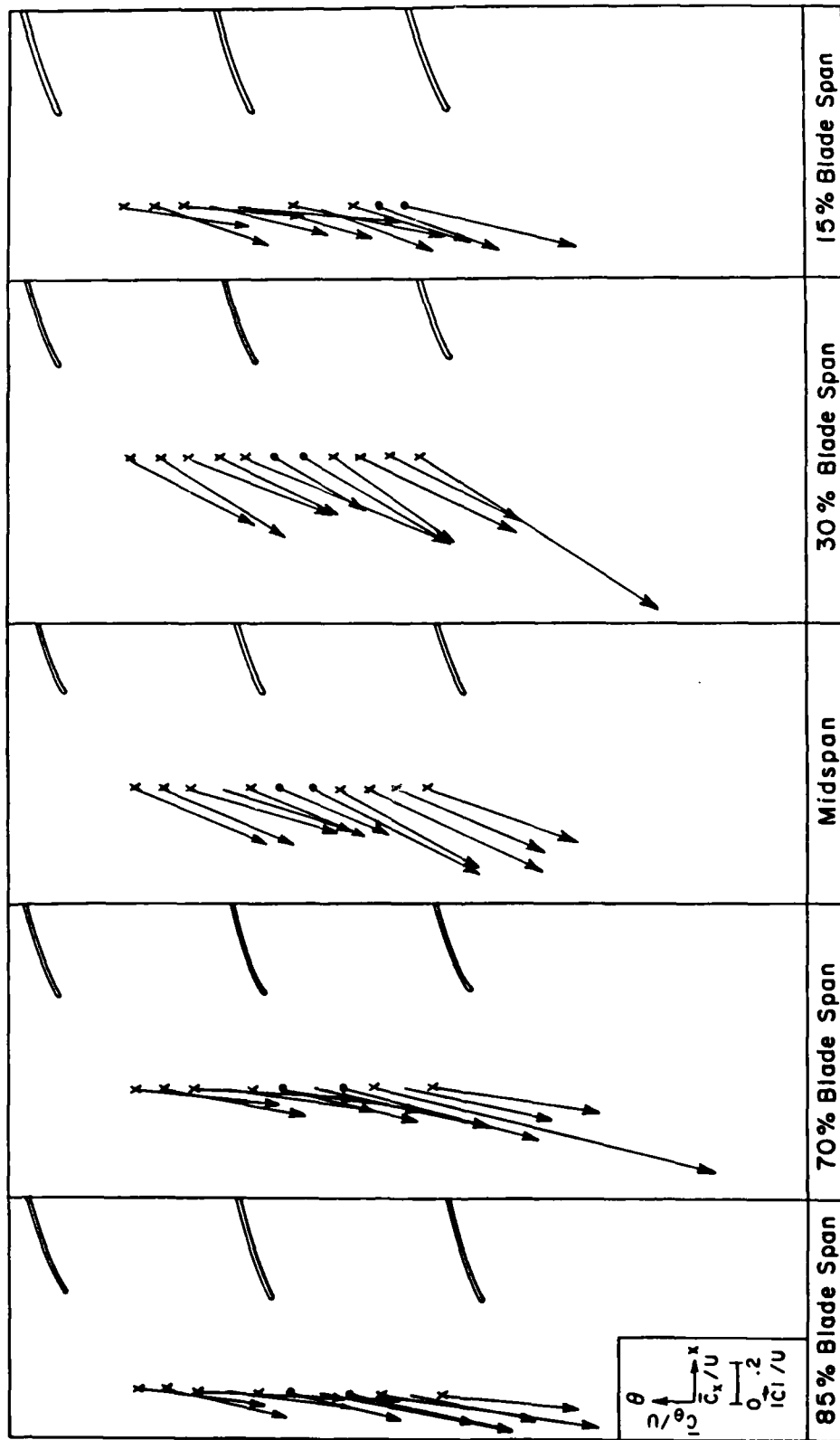
Figure 152   Axial Station #6 Absolute Axial Velocity vs. Relative Tangential Velocity Crossplot (Moderate Reverse Flow)

396

—— INSTANTANEOUS TRACE
—— 032 TRACE ENSEMBLE AVERAGE

DATE: 3 /29/85

SYNCHRONOUS TRIGGER
TRANSDUCER SERIAL NO.   C260
AMPLIFIER NO.   3
AXIAL STATION 6
CIRCUMFERENTIAL POSITION 6

CALIBRATION DATA:

	ZERO DRIFT (MV)	SENSITIVITY (MV/IN H_2O)	STD DEV (IN H_2O)
PRE-RUN	29.8	45.1	0.053
POST-RUN	-19.0	47.2	0.042
RUN AVG	-14.0	47.0	

PRESSURE DATA (IN H_2O):

AVERAGE 1.295
MAXIMUM 2.722
MINIMUM 0.151
CORRECTED AVG . . .   1.875
BLADE REFERENCE . .   2.949
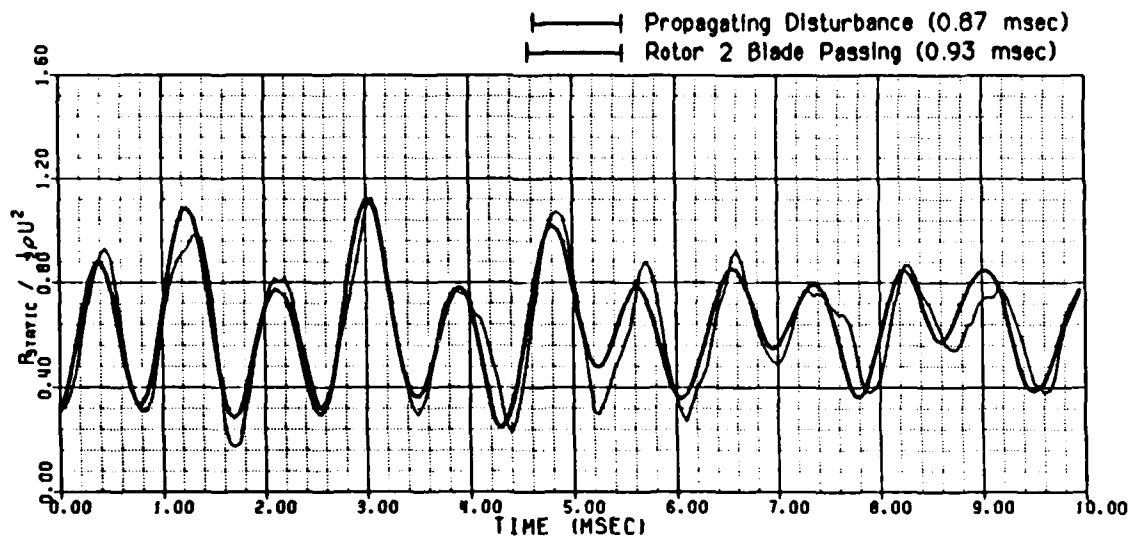
Figure 153   Axial Station #6 Wall Static Pressure Measurement
at Moderate Reverse Flow

────── INSTANTANEOUS TRACE
────── 032 TRACE ENSEMBLE AVERAGE

DATE: 3 /29/85

SYNCHRONOUS TRIGGER
TRANSDUCER SERIAL NO.   C259
AMPLIFIER NO.   3
AXIAL STATION 6
CIRCUMFERENTIAL POSITION 6
RADIAL POSITION 5
PROBE YAW ANGLE (DEG TDC) . . . . -78

CALIBRATION DATA:

	ZERO DRIFT (MV)	SENSITIVITY (MV/IN H$_2$O)	STD DEV (IN H$_2$O)
PRE-RUN	26.9	82.6	0.047
POST-RUN	398.2	79.2	0.043
RUN AVG	92.0	82.0	

PRESSURE DATA (IN H$_2$O):

AVERAGE . . . . . . -0.760
MAXIMUM 0.090
MINIMUM . . . . . . -1.419
CORRECTED AVG . . .   2.300
BLADE REFERENCE . .   2.949

├──────┤ Propagating Disturbance (0.87 msec)
├──────┤ Rotor 2 Blade Passing (0.93 msec)
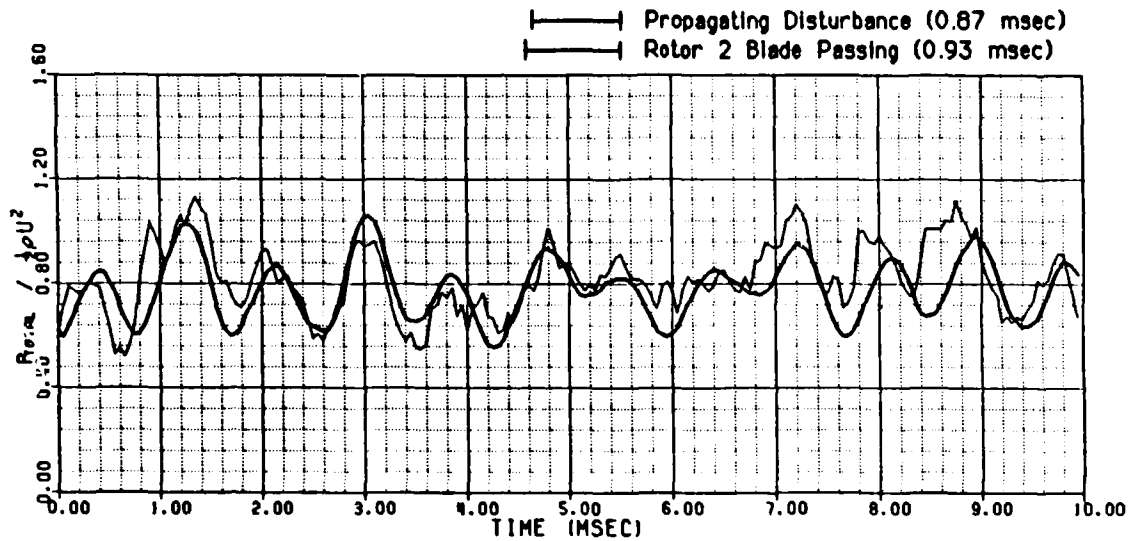
Figure 154 Axial Station #6 Total Pressure Measurement at
Moderate Reverse Flow and the 85% Blade Span Location

398
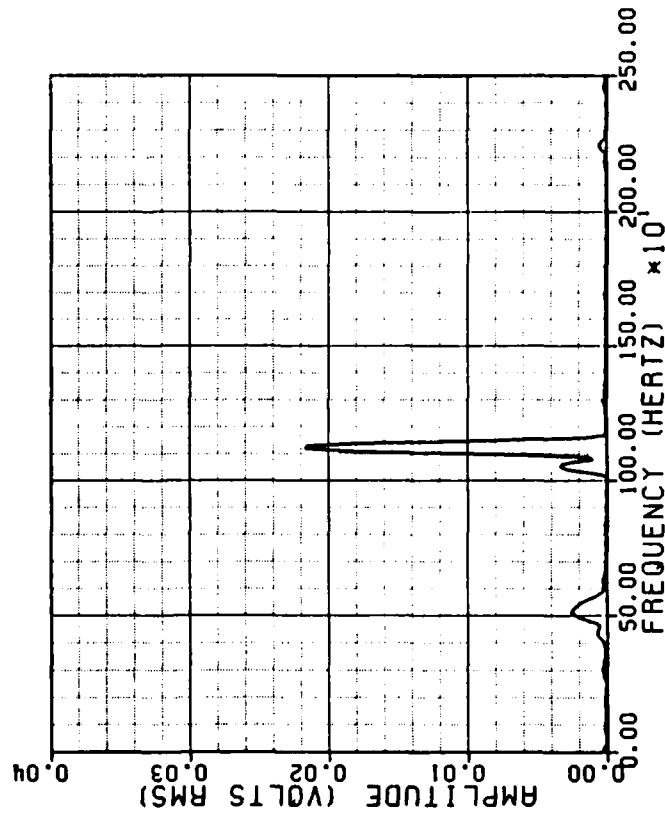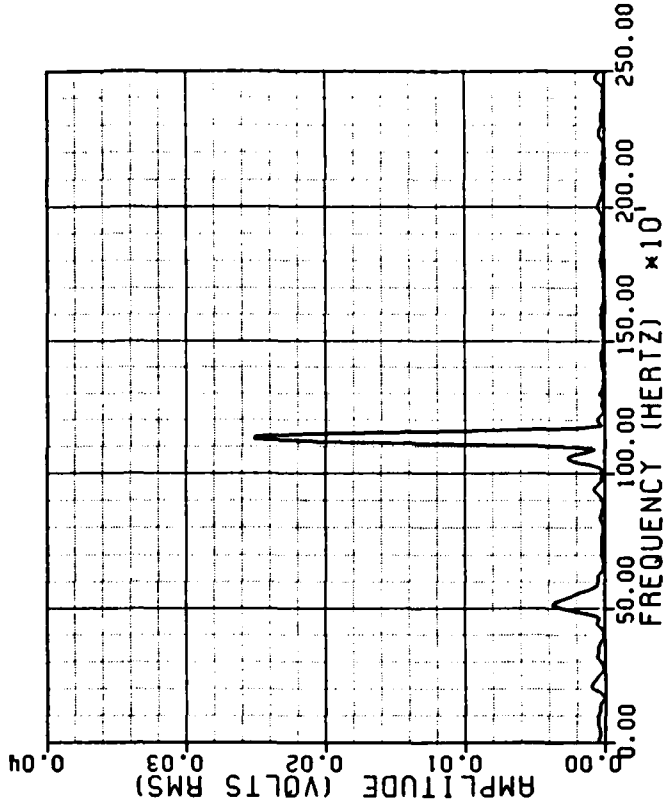
Figure 155   Axial Station #6 Wall Static and Total Pressure Spectral
Signatures at Moderate Reversed Flows
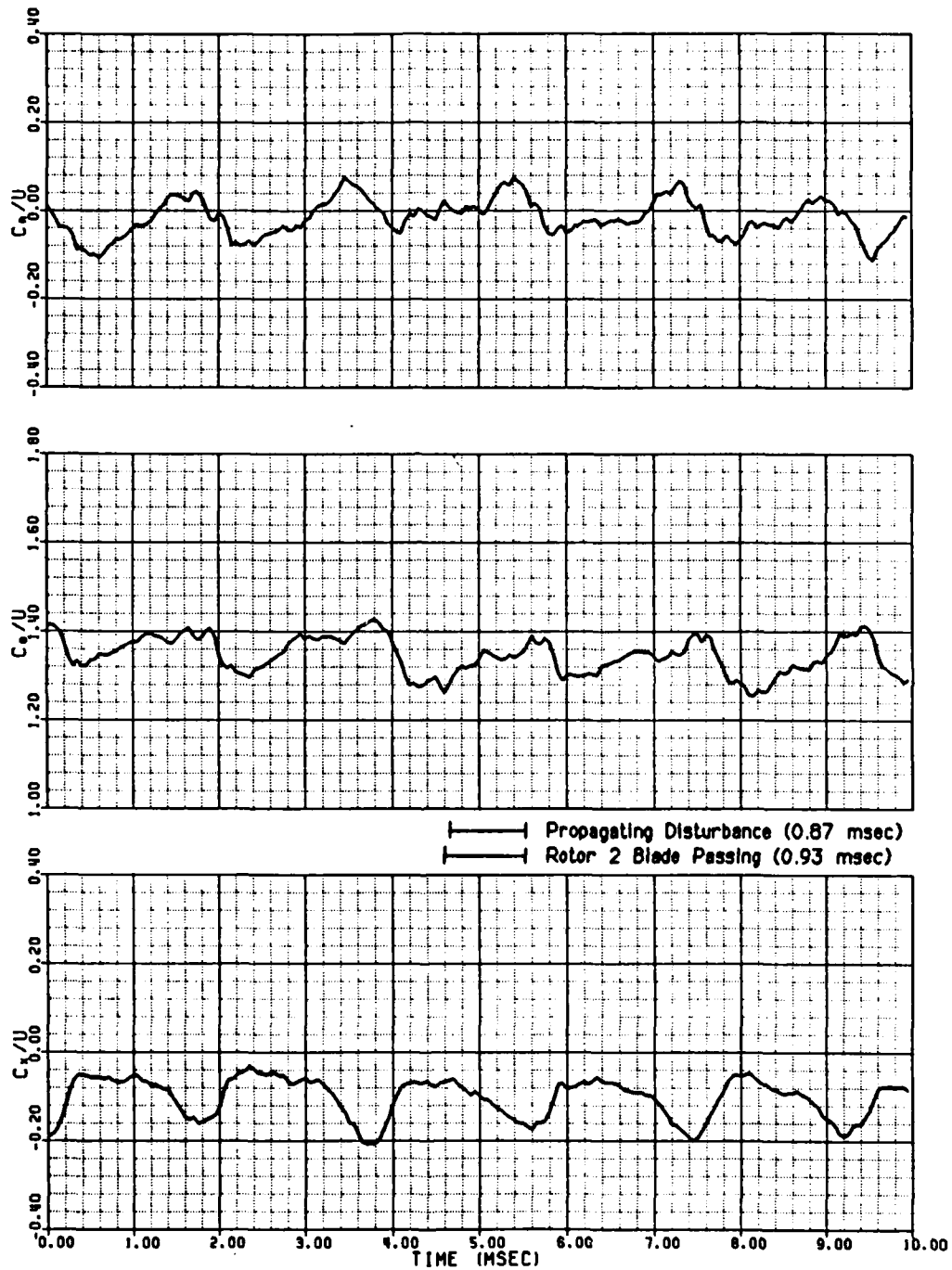
Figure 156 Axial Station #5 Velocity Field at Moderate
Reverse Flow and the 85% Blade Span Location

Figure 157   Axial Station #5 Effective Cooling Velocity Measurements
at Moderate Reversed Flow and the 85% Blade Span Location
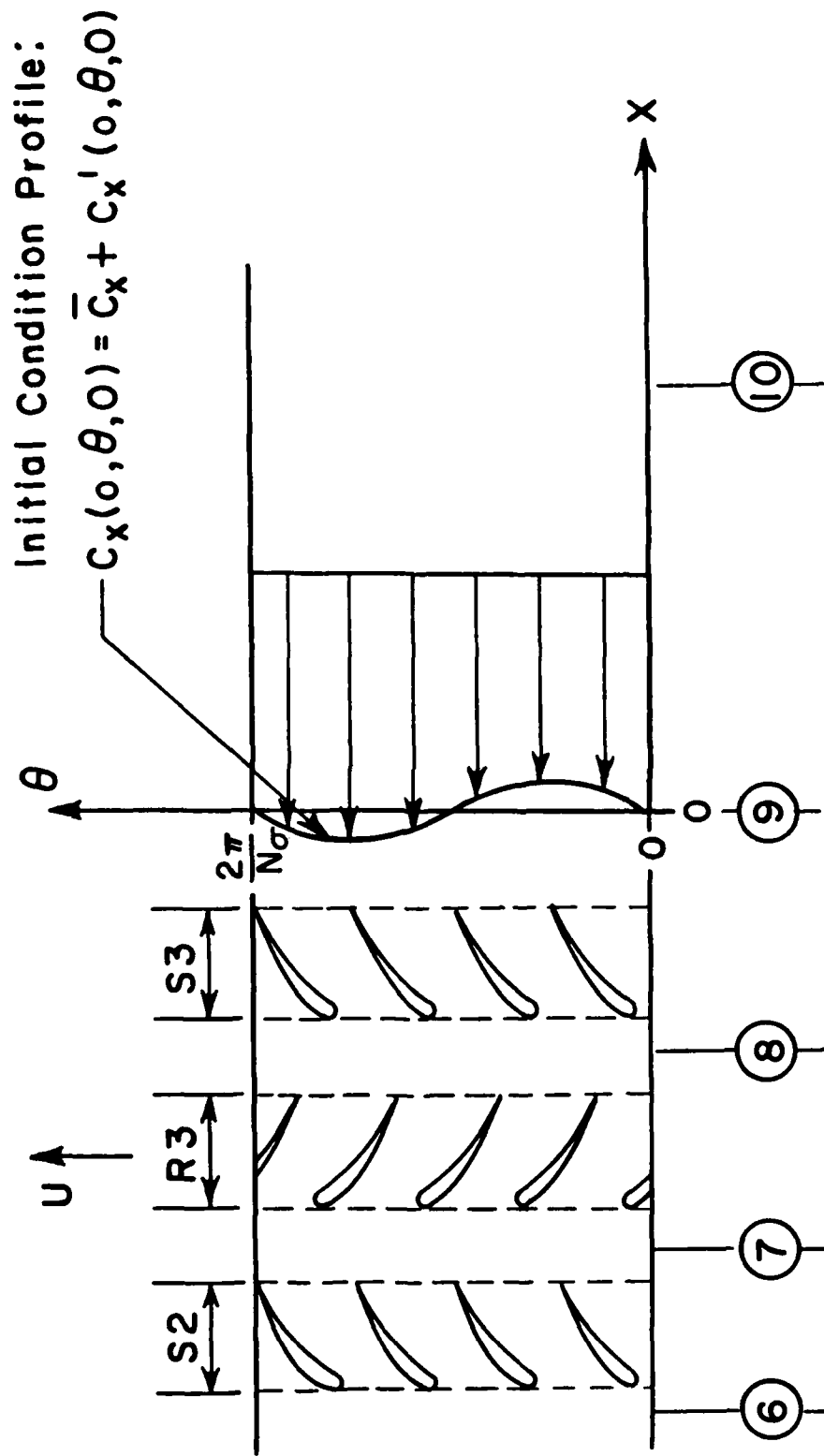
Figure 158   Two-Dimensional Coordinate System for Upstream Unsteady
Potential Flow Analysis

Possible Spinning Mode	Phase Shift Δt (msec)	Propogation Speed U_σ/U	No. Of Lobes N_σ
1	0.100	-6.98	~8
2	1.846	-0.38	~158
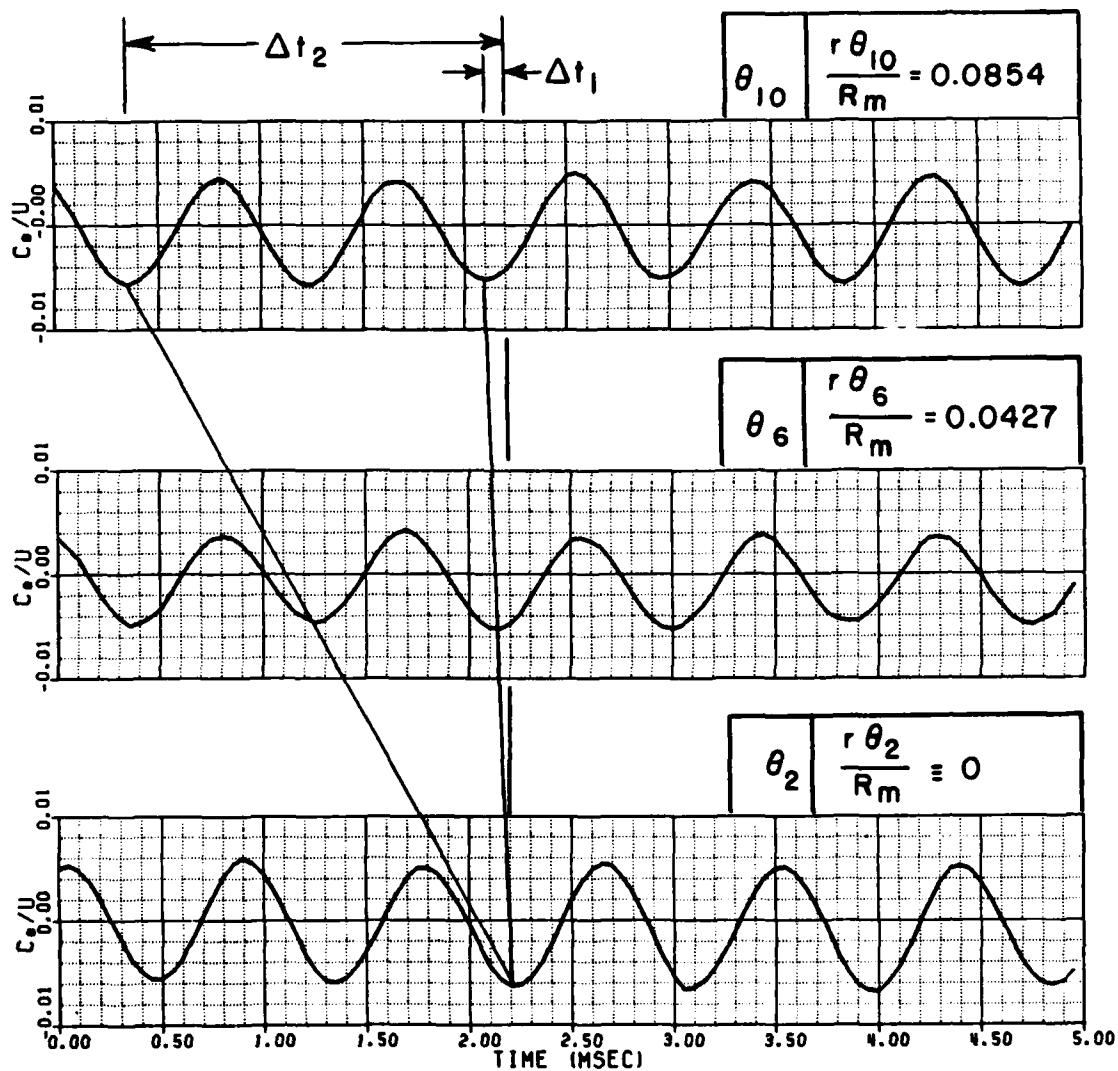
Figure 159 Upstream Tangential Velocity Component "Waterfall" Plot for Identification of Possible Spinning Disturbance Modes

403
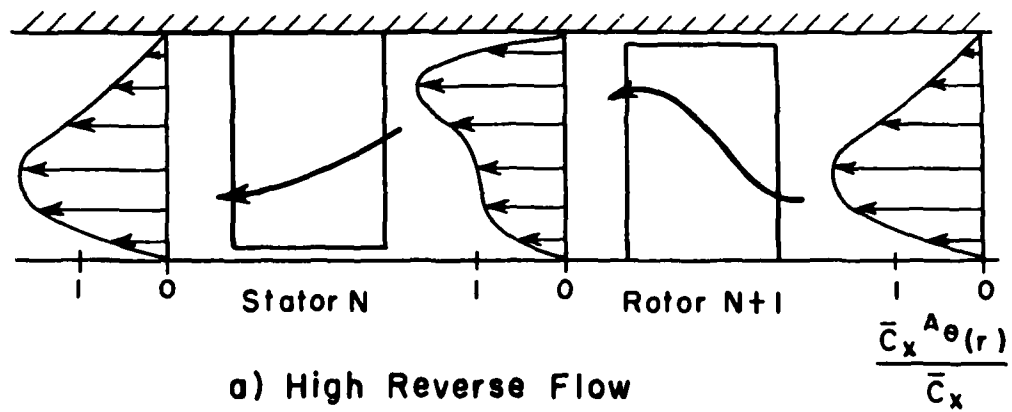
a) High Reverse Flow
(Axisymmetric)
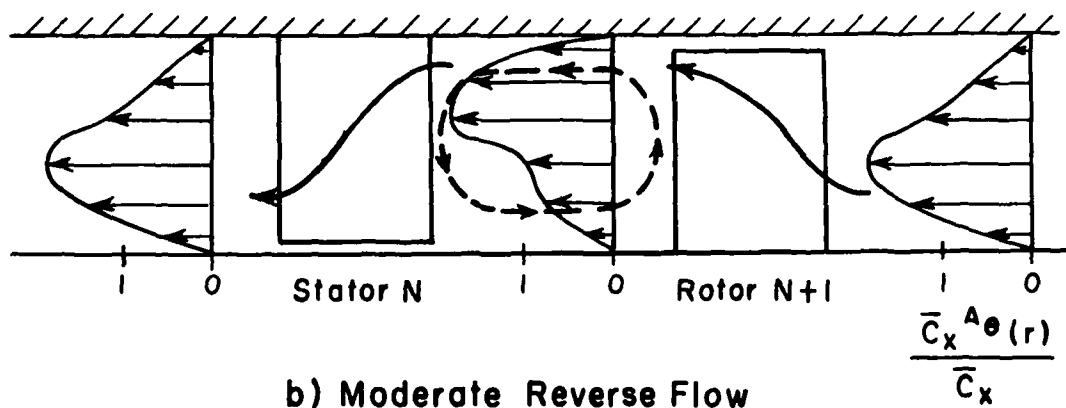
b) Moderate Reverse Flow
(Asymmetric)
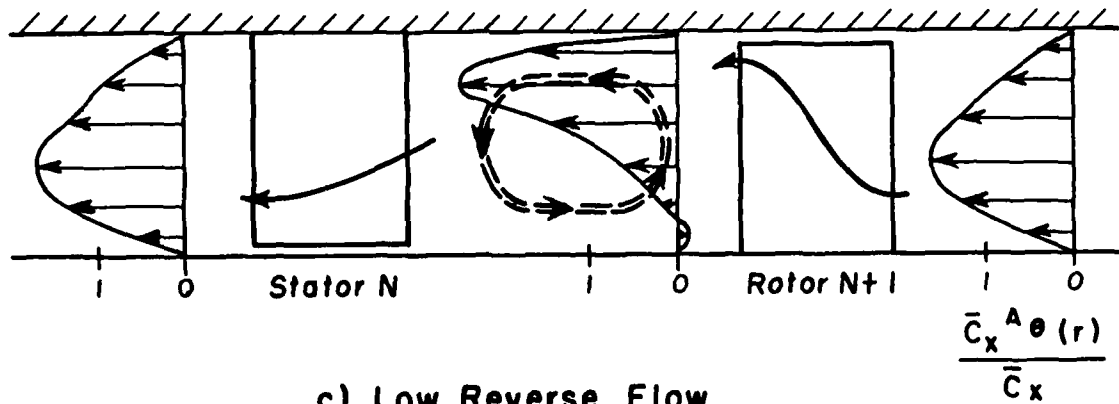
c) Low Reverse Flow
(Axisymmetric)

Figure 160   Radial Movement of Fluid during Reverse Flow

404
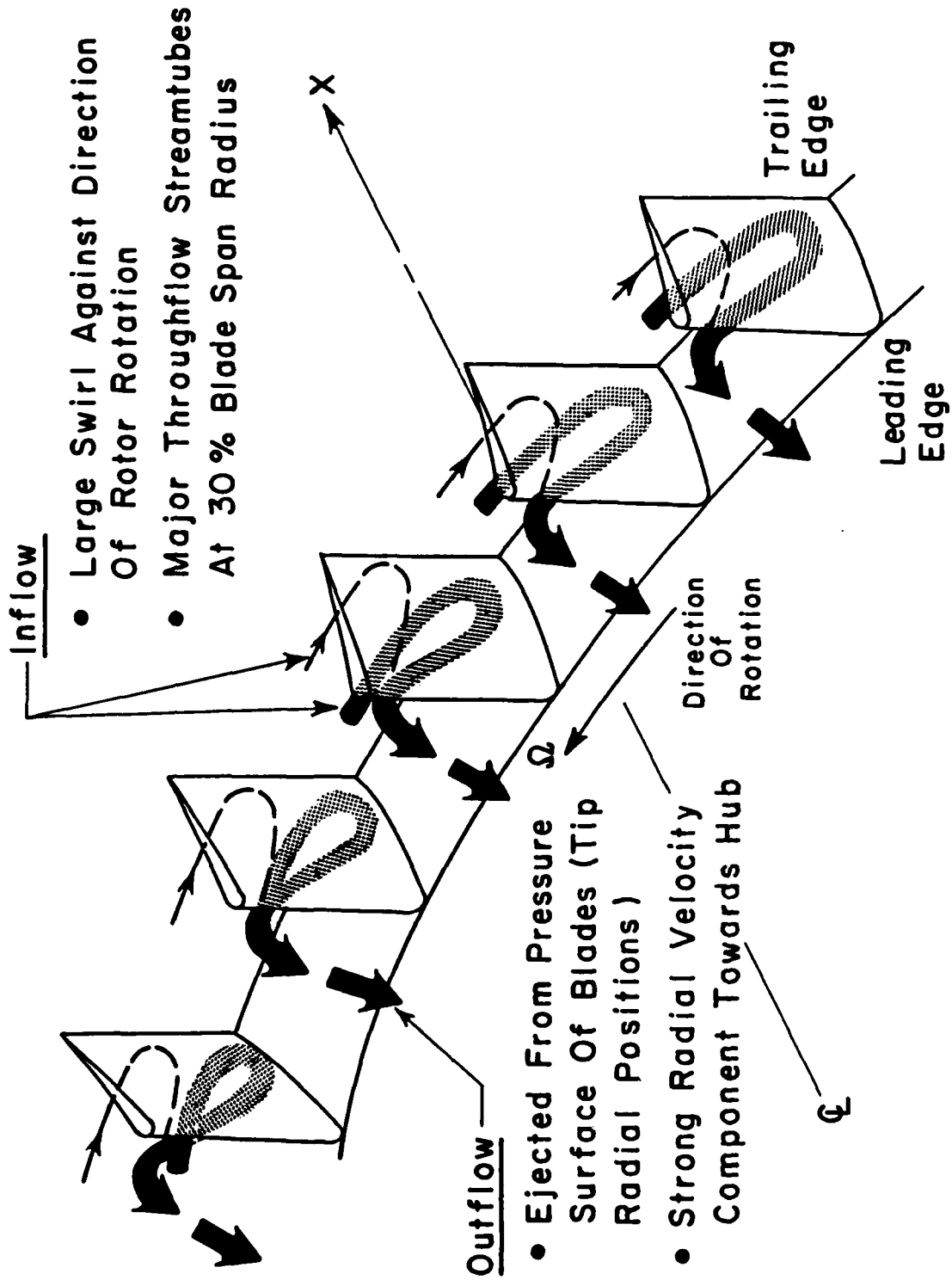
Figure 161   Three Dimensional Rotor Bladerow Flowfield Structure at High Reverse Flow
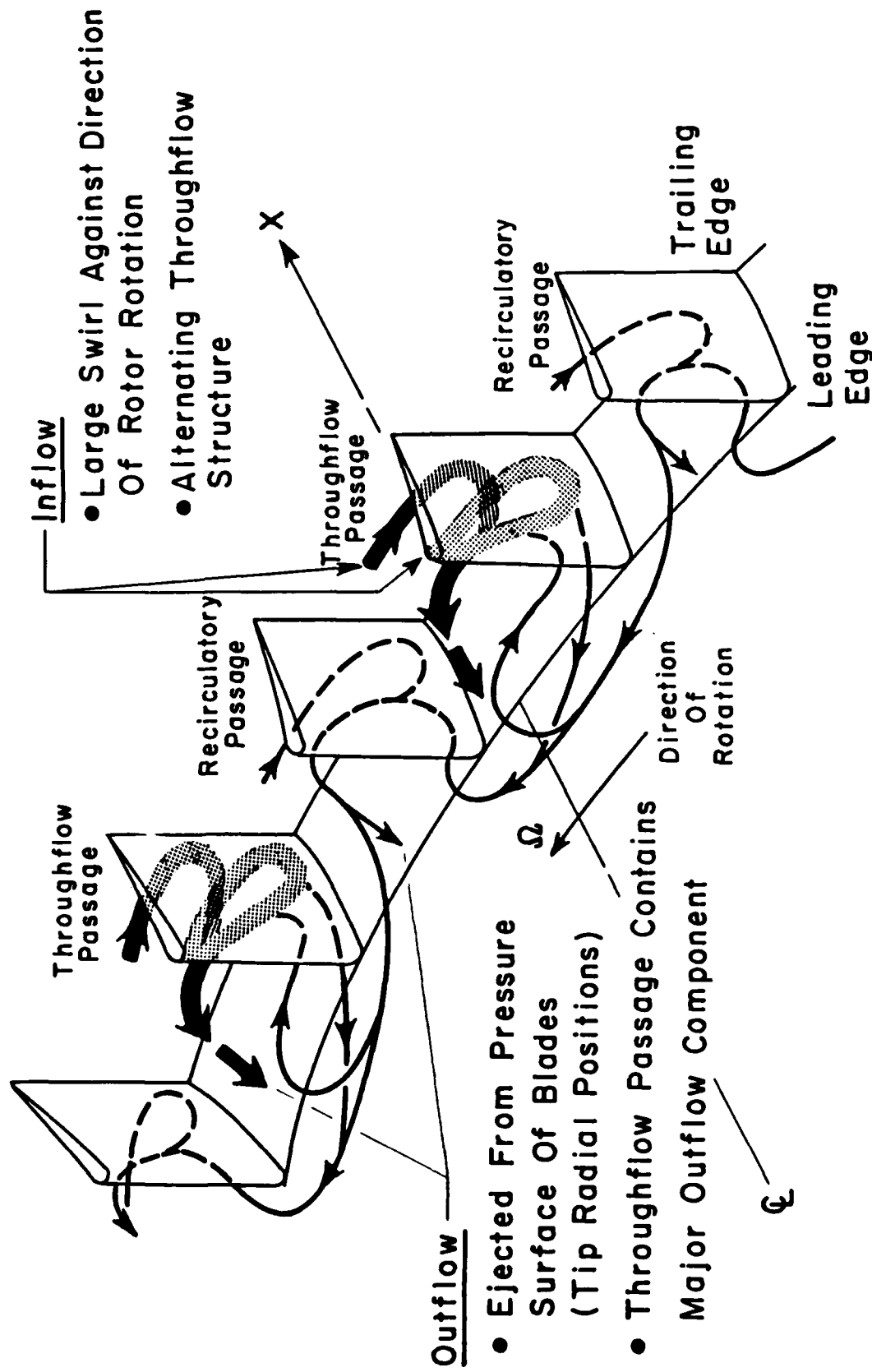
Figure 162   Three Dimensional Rotor Bladerow Flowfield Structure at Moderate Reverse Flow
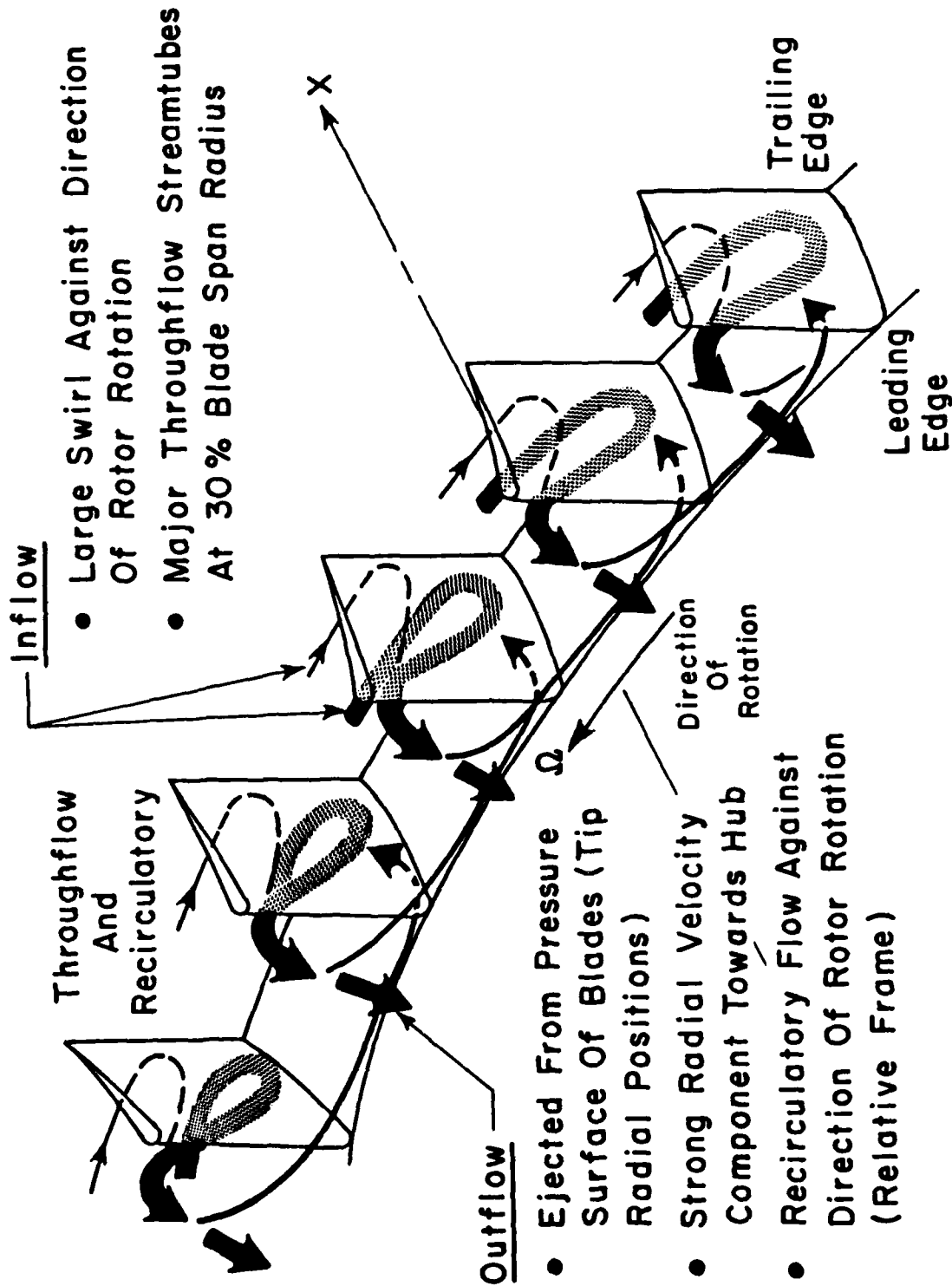
406

Figure 163 Three Dimensional Rotor Bladerow Flowfield Structure at Low Reverse Flow
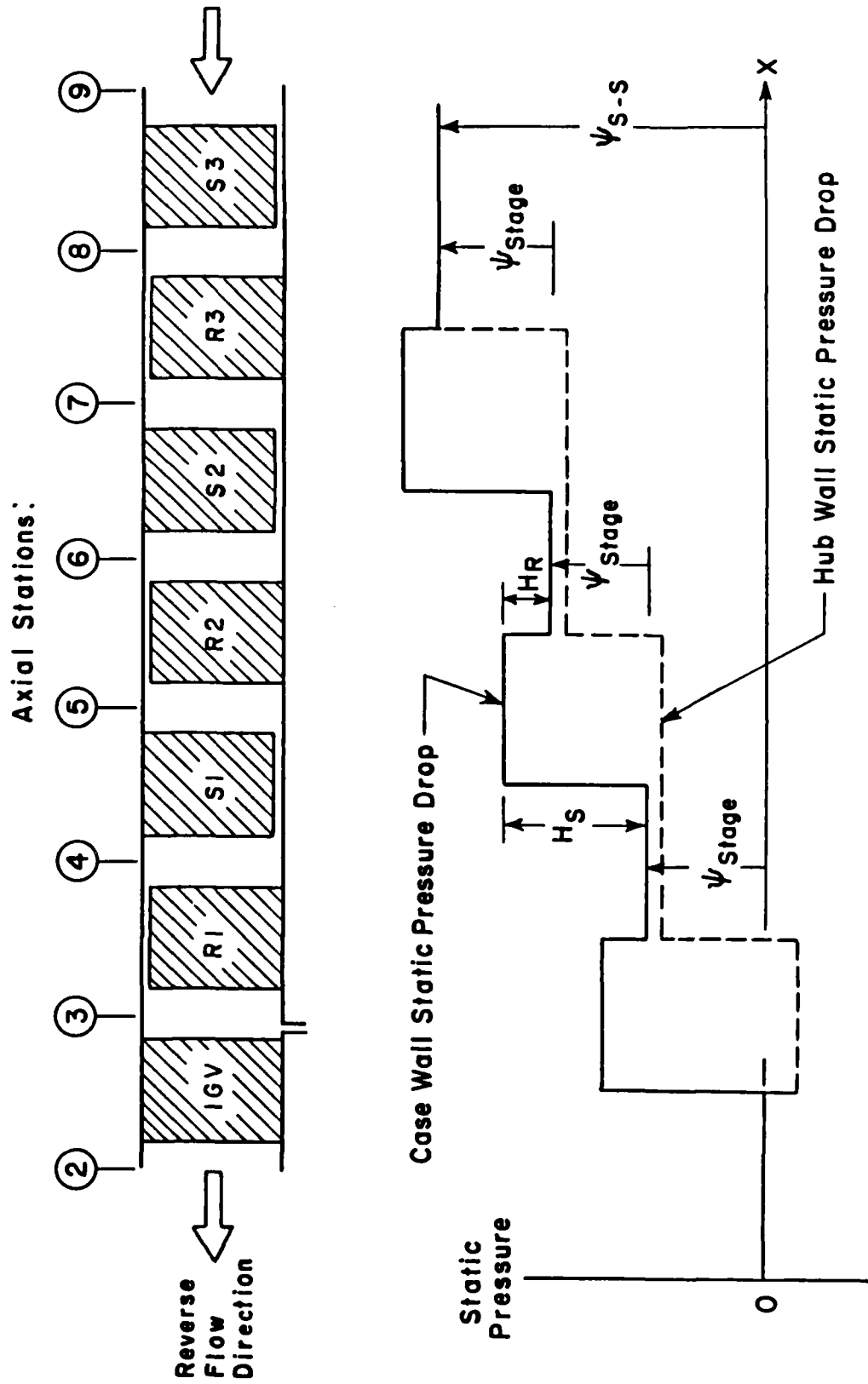
Figure 164 Overall Model of Reverse Flow Axial Compressor Performance

APPENDIX A

MASS FLOW CALIBRATION

The orifice plate was calibrated by measuring the mass flow through the facility and the pressure drop across the orifice plate. In order to determine the mass flow rate, the dynamic pressure profile across the inlet annulus of the compressor was measured at several mass flow rates. The figures at the end of this appendix illustrate four typical inlet dynamic pressure profiles. Mass flow was determined by using the measured dynamic pressure profiles to evaluate the following integral expression

$$\dot{m} = \rho A_c \overline{C}_x = 2\pi \int_{r_{hub}}^{r_{tip}} \sqrt{2\rho(P_T - P_s)} \; r \, dr \qquad (A-1)$$

where $(P_T - P_S)$ is the measured dynamic pressure profile. The integral of Equation A-1 was evaluated numerically using the trapezoidal rule with end correction. This quadrature scheme is essentially a fourth order method.

The inlet calibration results indicate that the inlet blockage ratio varies with Reynold's Number according to the following power law expression

$$\frac{A_B}{A_c} = c_1 \left(R_{e_{inlet}}\right)^{c_2} \qquad (A-2)$$

where

$$\frac{A_B}{A_C} = 1 - \frac{\overline{C}_x}{V_f} \qquad (A-3)$$

$$Re_{inlet} = \left(\frac{\rho V_f L}{\mu}\right)_{inlet} \qquad (A-4)$$

and

$$V_f = \sqrt{\frac{2(P_T - P_S)_{midspan}}{\rho}} \qquad (A-5)$$

$$L \quad = \quad \text{inlet reference length (1.25 ft)}$$

The coefficients C_1 and C_2 were evaluated by rewriting Equation A-2 as follows

$$\log_{10}\left(A_B/A_C\right) = \log_{10}(c_1) + c_2 \log_{10}\left(Re_{inlet}\right) \qquad (A-6)$$

In this $\log_{10}$ form, the slope of a straight line least squares curve fit of the blockage data is the exponent, C_2. The coefficient C_1 is given by ten raised to the y-intercept value of the linear curve fit. The $\log_{10}$ presentation of the blockage data (as well as a standard presentation) appears in Figure 45.

The orifice plate calibration data indicates that a slight Reynold's Number dependence exists, i.e.

$$K = K_{theoretical} + K_{correction} \qquad (A-7)$$

where

$$K_{theoretical} = \alpha_i \frac{A_{op}}{A_c} \sqrt{1 - \left(\frac{A_{op}}{A_{duct}}\right)^2} \qquad (A-8)$$

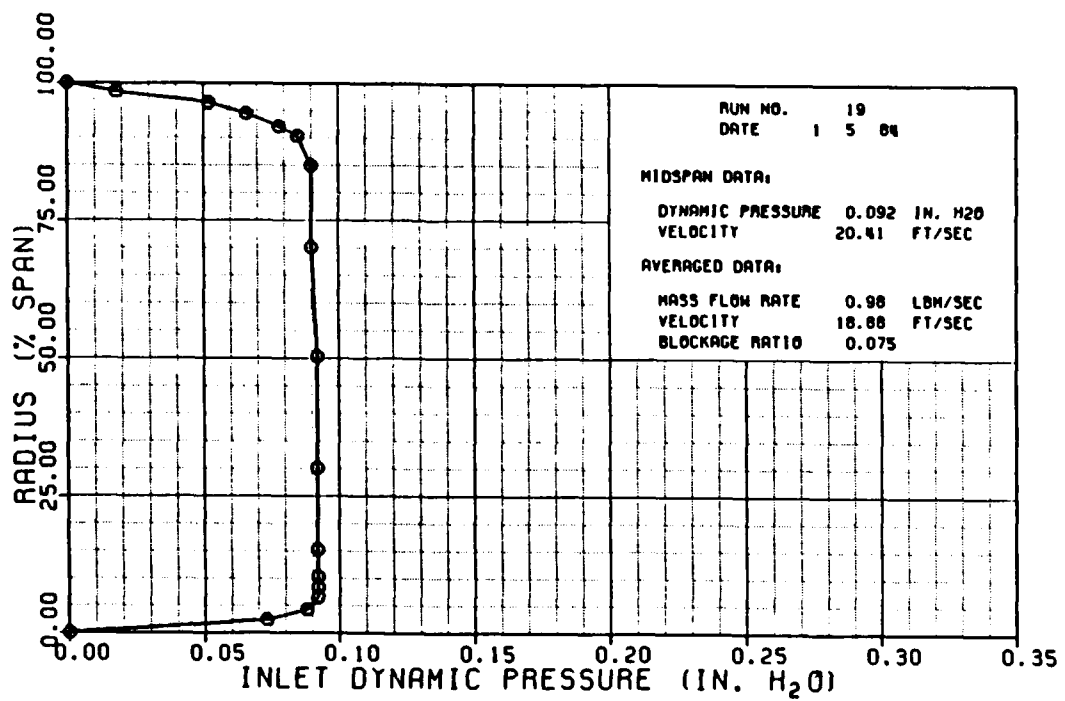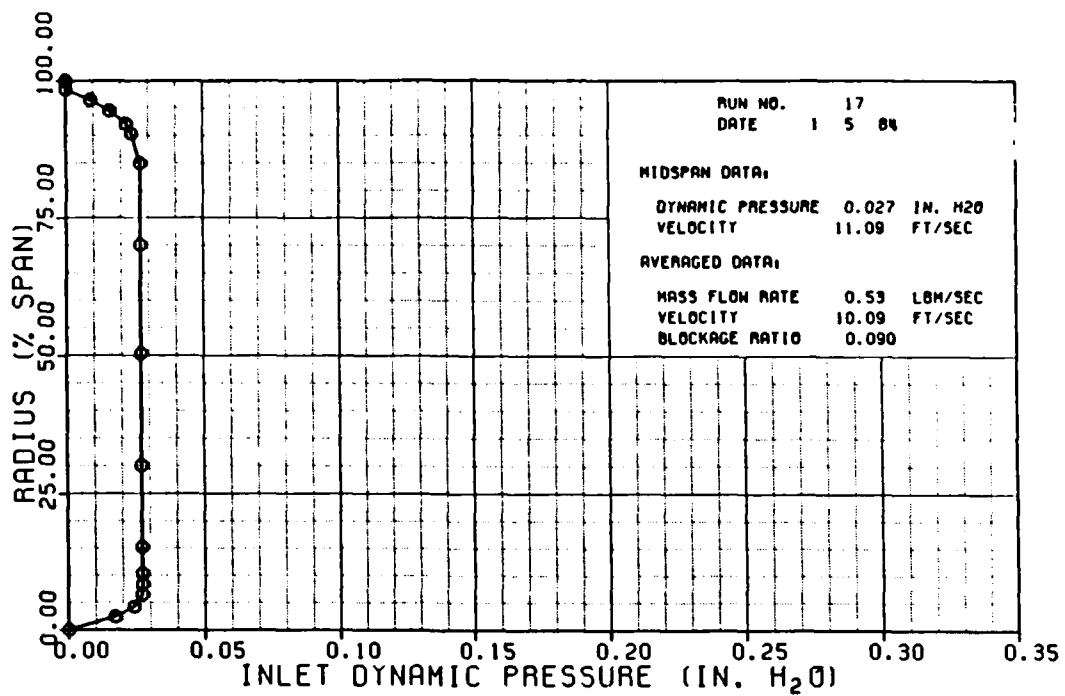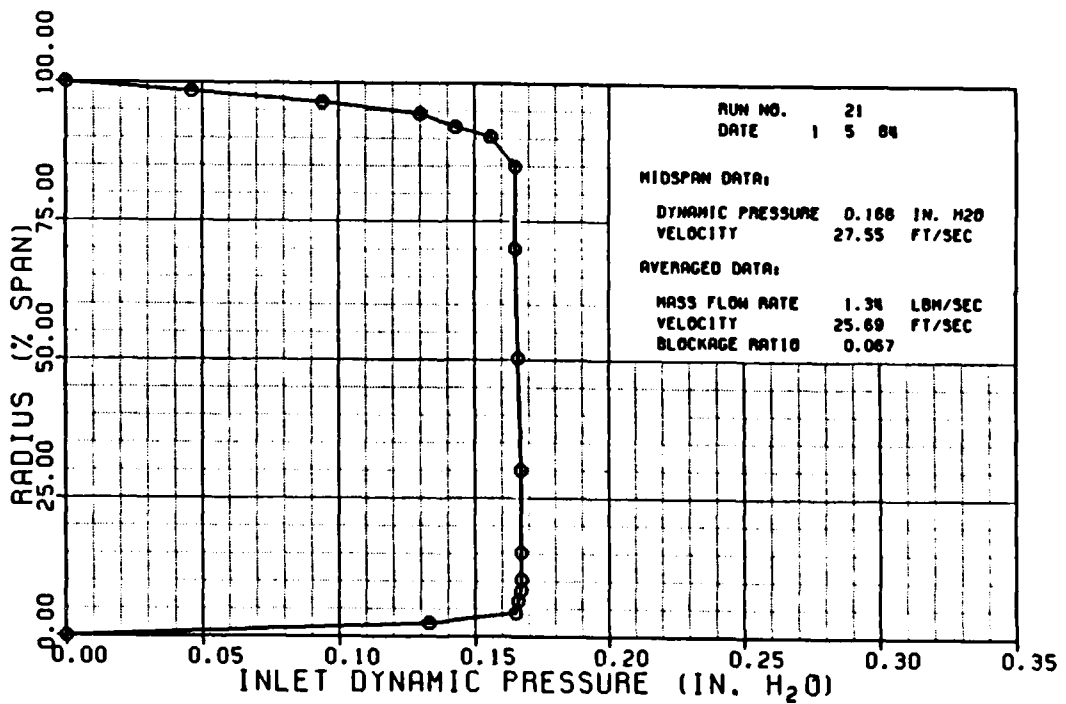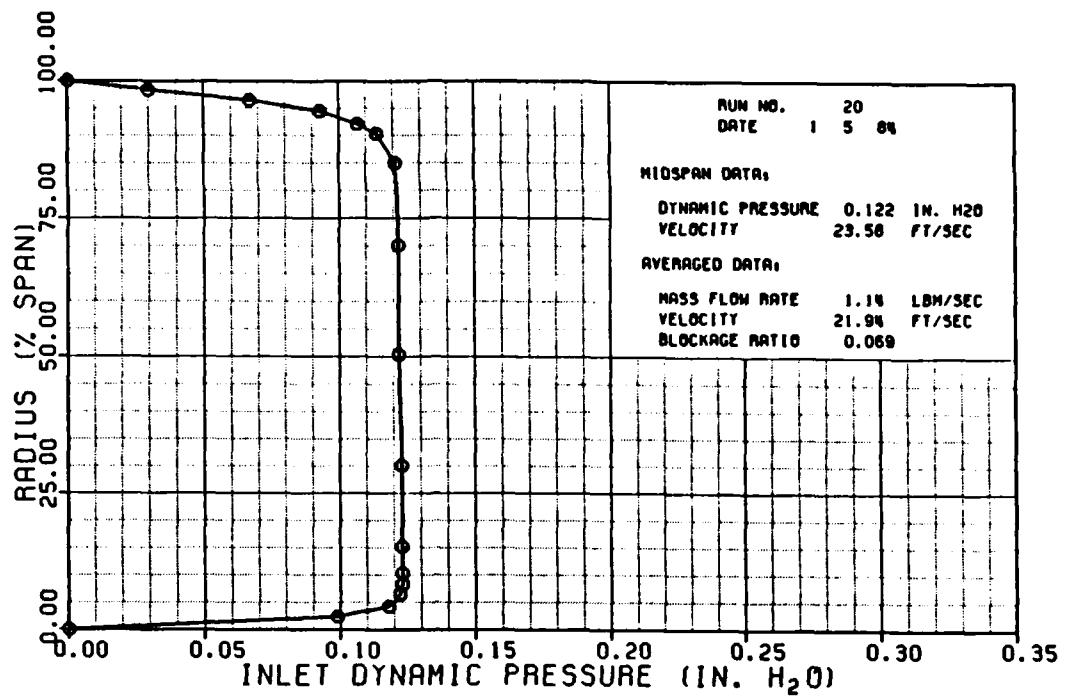$$K_{correction} = c_3 \left(R_{e\,op}\right)^{C_4} \qquad (A-9)$$

and α_i is the Reynold's Number invariant portion of the discharge coefficient given by Equation 4-2, A_{op} is the orifice area, A_{duct} is the crossectional area of the upstream ducting, and A_c is the compressor flow through area.

Substitution of Equation A-9 into A-7 and rearrangement yields

$$\log_{10}\left(K_{theoretical} - K\right) = \log_{10}\left(-c_3\right) + c_4 \log_{10}\left(R_{e\,op}\right) \qquad (A-10)$$

A linear least squares curve fit of the $\log_{10}$ form of the orifice plate calibration data yields the coefficents C_3 and C_4.

411

RUN NO. 17
DATE 1 5 84

MIDSPAN DATA:

DYNAMIC PRESSURE 0.027 IN. H2O
VELOCITY 11.09 FT/SEC

AVERAGED DATA:

MASS FLOW RATE 0.53 LBM/SEC
VELOCITY 10.09 FT/SEC
BLOCKAGE RATIO 0.090

RUN NO. 19
DATE 1 5 84

MIDSPAN DATA:

DYNAMIC PRESSURE 0.092 IN. H2O
VELOCITY 20.41 FT/SEC

AVERAGED DATA:

MASS FLOW RATE 0.98 LBM/SEC
VELOCITY 18.88 FT/SEC
BLOCKAGE RATIO 0.075

412

RUN NO.   20
DATE   1   5   84

MIDSPAN DATA:

DYNAMIC PRESSURE   0.122   IN. H2O
VELOCITY   23.58   FT/SEC

AVERAGED DATA:

MASS FLOW RATE   1.14   LBM/SEC
VELOCITY   21.94   FT/SEC
BLOCKAGE RATIO   0.069

RUN NO.   21
DATE   1   5   84

MIDSPAN DATA:

DYNAMIC PRESSURE   0.168   IN. H2O
VELOCITY   27.55   FT/SEC

AVERAGED DATA:

MASS FLOW RATE   1.34   LBM/SEC
VELOCITY   25.69   FT/SEC
BLOCKAGE RATIO   0.067

APPENDIX B

INSTRUMENTATION CALIBRATION DATA

Contents:

1) Scanivalve Pressure Transducer Calibration

2) Miniature Pressure Transducer Calibrations

 Base Calibration - S/N C257 (Static Probe)
           C260 (Static Probe)
           C258 (Total Probe)
           C259 (Total Probe)

 Pre-test and Post-test Calibration - S/N C260

3) Total Pressure Probe Directional Sensitivity Calibrations

      S/N C258
        C259

4) Amplifier Frequency Response (#1-#5)

5) Hot Wire Sensor Velocity Magnitude Calibrations

 Sensor 1 - 45° inclination
 Sensor 3 - 22.5° inclination

6) Hot Wire Sensor Directional Sensitivity Calibrations

7) Hot Wire Sensor Directional Sensitivity Coefficients

414

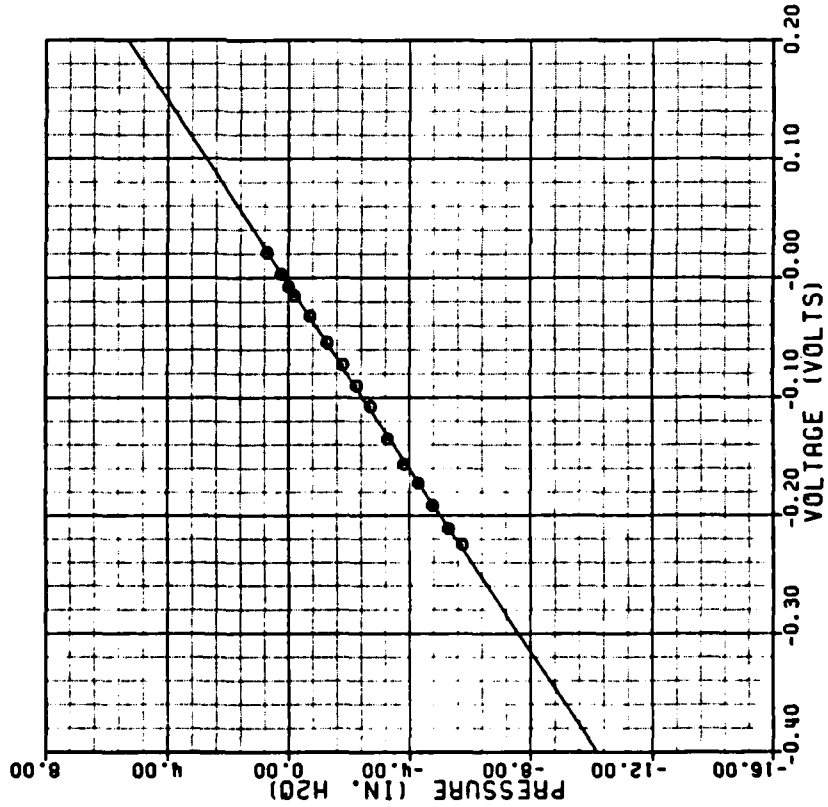# PRESSURE TRANSDUCER CALIBRATION

SCANIVALVE

DATE: 9 /3 /84

SLOPE	(IN. H20/VOLT)	27.755
Y-INTERCEPT	(IN. H20)	0.014
STD DEV	(IN. H20)	0.032
SENSITIVITY	(MV/IN. H20)	36.0

PRESSURE TRANSDUCER CALIBRATION

SERIAL NO.   C260

DATE: 10/27/84

SLOPE	(IN. H2O/VOLT)	22.259
Y-INTERCEPT	(IN. H2O)	0.045
STD DEV	(IN. H2O)	0.028
SENSITIVITY	(MV/IN. H2O)	44.9
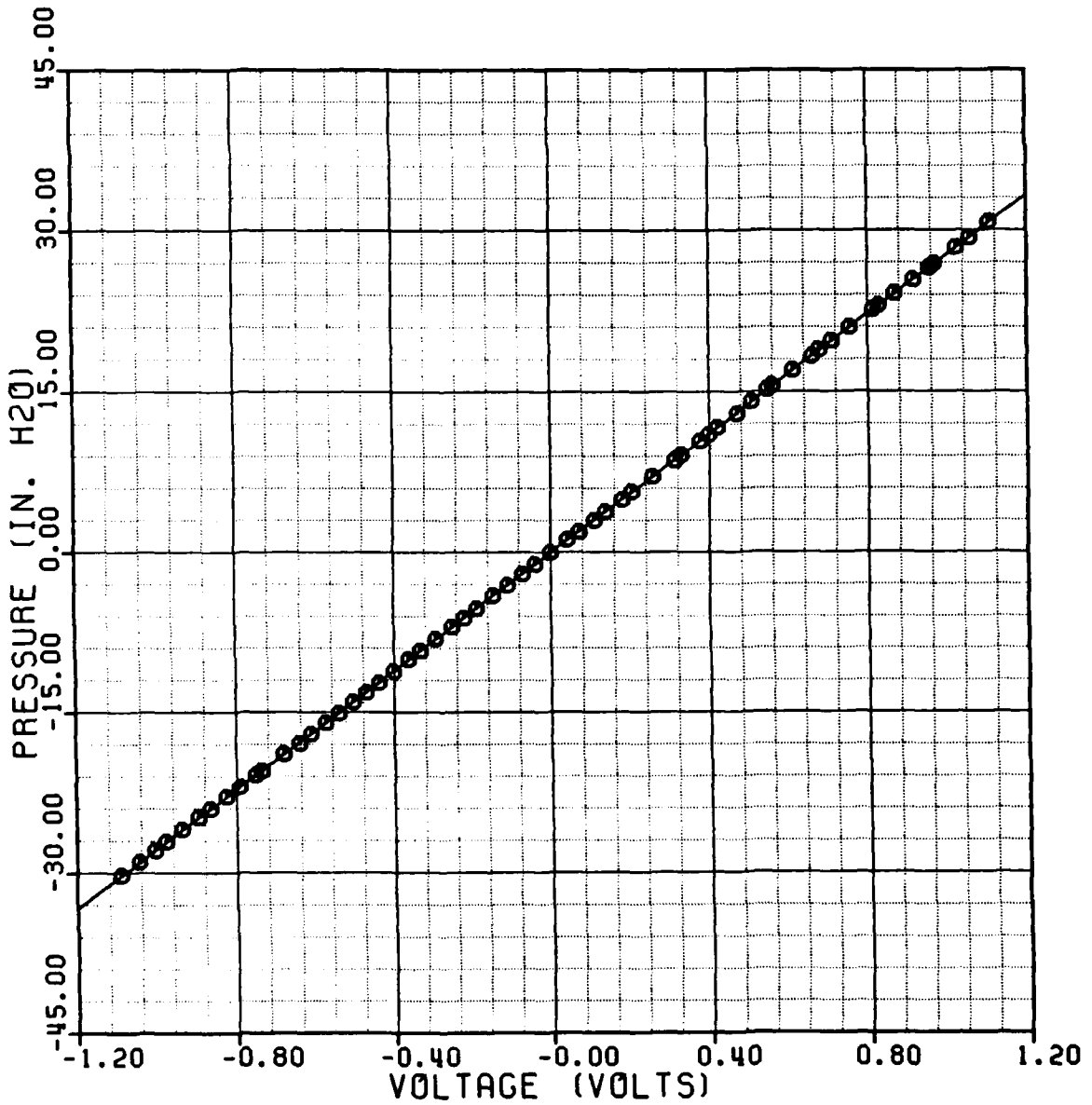
PRESSURE TRANSDUCER CALIBRATION

SERIAL NO.   C257

DATE: 10/27/84

SLOPE	(IN. H2O/VOLT)	25.848
Y-INTERCEPT	(IN. H2O)	0.158
STD DEV	(IN. H2O)	0.054
SENSITIVITY	(MV/IN. H2O)	38.7

416

PRESSURE TRANSDUCER CALIBRATION

SERIAL NO.   C259

DATE: 10/27/84

SLOPE	(IN. H2O/VOLT)	12.350
Y-INTERCEPT	(IN. H2O)	0.178
STD DEV	(IN. H2O)	0.034
SENSITIVITY	(MV/IN. H2O)	81.0
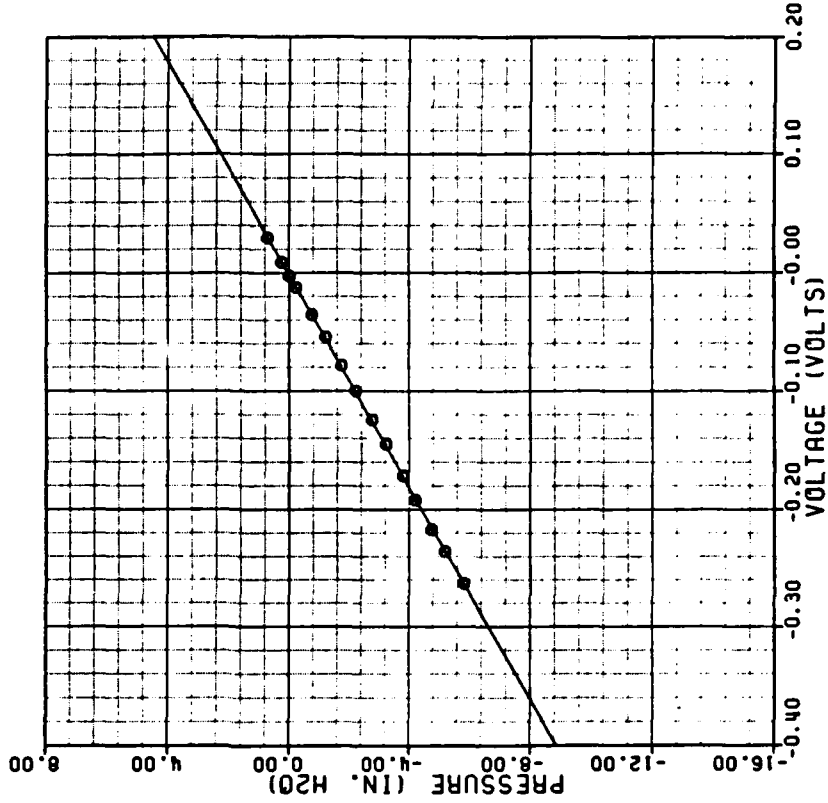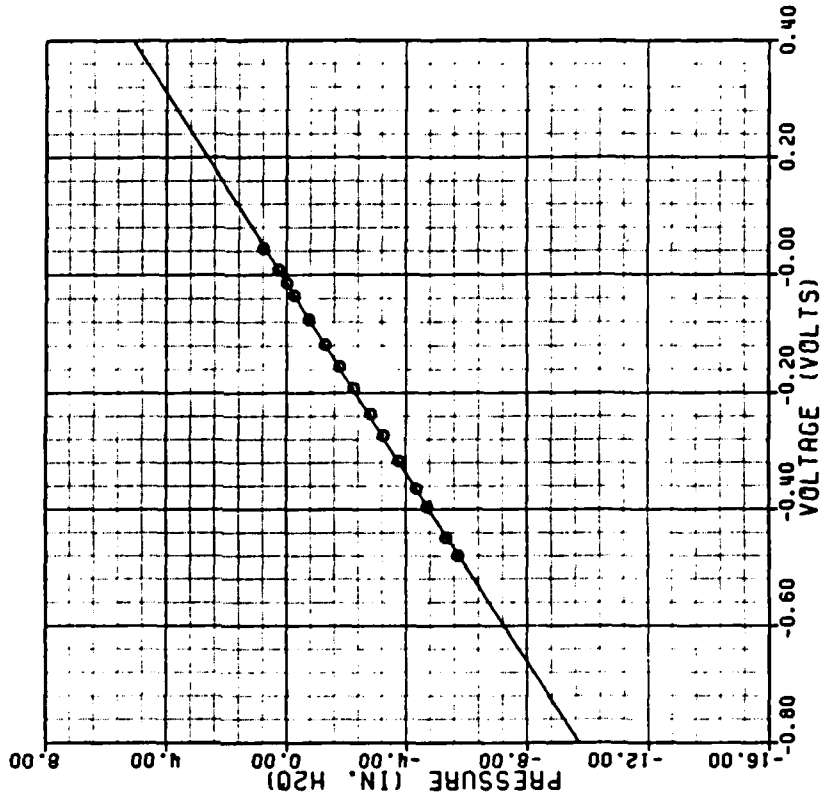
PRESSURE TRANSDUCER CALIBRATION

SERIAL NO.   C258

DATE: 10/27/84

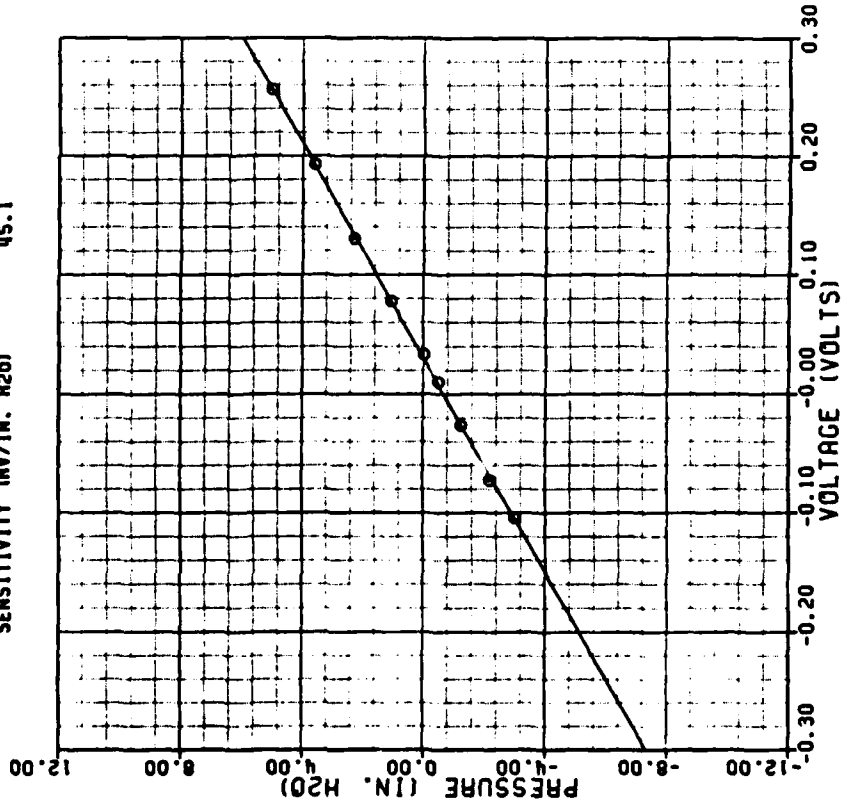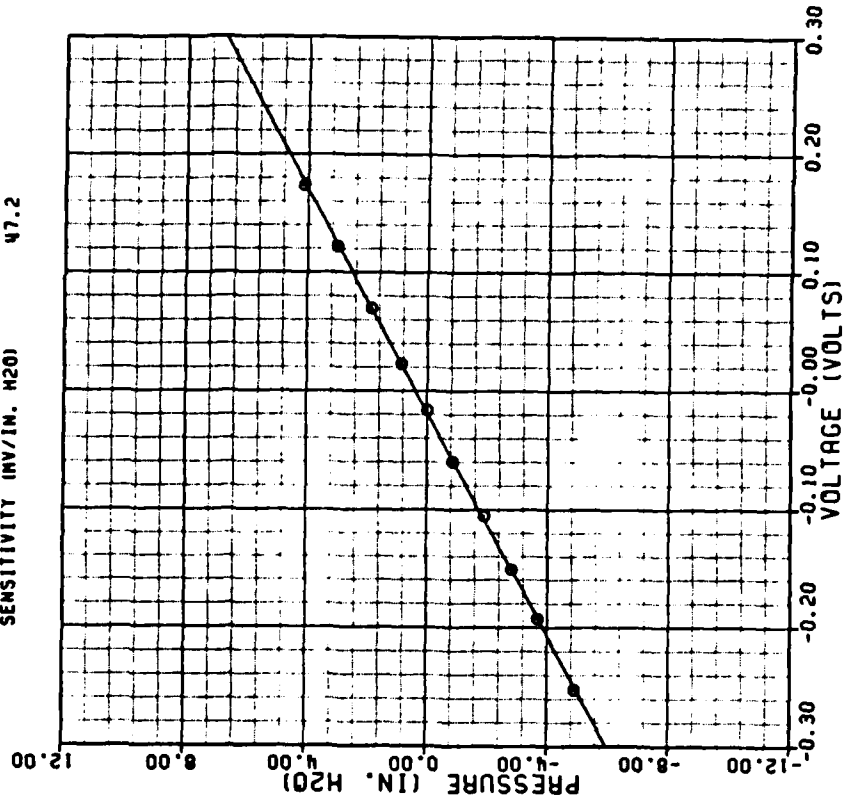|		
SLOPE	(IN. H2O/VOLT)	16.138
Y-INTERCEPT	(IN. H2O)	-0.033
STD DEV	(IN. H2O)	0.015
SENSITIVITY	(MV/IN. H2O)	62.0

417

PRESSURE TRANSDUCER CALIBRATION

TRANSDUCER SERIAL NO.   C260

AMPLIFIER NO.   3

DATE: 3 /29/85

TIME: 19:20

SLOPE   (IN. H2O/VOLT)   21.189
Y-INTERCEPT   (IN. H2O)   0.402
STD DEV   (IN. H2O)   0.042
SENSITIVITY   (MV/IN. H2O)   47.2

PRESSURE TRANSDUCER CALIBRATION

TRANSDUCER SERIAL NO.   C260
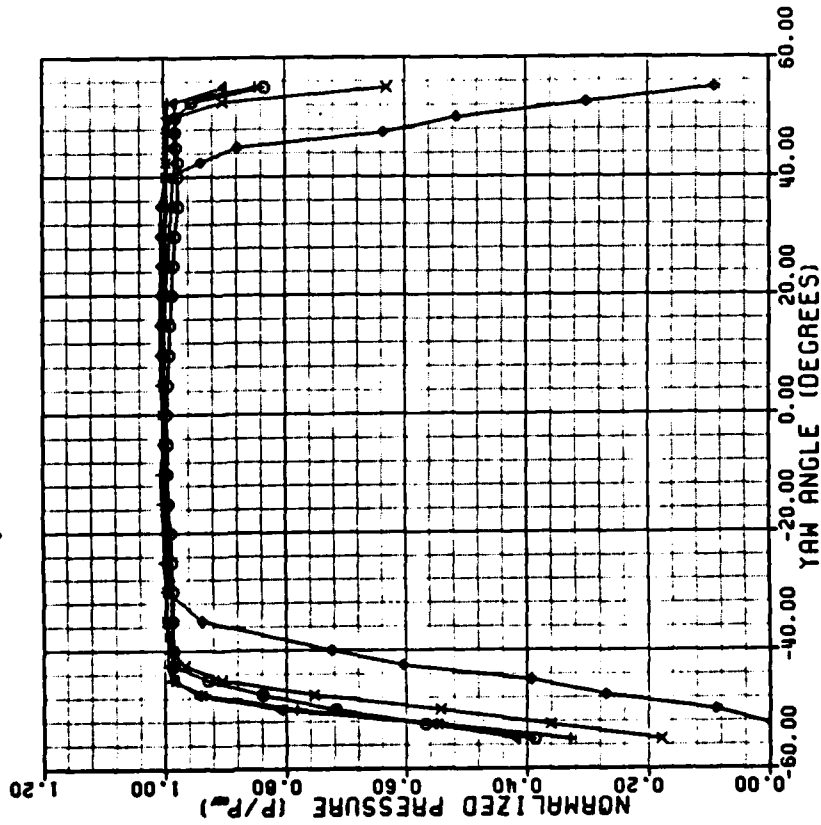
AMPLIFIER NO.   3

DATE: 3 /29/85

TIME: 16:43

SLOPE   (IN. H2O/VOLT)   22.187
Y-INTERCEPT   (IN. H2O)   -0.662
STD DEV   (IN. H2O)   0.053
SENSITIVITY   (MV/IN. H2O)   45.1

418

PROBE DIRECTIONAL SENSITIVITY

SERIAL NO. C258
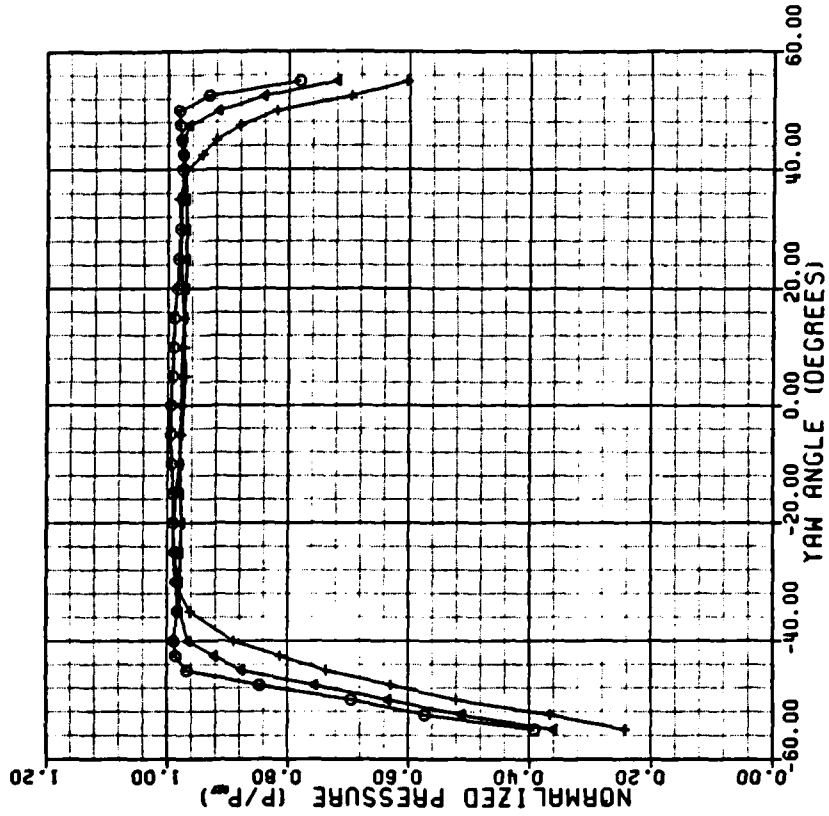DATE: 11/8/84
RUN NO. 2
P_∞ (IN. H20) 5.311

PITCH ANGLE LEGEND:

⊙	0.0	DEGREES
◄	-10.0	DEGREES
+	-20.0	DEGREES

PROBE DIRECTIONAL SENSITIVITY

SERIAL NO. C258
DATE: 11/8/84
RUN NO. 1
P_∞ (IN. H20) 5.330

PITCH ANGLE LEGEND:

⊙	0.0	DEGREES
◄	10.0	DEGREES
+	20.0	DEGREES
X	30.0	DEGREES
◆	40.0	DEGREES

419

PROBE DIRECTIONAL SENSITIVITY

SERIAL NO.   C259
DATE: 11/8 /84
RUN NO.   3
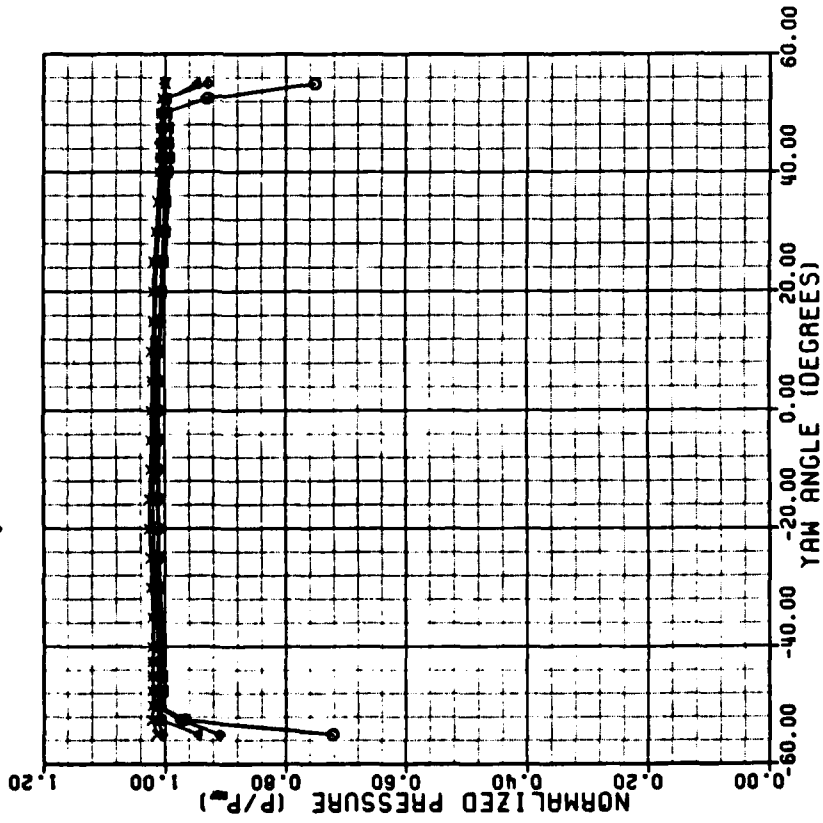P_{wr} (IN. H2O)   5.315

PITCH ANGLE LEGEND:

⊙   0.0   DEGREES
◢   -10.0   DEGREES
+   -20.0   DEGREES

PROBE DIRECTIONAL SENSITIVITY

SERIAL NO.   C259
DATE: 11/8 /84
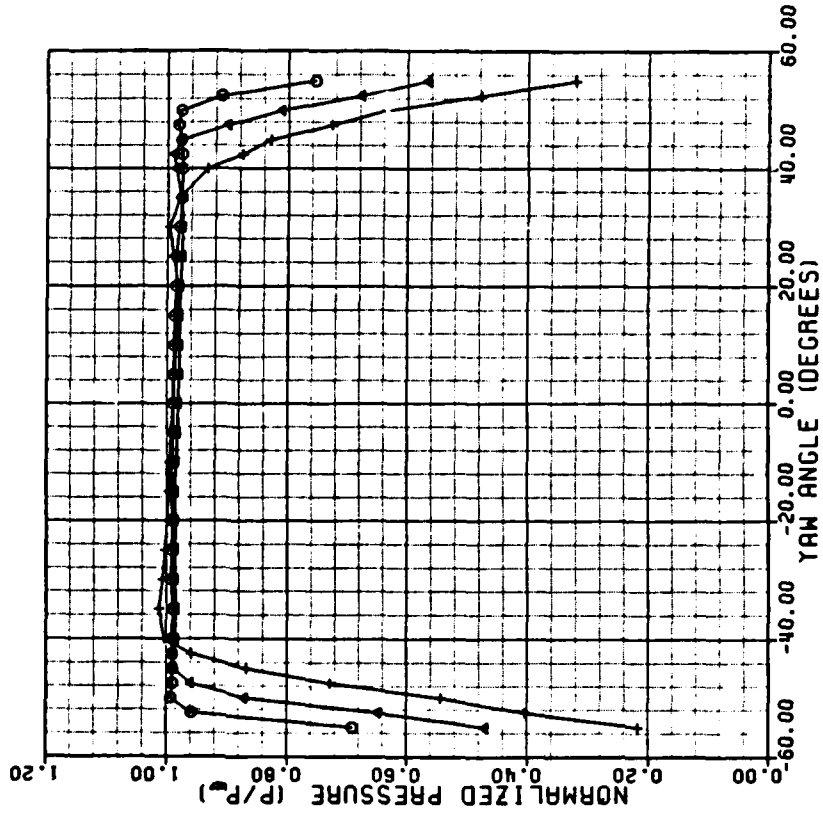RUN NO.   2
P_{wr} (IN. H2O)   5.323

PITCH ANGLE LEGEND:

⊙   0.0   DEGREES
◢   10.0   DEGREES
+   20.0   DEGREES
X   30.0   DEGREES
◆   40.0   DEGREES

420

AMPLIFIER FREQUENCY RESPONSE
AMPLIFIER NO. 2

CORNER FREQUENCY (HZ)   7177
REFERENCE GAIN   495

⊙ UNFILTERED OUTPUT
    DATE: 10/25/84

▣ FILTERED OUTPUT
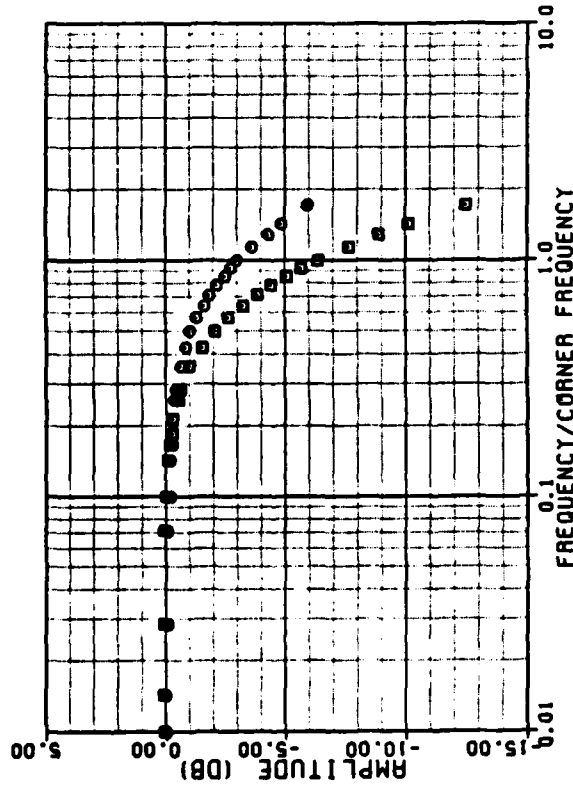   DATE: 10/25/84

AMPLIFIER FREQUENCY RESPONSE
AMPLIFIER NO. 1

CORNER FREQUENCY (HZ)   7040
REFERENCE GAIN   500

⊙ UNFILTERED OUTPUT
    DATE: 10/25/84

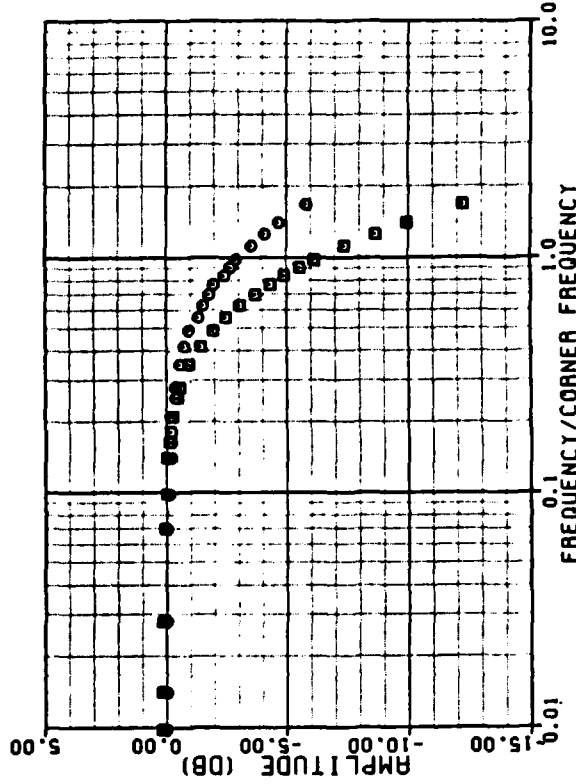▣ FILTERED OUTPUT
    DATE: 10/25/84

421

AMPLIFIER FREQUENCY RESPONSE
AMPLIFIER NO. 3

CORNER FREQUENCY (HZ)   6985
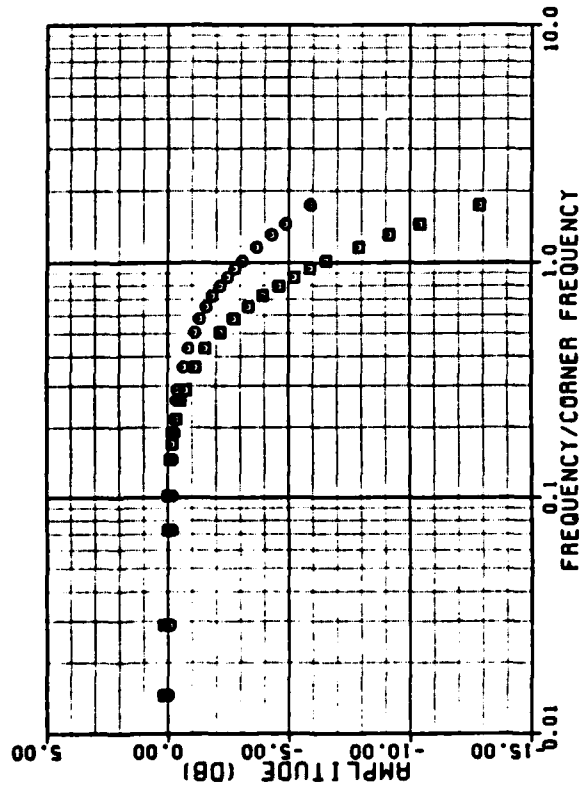REFERENCE GAIN   495

⊙   UNFILTERED OUTPUT
    DATE: 10/25/84

▣   FILTERED OUTPUT
    DATE: 10/25/84

AMPLIFIER FREQUENCY RESPONSE
AMPLIFIER NO. 3

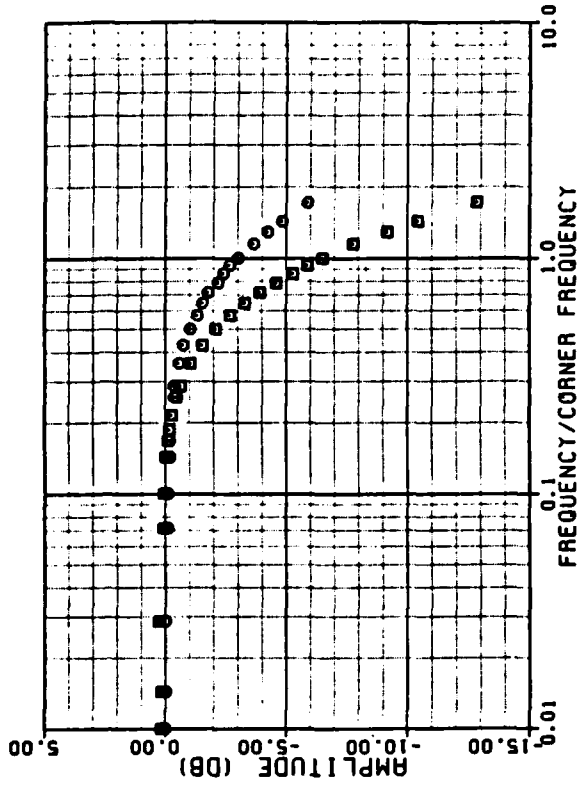CORNER FREQUENCY (HZ)   6917
REFERENCE GAIN   500

⊙   UNFILTERED OUTPUT
    DATE: 10/18/84

▣   FILTERED OUTPUT
    DATE: 10/18/84

422

AMPLIFIER FREQUENCY RESPONSE
AMPLIFIER NO. 5

AMPLIFIER FREQUENCY RESPONSE
AMPLIFIER NO. 4

423

SLANTED HOT WIRE
VELOCITY MAGNITUDE CALIBRATION

DATE: 2/12/85
SENSOR SERIAL NUMBER: 3
CALIBRATION TEMPERATURE: 79.0 DEG F

SECOND ORDER CURVE FIT
COEFFICIENTS

$$VELOCITY = A_0 + A_1 (VOLT) + A_2 (VOLT)^2$$

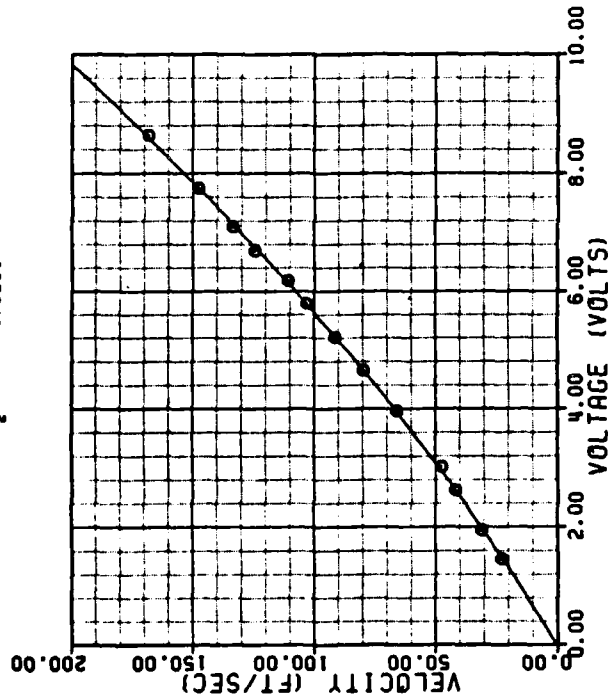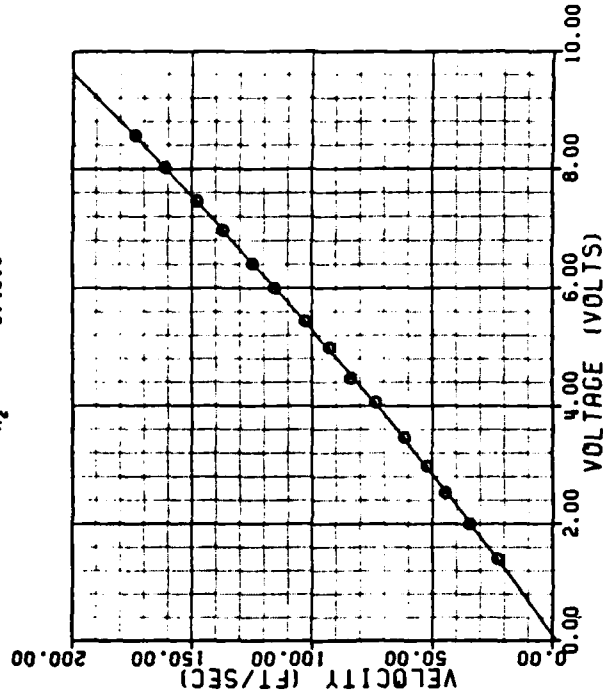$A_0 = -1.7380$
$A_1 = 17.1070$
$A_2 = 0.4016$

SLANTED HOT WIRE
VELOCITY MAGNITUDE CALIBRATION

DATE: 2/11/85
SENSOR SERIAL NUMBER: 1
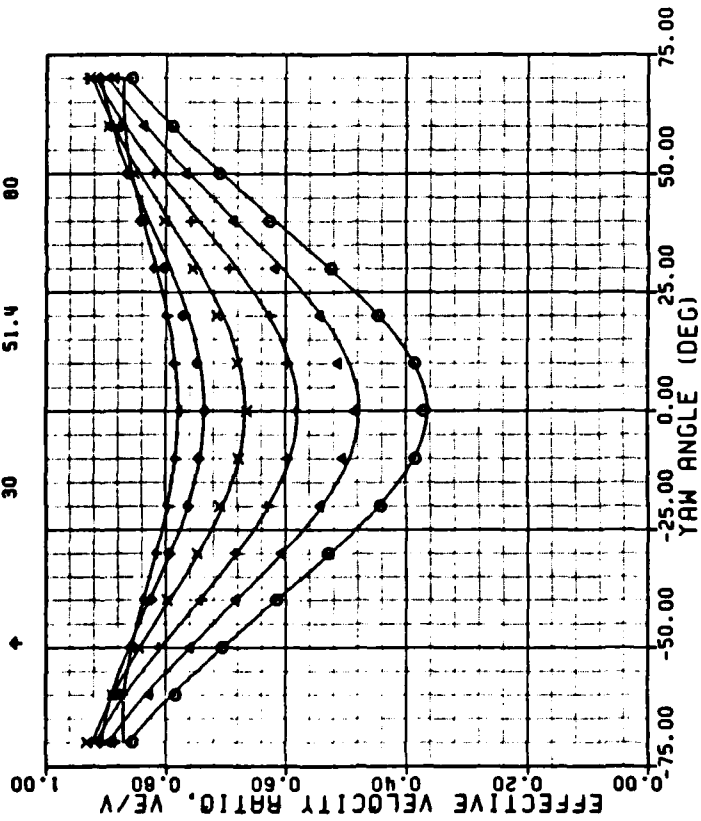CALIBRATION TEMPERATURE: 79.0 DEG F

SECOND ORDER CURVE FIT
COEFFICIENTS

$$VELOCITY = A_0 + A_1 (VOLT) + A_2 (VOLT)^2$$

$A_0 = 0.5402$
$A_1 = 14.1360$
$A_2 = 0.6251$

SLANTED HOT WIRE
DIRECTIONAL SENSITIVITY
CALIBRATION

DATE: 2/12/85
SENSOR SERIAL NUMBER: 3
AVG VELOCITY (FT/SEC):   51.9
AVG TEMPERATURE (DEG F):   79.6

SYMBOL	PITCH ANGLE (DEG TDC)	VELOCITY (FT/SEC)	TEMPERATURE (DEG F)
⊙	-10	51.3	79
◄	0	50.8	79
+	10	51.7	80
×	20	52.2	80
◆	30	53.3	80

EFFECTIVE VELOCITY RATIO, VE/V

YAW ANGLE (DEG)

SLANTED HOT WIRE
DIRECTIONAL SENSITIVITY
CALIBRATION

DATE: 2/11/85
SENSOR SERIAL NUMBER: 1
AVG VELOCITY (FT/SEC):   51.2
AVG TEMPERATURE (DEG F):   79.3

SYMBOL	PITCH ANGLE (DEG TDC)	VELOCITY (FT/SEC)	TEMPERATURE (DEG F)
⊙	-20	50.4	79
◄	-10	48.3	79
+	0	48.3	79
×	10	52.6	79
◆	20	55.9	80
✦	30	51.4	80

EFFECTIVE VELOCITY RATIO, VE/V

YAW ANGLE (DEG)

425

SLANTED HOT WIRE
DIRECTIONAL SENSITIVITY
CALIBRATION

DATE: 2/12/85
SENSOR SERIAL NUMBER: 3
AVG VELOCITY (FT/SEC): 101.3
AVG TEMPERATURE (DEG F): 79.4

SYMBOL	PITCH ANGLE (DEG TOC)	VELOCITY (FT/SEC)	TEMPERATURE (DEG F)
⊙	-10	99.9	79
▲	0	100.4	79
+	10	102.0	79
×	20	102.2	80
◇	30	102.1	80

SLANTED HOT WIRE
DIRECTIONAL SENSITIVITY
CALIBRATION

DATE: 2/11/85
SENSOR SERIAL NUMBER: 1
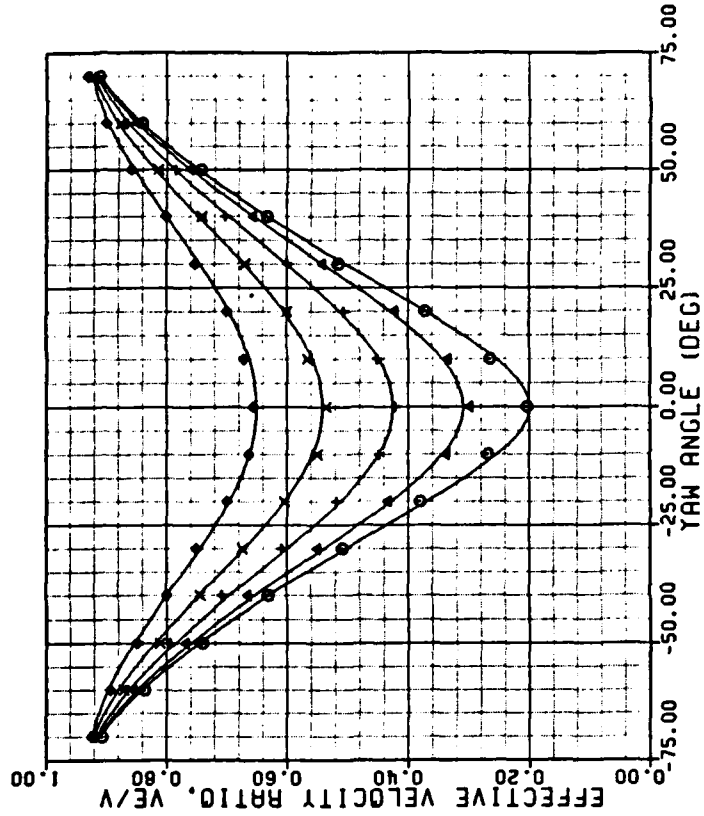AVG VELOCITY (FT/SEC): 100.3
AVG TEMPERATURE (DEG F): 79.2

SYMBOL	PITCH ANGLE (DEG TOC)	VELOCITY (FT/SEC)	TEMPERATURE (DEG F)
⊙	-20	101.2	79
▲	-10	97.7	79
+	0	98.3	79
×	10	99.7	79
◇	20	101.5	79
✦	30	103.6	80

426

SLANTED HOT WIRE
DIRECTIONAL SENSITIVITY
CALIBRATION

DATE: 2 /12/85
SENSOR SERIAL NUMBER: 3
AVG VELOCITY (FT/SEC):   149.0
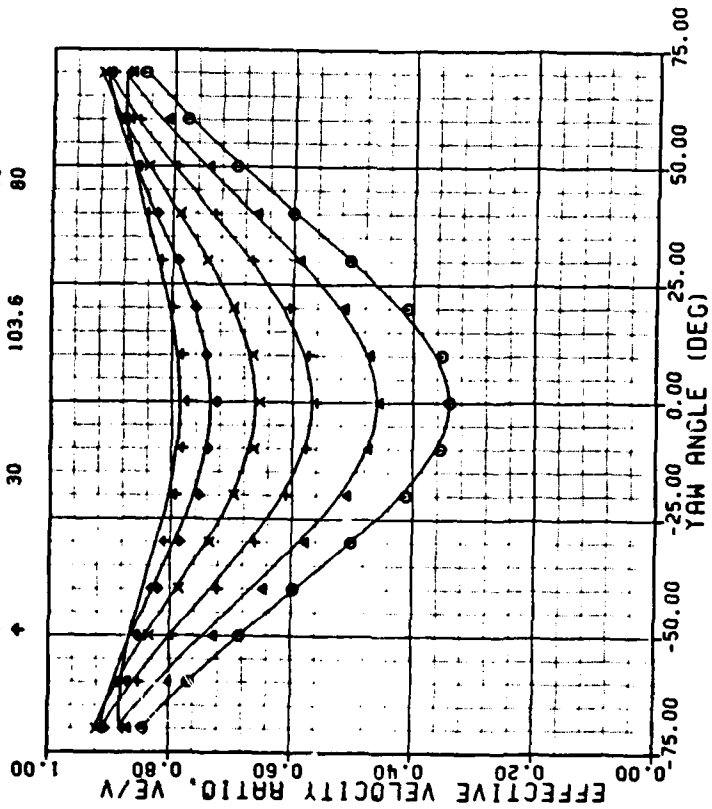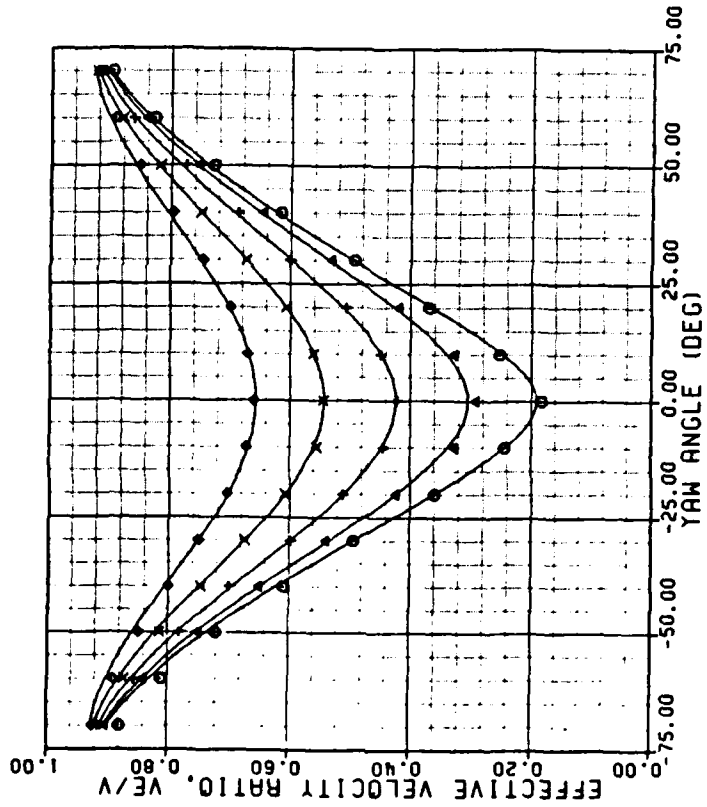AVG TEMPERATURE (DEG F):   79.4

SYMBOL	PITCH ANGLE (DEG TOC)	VELOCITY (FT/SEC)	TEMPERATURE (DEG F)
⊙	-10	149.1	79
◀	0	149.7	79
+	10	152.1	79
×	20	147.1	80
◇	30	147.1	80

SLANTED HOT WIRE
DIRECTIONAL SENSITIVITY
CALIBRATION

DATE: 2 /11/85
SENSOR SERIAL NUMBER: 1
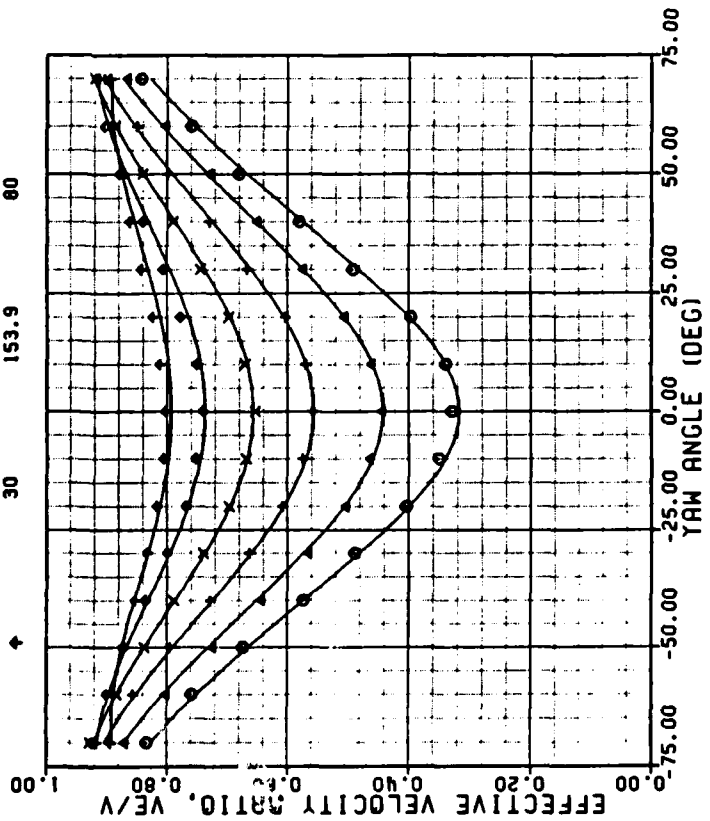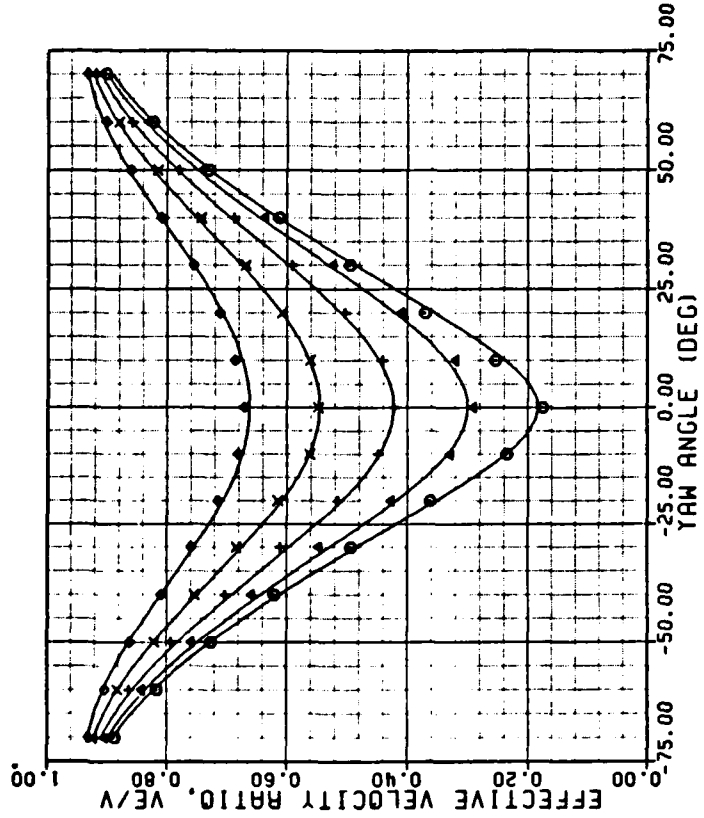AVG VELOCITY (FT/SEC):   149.9
AVG TEMPERATURE (DEG F):   79.2

SYMBOL	PITCH ANGLE (DEG TOC)	VELOCITY (FT/SEC)	TEMPERATURE (DEG F)
⊙	-20	151.3	79
◀	-10	148.7	79
+	0	150.3	79
×	10	146.7	79
◇	20	148.3	79
✦	30	153.9	80

427

HOT WIRE SENSOR

DIRECTIONAL SENSITIVITY COEFFICIENTS

	SENSOR #1 (45° inclination)	SENSOR #3 (22.5° inclination)
b_0	-0.18558E + 00	-0.80208E - 01
b_1	0.18182E - 01	0.17689E - 01
b_2	-0.85758E - 02	-0.76160E - 02
b_3	-0.37662E - 03	-0.76065E - 04
b_4	0.19117E - 04	0.16060E - 04
b_5	-0.39879E - 04	0.13058E - 05
b_6	0.66322E - 04	0.74768E - 04
b_7	0.32348E - 05	-0.74754E - 06
b_8	0.88284E - 05	0.78139E - 05
b_9	-0.87264E - 06	-0.95297E - 06

428

END

FILMED

12-85

DTIC